FRIEDRICH-SCHILLER-
UNIVERSITÄT
JENA Chemisch-Geowissenschaftliche
Fakultät

Uptake and intracellular fate of polymeric nanoparticles studied by light and electron microscopy –

from labeling strategies for polymers towards a correlative microscopy approach

Dissertation

(kumulativ)

Zur Erlangung des akademischen Grades

doctor rerum naturalium (Dr. rer. nat.)

Vorgelegt dem Rat der Chemisch-Geowissenschaftlichen Fakultät

der Friedrich-Schiller-Universität Jena

von Dipl.-Chem. Martin Reifarth,

geb. am 25.08.1986 in Nordhausen

Gutachter: 1. Prof. Dr. Ulrich S. Schubert, FSU Jena

2. Prof. Dr. Rainer Heintzmann, FSU Jena

Tag der öffentlichen Verteidigung: 21.11.2018

Dissertation, Friedrich-Schiller-Universität Jena, 2018

Table of Contents

Documentation of Authorship

This section contains a list about the individual authors' contribution to the publications reprinted in this thesis.

P1) M. Reifarth,[1] S. Hoeppener,[2] U. S. Schubert,[3] "Uptake and intracellular fate of engineered nanoparticles in mammalian cells: Capabilities and limitations of transmission electron microscopy—polymer-based nanoparticles", *Adv. Mater.* **2018**, *30*, 1703704.

	1	2	3
Development of the concept	x		
Preparation of the manuscript	x	x	
Correction of the manuscript			x
Supervision M. Reifarth		x	x
Proposed publication equivalents	0.5		

P2) M. Reifarth,[1] U. S. Schubert,[2] S. Hoeppener,[3] "Considerations for the uptake characteristic of inorganic nanoparticles into mammalian cells – Insights gained by TEM investigations", *Adv. Biosys.* **2018**, 1700254.

	1	2	3
Development of the concept	x		
Preparation of the manuscript	x		x
Correction of the manuscript		x	
Supervision M. Reifarth		x	x
Proposed publication equivalents	0.5		

P3) M. Reifarth,[1] W. Mueller,[2] B. Shkodra-Pula,[3] H. Goerls,[4] U. S. Schubert,[5] R. Heintzmann,[6] S. Hoeppener,[7] "Electron density of polymeric nanoparticles determined by image processing of transmission electron micrographs: Insights into heavy metal staining processes", *Part. Part. Syst. Charact.* 2019, *36*, 1800324.

	1	2	3	4	5	6	7
Development of the concept	x						x
TEM data acquisiton	x						
Preparation of the Os complex	x						
Development and improvement of the algorithm		x				x	
Preparation of the PLGA nanoparticles			x				
Performance of X-ray crystal structure analysis				x			
Preparation of the manuscript	x						x
Correction of the manuscript		x	x	x	x	x	
Supervision M. Reifarth					x	x	x
Proposed publication equivalents	1.0						

P4) M. Reifarth,[1] D. Pretzel,[2] S. Schubert,[3] C. Weber,[4] R. Heintzmann,[5] S. Hoeppener,[6] U. S. Schubert,[7] "Cellular uptake of PLA nanoparticles studied by light and electron microscopy: synthesis, characterization and biocompatibility studies using an iridium(III) complex as correlative label", *Chem. Commun.* **2016**, *52*, 4361-4364.

	1	2	3	4	5	6	7
Development of the concept	x						
Synthesis and characterization of the metal complex and polymers	x						
Synthesis and characterization of the nanoparticles			x				
Toxicity tests, uptake tests		x					
Preparation of cell samples for TEM/SIM investigations	x	x					
TEM and SIM imaging	x					x	
Supervision of polymer synthesis				x			
Preparation of the manuscript	x						
Correction of the manuscript		x	x	x	x	x	x
Supervision M. Reifarth					x	x	x
Proposed publication equivalents	1.0						

P5) T. Bus,[1] C. Englert,[2] M. Reifarth,[3] P. Borchers,[4] M. Hartlieb,[5] A. Vollrath,[6] S. Hoeppener,[7] A. Traeger,[8] U. S. Schubert[9] "3rd generation poly(ethylene imine)s for gene delivery", *J. Mater. Chem. B* **2017**, *5*, 1258-1274.

	1	2	3	4	5	6	7	8	9
Development of the concept	x	x			x	x		x	
Polymer and material synthesis		x							
Polymer and material characterization		x		x					
Biological tests *in vitro*	x								
CLSM microscopy studies	x								
SIM and STEM microscopy studies			x						
Preparation of the manuscript	x	x							
Correction of the manuscript			x		x		x	x	x
Supervision M. Reifarth							x		x
Proposed publication equivalents	0.25								

Publication P5 has already/will be used in the PhD thesis of C. Englert as well as T. Bus.

P6) M. Reifarth,[1] E. Preußger,[2] R. Heintzmann,[3] U. S. Schubert,[4] S. Hoeppener,[5] "Metal–polymer hybrid nanoparticles for correlative high-resolution light and electron microscopy", *Part. Part. Syst. Charact.* **2017**, *34*, 1700180.

	1	2	3	4	5
Development of the concept	x				x
Synthesis and characterization of hybrid particles	x				
Cell cultivation, fluorescence staining		x			
Determination of particle toxicity and uptake behavior		x			
Microscopy investigations	x				
Preparation of the manuscript	x				x
Correction of the manuscript		x	x	x	
Supervision M. Reifarth			x	x	x
Proposed publication equivalents	1.0				

Erklärung zu den Eigenanteilen des Promovenden/der Promovendin sowie der weiteren Doktoranden/Doktorandinnen als Koautoren an den Publikationen und Zweitpublikationsrechten bei einer kumulativen Dissertation

Für alle an dieser kumulativen Dissertation verwendeten Manuskripte liegen die notwendigen Genehmigungen der Verlage („Reprint permissions“) für die Zweitpublikation vor.

Die Koautoren der in dieser kumulativen Dissertation verwendeten Manuskripte sind sowohl über Nutzung als auch über die oben angegebenen Eigenanteile der weiteren Doktorandinnen/Doktoranden als Koautoren an den Publikationen und Zweitpublikationsrechten bei einer kumulativen Dissertation informiert und stimmen dem zu.

Die Anteile des Promovenden sowie der weiteren Doktoranden/Doktorandinnen als Koautoren an den Publikationen und Zweitpublikationsrechten bei einer kumulativen Dissertation sind in der Anlage aufgeführt („Documentation of Authorship“).

Martin Reifarth, Jena, den _____

Ich bin mit der Abfassung der Dissertation als publikationsbasiert, d.h. kumulativ, einverstanden und bestätige die vorstehenden Angaben. Eine entsprechend begründete Befürwortung mit Angabe des wissenschaftlichen Anteils des Doktoranden an den verwendeten Publikationen werde ich parallel an den Rat der Fakultät der Chemisch-Geowissenschaftlichen Fakultät richten.

Prof. Dr. Ulrich S. Schubert Jena, den _____

1. Introduction

Our worldview is dominated by visual observations. The eye represents our most important sensory organ; however, its performance is limited so that many of nature's details would remain hidden to us, if we only relied on what we are directly able to see. It is not surprising that mankind has always been attracted to take a view on the world beyond our observational capabilities; may it be the world on the microscopic scale or the extraterrestrial space. These worlds eventually became accessible with the availability of improved optical lenses in the late 16th and the beginning of the 17th century, which emerged in the construction of optical devices.[1] As such, the construction of the first telescopes by Galileo Galilei[1] and the Dutch scientists H.M. and Z. Janssen[2] as well as the construction of microscopes and their first applications in biology driven by Hooke and van Leeuwenhoek[2, 3] set milestones in science and fueled our understanding of the world. Since then, microscopy techniques have developed into an outstanding investigation tool in materials and life sciences, supporting the investigations of structural details of materials[4-6] or biological specimens under static[7] and even dynamic[8-10] conditions on the micro- and nanometer range.

In this size range, there are objects in the sub-tissue-level of biological specimens, *i.e.* mammalian cells, with a size below 10 µm and subcellular compartments with sizes in the range of 10 nm up to a few microns. These investigation objects can be efficiently addressed by high-performance microscopy techniques. Furthermore, modern microscopy methods facilitate the examination of even smaller cellular components, such as proteins and antibodies, that possess sizes in the low nanometer range.[11-13] In order to illustrate size ratios of biological objects of interest of investigation, see Figure 1.1for visualization.[14]

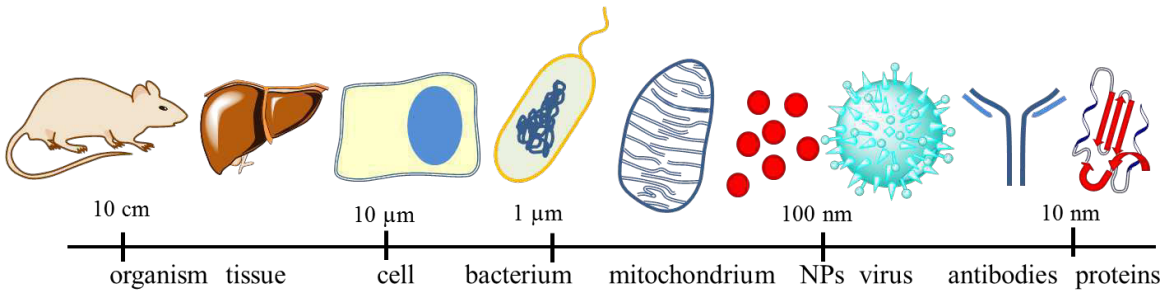

Figure 1.1: Sizes of cellular and subcellular investigation objects.

In this thesis, investigations of nanoscale objects, *i.e.* polymeric nanoparticles, within mammalian cells with strong focus on their uptake characteristics as well as their intracellular fate are addressed. These investigations are motivated by the growing interest for nanomaterials in (bio-)medicine during the last years, which is attributed to their manifold applications as therapeutic and diagnostic agents.[15-17] As the typical size of nanoparticle systems features a range from 10 to 1000 nm, nanoscale materials potentially show active interactions with the cells, which means, that nanoparticulate materials can be taken up and affected by the conditions present in the cellular interior. A fine-tuning of the nanoparticles' (NPs') properties enables their utilization as drug or gene delivery nanocarriers,[18-20] *i.e.* particle systems which are designed to be taken up into particular cell types in a targeted fashion, to facilitate a controlled release of pharmaceutically active compounds from the nanomaterials into the cellular interior. Novel developments in this area focus on the application of polymer-based nanomaterials. This is motivated by the potential biodegradability of some synthetic or natural polymers[21] and the manifold synthetic possibilities to introduce stimuli-responsive functional groups into these nanoparticle systems.[22-25] As a result, nanomaterials formed by tailor-made polymers represent eligible platforms for (stimulated) targeted drug-delivery. The development of novel nanomedical platforms requires a deeper elucidation of their mode-of-action on the cellular level. This includes a fundamental understanding of the particle uptake as well as their subsequent fate within the cells. These investigations are efficiently conducted, *e.g.* by flow cytometry,[26] which provides statistically valid data over a large number of uptake events. But also microscopy techniques represent adjuvant investigation tools, which can contribute useful information to the elucidation of the

particles' mode-of-action,[27, 28] since these approaches facilitate a direct visualization of the particles within the cellular environment.

In this thesis, namely the superresolution fluorescence technique of Structured Illumination Microscopy (SIM) and Transmission Electron Microscopy (TEM) were utilized to obtain peculiar insights into particle uptake, internalization as well as in the distribution/localization of NPs in the cellular framework. These studies were supplemented by confocal laser scanning microscopy (CLSM) investigations. This combination of different high resolution techniques was chosen, since each of these methods alone cannot provide a complete set of data, which unambiguously can answer questions on the localization and internal fate of nanoparticles in the cellular context. SIM and TEM represent to date techniques which provide the highest imaging resolution capabilities.

In order to justify the selection of these techniques, a deeper discussion of the performances of the individual techniques is required. In this context, the resolution of a microscope constitutes a basic parameter. Equation (1) describes the resolution of a microscope according to the Abbe criterion.

$$(1)\quad d = \frac{\lambda}{2\,NA}$$

with the wavelength of the utilized light λ and lens's numerical aperture NA.[‡] From this equation it becomes clear that the wavelength λ of the illumination source used in the microscopy experiments strictly dictates the resolution capabilities of the respective method.

In case of conventional light microscopy, the resolution is limited to ~ 200 nm in lateral direction and 500 to 700 nm in axial direction.[29] This means, in consequence, that light microscopy is in general inappropriate to investigate the morphology of NPs, which are typically < 250 nm for nanomedical applications, on the individual particle level. In order to achieve an enhanced resolution – *i.e.* a decreased value for the distance d according to equation (1) – there are in principle two strategies: (i) The application of high-NA optical devices, or (ii) the employment of short-wavelength radiation. The

[‡] The numerical aperture $NA = n \sin \alpha$ constitutes a dimensionless number which is calculated by the sine of the maximum opening angle α of the objective and the refractive index n of the environment in which the objective is working.

application of a high-NA objective can improve the image quality in light microscopy; however, the resolution of the system can only be improved to a limited extend, so that a resolution in the low nanometer range cannot be achieved.

There is a particular case of light microscopy, referred to as fluorescence microscopy, which relies on the selective accumulation of fluorophores (organic dyes or fluorescent proteins) in cellular organelles or the plasma membrane, respectively.[30-32] The selection of an appropriate combination of the excitation wavelength and filter sets facilitates the formation of high-quality microscopy images. With this method, it is even possible to obtain a resolution beyond Abbe's limit according to equation (1), if different experimental concepts are applied.[29, 33] A prominent example for such a superresolution microscopy technique is the aforementioned high-resolution method Structured Illumination Microscopy (SIM). This method is based on the projection of structured patterns with a targeted variation of phase and rotation properties onto the sample as well as the acquisition of a set of resulting fluorescence images. Sophisticated image processing algorithms enable the reconstruction of an image with improved resolution.[34] Although this method provides a resolution of ~ 100 nm in lateral direction (and approx. 250 nm in axial direction),[29] its resolution capabilities are still not sufficient to address individual particles.

This size range is easily addressed by Transmission Electron Microscopy (TEM), which represents a technique utilizing propagating electrons instead of visible light, since propagating electrons possess a wavelength in the picometer range. Thereby, the employment of an electron beam can significantly enhance the imaging performance, as the wavelength λ determines the resolution capability of a microscope as evidenced by Abbe's formula (1).[35] The first experimental attempts resulting in the development of TEM were conducted by Ruska and Knoll[36] who adapted concepts known from light optics to electron waves. Even though the first innovations in this field were driven by physicists and engineers, biologists became soon interested in the capabilities of electron microscopy imaging techniques. Initial work was conducted by Marton *et al.* already in 1935 who showed EM images of tissue sections.[37] Although the performance of EM was inferior to the well-established light microscopy at this stage, the development of sophisticated sample preparation methods boosted the

performance of electron microscopy for biological applications only in the early 1950s.[7] Since then, EM has developed into an outstanding technique in cell biology, providing knowledge about the ultrastructural details of the subcellular compartments and of cell structures. Fueled by optimized sample preparation protocols as well as a sustained improvement of instrumentation, EM high-resolution studies gained continuously increasing importance over the last decades.[7, 38-40]

In addition to the resolution capabilities of the microscopic technique, the performance of an imaging method is characterized by the possibility to introduce suitable labels into the sample in order to obtain a sufficient contrast in the resulting images. Considering the aim of this thesis to study nanoparticle-cell interactions, ideally the particulate systems are supposed to be identified unambiguously within the cellular environment. Simultaneously, cellular features need to be highlighted selectively, so that the particle localization and, with that, the intracellular particle fate can be discussed with respect to the role of subcellular compartments. In this regard, fluorescence microscopy exhibits the crucial benefit that an appropriate labeling strategy enables the direct assignment of the respective fluorescent signals in the resulting image to desired intracellular structures.[30-32] Moreover, the incorporation of fluorophores into the polymer material facilitates a labeling of the nanoparticles, which allows their distinct identification in the cellular environment.[41]

In TEM, the sample contrast is provided by the presence of electron-dense features, *e.g.* heavy atoms, within the sample.[7] Biological specimens possess an intrinsically low electron density owing to light elements being present in biological specimens. This contrast of selected cellular components can be sufficiently enhanced by the treatment of the sample with reactive heavy metal staining agents, which accumulate in a selective fashion in the cellular constituents, whereby ultrastructural features, *i.e.* organelles and membranes, can be imaged with a high contrast.[7] A thorough investigation of the cellular membrane morphology in response to the particle incubation, for instance, allows for the elucidation of the particle uptake mechanism and the investigation of their intracellular localization and fate. Particle internalization is often associated with active, *i.e.* energy-dependent, membrane processes. For instance macropinocytosis, phagocytosis, caveolin-dependent or clathrin-dependent uptake processes are associated with the formation of membrane invaginations or protrusions,

respectively,[42-46] which can be identified in TEM images (a more detailed discussion about these internalization processes can be found in Chapter 2). Furthermore, particle association to organelles as, for instance, intracellular vesicles, mitochondria, or the nucleus can be assessed. As a drawback of this method, the tedious sample preparation protocol and the incompatibility with live cell imaging has to be mentioned.[47] The main disadvantage, however, is the lack of contrast of polymeric nanomaterials in biological systems. Polymeric nanoparticles possess a similar electron density as their biological surrounding and generally do not show appropriate labeling levels.[48] Consequently, they cannot always be unambiguously identified within the cellular context. It will, thus, be a central task in this thesis to identify reliable strategies to label different polymeric NPs selectively to improve their contrast in TEM imaging.

Advantages and drawbacks of SIM and TEM are summarized in Figure 1.2. It can clearly be concluded that both fluorescence as well as TEM complement each other in a synergetic fashion. Thereby, the contrast features of fluorescence imaging can be utilized to unambiguously identify the localizations of the particles within the cellular structure and the resolution capabilities of TEM provide deeper insights into the particle fate. As a consequence, this thesis aims to develop a correlative approach to allow the investigation of the same cells with both techniques to obtain a set of complementary information, which reflect details of the particle uptake as well as on the localization of the nanoparticles within the cells. This approach, which is referred to as correlative light and electron microscopy (CLEM) critically depends on the design of suitable correlative dyes.

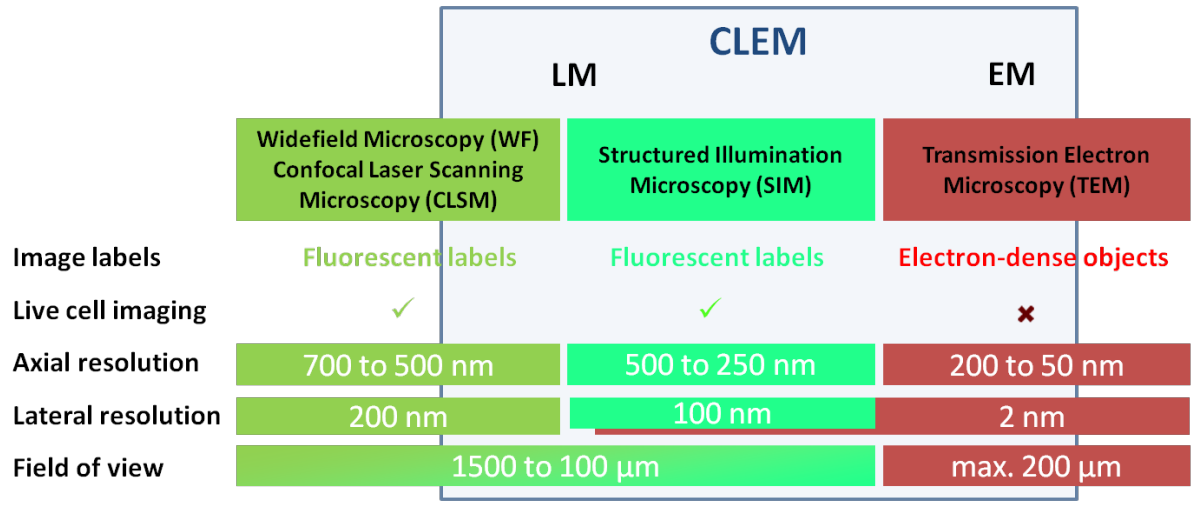

Figure 1.2: Comparison of fluorescence imaging techniques with transmission electron microscopy. From this overview, the advantages of a correlative approach become evident.

Consequently, this thesis is divided into four major parts. Chapter 2 will provide an overview about investigations which have been performed by TEM on the internalization of polymeric nanoparticles, thereby focusing on the uptake mechanism as well as of their localization in the cellular framework. In this context, also limitations and benefits of TEM for these studies will be highlighted. Furthermore, this chapter aims for providing a brief introduction into TEM sample preparation techniques, since sample preparation represents a key role in the experimental workflow of TEM investigations and, thus, also represents the bottleneck in the development of a correlative approach.

In Chapter 3 of the thesis, a strategy to assess the electron contrast of different polymeric nanomaterials on the basis of image analysis of TEM micrographs is presented. With that, also the response of polymer nanoparticles to standard heavy metals stains is evaluated. These studies provide a rough orientation of suitable polymer systems to be studied by TEM investigations. Additionally, a strategy was developed to increase the electron density of the polyester material poly(lactic acid), since polyesters represent materials which are usually not affected by conventional heavy metal staining. By using an iridium containing coordination compound which, furthermore, exhibits luminescent properties, a polymer dually labeled for TEM as well as for high-resolution fluorescence microscopy investigations could be synthesized. This correlative dual label represents a novel class of dyes and is well suited to introduce both, an enhanced electron density as well as a luminophore into a

polymer with pharmaceutical relevance. Here, the interdisciplinary character of this thesis becomes particularly obvious, since synthetic chemistry helped to address this persistent problem in microscopy.

In Chapter 4, uptake and intracellular fate of amino-rich polymers are investigated by means of TEM, whereby these materials represent structures which are generally well observable in TEM. These investigations have, furthermore, been complemented by (high-resolution) fluorescence imaging techniques. As an additional result, a protocol to achieve a correlation of both methods was developed and the advantage of this correlation approach was discussed. The workflow of this thesis is illustrated in Figure 1.3.

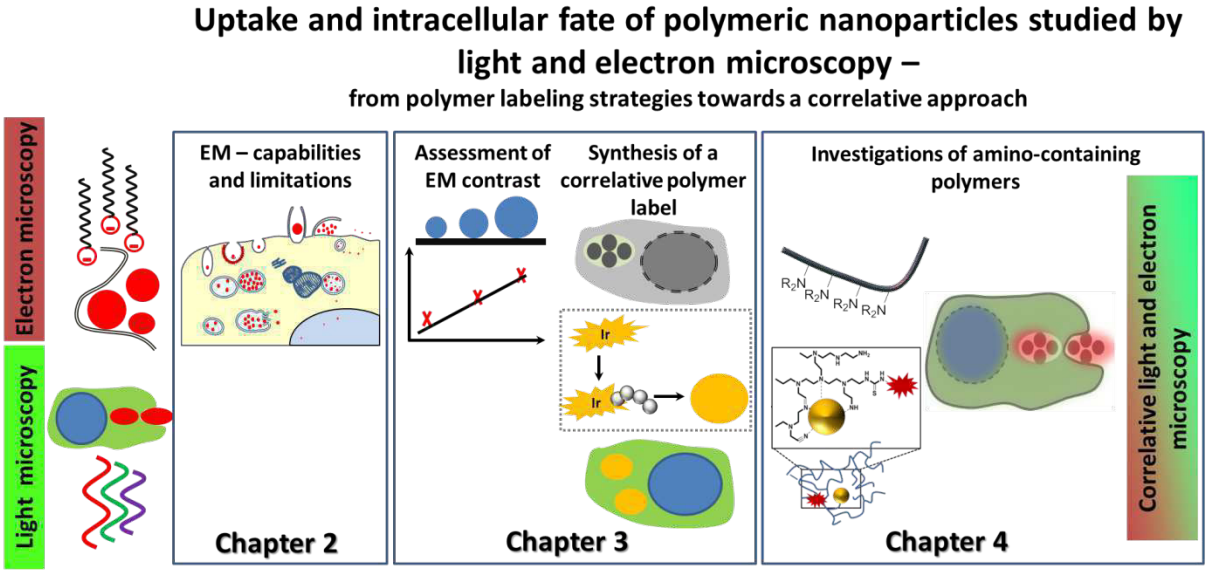

Figure 1.3: Schematic representation of the contents of this thesis.

In summary, this thesis discusses essential requirements to implement a comprehensive CLEM approach. Thereby, issues starting from the synthesis of a correlative dye, the quantification of electron contrast in TEM investigations up to the introduction of a correlative workflow to answer the question how nanoparticles are taken up and how they are processed by the cell are discussed.

2. Uptake of polymer-based nanoparticles studied by TEM: Capabilities, limitations, and experimental requirements

Parts of this chapter have been published: P1) M. Reifarth, S. Hoeppener, U. S. Schubert, *Adv. Mater.* **2018**, *30*, 1703704. P2) M. Reifarth, S. Hoeppener, U. S. Schubert, *Adv. Biosys.* **2018**, 1700254.

This chapter summarizes the state-of-the-art of imaging polymeric nanoparticles in mammalian cells by means of TEM. This method represents one of the main investigation tools used in this thesis; thus, major advantages and drawbacks for polymeric nanoscale objects in the cellular context are discussed. Electron microscopy of biological specimens relies on sophisticated sample preparation techniques which require experimental skills.[7] In order to investigate polymeric particles within the cellular context, the choice of the preparation protocol from a variety of possible procedures has to be carefully adjusted, since it might have a direct impact on the particle integrity. In addition, particular requirements also have to be taken into account if a correlation with fluorescence microscopy is supposed to be conducted on the same cellular feature. For this purpose, experimental challenges on the way to high-quality TEM images are discussed and summarized in this chapter.

2.1 On the experimental challenges of the preparation of biological specimens for transmission electron microscopy

Cell samples represent a demanding class of specimens to be analyzed by TEM. On the way towards obtaining a specimen that is compatible with TEM experimental conditions, several elaborate preparation steps are mandatory. An efficient preparation protocol includes in general (i) the preservation of the cellular ultrastructure close to its native state (fixation), (ii) sectioning of the

cellular samples in order to facilitate beam penetration, and (iii) the contrast amplification for ultrastructural features by improving their intrinsically weak electron contrast in the cellular environment (staining). During the preparation protocol, each individual preparation step has a severe impact of the quality of the EM sample.[7]

The classic preparation protocol initially requires effective sample fixation. Since the subsequent steps within the preparation protocol rely on the sample treatment with highly reactive chemicals, an efficient fixation is mandatory to preserve the sample's structure close to its native state. However, this also means that cell samples cannot be imaged in the living state. Sample fixation is classically performed with reactive aldehydes, *e.g.* glutaraldehyde, to achieve a crosslinking of the protein structures. Moreover, a sample treatment with the highly reactive compound osmium tetroxide (OsO_4) facilitates additional crosslinking with unsaturated lipids, which results in a fixation of double-layer membranes.[49]

As a prerequisite for TEM imaging, the samples must facilitate beam penetration. In order to access effective beam penetration, the sample has to be sliced down to ultrathin sections, *i.e.* sections with a thickness between 50 to 200 nm,[§] which is facilitated *e.g.* by embedding of the sample into a hard resin. This method requires infiltration of reactive monomeric compounds into the dehydrated cell samples which polymerize, *e.g.* triggered by elevated temperatures,[7] to form a three-dimensional polymer network incorporating the sample. The resulting resin block can, subsequently, be subjected to slicing owing to appropriate material properties, *i.e.* optimized stiff- and brittleness. Although these harsh preparation conditions seem to be invasive, resin-embedding constitutes a well-reproducible method and is, thus, widely applied. This approach was predominantly used in the experiments presented in this thesis by applying an Epon-based embedding strategy. Nevertheless, for addressing the issue to image polymeric nanoparticles within the cellular context, the suitability of this protocol must be considered carefully. Due to the hydrophobic conditions present in the cell during the monomer infiltrating step, the stability of the polymeric colloids, which can feature hydrophobic

[§] This is valid for conventional TEM approaches which are classically conducted under high-voltage conditions. There are EM approaches striving for imaging of thicker samples, however, at the expense of the image resolution.

properties themselves, might be limited.[50] Furthermore, the harsh reaction conditions during the curing process may alter the functionality of specific molecules present in the cell sample, *e.g.* fluorescent properties, which must be taken into consideration when the correlation of EM investigations with other techniques, such as the correlation with fluorescence microscopy, is in focus of investigations.

A rather mild preparation method is, for instance, introduced by sample vitrification instead of resin embedding, whereby the cell sample in its liquid state is exposed to liquefied gases (*i.e.* ethane or nitrogen) to form frozen water in a glassy state. Under these conditions, the formation of crystalline ice is prevented which could cause adverse effects on the cellular ultrastructure and result, *e.g.*, in membrane ruptures. The frozen samples provide a suitable hardness to allow ultrathin cryo-sectioning, followed by imaging of the frozen specimens (cryo-EM). However, this method requires careful sample handling to avoid undesired thawing (and with that the formation of ice crystals). Precedent infiltration of a cell sample with a sucrose solution as a cryo-protectant, nevertheless, enables thawing without affecting its integrity and, thus, handling the samples at room temperature. Due to the less-invasive character of this method, which is referred to as Tokyuyasu cryosectioning, it is also compatible with fluorescence imaging.[51] It has to be mentioned that there are additional methods available to achieve ultrathin sample sections which will not be discussed at this point. To obtain further insights into the variety of sample preparation techniques and their advantages and disadvantages with respect to the sample preservation, several comprehensive articles and book chapters exist.[7, 52-56]

Imaging of ultrathin samples alone would not provide high-quality images. This can be explained by the fact that a high contrast in a homogeneously thick sample is only achieved for a heterogeneous distribution of the electron densities of the sample, which is directly connected with the elements present in the biological specimen. Thereby, electron scattering depends on the atomic number Z, *i.e.* a strong contrast can be achieved for heavy atoms.[35] A biological sample, however, mostly consists of light elements with only a limited range of variations in atomic numbers (*i.e.* C, O, H, N, S) which provides only small differences in electron density. In order to significantly enhance the image contrast, an efficient preparation protocol includes the treatment of the sample with reactive heavy

metal species, which accumulate within the cellular structure in a selective fashion. As a result, ultrastructural cellular details, *i.e.* organelle and membrane features, are highlighted within a TEM micrograph.[7] Standard heavy metal staining includes the treatment with OsO_4 which can be considered as a contrast enhancement reagent additionally to its role as fixative, as well as uranyl acetate ($UO_2(OOCCH_3)_2$) and lead citrate ($Pb_3(C_6H_5O_7)_2$). The binding affinities as well as the resulting staining selectivity of the individual compounds will be discussed more in detail in Chapter 3. In Figure 2.1, the fundamental steps, necessary for the sample preparation of biological specimens for TEM, are summarized.

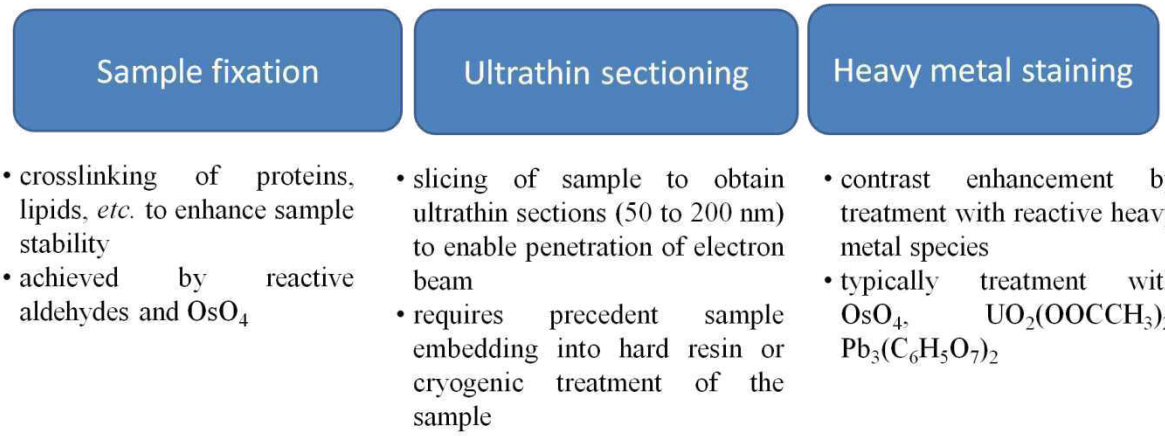

Figure 2.1: Schematic representation of the fundamental steps for preparing biological samples for TEM imaging. Sample preparation requires typically sample fixation, ultrathin sectioning and contrast enhancement by heavy metal staining.

To achieve a more pronounced sample contrast it is additionally possible to change the operational and, with that, the detection mode of the microscope. As previously mentioned, differences in the deflection angles of electrons propagating through the sample are a basic requirement for the image formation. In conventional TEM, electrons propagating through the specimen to be investigated are detected by the electron multiplying charge-coupled device (EMCCD) camera, which is placed in the direction of the electron beam (Figure 2.2A). Electron-lucent sample areas enable unimpeded beam penetration, which results in the image formation. As a result, less electron-dense sample areas are observable with high-intensity values in the image. On the other hand, dark image areas point towards electron-dense sample constituents which strongly affect the direction of propagating electrons. These

strongly deflected electrons are not able to reach the detector, and can additionally be suppressed by an aperture, which further increases the contrast of the resulting image.[7, 35]

Scanning transmission electron microscopy using a high-angle annular dark-field detection (HAADF-STEM) scheme represents an alternative operational mode of TEM. In this variation, the detector possesses a ring shape and is placed in such a way into the beam path that the unimpeded electrons are not detected. The highly scattered electrons, however, reach the annular detector and result in the image formation (Figure 2.2B). This method requires the point-wise scanning of the sample with a focused beam. In the formed image, bright areas represent electron-dense and, therefore, highly scattering sample areas (in the HAADF detection scheme only the highly scattered electrons are capable of reaching the detector) and dark areas representing electron-transparent samples. A major advantage of this mode is the strong dependence of the image contrast on Z, which results in an enhanced image contrast. However, this mode features a slightly reduced image resolution compared to conventional TEM.[35] Nevertheless, this method was frequently applied in the experiments conducted in this thesis to obtain highly contrasted EM images.

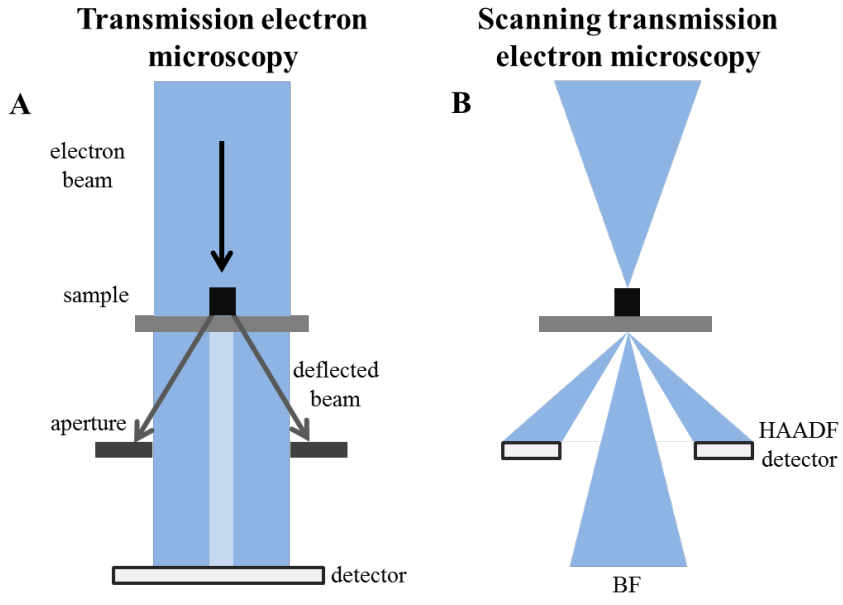

.

Figure 2.2: Comparison of the different operational modes transmission (A) and scanning transmission electron microscopy (B).

2.2 Nanoparticle-cell interactions studied by TEM: What is possible and what are the limitations?

Transmission electron microscopy represents an outstanding method to examine the interaction between nanoparticles and cells, *i.e.* mechanisms of particle uptake as well as the intracellular particle fate can be investigated. The strength of this method is attributed to the most outstanding features of TEM investigations, *i.e.* a resolution in the low-nanometer range as well as the visualization of intracellular, ultrastructural features such as membranes or organelles.

Cellular membranes represent important structures and their morphologies can be visualized efficiently by means of TEM. An approaching nano-object might induce alterations in the membrane structure from which valuable information about its subsequent uptake mechanism and intracellular localization can be concluded. Thereby, the mechanisms of cellular uptake are strongly related to different membrane appearances,[42, 43] which means, that that the mechanism of individual uptake events can be determined on the basis of electron micrographs. Particle uptake can be grouped into active, *i.e.* energy-dependent, as well as passive, *i.e.* diffusive, processes. Active processes include:

- Caveolin-dependent endocytosis: *Via* this mechanism, small particles are taken up. Caveolae represent small membrane invaginations which can efficiently be identified owing to their charactertistic flask-like shape. They participate in important cellular processes, *e.g.* singal transduction, protein endocytosis or cholesterol homeostasis.[44]
- Clathrin-mediated endocytosis (CME): CME is involved in intracellular signaling, membrane recycling, and the uptake of nutrients.[45] In TEM micrographs, this mechanism can be identified by the appearance of invaginations with a size of ~ 100 nm which are coated with the protein clathrin. Clathrin-coated pits can be identified due their characteristic morphological shapes (Figure 2.3). This mechanism is accountable for receptor-mediated endocytosis.[43]

- Clathrin-independent endocytosis: By this mechanism, *e.g.* many bacterial toxins and surface proteins are taken up.[46]
- Phagocytosis: This mechanism allows the uptake of significantly larger objects; however, this mechanism can only be observed in specialized cell types. Phagocytosis is accompanied by the formation of characteristic membrane protrusions (Figure 2.3).[43]
- Macropinocytosis: This mechanism represents an actin-driven endocytic process which enables the uptake of larger objects, such as aggregated particles. The particles taken up by means of macropinocytosis and are, subsequently, localized within large endosomes that contain a large amount of cellular fluids additionally to the particles. This mechanism is associated with the formation of membrane ruffles.[43]

Diffusion of particles through the membrane is possible for small particles. The particles internalized *via* passive mechanisms are found directly inside the cytosol and are not associated to intracellular vesicular structures. In Figure 2.3, a schematic representation of the membrane morphologies associated with different uptake mechanisms is shown. A more detailed discussion of cellular uptake can be found elsewhere.[42, 43]

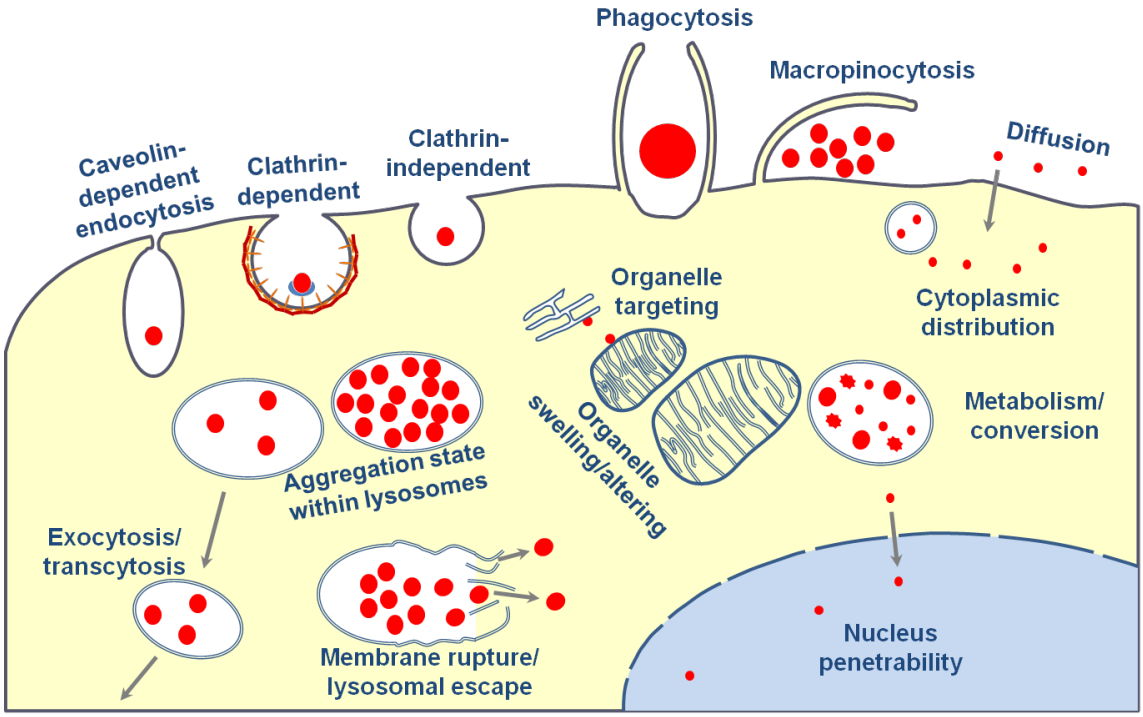

Figure 2.3: Schematic representation of different uptake mechanisms of cells with their characteristic alterations of the plasma membrane structure. TEM images provide, furthermore, insights into the intracellular localization as well as into the fate of the particles, *e.g.* their cytoplasmic distribution, the vesicular localization, the aggregation state within the lysosomes, organelle targeting, lysosomal escape, nucleus penetrability as well as particle conversion or metabolism among others. Reprinted with permission from ref. [48], copyright 2018, Wiley.

Additionally to the elucidation of uptake mechanisms by means of TEM investigations, TEM imaging can also provide useful information about the subsequent intracellular fate. For drug delivery applications, it is important to obtain information about a particle association with intracellular vesicles (*i.e.* endosomes or lysosomes) or their free distribution inside the cytosol, respectively. In TEM images, vesicular structures represent easily identifiable organelles owing to their electron-lucent character. Since double-layered membranes are well detectable in TEM images at a high resolution level, this method provides also access to, *e.g.* lysosomal membrane rupture, which represents a desired issue in the controlled release of substances.[57] Within the lysosomes it is furthermore possible to assess the aggregation state of the particles owing to the TEM resolution capability beyond the particle size. With that, also alterations in the particle morphology, *e.g.* introduced by intracellular degradation processes, become accessible.[58]

Particles which are freely distributed within the cytoplasm might address intracellular components.[58, 59] As an example, dysfunctional mitochondria are discussed to be involved into the development of numerous diseases; NP targeting of these organelles can boost the development of new nanomedical platforms.[60] Mitochondria are identified by their characteristic cristae, *i.e.* wrinkled double-layered membrane arrangements inside these organelles and can, thus, easily be identified by TEM imaging. Furthermore, the cellular nucleus represents an intracellular compartment, which is well distinguishable from the cytoplasm structure within the cellular environment. Since the nucleus hosts the cellular genetic information, nanoparticle penetration into the nucleus represents a subject of several investigations regarding, *e.g.* genotoxicity studies.[61, 62]

Nevertheless, also the drawbacks of TEM investigations on particle uptake have to be discussed. A major limitation of this method is based on the fact that electron microscopy is only possible for fixed cell samples and, hence, does not support live cell imaging.[47] Furthermore, limitations emerge from the limited field-of-view of this method. Even though TEM investigations can provide valuable information about the particle aggregation state and their association to different organelles and TEM can provide access to the exact particle number to the individual events, it has to be kept in mind that TEM images of ultrathin slices only represent a small volume of an entire cell. In order to draw conclusions from TEM micrographs with statistic validity, it is necessary to image numerous ultrathin sections and to develop an unbiased sampling method to obtain statistically valid data.[63-65] TEM *per se* is not a method which is suitable for high-throughput experimentation owing to the required sophisticated sample preparation as discussed in Chapter 2.1, so that the extraction of significantly valid data from TEM images remains a tedious and time-consuming task.

A summary of capabilities and limitations of TEM investigations to study uptake and intracellular fate of nanoparticles is summarized in Figure 2.4.

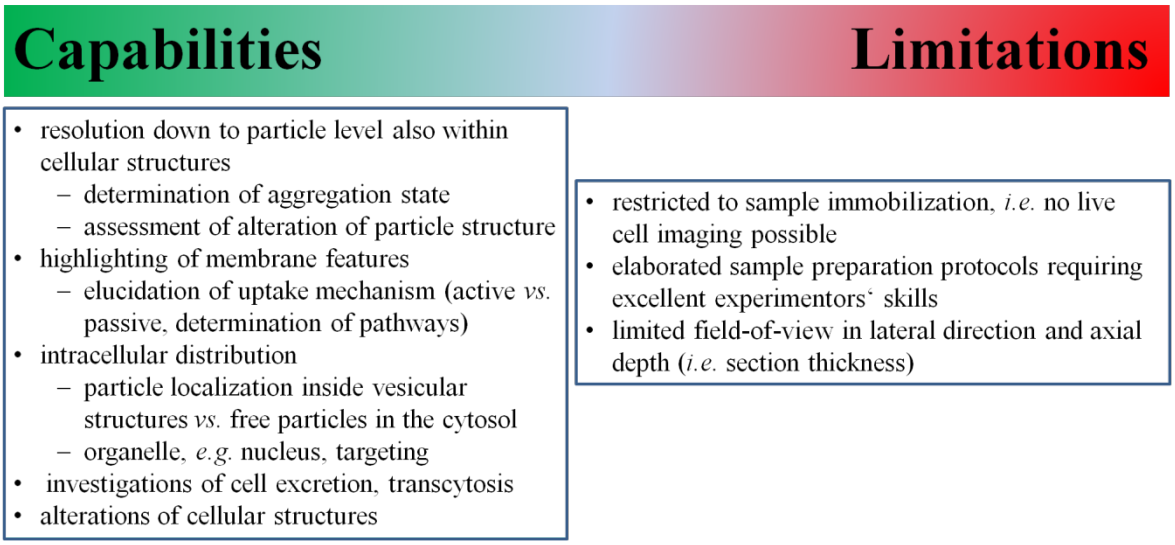

Figure 2.4: Summary of capabilities and limitations of TEM investigations for investigations of uptake and intracellular fate of nanoparticulate materials. Reprinted with permission from ref. [48], copyright 2018, Wiley.

2.3 Challenges for the observation polymer-based nanoparticles within cellular samples in TEM micrographs

Whereas inorganic nanoparticles, *i.e.* crystalline or amorphous (semi-)metal or (semi-)metal chalcogenide nanoscale materials, exhibit an inherently high electron density and represent easily identifiable objects in TEM micrographs of biological samples, the localization of polymeric nanomaterials constitutes a demanding task. Nevertheless, there are a few examples reported in literature in which the uptake of polymeric nanoparticles into cells could be observed. Lerch *et al.*, for instance, described the uptake of polystyrene (PS) beads into HeLa cells,[66] whereby the particles could be identified within intracellular vesicular structures, however, with only a poor TEM contrast. Similar contrast features for PS nanoparticles could be found in another study, in which their uptake into BMDM cells was observed.[67] PS beads represent structures that are stable towards the electron beam and seem to be unaffected by the harsh embedding conditions. On the contrary, polyesters such as polylactide (PLA) or poly(lactide-*co*-glycolide) (PLGA) were found to be severely affected under the electron beam. In a study conducted by Musyanovych *et al.*, the uptake of differently charged polylactide nanoparticles into HeLa cells was investigated.[68] In TEM micrographs, the authors found electron-lucent spots within vesicular structures which they identified as PLA nanoparticles. The authors thereby explained this observation by a degradation of the sensitive polymer material under the electron beam which results in the occurrence of electron-lucent areas. A further proof of the assumption that the electron-lucent spots correspond to the PLA nanomaterial was given by Barthel *et al.*.[69] In this study the authors decorated PLA particles with smaller electron-dense iron oxide particles. Within mesenchymal stem cells a clear association of the electron-lucent NPs with the electron-dense signals emerging from the nanocrystals could be obtained which served as TEM labels in this study proving the electron-lucent character of PLA particles. Likewise, electron-transparent structures could also be found for PLGA nanoparticles.[70, 71]

Whereas polyesters or polystyrene particles only contribute a low-electron contrast, polymeric nanostructures containing amino functionalities can efficiently be identified within TEM micrographs, since they possess a significantly enhanced electron density after straining.[72] This class of polymers is, if water-soluble, positively charged due to the basic properties of the amino functionalities. When exposed to negatively charged nucleic acids in aqueous solutions, these polymers are capable of forming polymeric complexes, *i.e.* polyplexes, owing to electrostatic interactions. Polyplexes are used for the transport of genetic material into the cells in order to transfect them. The facile visibility of polyplexes within cellular structures is explained by the efficient complexation ability of amino groups present in the polymer structure as well as of phosphate moieties of the nucleic acids with the heavy metal species used for staining. Thereby, the polyplex structures are stained simultaneously with the cellular constituents. However, due to the increased density of reactive functional groups within the polyplexes compared to the cellular interior, the staining efficiency of polyplexes is more pronounced.

In summary, polymeric nanomaterials generally constitute demanding objects for TEM-based investigations, since they intrinsically provide only a low electron density. As a consequence, strategies for increasing their electron density have to be found. An advanced strategy to address this issue is provided by the implementation of additional techniques and the correlation of the acquired images. In the next chapter, an approach to assess the contrasting capabilities of different polymer nanoparticles by means of image processing routines will be discussed. Furthermore, a suitable polymeric nanoparticle system for additional, complementary investigation by fluorescence microscopy as well as TEM will be introduced.

3. Assessment of electron densities of selected polymeric nanoparticles and the synthesis of a correlative label

Parts of this chapter have been published in: P3) M. Reifarth, W. Müller, B. Shkodra-Pula, H. Görls, U. S. Schubert, R. Heintzmann, S. Hoeppener, *Part. Part. Syst. Charact.* **2019**, *36*, 1800324, and P4) M. Reifarth, D. Pretzel, S. Schubert, C. Weber, R. Heintzmann, S. Hoeppener, U.S. Schubert, *Chem. Commun.* **2016**, *52*, 4361-4364.

One of the major challenges addressed in this thesis is related to the relatively weak electron contrast provided by polymeric nanomaterials. This makes it difficult to trace them in TEM within an organic matrix, such as the cellular environment.[48] The electron density can be enhanced by (i) the treatment of the nanomaterial with reactive heavy metal species, which accumulate chemically within the nanoparticulate polymer framework with a strong affinity ("passive staining") or by (ii) the active incorporation of strongly electron scattering species into the polymer ("active staining"). In this chapter, a method to assess the electron attenuation of a nanoparticle sample on the basis of image processing of TEM micrographs prior and subsequently to the treatment with heavy metal species is described. Polyesters were identified as a material whose electron density is not significantly enhanced by the treatment with standard heavy metal agents. As a consequence, the synthesis of a poly(lactic acid) species covalently attached to a luminescent iridium(III)-based coordination compound was performed to establish a NP system which can be investigated in a CLEM approach. The iridium compound acted as an electron microscopy label as well as a luminescent dye which can be efficiently utilized for fluorescence microscopy investigations.

In order to classify electron densities of common polymeric nanomaterials and to evaluate polymer staining mechanisms, an initial task was the development of a method capable of assessing electron density values by means of TEM micrograph image analysis. These investigations are motivated by

the fact that the preparation of biological specimens for TEM investigations relies on the treatment of the sample with heavy metal staining agents, which selectively bind to the cellular constituents. Along with the cellular structures, the polymeric nanoparticles may be co-stained. This is, however, only possible if the chemical composition of the polymer material allows for an active interaction with the heavy metals either by complexation or by a redox-reactive addition.

The development of an image processing-based routine to analyze TEM micrographs of particle samples was the initial task of the study. This algorithm is based on the assumption that for amorphous, ultrathin materials (which is valid for polymeric nanomaterials) the electron beam intensity can be characterized as a function of the sample thickness as well as a material-specific attenuation coefficient α which follows an exponential decay similar to the Lambert-Beer relationship.[35, 73-75]

(2) $I(\vec{r}) = I_0 e^{-\alpha(\vec{r})\cdot h(\vec{r})}$.

Here, $I(\vec{r})$ is the electron beam intensity at the position $\vec{r}$ at the detector (CCD camera intensity), I_0 represents the background intensity, $\alpha(\vec{r})$ is the material-specific attenuation coefficient and $h(\vec{r})$ denotes the sample thickness at the position $\vec{r}$.

A thorough analysis of a TEM micrograph of a nanoparticle sample can provide access to the electron attenuation coefficient α of a polymer nanoparticle system. For this purpose, the spatial distribution of the thicknesses of the homogenously electron-dense nanoparticles needs to be carefully assessed. This requires (i) an initial analysis of the TEM image to distinguish between background and particle signal and (ii) the determination of the particle coordinates (including the coordinates of the particle centers) as well as their diameters. With that knowledge, the sample thickness d at each image position $\vec{r}$, *i.e.* the respective sample height, can be calculated assuming a spherical shape of the particles. The local height across the individual particle can be described by:

(3) $h(\vec{r}) = \begin{cases} 2\sqrt{R^2 - (\vec{r} - \overrightarrow{r_C})^2}, & R^2 - (\vec{r} - \overrightarrow{r_C})^2 \geq 0 \\ 0, & else \end{cases}$,

whereby $\overrightarrow{r_C}$ represents the coordinates of the center of the particle and R its radius. From equations (2) and (3), the theoretical intensity function of an individual particle can be deduced:

$$(4)\ I(\vec{r}) = \begin{cases} I_0 exp(-2\alpha\sqrt{R^2 - (\vec{r} - \overrightarrow{r_C})^2}),\ R^2 - (\vec{r} - \overrightarrow{r_C})^2 \geq 0 \\ I_0,\ else \end{cases}.$$

The attenuation coefficient α can be determined by plotting the intensity profile of each individual particle signal with eq. (4) as a fit function. However, data elaboration of each individual signal would be associated with a computational effort and be error-prone. In order to reduce computation time, the sum of logarithmized pixel values of each individual particle was determined. This value represents a magnitude associated to the volume of the particle with a prefactor directly related to the electron attenuation coefficient α, assuming thereby an ideally spherical geometry of the particles. Furthermore, an image processing-based determination of the respective particle diameters with the diameter d = 2R was conducted. A comparison of these both values extracted from TEM micrographs provided access to α according to according to equation (5):

$$(5)\ \sqrt[3]{\frac{6}{\pi}\sum_{x',y'}^{\text{area}} \ln I_n(x',y') \cdot p} = \sqrt[3]{\alpha} \cdot \text{d}.$$

In this equation, I_n(x',y') denotes the reciprocal normalized pixel intensity, p the pixel area [μm^2]. and α represents the attenuation coefficient.

In order to increase the statistical validity of the method, the TEM signals of numerous particles were considered for data elaboration. In this context, particle diameters were plotted *vs.* their TEM image contrast according to the left-hand side of equation (5) and the data points were subjected to linear regression. The slopes of these plots correspond to $\alpha^{1/3}$.

This automatic image processing routine was implemented utilizing the toolbox DIPimage for MATLAB. Within this routine, a basic challenge was to implement reliable particle recognition and background suppression among others. Optimized image processing resulted in linear plots with the slope α^3 as depicted in Figure 3.1 (Figure 3.1A shows a raw image of polystyrene beads, Figure 3.1B highlights the particle signals taken into consideration for analysis and Figure 3.1C displays the linear

plot). In order to achieve a high quality linear fit of the data, a large number of data points possessing a relatively wide range of x- and y-values is beneficial. This was obtained for particle samples with a broad size-distribution, *i.e.* a high polydispersity.

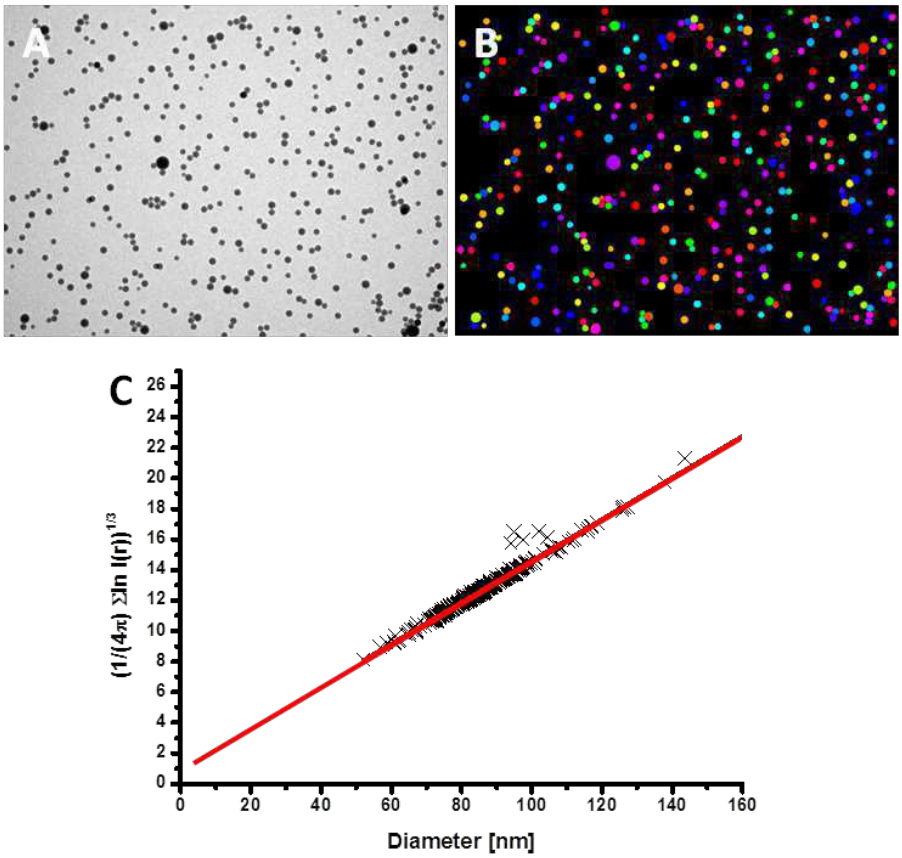

Figure 3.1: A) Background-corrected low-magnification TEM image of polystyrene nanoparticles. B) Labeled particles which were considered for further analysis. C) Linear regression of particle diameter *vs.* cubic route of sum of logarithmized intensities extracted from A). Reprinted with permission from ref. [76], copyright 2019, Wiley.

For investigations, common materials for polymer NP formulations were selected. Figure 3.2 depicts the chemical structures of the polymers used in the study.

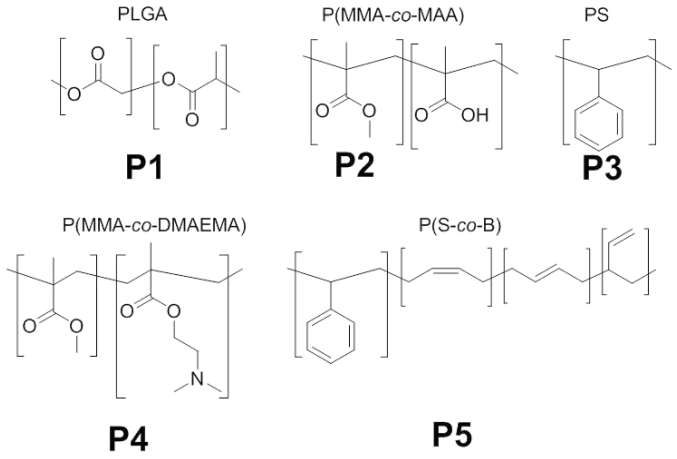

Figure 3.2: Schematic representation of polymeric systems used for the formulation of nanoparticle systems.

In Table 3.1, furthermore, the characteristics of the investigated nanoparticle systems are listed.

Table 3.1: Characteristics of the polymeric nanoparticles used in the study. The particles were either prepared by nanoemulsion (NE), nanoprecipitation (NPr) or emulsion preparation (EP), respectively.

NP sample	Polymer	Preparation method	Size [nm] (PDI) DLS	Zeta potential [mV]
P1	PLGA	NE	199 (0.138)	– 29 ± 1
P2	P(MMA-c*o*-MAA)	NPr	107 (0.110)	– 46 ± 1
P3	PS	EP	115 (0.105)	+ 33 ± 1
P4	P(MMA-*co*-DMAEMA)	NPr	124 (0.060)	+ 33 ± 1
P5	PS-*co*-PB	NE	214 (0.118)	– 5 ± 0.1

These particle samples were subjected to TEM imaging in a subsequent step. Therefore, the particle samples were incubated for 24 h with the respective staining agents, *i.e.* osmium tetroxide (OsO_4) as well as uranyl acetate ($UO_2(OOCCH_3)_2$) and were placed on a carbon-supported TEM copper grid by conventional blotting and drying. All particle samples were imaged under the similar beam conditions (focus position, magnification, background illumination, aperture size *etc.* was kept constantly). The resulting TEM micrographs were subjected to image processing analysis. In Table 3.2, the respective electron attenuation values of the **P1-3** unstained and in response to the staining agents are listed. At a first glance, similar electron attenuation values of stained with OsO_4 and $UO_2(OOCCH_3)_2$ as well as the unstained particle samples **P1-3** were determined. This indicated the inability of these agents to accumulate inside the particle interior. In fact, this means that particles prepared from the polymers

P1-3, *i.e.* polymers possessing phenyl and ester (and carboxy-) functionalities, are not stained by the standard heavy metal agents OsO_4 and $UO_2(OAc)_2$, since these functionalities are inert towards the reactive heavy metal species. These results are in accordance to literature reports.[77]

Table 3.2: Attenuation factors $\boldsymbol{\alpha}$ extracted from the original images of the polymer samples **P1-3**. Here, the individual entries in the table represent mean values of multiple measurements and their standard deviations.

NP sample	Non-stained NPs α [µm^{-1}]	OsO_4 staining α [µm^{-1}]	Uranyl acetate α [µm^{-1}]
PLGA, **P1**	1.13 ± 0.33	1.33 ± 0.21	1.35 ± 0.10
P(MMA-*co*-MAA), **P2**	1.64 ± 0.31	1.49 ± 0.30	1.71 ± 0.27
PS, **P3**	2.14 ± 0.05	2.24 ± 0.17	2.04 ± 0.13

The situation is expected to be different for particles bearing chemical functionalities which are known to exhibit a strong coordination or reactive capacity towards the staining materials. Owing to their importance in nanomedicine and in materials sciences,[20, 78-80] particles possessing amino-functionalities and isolated double bonds were selected. Their corresponding homopolymers represent water-soluble polymers (amino-containing structures) or compounds that represent viscous liquids under standard conditions (polydiene structures), so that they were not expected to form stable polymer colloids. For this purpose, amino- as well as double bond-containing monomers were copolymerized with other building blocks to yield solid, water-insoluble polymers, from which stable nanoparticles could be formed. As such, nanoparticles of poly(methyl methacrylate-*co*-2-dimethylaminoethyl methacrylate) P(MMA-*co*-DMAEMA), as previously synthesized by Yildirim *et al.*,[81] as well the commercially available poly(styrene-*co*-butadiene) were selected, since these polymers formed stable colloids (structures see Figure 3.2, nanoparticle characteristics see Table 3.1). The extracted electron densities of the particles are summarized in Table 3.3.

Table 3.3: Attenuation factors $\boldsymbol{\alpha}$ extracted from the original images of the polymer samples **P5-7**. Here, the individual entries in the table represent mean values of multiple and their standard deviations.

NP sample	Non-stained NPs α [µm^{-1}]	OsO_4 staining α [µm^{-1}]	Uranyl acetate α [µm^{-1}]
P(MMA-*co*-DMAEMA), **P4**	1.23 ± 0.06	2.41 ± 0.47	2.64 ± 0.16
P(S-*co*-B), **P5**	0.26 ± 0.03	4.73 ± 0.74	0.29 ± 0.05

Table 3.3 reveals a significant contrast enhancement for **P4** stained with OsO_4 and $UO_2(OAc)_2$ and **P5** upon OsO_4 staining. Since the ester and phenyl moieties as chemical functionalities were shown not to contribute to staining, the contrast enhancement of these polymer samples can clearly be ascribed to the selected functional groups in the polymeric framework. In case of **P4**, the complexation behavior of the amino groups was conditional on the accumulation of osmium and uranium inside the polymer structure. **P5** possessed only a small electron attenuation value which complicated the extraction of α; however, the values could be determined for all particle samples with a low standard deviation. Unstained particles revealed similar attenuation values as uranyl acetate stained particles which hinted towards the non-selecitvity of the polymer towards these staining agents. However, osmium staining resulted in the most significant contrast enhancement within this study.

This fact motivated further investigations on the underlying chemistry of this particular staining effect. Proton nuclear magnetic resonance spectroscopy (^{1}H-NMR) could provide an insight into the substitution pattern of the isolated double bonds in the polymer structure and revealed the presence of terminal as well as (*Z*)- and (*E*)-substituted C=C double bonds (Figure 3.2, **P5**, spectrum not shown here). For further investigations of the chemical staining mechanism, particular attention was placed on (*Z*)-substituted olefins. (*Z*)-Alkenes, *e.g.* unsaturated fatty acids, play an important role as building blocks of biomembranes, so that a deeper insight about their reaction mechanism with OsO_4 could elucidate the role of OsO_4 in membrane fixation and staining. The capability of OsO_4 as a fixative compound for membranes is controversially discussed in literature.[7, 49]

For this purpose, (*Z*)-cyclooctene as a model substance was selected. This substance was dissolved in an organic hydrophobic solvent, *i.e.* xylene, and a nanoscale emulsion was prepared from this solution by ultrasonication and stabilized by sodium dodecylbenzenesulfonate (SDBS) as surfactant. In the

resulting nanodroplets, the olefinic compound is enclosed in a hydrophobic environment of aromatic compounds (xylenes), such that they are exposed to a very similar chemical environment as present inside the nanoparticle sample prepared from *e.g.* **P5**, in which the olefinic building blocks face the phenyl moieties of polystyrene building blocks. These nanodroplets were exposed to the OsO_4 staining solution. Subsequently to staining, the droplets were purified by dialysis, the emulsion was destabilized and the solvent was removed *in vacuo* (Figure 3.3). First, the resulting chemical compound was analyzed by electron spray ionization time-of-flight mass spectrometry (ESI-ToF-MS).

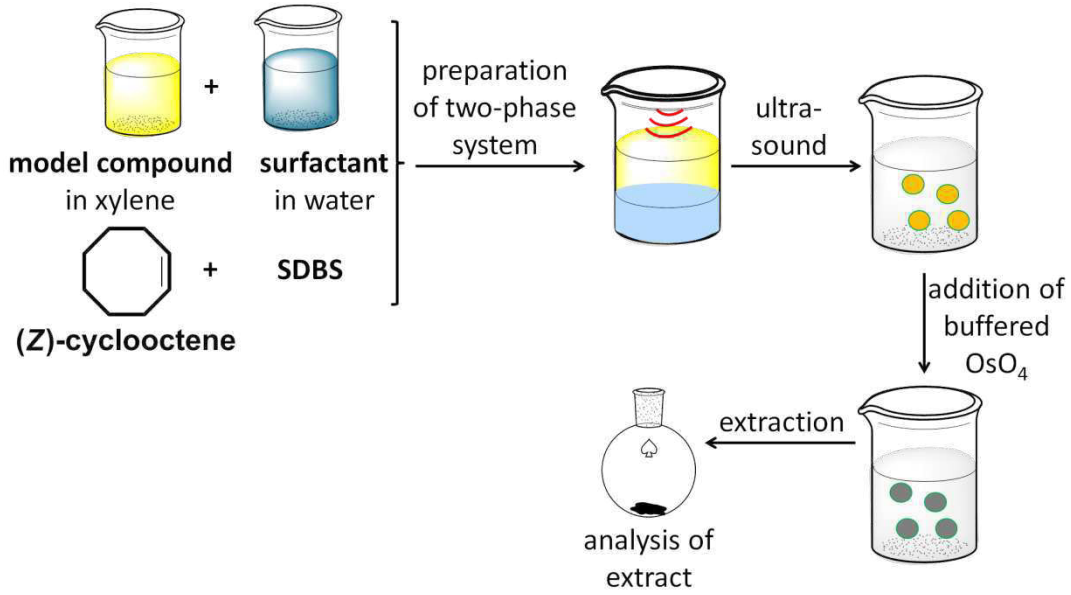

Figure 3.3: Workflow of the model experiment. (*Z*)-Cyclooctene was used as a model substance and was dissolved in xylene and overlaid water containing SDBS as surfactant. Ultrasonication of the emulsion resulted in the formation of nanodopletes. These droplets were exposed to the OsO_4 staining solution. After a short incubation period, the nanodroplets were purified and the formed substance was processed for further analyses. Adapted with permission from ref. [76], copyright 2019, Wiley.

The ESI-MS spectrum is depicted in Figure 3.4A. In the spectrum, three main signal distributions can be observed as indicated in the blue, red, and violet box. In the blue box, the signal distribution represents the H^+, Na^+ and K^+ adduct of a compound with the sum formula $C_{16}H_{28}O_5Os$ (Figure 3.4B). The occurrence of a species with this sum formula can be explained by the formation of coordinative Os^{VI} compound, in which two diolic species coordinate the Os atom in form of a cylic osmium acid ester as depicted in Figure 3.4B. A further proof of the assumed structure was provided by high-resolution MS, whereby the calculated and the measured exact mass are in good accordance, as well as

by the fact that the isotopic pattern observed in MS corresponds well with the measured data (Figure 3.4C). In addition, it was possible to crystallize this highly pure compound, and X-ray analysis validated the presence of the assumed species as well (Figure 3.4D). This data indicates that OsO_4 is capable of crosslinking olefinic structures by forming coordinative compounds.

As an important conclusion from this study it was identified that ester-based polymeric nanoparticles as structures do not respond significantly to the standard heavy metal stains. That means in fact that their identification in a TEM micrograph showing a cell sample incubated with the nanoparticles is not straightforward and relies either on their high contrast (unlikely in the framework of cells) or requires their degradation to form electron-lucent areas. Polyester materials can, thus, hardly be identified, *e.g.* within a cellular context.[82] One possible strategy to improve the electron contrast is the incorporation of a heavy metal already into the polymer structure to manufacture electron-dense polyester-based nanoparticles

Therefore, initially appropriate EM labels had to be synthesized. One elegant way to address this task is to apply luminescent metal complexes, which can act as both, EM as well as luminescent dye. For the synthesis of a polyester material bearing this functional moiety, lactide as monomer was utilzed, since the resulting homopolymer poly(lactic acid) (PLA) represents an important polymer class used in medicine *etc.* owing to its nontoxic and biodegradable character.[83-87] As electron-density enhancer, a cyclometalated iridium(III) coordination was selected based on the following properties: (i) Iridium represents a heavy metal of the 6th period of the periodic table of elements and, thus, is expected to enhance the electron contrast of the resulting polymer significantly and (ii) cyclometalated iridium(III) complexes are known for their strong luminescence, which finds numerous applications, *e.g.* in biomedical imaging[88, 89] or in organic light emission devices,[90] which makes them powerful labels for fluorescence microscopy.[**] The reaction scheme is presented in Figure 3.5.

[**] Even though the luminescent behavior of the described iridium(III) complex is based on phosphorescence, the applied imaging method is referred to as fluorescence microscopy in this thesis.

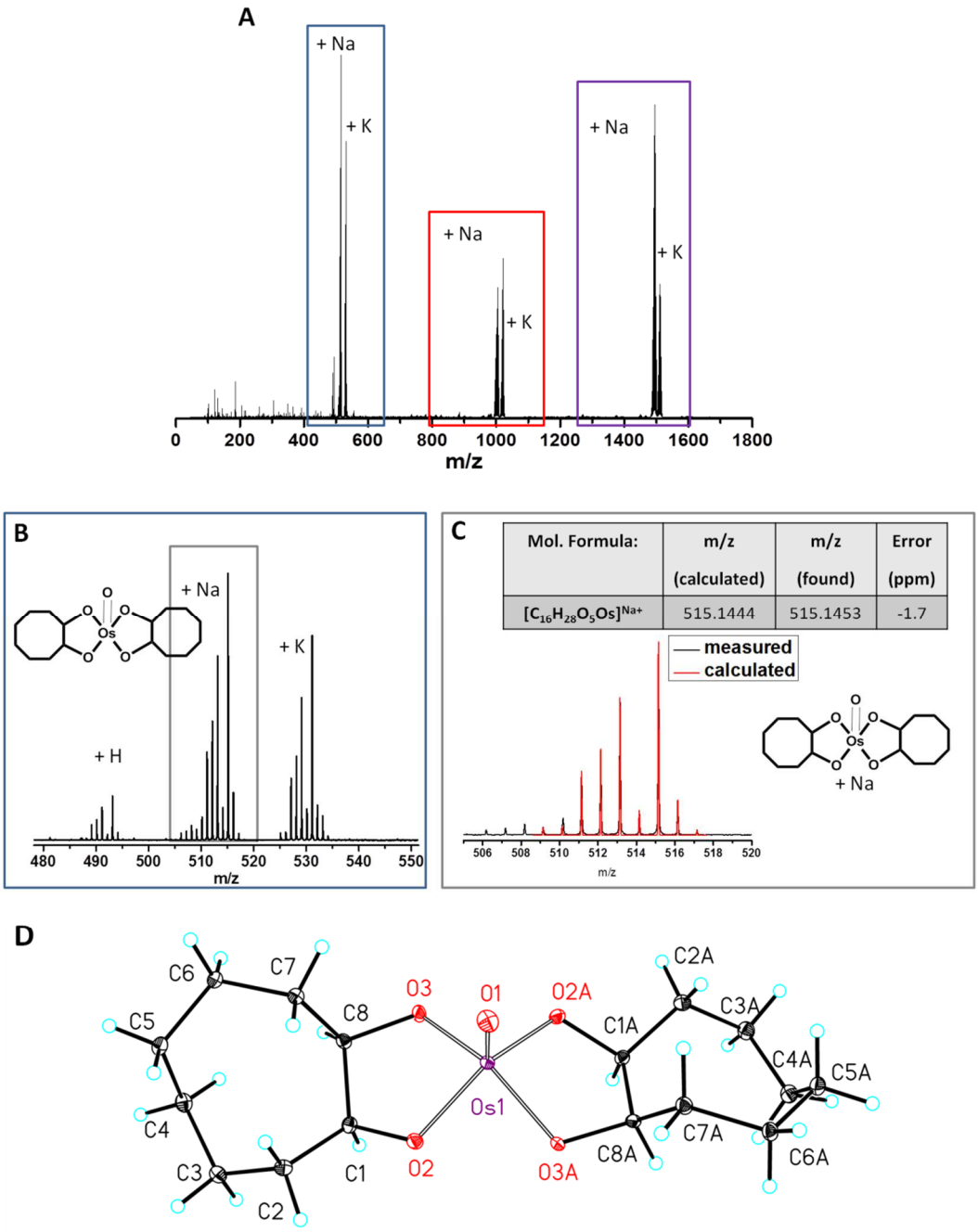

Figure 3.4 A: ESI-MS of (*Z*)-cyclooctene processed as represented in Figure 3.3. Three signal distributions are observed (blue, red and violet box). B: Depicts the signals as emphasized in the blue box. The occurrence of the signals can be explained by adducts of H^+, Na^+ and K^+ of the species as suggested in the structure as shown in the box. High-resolution MS (HRMS) data indicate the correctness of the suggested structure. Furthermore, the isotopic pattern of the measured sample (black line) and the calculated spectrum are in good agreement. D: Results of the crystal structure analysis of the resulting compound. Adapted with permission from ref. [76], copyright 2019, Wiley.

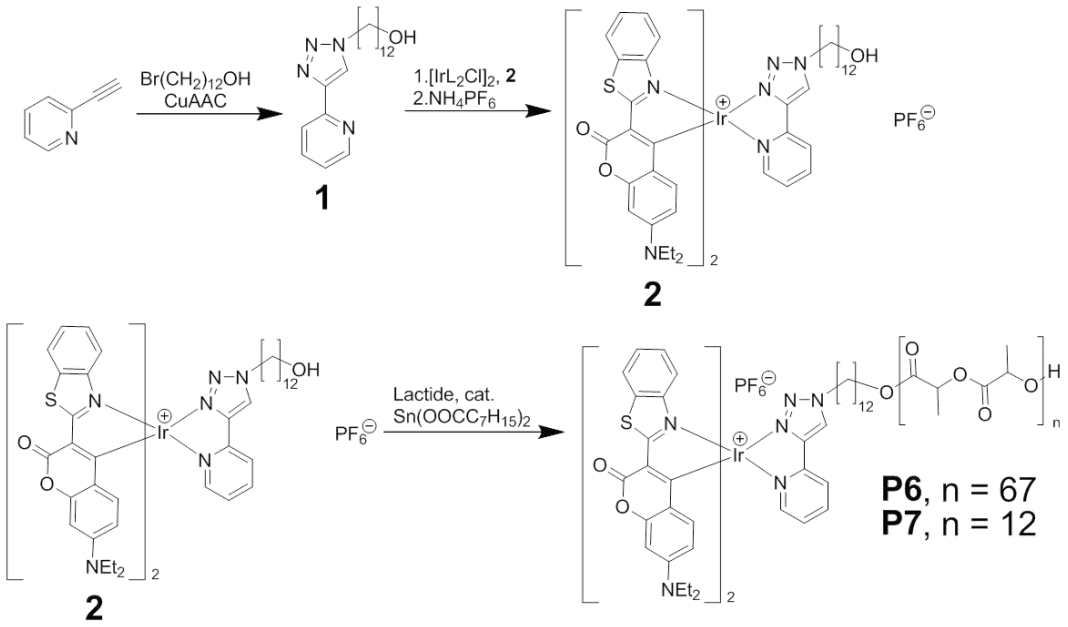

Figure 3.5: Schematic representation of the reaction of polymers **P6** and **P7**.

The synthesis of the Ir functionalized PLA starts from the synthesis of the anchor 4-(2-pyridyl)-1,2,3-triazole ligand **1**. Ligand **1** was synthesized via a copper(I) initiated alkyne-azide click reaction. The desired luminescent iridium complex **3** was obtained by the reaction of 1 with the μ-dichloro bridged precursor complex **2** (synthesis described by Haensch *et al.*[91]) subsequently to an ion exchange of the crude reaction product with NH_4PF_6. Compound **3** possesses a strong absorption maximum at 483 nm wavelength owing to the coumarin-6 ligands which cyclometalate the iridium(III) ion. The complex is perfectly suited to be used in fluorescence imaging since it is highly air- and water-stable and possesses appropriate absorption characteristics (it can be excited, *e.g.* by the 488 nm transition of an Ar^+ laser, which is commonly used in the field of fluorescence microscopy) as well as a large Stokes shift.

In order to achieve a metal content as high as possible (which is required to significantly enhance the polymer's electron density), the hydroxy-terminated luminescent complex was used directly as an initiator for a ring-opening polymerization of the monomer L-lactide. This strategy was preferred to alternative modification strategies, *e.g.* the direct attachment of the complex **3** to a carboxy-terminated polylactide *via* esterification or the utilization of the pristine ligand **1** as polymerization initiator and subsequent complexation by attachment of the precursor iridium coordinative compound **2** to the

ligand bearing polymer. This approach promised the highest degree of functionalization. The polymerization procedure was conducted in toluene under reflux using tin(II)-2-ethylhexanoate as catalyst. Two polymers **P6** and **P7** with different chain length were synthesized. The polymers were fully characterized with proton nuclear magnetic resonance (^{1}H NMR) spectroscopy, size-exclusion chromatography (SEC) and matrix-assisted laser desorption ionization time-of-flight mass spectrometry (MALDI-ToF-MS). The respective analytical data of the synthesized polymers are summarized in Table 3.4. It is noteworthy that the polymers could be synthesized with a narrow size-distribution (as indicated by dispersities Đ < 1.2 according to SEC measurements), which indicates a controlled polymerization procedure despite a possible sensitivity towards the harsh chemical reaction conditions of the initiator complex **3**.

Table 3.4: Selected characterization data of the synthesized polymers.

	[M]:[I]:[C]	Conv.[a] [%]	$M_{n,theo}$[b] [g·mol^{-1}]	$M_{n,NMR}$[c] [g·mol^{-1}]	$M_{n,SEC}$[d] [g·mol^{-1}]	$Đ_{SEC}$[d]	$M_{n,MALDI}$[e] [g·mol^{-1}]	$Đ_{MALDI}$[e]
P6	90:1:1	80	11,400	11,700	6,800	1.17	5,000	1.04
P7	15:1:1	82	2,900	3,000	2,180	1.21	2,460	1.06

[a]Conversion determined from the ^{1}H-NMR spectra of the polymerization mixtures.
[b]$M_{theo}=[M]_0:[I]_0 \cdot conv. \cdot 144$ g/mol + 1366 g/mol.
[c]Referred to ^{1}H-NMR peak at δ = 8.52 ppm (m, 1H).
[d]Eluent: DMAc-LiCl, PMMA calibration, RI detection.
[e]DCTB, NaCl.

The integrity of the complex subsequently to the polymerization procedure was proven by ^{1}H NMR spectroscopy, SEC as well as MALDI-ToF-MS. ^{1}H NMR revealed that the signals observed for the initiator were also present in the purified polymer (data not shown here, for further information see Reifarth *et al.*[92]). SEC with diode array detection (DAD) showed an absorption spectrum matching to the respective spectrum of the complex (Figure 3.7), which overlaps with the corresponding refractive index signal. This indicates covalent attachment of the complex to the polymer. In addition to that, MALDI-ToF-MS investigations were conducted using the short-chain length polymer **P6**. Owing to the positively charged character of the initiating complex, all polymer chains carry a positive charge and can, thus, be ionized well in MALDI-ToF-MS investigations. The MALDI spectrum reveals two major mass distributions corresponding to an even (E) or odd (O) number of lactic acid repeating units

and the complex (without the counter ion PF_6^-). Furthermore, an overlay of the calculated isotopic pattern and the measured zoom-in view of the MALDI spectrum indicates a good agreement of both, measured and calculated data, which makes the assumption of a covalent attachment of the complex to the polymer more evident. In summary, ^{1}H NMR, SEC as well as MALDI-ToF-MS, suggests the formation of an end-group functionalization of the polymer with a high fidelity.

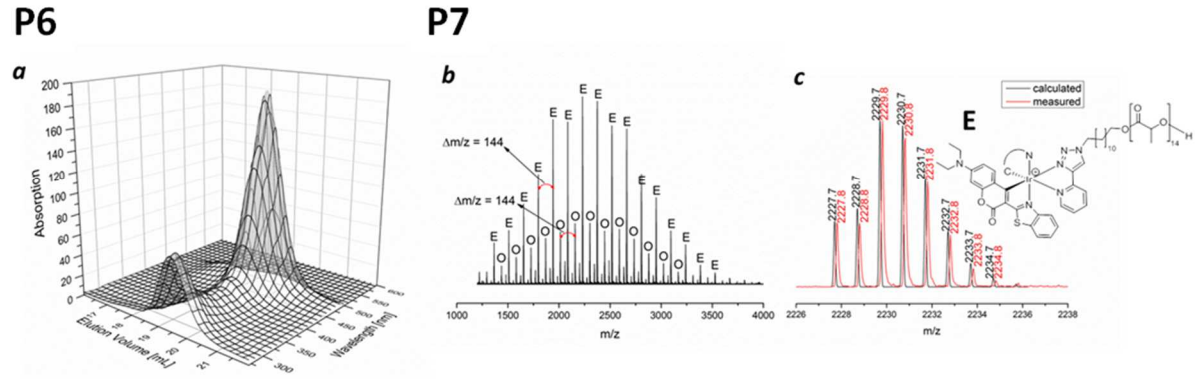

Figure 3.7 A: SEC trace of **P6** (eluent: DMAc-LiCl, PMMA calibration) with DAD detection). B: MALDI-ToF mass spectrum of **P7** (DCTB, NaCl). C: Mass spectrum of a selected isotopic pattern from B in comparison to the calculated abundancies. Adapted with permission from ref. [92], copyright 2016, RSC.

From the polymer **P6**, nanoparticles were formulated using a single-emulsion technique with poly(vinyl alcohol) as surfactant. Thereby, it was assumed that one complex unit is attached to the polymer chain. **NP1** was synthesized from the pure complex-initiated polymer **P6** and possesses, thus, an assumed mass-content of Ir of 2%, **NP2** formulated from a mixture of **P6** and isopropanol-initiated polymer in a mass ratio 1:1 provided an assumed Ir content of 1%. The particle samples possess diameters of 300 nm as well as small zeta potentials. Despite the low surface charge, the particles were stable and could even be lyophilized. The characteristics of the particle samples are summarized in Table 3.5.

Table 3.5: Characterization of the NP samples after preparation and after lyophilization.*

	After preparation		**After lyophilization**		**Zeta potential**
	d [nm]	PDI	d [nm]	PDI	[mV]
NP1[a]	323	0.201	301	0.213	0.2
NP2[b]	307	0.151	293	0.206	7.8

*Diameters and PDI determined by DLS measurements.
[a]Prepared from 100 wt.-% **P66**.
[b]Prepared from 50 wt.-% **P6** and 50 wt.-% unlabeled polymer.

The toxicity of the nanoparticle samples **NP1** and **NP2** as well as of the complex **3** against human embryonal kidney cells HEK-293 was assessed using a 2,3-bis-(2-methoxy-4-nitro-5-sulfophenyl)-2H-tetrazolium-5-carboxanilide (XTT) assay. After an incubation period of 24 h with different concentrations of the pristine complex **3**, a significant decrease of the cell viability could be detected for all applied concentrations. In contrast, the metabolic activity of the cell population in response to their treatment with **NP1** and **NP2** was not found to be severely affected at all concentration ranges (Figure 3.8). These results indicate an efficient encapsulation of the complex into the particles and the prevention of its leakage into the cells due to covalent polymer attachment. Furthermore, a concentration-dependent uptake of the particles was found by means of flow-cytometry (FC) measurements.

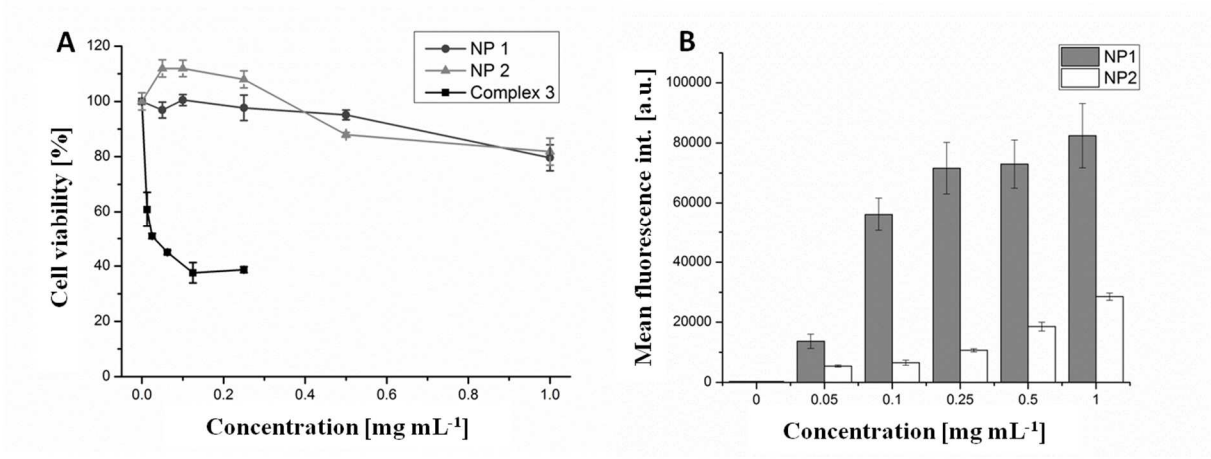

Figure 3.8A: Viability of HEK-293 cells after 24 hours of incubation. B: Flow cytometry investigations of concentration-dependent uptake of NP1 and NP2 after 24 h incubation time. Reprinted with permission from ref. [92], copyright 2016, RSC.

Since no severe adverse effect and an efficient uptake were observed for the highest particle concentration of 1 mg mL^{-1}, this concentration was applied for the imaging experiments. First, the superresolution technique SIM was performed to prove the suitability of the complex as luminescent label. For this purpose, the actin-cytoskeleton was stained by means of phalloidin-alexa 488 and the cell nucleus using Hoechst 33342. Although both, the complex **3** staining the particle samples **NP1** and **NP2** as well as the dye Alexa 488 are excited by the same laser line (488 nm) simultaneously, their emission can be efficiently separated by the choice of an appropriate filter system owing to the

large Stokes shift of **3** in comparison to Alexa 488. Acquisition of a z-stack through the entire cell body of a selected cell by means of SIM imaging proved the internalization of the particles into the cell. Unsurprisingly, both nanoparticle samples **NP1** and **NP2** provided appropriate signals in SIM.

A further proof for efficient internalization can be obtained by HAADF-STEM imaging of the sample. In Figure 3.9, the respective images are shown. Both particle samples, **NP1** and **NP2**, can be observed in the TEM micrographs, being incorporated into the cellular environment. However, the signal originating from the particles is only moderate. Additionally, it has to be mentioned that uranyl acetate and lead citrate staining was omitted, which is reflected in the fact that the cellular ultrastructure is not efficiently pronounced. Nonetheless, the particles could be found within electron lucent organelles which are, most likely, endosomal or lysosomal structures.

In summary, this approach showed that luminescent heavy metal complexes represent compounds that can efficiently be applied as both, fluorescence imaging labels as well as electron-density enhancers for bioimaging applications. Although the complexes represent efficient luminescent dyes perfectly suited for fluorescence microscopy (particularly due to the large Stokes shift which can facilitate, *e.g.* multichannel imaging), the contrast enhancement in electron microscopy is only moderate. A more efficient strategy would be the enhancement of the metal content. This could either be achieved by the synthesis of polymers with even shorter chain lengths, or by the application of multinuclear metal complexes that possess more metal ions per introduced complex unit.

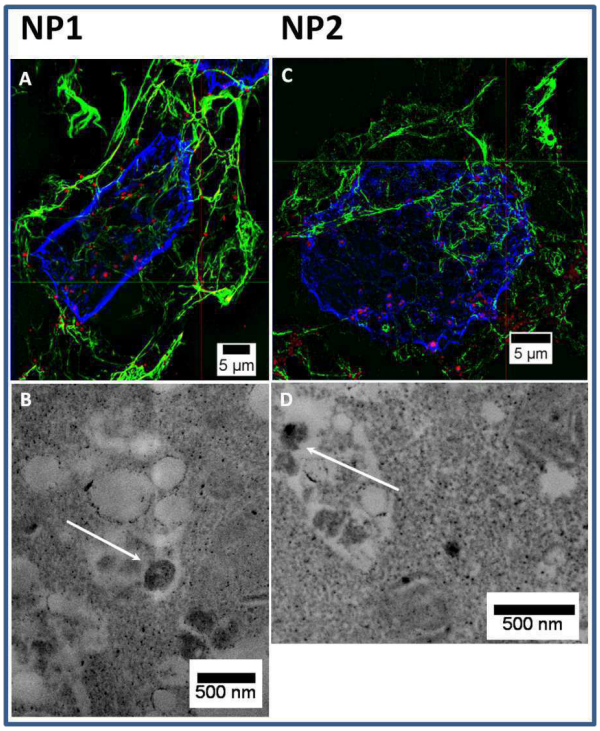

Figure 3.9A, B: Cells incubated with nanoparticle samples NP1 and C, D: NP2 for 24 h with 250 µg mL^{-1} particle concentration. A, C: HR SIM. 63×1.4 NA oil obj. Blue: nucleus. Green: cytoskeleton. Red: NP. B, D: HAADF-STEM images. Zoomed-in views of a cell incubated with NP1 (C) and NP2 (D). White arrows highlight the nanoparticles taken up into intracellular vesicles. Reprinted with permission from ref. [92], copyright 2016, RSC.

4. Uptake and intracellular fate of amino-containing polymeric nanostructures studied by TEM and fluorescence microscopy

Parts of this chapter have been published: P4) T. Bus, C. Englert, M. Reifarth, P. Borchers, M. Hartlieb, A. Vollrath, S. Hoeppener, A. Traeger, U. S. Schubert, *J. Mater. Chem. B* **2017**, *5*, 1258-1274 and P5) M. Reifarth, E. Preußger, R. Heintzmann, U. S. Schubert, S. Hoeppener, *Part. Part. Syst. Charact.* **2017**, *34*, 1700180.

In this chapter, studies focusing on the uptake and the intracellular fate of amino-containing polymeric nanostructures will be summarized. Nanomaterials based on this polymer class exhibit tremendous importance in the field of gene delivery, since they are known to interact electrostatically with nucleic acids in aqueous solution to form polyplexes. These polyplexes often mediate an active uptake, whereby the complexed nucleic acid can be transferred into cells and subsequently be released to enable a gene transfection of the infiltrated cell.[20, 93, 94] Interestingly, the structure of the amino-polymer based gene transfection vectors makes those polyplexes remarkable objects which can be investigated by means of fluorescence and electron microscopy. This is attributed to two adjuvant features of amino-containing polymers, as they (i) represent excellent nucleophiles (in particular primary amino functionalities) which support their functionalization with reactive small molecules and (ii) they possess outstanding coordinative properties which facilitates the selective accumulation of metal ions upon treatment with reactive heavy metal species. As a result of the first, these polymers can easily be labeled with luminescent species such as labels for fluorescence microscopy. Consequently to the latter point, a co-staining of the polyplexes with the staining agents occurs during conventional TEM sample preparation (see Chapter 3). In the resulting TEM micrographs, polyplexes were reported to be observed as dark structures, [48, 72, 95, 96] which can be explained by the fact that they

possess a density of reactive groups within their polyplex structure higher than the density of reactive functionalities in the surrounding cellular features.

In the scope of this thesis, this could efficiently be shown for two poly(ethylene imine) (PEI) based gene transfection agents, *i.e.* polyplexes which formed upon the treatment of linear PEI (**lPEI**) and polyplexes based on a novel polymer class referred to as 3rd generation poly(ethylene imine) (**P8**). Thereby, 3rd generation poly(ethylene imine) is a copolymer consisting of 2-ethyl-2-oxazoline, ethylene imine as well as primary amino group bearing monomer units. A superior gene transfection efficiency combined with a significantly reduced cytotoxicity of the structure could be obtained (data presented in Bus *et al.*[97]). It has to be mentioned that only the microscopy investigations, but not the synthesis, characterization and biological studies of the polymers and polyplexes are part of this thesis. Chemical structures of the polymers and characterization details are mentioned herein for an improved comprehension (Figure 4.1 and Table 4.1).

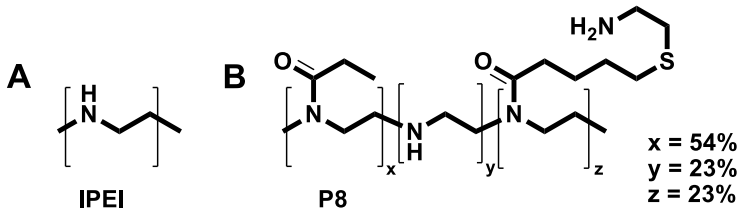

Figure 4.1: Schematic representation of the polymers used for gene transfection in Bus *et al.*.[97] A: Chemical structure of linear poly(ethylene imine) (**lPEI**). B: 3rd generation poly(ethylene imine) (**P8**).

Table 4.1: Size and zeta potential values of the polyplexes prepared from the polymers according to Figure 4.1 with plasmid DNA (N/P ratio of 30) in aqueous solution.

Polymer	z-Average [nm]	PDI	Zeta potential [mV]
lPEI	80 ± 2	0.17	33 ± 4.23
P8	154 ± 1	0.23	23 ± 0.12

Both polymers could efficiently be labeled with cyanine-5-NHS ester to form polyplexes upon exposure to plasmid DNA (pDNA). In addition to polymer labeling, the pDNA was as well labeled by means of Yo-Yo1, a dye molecule that exhibits fluorescent properties upon DNA intercalation. This

enabled high-resolution SIM live cell imaging. Moreover, (S)TEM imaging of HEK-293 cells incubated with the polyplexes were conducted. SIM imaging of cells incubated with lPEI polyplexes revealed a co-localization of pDNA with polymer labeling within lysosomal structures inside the cytoplasm. In the case of lPEI-based structures, the polyplex fluorescence signals possessed large spatial dimensions and are presumably co-localized within large lysosomes (Figure 4.2A, zoomed-in views B, C). These observations became more evident on the basis of STEM images (Figure 4.2D-F). Since STEM provides a resolution beyond the size of a single polyplex, it could be concluded from the images that a large number of polyplex structures was located in electron lucent intracellular vesicular structures, which appeared to be aggregated (particularly pronounced in Figure 4.2F). This aggregation explains the large spatial dimensions of the polyplex fluorescence signals. Furthermore, from STEM images it can be seen that polyplexes were not localized centrally inside the vesicle, but rather at one side of the vesicular structure in close vicinity to the membrane.

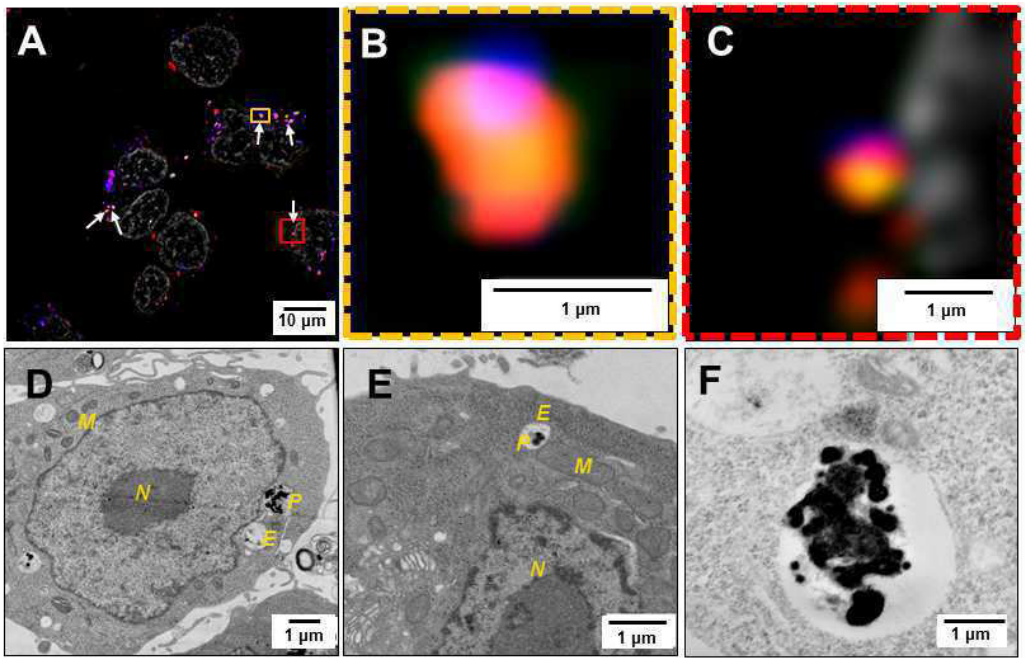

Figure 4.2: High resolution imaging. A: SIM data of a **lPEI** based polyplex within HEK-293 cells. Thereby, white arrow head indicates full co-localization of lysosomal and polyplex fluorescent signals. B-C: Magnified zoom of dash-lined frame in A (as indicated in yellow and red): **lPEI-Cy5** polyplex within the endosome. 63× Oil Obj. 1.4 NA. Grey: Hoechst 33342 Red: Lysosomal membrane (RFP). Green: Plasmid DNA labeling (YOYO-1). Blue: Polymer labeling (Cy-5). D-F: HAADF-STEM image of **lPEI** based. N = cell nucleus, M = mitochondria, E = endosomal compartment, P = polyplex. Reprinted with permission from ref. [97], copyright 2017, RSC.

In contrast to this, polyplexes formed of the polymer **P8** revealed a different behavior inside the cells. SIM images indicated lysosomes with a smaller spatial dimension co-localized with the polyplex signals (Figure 4.3A, zoomed-in views B, C). This finding could also be confirmed by means of STEM imaging (Figure 4.3D-F). With this method, the significantly smaller intracellular vesicles bearing the polyplex signals could be observed. Furthermore, a significantly reduced number of polyplexes within one vesicle was found. In addition to that, a membrane protrusion (Figure 4.3F) interacting with a polyplex at the outside of the cellular membrane was observed is indicative for an active uptake mechanism.

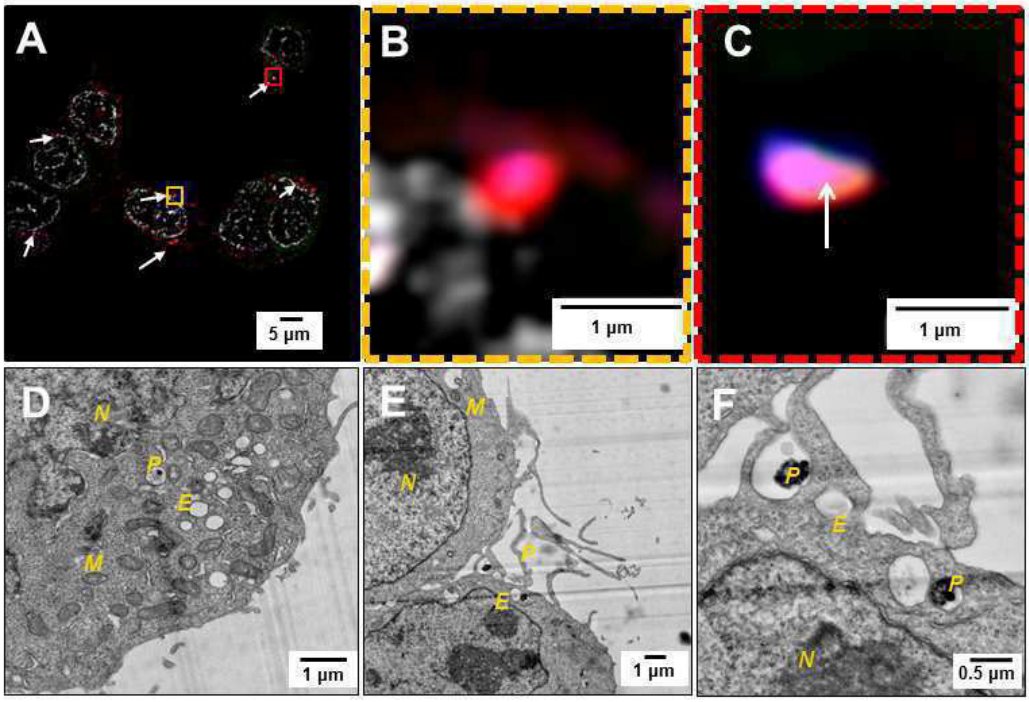

Figure 4.3: High resolution imaging. A: SIM data of **P8** based polyplexes within HEK-293 cells. White arrows: co-localization of P8-pDNA polyplexes within lysosomes. B-C: Zoom-in views of the yellow and red, dash-lined frame in A: P8-Cy5 polyplex within the endosome. 63× Oil Obj. 1.4 NA. Grey: Hoechst. Red: Lysosomal membrane (RFP). Green: Plasmid DNA labeling (YOYO-1). Blue: Polymer labeling (Cy-5). D-F: HAADF-STEM image. N = cell nucleus, M = mitochondria, E = endosomal compartment, P = polyplex. Reprinted with permission from ref. [97], copyright 2017, RSC.

These results point out the complementary character of high-resolution fluorescence as well as transmission electron microscopy. Both methods provided comparable information. Whereas the main advantage of structured illumination microscopy is constituted by its capability to unambiguously

differentiate between the components of the polyplex, *i.e.* polymer as well as pDNA, the advantage of STEM lies clearly in its resolution beyond the particle size.

The correlation of both methods, *i.e.* an overlay of images from the same cell section, consequently is a comprehensive approach to benefit from both techniques. In order to point out the capabilities and limitations of each of the methods individually, on the one hand, and to underline the meaningfulness of the correlative approach, on the other hand, a poly(ethylene imine) based model system mimicking a polyplex was synthesized. For this purpose, branched PEI (bPEI) was reacted with the highly reactive compound $HAuCl_4$ in *N,N'*-dimethylformamide to provide polymer particles with a size of 32 ± 7 nm bearing smaller gold nanoparticles with 10 ± 4 nm as described by Kretschmer *et al.* (Figure 4.4A-C).[98] These particles could be fluorescently labeld by the attachment of a reactive dye molecule, *i.e.* Rhodamine B isothiocyanate (Figure 4.4D). Owing to the labeling with gold particles as well as the fluorescent dye, the particles could be traced within a cellular context by electron and fluorescence microscopy, respectively.

The particles possess a zeta potential of 44.0 ± 0.1 mV (unlabeled particles) and 41.5 ± 2.3 mV (fluorescently labeled particles), respectively, and were expected to be taken up actively.[99] However, XTT assays revealed a severe toxicity of the particles (particles were toxic at concentrations >30 $\mu g \cdot mL^{-1}$, Figure 4.5A). Due to the fact that particles did not show adverse effects on the cellular viability below this threshold, these systems can be considered as suitable model systems for biologically relevant gene vectors.

Furthermore, the uptake efficiency by means of fluorescence-activated cell scanning (FACS) was determined for different incubation periods (Figure 4.5B). These investigations revealed a high uptake already after 30 min, which was more pronounced after 4 h. After 8 h, already 90% of the maximum fluorescence intensity (mean fluorescence intensity value after 24 h incubation time) was achieved, which suggests a rapid internalization of the particles that is almost completely finished after this incubation time.

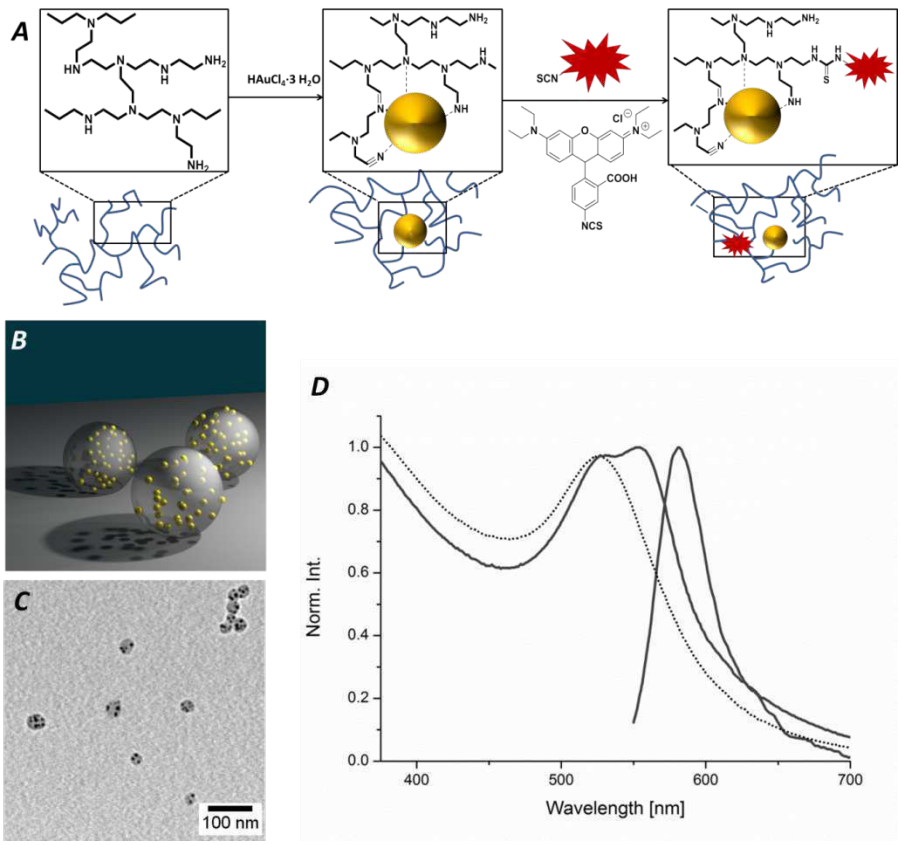

Figure 4.4: A: Synthesis scheme of the gold-PEI hybrid metal-polymer nanoparticles. B: Schematic representation of the particles and C: TEM images of the Rhodamine B-labeled gold-PEI nanoparticles. D: Absorption spectrum of non-functionalized (dotted line) and absorption and fluorescence emission sprectra of Rhodamine B-labeled (solid line) gold-PEI nanoparticles measured in DMF. Reprinted with permission from ref. [100], copyright 2017, Wiley.

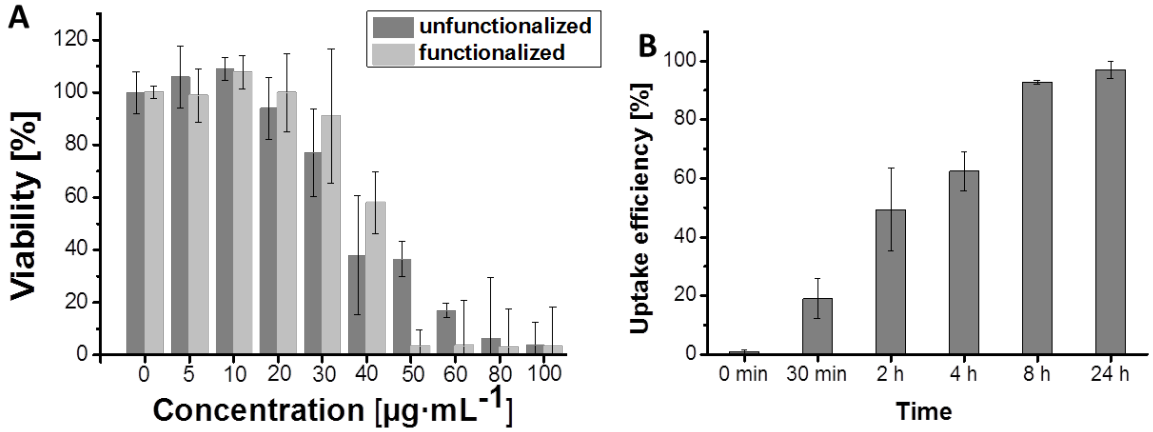

Figure 4.5: A: XTT cytotoxicity test with Rhodamine B-labeled nanoparticle samples and the unlabeled particle sample at different nanoparticle concentrations (0 to 100 µg/mL). In the course of these experiments incubation times of 24 h were chosen to enable uptake of the metal-polymer hybrid nanoparticles into HEK-293 cells. All data are expressed as mean and SD ($n \geq 3$). B: Time-dependent uptake efficiency determined by flow cytometry (labeled particles with a conc. of 25 µg/mL). All data are expressed as mean and SD ($n \geq 4$). Reprinted with permission from ref. [100], copyright 2017, Wiley.

In order to obtain a deeper understanding of the particle fate, fluorescence microscopy was applied. Therefore, the cells were incubated with the particles for 24 h and were stained with Hochest 33342 (nucleus staining) and Alexa Fluor 488 phalloidin (cytoskeleton staining). A representative cell image is depicted in Figure 4.5, whereby a SIM image is displayed in comparison to the corresponding laser widefield (LWF) image of the same cell. The laser widefield image Figure 4.5A revealed that particle signals (red) are localized within the cytoplasm. These signals possess a spatial dimension of about 1 to 2 µm and exhibit a non-circular shape (Figure 4.5B). On the basis of LWF images, it can be assumed that the shape of the particle signals originates from the fusion of smaller, particle bearing intracellular vacuoles into larger structures. This image is compared to the corresponding SIM image, whereby SIM, as a high-resolution technique, provides a resolution of approximately 100 nm.

Figure 4.5D shows a zoomed view of the morphology of the elongated particle structures imaged by SIM. With the enhanced resolution, a significantly more detailed fine structure of the particle signals is revealed. This underlines the assumption that the elongated particle signals represent smaller compartments in close vicinity to each other which might be in the process of fusion.

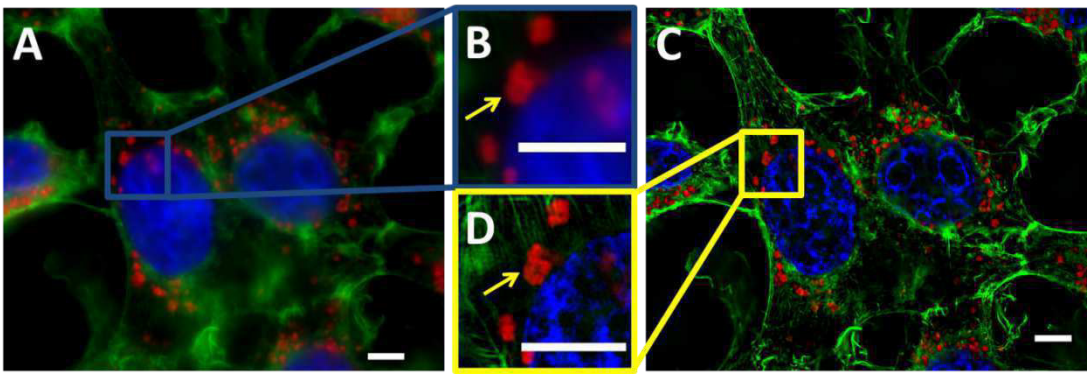

Figure 4.5: Fluorescence images of HEK-293 cells incubated with functionalized nanoparticles (25 µg·mL^{-1}, 24 h). 63× Oil Obj. 1.4 NA. Blue: Nucleus (Hoechst 33342). Green: Cytoskeleton (Alexa-green phalloidin). Red: Functionalized nanoparticle. A: Laser wide-field image. B: Magnification of the highlighted area in A. C: Structured illumination microscopy (SIM) image. D: Magnification of the highlighted area in C. SIM (D) is capable of resolving the particle arrangement inside lysosomes far better than conventional wide-field microscopy C. Scale bars: 5 µm. Reprinted with permission from ref. [100], copyright 2017, Wiley.

Although SIM imaging provides a significantly improved resolution in comparison to conventional methods, its resolution is still not sufficient to image the cell sample on the level of individual particles. Hence, questions about the number of particles internalized into the cellular compartments,

their arrangement as well as their association within the intracellular organelles cannot be eveluated by this technique. In order to address these issues, additional HAADF-STEM was conducted. For this purpose, cells were incubated with the particles for 24 h. Representative images are shown in Figure 4.6. From these images, it can be clearly seen that the particles are taken up by the cells since they are localized within the cellular interior. The particles are localized within vesicular structures. Furthermore, it can clearly be seen that the particles tend to form aggregates within the cellular structures. Figure 4.6A, B revealed additionally that particles are localized at the cellular membrane, and are engulfed by membrane protrusions. This observation suggests an active particle uptake, most likely micropinocytosis (flow cytometry investigations support this assumptions and are found in Reifarth *et al.*[100]). As a result of this uptake mechanism, the particles are internalized in membrane-surrounded endosomal/lysosomal compartments (Figure 4.6C, D).

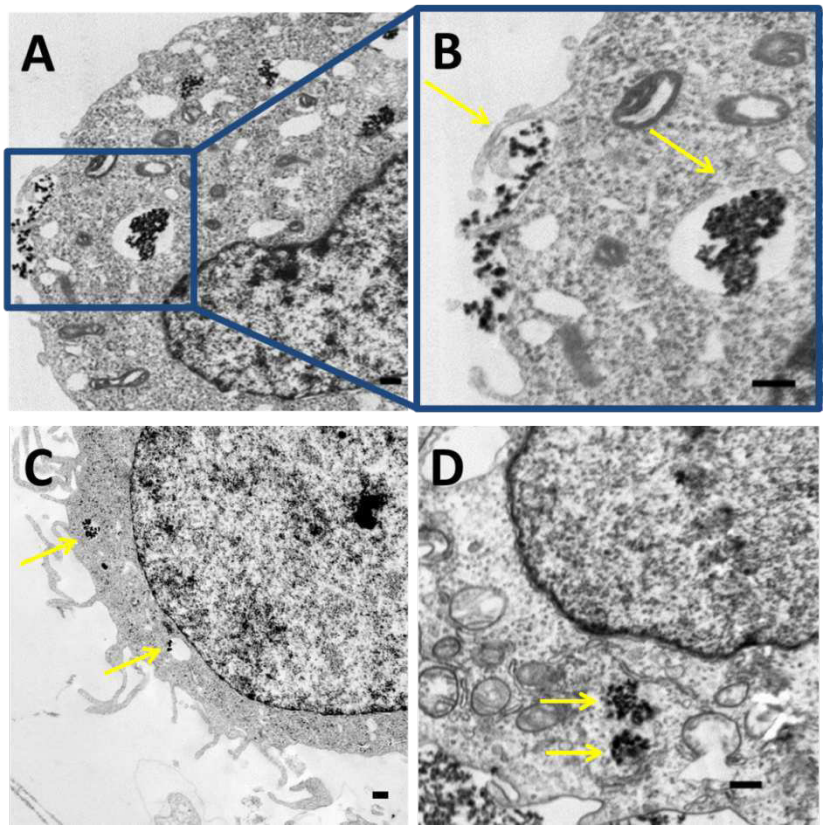

Figure 4.6: STEM images of HEK-293 cells after gold-PEI nanoparticle uptake after 24 h of particle incubation (conc. 25 µg·mL^{-1}). Particles inside the cellular body are highlighted by yellow arrows. (A) Macropinocytosis triggered uptake of nanoparticles and nanoparticle aggregates at the extracellular membrane. (B) Magnification thereof. (C), (D) Internalized particles. Intracellular localization of nanoparticle aggregates within membrane surrounded endosomal/lysosomal compartments. Scale bars: 0.5 µm. Reprinted with permission from ref. [100], copyright 2017, Wiley.

In order to conduct further investigations on the assumed lysosomal fusion processes, a correlative microscopy approach was carried out in the frame of this thesis. Therefore, a larger arrangement of the adherently grown cells was initially imaged by confocal laser scanning microscopy (CLSM) and, on the basis of this image, a region of interest to be subjected to further imaging was selected. Thus, a cell possessing particle signals with an elongated shape was selected (Figure 4.7). After fluorescence imaging, the standard EM preparation protocol was applied.

The results of this correlative data set can be found in Figure 4.7. Figure 4.7A represents a CLSM image of the particle incubated for 24 h, Figure 4.7B depicts the corresponding TEM data. An overlay of both data sets (Figure 4.7C) shows that the particle signals (red in fluorescence microscopy and dark areas in TEM) could be registered along with the cytoplasmic signals and the nucleus signal. Figure 4.7D reveals the fluorescent signals of the hypothesized endosomal/lysosomal fusion processes.

A closer look on the correlated data set provided insights into the particle arrangement within these intracellular organelles. Thereby, particularly the membrane features of the vesicular structures are of interest. As an example, a vesicle (encircled in yellow) in Figure 4.7E possesses a segmented appearance. This vesicle bears packages of Au-PEI particles which are located within the vesicle "chambers". This is a clear evidence for the merging of vesicles, which will be followed by the fusion of their cargos and consequently forming larger structures of endo-/lysosomes. A more evident example is provided by the structure highlighted in the orange dotted-lined box. Here, the original shape of the merging lysosomes is still observable.

In this example, the advantage of a CLEM approach becomes particularly obvious. On the basis of fluorescence microscopy, it was possible to identify special events, *e.g.* fusion events, and additional investigations could be performed on the basis of (S)TEM imaging. Based on (S)TEM only, the appearance of these structures would not be straightforward to identify. Due to the limited field-of-view provided by this method (in lateral direction as well as in axial direction caused by ultrathin sectioning), the identification of such fusion events becomes tedious. Hence, TEM imaging alone is

not capable of providing a complete set of information of the cell morphology due to its limited field-of-view. This gap is efficiently bridged by correlative light and electron microscopy.

In summary, in this chapter uptake and intracellular fate of amino-containing polymeric nanomaterials in cells was investigated by both, fluorescence as well as electron microscopy. In two studies, the expressive value of both methods could be demonstrated and their advantages and drawbacks were discussed. Furthermore, a correlation of both methods was successfully applied and it could be shown that a correlative approach provided a more complete set of information.

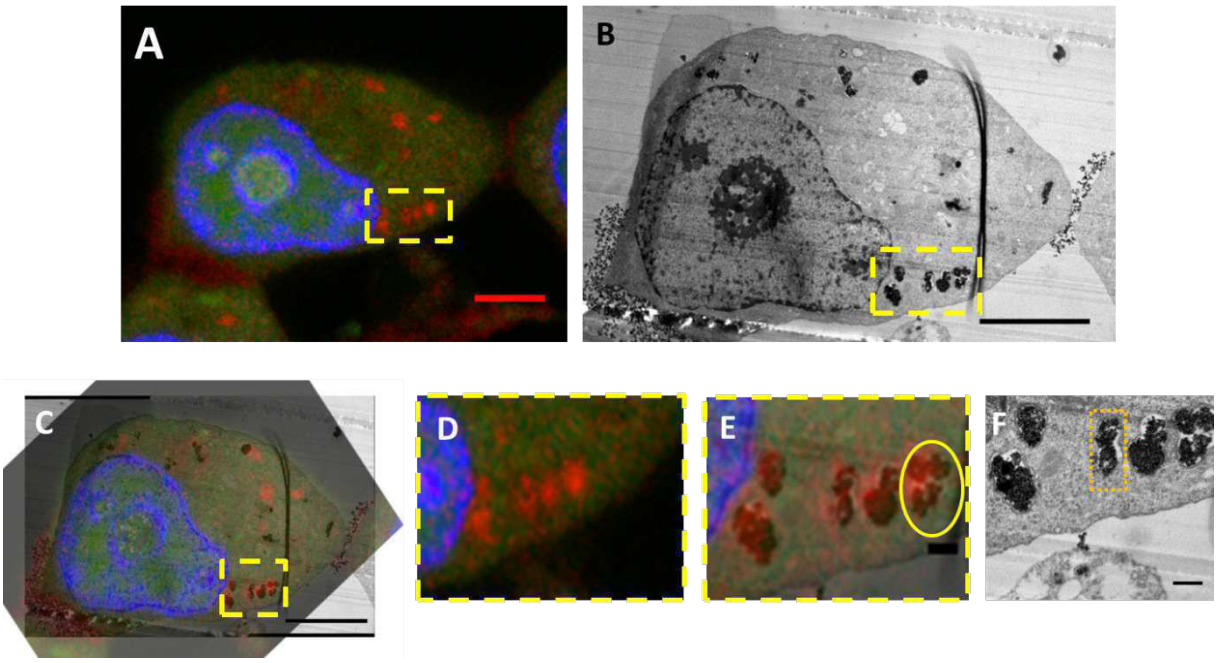

Figure 4.7: Correlative light and electron microscopy of a HEK-293 cell 24 h incubated with functionalized gold-PEI nanoparticles (25 µg·mL^{-1}). A: Cell imaged by CLSM. 63× Oil Obj. 1.4 NA. Blue: Nucleus (Hoechst 33342). Green: Cytoplasm (Hoechst 33342). Red: Functionalized nanoparticles (Rhodamine B). B: STEM image of the same cell. C: Overlay. D: Magnified image of A as indicated by yellow box. E: Magnified image of C as indicated by yellow box. F: High magnification STEM image of the selected area. Scale bars: A, B, C 5 µm. C: Scale bar extracted from STEM image. E,F: 0.5 µm. All STEM images are displayed with equalized histogram. Reprinted with permission from ref. [100], copyright 2017, Wiley.

5. Summary

In the past years, the development of new nanomedical strategies to achieve a targeted delivery of drug molecules into particular cell types has been actively investigated. In this field, particles are used as vectors to transfer pharmaceutically active compounds into the cellular interior and, subsequently, to release the drug molecule. The success of a nanomedical treatment relies on a careful adjustment of the properties of the applied nanoparticulate material, so that the nanocarriers approach particular cell types with a high specificity, are taken up by these cells efficiently, and release their cargo intracellularly in a controlled manner. This makes it indispensible to perform a thorough analysis of the underlying mechanisms and the deduction of comprehensive concepts of particle-cell interactions. The portfolio of possible investigation tools is vast, and the role of cellular imaging as analytical method has become more and more important. This thesis, hence, pursues the implementation of suitable imaging techniques into particle-cell interaction studies by applying two microscopy techniques providing information on a high resolution level: Fluorescence as well as transmission electron microscopy. These studies are exclusively restricted to polymer-based nanoparticles, which have gained increasing importance in drug delivery applications over the last years. It has already been acknowledged that TEM and fluorescence microscopy differ in their resolution capability (Chapter 1) as well as in the performance of displaying cellular structures with an appropriate contrast (Chapters 1 and 2), so that each of the techniques alone would not always provide all desired information. A comparison or even a correlation of both methods, however, may be highly beneficial to obtain a more complete insight.

The present thesis is motivated by the establishment and development of methods to implement both microscopy approaches into uptake studies and to discuss their informative value also in view of experimental challenges. Fluorescence microscopy, thereby, can be considered as a standard method due to the manageable experimental effort, whereas the investigation of polymeric nanomaterials within a cellular framework by means of TEM is demanding. This is attributed to a very similar

electron density of both, polymers and cell structure, so that the particles are not particularly emphasized within the cell structure. It was, thus, a central task to make polymeric nanoparticles visible in TEM micrographs to highlight them within the cellular interior. This can be achieved by introducing heavy atoms into the polymeric framework of the particle, which is possible by: (i) "Passive staining" of the polymer, *i.e.* the exposure of nanoparticle containing cell sample to selected heavy metal species, which accumulate inside the polymer structure (and at best in the cell structure with less efficiency), and (ii) "active staining" of the polymer, *i.e.* the targeted introduction of heavy metal species into the polymer structure, which are incubated with cell samples.

In order to obtain an insight in the heavy metal staining efficiency in a sense of strategy (i), in Chapter 3 of this thesis the "passive staining" capability of different heavy metal species towards selected polymeric nanoparticles was assessed. For this purpose, homopolymeric nanoparticle formulations of polystyrene, poly(methyl methacrylate) and poly(lactide-*co*-glycolide) as well as copolymer structures containing amines and double bonds were selected and exposed to heavy metal stains, *i.e.* OsO_4, and $UO_2(OAc)_2$. These particle samples, with and without heavy metal treatment, were subsequently subjected to TEM imaging under comparable instrument settings. The resulting TEM micrographs were analyzed by means of a custom-made image processing routine. In the scope of this algorithm, the electron contrast of the particle sample was determined and expressed as an electron attenuation coefficient α. In case of successful staining, the attenuation coefficient is supposed to be enhanced in comparison to the pristine particles. The results indicated that the homopolymers were not stained with OsO_4 and $UO_2(OAc)_2$. It was observed that OsO_4 and $UO_2(OAc)_2$ stained amino-containing particles, whereas OsO_4 was capable of enhancing the contrast of particles with isolated double bonds significantly. Owing to the importance of double bonds as building blocks in double-layered membranes and OsO_4 as fixative for membranal structures, a deeper insight into the chemistry of the staining and fixation mechanism of double bonds was obtained by ESI-MS measurements and crystal structure analysis by employing a model substance.

The targeted introduction of electron-dense functionalities into the polymer ("active staining") was also demonstrated in Chapter 3. The electron density of polylactide (PLA) was enhanced by actively incorporating a heavy metal ion into the polymer structure. For this purpose, an Ir^{3+}-based metal complex was synthesized. The complex was shown to be stable even under elevated temperatures, which enabled its utilization as initiator for the catalyzed ring-opening polymerization of lactide. Analysis (SEC, MALDI-ToF-MS, NMR) indicated the successful end-group functionalization of the resulting polylactide polymer, which was subsequently formulated into nanoparticles. Cytotoxicity assays indicated mild adverse effects and flow cytometry revealed a moderate uptake efficiency. In subsequent imaging experiments it could be shown that PLA particles labeled with the iridium complex were observable in TEM micrographs as well as structured illumination microscopy (SIM) images within cells. These experiments demonstrated that a luminescent iridium coordinative compound represents a suitable label for polymeric nanoparticles in uptake studies performed by transmission electron as well as high-resolution fluorescence microscopy. As concluded from Chapter 3, amino-containing polymers can be addressed well by "passive staining", which means that nanoformulations based on this polymer class are efficiently visualized in the cellular context within micrographs. Furthermore, the nucleophilic character of amines enables the attachment of reactive fluorescent labels to the polymer structure, which supports their investigation *via* fluorescence microscopy. These features, along with the importance of this material class as gene delivery agents, motivated microscopy investigations on polymers containing amino-functionalities in Chapter 4. In a first study presented in this chapter, uptake and intracellular fate of polyplexes based on linear poly(ethylene imine) derivatives could be investigated, whose architecture was optimized in such a way that a high transfection efficiency accompanied with low cytotoxicity was obtained. TEM investigations revealed that polyplexes made of this polymer class were taken up *via* active uptake processes (as indicated by membrane interactions) and that the polyplexes were found individually inside intracellular vesicles. These observations could be confirmed by SIM imaging. For comparison, also polyplexes prepared from linear poly(ethylene imine) were prepared. TEM and SIM imaging indicated that multiple polyplexes were observed inside intracellular vesicles, where they aggregated. Another study described in chapter 4 discusses the advantages and drawbacks of the individual

microscopy techniques. For this purpose, nanoparticles based on branched poly(ethylene imine) were prepared, which were labeled with gold nanoparticles as TEM labels, on the one hand, and a fluorescent dye, on the other hand, to provide enhanced signals in both fluorescence and electron microscopy. Superresolution fluorescence microscopy provided an insight into the distribution of the particles and indicated a clustering of the particles inside the cells. However, its resolution is not sufficient to image individual particles. TEM provides an improved resolution capable of resolving individual particles, which is, however, accompanied by a limited field-of-view of this technique. These drawbacks could be circumvented by a correlation of both methods. The correlation of both methods facilitated a deeper insight into lysosomal fusion processes, whereby fluorescence imaging provided an overall image of the cell and TEM was capable of resolving the cellular structure at the highest possible resolution level.

In conclusion, in this thesis fluorescence as well as transmission electron microscopy are discussed regarding their suitability to contribute complementary information about nanoparticle-cell interactions. As a major challenge, the difficulty to trace polymeric nanoparticles in TEM micrographs of cells was identified. Furthermore, a correlation of fluorescence with transmission electron microscopy could be successfully demonstrated. As an outlook, the correlative approach can be optimized in such a way that an overlay of TEM and fluorescence data is achieved with a high precision. The highly specific fluorescent particle signals, thereby, provide information about the intracellular particle localization and supplement TEM data. Hence, correlative light and electron microscopy can be considered as a strategy to highlight polymeric particles in TEM micrographs (Figure 5.1).

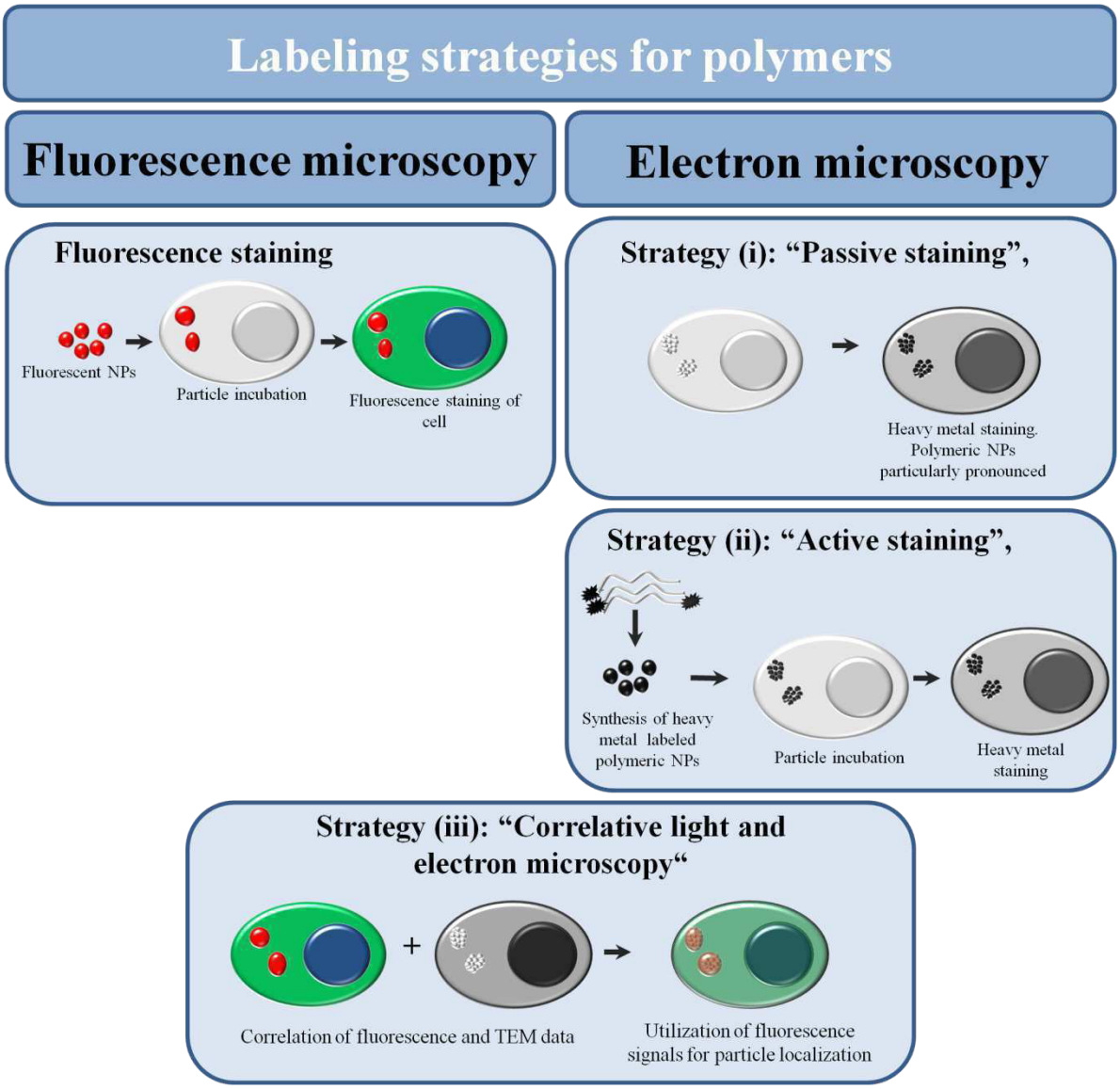

Figure 5.1: Summary and outlook of polymer labeling strategies discussed this thesis. For fluorescence microscopy, polymeric nanoparticles have to be fluorescently labeled, which can be considered as a standard method nowadays. For electron microscopy, three strategies are suggested in this thesis: (i) "Passive staining", *i.e.* the exposure of the cell sample to conventional heavy metal agents, which accumulate in the cellular structure and to a higher extent in the polymeric particles, (ii) "active staining", *i.e.* the targeted introduction of heavy metal functionalities into the particles and (iii) a correlative approach, whereby the more specific fluorescence signals of the particles are utilized for particle localization in the TEM micrograph.

6. Zusammenfassung

Die gezielte Abgabe von Wirkstoffmolekülen in besondere Zelltypen stellt den Gegenstand intensiver Forschungsbemühungen dar. Als Lösungsansatz mit aktueller Relevanz seien hier nanomedizinische Strategien zu nennen, die nanoskalige Materialien als Vektoren verwenden, um pharmazeutisch wirksame Stoffe in Zellen einzubringen und diese im Zellinneren freizusetzen. Der Erfolg einer nanomedizinischen Behandlung erfordert eine sorgfältige Anpassung der Eigenschaften der Partikel, sodass die Nanovektoren besondere Zelltypen mit einer hohen Spezifität adressieren, in diese Zellen mit hoher Effizienz aufgenommen werden und am Ort den Wirkstoff kontrolliert abgeben können. Dabei ist eine gründliche Analyse zugrundeliegender Mechanismen und die Ableitung umfassender Konzepte zum Verständnis der Wechselwirkungsbeziehung zwischen Nanopartikeln und Zellen unabdingbar. Zu diesem Zwecke steht eine große Auswahl geeigneter Untersuchungsmethoden zur Verfügung, wobei bildgebenden Methoden eine immer größer werdende Bedeutung zukommt. Die Anwendung hochauflösender Mikroskopiemethoden, d.h. Fluoreszenz- und Transmissionselektronenmikroskopie, steht aus diesem Grunde im Mittelpunkt der vorliegenden Arbeit. Da polymerbasierte Nanoformulierungen auf dem Gebiet der kontrollierten Wirkstoffabgabe unlängst einen Bedeutungszuwachs erlangt haben, beschränkten sich die hier vorgestellten Studien ausschließlich auf diese Materialklasse. TEM und Fluoreszenzmikroskopie unterscheiden sich in ihrem Auflösungsvermögen (Kapitel 1) sowie in ihrer Eignung, zelluläre Strukturen mit geeignetem Kontrast darstellen zu können (Kapitel 1 und 2). Beide Methoden weisen folglich Vor- und Nachteile auf, sodass ein umfassender Einblick in Nanopartikel-Zell-Wechselwirkungen vor allem durch eine vergleichende Betrachtung oder sogar die Korrelation beider Methoden erreicht werden kann.

Als experimentelles Ziel dieser Arbeit stellte sich demzufolge die Etablierung und Weiterentwicklung von Fluoreszenz- und Elektronenmikroskopiemethoden heraus mit dem Ziel, beide Methoden in Nanopartikel-Zell-Untersuchungen einzubeziehen. Darüber hinaus wird deren Aussagegehalt auch im Hinblick auf ihren experimentellen Aufwand diskutiert. Fluoreszenzmikroskopie stellt heutzutage eine

Standardmethode dar, die mit einem überschaubaren experimentellen Aufwand einhergeht. TEM-Untersuchungen hingegen erwiesen sich als anspruchsvoll, was auf die Tatsache zurückzuführen ist, dass sich in TEM-Aufnahmen die Morphologien der Partikel sich nicht ohne Weiteres vom zellulären Hintergrund hervorheben. Dies ist dadurch begründbar, dass der Elektronenkontrast polymerer Nanomaterialien dem des Zellinneren recht ähnlich ist. In der vorliegenden Arbeit wurden deshalb Strategien erarbeitet, die eine eindeutige Identifizierbarkeit polymerer Nanomaterialien im zellulären Kontext ermöglichen.

Zunächst erschien hierfür die gezielte Kontrasterhöhung der Nanopartikel zielführend. Dies ist erreichbar durch „passives Anfärben“, d.h. eine Anfärbung der Nanopartikel enthaltenden Zellproben mit ausgewählten Schwermetallreagenzien, die sich innerhalb der Nanopartikel (in geringerem Maße aber in der Zellstruktur) anhäufen, sowie „aktives Anfärben“, d.h. einer gezielten Einbringung schwermetallhaltiger Funktionalitäten in die Polymerstruktur, die in ihrer Nanoformulierung den Zellen ausgesetzt werden soll.

Der ersten Strategie folgend wurde das Anfärbevermögen ausgewählter Schwermetalle in Kapitel 3 untersucht. Hierfür wurden Nanopartikel basierend auf den Homopolymeren Polystyrol, Polymethylmethacrylat sowie Poly(laktid-*co*-glyolid) sowie Copolymere, die als funktionelle Gruppen Amine sowie isolierte Doppelbindugen enthielten, untersucht. Diese wurden OsO_4 und $UO_2(OAc)_2$ ausgesetzt und metallfreie sowie schwermetallbehandelte Nanopartikel im Elektronenmikroskop untersucht. Mit Hilfe eines im Rahmen dieser Arbeit entwickelten Auswertealgorithmus wurden die TEM-Aufnahmen analysiert und der Partikelkontrast in einer zu bestimmenden Elektronenabschwächungskonstante α des jeweiligen Materials ausgedrückt. Ein hohes Anfärbevermögen zeichnet sich hierbei durch eine vergrößerte Elektronenabschwächungskonstante aus. Die Ergebnisse dieser Studie zeigten, dass OsO_4 und $UO_2(OAc)_2$ die homopolymeren Strukturen nicht anfärben. Es wurde ferner beobachtet, dass OsO_4 und $UO_2(OAc)_2$ aminhaltige Polymere anzufärben vermochten und dass sich Doppelbindungen durch OsO_4 deutlich anfärben ließen. Aus diesem Grunde – sowie wegen der außerordentlichen Bedeutung ungesättigter Kohlenwasserstoffe als wesentliche Bestandteile biologischer Membranen – wurde der zugrundeliegende chemische

Mechanismus der OsO_4-Färbung in einem Modellexperiment näher untersucht. ESI-MS und Kristallstrukturanalyse lieferten hierbei Einblicke in den chemischen Mechanismus von Anfärbung und Fixierung.

Die aktive Anfärbung von Polymeren wurde ebenfalls in Kapitel 3 nachgewiesen. Die Elektronendichte von Polylaktid wurde gezielt durch die aktive Anbindung einer koordinationschemischen Schwermetallverbindung an die Polymerkette erreicht. Hierbei wurde Ir als elektronendichtes Atom benutzt. Der Komplex, der eine hohe Stabilität unter erhöhten Temperaturen aufwies, wurde als Initiator für eine katalysierte Ringöffnungspolymerisation von Laktid verwendet. Die erfolgreiche Endgruppenfunktionalisierung des resultierenden Polymers konnte mit geeigneten Analysenmethoden (SEC, MALDI-ToF-MS, NMR) untersucht werden und wurde für die Herstellung von Nanopartikeln verwendet. Zelltoxizitäts-Assays zeigten eine geringe Giftigkeit und Durchflusszytometriemessungen moderate Aufnahmeraten der Partikel an. In TEM-Aufnahmen von Zellproben konnten die Nanopartikel auf Grund ihrer erhöhten Elektronendichte nachgewiesen werden. Zudem wurde der lumineszente Charakter des Komplexes ausgenutzt, um die Partikel mit hochauflösender Fluoreszenzmikroskopie (strukturierte Beleuchtung) zu untersuchen.

Aus den Untersuchungen in Kapitel 3 ging hervor, dass aminhaltige Polymere effizient durch Schwermetallsalze passiv gefärbt werden können. Der nukleophile Charakter der Aminofunktionalität ist ferner hervorragend geeignet, reaktive Fluoreszenzfarbstoffe kovalent an diese Polymere anzubinden. Die Bedeutung dieser Polymerklasse als Überträgermaterialien für genetisches Material macht überdies Nanomaterialien auf Basis aminhaltiger Polymere zu attraktiven Untersuchungsobjekten für mikroskopische Studien (Kapitel 4). In einer ersten Studie wurden die Aufnahme und das innerzelluläre Verhalten von Polyplexen untersucht, die sich chemisch von linearem Polyethylenimin ableiten. Die Architekturen dieser Polymere wurden dahingehend optimiert, dass ihre Polyplexe eine hohe Transfektionseffizienz aufwiesen, die mit einer geringen Zelltoxizität einhergingen. TEM-Untersuchungen zeigten, dass Polyplexe im Sinne eines aktiven Mechanismus in die Zelle aufgenommen wurden und dass sich Polyplexe einzeln innerhalb innerzellulärer Vesikel aufhielten. SIM-Untersuchungen ergänzten diese Befunde. Vergleichend wurden Polyplexe von

linearem Polyethylenimin angefertigt und diese zu Zellkultutren hinzugegeben. TEM- und SIM-Untersuchungen zeigten, dass die Polyplexe nicht einzeln innerzellulär nachzuweisen waren, sondern dass diese angehäuft in Vesikeln beobachtbar waren. In einer anderen in Kapitel 4 beschriebenen Studie werden Vor- und Nachteile der einzelnen Mikroskopiemethoden an einem geeignetem Partikelmodell diskutiert. Diese Partikelprobe besteht aus verzweigtem Polyethylenimin, das mit kleineren Goldpartikeln sowie einem Fluoreszenzfarbstoff markiert wurde und somit einen erhöhten Kontrast sowohl im Fluoreszenzmikroskop als auch im Elektronenmikroskop aufweist. Hochauflösende Fluoreszenzmikroskopie ermöglichte einen ersten Einblick in die innerzelluläre Verteilung der Partikel und deutete auf eine Anhäufung mehrerer Partikel im Zellinneren hin. Die Auflösung dieser Methode war dennoch nicht ausreichend, um einzelne Partikel zu visualisieren. Untersuchungen einzelner Zellen mit TEM konnten detaillierte Einblicke in die Partikelaufnahme liefern, wobei die Untersuchungen auf einzelne Zellareale beschränkt werden muss. Es erschien folgerichtig, die beiden Methoden miteinander zu korrelieren, um den Vorteil der Hochauflösung des TEMs mit dem mikroskopischen Weitblick des Lichtmikroskops zu vereinen. Mit Hilfe der korrelativen Mikroskopie war es möglich, lysosomale Verschmelzungsprozesse zu beobachten.

Zusammenfassend sei erwähnt, dass in der vorliegenden Arbeit Fluoreszenz- und Transmissionselektronenmikroskopie Verwendung fanden um Nanopartikel-Zell-Wechselwirkungen zu untersuchen. Dabei wurden die Vorteile beider Methoden ausgenutzt, um einen besseren Einblick in die innerzellulären Prozesse zu erhalten, die mit den individuellen Methoden nur unzureichend untersucht werden können. Als größte Herausforderung stelle es sich hierbei heraus, Polymernanopartikel im Zellkörper im TEM herauszuheben. Hierfür stehen zwei Strategien zur Verfügung, die entweder ein „aktives Anfärben“ des Polymers oder ein „passives Anfärben“ der Partikel ausnutzen. Ferner konnte die Korrelation von Fluoreszenz- und Elektronenmikroskopie realisiert werden. Als Ausblick dieser Arbeit kann die Korrelation beider Methoden experimentell so optimiert werden, dass das Übereinanderlegen beider Datensätze mit höchstmöglicher Genauigkeit geschieht. Die spezifischen Fluoreszenzsignale der Partikel können dabei Informationen über deren Lokalisierung innerhalb der Zelle bereitstellen und so in hervorragender Weise TEM-Daten ergänzen.

Die Korrelation von Licht- und Elektronenmikroskopie kann somit als Strategie (iii) verstanden werden, um polymere Nanopartikel in TEM-Aufnahmen hervorzuheben (Abbildung 6.1).

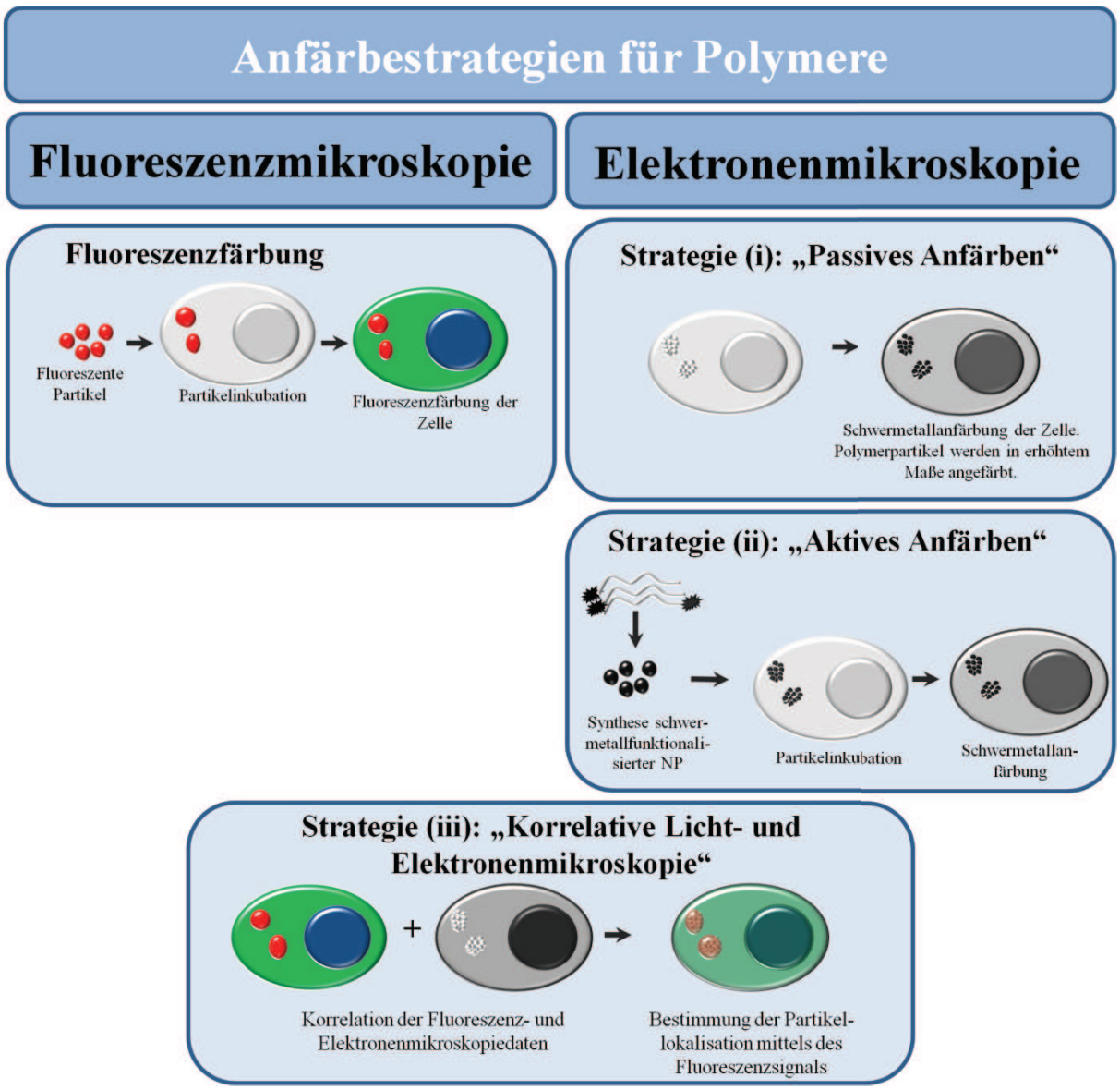

Abbildung 6.1: Zusammenfassung der in dieser Arbeit diskutierten Anfärbestrategien für Polymere. Um für das Fluoreszenzmikroskop kontrastiert zu sein, müssen die Nanopartikel mit einem Fluoreszenzfarbstoff gefärbt werden. Dies stellt heutzutage eine Standardmethode das. Um eine geeigneten Kontrast für das Elektronenmikroskop beizutragen, wurden im Rahmen dieser Arbeit drei Strategien diskutiert: (i) „Passives Anfärben“, d.h. das Inkubieren der Zellprobe konventionellen Schwermetallanfärbereagenzien, die sich in der Zellstruktur in geringerem und in der Partikelstruktur in hohem Maße anhäufen, (ii) „aktives Anfärben“, d.h. der gezielten Einbringung von Schwermetallen in die Polymerstruktur und (iii) einem korrelativen Ansatz, bei dem die spezifischen Fluoreszenzsignale ausgenutzt werden, um die Partikel im TEM-Mikrographen zu lokalisieren.

7. Acknowledgements

At this point, I want to express my honest gratitude to all people who supported me over the last years during my PhD time. First of all, I want to thank Prof. Dr. Ulrich S. Schubert for giving me the opportunity to work on this highly interesting interdisciplinary topic. It was a pleasure to work in his well-equipped labs in the ZAF. I was able to carry out all experiments in the same house – and I am well aware that this cannot be taken for granted. Furthermore, I want to thank Prof. Dr. Rainer Heintzmann for being my second supervisor. I want to thank him for introducing me into the very exciting world of microscopy with all his enthusiasm, for social activities and for fruitful discussions.

I sincerely would like to thank PD Dr. Stephanie Höppener for her continuous supervision over the past years, for giving me useful advices and for sometimes bringing back me on the right track. Even though times during this project have not always been easy, I hope she agrees to say that we eventually could manage it successfully. I also want to thank her for so many constructive discussions particularly in the writing phase, which helped me a lot to improve my manuscripts. Furthermore, I want to thank her for organizing social activities.

The work in a group would only be half as effective if there was not a good working atmosphere. Hence, I want to thank all the members of the “new” and “old” nanogroup members for making my time at work nicer: Pelin Sungur, Steffi Stumpf, Karina Zub, Aisha Womilijou and Limin Wong as well as Dr. Almut Schwenke, Dr. He Liu, Melanie Herzig, and Dr. Florian Kretschmer. Thank you for all valuable discussions – may they have been work-related or concerning topics apart from sciences. It was a pleasure to be part of this international group.

For me as a chemist it was not always easy to work on an interdisciplinary topic covering aspects of physics and biology. On the physics side, I would like to thank the group of Prof. Dr. Heintzmann, and in particular Dr. Walter Müller for a lot of useful discussions and for showing me that MATLAB is indeed sometimes a useful tool. On the biology side, there are many people to thank. First of all, I want to thank Elisabeth Preußger and Carolin Kellner for performing all the cell cultivation and

fluorescence staining experiments for me, for all discussions and useful advices concerning cell preparation/staining protocols, and for never complaining about me coming up with new requests ("anbei wieder einmal eine Wunschliste – schafft ihr das diese Woche noch?"). Thank you for your patience with me! Furthermore, I would like to thank Dr. David Pretzel for uncomplicated cooperations. I would also like to thank Tanja Bus, Dr. Alexandra Rinkenauer and Dr. Anja Träger, who helped me with their useful advices and sometimes direct criticism, and often showed me that a chemist underestimates the complicity of cell biology.

From the good old times in the synthesis lab, I would like to thank all my lab colleges in lab 128 for a constructive working atmosphere: Dr. Matthias Hartlieb, Dr. Turgay Yildirim (thank you for the cooperation, even though the results did not make it into this thesis), Dr. Meike Leiske, Anne-Kristin Trützschler and Dr. Christoph Englert. Furthermore, I thank Dr. Stephanie Schubert for introducing me into some aspects of nanoparticle preparation and Dr. Christine Weber for the introduction into polymer synthesis. Blerina Shkodra-Pula is acknowledged for providing me PLGA nanoparticles and Dr. Helmar Görls for determining the crystal structure analysis.

Last, but not least, I want to thank my friends for showing me that there is also a world apart from science, and for simply being there in some hours of darkness. And with that, also Stefan: Thank you for the nice time. You had to leave this world so early. Der letzte Satz dieser Arbeit gilt meinen Eltern und meiner Familie in deutscher Sprache: Danke für Eure Unterstützung während der Zeit meines Studiums, und natürlich auch darüber hinaus.

8. References

1. B. Vohnsen, *Phys. Scripta* **2004**, *T109*, 75-79.
2. H. Riesenberg, J. Bergner and H. Beyer, *Handbuch der Mikroskopie*, Verl. Technik, Berlin, **1988**.
3. M. Mulisch, U. Welsch and E. Aescht, *Romeis-Mikroskopische Technik*, Spektrum, Akad. Verlag, Heidelberg, **2010**.
4. A. R. Clarke and C. N. Eberhardt, *Microscopy techniques for materials science*, Woodhead Publishing, Cambridge, **2002**.
5. J. P. Patterson, Y. Xu, M.-A. Moradi, N. A. J. M. Sommerdijk and H. Friedrich, *Acc. Chem. Res.* **2017**, *50*, 1495-1501.
6. H. Jinnai, T. Higuchi, X. Zhuge, A. Kumamoto, K. J. Batenburg and Y. Ikuhara, *Acc. Chem. Res.* **2017**, *50*, 1293-1302.
7. J. J. Bozzola and L. D. Russell, *Electron microscopy: Principles and techniques for biologists*, Jones & Bartlett Learning, **1999**.
8. B. Traenkle and U. Rothbauer, *Front. Immunol.* **2017**, *8*, 1030.
9. J. Yu, *Annu. Rev. Phys. Chem.* **2016**, *67*, 565-585.
10. W. Yang and R. Yuste, *Nat. Meth.* **2017**, *14*, 349-359.
11. E. Park, E. B. Campbell and R. MacKinnon, *Nature* **2016**, *541*, 500.
12. R. Fernandez-Leiro and S. H. W. Scheres, *Nature* **2016**, *537*, 339.
13. F. Merino and S. Raunser, *Angew. Chem. Int. Ed.* **2017**, *56*, 2846-2860.
14. http://zeiss-campus.magnet.fsu.edu/articles/superresolution/introduction.html, *last accessed 2018-03-17*.
15. T. Kang, F. Li, S. Baik, W. Shao, D. Ling and T. Hyeon, *Biomaterials* **2017**, *136*, 98-114.
16. L. Zhu, Z. Zhou, H. Mao and L. Yang, *Nanomedicine* **2017**, *12*, 73-87.
17. M. Swierczewska, H. S. Han, K. Kim, J. H. Park and S. Lee, *Adv. Drug Deliv. Rev.* **2016**, *99, Part A*, 70-84.
18. M. R. Mohammadi, A. Nojoomi, M. Mozafari, A. Dubnika, M. Inayathullah and J. Rajadas, *J. Mater. Chem. B* **2017**, *5*, 3995-4018.
19. D. Wu, M. Si, H.-Y. Xue and H.-L. Wong, *Int. J. Nanomedicine* **2017**, *12*, 5879-5892.
20. A. C. Rinkenauer, S. Schubert, A. Traeger and U. S. Schubert, *J. Mater. Chem. B* **2015**, *3*, 7477-7493.
21. A. Kumari, S. K. Yadav and S. C. Yadav, *Colloids Surf. B Biointerfaces* **2010**, *75*, 1-18.
22. S. Ganta, H. Devalapally, A. Shahiwala and M. Amiji, *J. Controlled Release* **2008**, *126*, 187-204.
23. J. Zhuang, M. R. Gordon, J. Ventura, L. Li and S. Thayumanavan, *Chem. Soc. Rev.* **2013**, *42*, 7421-7435.
24. F. Wendler, K. R. A. Schneider, B. Dietzek and F. H. Schacher, *Poly. Chem.* **2017**, *8*, 2959-2971.
25. T. Yildirim, I. Yildirim, R. Yanez-Macias, S. Stumpf, C. Fritzsche, S. Hoeppener, C. Guerrero-Sanchez, S. Schubert and U. S. Schubert, *Polym. Chem.* **2017**, *8*, 1328-1340.
26. Y. Ibuki and T. Toyooka, in *Nanotoxicity: Methods and Protocols*, ed. J. Reineke, Humana Press, Totowa, NJ, **2012**, pp. 157-166.
27. R. Tantra and A. Knight, *Nanotoxicology* **2011**, *5*, 381-392.
28. R. M. Goodhead, J. Moger, T. S. Galloway and C. R. Tyler, *Nanotoxicology* **2015**, *9*, 928-939.
29. L. Schermelleh, R. Heintzmann and H. Leonhardt, *J. Cell Biol.* **2010**, *190*, 165-175.
30. H. Zhu, J. Fan, J. Du and X. Peng, *Acc. Chem. Res.* **2016**, *49*, 2115-2126.
31. K. Nienhaus and G. Ulrich Nienhaus, *Chem. Soc. Rev.* **2014**, *43*, 1088-1106.
32. J. E. Pawley, *Handbook of biological confocal microscopy*, Springer-Verlag, New York, **2006**.
33. C. Cremer and U. Birk, *Front. Phys.* **2016**, *4*, 11.
34. A. Jost and R. Heintzmann, *Annu. Rev. Mater. Res.* **2013**, *43*, 261-282.

35. L. Reimer, *Transmission electron microscopy: physics of image formation and microanalysis*, Springer, Berlin, **1993**.
36. M. Knoll and E. Ruska, *Ann. Phys. (Berlin)* **1932**, *404*, 607-640.
37. L. Marton, *Bull. Acad. Roy. Med. Belg.* **1935**, *21*, 600-617.
38. G. Knott and C. Genoud, *J. Cell Sci.* **2013**, *126*, 4545-4552.
39. C. J. Peddie and L. M. Collinson, *Micron* **2014**, *61*, 9-19.
40. D. J. Flannigan and A. H. Zewail, *Acc. Chem. Res.* **2012**, *45*, 1828-1839.
41. A. Vollrath, S. Schubert and U. S. Schubert, *J. Mater. Chem. B* **2013**, *1*, 1994-2007.
42. T.-G. Iversen, T. Skotland and K. Sandvig, *Nano Today*, **2011**, *6*, 176-185.
43. B. Yameen, W. I. Choi, C. Vilos, A. Swami, J. Shi and O. C. Farokhzad, *J. Controlled Release* **2014**, *190*, 485-499.
44. R. G. Parton and K. Simons, *Nat. Rev. Mol. Cell Biol.* **2007**, *8*, 185-194.
45. T. Kirchhausen, *Annu. Rev. Biochem.* **2000**, *69*, 699-727.
46. K. Sandvig, M. L. Torgersen, H. A. Raa and B. van Deurs, *Histochem. Cell. Biol.* **2008**, *129*, 267-276.
47. N. de Jonge and D. B. Peckys, *ACS Nano* **2016**, *10*, 9061-9063.
48. M. Reifarth, S. Hoeppener and U. S. Schubert, *Adv. Mater.* **2018**, *30*, 1703704.
49. D. Belazi, S. Solé-Domènech, B. Johansson, M. Schalling and P. Sjövall, *Histochem. Cell Biol.* **2009**, *132*, 105-115.
50. R. Kalluru, F. Fenaroli, D. Westmoreland, L. Ulanova, A. Maleki, N. Roos, M. Paulsen Madsen, G. Koster, W. Egge-Jacobsen, S. Wilson, H. Roberg-Larsen, G. K. Khuller, A. Singh, B. Nystrom and G. Griffiths, *J. Cell Sci.* **2013**, *126*, 3043-3054.
51. K. Cortese, A. Diaspro and C. Tacchetti, *J. Histochem. Cytochem.* **2009**, *57*, 1103-1112.
52. P. Chlanda and J. Krijnse Locker, *Biochem. J.* **2017**, *474*, 1041-1053.
53. K. L. McDonald, *J. Microsc.* **2009**, *235*, 273-281.
54. P. Webster, H. Schwarz and G. Griffiths, *Methods Cell Biol.* **2008**, *88*, 45-58.
55. J. Dubochet, M. Adrian, J.-J. Chang, J.-C. Homo, J. Lepault, A. W. McDowall and P. Schultz, *Q. Rev. Biophys.* **2009**, *21*, 129-228.
56. K. T. Tokuyasu, *Histochem. J.* **1980**, *12*, 381-403.
57. A. K. Varkouhi, M. Scholte, G. Storm and H. J. Haisma, *J. Controlled Release* **2011**, *151*, 220-228.
58. J. D. Lopez-Castro, A. V. Maraloiu, J. J. Delgado, J. J. Calvino, M. G. Blanchin, N. Galvez and J. M. Dominguez-Vera, *Nanoscale* **2011**, *3*, 4597-4599.
59. A. R. Mishra, J. Zheng, X. Tang and P. L. Goering, *Toxicol. Sci.* **2016**, *150*, 473-487.
60. R. K. Pathak, N. Kolishetti and S. Dhar, *Wiley Interdiscip. Rev. Nanomed. Nanobiotechnol.* **2015**, *7*, 315-329.
61. I. G. Macara, *Microbiol. Mol. Biol. Rev.* **2001**, *65*, 570-594.
62. K. Huang, H. Ma, J. Liu, S. Huo, A. Kumar, T. Wei, X. Zhang, S. Jin, Y. Gan, P. C. Wang, S. He, X. Zhang and X.-J. Liang, *ACS Nano* **2012**, *6*, 4483-4493.
63. C. Rosman, S. Pierrat, A. Henkel, M. Tarantola, D. Schneider, E. Sunnick, A. Janshoff and C. Sönnichsen, *Small* **2012**, *8*, 3683-3690.
64. A. Elsaesser, C. A. Barnes, G. McKerr, A. Salvati, I. Lynch, K. A. Dawson and C. V. Howard, *Nanomedicine (Lond.)* **2011**, *6*, 1189-1198.
65. B. Rothen-Rutishauser, D. A. Kuhn, Z. Ali, M. Gasser, F. Amin, W. J. Parak, D. Vanhecke, A. Fink, P. Gehr and C. Brandenberger, *Nanomedicine* **2013**, *9*, 607-621.
66. S. Lerch, S. Ritz, K. Bley, C. Messerschmidt, C. K. Weiss, A. Musyanovych, K. Landfester and V. Mailänder, *Nanomedicine* **2015**, *11*, 1585-1596.
67. R. Firdessa, T. A. Oelschlaeger and H. Moll, *Eur. J. Cell Biol.* **2014**, *93*, 323-337.
68. A. Musyanovych, J. Dausend, M. Dass, P. Walther, V. Mailänder and K. Landfester, *Acta Biomater.* **2011**, *7*, 4160-4168.
69. A.-K. Barthel, M. Dass, M. Dröge, J.-M. Cramer, D. Baumann, M. Urban, K. Landfester, V. Mailänder and I. Lieberwirth, *Beilstein J. Nanotechnol.* **2014**, *5*, 1905-1917.
70. Y. Lemmer, L. Kalombo, R.-D. Pietersen, A. T. Jones, B. Semete-Makokotlela, S. Van Wyngaardt, B. Ramalapa, A. C. Stoltz, B. Baker, J. A. Verschoor, H. S. Swai and C. de Chastellier, *J. Controlled Release* **2015**, *211*, 94-104.

71. R. Kalluru, F. Fenaroli, D. Westmoreland, L. Ulanova, A. Maleki, N. Roos, M. Paulsen Madsen, G. Koster, W. Egge-Jacobsen, S. Wilson, H. Roberg-Larsen, G. K. Khuller, A. Singh, B. Nyström and G. Griffiths, *J. Cell Sci.* **2013**, *126*, 3043-3054.
72. S. Mishra, P. Webster and M. E. Davis, *Eur. J. Cell Biol.* **2004**, *83*, 97-111.
73. R. E. Burge and N. R. Silvester, *J. Biophys. Biochem. Cytol.* **1960**, *8*, 1-11.
74. F. Wang, H.-B. Zhang, M. Cao, R. Nishi and A. Takaoka, *Micron* **2010**, *41*, 769-774.
75. I. Pozsgai, *Ultramicroscopy* **1997**, *68*, 69-75.
76. M. Reifarth, W. Müller, B. Shkodra-Pula, H. Görls, U. S. Schubert, R. Heintzmann and S. Hoeppener, *Part. Part. Syst. Charact.* **2019**, *36*, 1800324.
77. G. H. Michler, *Electron microscopy of polymers*, Springer Heidelberg, **2008**.
78. H. Hosseinkhani, F. Abedini, K.-L. Ou and A. J. Domb, *Polymer. Adv. Tech.* **2015**, *26*, 198-211.
79. S. K. Samal, M. Dash, S. Van Vlierberghe, D. L. Kaplan, E. Chiellini, C. van Blitterswijk, L. Moroni and P. Dubruel, *Chem. Soc. Rev.* **2012**, *41*, 7147-7194.
80. A. Tohsan and Y. Ikeda, *Chemistry, manufacture and applications of natural rubber*, Woodhead/Elsevier, Cambridge, **2014**.
81. T. Yildirim, A. C. Rinkenauer, C. Weber, A. Traeger, S. Schubert and U. S. Schubert, *J. Polym. Sci., Part A: Polym. Chem.* **2015**, *53*, 2711-2721.
82. A. Höcherl, M. Dass, K. Landfester, V. Mailänder and A. Musyanovych, *Macromol. Biosci.* **2012**, *12*, 454-464.
83. C. M. Thomas and J.-F. Lutz, *Angew. Chem. Int. Ed.* **2011**, *50*, 9244-9246.
84. N. Hernandez, R. C. Williams and E. W. Cochran, *Org. Biomol. Chem.* **2014**, *12*, 2834-2849.
85. R. Auras, B. Harte and S. Selke, *Macromol. Biosci.*, **2004**, *4*, 835-864.
86. R. E. Drumright, P. R. Gruber and D. E. Henton, *Adv. Mater.* **2000**, *12*, 1841-1846.
87. J. M. Anderson and M. S. Shive, *Adv. Drug Deliv. Rev.* **1997**, *28*, 5-24.
88. K. K.-W. Lo and K. Y. Zhang, *RSC Adv.* **2012**, *2*, 12069-12083.
89. Y. You, *Curr. Opin. Chem. Biol.* **2013**, *17*, 699-707.
90. X. Yang, G. Zhou and W.-Y. Wong, *Chem. Soc. Rev.* **2015**, *44*, 8484-8575.
91. C. Haensch, M. Chiper, C. Ulbricht, A. Winter, S. Hoeppener and U. S. Schubert, *Langmuir* **2008**, *24*, 12981-12985.
92. M. Reifarth, D. Pretzel, S. Schubert, C. Weber, R. Heintzmann, S. Hoeppener and U. S. Schubert, *Chem. Commun.* **2016**, *52*, 4361-4364.
93. K. Kim, W. C. W. Chen, Y. Heo and Y. Wang, *Prog. Polym. Sci.* **2016**, *60*, 18-50.
94. P. Zhang and E. Wagner, *Top. Curr. Chem.* **2017**, *375*, 26.
95. X. Zhong, D. Panus, W. Ji and C. Wang, *Mol. Pharm.* **2015**, *12*, 932-940.
96. N. Zuidam, G. Posthumab, E. de Vries, D. Crommelin, W. Hennink and G. Storm, *J. Drug Target*. **2000**, *8*, 51-66.
97. T. Bus, C. Englert, M. Reifarth, P. Borchers, M. Hartlieb, A. Vollrath, S. Hoeppener, A. Traeger and U. S. Schubert, *J. Mater. Chem. B* **2017**, *5*, 1258-1274.
98. F. Kretschmer, U. Mansfeld, S. Hoeppener, M. D. Hager and U. S. Schubert, *Chem. Commun.* **2014**, *50*, 88-90.
99. E. Fröhlich, *Int. J. Nanomedicine* **2012**, *7*, 5577-5591.
100. M. Reifarth, E. Preußger, U. S. Schubert, R. Heintzmann and S. Hoeppener, *Part. Part. Syst. Charact.* **2017**, *34*, 1700180.

List of abbreviations

α	electron attenuation coefficient
bPEI	branched poly(ethylene imine)
CLEM	correlative light and electron microscopy
CLSM	confocal laser scanning microscopy
CME	clathrin-mediated endocytosis
cryo-EM	electron microscopy under cryogenic conditions
CuAAC	copper-catalyzed alkyne-azide cycloaddition
Đ	dispersity index of polymers
DAD	diode array detection
DCTB	trans-2-[3-(4-tert.-butylphenyl)-2-methyl-2-propenylidene]malononitrile
DLS	dynamic light scatterin
DMAc	*N,N'*-dimethylacetamid
DMF	*N,N'*-dimethylformamide
DNA	deoxyribonucleic acid
EM	electron microscopy
(EM)CCD	(electron multiplying) charge-coupled device
EP	emulsion polymerization
ESI-ToF-MS	electron spray ionization time-of-flight mass spectrometry
FACS	fluorescence-activated cell scanning
FC	flow cytomety
HAADF	high-angle annular dark-field detection
$HAuCl_4$	chloroauric(III) acid
HEK-293	human embryonal kidney cell
(^{1}H)-NMR	(proton) nuclear magnetic resonance spectroscopy
I	intensity (of electron beam)
LiCl	lithium chloride
LM	light microscopy
lPEI	linear poly(ethylene imine)
LWF	laser widefield
MALDI-ToF-MS	matrix-assisted laser desorption ionization time-of-flight mass spectrometry
N/P ratio	nitrogen over phosphorous ratio
NA	numerical aperture
NaCl	sodium chloride

NE	nanoemulsion
NHS	*N*-hydroxysuccinimid
NP	nanoparticle
NPr	nanoprecipitation
OsO_4	osmium tetroxide
p	pixel area [μm^2]
P(MMA-*co*-DMAEMA)	poly(methyl methacrylate-*co*-2-dimethylaminoethyl methacrylate)
P(MMA-*co*-MAA)	poly(methylmethacrylate-*co*-methacrylic acid)
PDI	polydispersity index
pDNA	plasmid deoxyribonucleic acid
PEI	poly(ethylene imine)
PLA	poly(lactic acid), polylactide
PLGA	poly(lacti-*co*-glycolic acid)
PMMA	poly(methylmethacrylate)
PS	polystyrene
R	particle radius
RI	refractive index
SD	standard deviation
SDBS	sodium dodecylbenzenesulfonate
SEC	size-exclusion chromatography
SIM	structured illumination microscopy
STEM	scanning transmission electron microscopy
TEM	transmission electron microscopy
XTT	2,3-bis-(2-methoxy-4-nitro-5-sulfophenyl)-2*H*-tetrazolium-5-carboxanilide
Z	atomic number

Curriulum Vitae

Personal data:

Name:	Martin Reifarth
Date and place of birth:	August 25th 1986 in Nordhausen
Nationality:	German

Education:

12/2013 to present	**Doctoral project**, Friedrich-Schiller-Universität Jena Institute of organic chemistry and macromolecular chemistry (IOMC) *and* Institute of physical chemistry (IPC) „Uptake and intracellular fate of polymeric nanoparticles studied by light and electron microscopy" Supervision: PD Dr. Stephanie Höppener/Prof. Dr. Ulrich S. Schubert *and* Prof. Dr. Rainer Heintzmann
12/2012 to 09/2013	**Diploma thesis**, Friedrich Schiller University Jena Institute of physical chemistry (IPC) „Refractive index matching in optical microscopy" Supervision: Prof. Dr. Rainer Heintzmann
10/2008 to 09/2013	**Chemistry**, **Diploma** (equivalent to MSc.), Friedrich Schiller University Jena Specialization: Spectroscopy and photochemistry, Theoretical Chemistry/Computational chemistry, additional lectures in theoretical physics
09/2005 to 07/2008	**Chemical lab technician**, **apprenticeship**, Eurofins-AUA „Agrar- und Umweltanalytik
08/1997 to 07/2005	**University entrance qualification**, Gymnasium Albert Schweizer Sömmerda

Jena, _____ _____

Martin Reifarth

Publication list

Peer-reviewed articles

[1] M. Reifarth, D. Pretzel, S. Schubert, R. Heintzmann, S. Hoeppener, U. S. Schubert: "Cellular uptake of PLA nanoparticles studied by light and electron microscopy: synthesis, characterization and biocompatibility studies using an iridium(III) complex as correlative label", *Chem. Commun.* **2016**, *52*, 4361-4364.

[2] M. Reifarth, E. Preußger, R. Heintzmann, U. S. Schubert, S. Hoeppener, "Metal–Polymer Hybrid Nanoparticles for Correlative High-Resolution Light and Electron Microscopy", *Part. Part. Syst. Charact.* **2017**, *34*, 1700180.

[3] T. Bus, C. Englert, M. Reifarth, P. Borchers, M. Hartlieb, A. Vollrath, S. Hoeppener, A. Traeger, U. S. Schubert: "3rd generation poly(ethylene imine)s for gene delivery", *J. Mater. Chem. B* **2017**, *5*, 1258-1274.

[4] M. Reifarth, S. Hoeppener, U.S. Schubert: "Uptake and Intracellular Fate of Engineered Nanoparticles in Mammalian Cells: Capabilities and Limitations of Transmission Electron Microscopy—Polymer-Based Nanoparticles", *Adv. Mater.* **2018**, *30*, 1703704.

[5] M. Reifarth, U. S. Schubert, S. Hoeppener: "Considerations for the Uptake Characteristic of Inorganic Nanoparticles into Mammalian Cells—Insights Gained by TEM Investigations", *Adv. Biosys.* **2018**, 1700254.

[6] A.-K. Truetzschler, T. Bus, M. Reifarth, J. C. Brendel, S. Hoeppener, A. Traeger, U. S. Schubert: "Beyond Gene Transfection with Methacrylate-Based Polyplexes—The Influence of the Amino Substitution Pattern" *Bioconjugate Chem.* **2018**, *29*, 2181-2194.

[7] M. Reifarth, E. Preußger, R. Heintzmann, U. S. Schubert, S. Hoeppener, "Metal–Polymer Hybrid Nanoparticles for Correlative High-Resolution Light and Electron Microscopy", *Part. Part. Syst. Charact.* **2017**, *34*, 1700180.

Poster presentations:

[1] M. Reifarth, P.Sungur, S. Stumpf, S. Schubert, S. Hoeppener, R, Heintzmann, U. S. Schubert: "Luminescent Nanoparticles for *In Vitro* Studies Using Light and Electron Microscopy", European Polymer Congress, June 21st to 26th 2015, Dresden, Germany.

[2] M. Reifarth, S. Schubert, S. Hoeppener, R. Heintzmann, U. S. Schubert: „Cellular uptake of polymeric nanoparticles using light and electron microscopy", 51st Winter seminar – biophysical chemistry, molecular biology and cybernetics of cell functions, January 7th to 16th 2016, Klosters, Switzerland

Declaration of Authorship/Selbständigkeitserklärung

Ich erkläre, dass ich die vorliegende Arbeit selbständig und unter Verwendung der angegebenen Hilfsmittel, persönlichen Mitteilungen und Quellen angefertigt habe.

I certify that the present work is original and the result of my own investigations, except as acknowledged, and has not been submitted, either in part or whole, for a degree at this or any other university.

Jena, _____ _____

Martin Reifarth

Publications P1-P6

P1) M. Reifarth, S. Hoeppener, U.S. Schubert: "Uptake and Intracellular Fate of Engineered Nanoparticles in Mammalian Cells: Capabilities and Limitations of Transmission Electron Microscopy—Polymer-Based Nanoparticles", *Adv. Mater.* **2018**, *30*, 1703704.

P2) M. Reifarth, U. S. Schubert, S. Hoeppener: "Considerations for the Uptake Characteristic of Inorganic Nanoparticles into Mammalian Cells—Insights Gained by TEM Investigations", *Adv. Biosys.* **2018**, 1700254.

P3) M. Reifarth, W. Mueller, B. Shkodra-Pula, H. Goerls, U.S. Schubert, R. Heintzmann, S. Hoeppener: "Electron density of polymeric nanoparticles determined by image processing of transmission electron micrographs: Insights into heavy metal staining processes", submitted.

Publsihed as: Reifarth *et al.*, *Part. Part. Syst. Charact.* 2019, *36*, 1800324.

P4) M. Reifarth, D. Pretzel, S. Schubert, R. Heintzmann, S. Hoeppener, U. S. Schubert: "Cellular uptake of PLA nanoparticles studied by light and electron microscopy: synthesis, characterization and biocompatibility studies using an iridium(III) complex as correlative label", *Chem. Commun.* **2016**, *52*, 4361-4364.

P5) T. Bus, C. Englert, M. Reifarth, P. Borchers, M. Hartlieb, A. Vollrath, S. Hoeppener, A. Traeger, U. S. Schubert: "3rd generation poly(ethylene imine)s for gene delivery", *J. Mater. Chem. B* **2017**, *5*, 1258-1274.

P6) M. Reifarth, E. Preußger, R. Heintzmann, U. S. Schubert, S. Hoeppener, "Metal–Polymer Hybrid Nanoparticles for Correlative High-Resolution Light and Electron Microscopy", *Part. Part. Syst. Charact.* **2017**, *34*, 1700180.

Publication P1

"Uptake and Intracellular Fate of Engineered Nanoparticles in Mammalian Cells: Capabilities and Limitations of Transmission Electron Microscopy—Polymer-Based Nanoparticles"

Martin Reifarth, Stephanie Hoeppener, Ulrich S. Schubert

Adv. Mater. **2018**, *30*, 1703704.

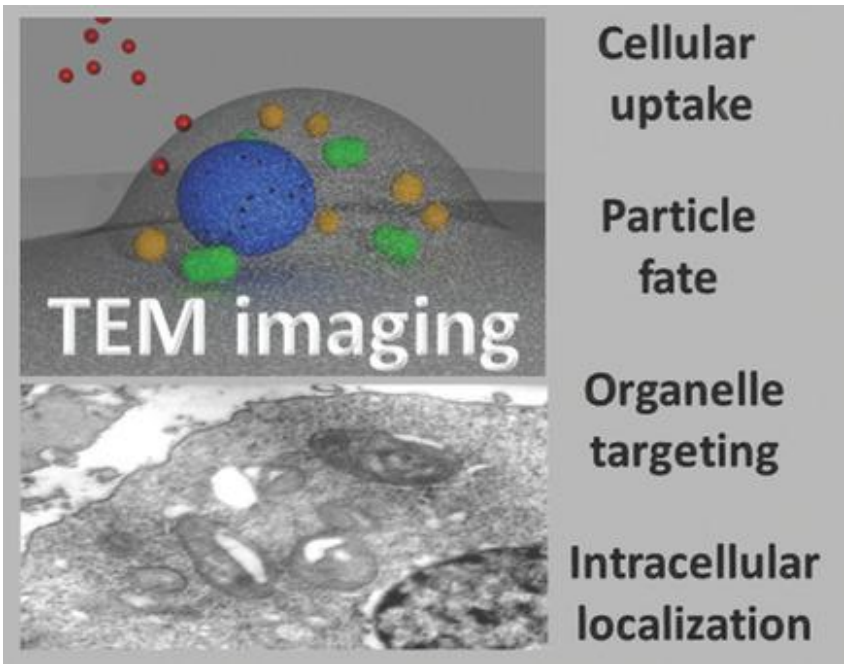

ADVANCED MATERIALS
www.advmat.de

Uptake and Intracellular Fate of Engineered Nanoparticles in Mammalian Cells: Capabilities and Limitations of Transmission Electron Microscopy—Polymer-Based Nanoparticles

Martin Reifarth, Stephanie Hoeppener, and Ulrich S. Schubert*

In order to elucidate mechanisms of nanoparticle (NP)–cell interactions, a detailed knowledge about membrane–particle interactions, intracellular distributions, and nucleus penetration capabilities, etc. becomes indispensable. The utilization of NPs as additives in many consumer products, as well as the increasing interest of tailor-made nanoobjects as novel therapeutic and diagnostic platforms, makes it essential to gain deeper insights about their biological effects. Transmission electron microscopy (TEM) represents an outstanding method to study the uptake and intracellular fate of NPs, since this technique provides a resolution far better than the particle size. Additionally, its capability to highlight ultrastructural details of the cellular interior as well as membrane features is unmatched by other approaches. Here, a summary is provided on studies utilizing TEM to investigate the uptake and mode-of-action of tailor-made polymer nanoparticles in mammalian cells. For this purpose, the capabilities as well as limitations of TEM investigations are discussed to provide a detailed overview on uptake studies of common nanoparticle systems supported by TEM investigations. Furthermore, methodologies that can, in particular, address low-contrast materials in electron microscopy, i.e., polymeric and polymer-modified nanoparticles, are highlighted.

1. Introduction

Several thousand tons of engineered nanoparticles (NPs) per year are produced worldwide.[1] Applications of nanoparticles cover the fields of materials science, electronics,[1,2] dyes, pigments and paint technology,[3] catalysis,[4] antibiotics as well as antifouling,[5] and many others. Unsurprisingly, nanoparticles have found their way into the environment and have recently been discussed as being potential pollutants.[6] Furthermore, we face nanomaterials directly in our everyday life since they are used in food industry,[7] as additives in personal care products,[8] as contrast agents in medical imaging applications,[9] etc. Moreover, NPs have gained recent interest due to their outstanding properties which make them potentially applicable in biomedicine,[10] e.g., as probes in optical (bio)sensing,[11] or as drug delivery agents[11c,12] resulting in the establishment of potentially superior and novel theranostic approaches inter alia. In the field of drug delivery, in particular, polymeric nanoparticulate materials have gained increasing attention in recent years.[13] Owing to the potential biodegradability of some polymeric material, the biocompatibility of the polymers and their degradation,[14] as well as the manifold synthetic possibilities, which enable the introduction of, e.g., stimuli-responsive functionalities,[15] polymeric nanoparticles exhibit excellent properties which make them suitable materials, e.g., to achieve controlled release.

The toxicological potential of nanomaterials and their biomedical impact raise increasingly the issues what impact nanoparticles have on biological specimens and how their biological functions are affected. These questions have to be discussed thoroughly in vivo and in vitro to achieve a clear elucidation of promises and threats of the particles. On the cellular level this discussion includes an accurate assessment of the internalization mechanism of particles into cells, i.e., their cellular uptake mechanism, as well as the particles' intracellular fate. In general, uptake studies rely on a large portfolio of different characterization tools, including biophysical studies, the investigation of protein expression, flow cytometry based methods, etc. In order to obtain a deeper insight on the cellular level, advanced imaging techniques are indispensable.[16] Traditionally, fluorescence based techniques are used to provide a detailed view on cellular processes.[17] For this purpose, appropriate labeling facilitates a distinct assignment of the corresponding fluorescence signal to the NPs inside the cells as well as to the cellular components. These features make fluorescence microscopy a powerful method; however, light microscopy based techniques

M. Reifarth, Dr. S. Hoeppener, Prof. U. S. Schubert
Laboratory of Organic and Macromolecular Chemistry (IOMC)
Friedrich Schiller University Jena
Humboldtstr. 10, 07743 Jena, Germany
E-mail: s.hoeppener@uni-jena.de
M. Reifarth, Dr. S. Hoeppener, Prof. U. S. Schubert
Jena Center of Soft Matter (JCSM)
Friedrich Schiller University Jena
Philosophenweg 7, 07743 Jena, Germany
The ORCID identification number(s) for the author(s) of this article can be found under https://doi.org/10.1002/adma.201703704.

DOI: 10.1002/adma.201703704

only provide restricted resolution capabilities as dictated by Abbe's resolution limit. Classical fluorescence microscopy supports a resolution of ≈200 nm in lateral and 500–700 nm in axial direction,[18] hence, hampering the visualization of individual particles due to their small size being in the nanometer range. Although recent advances in the field of superresolution fluorescence microscopy techniques[19] improved the fluorescence based imaging capabilities,[18] single particle imaging in the cellular context by means of superresolution microscopy still remains an experimentally demanding task.[20]

EM represents a more suitable technique, since it provides a resolution in the nanometer range, in particular for transmission electron microscopy (TEM) which facilitates the localization of nanoparticles in the cellular framework and provides, moreover, access to the ultrastructural information level of the cell system. Fueled by optimized preparation and staining protocols as well as a sustained improvement of instrumentation, TEM high-resolution studies gained continuously increasing importance over the last decades.[21] Thereby, their benefits are based on the capability to image organelles and membrane structures with an appropriate contrast with a resolution unmatched with other techniques. Consequently, TEM plays an important role in biological investigations on cellular systems since no alternative techniques support a direct view on changes induced on the subcellular or even on the macromolecular level.[21a] However, also drawbacks of electron microscopy have to be discussed. The relatively time-consuming sample preparation techniques—including fixation, embedding, heavy metal staining, and slicing—represent experimentally demanding steps which require experienced skills. Moreover, the excellent resolution capabilities of TEM are impaired by a small field-of-view which impedes studies on larger biological specimens, such as entire organisms. The major drawback of EM studies of biological specimens is related to the fact that sample preparation protocols include immobilization of the samples, either by resin embedding or by treatment under cryogenic conditions.[21a,22] Thus, this technique only provides a static snapshot of the sample, prohibiting the investigation of dynamic cellular processes.

Polymeric nanoparticles, which are discussed within the scope of this review, enter increasingly the focus of scientific research during the last years.[13b,c,23] It has to be emphasized that they are significantly more difficult to be investigated by EM techniques since they feature only low contrast due to the fact that they basically consist of the same elements being present in the cell itself (carbon, hydrogen, oxygen, nitrogen, sulfur etc.). Furthermore, their stability toward the conditions of the sample preparation and measurement needs to be carefully adjusted.

Motivated by the excellent capabilities of EM imaging in nanoparticle research as well as the increasing interest within the past years we will highlight important studies focusing on the uptake and intracellular fate of polymeric nanomaterials as well as polymer-metal (oxide) hybrid nanocomposites in mammalian cells in this review. This includes a thorough discussion on particle–membrane interactions, their subcellular distribution, their aggregation state inside the cells, etc. The gained information facilitates deeper insights into the mode-of-action of polymer nanoparticles and different polymer classes and provides a better understanding of their toxicity, which ultimately boosts the nanoparticles' applicability as biomedical platforms. Special focus is placed in this review on studies which utilized electron microscopy as a valuable tool to obtain information on the internalization and the fate of nanoparticles in different cells. Since scientific progress is associated with the accessibility of a large number of biocompatible and biodegradable polymers which promise a more flexible utilization, e.g., for targeted delivery applications, those particle systems will be discussed intensively.

Martin Reifarth studied chemistry at the Friedrich Schiller University Jena, Germany. Since December 2013, he has been working on his Ph.D. thesis in the groups of Prof. Ulrich S. Schubert and Prof. Rainer Heintzmann, focusing on the uptake and intracellular fate of polymer-based nanoparticles studied by fluorescence and transmission electron microscopy. Alongside high-resolution microscopy, his research interests cover nanoparticle synthesis and characterization.

Stephanie Hoeppener studied physics at the Westfälische Wilhelms-University Münster, Germany, where she earned her Ph.D. degree in 2001 under the supervision of Prof. H. Fuchs and Prof. L. F. Chi. Thereafter; she joined the group of Prof. J. Sagiv at the Weizmann Institute of Science, Israel, as a Minerva fellow. In 2003 she moved to the group of Prof. U. S. Schubert, Eindhoven University of Technology, The Netherlands. Since 2009, she has been the project leader for Nanolithography and Surface Functionalization, and is responsible for electron microscopy in the Jena Center for Soft Matter at the Friedrich Schiller University Jena, Germany.

2. Short Introduction into Polymer-Based Particle Systems—Synthesis Strategies, and Characterization

Engineered nanomaterials include inorganic, i.e., (semi-)metal or (semi-)metal chalcogenide based, and all-polymer nanoscale objects (**Figure 1**A–D). Additionally, also inorganic nanoparticles exist which feature a macromolecular coating, thus, representing hybrid composites of inorganic and all-polymer systems.

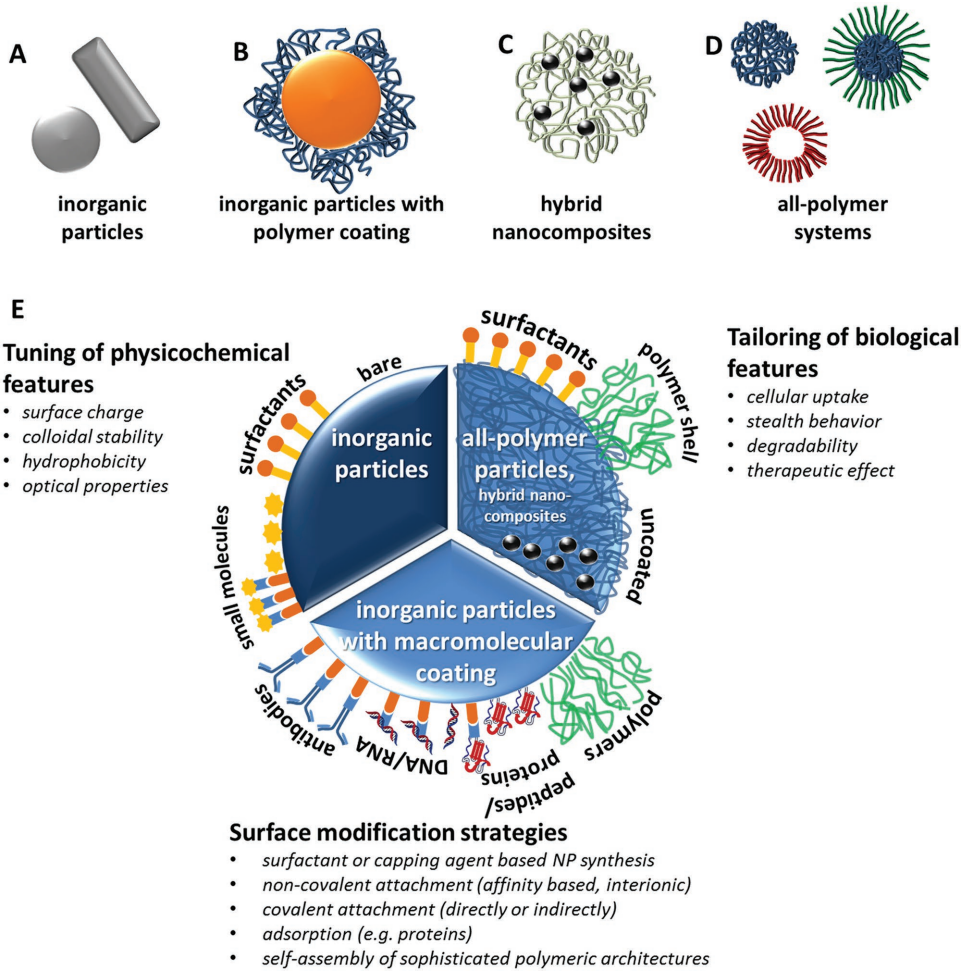

Figure 1. Overview of different classes of nanomaterials. A) Inorganic particles, i.e., particles consisting of (semi-) metals or (semi-) metal oxides, are accessible in different shapes. B) Different synthetic methods facilitate the attachment of a polymer coating at the particle surface. C) Hybrid nanocomposites constitute nanoscale materials assembled of small inorganic nanoparticles incorporated in a polymeric framework. D) All-polymer systems represent nanomaterials consisting of polymers only. Depending on the polymer architecture, nanoparticles, micellular structures, or vesicles etc. may form due to self-assembly processes. E) Possible surface modifications of inorganic or all-polymer particles: the surface modification alters the physicochemical as well as the biological properties of the particles, and influences the uptake as well as the mode-of-action of nanoparticle systems.

The class of hybrid nanocomposites includes furthermore inorganic NPs incorporated in a polymeric framework.

A predominant role for the biological performance and uptake of nanoparticles plays in particular the surface of the nanoparticles, since the particle surface represents the interface responsible for cell interaction.[24] Surface modification of NPs tunes their physicochemical properties, such as, surface charge, optical properties, and/or stability as well as their biological properties, like cellular uptake, degradability, stealth behavior, etc. (Figure 1E). It has to be mentioned that each of these functionalization steps alters the biological activity of the nanoparticle systems and a careful evaluation of the biological response of cellular systems has to be conducted for each nanoparticle system. The possibility to attach a variety of (reactive) functionalities onto inorganic NPs' surfaces enables the indirect covalent or noncovalent attachment of ligands, such as, sugars, antibodies, nucleic acids, proteins, or peptides, e.g., by means of click-chemistry, ionic or hydrophobic interactions, or interface affinities. Furthermore, there are various methods to introduce covalent and noncovalent polymer coatings onto inorganic particles which can alter the particles' behavior to result in an increased biocompatibility or decreased cytotoxicity in vitro and in vivo as well as in targeted delivery strategies.[10b] As an example, functionalization of NPs with polyethylene glycol (PEG) often results in an improved particle performance.[25] PEG is known to induce a stealth behavior which renders the particles "undetectable" for the immune system. Furthermore, protein adsorption onto the particle surface can be reduced, resulting in a decreased particle agglomeration. PEGylation of particles also results in prolonged blood circulation in vivo.

All-polymer nanoparticles are accessible as uncoated or surfactant-modified structures based on hydrophobic polymers.[26] The utilization of polymeric nanoparticles as vehicles for drug delivery applications has gained increasing interest during the last years and the field encountered tremendous interest.[13a,b] This is related to their excellent endocytosis efficiency, passive and active tumor-targeting, and the possibility of encapsulating a wide range of therapeutic agents with a high encapsulation

efficiency.[27] Polymeric nanoparticles can be formed by a large variety of different monomers. This allows an efficient tuning of their properties for many applications by engineering their size, shape, surface charge, as well as by introducing targeting units to control their interaction.

Moreover, self-assembled nanoparticle structures, such as micelles or vesicles, can be obtained by tailored block copolymer architectures in aqueous solution.[28] Additionally, biodegradable polymers can be employed with exceptional drug release capabilities.

Starting from water-insoluble polymers, nanoprecipitation represents a facile strategy to access polymer nanoparticles.[29] This method utilizes a water-miscible solvent, e.g., acetone or tetrahydrofurane, to dissolve the polymer, whereas water represents a nonsolvent for the polymer. A careful dropping of the polymer solution into the nonsolvent or a careful addition of the nonsolvent to the polymer solution, respectively, yields polymer nanoparticles, if all components' concentrations are optimized to achieve nanoprecipitation rather than polymer flocculation.[26] This method does not necessarily require the use of surfactants and enables also the encapsulation of hydrophobic substances. Nanoemulsion techniques represent a different approach to access polymeric nanostructures. This method starts from a polymer solution in a solvent that is not miscible with water, e.g., dichloromethane or ethyl acetate. Within this method, a two-phase system consisting of the polymer solution and water is emulsified by means of ultrasonication, followed by solvent evaporation to allow the "hardening" of the NPs.[14] In order to stabilize the aqueous emulsion the use of surfactants is essential. With this method, the encapsulation of hydrophobic substances is possible. A further modification of the protocol is the double-emulsion method, which enables encapsulation of hydrophobic as well as hydrophilic substances.[30] On the basis of this method, also the incorporation of small metal (oxide) particles into a polymer framework is possible, which results in the formation of larger metal (oxide)-polymer nanocomposites; e.g. nanoparticulate systems based on polyesters have been reported (for a more detailed discussion, see Section 5.1).

In order to prove the success of nanoparticle syntheses and surface modifications, a variety of investigation tools is available (**Figure 2**). Light scattering methods, such as, dynamic and static light scattering (DLS and SLS), provide statistically significant data of the size distribution and geometrical features of particles in solution and indicate aggregation effects.[31] UV–vis and Raman spectroscopy as well as zeta-potential measurements provide insights into their surface properties.[32] However, electron microscopy methods (scanning electron microscopy (SEM) and TEM) provide the most commonly used possibilities to directly image individual particles and to provide information on the particle size, and the particle shape, respectively.[32] TEM investigations, in particular, facilitate the observation of morphology changes subsequently to a surface modification step. With that, e.g., the successful attachment of a polymer shell on a particle surface can be investigated due to different electron densities of the inorganic core particle and the less electron-dense polymeric shell.[33] Furthermore, TEM investigations provide insights into the particles' aggregation state, whereby particularly TEM imaging under cryo conditions can be applied to examine the particle aggregation behavior in aqueous solution.[32]

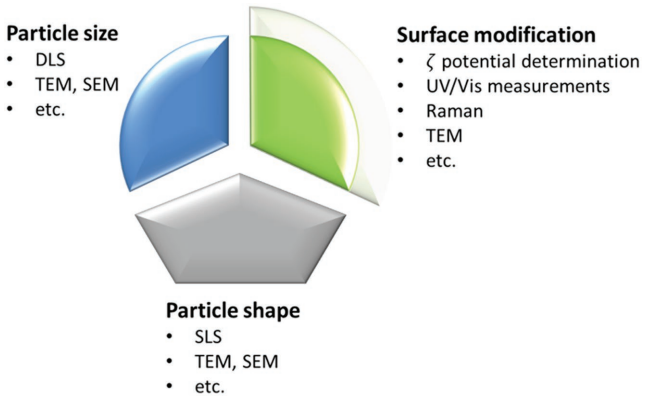

Figure 2. Overview of selected particle characterization methods.

Next to a careful elucidation of the nanoparticles' physicochemical properties, which are of tremendous importance for their interactions with mammalian cells (see Section 4.), special requirements are placed on the preparation of cellular systems treated with the respective nanoparticles. This step is of utmost importance as issues like sample stability and a preservation of the cells close to their native state have to be taken into consideration. Additionally, the quality of ultrastructural investigations and the possibility to localize polymer nanoparticles in the cellular matrix critically depends on the quality of the prepared specimens.

3. Preparation of Cell Specimens for TEM Investigation

This section will provide a general overview of requirements and preparation strategies to enable the investigation of cellular samples by TEM and to facilitate the imaging and localization of polymeric nanoparticles within the cellular environment. We will provide at this stage only a general overview, as the protocol of choice critically depends on the cellular system and has to be adapted for the individual aspects of interest for each system. For detailed information we refer to a number of comprehensive book chapters as well as review articles on this subject.[21a,34]

Major goals of the preparation procedure are (1) to preserve the ultrastructure of the cells close to their native state (fixation), (2) to prepare thin slices (typically 50–150 nm) of the cellular samples, in order to facilitate TEM imaging (embedding and slicing), and (3) to highlight ultrastructural features and/or the nanoparticles by improving their intrinsically weak electron contrast in the cellular environment (staining).

The classical standard procedure for cell preparations includes first the fixation step, which most frequently is performed by treatment of the cell sample with glutaraldehyde. This step results in the cross-linking of proteins and inactivates the enzyme activity. Additionally, osmium tetroxide (OsO_4) is used in a postfixation agent OsO_4 interacts with unsaturated lipids, among others, which are present, e.g., in double-layered

membranes,[35] and a reduction of the Os takes place. As a side effect, OsO_4 introduces already a first staining due to the accumulation of the heavy element Os and, hence, improves the contrast of all cellular or nanoparticle components which bear unsaturated carbon bonds. The systematic chemical fixation involving glutaraldehyde and osmium tetroxide treatment immobilizes and stabilizes proteins as well as lipid structures;[38] nevertheless, the integrity and functionality of these structures might be affected, which results in an alteration of their morphology.

In order to obtain ultrathin sections of the biological specimens, their embedding into a polymeric network becomes mandatory. For this purpose, resin embedding techniques represent the standard sample preparation method. As a consequence, the samples need to be dehydrated and infiltrated with reactive monomeric compounds. Triggered by exposure to heat (curing temperatures typically ≈60–70 °C), the monomers form a resin with a 3D network.[21a] At a first glance, these rather harsh protocol steps might be considered as invasive; however, they represent a powerful and well-established, reproducible method and are, thus, widely applied. Standard resin embedding media are, e.g., Epon 812 (and improvements thereof), araldite, Spurr's medium, and LR white.[21a] In the context of uptake studies of polymeric nanoparticles, the suitability of these standard techniques needs to be adjusted carefully. Therefore, it has to be kept in mind that the stability of polymer colloids might be limited under the presence of the hydrophobic resin monomers infiltrating the biological sample, since the polymeric nanomaterial itself features hydrophobic properties.[37] The preparation step is finalized by slicing the resin blocks into small and thin sections by ultramicrotomy, which are subsequently attached to the microscopy grids.

In a final step additional staining is performed to further increase the contrast of the samples. Similar to OsO_4 which attaches to unsaturated lipids, other staining agents can be employed to highlight other cellular structures. Staining with uranyl acetate ($UO_2(OOCCH_3)_2$) as well as lead citrate ($Pb_3(C_6H_5O_7)_2$), which interact efficiently with different functional groups in the biological sample, result in a specific highlighting of different (membrane) structures. Additonally, uranyl acetate and lead citrate are assumed to be involved in reacting with phosphate groups present in nucleic acids, amino groups in form of protein features, and carboxy functionalities among others.[21a,38] Hence, ultrastructural details such as membrane morphologies, organelles, etc. are amplified in terms of their contrast in TEM imaging.

There are many variations and combinations of different fixation, embedding and staining, and the necessity to adapt and optimize these conditions is evident. Furthermore, these chemical fixation protocols can be considered to be rather harsh. In order to circumvent these harsh conditions alternative, milder sample preparation methods have been established. These techniques include vitrification steps, i.e., freezing of the sample to achieve a physical immobilization of lipids and proteins in such a way that the formation of ice crystals is prevented to avoid membrane or organelle rupture. This can be achieved, e.g., by plunge-freezing, i.e., the rapid placement of a small sample fraction into liquid nitrogen or ethane. However, due to reduced cooling rates this preparation protocol is restricted to thin samples only. Alternatively, high-pressure freezing, i.e., deep-freezing protocols under reduced temperature and at elevated pressures have been developed.[39] The resulting frozen samples can be imaged directly under cryogenic conditions (cryo-EM). Thereby investigations on relatively thick samples are often favored, since imaging over an increased sample volume results in an enhanced signal-to-noise ratio.[40] However, a distinct assignment of the 3D ultrastructures in axial direction within a thick section requires the acquisition of multiple images from different tilt angles in a sense of a tomography series and subsequent reconstruction of the 3D structure.[41] Alternatively to cryo-EM, a method employing sucrose-solution as cryo-protectant was established to prevent elaborate TEM imaging under cryo-conditions. With that, thawing of the obtained sections to room temperature is enabled. The method, which is referred to as Tokuyasu cryosectioning, is also compatible with fluorescence imaging.[42] Additionally to the techniques in which embedding is avoided, freeze-substitution techniques utilize a slow infiltration of reactive monomers into the biological specimen under reduced temperature. This method represents a mild embedding procedure also compatible with fluorescence imaging.[43] The pros and cons of the individual approaches with respect to membrane imaging are reviewed by Chlanda and Krijnse Locker.[44]

In conclusion, resin-embedding techniques constitute the standard sample preparation technique and represent, hence, the best known, established protocols. However, they rely on a harsh dehydration and monomer infiltration procedure and it has to be kept in mind that the investigated polymeric nanomaterial, which exhibits hydrophobic properties itself, might lack stability under these hydrophobic conditions. In order to reduce the exposure of the polymeric nanomaterials toward hydrophobic solvents and monomers used for resin embedding or to prevent morphological changes, cryo-based methods represent mild alternatives to the conventional standard resin-embedding methods. Freeze-substitution techniques working at reduced temperatures, as well as also Tokuyasu cryosectioning or TEM under cryogenic conditions, respectively, constitute the least invasive methods. However, the applicability of these techniques has to be discussed with respect to experimental effort, the availability of instrumentation, as well as their potential to access ultrastructural details of the biological sample, which can be reduced in comparison to conventional methods.

All cell preparation techniques include laborious sample preparation protocols involving a physical sectioning of the cells. Recent developments in electron microscopy aim for the imaging of hydrated samples. These techniques include, e.g., environmental scanning electron microscopy.[45] Conventional SEM represents an EM method, in which a small electron spot is used to scan the sample and the secondary electrons and/or back-scattered electrons are detected, resulting in an image of the sample surface.[21a] As a hybrid method in between SEM and TEM scanning transmission electron microscopy (STEM) can be used.[46] Here a focused electron beam scans the sample and the electrons transmitted through the sample are detected. Advantages of the utilization of STEM are the possibility to investigate thicker samples and the fact that, by utilizing high angle annular dark field detectors, a material specific contrast and, thus, an improved image contrast can be achieved. This

approach can as well be applied to wet samples,[47] which are prepared in special liquid cells consisting of two electron-transparent windows of silicon nitride. This approach is compatible with fluorescence microscopy investigations in a correlative fashion.[48] These novel approaches aim for imaging cells in a natural state, however, still the image quality with respect to resolution and contrast is inferior compared to conventional TEM images.

4. Capabilities and Limitations of Transmission Electron Microscopy in Cellular Uptake and Intracellular Fate

There are several capabilities of transmission electron microscopy to investigate nanoparticle interactions with biological specimens which can boost the understanding of the particles' mode-of-action and internalization. Owing to the fact that EM provides a resolution in the nanometer range, which is to date unmatched with other techniques, this method is perfectly suitable to image individual nanoparticles within the biological context. In addition, heavy metal staining protocols result in the accumulation of electron-dense material in subcellular structures (such as membranes, proteins, or nucleic acids), allowing the observation of morphological ultrastructural details within the cell. A thorough investigation of nanoparticle–cell interactions includes an elucidation of the particle uptake as well as the particles' subsequent intracellular fate. Cellular uptake mechanisms, which can be grouped into active or passive processes, are mechanistically related to the response of the plasma membrane to the approaching nanoobject.[49] Since TEM is capable of imaging characteristic membrane features, this method enables the elucidation and determination of individual particle uptake events and it provides access to determine their uptake mechanism. A schematic illustration of typical uptake mechanisms highlighting their characteristic membrane features associated with the particular uptake mechanisms is depicted in **Figure 3** and a more detailed discussion of these processes is reviewed elsewhere.[49]

Active uptake mechanisms represent energy-dependent processes and are associated with membrane protrusions or invaginations. Small particles can be taken up via caveolin-dependent endocytosis. Caveolae constitute small membrane invaginations with a typical size of ≈60–80 nm which participate in different cellular processes, such as signal transduction, cholesterol homeostasis or the endocytosis of proteins, among others.[50] These structures are present in many cell types, including fibroblasts, smooth muscle cells, endothelial cells, and in particular in adipocytes.[49b] Due to their characteristic flask-shaped structures they can be reliably identified by means of TEM. Clathrin-mediated endocytosis (CME), one of the most intensively studied uptake mechanisms, involves intracellular signaling, membrane recycling, and the uptake of nutrients.[51] CME can be identified by membrane invaginations with a size of ≈100 nm which are coated with the morphologically distinguishable protein clathrin. The clathrin-coated membrane pits, which are observable in all cell types, are able to bind specific receptors by which the majority of all receptor-mediated uptake processes are facilitated.[49b] Clathrin-independent endocytosis facilitates the internalization of abundant bacterial toxins, surface proteins, and is discussed to participate in intercellular signaling, plasma membrane repair, etc.[52] Larger particles are taken up via phagocytosis, a mechanism that is only possible for specialized cell types. This uptake mechanism can be identified by characteristic membrane protrusions.[49b] In contrast,

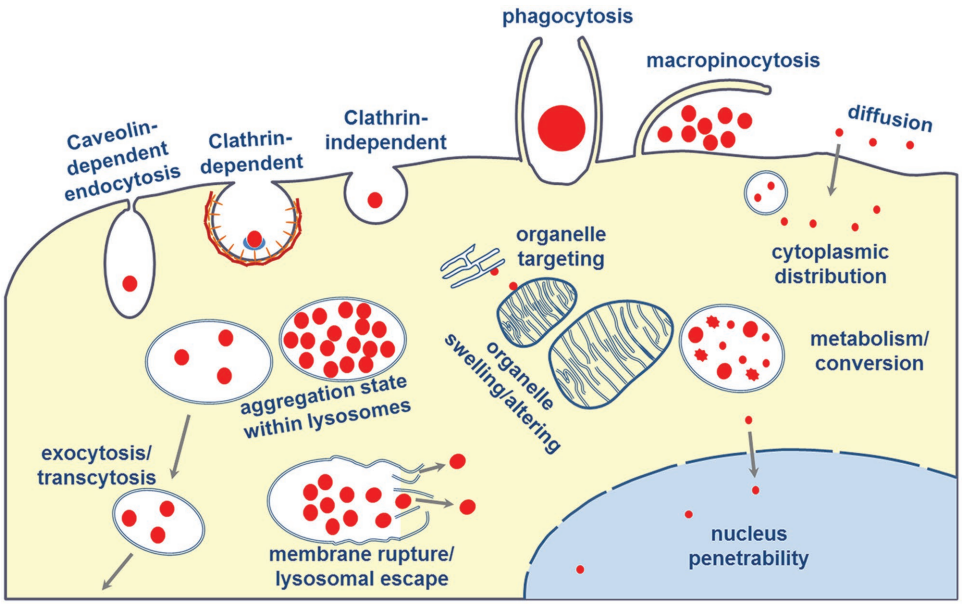

Figure 3. Individual events observable by means of transmission electron microscopy on ultrathin cell sections. A profound inspection of membrane features allows the identification of particle uptake mechanisms. Furthermore, TEM images provides insight into the intracellular localization as well as into the fate of the particles, e.g., the cytoplasmic distribution, the vesicular localization, the aggregation state within the lysosomes, organelle targeting, lysosomal escape, nucleus penetrability as well as particle conversion or metabolism, among others.

macropinocytosis represents an actin-driven endocytic uptake mechanism, facilitating the internalization of large structures, such as, aggregated particles. This uptake mechanism is characterized by the occurrence of membrane ruffles. Furthermore, particles internalized by macropinocytosis are found in large vesicles which are mainly filled with cellular fluids.[49b] Passive uptake is possible for small particles, which internalize via diffusive mechanisms through the cellular membrane directly into the cytosol.

After internalization particles are either associated with intracellular vesicles (endosomes or lysosomes) or are freely distributed inside the cytosol. This is clearly distinguishable on the basis of TEM investigations since intracellular vesicles represent less electron dense structures inside the electron denser cytosol. In addition, mitochondria can be identified by their inner double-layered membranes which possess a characteristic "wrinkled" shape (i.e., cristae). Authophagosomes are observable as double- or multilayer spherical organelles.[53]

Due to the fact that TEM provides a resolution sufficiently high enough to identify individual particles, EM data generate valuable information on the particle aggregation state within the lysosomes as well. However, it has to be mentioned that on the basis of TEM data only, it is frequently impossible to clearly differentiate, e.g., between lysosomes and endosomes. For this purpose, supplementary fluorescence imaging represents an important tool to provide direct evidence for the nature of the intracellular compartments. Additionally, the capability of EM to observe the rupture of vesicular membrane structures is an adjuvant feature to validate, e.g., the suitability of particles as drug delivery agents, since lysosomal escape of particles or particle cargos constitutes a desired requirement in controlled drug release.[54] Conversely, particle systems might also be exocytosed or transcytosed, which is important to investigate, for instance, to understand particle transfer through cellular barriers.[55] In addition, NPs can be metabolized or converted into smaller or morphologically different nanoobjects within the cellular interior, which might address particular organelles and/or affect their structures or functionalities.[56] Finally, nucleus penetration, as a desired or undesired feature of engineered particles, can cause genotoxic effects on the cell and is therefore subject of several investigations.[57]

Another important question is the degradation of nanoparticles in the intracellular context. This issue can be efficiently addressed by EM investigations as particle shapes and sizes can be accessed on the individual particle level. However, next to these possibilities TEM features also drawbacks. The necessity to obtain samples, which can be investigated under ultrahigh vacuum (UHV) conditions requires their fixation and, hence, it is not possible to measure them in a living state. Even though liquid cells are available these days, the high energy-dose of the electron beam prevents the compatibility of electron microscopy with live cell imaging.[58] Hence, EM investigations are merely restricted to imaging fixed cell samples and investigations of dynamic events are prohibited. Furthermore, the choice of the subsequent sample preparation protocol needs to be carefully adjusted with respect to the stability of the polymeric nanomaterials in response to the hydrophobic and highly reactive chemicals used for embedding and chemical fixation of the cells (for a more detailed discussion, see Section 3).

Electron microscopy represents a method which generally is not designed for high-throughput investigations. Therefore, only a careful analysis of statistical data obtained on the basis of TEM images can result in an increased reliability of the interpretation, e.g., of a suspected mode-of-action of a nanoparticle system. For instance, particle numbers associated with organelle localization could underline suspected mechanisms and, thus, boost the meaningfulness of the obtained data. There are several obstacles to address in order to acquire statistically relevant data on the basis of TEM images. TEM images of an embedded sample represent only a thin slice, i.e., a small sample volume of the entire cell. In order to deduct the particle uptake into an entire cell volume from images acquired on thin slices, statistically based knowledge about the shape of a single cell becomes mandatory.[59] For this purpose, stereological information can be obtained either on the basis of light-microscopy approaches[59a,c] (**Figure 4**) or by an unbiased sampling method for electron microscopy,[61b] resulting in a 3D model of an average cell that can be found in the sample. Due to the high number of cells which are necessary to be imaged, accompanied

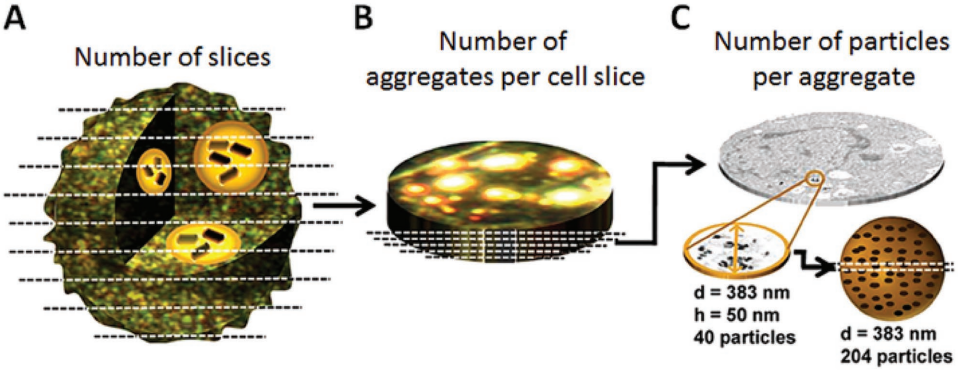

Figure 4. Scheme of the stereological approach for the estimation of the particle number per cell. A) Acquisition of the number of slices necessary to image an entire cell (N_{slice} = diameter of the cell/slice thickness). Dark-field microscopy (DFM) images facilitate the determination of the diameter. B) Measurement of the number of aggregates found in a single slice ($N_{aggregates}$) as indicated by the number of signals provided by DFM. C) Determination of the number of particles per aggregate ($N_{particles}$) on the basis of TEM, which have been corrected for the 3D volume of the aggregate. The total number of particles per cell can be calculated by $N = N_{slice} \times N_{aggregates} \times N_{particles}$. Reproduced with permission.[59a] Copyright 2012, Wiley-VCH.

with a thorough handling of the statistical data, this method represents a rather time-consuming approach. If general statistical analysis is performed by investigation of a large number of individual cells, the cells can be, e.g., categorized into uptake positive and negative groups. Based on these data a measure for the relative uptake efficiency can be provided.

Rosman et al. for instance investigated the uptake of spherical particles (AuNPs, diameter ≈43 nm) coated with cetyl trimethyl ammonium bromid (CTAB), as well as with amino- and carboxyfunctionalized PEG and compared their uptake with equally coated nanorods[59a] and defined a stereologic protocol to quantify the number of nanoparticles taken up by the cell. In this study, the authors used dark-field microscopy (DFM) combined with TEM to study the average number of particles internalized into epithelial Madin–Darby canine kidney cells. For this purpose, the authors initially sliced the cells into sections with 1 µm thickness and investigated them by means of DFM. These images reveal the cellular shape and strong scattering signals emerging from the nanoparticles. Since DFM, as a light-microscopy based approach, is not capable of resolving individual particles, scattering signals represent particle clusters within the cellular interior. The authors used the DFM images to count the slices necessary to reconstruct an entire cell and counted the number of scattering signals within one slice which represent the number of particle aggregates within the cell. Subsequent TEM imaging on ultrathin slices (50 nm thickness) revealed the average number of particles per aggregate. The determination of the number of slices per cell and the number of aggregates on the 1 µm thick slice, and the number of particles per aggregate based on TEM facilitated an estimation of an average number of particles per cell. A schematic overview of the workflow is displayed in Figure 4. The authors' data indicated an enhanced uptake of CTAB-modified particles, whereas PEGylated particles were shown not to be taken up in such a large amount. Comparing the uptake of surface-coated spherical particles with their rod-shaped analogues revealed that the number of internalized particles is rather dependent on the stabilizing agent than on the particle shape itself.

Rothen-Rutishauser et al. applied statistical TEM investigations to study the internalization of AuNPs (≈13 nm) coated with the polymer poly(isobutylene-*alt*-maleic anhydride) and labeled them with a fluorescent dye in alveolar tumor cells A549 with respect to different uptake mechanisms.[59c] In this study, the authors used confocal laser scanning microscopy (CLSM) to achieve stereological information about the cells. CLSM images reveal the number of particle events, i.e., the number of fluorescent spots corresponding to nanoparticle labeling, which most likely represent filled endosomes, within the cellular interior. Furthermore, the authors carried out TEM imaging and counted the number of internalized particles per cell. The authors applied different inhibitors to block distinct uptake pathways and compared the number of particle events per cell as indicated by CLSM with the number of particles internalized based on TEM images. The results suggested that an average fluorescent signal corresponds to a cluster of 150 NPs. The authors identified caveolin-mediated endocytosis as the main uptake pathway, based on the fact that ≈95% of the particles were localized within vesicles in the control as well as in inhibitor treated cells.

In another study, the uptake of 50 nm sized AuNPs into the mouse fibroblast cell line 3T3-L1 was assessed by counting the number of individual particles with respect to their cytoplasmic localization.[59b] In this study, the authors established an unbiased sampling by counting the number of cells automatically prior to sample preparation for TEM. The determined number of cells was embedded into a resin block that possessed a cylindrical shape. From this cylinder, ultrathin sections were cut at known locations within the cylinder and a certain fracture of the sample was analyzed by TEM. The known number of embedded cells, along with the number of slices analyzed per sample and the determination of the number of cells per slice facilitated the estimation of the number of particles per cell. The data indicated that more than 70% of the particles were found within vesicular structures and only a few particles could be detected in the cytosol or in other intracellular features. The necessity to generate quantitative data will gain even more significance in future to scope with the inherent heterogeneity of biological samples and the uncertainties that arise from the limited thickness resolution available by TEM investigations.

In summary, the new developments and the availability of new measurement modes as well as improved resolution capabilities fuel a dynamic development of the field of electron microscopy for the study of internalization processes and the mode-of-action of nanoparticles in cellular environments. The integration of new methods and protocols promises, along with the mere visualization of nanoparticles in the intracellular environment, advanced possibilities for studying cellular uptake mechanisms as well as to develop a thorough understanding of intracellular processes. This knowledge will help to expand the possibilities and the understanding of cellular processes which, in turn, will enable a careful design of different nanoparticle systems for a broad range of applications. For a comprehensive summary of capabilities and limitations of TEM investigations, see **Figure 5**.

5. Cellular Uptake and Intracellular Fate of Metal (Oxide)-Polymer Hybrid Nanocomposites and All-Polymer Particles

Within this chapter, we intend to provide an overview about the most relevant literature with respect to the investigation of uptake and intracellular fate of polymer-based nanoparticles, i.e., all-polymer particles and metal (oxide)-polymer nanocomposite.

Although all-polymer nanoparticles have extensively been studied, the number of publications which utilize TEM investigations to study the uptake and intracellular trafficking of these systems is relatively small compared to studies focusing on inorganic nanoparticles. This can easily be explained by the fact that these systems generally provide only a poor contrast in TEM investigations, as they mainly consist of the same atomic constituents as the intracellular environment (C, H, O, N, S, etc.). Thus, their visualization by TEM is frequently not straightforward. This fact is sometimes addressed by the utilization of metal (oxide)-polymer nanocomposites as tracers for the polymer-guided uptake of the nanoparticle systems.

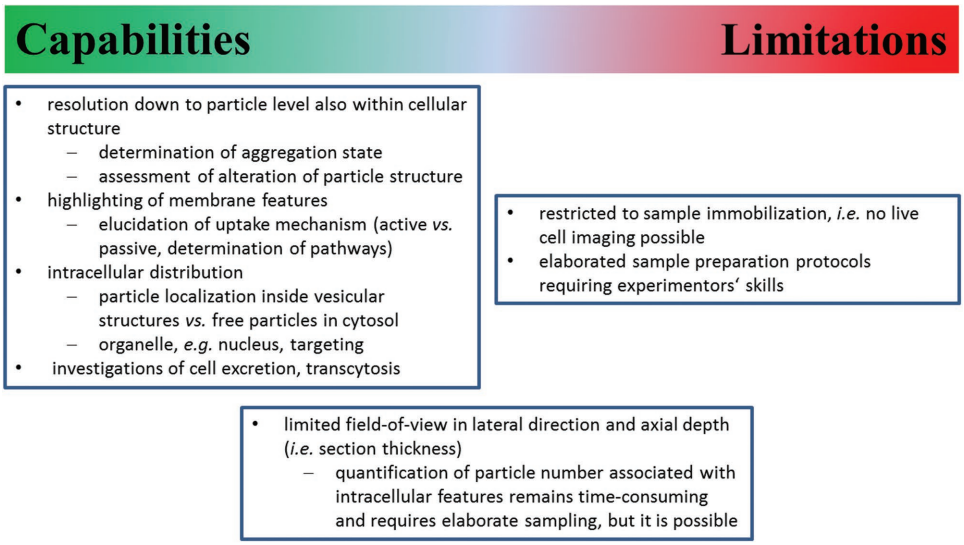

Figure 5. Capabilities and limitations of transmission electron microscopy to study particle uptake and intracellular fate. Due to a resolution down to the particle level within the cellular structures, TEM investigations provide valuable information about cell–particle interactions. However, TEM lacks the possibility to conduct live cell experiments and requires elaborated sample preparation. TEM investigations facilitate statistical analysis of particle numbers associated with different cellular compartments, which cannot be achieved with any alternative technique. Nevertheless, for this purpose, time-consuming data elaboration based on a sophisticated sampling is required.

5.1. Metal (Oxide)–Polymer Nanocomposites

One possibility to circumvent the problem of low electron contrast of polymeric systems is the use of metal-polymer hybrid nanoparticles. Here, an enhanced electron contrast can be achieved by labeling polymeric NPs with small inorganic particles, Here, an enhanced electron contrast of polymeric nanoparticles can be achieved by labeling polymeric NPs with small inorganic particles, e.g., by the synthesis of metal (oxide)-polymer hybrid nanoparticles. These systems are summarized in **Table 1**. In these examples, the inorganic component mainly provides the contrast in TEM.

In contrast to the above mentioned studies, in which the polymers were used mainly in a sense of a surface modifier for inorganic particles, there are also a number of studies directly applying inorganic NPs as EM labels for polymers. For example, Kilchrist et al. studied the uptake of electrostatically complexed cationic MAPKAP kinase 2 inhibitor (MK2i) peptides with the anionic, pH responsive poly(propyl acrylic acid),[83] which resulted in an increased uptake of peptides and intracellular trafficking in smooth muscle cells. TEM confirmed that the MK2i-nanoparticles were localized in macropinosomes and endosomal escape facilitated the cytosolic delivery of the peptide—an important requirement to provide a biological activity of the peptide. The authors studied the uptake not by visualizing the polymer nanoparticle itself, but the authors utilized small gold-peptide functionalized markers to trace the uptake, which is sometimes controversially discussed since it might influence the uptake characteristic.

Ravikumar et al. labeled poly(lactic-*co*-glycolic acid) (PLGA) nanoparticles[84] prepared by double emulsion polymerization and incorporated additional iron oxide nanoparticles (IONPs) nanoparticles to enable their tracing in human type-1 alveolar epithelial cells by TEM imaging (**Figure 6**). By utilizing these tracers the degradation of the IONPs loaded PLGA nanoparticles could be followed, resulting finally in the observation of free IONPs nanoparticles after degradation of the polymer matrix.

Table 1. Metal (oxide)–polymer nanocomposites discussed the second part of the review.

Inorganic system[a)]	Polymer coating	Reference
Au	Polyethylene glycol	[59a,60–67]
	Poly(2-hydroxypropylmethacrylamide)	[68]
	Poly(L-lysine)	[69]
	Gelatin	[70]
	Poly(ethylene imine)	[71]
Au@IONP	Poly(ethylene imine)	[72]
IONP	Polyethylene glycol	[73]
	Heparin	[74]
	Poly(maleic anhydride-*alt*-1-octadecene) (PMAOD)	[75]
	Dextran	[76–78]
	Protamine	[74,79]
	Poly(acrylic acid)	[80]
	Poly(ethylene imine)	[77,81]
	Poly(diallyldimethylammonium chloride)	[77]
	Poly(styrene sulfonate)	[77]
	Chitosan	[77,82]
	Poly-L-lysine	[83]
	Poly(isobutylene-*alt*-1-tetradecene-maleic anhydride)	[84]

[a)]Abbreviations: IONP, iron oxide nanoparticles; Au, gold nanoparticles.

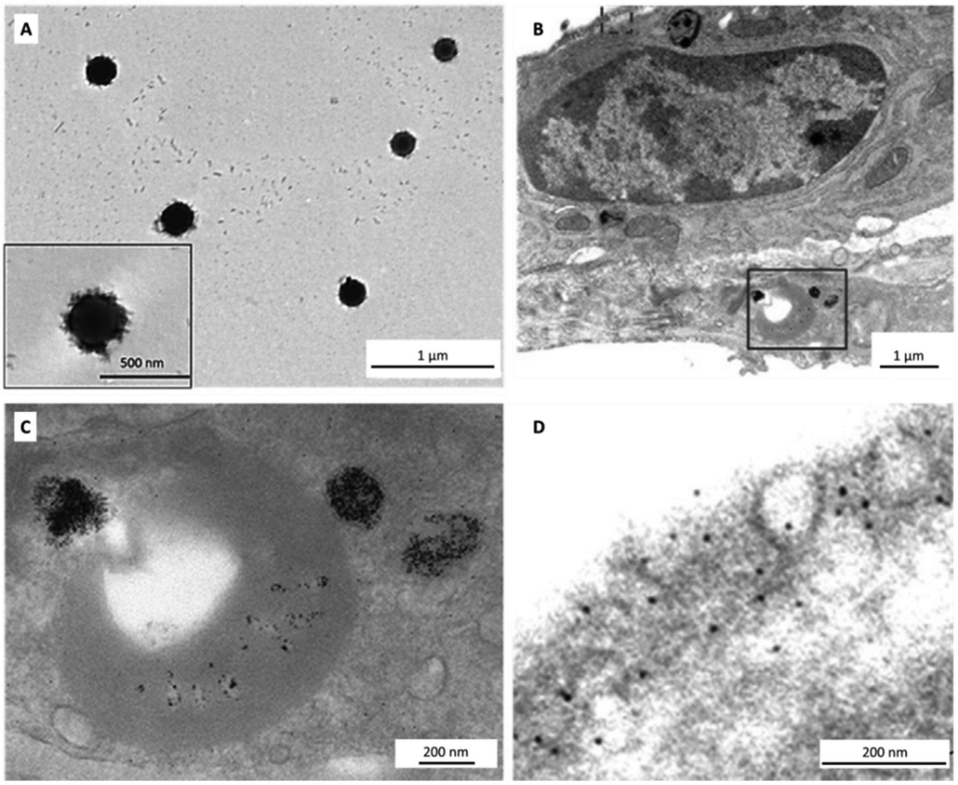

Figure 6. TEM micrographs of A) the PLGA-IONP nanoparticles. IONPs. Degradation study of the IONP nanoparticles in alveolar septal cells: B) Overview, C) magnified view of the solid line surrounded rectangular area of (B), and D) magnified view of the free iron oxide nanoparticles located within the alveolar type-1 epithelium (dashed rectangular area in (B)). Reproduced with permission.[86] Copyright 2016, Elsevier.

In a recent study, a hybrid metal–polymer nanocomposite based on branched poly(ethylene imine) (bPEI) which was labeled with Rhodamine B was studied.[87] This system is excellently suited for uptake studies by means of TEM and fluorescence microscopy. For this purpose, spherical bPEI particles containing smaller gold particles were incubated into HEK-293 cells and their uptake was studied by TEM as well as by fluorescence microscopy. Within the cytoplasm, laser widefield fluorescence microscopy investigations revealed signals with segmented spherical and elongated shapes which can be associated with the particle fluorescence. These structural details became more pronounced on the basis of the superresolution technique structured illumination microscopy (SIM). TEM investigations indicated a macropinocytic uptake which could furthermore be verified on the basis of flow-cytometry measurements, whereby a significantly reduced uptake of the particles was observed in the presence of a micropinocytosis inhibitor. The particles were only found in vesicular structures and only a few particles were observed outside these structures. To compare the informative content of the acquired images, a correlative light and electron microscopy (CLEM) investigation was performed. TEM images revealed that these structures correlate to lysosomal structures which approach each other and, in consequence, fuse. With this contribution, the uptake and intracellular fate of this metal–polymer nanocomposite by means of CLEM could be demonstrated.

In these examples the nanoparticles serve as an electron dense marker which is relatively easily traced by conventional TEM investigations. However, the influence of the metal particles is not always evident and might cause adverse effects on the cells. Omitting these nanoparticle tracers in all-polymer nanoparticle systems, on the other hand, complicates the investigation of uptake and internalization processes, because they frequently lack inherent material contrast in the cellular framework.

5.2. All-Polymer Nanoparticles

For all-polymer nanoparticles it has to be taken into consideration that TEM sample preparation includes fixation and staining with heavy metal salts to enhance the sample contrast, since the untreated biological specimen only provides a poor electron density contrast. The standard staining procedure includes exposure to osmium tetroxide, uranyl acetate and lead citrate, whereby chemical features within the cellular framework are emphasized in a selective fashion (see Section 3). This results in the efficient observability of ultrastructural details. Additionally to the contrast enhancement of the sample components as a result of heavy metal treatment, polymeric NPs bearing functional groups, which interact with the standard staining agents can be efficiently visualized within the context of the cellular environment. Since the density of the reactive functionalities in the well-defined synthetic polymeric NPs is sometimes higher than in the sample's proteins or nucleic acids, the contrast of the particles is frequently significantly

more enhanced than the biological surrounding, thus, allowing their distinct identification in TEM images. Polymer classes that can be highlighted particularly well by standard agents are, e.g., polyplexes consisting of amino-bearing polycationic polymers. Polymeric nanoparticles possessing functional groups unaffected by the standard staining procedures, however, do not experience a specific contrast enhancement. Nevertheless, in some cases, they can be identified as bright structures, e.g., in case of polystyrene (PS) nanoparticles or polylactic-*co*-glycolic acid NPs, which allows their identification inside the more electron-dense biological surrounding. The identification of these NP systems is, unfortunately, not always straightforward. In the following, representative examples of different polymer classes and their identification in the cellular environment will be summarized and their biological uptake characteristics as well as their typical internalization in different cellular systems will be discussed.

5.2.1. Nanoparticles Based on Commercial Polymers

Eudragit represents the brand name for several methacrylate-based polymers. The introduction of anionic, cationic, or neutral comonomers, based on methacrylate or methacrylate esters, respectively, facilitates to adjust Eudragit's properties.[88] The commercially available compound Pluronic represents an ABA triblock copolymer consisting of the hydrophilic poly(ethylene glycol) (block A) and the hydrophobic poly(propylene glycol) (block B).[89] Both polymer systems are known to be non-critical in biological systems.

Abdel-Wahhab et al. fabricated particles from Eudragit RL, an amino-containing Eudragit polymer, with a size of 330 nm and a positive zeta-potential, by the double emulsion method (**Figure 7**A) and studied their uptake into human monocytic THP-1 cells by phagocytosis.[90] The nanoparticles could be localized inside as well as outside the cell due to their characteristic appearance (Figure 7B,C). A closer inspection of the cellular structures revealed no alterations of the cellular system after exposure to the nanoparticles. Furthermore, the authors carried out in vivo studies on Sprague–Dawley rats and observed moderate hematological disturbances in animal models. The authors discussed that for an increase in saturation solubility and the adhesiveness to surfaces and membranes, the availability of smaller particles is desired, which, however, cannot be accomplished by the utilized double emulsion formulation method. The authors excluded effects due to the aggregation of the nanoparticles and verified the size of the particles at different pH values. Addition of serum to the medium resulted in the formation of larger aggregates.

Waiczies et al. investigated the increased uptake of ^{19}F enriched Pluronic nanoparticles (perfluorocompounds) in dendritic cells by manipulating their aminophospholipid composition.[91] Incorporating fluorinated compounds into the nanoparticles significantly enhanced their hydrophobicity, which was regarded as an important factor to control their ability to cross biological membranes and, thus, to facilitate their uptake. The nanoparticles can serve as an efficient tracer for magnetic resonance imaging (MRI) to increase the signal sensitivity and the detection limit. The authors found an at least one order of magnitude higher uptake in the cytoplasm of NPs when the NPs were enriched with 1,2-dipalmitoyl-sn-glycero-3-phosphoetanolamine. TEM investigations revealed a striking difference in the cytoplasmic uptake. The nanoparticles could be observed as white globules embedded into the cell cytoplasm and the authors found their clustering in a lipid membrane capsule within amorphous, grey compartments.

Madaan et al. investigated the mode-of-action of different commercially available polymeric drug carriers for Paclitaxel,[92] a widely used anticancer drug, which is virtually insoluble in aqueous solutions. The authors compared the performance of three different Paclitaxel formulations, Nanoxel, Intaxel, and Abraxane. Nanotaxel is a newly developed, pH sensitive, biodegradable, Cremophor-free, nanoparticle based tumor targeted *N*-isopropyl acrylamide and vinyl pyrrolidone containing copolymer forming 80 nm micellar containers in water. The small size and its amphiphilic character allow enrichment of the Nanoxel into tumor tissue featuring an enhanced vascular permeability and the release of the drug by surface erosion. The authors employed TEM in their study to investigate and compare the intracellular uptake of the three Paclitaxel formulations in various human cancer cell lines, such as, A549, HBL-100, and PA-1. Nanoxel and Abraxane were internalized after 30 min in well-defined and intact endocytic vesicles, whereas Intaxel revealed the presence of many swollen mitochondria being indicative for the evolution of oxidative stress and did not demonstrate the formation of endocytic vesicles. These particles, thus, are potentially taken up by non-endocytic mechanisms.

This polymer classes do not provide a strong contrast in TEM imaging. Nevertheless, the resolution capabilities of TEM have been proven to be sufficient to elucidate an active uptake of the described structures. Potentially, the results of these studies would become more evident if there was further evidence

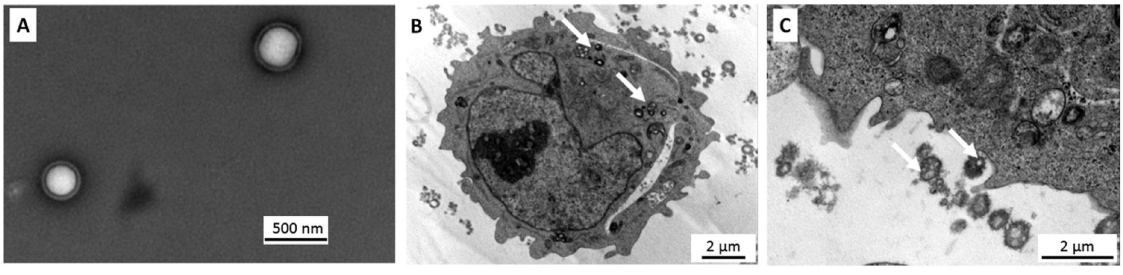

Figure 7. A) TEM image of the prepared Eudragit RL nanoparticles. THP-1 cells exposed to Eudragit nanoparticles. B) Internalized particles and C) membrane-near nanoparticles prior to the stage of uptake. Reproduced with permission.[90] Copyright 2014, MDPI.

for their uptake. In this regard, correlation with fluorescence microscopy would provide valuable additional information.

5.2.2. Polystyrene (PS)

PS represents one of the most extensively used polymers. As a polymer with aromatic side chains, it is hardly biodegradable, nevertheless, its high biocompatibility facilitates the use of PS as food packaging, but also as container material of cosmetics, pharmaceuticals, cleaning agents among others.[93] Polystyrene beads , for example, can be fabricated via emulsion polymerization techniques,[94] by which well-dispersed nano or microsized particles are accessible. Furthermore, their surface charge properties can be controlled by using polymers as surfactants that possess amino- or carboxy-functionalities during the emulsion process.[95] These groups may additionally function as anchor groups and can be used for instance to attach fluorescent dyes to the particles' surface. Fluorescent PS nanobeads have, owing to their narrow size-distribution and synthetic accessibility, been abundantly used in the area of confocal laser-scanning microscopy, e.g., to assess the alignment or stability of a confocal laser-scanning microscope,[96] or as fluorescent markers to achieve a drift correction[97] among many others.

Ng et al. studied the uptake of PS NPs in MRC 5 human embryonic lung fibroblast and primary small airway epithelial cells and polystyrene microspheres in lung fibroblast by conventional TEM imaging.[98] The authors took advantage of the fact that the polystyrene nanoparticles do not participate in the staining process and appear with a bright contrast. In these studies the uniform size of the polymer particles significantly contributes to their easy detection by TEM imaging since they hardly can be confused with vacuoles or lysosomes of the cell (**Figure 8**).

Rothen-Rutishauser et al. investigated different particle systems regarding their uptake characteristic into human red blood cells.[99] These serve as a model for non-phagocytic cells which do not have phagocytic receptors on their surface as well as no actin-myosin system. The authors discussed difficulties to visualize polymer nanoparticles in the cellular framework in their article. However, they could visualize the uptake of 200 nm polystyrene particles, which are shown to be membrane bound. Nevertheless, 100 nm particles could not be identified within the cell. Lerch et al. introduced a nanoparticle based sensor system to trace the local pH values within the cellular environment in a dynamic fashion[100] (**Figure 9**A,B) and studied the acidification process during intracellular trafficking of the internalized PS-nanoparticles in living cells by fluorescence microscopy. TEM investigations were utilized to further confirm the intracellular localization of the nanoparticles. The authors synthesized, for this purpose, amino-functionalized polystyrene nanoparticles by an emulsifier-free copolymerization approach. Utilizing an *N*-hydroxysuccinimidyl ester (NHS) mediated coupling reaction the dual-wavelength pH-sensitive carboxy seminaphthorhodafluor-1 (SNARF-1) dye could be covalently bound onto the NPs' surface. These dyes show dual emission depending if the dye is in the protonated or the deprotonated state and are, therefore, able to quantitatively indicate the local pH-value of the environment of the NPs (Figure 9A). The emission maxima were calibrated in the cellular environment by radio metric pH quantification. Pseudocolored CLSM images revealed vesicular structures with a bimodal pH distribution with maxima found at pH 6.8 and pH 6.0 at early time points of the cellular uptake. At later time points the pH values shifted to equilibrium of pH 5.2 after 4 to 6 h, respectively. TEM investigations (Figure 9C–F) could confirm the presence of nanoparticles in endosomal/lysosomal compartments. At early time points single, functionalized nanoparticles or clusters (≤5 particles) surrounded by a dark contrasted phospholipid membrane were found in the cytoplasm close to the plasma membrane. At later time points larger packages (5–10 particles) of NPs were found near the cell nucleus, suggesting fusion of the vesicular compartments during the ripening process. After 3 h, the nanoparticles were localized in endosomal/lysosomal vesicles and in multivesicular bodies densely filled with nanoparticles. To confirm the endosomal character of the vesicles, an additional quantitative-colocalization analysis with the green fluorescent protein (GFP) labeled endosomal marker Rab GTPases was performed by CLSM. The marker is a regulating protein for intracellular trafficking as well as for fusion of endosomal structures and is known to occur in distinct endosomal compartments. TEM investigations were, moreover, utilized to conclude on the uptake mechanism which is proposed to be governed by macropinocytosis. The dark rim surrounding the particle might be indicative for a selective staining of the amine modifiers attached to the particles' surface. In this study TEM provided important additional information on the intracellular particle distribution and is a very nice example that different techniques can synergetically be implemented into the analysis process.

Firdessa et al. utilized fluorescently labeled, carboxyl terminated polystyrene nanoparticles of different sizes to investigate their uptake characteristics in three different cell lines (bone marrow derived macrophages BMDM, 293T kidney epithelial cells and L929 fibroblasts) as well as the impact of the infection

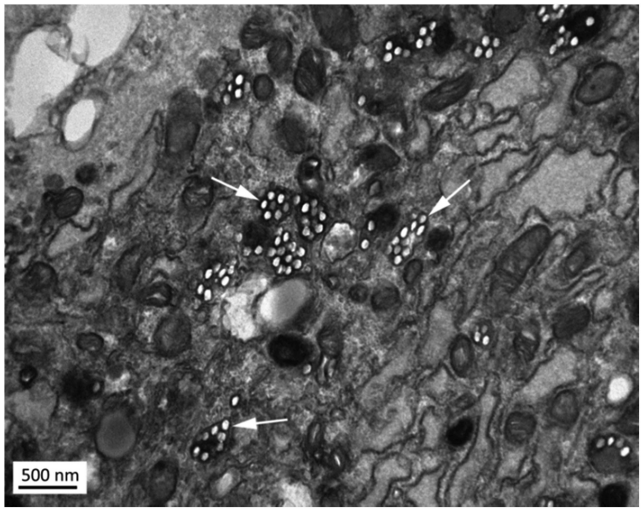

Figure 8. PS nanoparticles internalized in lung fibroblast after a treatment of 72 h. The nanoparticles show a bright contrast and can be found in the cytosol (indicated by the white arrows). Reproduced with permission.[98] Copyright 2010, Formatex Research Center.

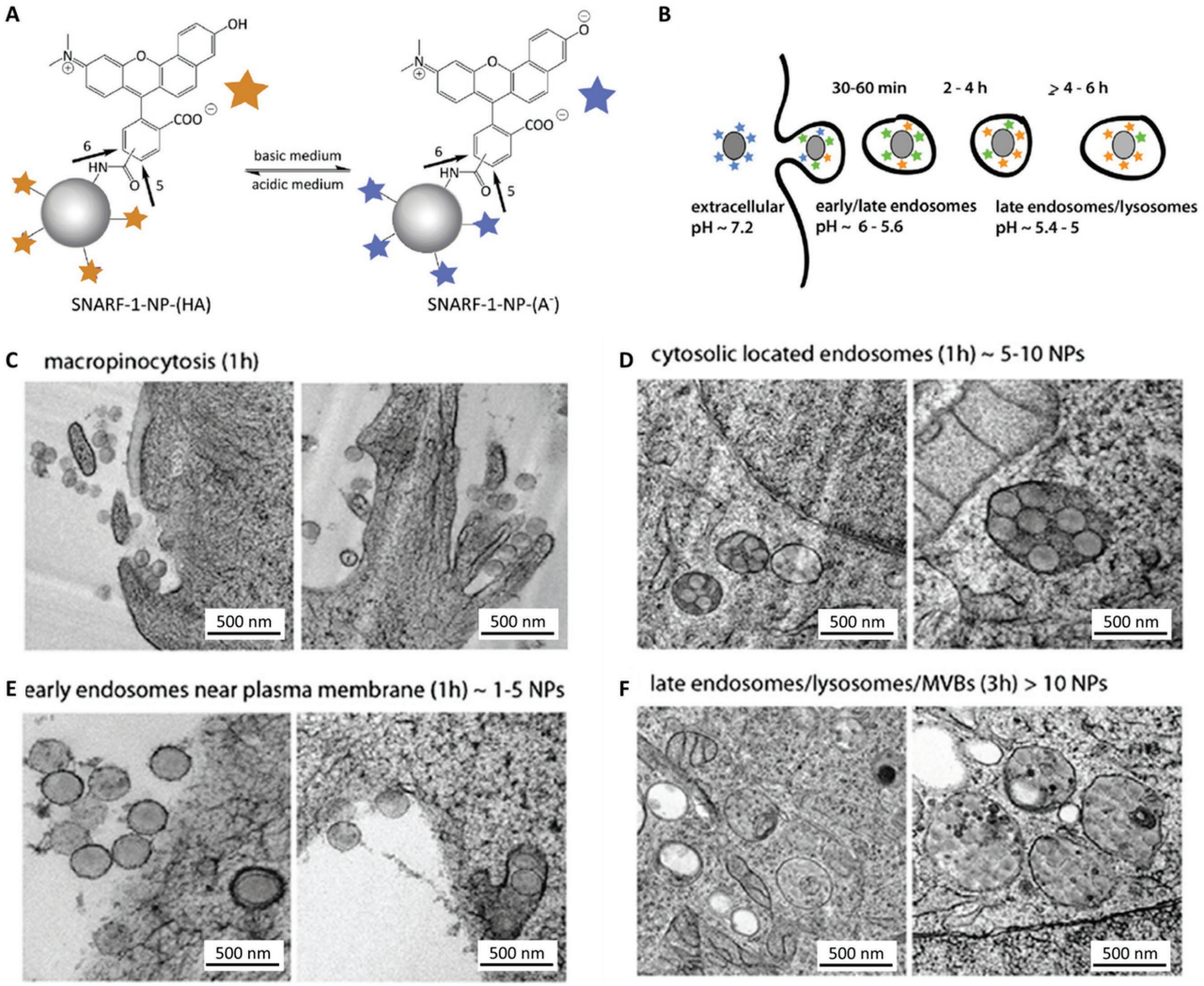

Figure 9. A) A pH-responsive nanoparticle system based on amino-functionalized PS particles. The covalently attached fluorescence dye (SNARF-1) features two pH-dependent fluorescence maxima. These allow chasing the particles within the cells and to elucidate a time dependent trafficking along the endosomal pathway (B). C–F) TEM micrographs of typical cellular compartments at different time points. Reproduced with permission.[100] Copyright 2015, Elsevier.

stage of the cells on the internalization.[101] The authors observed a rapid internalization of the nanoparticles via endocytosis and their accumulation in intracellular vesicles. Soon after internalization, a trafficking of the nanoparticles to organelles with acidic pH value was revealed. Initially, the authors investigated the ultrastructural characteristics of the plasma membrane to conclude on possible uptake mechanisms. The authors found evidence for the occurrence of several uptake routes that all were taking place simultaneously, and the involvement of complex nanoparticle-cell interactions in nanoparticle uptake by mammalian cells. Significant differences in the uptake efficiencies were found to be highly dependent on the cell type as well as on the particle size and time-dependent uptake characteristics could be revealed. The uptake of nanoparticles increased with particle sizes for 293T and L929 cells compared to BMDM. Furthermore, infections and the activation status of BMDM had an influence on the uptake. TEM investigations were employed to elucidate the uptake mechanism of 100 nm PS nanoparticles in BMDM. The authors found evidence for the occurrence of an endocytic uptake, early phagocytosis, macropinocytosis, clathrin-dependent endocytosis processes and early caveolin-dependent endocytosis. Additionally, also clathrin- and caveolin-independent uptake was observed. To support their findings, the authors also investigated the morphology of endosomes containing nanoparticles and tried to correlate their size and morphology to the respective uptake mechanisms. Endosomes formed by clathrin- and caveolin-independent uptake seemed to maintain the tubular-vesicular structure, whereas the morphology of vesicles formed by caveolae-dependent endocytosis appeared to maintain their flask-like shape. The authors concluded that the ultrastructural morphology of nanoparticles at the plasma membrane corresponds directly to their distinct uptake mechanisms. After longer residence times (6 h) the nanoparticles were finally localized in late endosomes/lysosomes and were never trafficked into the nucleus. This study exemplifies the various possibilities that emerge from the TEM

investigations, which can probe the morphology of intracellular compartments as well as to enable investigation of the cellular environment of individual particles and nanoparticle clusters.

Dass et al. compared the uptake of polyisoprene and NH_2-functionalized polystyrene nanoparticles into human cervical carcinoma epithelial (HeLa) cells.[102] Whereas polystyrene particles were internalized as particle aggregates, polyisoprene particles were internalized in endosome-like compartments. The authors concluded that the particle uptake mechanism is governed by the particle structure as well as by their chemical composition. In their study polystyrene appeared with a bright contrast, whereas polyisoprene featured a dark contrast after staining the sample with OsO_4 as well as with uranylacetate. These studies emphasize the importance of the chemical composition of nanoparticles and represent a key to obtain selectivity and directionality in the uptake process.

Musyanovych et al. investigated the uptake of surface charged fluorescently labeled PS in comparison to pure poly(L-lactic acid) (PLLA) nanoparticles into HeLa cells.[103] The results of the study are discussed in detail in Section 5.2.3. Interestingly, the authors discussed a way to significantly increase the contrast of the PS particles. For this purpose, a ruthenium tetroxide (RuO_4) fixation instead of a treatment with OsO_4 was carried out. Since the more reactive RuO_4 affected the aromatic structures present in the polystyrene particles (in contrast to OsO_4), an enhanced electron density could efficiently be introduced into the PS beads, whereby their structure became highlighted within the cellular context.

Tautzenberger et al. utilized nanoparticles formed by copolymerization of styrene with vinyl phosphonic acid via miniemulsion polymerization.[104] These phosphonate-functionalized nanoparticles were shown to be efficiently taken up by mesenchymal stem cells (MSC) without using transfection agents and no influence on the cell viability even at long cultivation times was observed. TEM investigations could reveal the position of the nanoparticles in the cellular environment in untreated cells as well as in cells cultivated under osteogenic and adipogenic conditions. The particles revealed a dark contrast in TEM imaging. In undifferentiated cells, these clusters appeared to be surrounded by a membrane-like structure which clearly indicated their endosomal nature. However, in osteogenic and adipogenic MSCs the clusters only rarely featured a membrane encapsulation. Furthermore, no particles were found in all cases in the cell nucleus, the Golgi apparatus or the mitochondria. The authors pointed out that the exact uptake mechanism is still unknown and should be subject of further investigations.

In a different study conducted by Tautzenberger et al. the effect of phosphonate-functionalized polystyrene particles with vinyl phosphonic acid as comonomer (VPA) fabricated via microemulsion polymerization[105] were investigated with respect to osteoclast formation as well as to trigger the activity and inflammatory response of osteoclasts and osteoblasts. TEM investigations were conducted in order to verify the localization of the nanoparticles in the cellular environment of osteoclasts and the authors could show a significant clustering of the nanoparticles within the cells. Moreover, the nanoparticles localized outside but close to the nuclei of multi-nucleated cells. Most particles were found to be densely packed and internalized into compartments surrounded by a membrane-like structure, which appeared similar to endosomes. The nanoparticles featured a slightly bright appearance due to their low sensitivity toward the common staining procedures. However, TEM did not reveal any details on the uptake mechanism of the phosphate-functionalized nanoparticles. The authors concluded from their studies that the treatment of osteoclasts does not impair their formation and their function as well as that the pro-inflammatory cytokine expression levels of the osteoclasts remain unaffected. Thus, the authors could verify that the VPA particles did not affect cell function directly or indirectly and did not provoke any inflammatory response in this cell type. TEM investigations in both of these studies took advantage of the fact that the resolution capabilities and staining of the samples provides access to the membrane features of cellular organelles. This is a level of detail, which can be hardly achieved by optical methods alone.

Based on these literature examples, PS particles seem to be well-suited to be studied by means of TEM. The particles are stable toward the standard embedding protocol and appear with a bright TEM contrast owing to a reduced electron density compared to the background. Even though PS is of limited relevance for drug delivery applications itself, nanoparticles based on this polymer can serve as an excellent model system and can certainly also be incorporated into copolymer assemblies. Moreover, these particles can be effectively modified, e.g., with fluorescence dyes or other active motifs.

5.2.3. Polyesters

Polyesters have long been established as highly biocompatible polymeric materials. Owing to their facile synthetic accessibility as well as their effective biodegradability, they represent an important polymer class in pharmaceutical research. PLGA, as a prominent representative, has been used for drug delivery or tissue engineering and found a large number of applications. It has extensively been studied to establish platforms for the controlled delivery of small drug molecules, proteins etc. PLGA constitutes, furthermore, an FDA approved compound.[106] Poly(lactic acid) (PLA) or the enantiopure PLLA features similar properties as PLGA and has been discussed as renewable and biodegradable material, which facilitates its application as, e.g., environmentally friendly packaging material.[107] Furthermore, the facile synthetic accessibility of PL(L)A and PLGA nanoparticles via nanoprecipitation or nanoemulsion techniques opens the possibility to encapsulate drug molecules, proteins, etc.[108] Due to the biocompatibility and biodegradability of the polymers, PL(L)A and PLGA nanoparticles are excellently suited for achieving a controlled release of pharmaceutically active compounds within the cells and, hence, nanoparticles based on polyesters represent a prominent platform for drug delivery.[109]

It has to be emphasized that polyester structures do not respond to the standard heavy metal fixation and staining applied during the TEM sample preparation process. Thus, these particle systems are not efficiently highlighted in TEM images.

Poly(Lactic Acid) or Poly(L-Lactic Acid): Barthel et al. investigated the degradation of PLLA nanoparticles incorporated into mesenchymal stem cells over a time period of 14 d.[110] The biodegradable polymer is decomposed by hydrolysis in the cellular environment, possibly catalyzed by enzymes. In order to study the degradation process magnetite nanocrystals were incorporated into the framework of the PLLA nanoparticle (**Figure 10**A), which were gradually released from the surface of the nanoparticle during the degradation process. The authors statically analyzed the number of free magnetite nanocrystals as well as the number of nanoparticles localized in endosomes. PLLA nanoparticles appeared to be unstable in the electron beam and degraded, which explains their appearance in a capsular-like shape with a bright contrast (Figure 10B). This effect is enhanced due to the ineffective staining of PLLA. The authors found particles as well as free magnetite crystals in endosomal structures with a multitude of morphologies due to their intercellular PLLA decomposition. Large endosomes with a diameter >1 µm were observed containing PLLA and magnetite concentrated on one side of the endosome. Additionally, material was found also in smaller endosomes (≈500 nm in diameter) densely filled with external material and giant endosomes (several µm in diameter) with irregularly distributed material. The authors deduced the evolution from smaller, early endosomes with only few PLLA particles to larger, late endosomes with more external material, to the final lysosome. Since no clear interpretation of these observations was possible, the authors performed additional statistical analyses and endosome classification (according to the number of visible PLLA particles, their mean diameter, the number of magnetite clusters and the number of free magnetite crystals, size of the endosome and if endosomes are surrounded by a membrane). The key findings of this analysis provided basic trends. The PLLA nanoparticle density increases over time suggesting the occurrence of fusion processes, which could also be verified by TEM imaging. Moreover, the particle diameter decreases slightly; however, 14 d after incubation a slightly increased diameter of the PLLA particles was observed. The average number of free magnetite particles per endosome increased in the first 2 d after incubation, suggesting that the particle release is rather fast and remains constant thereafter. It was, moreover, found that the fraction of endosomes containing at least one free magnetite cluster reached 100% after 24 h (80%). All data suggest that the surface triggered hydrolysis starts very early (already after 24 h), however, PLLA nanoparticles were still found even after 14 d within the cells (Figure 10C–F). This study nicely reflects the significant amount of information that can be extracted form highly resolved cellular samples and their respective ultrastructures. Also the possibility to address the aggregation state as well as the number of individual magnetite crystals provides advantages compared to other techniques. Here elaborated and more sophisticated analysis might further extend the level of information significantly.

Musyanovych et al. studied the influence of different surface charges of fluorescently labeled PS and PLLA nanoparticles in HeLa cells.[103] For this purpose, different surfactants were used to functionalize the 100–160 nm particles which were synthesized by a miniemulsion process, resulting in positively charged (using cetyltrimethylammonium chloride (CTMA-Cl) as surfactant), negatively charged (sodiumdocedyl sulfate) or nonionic particles (Lutensol AT50). Within incubation times of 24 h with PLLA nanoparticles, the cationic nanoparticles resulted in significant changes of the cell morphology. In particular, swollen vesicles containing few nanoparticles as well as swollen mitochondria with broken cristae were found and were indicative for toxic effects induced by the cationically charged PLLA nanoparticles. Moreover, evidence for a macropinocytosis or lipid raft-dependent uptake mechanism was found, whereas observed coated pits, found at the cell membrane surface, were not associated with the particles and, moreover, were smaller in size compared to the particle diameters. Based on these findings, the clathrin pathway was excluded as a possible uptake mechanism. In contrast, nonionic and anionic particles were taken up in vesicles, which contained several

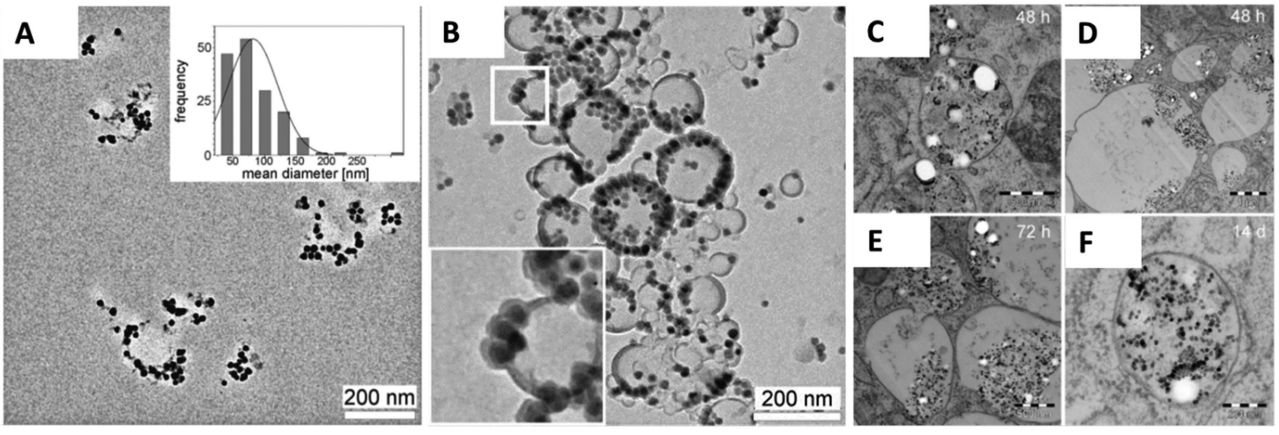

Figure 10. A) PLLA-magnetite nanoparticles embedded by high pressure freezing, freeze substitution, and microtomy into 60 nm slices. B) Particles imaged in TEM after drop-casting and carbon-coating. The particles appeared in a capsule-like shape due to instability in the electron beam. C–F) TEM bright field micrographs of endosomes observed in the MSCs at different residence times of PLLA nanoparticles. These images only provide an excerpt of the different endosomes observed for each observation time. At the 48 h time point, ≈500 nm sized endosomes become filled with external material (C). Additionally, "giant endosomes" were found (D). These could be found after 72 h as well (E), among other structures. Even after 14 d, the MSCs contain endosomes engulfing PLLA nanoparticles and magnetite nanocrystals (F). Reproduced with permission.[110] Copyright 2014, Beilstein.

nanoparticles. However, for anionic particles the number of completely filled endosomes was three times larger compared to the nonionic particles. Additional studies were performed with similarly functionalized PS nanoparticles. Nonionic PS particles were hardly taken up by the cells and the cellular morphology remained unchanged, whereas anionic and most of the cationic PS particles were efficiently internalized in endosomes, which were completely filled with nanoparticles. Also here no morphological changes of the ultrastructure of the cell were observed for anionic particles, but similar to the results obtained for PLLA, positively charged PS particles induced changes on the ultrastructural level. Expanded vesicles and swollen mitochondria were found, however, the effects were less pronounced compared to the cationic PLLA nanoparticles. The authors concluded that the combination of CTMA-Cl and PLLA increases the morphological changes and, therefore, the toxic character of PLLA nanoparticles. Additionally, the lower uptake rates of the nonionic particles were ascribed to their reduced capability to interact with the cells, potentially due to the presence of poly(ethylene glycol) chains originating from the Lutensol AT50 surfactant. Moreover the authors discussed the contrast of the nanoparticles in TEM investigations. PLLA particles appeared with a bright contrast in TEM imaging, due to their low staining potential with heavy metals.

This example illustrates that the different modes-of-action of the differently charged particles could be elucidated by assessing the structural differences in the cells.

Poly(lactic acid-co-glycolic acid): Lemmer et al. tested the effect of a nanoformulation of PLGA nanoparticles, containing mycobacterial mycolic acid (MA) as a targeting moiety and isoniazid (INH) as anti-mycobacterium tuberculosis (Mtb) drug, obtained by double emulsion solvent evaporation, on mycobacterium containing cells.[111] The authors based their studies entirely on TEM investigations and quantitative evaluations of particle numbers and an in-depth analysis of the intracellular cell morphology. Moreover, gold particles decorated with bovine serum albumin (Au-BSA) were used to identify the nature of cell compartments and the fate of nanoparticles over longer periods of times was evaluated to study the fate of nanoparticles within macrophages. The authors demonstrated that MA induced a three- to fourfold enhanced uptake into infected macrophages. The nanoparticles could be localized in phagosomes surrounded by the typical membranes (**Figure 11**A–D). In order to clearly identify the phagosomal nature (phagolysosomes or immature phagosomes), the authors analyzed the luminal presence of either electron-dense markers, such as, Au-BSA chased to lysosomes prior to incubation of the macrophages with the PLGA/PLGA-MA nanoparticles, or by the presence of the characteristic electron-dense lysosomal contents. By analyzing these data, the authors confirmed also an enhanced uptake of MA-functionalized nanoparticles into mycobacterium-infected macrophages. Newly formed nanoparticle-containing phagosomes where converted into phagolysosomes within short periods of time. The phagolysosomes were observed to fuse and to deliver their content to mycobacterium-containing phagolysosomes but not to immature phagosomes. Moreover, it could be demonstrated that the nanoparticles tend to colocalize with the mycobacteria in the phagolysosomal compartments. Additionally, the authors followed the degradation of the nanoparticles in the cellular compartments and could detect long residence times of more than 9 d. Nanoparticles evidently developed blebs and, toward long residence times, much smaller nanoparticles were found in phagolysosomes. The authors tested two size distributions of nanoparticles (800–900 nm and 220–250 nm) and found that the smaller fraction of nanoparticles colocalized faster with mycobacteria infected phagolysosomes. In this example the problem of unambiguous identification of organelles within the cellular environment was elegantly addressed by colloidal staining. This can be optimized for other studies, e.g., by introducing

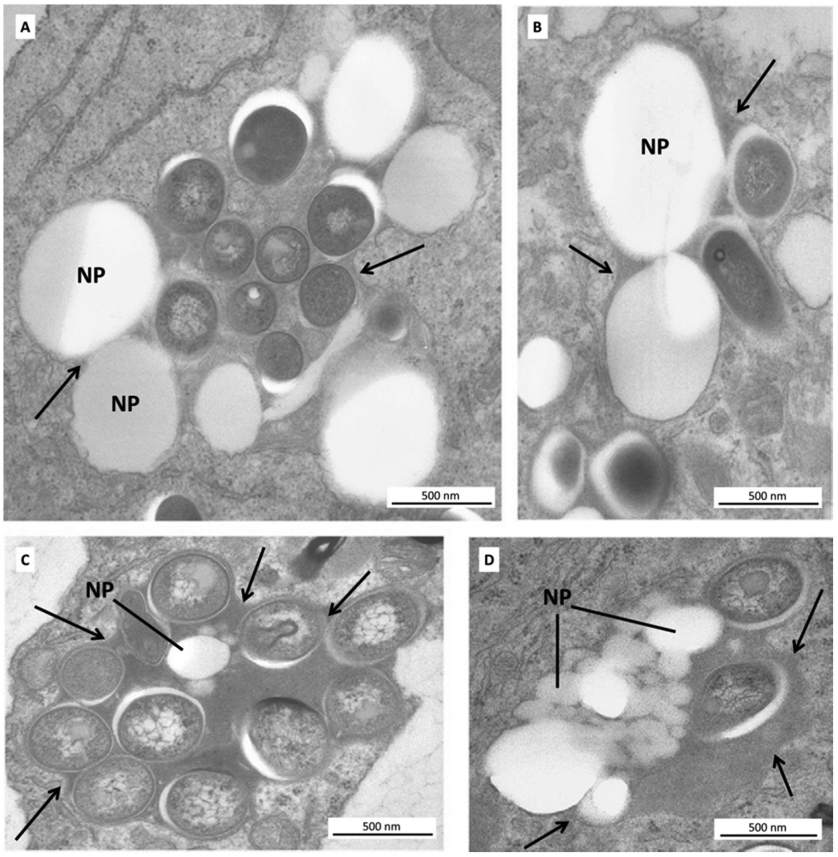

Figure 11. Micrographs of PLGA- and PLGA/MA-functionalized nanoparticles localized in mycobacterium-containing phagolysosmes. A,C,D) BMDM infected with *M. bovis* or B) *M. avium* after 4 h. Large PLGA nanoparticles after A) 5 d and B) 9 d. C) Small PLGA nanoparticles after 5 d and D) small PLGA/MA nanoparticles after 6 d. All samples show phagolysosomes containing at least two mycobacteria. Arrows indicate the phagosome membranes. Adapted under the terms of the CC-BY 4.0 licence.[111] Copyright 2015, Elsevier. Image captions and scale bars have been changed in this figure.

antibodies or tailored targeting units. However, application of such markers previously to the incubation of the nanoparticles might already alter the cellular response. These issues have always to be ruled out by sufficient control experiments prior to the investigation.

Wang et al. studied the uptake of poly-D,L-lactide-block-poly(ethylene glycol) (PELA) micro- and nanoparticles into endosomes and lysosomes of osteoblast cells.[112] In the extracellular space, the authors found emerging organelles which were loaded with nanoparticles. Many nanoparticles were internalized in the cell. In contrast to the PLGA particles, the PELA particles showed a dark contrast in TEM images.

Win and Feng were able to visualize biodegradable Coumarin-6 loaded PLGA nanoparticles coated with polyvinyl alcohol or the water-soluble vitamin E derivative TPGS.[113] The particles featured a dark contrast in the TEM investigations and could be localized within the cell as well as in the nucleus of Caco-2 cells. Moreover, the authors demonstrated the suitability of cryo-SEM to localize the nanoparticles within the cellular framework and point out that cryo-SEM might be an attractive alternative for TEM investigations due to its simplified preparation requirements; however, the resolution capabilities of TEM remain significantly higher. Moreover, cryo-SEM investigations provide only a small depth of information. Thus, mainly nanoparticle interactions with the extracellular membrane are accessible, rather than ultrastructural details become clearly highlighted. An alternative might be utilization of STEM holders, which are available for SEMs as well. However, the ability of electrons to transmit through the entire cell remains one of the critical issues.

Kalluru et al. utilized TEM investigations to address the controversially discussed issue, whether nanoparticles formed by PLGA remain membrane-bound or if they escape into the cytoplasm after internalization in macrophages infected with *Mycobacterium bovis* BCG bacteria which are intracellular residents of macrophages.[37] The authors could demonstrate that the BCG bacteria localize preferentially in early phagosomes, whereas the PLGA particles remained in low pH- and hydrolase-rich phagolysosomes. The authors prepared antibiotic loaded PLGA nanoparticles by standard oil-in-water emulsion with subsequent selective centrifugations and obtained particles with a size of 50–400 nm which can be internalized by phagocytosis. Several experimental issues had to be addressed in this study. First, conventional fixation and embedding protocols dissolved the PLGA nanoparticles and the authors had to apply Tokuyasu thawed cryo-sectioning to avoid the exposure to solvents. This approach also enabled the application of immunogold labeling. In order to localize the low contrast components of the system in TEM the authors selectively labeled early and late endocytic organelles in living cells after the uptake of the PLGA in a three-step labeling procedure. For this purpose, the cells were incubated with 15 nm gold-BSA particles, which preferentially accumulated in lysosomes, followed by an additional incubation with 5 nm gold-BSA for shorter times to label predominantly early endocytic organelles. After thaw-cryo-sectioning the sections were additionally labeled with LAMP2 antibody via rabbit anti-mouse followed by 10 nm protein-A-gold treatment as a membrane marker. This procedure allowed distinguishing the PLGA nanoparticles from the BCG bacteria by colocalizing them with the 15 nm gold nanoparticles. The authors' results clearly indicated that the BCG bacteria do not colocalize with the administered PLGA nanoparticles and that the majority of nanoparticles were localized in phagolysosomes. Additionally, the authors discussed a prolonged residence time of PLGA nanoparticles loaded with antibiotics and their ability to clear the macrophages from bacterial infection. In this contribution it was critically demonstrated that the choice of sample preparation is highly important in order to obtain meaningful results and that adaptations of the classical approaches might be required to preserve the NPs integrity (and, e.g., not to confuse them with particle degradation processes, etc.). Simultaneously, this example nicely demonstrates that colloidal staining techniques provide a powerful tool to assign particle uptake to specific organelles and represents an alternative to fluorescence labeling. This example emphasizes the necessity to accumulate a large toolbox of preparation and staining protocols which can be adapted to specific research issues and that are also compatible with the integrity of the nanoparticles itself.

Contrast Enhancement Strategies: Polyesters, in general, provide only a poor contrast in TEM imaging and are often only observable as electron-lucent spots within the cellular framework. As described by Barthel et al.,[110] the particles are unstable under the electron beam conditions, which would indicate that the electron-lucent spots represent polyester material which bleached under the beam. In order to achieve a more pronounced particle signal, some authors have incorporated heavy metal containing subunits to their polymer nanoparticle systems to achieve a sufficient contrast in TEM imaging. This strategy is sometimes also used to incorporate suitable markers to allow studying the uptake by complementary techniques.

Sun et al. addressed the issue of poor contrast of polylactide NPs in electron microscopy.[116] The authors proposed to encapsulate copper chlorophyll in the matrix of 20–50 nm PLA nanoparticles as intrinsic contrasting agent. For in vivo studies of the particle uptake in brain tissue, the nanoparticles were additionally coated with T-80. Copper chlorophyll is a stable derivative of chlorophyll, in which the central Mg atom of the macrocycle is replaced by a copper atom (**Figure 12**A). It can be encapsulated into polymer nanoparticles by nanoprecipitation without the need of additional surfactants. The authors suggested that the utilization of analytical electron microscopy (Figure 12B,C) may supply additional chemical data and, so far, its capabilities for investigation of polymer nanoparticle arrangements within the tissue context have not been fully explored. Consequently, the authors conducted energy-dispersive X-ray spectroscopy (EDS) investigations on the particles as well as on the surrounding tissue (Figure 12D). Elevated Cu signals were detected for the copper chlorophyll labeled nanoparticles. The authors could visualize the T-80 modified chlorophyll containing particles by TEM investigations. The NPs revealed a strong dark contrast in the TEM micrographs and were located at the membrane and in close vicinity of the microvasculum, which was interpreted as evidence for endocytosis and subsequent transcytosis processes. This study implements an important and powerful additional measurement tool which is available in many TEM systems. EDS provides additional chemical information, in particular, if metal ions are present in the polymer structure. For all-polymer nanoparticles this

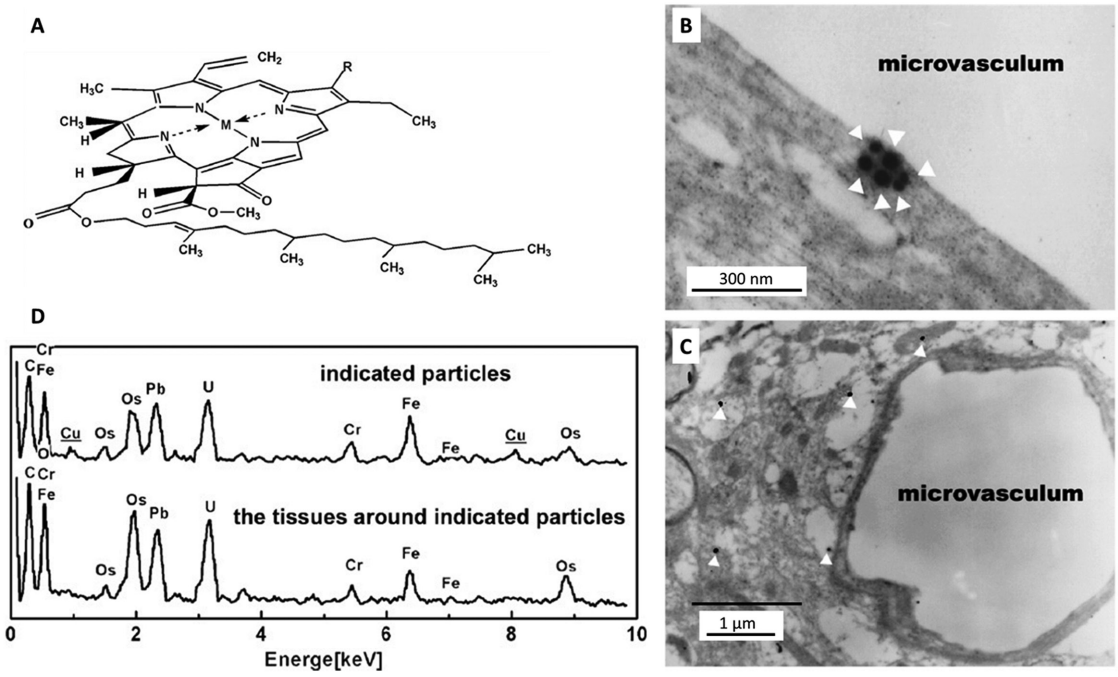

Figure 12. A) Structure of chlorophyll (M = Mg) and copper chlorophyll (M = Cu), R = CH_3 or CHO. B,C). Distribution of the copper–chlorophyll-labeled particles with T-80 coating in brain tissue. B) The particles are located at the wall of the microvasculum and C) around the microvasculum. The particles are highlighted by white arrows. D) EDS spectra obtained on the particles depicted in (B,C) and on the brain tissue without nanoparticles. Reproduced with permission.[114] Copyright 2006, Elsevier.

approach is less effective as low molar mass elements are less sensitively detected. Electron energy loss spectroscopy (EELS) could potentially be used for lighter elements, however, these elements should be specific for the nanoparticle system and not be present in the cellular sample. Both methods can be considered as a tool to investigate the spatial distribution of the elemental composition of the sample, however, with a reduced lateral resolution.

In our own previous work,[115] we showed that a heavy metal coordination compound represents a suitable label for TEM imaging. We utilized a luminescent iridium(III) complex bearing a hydroxyl moiety and used it as initiator for a cationic ring-opening polymerization to synthesize PLA. The polymer formed stable nanoparticles using an emulsion process. Owing to its electron-dense character, the particles could be identified by TEM measurements in HEK-293 cells at a rather low Ir-content of 1–2%. This system is of particular interest due to its luminescent character which made the iridium complex also a suitable label for fluorescence microscopy. We could demonstrate that the particles could as well be observed within the cells by means of structured illumination microscopy (SIM). Thereby, correlative dyes become available, which enable the investigation of the same cell with two high-resolution microscopy techniques. Frequently, metal complexes can provide in this respect an enhanced luminescence lifetime compared to classical fluorescence dyes. Furthermore, the coordinated metal ion into the polymer framework increases the electron contrast of the particle efficiently.

Panyam et al. introduced fluorescence and electron microscopy probes for the investigation of cellular and tissue uptake of poly(D,L-lactide-*co*-glycolide).[116] For this purpose, the authors fabricated BSA (as a model protein) loaded PLGA nanoparticles containing 5-coumarin as a fluorescent label and with osmium tetroxide as an electron microscopy label by double emulsion-solvent evaporation. Due to the lipophilic properties and its solubility in organic solvents, osmium tetroxide can be efficiently dissolved with the polymer prior to emulsification. For both labels non-altered physico-chemical properties of the particles were found as well as no significant cytotoxic effects could be observed over a time period of 48 h, however, the authors explicitly state the necessity to also evaluate long term effects. It was possible to clearly localize the osmium tetroxide functionalized nanoparticles, which appear as 100–200 nm large dark spherical structures within the tight muscle tissue of mice, being specifically localized in the extracellular matrix of the muscle tissue. The authors suggest that the negatively charged particles are attracted to cationic molecules of the extracellular membrane. Some nanoparticles were also observed to be internalized in the sarcoplasm. The authors do not explicitly discuss the influence of the post-staining of the cells with osmium tetroxide, however, control experiments with PLGA nanoparticles revealed that in these experiments the nanoparticle structures could not be identified due to their similarity to intracellular vesicular structures, stressing the importance to directly load the osmium tetroxide into the PLGA particles.

5.2.4. Polyplexes

Synthetic gene delivery systems frequently utilize the polycationic character of suitable polymers to complex DNA. These condense the polymer/DNA into a compact nanoparticulate

structure, referred to as polyplexes. The polyplexes are actively used for cell transfection with DNA and, therefore, their uptake and their intracellular fate are of tremendous importance. Polyplexes should feature the following properties: Endocytotic uptake, DNA escape from the endocytic vesicles and, finally, the DNA should traffic through the cytoplasm toward the nucleus before gene expression can be accomplished (**Figure 13**). Since a variety of synthetically derived polymers are positively charged in aqueous solutions, an electrostatic interaction with the negatively charged plasma membrane facilitates a good endocytic uptake. TEM investigations can provide here a profound knowledge on the nanoparticle internalization as well as to trace their endosomal escape into the cytoplasm. A detailed knowledge of these processes is a prerequisite to further improve and to tailor their uptake.

Polyplexes provide, in contrast to many other polymeric nanoparticles, an excellent contrast in TEM investigations, owing to the nitrogen-rich functionalities present in the utilized polymers, which can be efficiently stained by contrasting agents due to complexation of the highly reactive heavy metal species. Furthermore, the chemical fixatives as, e.g., formaldehyde and glutaraldehyde, actively react with amino functionalities, whereby the polyplex structure is immobilized efficiently within the cellular framework.

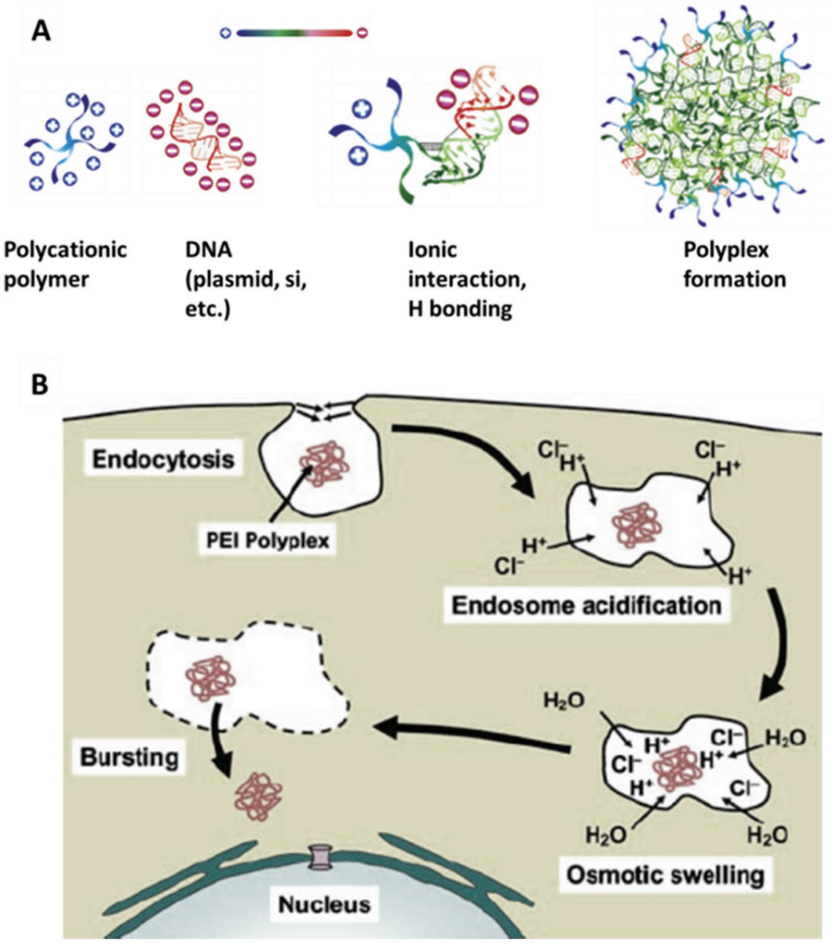

Figure 13. A) Schematic representation process of the formation of polyplexes. Reproduced with permission.[117a] Copyright 2014, Elsevier. B) Schematic representation of the intracellular trafficking of polyplexes for gene transfection applications. Reproduced with permission.[117b] Copyright 2008, AAPS.

Zhou et al. studied the transfection of plasmid DNA (pDNA), encoding the enhanced green fluorescent protein reporter gene, into the cultured cochlear epithelium of neonatal mice. pDNA was transfected by 20–100 nm 25 kDa linear poly(ethylene imine) (lPEI) nanoparticles.[118] The nanoparticles revealed a significant tendency toward aggregation in l-PEI PBS solution. The authors could demonstrate that high l-PEI to pDNA ratios of more than 7:1 resulted in a significant damage of the sensory epithelial cells as could be revealed by immunofluorescence and TEM imaging. After incubation with polyplexes nanoparticles were found to be localized in the cell bodies of the hair cells as well as in their supporting cells. Immediately after transfection, a large number of bubbles within the sensory epithelial cells were observed. Additionally, stereocilla were partially damaged and the number of mitochondria decreased. After 24 h, the sensory epithelium was found to detach from the basilar membrane, with clear evidence for the rupture of the cell membrane and a significant reduction of cytoplasm of the cell. In some sections condensed chromatin in the nucleus and apoptotic bodies were identified. After additional 24 h of incubation the cells died. This example stresses the ability to follow the evolution of particle transfer by studying morphological changes even down to the level of individual membranes.

Zuidam et al. studied the uptake and internalization of the cationic polymer poly(2-(dimethylamino)ethyl methacrylate) (pDEMAEMA)/DNA polyplexes in human ovarian carcinoma cells (OVCAR-3).[119] The authors studied effects of the zeta potential, size and the effect of the tertiary amine groups by comparison with the quaternary ammonium analogue poly(2-(trimethylamino)ethyl methacrylate) (pTMAEMA), as well as the effect of PEGylation on the uptake, due to the shielding of surface charges. Endocytosed polyplexes were found for particles with a positive zeta potential and sizes of 150–200 nm. Smaller or larger particles were not internalized. The authors could elucidate by TEM investigations that the polyplexes start to be taken up by the cells only after prolonged incubation times of 2 d and the aggregates of the polyplexes could be found mainly in lysosomal structures, which could be identified by utilizing LAMP-1 immunogold-labeling. An inferior transfection efficiency was observed for the p(TMAEMA) polyplexes, which is ascribed to a lack of amine buffering capacity, which is known to occur, e.g., for PEI and p(DMAEMA), and which destabilizes endosomal membranes by the so-called "proton sponge" effect.[120]

Zuckerman et al. investigated the rapid clearance of cationic, cyclodextrin-containing polymer-based siRNA delivery vehicles after administration.[121] Despite the fact that these vehicles can induce targeted delivery in tumors via intravenous injection, their residence times during circulation are rather short. Although pore sizes in the renal filtration barrier of the kidney are rather small, even the transfer of particles as large as 100 nm could be observed. The authors investigated the area of the renal filtration barrier and could visualize the particles localization as well as their disassembly in the glomerular basement membrane (GBM) and could provide a model mechanism for the efficient clearance of the drug vehicles. For the development of a model, the TEM investigations are of utmost importance and can provide direct evidence for processes taking place in different locations. The vehicles deposit preferentially in the GBM in which they transiently accumulate due to their positive surface charge, TEM investigations could reveal that after short residence times, a disintegration of the particles, which can be efficiently stained with uranyl acetate, takes place by abundant negatively charged proteoglycans, i.e., heparin sulfate. TEM investigations indicated subsets of nanoparticles with irregular borders and heterogeneous staining intensity, whereby objects more closely located at the GBM showed a more pronounced loss of shape and staining intensity, which suggests that the siRNA was released and passed out to the urinal side. Based on these observations the authors could identify a clearance mechanism for this class of nanoparticles and suggested that this pathway will be important for all nanoparticles featuring sizes of up to ≈100 nm, a positive zeta potential and which are assembled primarily by electrostatic interactions. Moreover, they could demonstrate that the polyplexes can form during circulation as well as they can reform after all small components have translocated through the barriers.

Zhong et al. investigated polyplex-induced early autophagy with only minimal induction of apoptosis or necrosis in mouse fibroblast of PEI/DNA polyplexes in order to understand the cellular stress response upon transfection.[122] The authors investigated the impact of autophagy modulation on transgene expression. Based on TEM investigations, they identified the formation in the cytoplasm of polyplex-transfected cells according to their characteristic structural features, i.e., their double-membrane vesicular structure which contains cytoplasmic material or organelles as well as by their size of ≈600 nm. The authors suggested that controlling the autophagy modulation with small molecules by co-delivery via appropriately designed dual functional polymeric vehicles is possible.

Mishra et al. utilized extensive TEM investigations to demonstrate the differences in polyplex/DNA uptake characteristics utilizing the two different polycationic polymers branched poly(ethylene imine (b-PEI) and β-cyclodextrin, containing the respective polymer and their PEGylated counterparts.[123] PEGylation resulted in an improved salt stability of the nanoparticles under physiological conditions and prevented aggregation of the nanoparticles, which featured a size of ≈100 nm. Unmodified polyplexes aggregated into irregularly shaped clusters with diameters of 300–500 nm. TEM imaging demonstrated different uptake patterns in BHK-21 cells. Aggregates of unmodified b-PEI polyplexes could be found on the cell membranes, frequently associated with invaginations of the membrane. The cytoplasmic side of the membrane appeared thicker and darker in TEM imaging, which was interpreted as indicative for clathrin accumulation in this area. Internalization of the large aggregates proceeded via large vesicles that mimic the shape of the aggregates. At later times, accumulation of the polyplexes near the cell nucleus and an increase in their size were observed while some free polyplexes without surrounding membrane are moreover found in the cytoplasm. In particular, inside the vesicular structures a degradation of the polyplexes can be observed, which is indicated by the loss of defined borders of the aggregate structures. A similar behavior was found for unmodified β-cyclodextrin polyplexes, however, the membranes usually do not completely surround the polyplexes in this case. At later times, many polyplexes are located freely in the cytoplasm, whereby the cytoplasm appears in some cases to contact the polyplexes, whereas in other cases a void space is observed between both. Here TEM investigations provide direct evidence for the degradation of the nanoparticles due to the fact that their shape and size can be faithfully determined. For both polyplexes no internalization in the cell nucleus was observed. In contrast, PEGylated b-PEI particles did not show aggregation but appeared as individual polyplexes. Extracellularly they are located irregularly across small stretches of the cell membranes. Single nanoparticles are localized in invaginations of the membrane or are found in small vesicles near the membrane inside the cell. Close to the nucleus the size of vesicles significantly increased and they accumulated moderate numbers of individual, non-aggregated polyplexes, which suggests a fusion of polyplex containing vesicles. These vesicles feature a round and smooth appearance. Besides the incorporation in vesicles, free polyplexes are found in the cytoplasm, but also here no polyplexes were observed in the nucleus. PEGylated β-cyclodextrin polyplexes could not be traced inside the cells and the authors related this to the inability to sufficiently stain the β-cyclodextrin by the commonly applied staining procedures or simply by the dissociation of the polyplex during the staining process. The authors additionally utilized immunogold-labeling to localize the DNA transfected with β-cyclodextrin polyplexes within the cellular structure. For this purpose, biotin labeled pDNA was used. Clusters of five to ten gold nanoparticles mainly arranged in a circular arrangement indicating the position of the pDNA, and free DNA could be identified in the cytoplasm which proved the release of the DNA from the polyplexes. Few Au nanoparticles were also found in the nucleus. As a consequence, the authors concluded that the dissociation of the pDNA-polyplexes occurred prior to the entry of pDNA into the nucleus. The authors attributed the differences in the uptake and release of unmodified b-PEI nanoparticles and their PEGylated counterparts to the presence and/or the reaction with primary amines which might impair the proton-sponge effect that triggers the release of the polyplexes into the cytoplasm. Thereby, endosomal escape of the polyplex and its release into the cytoplasm is mandatory for an efficient gene transfection. In contrast, unmodified polyplexes may escape from the intracellular vesicles more easily because of their filling capacities and the distorted shape of the surrounding membrane. The authors utilized volume density analysis[124] to quantify the polyplex uptake. For this purpose, a lattice is overlaid on randomly collected images and the

fraction of vertices on polyplexes was compared to vertices on the cell cytoplasm. This example utilizes TEM staining protocols to highlight specific aspects of the process. By this means, the authors were able to follow the fate of the particles as well as of the complexed DNA within the cellular system. Thus, it represents a very illustrative study which highlights the increased level of information that can be obtained by sequentially addressing different aspects of the process in a selective fashion by optimized staining steps.

Gonçalves et al. investigated the internalization and trafficking of pDNA complexed with histidylated polylysine (His-pLK) 110 nm polyplexes,[125] which condense pDNA and lead to a destabilization of membranes in an acidic pH value, thereby facilitating the endosomal release of pDNA in HepG2 cells. The authors emphasized the critical role of uptake and intracellular localization of the polyplexes to optimize their mode of action. In their studies pDNA was taken up both via clathrin-dependent and clathrin-independent, most likely macropinocytic processes. This could be confirmed by TEM investigations where the polyplexes were identified as electron dense structures. Small polyplexes were observed in clathrin-coated vesicles and large polyplexes were localized in uncoated vesicles near the plasma membrane which showed membrane ruffles. In combination with additional studies, the authors could conclude that polyplexes internalized by macropinocytosis and pDNA recycling significantly decreased the transfection efficiency. Moreover, segregation between His-pLK and pDNA could be observed already 30 min after internalization.

Cartier et al. based their investigations on early steps of polyplex-mediated transfection mostly on the morphological analysis of TEM data and gained a deep insight on the internalization mechanism.[126] The authors utilized a synthetic peptide K_{16}-NLS (CKKKKKKKKKKKKKKKGGGPKKKRKVG) containing 16 lysine residues for DNA binding and formed peptide/DNA polyplexes with a size between 300 nm and 3 µm in diameter. The polyplexes consisted of 30–50 spherical subunits with sizes of 30–70 nm. The peptide/DNA polyplexes could be visualized by TEM as dark, stained aggregates 30 min after transfection and were found close to the cell surface or were localized in invaginations of the plasma membrane (**Figure 14**). Intracellular compartments hosting aggregates were additionally found. The size of these aggregates was significantly smaller ranging from 200 nm to 1 µm. Based on their morphological studies, the authors hypothesized that the tumor cells (HCT116) behave like non-professional phagocytes and, therefore, are able to internalize large particles. The authors confirmed their interpretation that the found aggregates host the DNA by employing immunogold labeling utilizing digoxigenin-labeled plasmid DNA. A detailed investigation of the polyplex-cell membrane region revealed that only few focal points were formed and the internalized polyplexes were located in large vacuoles shortly after engulfment. The authors also analyzed the intracellular pathway of the polyplexes after uptake utilizing labeled and unlabeled peptide/DNA polyplexes. Four hours after transfection large vacuoles, containing DNA, were observed and the morphology of the DNA-containing structures was indicative for the degradation of the large aggregates. Moreover, vacuoles with dark condensed structures were also observed, even though no DNA could be identified in these regions, which was interpreted as an indication for an advanced degradation stage. The authors concluded from their observations that the cellular uptake of peptide/DNA polyplexes was facilitated by a non-specific phagocytosis-like mechanism, which leads to the fusion of phagosomes with lysosomes. Additionally, the authors investigated the influence of chloroquine, an agent promoting the endosomal escape of endocytosed DNA complexes, and $CaCl_2$, which was added as an enhancing factor for transfection. Chloroquine was shown to affect the intracellular structure of the cells, as in the absence of chloroquine a significantly larger number of small vacuoles was observed in the cytoplasm. $CaCl_2$, however, did not result in any morphological changes of the cellular ultrastructure, which suggests the involvement of $CaCl_2$ in a later stage of the gene transfer, possibly after the DNA escapes into the cytoplasm. Cells treated with $CaCl_2$ alone (no polyplexes, no chloroquine) revealed the degradation of mitochondria localized in authophagosomes, which looked very similar to the condensed structures found in vacuoles 4 h after transfections carried out with peptide/DNA complexes in the presence of chloroquine. The authors concluded from these observations a fusion of phagosomes, containing internalized complexes, and authophagosomes, containing damaged mitochondria, at later stages of the transfection. The authors gained superior insight in the occurring processes by in-depth investigations of specific membrane features, which, due to their small size, are not accessible by other techniques.

Bus et al. introduced a new, PEI based material suitable for gene delivery.[127] In their study, a library of water-soluble copolymers, consisting of ethyl-(2-oxazoline), ethylene imine and primary amine bearing monomers, was synthesized and the capabilities of the polymers to form stable polyplexes were investigated. It was shown that the polymers efficiently bind plasmid DNA (pDNA) and small interfering RNA (siRNA). A high transfection performance, accompanied by a low cytotoxicity was observed for pDNA containing polyplexes. In contrast, l-PEI revealed, in addition, high transfection efficiency; however, l-PEI possesses a high cytotoxic potential. The polyplexes formed by pDNA and the new material could be highlighted efficiently in STEM. STEM images revealed that most of the polyplexes were localized as individual particles within vesicular structures in contrast to polyplexes formed by l-PEI, which were observed in form of particle clusters. The authors attributed these findings to an aggregation of l-PEI based polyplexes due to protein interaction in the medium, whereas polyplexes based on the new material are supposed not to interact with serum proteins. Furthermore, a macropinocytic uptake was hypothesized for both materials on the basis of TEM images, which was furthermore, confirmed by inhibition experiments. The authors complemented the STEM data with superresolution fluorescence microscopy images. The utilization of STEM, which is rarely used for the investigation of cellular samples so far, provides here the possibility to introduce additional contrast or to improve the visibility of selective staining which might be compromised by the staining procedures of the nanoparticles compared to the cellular "background". With that, it is possible to carry out investigations at low staining levels. This approach is of particular interesting for systems, which are not compatible with common staining routines or systems which contain specific elements that provide a STEM material contrast.

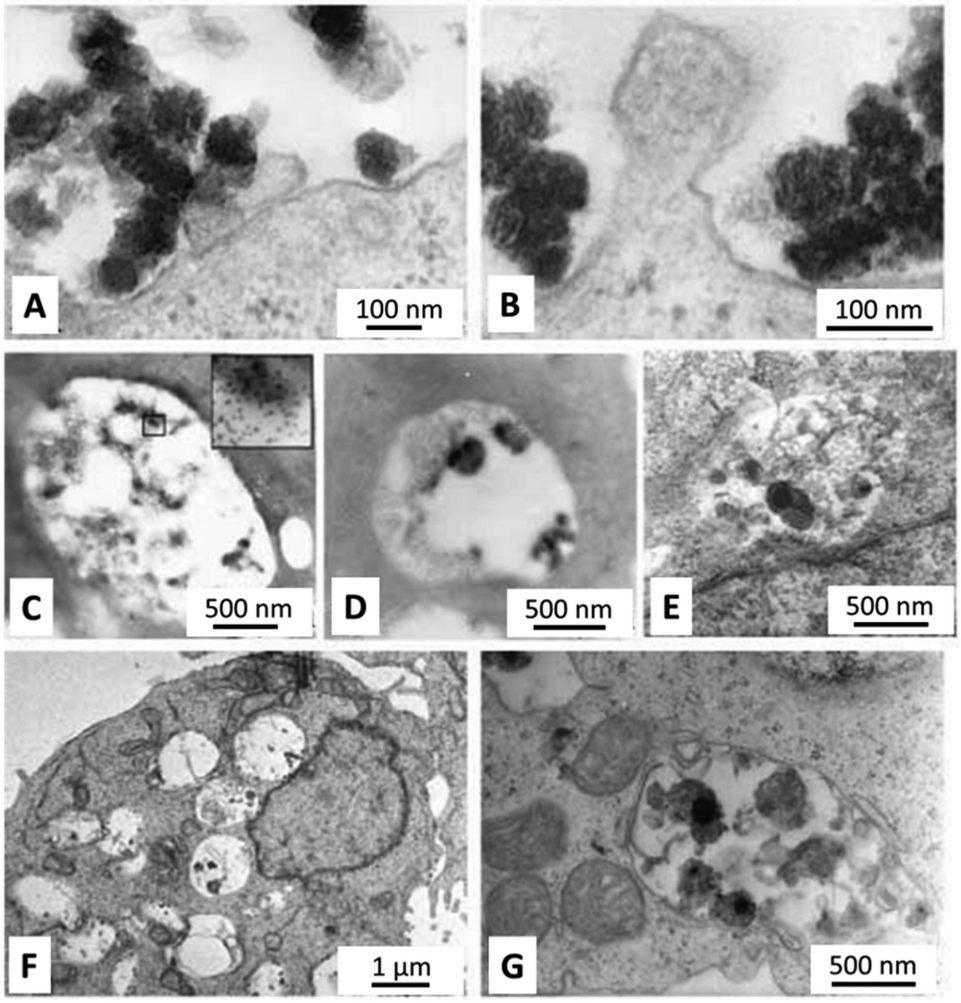

Figure 14. TEM investigations of the transfection process. A,B) Polyplex–cell-surface interaction sites. C,D) Polyplexes localized in secondary lysosomes show degradation after 4 h. (DNA labeled with digoxigenin indicated by gold grains). E) Unlabeled DNA. F) Formation of large vacuoles. G) Cytotoxic effect of calcium indicated by dying mitochondria insides of an autophagosome (control experiment with calcium but without DNA complexes and cholorquine). Reproduced with permission.[126] Copyright 2003, SAGE.

5.2.5. Chitosan and Gelatin

Chitosan and gelatin represent biopolymers with excellent biocompatible properties. Chitosan, as the deacetylated polymer chitin (present in mollusks, crustaceans, insects, fungus, algae, etc.), is a biodegradable polymer which features abundant possibilities for chemical modifications, owing to its reactive amino side groups.[128] Gelatin represents a protein compound which is accessible by partial hydrolysis of the fibrous protein constituent collagen.[129]

Park et al. complemented confocal laser scanning microscopy studies of the uptake of near-infrared (NIR) fluorescent labeled, hydrophobically modified glycol chitosan nanoparticles with a size of 350 ± 45 nm in HeLa H2B-GFP cells by TEM investigations.[130] The nanoparticles were additionally loaded with Ce6, a photosensitizer for photodynamic therapy. CLSM studies with samples treated with different inhibitors clearly showed that the uptake of the hydrophobically modified glycol chitosan nanoparticles proceeds mainly via macropinocytosis but also other uptake mechanisms are involved into the internalization process. Depending on the internalization pathway also a different intracellular fate of the nanoparticles within the cytoplasm was observed. Nanoparticles internalized via clathrin- and caveolin-independent endocytosis enabled nanoparticles to traffic from the degradative pathway into the lysosomes. The authors utilized TEM investigations and the nanoparticles were localized in late endosomes, lysosomes and some were located in the cytoplasm. Nevertheless, vesicles containing the nanoparticles, which are indicative for lysosomal structures, had to be visualized by means of immunostaining of the lysosomes utilizing the anti-LAMP2 antibody, since the nanoparticles only provide moderate electron contrast. In this study TEM investigations verified the results obtained by CLEM studies and provided a detailed picture of the uptake process.

Vivek et al. investigated a pH-responsive drug delivery system formed by 100–150 nm chitosan based nanoparticles loaded with Tamoxifen,[131] which was complexed to the nanoparticles. Thereby, the attractive properties of chitosan, i.e., cell

affinity, enzymatic biodegradability, antimicrobial activity, epithelial permeability as well as nontoxicity, non-immunogenic, non-carciogenic properties, etc. were discussed. The system under investigation is a pH-responsive system as the drug delivery vehicles tend to release their drugs more quickly at pH-values of 4.0 and 6.0 compared to a pH-value of 7.4. The authors found in their study that the chitosan drug delivery system revealed a higher efficiency compared to the free drug for MCF-7 cells. TEM investigations were performed and could demonstrate an internalization of the nanoparticles by nanoparticle-mediated endocytosis, and were distributed within the cytoplasm as well as in the nucleus. Fragmentation of the cell as well as of the nuclear membrane was observed by TEM. This was confirmed by additional measurements, which indicated a decreased viability of the cells treated with the chitosan system compared to the pristine drug alone. The authors concluded that the application of both, the free drug and in particular the chitosan drug delivery system, arrested the growth of cancer cells and induced significant morphological changes, which were indicative for cell death. The nanoparticles appeared with a slightly dark contrast in these studies. This study represents an example where the cell morphology was heavily affected. In these cases a careful evaluation of the live-state of the cells is an important step in the final data analysis and for cross-checking the condition of the cells.

Li et al. investigated the effect of Paclitaxel loaded chitosan nanoparticles.[132] The particles were synthesized by a solvent evaporation and emulsification crosslinking method with trisodium citrate as the crosslinking agent, resulting in non-aggregating particles with a size of 116 ± 15 nm. To verify their results obtained by fluorescence microscopy, which suggested a non-specific absorptive endocytosis with subsequent Paclitaxel release from the particles, the authors employed TEM investigations. They could demonstrate a strong destructive effect of the chitosan on the membrane integrity of A2780 cells. The membrane of treated cells was damaged and a concentration of the chromatin into multiple aggregates at the boundary of the membranes was observed along with the formation of an apoptotic body. After 24 h incubation time, the cytoplasm showed signs of condensation and chromosome aggregation was observed. Apoptotic bodies were, moreover, found in the nuclei of cells after incubation for 72 h. Nevertheless, inside the cell no distinct particle signal could be observed.

Malatesta et al. scope the problem of the low contrast of chitosan nanoparticles in electron microscopy by applying 3,3′-diaminobenzidine (DAB) photoconversion.[133] The authors aimed on correlating fluorescence and TEM images. This technique[134] requires the presence of an additional fluorophore in the nanoparticle structure (e.g., fluorescein 5(6)-isothiocyanate (FITC)). When the fluorophore is exposed to light of a suitable wavelength, the excitation of the molecule from the ground to an elevated energy level can proceed in combination with the population of an excited triplet state under certain circumstances. In the presence of non-reactive triplet oxygen, a highly reactive singlet oxygen species may be formed, which triggers the oxidation of the DAB and results in the formation of an electron-dense, osmiophilic precipitate (**Figure 15**A). This electron-dense structure is observable in TEM. In their study[133] the authors investigated the uptake of FITC-labeled chitosan nanoparticles in B50 cells and studied their intracellular fate.

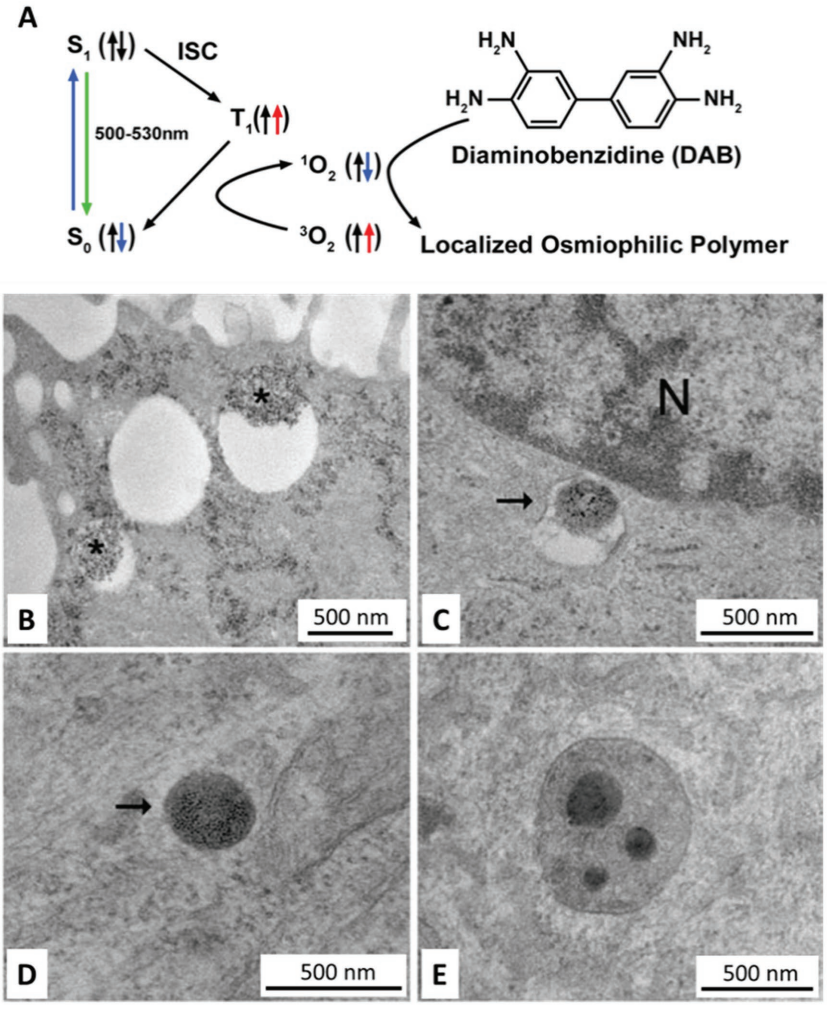

Figure 15. A) Schematic representation of the DAB photoconversion to obtain electron-dense, osmiophilic precipitates observable by TEM in B50 cells. Adapted with permission.[135] Copyright 2011, PLOS. B) Micrographs of internalized nanoparticles (highlighted by asterisks) in endosomes at the cell periphery. The particles can be identified by the fine, granular, dark structure of the reaction product of the photoconversion. C) Endosome-internalized nanoparticle close to the nuclear envelope (N = nucleus), and D) nanoparticle distributed freely in the cytoplasm. E) Also residual bodies show still the presence of photoconversion products as a result of particle uptake. Adapted under the terms of the CC-BY 4.0 licence.[133] Copyright 2012, The Authors. Published by PAGEPress. Image captions and scale bars have been changed in this figure.

The nanoparticles were formed by an ionotropic gelation with tripolyphosphate pentasodium salt and produced particles with diameters of 125 ± 110 nm with a high dispersity. Associated fluorescence microscopy studies revealed their distribution within the cytoplasm with a tendency toward localizing closer to the nucleus after longer incubation times, and a colocalization of the fluorescently labeled chitosan nanoparticles with intracellular membranes. This was interpreted as a hint toward an endocytotic uptake. After DAB photoconversion, the chitosan nanoparticles could be visualized by TEM in form of fine granular reaction products and additional information on their intracellular distribution could be obtained (Figure 15B–F). Chitosan nanoparticles were found as single particles internalized mostly in electron-lucent vacuoles all over the cytoplasm but were never associated to the cell nucleus. Free particles were found in the cytoplasm and at longer incubation times also inside multivesicular or in residual bodies (Figure 15E), whereby their morphology was often altered and only the dark contrast originating from the reaction product could be used to identify the particles. The authors highlight that the DAB photoconversion is compatible with different cell embedding media after the precipitates have been formed. As such, e.g., epoxy resins after osmium post-fixation or acrylic resin without osmium post-fixation can be used. This approach represents a very promising tool, which will certainly provide more impact in the future.

Gupta et al. studied the cellular uptake of cross-linked, rather small (≈37 nm) gelatin nanoparticles prepared via water-in-oil microemulsion into human fibroblasts to study adhesion, morphology and cytoskeleton organization.[136] Initially, the authors could observe the presence of vacuoles in the cell body, membrane abnormalities as well as the formation of lamellapodia and filopodia on glass substrates by SEM investigations. The authors suggested that the vacuoles were formed upon phagocytosis of the gelatin nanoparticles, which led to a disruption of the cell cytoskeleton and the formation of membrane protrusions. Closer inspection of the cells by TEM revealed that a large number of gelatin particles was taken up, often at a ratio that the cell area was compromised by the nanoparticles. Particles were localized in several electron-lucent voids surrounded by intact mitochondria; however, only with a low electron contrast. The nuclear membrane as well as the cytoplasm remained intact, even though gelatin nanoparticles were found in the nucleus as well. Gelatin nanoparticles were localized in phagolysosomes, however, the contrast in TEM imaging of the gelatin particles was rather low which complicates their identification.

Chitosan particles open, owing to the amino-functionalities present in the structure, the possibility to be stained by the standard heavy metal agents in a similar fashion as polymers used for gene delivery. However, their electron contrast appears to be reduced in contrast to the polyplexes described in Section 5.2.4. These systems could potentially benefit from investigations performed by STEM.

5.2.6. Particle Replication in Nonwetting Templates (PRINT) and Polypyrrol

Besides particle systems with biomedical relevance, also other polymers have been utilized for studying nanoparticle uptake. In these, rather academic, studies either non-common polymers for drug delivery applications or special fabrication techniques to obtain unusual, but well-defined, nanoparticle architectures were used.

Gratton et al. addressed the question how the size, shape, and surface chemistry influence the biodistribution, cellular internalization and intracellular trafficking of nanoparticles in HeLa cells.[137] The authors utilized the top-down lithographic fabrication method PRINT to generate nanoparticle sets of micro and nanoparticles made from cationic, cross-linked poly(ethylene glycol) hydrogels in which only one variable is independently altered at a time. Series of micrometer sized cubic and two cylindrical systems were tested. TEM studies could reveal a detailed understanding of the internalization process of the particles and showed shape-dependent uptake kinetics. Cylindrical particles with an aspect ratio of 1 were taken up by multiple, non-specific, notably energy-dependent phagocytosis and a clathrin-mediated mechanism. This study benefits from the fact that membrane-particle interactions can be precisely determined by imaging the nanoparticles as well as the membranes at the same time. Both features can be accessed with a high resolution. The incorporation of TEM tomography would potentially allow for a more precise estimation of the contact areas between both components. Internalization of surface associated nanoparticles is mediated by actin rearrangement near the plasma membrane and extensions into the extracellular space. In contrast, rod-like shaped particles were translocated deeper into the cell contacts and resided close to the nuclear membrane at a fourfold increased internalization speed. The authors identified also the importance of the absolute size and/or volume of the particles on their uptake. This was explained by the larger surface area, which might be in contact with the cell and, thus, more multivalent cationic interactions are involved in the uptake. Also the effect of the surface charge was investigated. For this purpose, particles were treated with acetic anhydride to passivate the surface amine groups by forming amides, which alters the surface charge from positive to negative, and it was found that positively charged particles were rapidly internalized, whereas negatively charged particles were hardly taken up by the cells. The authors could also verify that the maximum size of particles being internalized is up to 3 μm. Interestingly, the appearance of the particles in the cellular framework varied and particles were found to provide dark and bright contrasts within different cells.

An illustrative example for utilizing nonconventional polymers for drug delivery applications was reported by Kim et al.[138] The authors systematically investigated the uptake and effect of differently sized polypyrrol (PPy) nanoparticles (20, 40, 60, 80, and 100 nm, respectively), formulated by chemical oxidation polymerization, into lung fibroblasts (IMR90) and mouse alveolar macrophages (J774A.1). TEM investigations could reveal different uptake mechanisms for both cell lines. While fibroblasts internalized the nanoparticles mainly via endocytosis, macrophages utilized a combination of phagocytosis and endocytosis. Endocytosis was identified by characteristic invaginations of the plasma membrane, whereas the formation of protrusions of the plasma membrane was indicative for phagocytosis. In both cell lines nanoparticle localization in endosomes, late endosomes/multivesicular bodies and

endolysosomes and finally in lysosomes occurred, following the pathway of the endosome network. No accumulation of nanoparticles in the cytoplasm or in mitochondria was observed. In fibroblasts, a significantly larger amount of nanoparticles was localized in endosomes, whereas macrophages revealed a preferential accumulation in multivesicular bodies and the late endosomes, which was in accordance with the proposed different uptake mechanisms observed for both cell lines. The authors, moreover, found a size- and dose-dependent effect on cell viability, oxidative stress and apoptosis/nectrosis and could explain the more adverse effect of PPy nanoparticles on macrophages due to the involvement of phagocytosis. Decreased viability in fibroblasts was related to early/late apoptosis, whereas macrophages preferentially undergo necrosis. Among all tested nanoparticles, 60 nm PPy nanoparticles caused the highest adverse effect in both cell lines, whereas the innate immune response was most efficiently affected by 40 and 80 nm PPy nanoparticles on macrophages.

6. Conclusion

The overview about illustrative examples involving TEM imaging to investigate internalization and localization of polymeric nanoparticles in cells nicely demonstrates the various possibilities to provide additional insight into these processes that are barely obtainable by any other technique. In this context a critical summary of advantages and disadvantages for the investigation of biological samples is presented with particular focus on the reviewed examples of polymer nanoparticle uptake studies. Nevertheless, these considerations are certainly also valid for other nanoparticle systems. The main advantage of TEM investigations is based on the ability to provide an in-depth study of nanoparticles, their interaction with membranes and organelles. At the same time, their biological effect on the whole cell level, e.g., in form of alterations of the ultrastructural features can be accessed. This high resolution level also provides a direct evidence for the aggregation state of the nanoparticles in the cellular matrix, which is rather difficult to achieve by other methods. The possibility to investigate the shape of the particles within specific organelles is an additional powerful tool which provides knowledge of the particle fate; i.e., degradation, swelling, etc. of the particles with high sensitivity.

New developments, measurement modes, greatly improved preparation protocols as well as significantly improving resolution capabilities of modern TEM methods bear great promises for further research achievements and the role of TEM will, in our opinion, become even more important in the near future. Moreover, the investigation of ultrastructural features will further boost the understanding of cellular responses and will provide further design strategies for various nanoparticle systems, in particular, for drug-delivery applications. However, polymeric systems often lack electron-density (particularly polyesters) which makes it difficult to identify them unambiguously within the cellular environment. We suggest that the combination of TEM with other analytical tools and physico-chemical as well as biological investigations will further improve the understanding of the underlying processes. In this development, correlative methods, combining information gained by complementary techniques, are highly desired, e.g., CLEM techniques are very promising.

Acknowledgements

The authors are grateful for the financial support in the frameworks of "Carl-Zeiss-Strukturmaßnahme" as well as the ProExzellenzinitiative "Nanopolar" of the federal state of Thuringia. The authors furthermore acknowledge the funding as a part of the Sonderforschunsgbereich "PolyTarget" (SFB 1278), project C04.

Conflict of Interest

The authors declare no conflict of interest.

Keywords

mammalian cells, polymeric nanoparticles, transmission electron microscopy, ultracellular structure, uptake

Received: July 3, 2017
Revised: August 14, 2017
Published online: January 11, 2018

[1] F. Piccinno, F. Gottschalk, S. Seeger, B. Nowack, *J. Nanopart. Res.* **2012**, *14*, 1109.
[2] K. Rajan, I. Roppolo, A. Chiappone, S. Bocchini, D. Perrone, A. Chiolerio, *Nanotechnol. Sci. Appl.* **2016**, *9*, 1.
[3] W. J. Stark, P. R. Stoessel, W. Wohlleben, A. Hafner, *Chem. Soc. Rev.* **2015**, *44*, 5793.
[4] a) T. Mitsudome, K. Kaneda, *Green Chem.* **2013**, *15*, 2636; b) B. S. Takale, M. Bao, Y. Yamamoto, *Org. Biomol. Chem.* **2014**, *12*, 2005.
[5] a) M. Rai, A. Yadav, A. Gade, *Biotechnol. Adv.* **2009**, *27*, 76; b) S. Prabhu, E. K. Poulose, *Int. Nano Lett.* **2012**, *2*, 32; c) G. Franci, A. Falanga, S. Galdiero, L. Palomba, M. Rai, G. Morelli, M. Galdiero, *Molecules* **2015**, *20*, 8856.
[6] a) M. N. Moore, *Environ. Int.* **2006**, *32*, 967; b) V. Srivastava, D. Gusain, Y. C. Sharma, *Ind. Eng. Chem. Res.* **2015**, *54*, 6209; c) M. A. Maurer-Jones, I. L. Gunsolus, C. J. Murphy, C. L. Haynes, *Anal. Chem.* **2013**, *85*, 3036.
[7] a) M. Das, N. Saxena, P. D. Dwivedi, *Nanotoxicology* **2009**, *3*, 10; b) R. J. B. Peters, G. van Bemmel, Z. Herrera-Rivera, H. P. F. G. Helsper, H. J. P. Marvin, S. Weigel, P. C. Tromp, A. G. Oomen, A. G. Rietveld, H. Bouwmeester, *J. Agric. Food Chem.* **2014**, *62*, 6285.
[8] a) S. W. Fage, J. Muris, S. S. Jakobsen, J. P. Thyssen, *Contact Dermatitis* **2016**, *74*, 323; b) A. Weir, P. Westerhoff, L. Fabricius, K. Hristovski, N. von Goetz, *Environ. Sci. Technol.* **2012**, *46*, 2242.
[9] a) E. Boisselier, D. Astruc, *Chem. Soc. Rev.* **2009**, *38*, 1759; b) T. Curry, R. Kopelman, M. Shilo, R. Popovtzer, *Contrast Media Mol. Imaging* **2014**, *9*, 53.
[10] a) S. Zeng, K.-T. Yong, I. Roy, X.-Q. Dinh, X. Yu, F. Luan, *Plasmonics* **2011**, *6*, 491; b) Y.-C. Yeh, B. Creran, V. M. Rotello, *Nanoscale* **2012**, *4*, 1871; c) C. Carnovale, G. Bryant, R. Shukla, V. Bansal, *Prog. Mater. Sci.* **2016**, *83*, 152; d) R. Arvizo, R. Bhattacharya, P. Mukherjee, *Expert Opin. Drug Delivery.* **2010**, *7*, 753.
[11] a) L. A. Austin, M. A. Mackey, E. C. Dreaden, M. A. El-Sayed, *Arch. Toxicol.* **2014**, *88*, 1391; b) P. D. Howes, R. Chandrawati,

M. M. Stevens, *Science* **2014**, *346*, 53; c) F. Peng, Y. Su, Y. Zhong, C. Fan, S.-T. Lee, Y. He, *Acc. Chem. Res.* **2014**, *47*, 612.
[12] a) E. Blanco, H. Shen, M. Ferrari, *Nat. Biotechnol.* **2015**, *33*, 941; b) A. Z. Wilczewska, K. Niemirowicz, K. H. Markiewicz, H. Car, *Pharm. Rep.* **2012**, *64*, 1020; c) W. H. De Jong, P. J. A. Borm, *Int. J. Nanomed.* **2008**, *3*, 133.
[13] a) F. Masood, *Mater. Sci. Eng. C* **2016**, *60*, 569; b) T. Patel, J. Zhou, J. M. Piepmeier, W. M. Saltzman, *Adv. Drug Delivery Rev.* **2012**, *64*, 701; c) M. Elsabahy, K. L. Wooley, *Chem. Soc. Rev.* **2012**, *41*, 2545.
[14] A. Kumari, S. K. Yadav, S. C. Yadav, *Colloids Surf., B* **2010**, *75*, 1.
[15] a) S. Ganta, H. Devalapally, A. Shahiwala, M. Amiji, *J. Controlled Release* **2008**, *126*, 187; b) J. Zhuang, M. R. Gordon, J. Ventura, L. Li, S. Thayumanavan, *Chem. Soc. Rev.* **2013**, *42*, 7421; c) F. Wendler, K. R. A. Schneider, B. Dietzek, F. H. Schacher, *Polym. Chem.* **2017**, *8*, 2959; d) T. Yildirim, I. Yildirim, R. Yanez-Macias, S. Stumpf, C. Fritzsche, S. Hoeppener, C. Guerrero-Sanchez, S. Schubert, U. S. Schubert, *Polym. Chem.* **2017**, *8*, 1328.
[16] R. Tantra, A. Knight, *Nanotoxicology* **2011**, *5*, 381.
[17] a) A. Vollrath, S. Schubert, U. S. Schubert, *J. Mater. Chem. B* **2013**, *1*, 1994; b) C. C. Fleischer, C. K. Payne, *Acc. Chem. Res.* **2014**, *47*, 2651; c) M. Schäferling, *Wiley Interdiscip. Rev. Nanomed. Nanobiotechnol.* **2016**, *8*, 378.
[18] L. Schermelleh, R. Heintzmann, H. Leonhardt, *J. Cell Biol.* **2010**, *190*, 165.
[19] a) B. O. Leung, K. C. Chou, *Appl. Spectrosc.* **2011**, *65*, 967; b) S. W. Hell, *Science* **2007**, *316*, 1153.
[20] a) A. Reisch, P. Didier, L. Richert, S. Oncul, Y. Arntz, Y. Mély, A. S. Klymchenko, *Nat. Commun.* **2014**, *5*, 4089; b) D. van der Zwaag, N. Vanparijs, S. Wijnands, R. De Rycke, B. G. De Geest, L. Albertazzi, *ACS Appl. Mater. Interfaces* **2016**, *8*, 6391.
[21] a) J. J. Bozzola, L. D. Russell, *Electron Microscopy: Principles and Techniques for Biologists*, Jones & Bartlett Learning, London, Boston **1999**; b) G. Knott, C. Genoud, *J. Cell Sci.* **2013**, *126*, 4545; c) C. J. Peddie, L. M. Collinson, *Micron* **2014**, *61*, 9; d) D. J. Flannigan, A. H. Zewail, *Acc. Chem. Res.* **2012**, *45*, 1828.
[22] S. M. Wilson, A. Bacic, *Nat. Protoc.* **2012**, *7*, 1716.
[23] C. Vauthier, K. Bouchemal, *Pharm. Res.* **2009**, *26*, 1025.
[24] A. Verma, F. Stellacci, *Small* **2010**, *6*, 12.
[25] K. Knop, R. Hoogenboom, D. Fischer, U. S. Schubert, *Angew. Chem., Int. Ed.* **2010**, *49*, 6288.
[26] S. Schubert, J. J. T. Delaney, U. S. Schubert, *Soft Matter* **2011**, *7*, 1581.
[27] A. H. Faraji, P. Wipf, *Bioorg. Med. Chem.* **2009**, *17*, 2950.
[28] Y. Mai, A. Eisenberg, *Chem. Soc. Rev.* **2012**, *41*, 5969.
[29] a) T. Yildirim, A. Traeger, E. Preussger, S. Stumpf, C. Fritzsche, S. Hoeppener, S. Schubert, U. S. Schubert, *Macromolecules* **2016**, *49*, 3856; b) A. Vollrath, D. Pretzel, C. Pietsch, I. Perevyazko, S. Schubert, G. M. Pavlov, U. S. Schubert, *Macromol. Rapid Commun.* **2012**, *33*, 1791; c) T. Yildirim, A. C. Rinkenauer, C. Weber, A. Traeger, S. Schubert, U. S. Schubert, *J. Polym. Sci., Part A: Polym. Chem.* **2015**, *53*, 2711.
[30] a) M. Iqbal, N. Zafar, H. Fessi, A. Elaissari, *Int. J. Pharm.* **2015**, *496*, 173; b) I. Katouzian, S. M. Jafari, *Trends Food Sci. Technol.* **2016**, *53*, 34.
[31] a) R. Pecora, *J. Nanopart. Res.* **2000**, *2*, 123; b) S. K. Brar, M. Verma, *Trends Anal. Chem. TRAC* **2011**, *30*, 4.
[32] P.-C. Lin, S. Lin, P. C. Wang, R. Sridhar, *Biotechnol. Adv.* **2014**, *32*, 711.
[33] a) J. Wotschadlo, T. Liebert, J. H. Clement, N. Anspach, S. Höppener, T. Rudolph, R. Müller, F. H. Schacher, U. S. Schubert, T. Heinze, *Macromol. Biosci.* **2013**, *13*, 93; b) K. Babiuch, R. Wyrwa, K. Wagner, T. Seemann, S. Hoeppener, C. R. Becer, R. Linke, M. Gottschaldt, J. Weisser, M. Schnabelrauch, U. S. Schubert, *Biomacromolecules* **2011**, *12*, 681; c) D. J. Kim, S. M. Kang, B. Kong, W.-J. Kim, H.-j. Paik, H. Choi, I. S. Choi, *Macromol. Chem. Phys.* **2005**, *206*, 1941.
[34] a) P. Webster, H. Schwarz, G. Griffiths, *Methods Cell Biol.* **2008**, *88*, 45; b) J. Dubochet, M. Adrian, J.-J. Chang, J.-C. Homo, J. Lepault, A. W. McDowall, P. Schultz, *Q. Rev. Biophys.* **1998**, *21*, 129; c) K. T. Tokuyasu, *Histochem. J.* **1980**, *12*, 381.
[35] D. Belazi, S. Solé-Domènech, B. Johansson, M. Schalling, P. Sjövall, *Histochem. Cell Biol.* **2009**, *132*, 105.
[36] a) J. A. Kiernan, *Micros. Today* **2000**, *1*, 8; b) S. Takatori, R. Mesman, T. Fujimoto, *Biochemistry* **2014**, *53*, 639; c) D. Hopwood, *Histochem J.* **1972**, *4*, 267.
[37] R. Kalluru, F. Fenaroli, D. Westmoreland, L. Ulanova, A. Maleki, N. Roos, M. Paulsen Madsen, G. Koster, W. Egge-Jacobsen, S. Wilson, H. Roberg-Larsen, G. K. Khuller, A. Singh, B. Nystrom, G. Griffiths, *J. Cell Sci.* **2013**, *126*, 3043.
[38] E. S. Reynolds, *J. Cell Biol.* **1963**, *17*, 208.
[39] a) D. Studer, B. M. Humbel, M. Chiquet, *Histochem. Cell Biol.* **2008**, *130*, 877; b) J. R. McIntosh, *J. Cell Biol.* **2001**, *153*, F25.
[40] a) M. Kudryashev, D. Castaño-Díez, H. Stahlberg, *Comput. Struct. Biotechnol. J.* **2012**, *1*, e201207002; b) C. A. Diebolder, A. J. Koster, R. I. Koning, *J. Microsc.* **2012**, *248*, 1.
[41] a) I. Hurbain, M. Sachse, *Biol. Cell* **2011**, *103*, 405; b) V. Lučić, A. Rigort, W. Baumeister, *J. Cell Biol.* **2013**, *202*, 407.
[42] K. Cortese, A. Diaspro, C. Tacchetti, *J. Histochem. Cytochem.* **2009**, *57*, 1103.
[43] K. L. McDonald, *J. Microsc.* **2009**, *235*, 273.
[44] P. Chlanda, J. Krijnse Locker, *Biochem. J.* **2017**, *474*, 1041.
[45] L. Muscariello, F. Rosso, G. Marino, A. Giordano, M. Barbarisi, G. Cafiero, A. Barbarisi, *J. Cell. Physiol.* **2005**, *205*, 328.
[46] A. A. Sousa, R. D. Leapman, *Ultramicroscopy* **2012**, *123*, 38.
[47] A. Bogner, G. Thollet, D. Basset, P. H. Jouneau, C. Gauthier, *Ultramicroscopy* **2005**, *104*, 290.
[48] a) N. Liv, I. Lazi , P. Kruit, J. P. Hoogenboom, *Ultramicroscopy* **2014**, *143*, 93; b) K. Böse, M. Koch, C. Cavelius, A. K. Kiemer, A. Kraegeloh, *Part. Part. Syst. Charact.* **2014**, *31*, 439.
[49] a) T.-G. Iversen, T. Skotland, K. Sandvig, *Nano Today* **2011**, *6*, 176.; b) B. Yameen, W. I. Choi, C. Vilos, A. Swami, J. Shi, O. C. Farokhzad, *J. Controlled Release* **2014**, *190*, 485.
[50] R. G. Parton, K. Simons, *Nat. Rev. Mol. Cell Biol.* **2007**, *8*, 185.
[51] T. Kirchhausen, *Annu. Rev. Biochem.* **2000**, *69*, 699.
[52] K. Sandvig, M. L. Torgersen, H. A. Raa, B. van Deurs, *Histochem. Cell. Biol.* **2008**, *129*, 267.
[53] S. Barth, D. Glick, K. F. Macleod, *J. Pathol.* **2010**, *221*, 117.
[54] A. K. Varkouhi, M. Scholte, G. Storm, H. J. Haisma, *J. Controlled Release* **2011**, *151*, 220.
[55] P. L. Tuma, A. L. Hubbard, *Physiol. Rev.* **2003**, *83*, 871.
[56] a) J. D. Lopez-Castro, A. V. Maraloiu, J. J. Delgado, J. J. Calvino, M. G. Blanchin, N. Galvez, J. M. Dominguez-Vera, *Nanoscale* **2011**, *3*, 4597; b) A. R. Mishra, J. Zheng, X. Tang, P. L. Goering, *Toxicol. Sci.* **2016**, *150*, 473.
[57] a) I. G. Macara, *Microbiol. Mol. Biol. Rev.* **2001**, *65*, 570; b) K. Huang, H. Ma, J. Liu, S. Huo, A. Kumar, T. Wei, X. Zhang, S. Jin, Y. Gan, P. C. Wang, S. He, X. Zhang, X.-J. Liang, *ACS Nano* **2012**, *6*, 4483.
[58] N. de Jonge, D. B. Peckys, *ACS Nano* **2016**, *10*, 9061.
[59] a) C. Rosman, S. Pierrat, A. Henkel, M. Tarantola, D. Schneider, E. Sunnick, A. Janshoff, C. Sönnichsen, *Small* **2012**, *8*, 3683; b) A. Elsaesser, C. A. Barnes, G. McKerr, A. Salvati, I. Lynch, K. A. Dawson, C. V. Howard, *Nanomedicine (Lond.)* **2011**, *6*, 1189; c) B. Rothen-Rutishauser, D. A. Kuhn, Z. Ali, M. Gasser, F. Amin, W. J. Parak, D. Vanhecke, A. Fink, P. Gehr, C. Brandenberger, *Nanomedicine (Lond.)* **2013**, *9*, 607.
[60] P. Nativo, I. A. Prior, M. Brust, *ACS Nano* **2008**, *2*, 1639.
[61] W. Lu, C. Xiong, R. Zhang, L. Shi, M. Huang, G. Zhang, S. Song, Q. Huang, G.-y. Liu, C. Li, *J. Controlled Release* **2012**, *161*, 959.

[62] G. K. Hinkley, P. Carpinone, J. W. Munson, K. W. Powers, S. M. Roberts, *Part. Fibre Toxicol.* **2015**, *12*, 9.
[63] A. L. Tam, M. P. Melancon, M. Abdelsalam, T. A. Figueira, K. Dixon, A. McWatters, M. Zhou, Q. Huang, O. Mawlawi, K. Dunner, C. Li, S. Gupta, *J. Biomed. Nanotechnol.* **2016**, *12*, 296.
[64] M. McCully, Y. Hernandez, J. Conde, P. V. Baptista, J. M. Fuente, A. Hursthouse, D. Stirling, C. C. Berry, *Nano Res.* **2015**, *8*, 3281.
[65] X. Liu, H. Li, Y. Chen, Q. Jin, K. Ren, J. Ji, *Adv. Healthcare Mater.* **2014**, *3*, 1439.
[66] R. Gromnicova, M. Kaya, I. A. Romero, P. Williams, S. Satchell, B. Sharrack, D. Male, *PLoS One* **2016**, *11*, e0161610.
[67] J. Yue, T. J. Feliciano, W. Li, A. Lee, T. W. Odom, *Bioconjugate Chem.* **2017**, *28*, 1791.
[68] C. Freese, R. E. Unger, R. C. Deller, M. I. Gibson, C. Brochhausen, H.-A. Klok, C. J. Kirkpatrick, *Biomater. Sci.* **2013**, *1*, 824.
[69] R. Shukla, V. Bansal, M. Chaudhary, A. Basu, R. R. Bhonde, M. Sastry, *Langmuir* **2005**, *21*, 10644.
[70] S. Suarasan, M. Focsan, M. Potara, O. Soritau, A. Florea, D. Maniu, S. Astilean, *ACS Appl. Mater. Interfaces* **2016**, *8*, 22900.
[71] M. Thomas, A. M. Klibanov, *Proc. Natl. Acad. Sci. USA* **2003**, *100*, 9138.
[72] M. Arsianti, M. Lim, S. N. Lou, I. Y. Goon, C. P. Marquis, R. Amal, *J. Colloid Interface Sci.* **2011**, *354*, 536.
[73] D. P. Cormode, G. O. Skajaa, A. Delshad, N. Parker, P. A. Jarzyna, C. Calcagno, M. W. Galper, T. Skajaa, K. C. Briley-Saebo, H. M. Bell, R. E. Gordon, Z. A. Fayad, S. L. C. Woo, W. J. M. Mulder, *Bioconjugate Chem.* **2011**, *22*, 353.
[74] G. T. Grottone, R. R. Loureiro, J. Covre, E. B. Rodrigues, J. Á. P. Gomes, *Curr. Eye Res.* **2014**, *39*, 403.
[75] M. Heine, A. Bartelt, O. T. Bruns, D. Bargheer, A. Giemsa, B. Freund, L. Scheja, C. Waurisch, A. Eychmüller, R. Reimer, H. Weller, P. Nielsen, J. Heeren, *Beilstein J. Nanotechnol.* **2014**, *5*, 1432.
[76] A. J. Giustini, R. Ivkov, P. J. Hoopes, *Nanotechnology* **2011**, *22*, 345101.
[77] S. Schwarz, J. E. Wong, J. Bornemann, M. Hodenius, U. Himmelreich, W. Richtering, M. Hoehn, M. Zenke, T. Hieronymus, *Nanomedicine* **2012**, *8*, 682.
[78] H. L. McConnell, D. L. Schwartz, B. E. Richardson, R. L. Woltjer, L. L. Muldoon, E. A. Neuwelt, *Nanomedicine* **2016**, *12*, 1535.
[79] T. J. England, P. M. W. Bath, M. Abaei, D. Auer, D. R. E. Jones, *Cytotherapy* **2013**, *15*, 384.
[80] N. K. Iversen, S. Frische, K. Thomsen, C. Laustsen, M. Pedersen, P. B. L. Hansen, P. Bie, J. Fresnais, J.-F. Berret, E. Baatrup, T. Wang, *Toxicol. Appl. Pharm.* **2013**, *266*, 276.
[81] G. Liu, Z. Wang, J. Lu, C. Xia, F. Gao, Q. Gong, B. Song, X. Zhao, X. Shuai, X. Chen, H. Ai, Z. Gu, *Biomaterials* **2011**, *32*, 528.
[82] S. H. Bakhru, E. Altiok, C. Highley, D. Delubac, J. Suhan, T. K. Hitchens, C. Ho, S. Zappe, *Int. J. Nanomedicine* **2012**, *7*, 4613.
[83] Y.-K. Chang, Y.-P. Liu, J. H. Ho, S.-C. Hsu, O. K. Lee, *J. Orthop. Res.* **2012**, *30*, 1499.
[84] B. Santini, I. Zanoni, R. Marzi, C. Cigni, M. Bedoni, F. Gramatica, L. Palugan, F. Corsi, F. Granucci, M. Colombo, *PLoS One* **2015**, *10*, e0126366.
[85] K. V. Kilchrist, B. C. Evans, C. M. Brophy, C. L. Duvall, *Cell. Mol. Bioeng.* **2016**, *9*, 368.
[86] P. Ravikumar, J. U. Menon, P. Punnakitikashem, D. Gyawali, O. Togao, M. Takahashi, J. Zhang, J. Ye, O. W. Moe, K. T. Nguyen, C. C. Hsia, *Nanomedicine* **2016**, *12*, 811.
[87] M. Reifarth, E. Preußger, U. S. Schubert, R. Heintzmann, S. Hoeppener, *Part. Part. Syst. Charact.* **2017**, *34*, 1700180.
[88] S. Thakral, N. K. Thakral, D. K. Majumdar, *Expert Opin. Drug Delivery.* **2013**, *10*, 131.
[89] A. Pitto-Barry, N. P. E. Barry, *Polym. Chem.* **2014**, *5*, 3291.
[90] M. Abdel-Wahhab, K. Abdel-Wahhab, F. Mannaa, N. Hassan, R. Safar, R. Diab, B. Foliguet, L. Ferrari, B. Rihn, *Materials* **2014**, *7*, 1555.
[91] S. Waiczies, S. Lepore, K. Sydow, S. Drechsler, M. C. Ku, C. Martin, D. Lorenz, I. Schutz, H. M. Reimann, B. Purfurst, M. A. Dieringer, H. Waiczies, M. Dathe, A. Pohlmann, T. Niendorf, *Sci. Rep.* **2015**, *5*, 8427.
[92] A. Madaan, P. Singh, A. Awasthi, R. Verma, A. T. Singh, M. Jaggi, S. K. Mishra, S. Kulkarni, H. Kulkarni, *Clin. Transl. Oncol.* **2013**, *15*, 26.
[93] C. Loos, T. Syrovets, A. Musyanovych, V. Mailänder, K. Landfester, G. U. Nienhaus, T. Simmet, *Beilstein J. Nanotechnol.* **2014**, *5*, 2403.
[94] a) B. Liu, Z. Fu, Y. Han, M. Zhang, H. Zhang, *Colloid Polym. Sci.* **2017**, *295*, 749; b) J. Ramos, J. Forcada, R. Hidalgo-Alvarez, *Chem. Rev.* **2014**, *114*, 367.
[95] C. Pichot, *Curr. Opin. Colloid Interface Sci.* **2004**, *9*, 213.
[96] R. M. Zucker, in *Confocal Microscopy: Methods and Protocols* (Ed: S. W. Paddock), Springer New York, New York, NY **2014**, p. 321.
[97] a) P. Dedecker, G. C. Mo, T. Dertinger, J. Zhang, *Proc. Natl. Acad. Sci. USA* **2012**, *109*, 10909; b) A. Szymborska, A. de Marco, N. Daigle, V. C. Cordes, J. A. G. Briggs, J. Ellenberg, *Science* **2013**, *341*, 655.
[98] C. Ng, J. Li, R. Perumalsamy, F. Watt, L. Yung, B. Bay, *Microsc. Sci. Technol. Appl. Educ.* **2010**, *1*, 316.
[99] B. M. Rothen-Rutishauser, S. Schurch, B. Haenni, N. Kapp, P. Gehr, *Environ. Sci. Technol.* **2006**, *40*, 4353.
[100] S. Lerch, S. Ritz, K. Bley, C. Messerschmidt, C. K. Weiss, A. Musyanovych, K. Landfester, V. Mailander, *Nanomedicine* **2015**, *11*, 1585.
[101] R. Firdessa, T. A. Oelschlaeger, H. Moll, *Eur. J. Cell Biol.* **2014**, *93*, 323.
[102] M. Dass, K. Landfester, P. Walther, *Microsc. Microanal.* **2007**, *13*, 220.
[103] A. Musyanovych, J. Dausend, M. Dass, P. Walther, V. Mailander, K. Landfester, *Acta Biomater.* **2011**, *7*, 4160.
[104] A. Tautzenberger, S. Lorenz, L. Kreja, A. Zeller, A. Musyanovych, H. Schrezenmeier, K. Landfester, V. Mailander, A. Ignatius, *Biomaterials* **2010**, *31*, 2064.
[105] A. Tautzenberger, L. Kreja, A. Zeller, S. Lorenz, H. Schrezenmeier, V. Mailander, K. Landfester, A. Ignatius, *Biomaterials* **2011**, *32*, 1706.
[106] H. K. Makadia, S. J. Siegel, *Polymers* **2011**, *3*, 1377.
[107] M. Jamshidian, E. A. Tehrany, M. Imran, M. Jacquot, S. Desobry, *Compr. Rev. Food Sci. Food Saf.* **2010**, *9*, 552.
[108] P. Lai, W. Daear, R. Löbenberg, E. J. Prenner, *Colloids Surf., B* **2014**, *118*, 154;
[109] a) E. Rytting, J. Nguyen, X. Wang, T. Kissel, *Expert Opin. Drug Delivery.* **2008**, *5*, 629; b) B. Tyler, D. Gullotti, A. Mangraviti, T. Utsuki, H. Brem, *Adv. Drug Delivery Rev.* **2016**, *107*, 163.
[110] A.-K. Barthel, M. Dass, M. Dröge, J.-M. Cramer, D. Baumann, M. Urban, K. Landfester, V. Mailänder, I. Lieberwirth, *Beilstein J. Nanotechnol.* **2014**, *5*, 1905.
[111] Y. Lemmer, L. Kalombo, R. D. Pietersen, A. T. Jones, B. Semete-Makokotlela, S. Van Wyngaardt, B. Ramalapa, A. C. Stoltz, B. Baker, J. A. Verschoor, H. S. Swai, C. de Chastellier, *J. Controlled Release* **2015**, *211*, 94.
[112] W. Wang, S. Zhou, L. Guo, W. Zhi, X. Li, J. Weng, *Int. J. Nanomedicine* **2010**, *5*, 557.
[113] K. Y. Win, S. S. Feng, *Biomaterials* **2005**, *26*, 2713.
[114] W. Sun, H. Wang, C. Xie, Y. Hu, X. Yang, H. Xu, *J. Controlled Release* **2006**, *115*, 259.
[115] M. Reifarth, D. Pretzel, S. Schubert, C. Weber, R. Heintzmann, S. Hoeppener, U. S. Schubert, *Chem. Commun.* **2016**, *52*, 4361.

[116] J. Panyam, S. K. Sahoo, S. Prabha, T. Bargar, V. Labhasetwar, *Int. J. Pharm.* **2003**, *262*, 1.
[117] a) S. T. Chou, K. Hom, D. Zhang, Q. Leng, L. J. Tricoli, J. M. Hustedt, A. Lee, M. J. Shapiro, J. Seog, J. D. Kahn, A. J. Mixson, *Biomaterials* **2014**, *35*, 846; b) A. El-Sayed, S. Futaki, H. Harashima, *AAPS J.* **2009**, *11*, 13.
[118] H. Zhou, X. Ma, Y. Liu, L. Dong, Y. Luo, G. Zhu, X. Qian, J. Chen, L. Lu, J. Wang, X. Gao, *Mol. Med. Rep.* **2015**, *11*, 4381.
[119] N. Zuidam, G. Posthumab, E. de Vries, D. Crommelin, W. Hennink, G. Storm, *J. Drug Targeting* **2000**, *8*, 51.
[120] a) P. Midoux, C. Pichon, J.-J. Yaouanc, P.-A. Jaffrès, *Br. J. Pharmacol.* **2009**, *157*, 166; b) M. W. Amjad, P. Kesharwani, M. C. I. Mohd Amin, A. K. Iyer, *Prog. Polym. Sci.* **2017**, *64*, 154.
[121] J. E. Zuckerman, C. H. Choi, H. Han, M. E. Davis, *Proc. Natl. Acad. Sci. USA* **2012**, *109*, 3137.
[122] X. Zhong, D. Panus, W. Ji, C. Wang, *Mol. Pharm.* **2015**, *12*, 932.
[123] S. Mishra, P. Webster, M. E. Davis, *Eur. J. Cell Biol.* **2004**, *83*, 97.
[124] H. J. Gundersen, P. Bagger, T. F. Bendtsen, S. M. Evans, L. Korbo, N. Marcussen, A. Moller, K. Nielsen, J. R. Nyengaard, B. Pakkenberg, F.B. Sorensen, A. Vesterby, M.J. West, *APMIS* **1988**, *96*, 857.
[125] C. Gonçalves, E. Mennesson, R. Fuchs, J. P. Gorvel, P. Midoux, C. Pichon, *Mol. Ther.* **2004**, *10*, 373.
[126] R. Cartier, M. Velinova, C. Lehman, B. Erdmann, R. Reszka, *J. Histochem. Cytochem.* **2003**, *51*, 1237.
[127] T. Bus, C. Englert, M. Reifarth, P. Borchers, M. Hartlieb, A. Vollrath, S. Hoeppener, A. Traeger, U. S. Schubert, *J. Mater. Chem. B* **2017**, *5*, 1258.
[128] V. Zargar, M. Asghari, A. Dashti, *ChemBioEng Rev.* **2015**, *2*, 204.
[129] M. C. Gómez-Guillén, B. Giménez, M. E. López-Caballero, M. P. Montero, *Food Hydrocolloids* **2011**, *25*, 1813.
[130] S. Park, S. J. Lee, H. Chung, S. Her, Y. Choi, K. Kim, K. Choi, I. C. Kwon, *Microsc. Res. Tech.* **2010**, *73*, 857.
[131] R. Vivek, V. Nipun Babu, R. Thangam, K. S. Subramanian, S. Kannan, *Colloids Surf., B* **2013**, *111*, 117.
[132] F. Li, J. Li, X. Wen, S. Zhou, X. Tong, P. Su, H. Li, D. Shi, *Mater. Sci. Eng., C* **2009**, *29*, 2392.
[133] M. Malatesta, M. Giagnacovo, M. Costanzo, B. Conti, I. Genta, R. Dorati, V. Galimberti, M. Biggiogera, C. Zancanaro, *Eur. J. Histochem.* **2012**, *56*, e20.
[134] A. R. Maranto, *Science* **1982**, *217*, 953.
[135] X. Shu, V. Lev-Ram, T. J. Deerinck, Y. Qi, E. B. Ramko, M. W. Davidson, Y. Jin, M. H. Ellisman, R. Y. Tsien, *PLoS Biol.* **2011**, *9*, e1001041.
[136] A. K. Gupta, M. Gupta, S. J. Yarwood, A. S. G. Curtis, *J. Controlled Release* **2004**, *95*, 197.
[137] S. E. A. Gratton, P. A. Ropp, P. D. Pohlhaus, J. C. Luft, V. J. Madden, M. E. Napier, J. M. DeSimone, *Proc. Natl. Acad. Sci. USA* **2008**, *105*, 11613.
[138] S. Kim, W. K. Oh, Y. S. Jeong, J. Y. Hong, B. R. Cho, J. S. Hahn, J. Jang, *Biomaterials* **2011**, *32*, 2342.

Publication P2

"Considerations for the Uptake Characteristic of Inorganic Nanoparticles into Mammalian Cells—Insights Gained by TEM Investigations"

Martin Reifarth, Ulrich S. Schubert, Stephanie Hoeppener

Adv. Biosys. **2018**, 1700254.

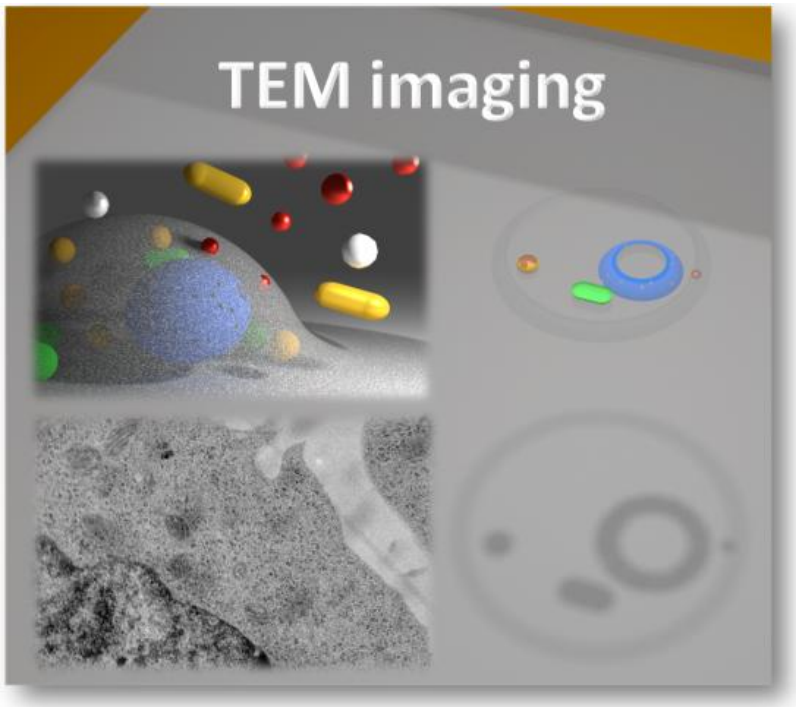

ADVANCED BIOSYSTEMS
www.adv-biosys.com

Considerations for the Uptake Characteristic of Inorganic Nanoparticles into Mammalian Cells—Insights Gained by TEM Investigations

*Martin Reifarth, Ulrich S. Schubert, and Stephanie Hoeppener**

The internalization of nanoparticles into mammalian cells relies on a complex interplay of several parameters, which enable and dictate uptake and fate of nanoparticles in the cellular system. Due to the complexity of the involved processes, a careful experimental design has to be developed to elucidate peculiarities of the uptake processes of new nanoparticle systems into cells. Individual parameters can be hardly considered alone but have to be carefully evaluated, as striking alterations of the particle internalization and fate might be induced. In this review, essential parameters are summarized and illustrative examples are presented demonstrating the consequences of the different parameters. Special focus is placed in this context on studies, which utilize transmission electron microscopy (TEM) to elucidate the particles' impact on the cells and to verify the nanoparticle uptake, localization as well as their effect on the cellular environment. Even though TEM is only one representative of a large number of very valuable investigation tools, the exceptional value, in particular, in view of the high resolution capabilities of TEM investigations is demonstrated by the chosen examples.

1. Introduction

The investigation of nanoparticle systems as drug delivery or probe systems to study cellular uptake has gained tremendous importance during the last years.[1] In nano-biotechnology, the comprehensive understanding of the nanoparticles' properties and their uptake efficiency into different cell types represents a major task. In general, these investigations comprise a variety of different studies. These utilize, e.g., fluorescence-activated cell scanning analysis[2] (FACS) to determine the internalized particle concentrations or studies are frequently conducted in conjunction with viability assays and inhibition experiments as well as biochemical analysis. In particular, standardized assays and the treatment of cells with chemical compounds which block individual uptake pathways[3] can help to distinguish between individual uptake mechanisms for respective nanoparticle systems. Cells internalizing nanoparticles respond to the nanoparticles and different intracellular processes will be initiated, possibly resulting in the impairment of the cellular key functions.[4] Even though these investigations provide data with statistical relevance, they can merely provide an overall picture of the uptake mechanism, as issues of different uptake mechanisms in anisotropic nanoparticle suspensions are barely assessable. Simultaneously, the influence of the biological environment, e.g., the presence of serum proteins, salts, or altered pH conditions, may have a severe impact on the particle properties, which can entail various biological implications. As such, the role of high resolution imaging techniques, which provide a clear evidence for the nanoparticles' fate in the cellular environment,[5] their localization and targeting to different cellular organelles, as well as evidence for uptake and release mechanisms, have gained increasing importance. In particular, transmission electron microscopy (TEM) investigations provide attractive possibilities to study the interaction of particles with biological barriers, i.e., the extracellular membrane or the nuclear membrane, their accumulation into cellular organelles or their spatial distribution on the scale of individual nanoparticles[6] (e.g., uptake as individual nanoparticles or in form of large clusters, etc.). In addition TEM can simultaneously image also the cellular membranes and organelles to determine respective morphological changes[7] upon nanoparticle interaction.[8–11] Thus, attractive possibilities to acquire additional information on the particle fate inside the cell emerge from TEM investigations.

It can be stated here, that the utilization of electron microscopy has been conducted during the last decades[5] and, in view of some extent electron microscopy investigations of particle uptake, can be regarded in this sense as a routinely applied technique. However, frequently TEM is only utilized to characterize the nanoparticle system or to prove particle internalization. Only a fraction of reported studies utilize TEM analysis to reveal details of nanoparticle uptake and internalization or even deduce uptake pathways from these studies. This might be related to the fact that sometimes the interpretation of TEM data is not straightforward but a number of experimental limitations have to be taken into account for such studies. In a recent review, the advantages and disadvantages of TEM investigations in the context of the

M. Reifarth, Prof. U. S. Schubert, Dr. S. Hoeppener
Laboratory of Organic and Macromolecular Chemistry (IOMC)
Friedrich Schiller University Jena
Humboldtstr. 10, 07743 Jena, Germany
E-mail: s.hoeppener@uni-jena.de
M. Reifarth, Prof. U. S. Schubert, Dr. S. Hoeppener
Jena Center for Soft Matter (JCSM)
Friedrich Schiller University Jena
Philosophenweg 7, 07743 Jena, Germany

DOI: 10.1002/adbi.201700254

localization of polymer nanoparticles in a rather large structure, i.e., a cell, have been summarized and practical solutions for improving these shortcomings have been summarized.[12] These include critically also the fact that TEM requires the preparation of thin slices, thus, TEM can merely provide a picture of the entire cell, which is a severe limitation for the quantitative assessment of particle uptake.[13,14] Furthermore, dynamic processes are difficult to study, since no live cell studies can be performed. These issues are of general nature and certainly apply also for investigations performed on inorganic nanoparticle systems. Traditionally the uptake of inorganic nanoparticles has been in focus of studies, since they are easily detectable in the framework of a cell by means of transmission electron microscopy studies. In general, literature on nanoparticle uptake into cells is vast,[15,16] but, at the same time, rather diverse and frequently no general conclusion about the uptake of a certain material can be drawn from the existing literature, despite the fact that many different groups studied even very similar nanomaterials. This can be rationalized when considering the many different parameters and nanoparticle properties, which affect the uptake of nanoparticles into cells.

This requests a very careful comparison of experimental conditions applied in different studies, if general patterns of particle uptake and fate for a particular class of nanoparticles are deduced.

Independently of these controversies, and sometimes contradictory results obtained from multiple studies, it has to be concluded that particle uptake and internalization of nanoparticles into cells depends on a number of important key factors, which include, e.g., the particle size,[17,18] their shape,[16,17] their aggregation state,[19] their surface charge,[20] their tendency to form a protein corona,[21] their crystalline state,[9,22,23] as well as the fact if the materials are inert under biological conditions or if dissociation of ions to the environment can occur. The respective factors have been studied by many different investigation tools and in particular TEM has contributed to a better understanding of the uptake and internalization of inorganic particles. In the literature, a few reports are found, in which the experimental conditions in uptake studies are systematically varied. It was, for instance, identified that the presence of salts in the incubation medium plays a significant role on the uptake characteristics of gold nanoparticles (AuNPs),[24] which entails implications on the uptake behavior into different cell lines and may result in different cytotoxicities.[19] Also conditions of cell incubation, used media and additives in buffer solutions, etc., may strongly affect the obtained results.[25] In this review, we summarize illustrative examples which demonstrate the value of TEM for the elucidation of the metabolic pathway of inorganic nanoparticles taken up by cells and discuss the main important parameters, which influence particle uptake and metabolism. These studies frequently provided profound knowledge and insight into the processes taking place inside a cell and can be regarded as important information to investigate the fate of the nanoparticles in the cell. Even though TEM is hardly the only method which is included in these studies, it has to be acknowledged that in particular studies on morphological changes of organelles, membranes, or other internal cell structures greatly benefit from the high resolution capabilities of this technique. Intracellular organelles, whose morphology is characterized by peculiar membrane topologies, i.e., mitochondria, the endoplasmic reticulum, or other cellular organelles, can be identified.[7] Inorganic nanoparticles may associate and interact with the organelle structures and are, owing to their often electron-dense appearance in TEM, particularly well observable within the intracellular environment or at the extracellular membrane.

Martin Reifarth studied chemistry at the Friedrich Schiller University, Jena, where he graduated in the group of Prof. Rainer Heintzmann. Currently, he is working on his Ph.D. thesis in the groups of Prof. Schubert and Prof. Heintzmann, in whose scope he investigates uptake and intracellular fate of nanoparticles by means of electron and fluorescence microscopy. His research interests cover—in addition to high-resolution microscopy—nanoparticle synthesis and characterization.

Ulrich S. Schubert was born in Tübingen (Germany) in 1969. He studied chemistry in Frankfurt and Bayreuth and at the Virginia Commonwealth University, Richmond (USA). Work toward his Ph.D. was performed at the Universities of Bayreuth and South Florida. After postdoctoral research with Prof. J.-M. Lehn at the University of Strasbourg (France), he moved to the TU Munich, where he habilitated in 1999. From 1999 to 2000 he was a professor at the University of Munich, and from 2000 to 2007 a full professor at the TU Eindhoven in the Netherlands. Since 2007, he has been a full professor at the Friedrich Schiller University Jena.

Stephanie Hoeppener studied physics at the Westfälische Wilhelms-University Münster, Germany, where she earned her Ph.D. degree in 2001 under the supervision of Prof. H. Fuchs and Prof. L. F. Chi. Thereafter, she joined the group of Prof. J. Sagiv at the Weizmann Institute of Science, Israel, as a Minerva fellow. In 2003 she moved to the group of Prof. U. S. Schubert, Eindhoven University of Technology, The Netherlands. Since 2009, she has been the project leader for Nanolithography and Surface Functionalization, and is responsible for electron microscopy in the Jena Center for Soft Matter at the Friedrich Schiller University Jena, Germany.

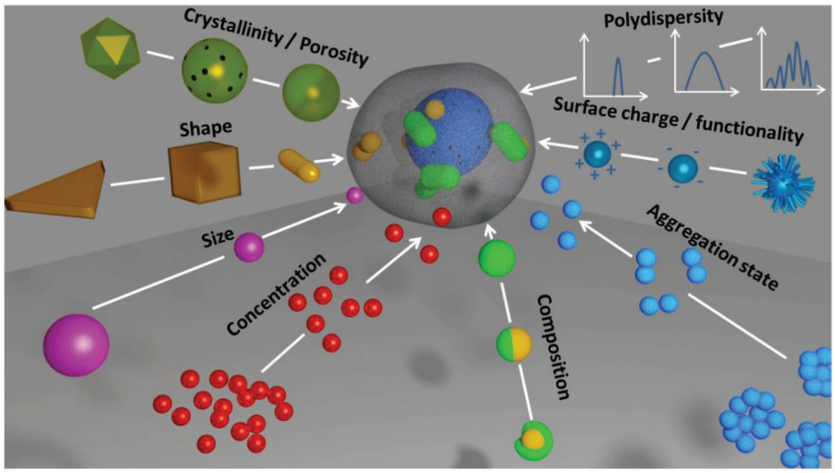

Figure 1. General overview of main parameters which influence the uptake and internalization of nanoparticles into cells. A multitude of different aspects has to be taken into account when studying the uptake and intracellular fate of nanoparticles in cellular systems. Frequently, systems cover more than one parameter which is regarded as a key factor determining the cellular response.

These possibilities motivated the preparation of this review article, which highlights in particular studies, which strongly rely on the results obtained by transmission electron microscopy studies to approach peculiarities of the uptake of nanoparticles with respect to their physicochemical properties. In this sense, the review does not aim on providing a complete overview on existing literature but rather highlights selected, individual studies where the utilization of TEM investigations contributed to a profound understanding of the intracellular processes with respect to the overall properties of the nanoparticle systems under investigation. In this context, various parameters contribute to the nanoparticle uptake and important properties of the systems under investigation are discussed (**Figure 1**). Many studies have addressed these issues and slowly a general consensus of important system parameters influencing the particle uptake is developing. Important parameters that have been identified include properties of the nanoparticles, i.e., the material the nanoparticles consist of, their size, and their shape and crystallinity, as well as the surface of the nanoparticles. The latter includes the availability of functional groups, e.g., sugars, antibodies, or positively or negatively charged entities. This is related to the fact that the particle surface represents the dominating interface between the cellular membrane and the nanoparticle and determines their interaction with the cellular boundaries and triggers specific uptake pathways. Furthermore, the effect of the formation of a particle–protein corona in relevant biological media is an effect whose influence has been in focus more recently due to a better understanding of the underlying effects. Moreover, the tendency of nanoparticle clusters to form larger aggregates is a critical point which can tremendously influence the uptake of particles.

In general, uptake events can be divided into passive and active processes. These include energy-dependent internalization mechanisms, i.e., phagocytosis, pinocytosis, receptor-mediated endocytosis, etc.,[26,27] or passive diffusion of the particles through membranes (**Figure 2**A). As a consequence of these uptake mechanisms, the subsequent localization of the nanoparticles within the cellular environment will be determined, which also has severe impact on the metabolic pathway of the nanoparticles after uptake. The processes involved in the uptake of nanoparticles are moreover strongly associated with the formation of characteristic changes induced by the interaction of the nanoparticles with the cellular membrane as well as their intracellular localization after internalization. For example, particles taken up by energy-dependent internalization mechanisms are related to the formation of membrane protrusions or invaginations[26] (Figure 2B–D). These nanoparticles are consequently localized into vesicular structures inside the cell, whereas nanoparticles that have been internalized via passive diffusion processes are frequently localized freely within the cytosol.

The membrane interactions play in this context an important role and can be efficiently visualized by TEM investigations. These investigations provide clear evidence for the uptake mechanisms and can support other investigation tools. Moreover, the visualization of peculiarities of the uptake and interaction events allows concluding on the uptake mechanism itself.

The situation can be even more complex, as frequently not only one process is involved in the uptake of nanoparticles into cells but sometimes different pathways are involved. As an illustrative example, Gromnicova et al.[30] investigated the uptake of small Au nanoparticles with a diameter of <5 nm into different epithelial cells (human kidney cells ciGENC and brain epithelium cells hCMEC/D3). The nanoparticles were surface functionalized with short poly ethylene glycol (PEG) units as well as with galactose. The galactose moieties are prone to stimulate active uptake mechanisms, which resulted in nanoparticles that were localized into vesicles, however, also a significant amount of nanoparticles was found freely into the cytosol, which is indicative for passive uptake. Statistical analysis of TEM investigations revealed a four times higher number of Au nanoparticles localized in vesicles than in the cytosol, indicating that active uptake is the dominating but not the exclusively relevant pathway for particle internalization. In this case two different particle features influenced the uptake; the small size, which facilitates passive uptake and the galactose functionalization of the particle surface which can stimulate receptor-mediated uptake.

In the following, illustrative studies involving TEM as a major investigation tool are discussed to summarize the main important parameters which can influence the particle uptake.

2. Particle Properties and Resulting Implications on Particle–Cell Interaction

2.1. Size and Size Distribution

One of the central and most important nanoparticle properties is the particle size and a large number of publications have addressed this issue. A comprehensive review highlighting

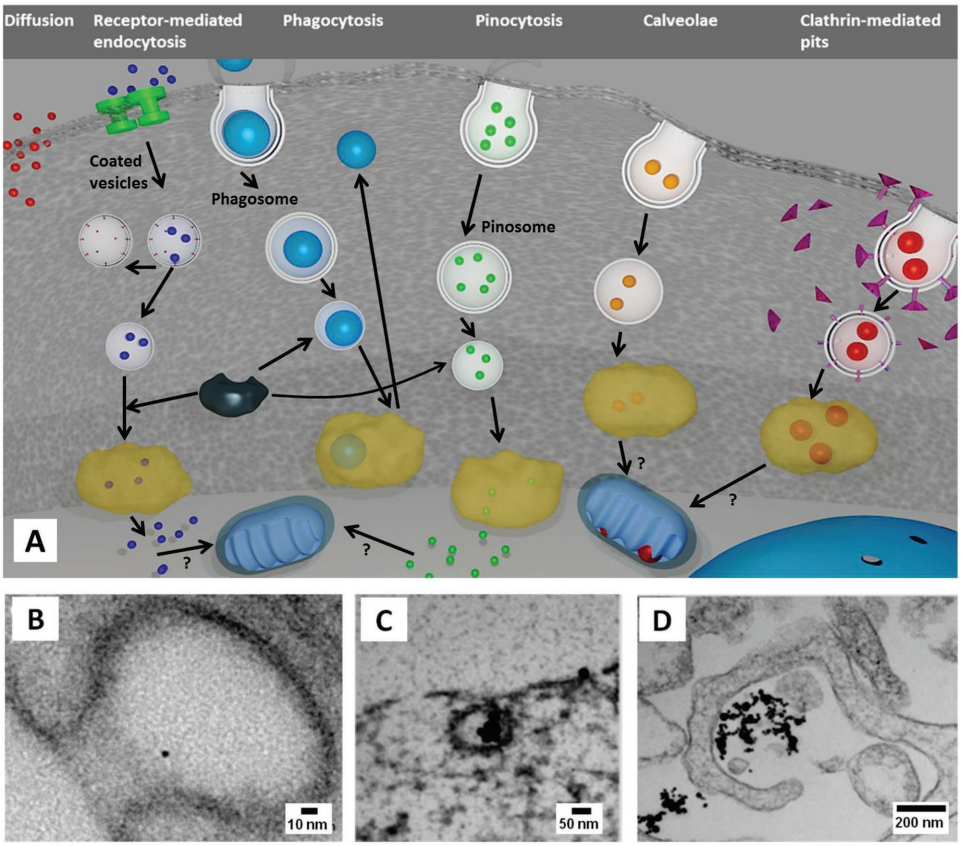

Figure 2. A) Overview of different uptake pathways of nanoparticles in cells. B–D) Typical TEM images of membrane structures associated with different uptake processes. B) Caveolin-dependent endocytosis. Caveolae represent invaginations with small diameters, which are detectable due to their characteristic flask-like shapes. Adapted with permission.[28] Copyright 2012, Springer. C) Clathrin-dependent endoycytosis: Clathrin-coated pits are larger in diameter compared to caveolae. Furthermore, the occurrence of an electron-dense coating of the invagination constitutes their typical feature of appearance. D) Macropinocytosis is associated with the formation of protrusions. Adapted with permission.[29] Copyright 2015, Springer. Scale bars of the images were modified.

detailed aspects of the size dependence of nanoparticle uptake is available elsewhere.[17,18] It has to be mentioned here, that the influence of particle size is frequently studied by comparing a limited number of different nanoparticle sizes and systematic investigations utilizing larger libraries of differently sized nano-objects remain rare.[31–35] It is generally acknowledged that for particles with diameters between 50 and 200 nm different endocytic processes are regarded as the predominant uptake mechanisms. This derives, among the utilization of other investigation tools, in particular from TEM investigations of the particle interaction with the plasma membrane and the analysis of their postuptake localization within the cells, which indicates their appearance inside intracellular vesicles. Most studies concentrate on the uptake of small and medium sized particles.[36] As an example, Hillyer and Albrecht[37] systematically compared the uptake of 4, 10, 28, and 58 nm gold nanoparticles in the gastrointestetinal tract (GIT) tissue of mice by quantitative TEM investigations. The authors found clear evidence that smaller particles crossed the GIT more easily compared to the larger ones and elucidated that the passage through the gut occurred via a persorption mechanism.

However, it has been additionally found that the particle size has a crucial impact on the toxicity of the nanoparticle system. A respective study, which compares the impact of the particle size, was reported by Yu et al.[32] The authors investigated the uptake of 30, 48, 118, and 535 nm silica particles into mouse keratinocytes (HEL-9). Internalization of all particles into vesicular structures inside the cytoplasm was found by TEM investigations. These studies were complemented with lactate dehydrogenase as well as the mitochondrial viability assays (MTT), which revealed that the cytotoxicities of particles with diameters of 30 and 48 nm were significantly increased at a concentration of 100 μg mL^{-1} compared to the larger particles with a diameter of 118 and 535 nm. The authors found also evidence for differences in their internal localization within the cell. While the small particles were clustered within the vesicular structures inside the cells, the large 535 nm silica particles were taken up as individual particles. The adverse effect on the cell viability of small nanoparticles could be also demonstrated by Tarantini et al.[38] The authors compared the internalization and effect of nonfunctionalized silica particles with sizes of 15 and 55 nm at low concentrations, respectively. TEM images revealed particle localization mainly within vesicles and, to a lesser extent, also freely in the cytoplasm in form of clustered aggregates consisting mainly of particles with a diameter of 15 nm and as individual particles if the particle dimensions are 55 nm. The authors showed that in particular the small particles induced cytotoxicity associated with apoptosis and, at higher concentrations, even result in chromosomal damage

along with proinflammatory effects. By contrast, these adverse effects were not observed for the larger particles.

For particles with a diameter below 25 nm, passive uptake, i.e., diffusive internalization into the cell body, is observed. Passive transport represents an occasional phenomenon and has been reported for different nanoparticle systems with diameters of <25 nm, which include SiO_2,[33,39] Au,[30,40–42] and Ag.[34] However, it has to be mentioned that passive transport is frequently accompanied by other active processes which might be involved as alternative uptake routes. The passive uptake of ≈15 nm ligand-free Au nanoparticles, fabricated by pulsed laser ablation and subsequent surface oxidation, into bovine endothelial cells was studied by Taylor et al.[41] The authors found a stimulated uptake of Au particles inside the cytosol, which were not associated to any vesicular structures, indicating passive uptake. In this context, TEM investigations represent a very valuable method to discriminate between individual particles being distributed freely in the cytosol or small aggregates of nanoparticles which might be associated to small vesicular structures. There is currently no other high resolution imaging tool, rather than TEM, available that can address this issue with comparable reliability. In particular, metal nanoparticles, i.e., gold nanoparticles, are easily recognizable objects in the cellular context. Owing to their high atomic number and the crystallinity, these nanoparticles possess a strong electron contrast, which is sufficient to recognize them in the cellular context. This holds even true when individual small nanoparticles have to be identified in the context of the cytosol, which usually is more electron-dense than the electron-lucent inside of vesicular organelles. It has to be mentioned here, that the particle size is not the only criterion which needs to be taken into account. An example was reported by Mustafa et al.[40] The authors utilized citrate stabilized Au nanoparticles with a size of 12 nm to study their concentration dependent uptake into mouse osteoblasts. These particles are formally prone to diffusive transport due to their small size. This diffusive entrance could be revealed for low concentrated nanoparticle solutions, whereas higher nanoparticle concentrations above 160 μg mL^{-1} resulted in endocytic uptake, which was characterized by the formation of membrane invaginations. The concentration and associated with that the aggregation of nanoparticles in the cellular environment is in this respect a critical factor which has to be taken into account when studying the uptake of nanoparticles into cells (for a detailed summary of the uptake mechanisms, see also Section 1 as well as Figure 1).

Special demands for internalization targeting the penetration of the nanoparticles to the nucleus have to be considered. These particles are supposed to possess a size <30–40 nm, since they have to bypass excretion pathways and a passage through nuclear pore complexes is required.[43,44] This pathway is rather difficult to address since in evolution eukaryotic cells have found ways to protect their genetic material from external materials.[45] Intranuclear passage of nanoparticles to the cell nucleus can feature undesired effects, i.e., genotoxicity or can be actively used for gene delivery applications.[43] As a necessary condition for particle uptake into the nucleus, particles have to be taken up into the cytoplasm,[46–48] which takes place by different mechanisms of uptake, either by endosomal escape[49] or passive diffusion processes. Afterward, the nuclear envelope needs to be crossed, which acts as a natural barrier. Ultrasmall particles with diameters <5 nm generally internalize efficiently into the nuclei, since they follow a passive uptake route and are, thus, immediately distributed into the cytoplasm. Furthermore, their small size supports the passage through the small nuclear pores. However, also larger particles >30 nm can be found into the nucleus.[8,40,50–52]

Surprisingly few studies address the uptake and internalization of large particles with a size larger than 300 nm into cells.[31–33] These particles are frequently observed to be localized individually inside the cytoplasm enclosed into vesicular structures, which indicates an uptake of these particles via endocytic processes without precedent aggregation processes. One reason for the limited number of studies on large particle systems might be related to impediments of classical TEM analysis, which requires the preparation of ultrathin specimens. Inorganic nanoparticles represent rather "hard" materials, which frequently possess also enhanced brittleness. As a consequence, the mechanical stress induced during mechanical sectioning by an ultramicrotome might result in a levering out of the particle from the cell slice rather than in the slicing of the nanoparticle in the cellular framework. This effect is less pronounced for particles of a diameter smaller than the slice thickness and for "soft" nanoparticles, i.e., amorphous silica or polymer nanoparticles,[53] which are likely to be sliced simultaneously with the surrounding cellular sample.

There are hardly any studies directly addressing the polydispersity of nanoparticles that do not undergo aggregation prior to their uptake. Investigations on highly dispersive nanoparticle systems would be very valuable and might provide additional insight into the size dependence of intracellular uptake, as in these cases the chemistry and physicochemical properties of the nanoparticles would be perfectly identical. These parameters have a strong influence on the uptake pathway and frequently play an even more important role than the size of the nanoparticles.

2.2. Aggregation

In many publications, the size effect on the uptake of nanoparticles is severely masked by different other effects. When it comes to the evaluation of size effects, a critical point is the formation of aggregates, which can form due to the instability of the nanoparticle solutions over time or aggregation in response to properties of the utilized solvent or the cellular environment. In these cases, mainly the aggregate size dominates the uptake characteristic rather than the size of the individual nanoparticle. Calero et al. could nicely demonstrate that small dimercaptosuccinic acid functionalized iron oxide nanoparticles (IONPs) with a size of ≈15 nm, despite their small size, feature an active pathway into human breast cancer (MCF-7) cells[29] rather than a passive process as could be expected for particles of this size. By TEM imaging, the authors could show the formation of particle clusters inside the culture medium, which subsequently governed the active uptake. Further investigations and analysis of the TEM images revealed a dependence of the uptake mechanism on the size of the formed clusters. Aggregates with a size below 200 nm stimulated membrane responses characteristic

for a clathrin-mediated uptake (compare Figure 2C), whereas the uptake of larger particle clusters is attributed to a micropinocytosis mediated uptake (compare Figure 2D). This study is a nice example highlighting the valuable contributions TEM imaging can provide. It can i) reveal the formation of large particle clusters, ii) prove the occurrence of differently sized particle aggregates, and iii) finally help to determine the individual uptake pathway by analysis of the membrane features and postinternalization localization of the particles.

The aggregation of nanoparticles might be induced by particle surface charge screening as a result of the high ionic strength in culture media,[54] the formation of protein coronae (see Section 2.6), or the pH conditions which might have an influence, e.g., on $-NH_2$ or $-COOH$-terminated particles.[25] As previously mentioned, these clustering phenomena have to be carefully considered. An uptake of rather large nanoparticles takes place via macropinocytosis, whereas smaller particles are, e.g., taken up via more specific pathways. Even though frequently the uptake is governed by the internalization of aggregates, it is also possible that this effect is less dominating. For example, Mu et al. discussed this effect by utilizing small spherical silica nanoparticles with a diameter of ≈14 nm to investigate their uptake in A549 cells.[39] The particles were exposed to cell culture medium and by dynamic light scattering (DLS) as well as by TEM studies the authors revealed the initial formation of large aggregates with hydrodynamic diameters of ≈500 nm. Generally, the occurrence of particle aggregation would result in the uptake of entire aggregates by active uptake mechanisms. However, in this case, TEM studies clearly revealed also the involvement of passive uptake pathways as emphasized by the detection of loosely agglomerated or well dispersed nanoparticles in the cytosol. No vesicle-associated particles or particles localized in the nucleus could be found at low particle concentrations after incubation times of 24 h. These studies were confirmed by TEM investigations of cell cultures which were exposed to the nanoparticles at 4 °C. At this temperature, it is expected that active, energy-dependent uptake mechanisms are considerably suppressed. Despite the low incubation temperature, a significant number of individual nanoparticles were internalized into the A549 cells, which is regarded as an additional confirmation of the preferential passive uptake of the silica nanoparticles. By performing additional impedance spectroscopy measurements on a tethered bilayer membrane model system, the authors moreover could reveal that the formation of a densely packed monolayer at the membrane is a prerequisite of passive diffusion through such barriers.

Even though aggregation is an important factor, this effect is sometimes neglected in studies of the intracellular uptake. The characterization of the applied nanoparticle systems should routinely consider this issue. Special emphasis should be placed to conduct aggregation studies in the relevant cell culture media and at the respective concentrations to ensure reproducible particle sizes or aggregate dimensions. This also ensures a safe interpretation of the obtained results, as particle clustering can be also a phenomenon occurring at a later stage in the cellular environment, e.g., due to endosomal/lysomal fusion processes. An example for particle clustering at the membrane was reported by Mustafa et al.[40] 12 nm gold nanoparticles were incubated on MC3T3-E1 cells at different concentration ranges. The authors conducted control experiments to validate that no aggregation of the particles took place in the cell medium, but particles formed aggregates only at the cell membrane. The authors concluded from their studies that the size of the individual nanoparticles becomes rather insignificant but is governed by the size of the aggregates formed at the cellular membrane. Carenza et al. demonstrated on the example of maghemite nanoparticles the complexity of the aggregation process.[55] The particles were stabilized with tetrametyhlammonium hydroxide and sodium citrate and tend to form aggregates. The authors could control the size of the formed aggregates by the ionic strength and the properties of the media used in the course of their experiments. As such, aggregation of nanoparticles resembles a complex interplay of different experimental conditions which will have a strong influence on the observed cellular uptake response which should be carefully controlled in view of a reliable interpretation of obtained nanoparticle uptake studies. At the same time, the state of aggregation of nanoparticles dramatically influences the uptake mechanism of the particles into the cells, which can be nicely discriminated by TEM investigations by the appearance of the respective membrane features, which are indicative for specific uptake routes.

The occurrence of particle aggregates does not only exhibit an influence on the uptake characteristics, it has also been reported to show an impact on particle toxicity.[38]

2.3. Shape

With improved synthesis protocols, the availability of nonspherical nanoparticle systems significantly increased during the last decades. Consequently, the investigation of this parameter on the uptake of these particle systems has gained increasing attention. As such, it has been explored that "unusual" geometries can add valuable physicochemical as well as biological features to the nanoparticulate systems.[16] Additionally, physical properties, i.e., the availability of plasmonic resonances or the strong enhancement of Raman signals,[56] can introduce interesting properties for therapeutic approaches. These include for gold nanorods, e.g., plasmonic absorbance in the near infrared (NIR) range[57] or the possibility to establish hyperthermia applications,[58] which utilize the interaction of the nanoscale object with electromagnetic radiation to selectively heat the nanomaterial.[59] As a major consequence of nonspherical geometries, the interaction of the nano-objects with the cellular membranes is altered, i.e., the effective interaction area in case of rods might be significantly different compared to spherical particles, moreover, preferential uptake in a certain orientation might occur.

Zhang[60] et al. investigated the uptake of gold nanorods (14 nm × 57 nm) coated with poly(diallyldimethyl ammoniumchloride) (PDDAC) into human breast cancer cells (MDA-MB-231). These studies were performed at different times after particle incubation. After 15 min, gold nanorods adhered at the plasma membrane and the authors could observe an uptake event, which provided evidence for a vertical internalization of the nanorod. After the internalization, the nanorods were localized in small vesicles in close vicinity to the membrane. The authors observed an electron-dense coating of the vesicles, which they attributed to the presence of clathrin, thus,

evidence for a clathrin-mediated uptake of the nanorods was found. Investigations at later time points after incubation could moreover demonstrate that the nanorods undergo an ordinary lysosomal maturation process. After 6 h, the individual vesicles hosted a large number of aggregated nanorods, which is indicative for lysosomal fusion processes. Furthermore, the authors found also evidence for the excretion of the nanorods from the cells. After 30 min, the authors could identify two populations of nanorods interacting with the extracellular membrane. Next to the pristine nanorods with no remarkable surface decoration, rods which showed a coating consisting of an electron dense material were found. The later nanorods are supposed to have been excreted by exocytosis processes. These rods can undergo re-endocytosis as could be deduced from a detailed analysis of the TEM data, which was supplemented by other techniques. In this study, the authors were able to elucidate the complete intracellular fate cycle of the nanorods. However, it remains unclear if the uptake and internalization are governed by the unique structure of the nanorods or are dominated by the PDDAC coating.

Sun et al. investigated the impact of iron oxide nanobricks on mouse-brain derived microvessel endothelial cells (bEnd.3) in comparison to identically functionalized nanospheres.[61] Both nanobricks and spheres were silanized to attach carboxy groups onto their surfaces, resulting in negatively charged materials (ζ-potential −39 mV for spheres, −45 mV for bricks). According to TEM investigations, the spheres featured a size of 8 nm, whereas the bricks feature dimensions of $15 \times 10 \times 5$ nm^3. TEM investigations revealed that nanospheres were loosely bound at the membrane of the bEnd.3 cells and internalized; however, not in significant amounts. By contrast, a significantly higher number of nanobricks was found inside the bEnd.3 cells. The iron amount was quantified by applying a ferrozine assay, which confirmed the enhanced uptake of bricks as suggested by TEM results. As uptake mechanism for both formulations, caveolae-mediated uptake was identified. The authors suggested that an enhanced uptake of nanobricks is a direct result of different geometric features, i.e., that an enhanced contact area with the cell surface leads to an increased interaction between surface features and the particle surface. In their studies, the authors utilized TEM as a powerful tool to underline this hypothesis. A possible impediment might be a direct result of the rather small dimensions of the nanobricks compared to the thickness of the investigated sections. Considering a section of a cell sample, it is likely that its cellular membranes are not oriented exactly perpendicular to the cutting surfaces. As a consequence nanobricks adhering at the cellular membrane might be displayed as "blurry" objects, since their individual tilts are not displayed correctly in a TEM image projection. In order to precisely determine the orientation of the nanostructures during the uptake, sample images should be acquired at different angles, in the best case even by applying electron tomography investigations to circumvent these problems.

Gold nanomaterials are also accessible in many other geometries. For example, Yue et al. investigated the uptake of gold nanostars (≈40 nm) in comparison to differently sized spherical particles (diameters ≈13 and 50 nm) into U87 glioblastoma cells.[62] These studies indicated that the star shape results in an enhanced liberation of the nanostars from intracellular vesicles, which can be explained by membrane rupture processes initiated by the star spikes. Despite the shape driven rupture and cellular interactions, it has to be taken into account that other influences might have a stronger impact on the nanoparticles' fate in the cellular environment.

To clarify the influence of the shape on the uptake, a comparison of particles with different shapes should be accompanied by an investigation of their identical spherical analogues. Such an investigation was performed by Rosman et al.[13] The authors investigated the uptake of gold nanorods (≈38×17 nm^2) coated with hexadecyltrimethylammonium bromide (CTAB) as well as aminofunctionalized and carboxyfunctionalized PEG and exposed them to alveolar cancer cells and compared their uptake efficiency with the respective spherical particles.[13] The authors of this study used statistical image analysis using a sophisticated sampling method. Image analysis revealed that the influence of the shape in that case was not that distinct; in fact, the surface coating had a stronger influence on the uptake efficiency.

Different shapes of nanoparticles can be also associated with different crystallinities of the materials used for particle synthesis and should be taken into account for cell uptake investigations.

2.4. Crystallinity

In addition to particle shape, also the particle morphology, i.e., the crystallinity or amorphous appearance of the material, plays in important role concerning the bioactivity of nanoparticles. Abundant investigations on the morphologies of particles and their biological effects have been reported for TiO_2 NPs. Therefore, it has to be kept in mind that TiO_2 exists in four different phases: the anatase-phase, the rutile-phase, the brookite-phase, and the amorphous phase, which show differences in their photocatalytic activity and were observed to have different effects in in vitro experiments.[63]

As an example, anatase, being more chemically reactive, will cause oxidative stress and inflammatory response; by contrast, this effect is significantly decreased for TiO_2 nanoparticles consisting of rutile.[64] A very detailed investigation about the influence of the particle crystal structure on the biological effects was reported by Ryabchikova et al.[9] The authors investigated the uptake of amorphous, anatase, rutile, and brookite TiO_2 utilizing TEM as their main investigation tool. Studies on the early stages and after prolonged incubation times of TiO_2 nanoparticle interactions with MDCK cells were performed. In particular, early steps are supposed to represent key factors which determine the mechanism of the cellular response. Significant differences in the appearance of the TiO_2 modifications were found. Amorphous TiO_2 nanoparticles were observed to be spherical (size 4–5 nm and rarely 10–15 nm) with fine, electron dense filamentous material in between the particles, forming a band-like aggregate (**Figure 3**A). Anatase (Figure 3B) and brookite (Figure 3C) nanoparticles appeared as fine, individual needle-like structures in loose aggregated forms and anatase appeared to be more electron-dense in TEM investigations. Rutile (Figure 3D), however, formed long needles with a diameter of 4–5 nm which aggregated in form of palm-leave-like structures with sizes varying from 30 to 50 nm up to 5–6 μm.

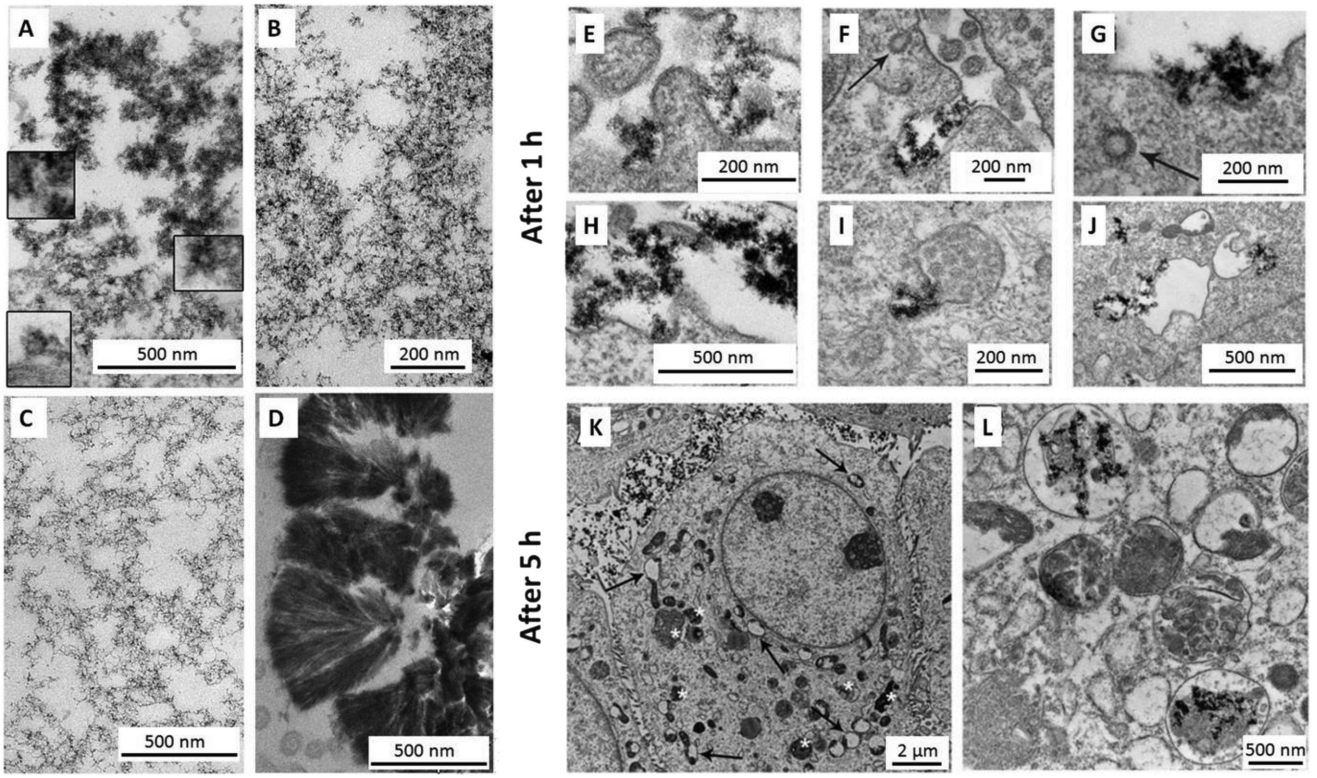

Figure 3. A–D) TEM micrographs of the TiO_2 nanoparticles. A) Amorphous, B) anatase, C) brookite, D) rutile in ultrathin sections. Insets in (A) represent particles at higher magnification. E–J) Different membrane and intracellular structures hosting amorphous TiO_2 particles after 1 h of incubation. E) Direct contact of the nanoparticles with cell plasma membrane, F) invagination of plasma membrane containing nanoparticles, G,H) nanoparticles in "coated pits," I,J) nanoparticles in endosomes. Arrows show empty "coated pits." K,L) Amorphous TiO_2 nanoparticle uptake after 5 h of incubation. K) The cells show a significant degree of cytoplasm and nucleus swelling as well as of the mitochondria (as indicated by white stars). L) Moreover, nanoparticles are located in phogosomes. Reproduced with permission.[9] Copyright 2010, Battelle Memorial Institute.

The authors could observe clear differences in the cell response of the MDCK cells for the four different modifications of TiO_2, which is a clear result of the different particle morphologies, and it could be demonstrated that the crystalline modification governed the pattern of the plasma membrane interaction with the cell. After 1 h of incubation, amorphous TiO_2 nanoparticles covered large areas of the MDCK cell surface and nanoparticles were located in all folds and cavities of the plasma membrane, facilitating a deep penetration into the cell. Based on TEM results, the authors could conclude that amorphous TiO_2 nanoparticles are mainly internalized via surface folds and invaginations characteristic for uptake processes and only very rarely via receptor-mediated endocytosis events. Anatase TiO_2 needles and dense agglomerations thereof were similarly taken up by penetration through folds and invaginations; however, significantly more often also the presence of anatase in "coated" membrane pits and endosomes was observed. These findings were supported by other studies which report the involvement of a macrophage receptor with collagenous structure[65] in the internalization process of anatase nanoparticles. Based on their observation, the authors proposed different modes of action for the internalization of the TiO_2 nanoparticles. For example, a direct interaction of amorphous, anatase, and brookite single nanoparticles with the plasma membrane is suggested, which is mediated by a simple mechanical binding of the nanoparticles to membrane macromolecules. The authors suggest that brookite will induce a decrease in the liquidification of the cell plasma membrane, which hardens the membrane and prevents the internalization of the nanoparticles. On the other hand, amorphous TiO_2 NPs are suspected to liquify the cell membrane, which facilitates a more rapid uptake of the nanoparticles. Alternatively, also the different chemical activity of TiO_2 modifications could account for differences in the uptake mechanism.

In a similar fashion, Gitrowski et al. utilized Coco-2 cells to investigate the uptake of different forms of TiO_2 nanoparticles (bulk and nanoforms, as well as of different crystal structures anatase and rutile) by the gut epithelium.[23] According to their findings, membrane invaginations with particles captured within the folding membrane were observed, pointing toward the involvement of a macropinocytosis-mediated uptake. The authors critically mention that a quantitative analysis of the particles within the cells was not possible, but found a qualitative evidence of more rounded particles being accumulated in the cells compared to striated particles, suggesting that the anatase crystal form may be preferentially accumulated in cells and rutile TiO_2 is taken up the least. The different accumulation efficiency was interpreted by the involvement of additional pathways for nanoparticle uptake, which facilitates the Caco-2 cells to actively exclude the rutile form. However, the authors could not definitely provide a complete elucidation of the uptake process.

SiO_2 particles are accessible as amorphous particles as well as species, which feature porous properties. A study focusing on the impact of porous nanoparticles in comparison to their nonporous analogues was reported by Maurer-Jones et al.[22] The authors investigated the uptake of silica NPs with ≈25 nm diameter possessing different porosities into primary culture mast cells of Swiss albino mice. Inductively coupled plasma emission spectroscopy (ICP-ES) measurements revealed a more efficient uptake for mesoporous particles compared to their amorphous counterparts, which is explained by a particle aggregation effect. However, a difference in uptake mechanism was concluded by the authors by a difference in the toxicity of the nanomaterials. MTT toxicity tests revealed that nonporous silica NPs caused adverse effects on the cell viability, whereas porous materials did not show an influence at a concentration level of 100 μg mL^{-1}. The authors discussed these findings and concluded that the external surface area of the nanoparticles, i.e., the surface of the particles that actually contacts the cell upon membrane attachment, represents the critical parameter for toxicity. The adverse effect is explained by membrane-bound proteins interacting with the particles' surface, resulting in an alteration of their key functions. The cell contactable surface area is larger for nonporous particles compared to the perforated external surface of porous particles (in contrast to the all-over surface which is larger for porous particles).

2.5. Particle Dissociation and Inertness of Nanoparticles

Inorganic nanomaterials can be grouped into inert particles, i.e., particles whose integrity is not affected by the intracellular environment, and particles which undergo morphology changes or dissociation processes as a result of uptake. A material which prominently experiences particle alterations inside a cell is nanosilver. There are a few reports in literature in which TEM investigations provide direct evidence for this property.[66,67] In those studies, TEM images recorded after short incubation periods revealed uptake of AgNPs into vesicles inside the cytoplasm. After prolonged incubation periods, the particles were still internalized; however, TEM images indicated a significant reduction of their diameters. This observation can be explained by the capability of AgNPs to release silver ions (Ag^+), which may diffuse into the cytoplasm resulting in disintegration and reprecipitation of secondary AgNPs.[66,67] This "Trojan-horse mechanism"[68] was investigated by Mishra et al.[66] In this study, particles (15, 50, and 100 nm) were exposed to cells in subcytotoxic concentrations (≤10 μg mL^{-1}). TEM investigations revealed an efficient uptake of all particles mainly into vesicular structures. A rapid uptake of 15 nm sized particles was observed, followed by the uptake of larger particles. Although the particles were applied at subcytotoxic concentrations, a significant bioactivity could be observed. For example, evidence for an enhanced lysosomal activity as well as indications for autophagy was found by means of fluorescence-based techniques. TEM images further revealed the formation of double-layered structures which were identified as autophagosomes. The authors attributed the bioactivity of the vesicle-bound particles to lysosomal membrane permeabilization and the leakage of silver ions Ag^+ into the cytosol. The antimicrobial activity of AgNPs is mainly attributed to the capability of silver in its ionic form to generate coordinative compounds with functional groups, such as thiols or amines, which are present in proteins and enzymes. Hence, the bacterial protein structure is affected, resulting in altering or inactivation of the proteins' key functions.[69]

Moreover, TEM images indicated a disintegration of large particles (≈100 nm) into smaller sized particles within vesicles.[68] It is suggested that AgNPs undergo disintegration processes within the cellular interior resulting in the subsequent formation of smaller, secondary colloids.

The fact that AgNPs readily release silver Ag^+ into the cytosol has direct implications on biological functionalities.[70] In this context, in particular the genotoxic effect emerging from silver nanoparticulate formulations was discussed in studies involving TEM investigations[8,32,34,66,71,72] (**Figure 4**). TEM images revealed in most cases that AgNPs were not present inside the cellular nucleus,[34,71] even though sometimes small particle system were

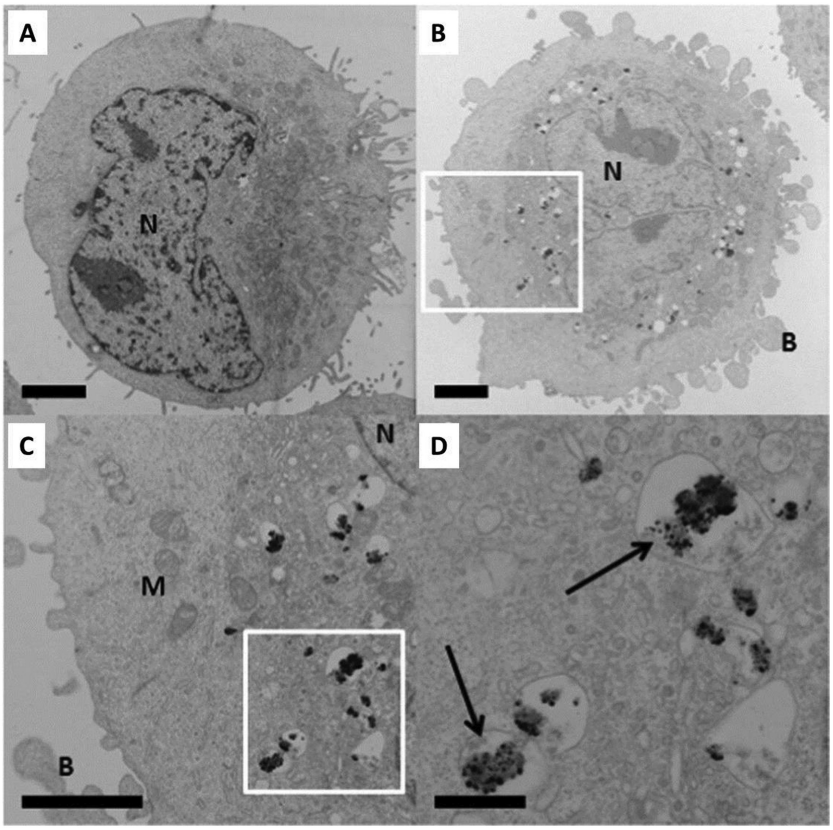

Figure 4. TEM micrographs of HaCaT cells with Ag nanoparticles internalized into vesicular structures. Vesicles are filled with strongly aggregated particle clusters (as indicated by the arrows). The bars are 2 μm for A–C) and 500 nm for D). Reproduced with permission.[72] Copyright 2014, Elsevier.

examined.[71] The fact, that a genotoxic effect was nevertheless observed would suggest that genotoxicity is a result of free Ag^+ inside the cellular interior. These experiments could successfully be complemented with the incubation of the cells with $AgNO_3$, which dissolved into Ag^+ and NO_3^- in aqueous solution, and upon exposure genotoxicity was observed as well. This assumption becomes even more evident based on the results of a different study, in which cell sections exposed to AgNPs were subjected to scanning transmission electron microscopy energy dispersive X-ray spectroscopy (STEM)-(EDS) measurements. The Ag EDS signal could be assigned to the STEM signals of the particles located within vesicles, but STEM-EDS indicated as well a significant amount of Ag distributed allover the cytoplasm and nucleus, which was explained by Ag^+ diffusion into the cellular interior.

In contrast to AgNPs, IONPs possess a valuable biocompatibility and biodegradability in biological specimens. This is attributed to the fact that particles are degraded into water-soluble iron species that are available to the body and can enter the body iron pool without adverse effects and participate in the physiological iron homeostasis.[73] Negative effects of the iron oxide nanoparticles can be expected in case of an overload, which might result in cellular damage due to the formation of reactive oxygen species (ROS).[74] These properties render IONPs a very powerful system to study different aspects of cellular uptake as well as it introduces attractive possibilities to develop therapeutic approaches.

As a primary step, IONPs are decomposed inside the cell and transferred into a storable form of iron. In order to understand the process of decomposition Lopez-Castro et al. investigated spleen samples of mice exposed to IONPs for several days.[75] Particles that possess a certain size have been observed to be converted into smaller objects with a size of ≈8 nm. These structures could be identified as ferritin, which represents a protein that acts as an iron reservoir (**Figure 5**). STEM investigations revealed large structures that can be attributed to particle signals and small structures which could be identified as ferritin signals. Image processing enabled a particle/protein counting to obtain kinetic data on the iron conversion.

In a similar fashion, Kolosnjaj-Tabi et al. investigated the fate of IONP-coated AuNPs (core size ≈ 5 nm, overall size 13 nm) in mice after intravenous injection.[76] The authors conducted a long-time experiment investigating the size evolution of the particles via TEM image processing and could conclude that the IONP coat readily decomposed inside the mice's spleens after 14 d postinjection. After 90 d, they concluded complete dissolution of iron oxide. Furthermore, a significant decrease of the Au

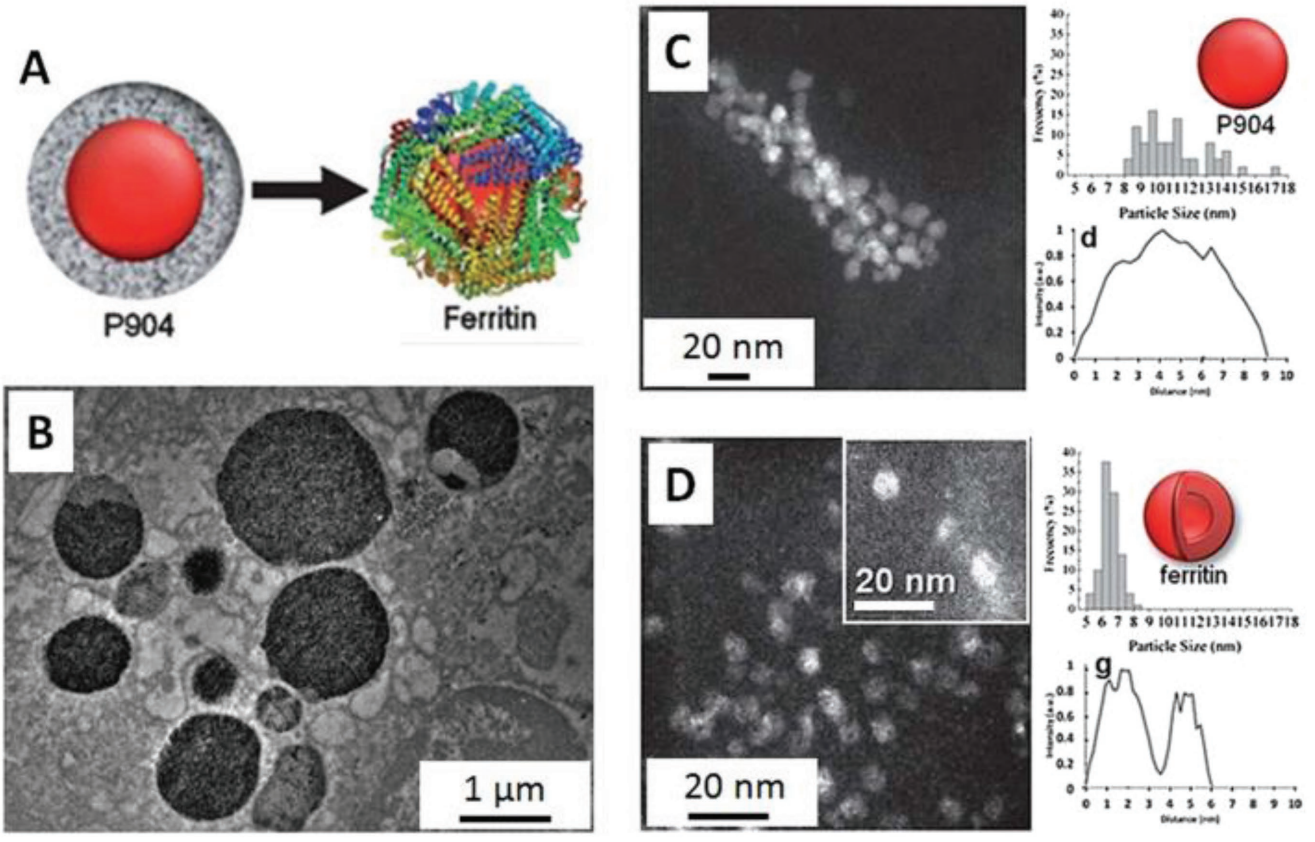

Figure 5. A) Schematic representation of the degradation of SPION nanoparticles (P904). Over time, the iron oxide core of the nanoparticles degrades after being taken up by macrophages and the iron oxide core is incorporated into the nontoxic iron-storing ferritin. B) TEM micrograph of P904 nanoparticles accumulated in the phagosomes of macrophages of the spleen. C,D) Time dependent evolution of the nanoparticle shape. High-angle annular dark-field (HAADF)-STEM images recorded on spleen samples show the degradation of the particles over a time period of C) 1 and D) 30 d (inset: characteristic appearance of the ferritin particles). Characteristic changes in the line profiles across the particles indicate degradation (C, D left). Adapted with permission.[75] Copyright 2011, Royal Society of Chemistry.

core size was observed: the AuNP core shrunk from 5 to 3 nm in size. The authors' findings show that AuNPs may undergo degradation in physiological environment, even though literature indicates that this class of materials is chemically inert under those conditions.

Evidence for cells featuring nonapoptotic (e.g., necrotic) cell death due to indications of cytoplasmic membrane rupture induced by TiO_2 was also found. In mainly all studies, TiO_2 nanoparticles induced elevated levels of ROS; however, cytotoxic effects of the nanoparticles could not inevitably ascribed to the increase of ROS. In these cases, particle alterations inside the intracellular environment could be detected. These often go along with a toxicity of the nanoparticulate material, which is a result of the production of reactive oxygen species inside the cell. Whereas moderate levels of ROS play an important role in signaling and regulation of cellular key functions,[77] increased ROS concentrations severely affect the cell viability, e.g., by lipid peroxidation, protein altering, DNA damage,[78,79] and eventually cell death.[80] However, not only ion release from the nanoparticulate material triggers the increased production of ROS, but also the direct stimulation of mitochondrial activity by NPs themselves.[78,81] As a class of nanomaterials which has been prominently investigated regarding its toxic potential, TiO_2 nanoparticles are known to induce damage to lipids, proteins, and DNA and, consequently, result in damage of subcellular organelles or induce cell death. In mainly all studies, TiO_2 nanoparticles induced elevated levels of ROS; however, cytotoxic effects of the nanoparticles cannot clearly be ascribed to the increase of ROS so far.

A very interesting approach that addresses this problem was introduced by Chan et al.[10] The authors examined the interaction of anatase 25 nm TiO_2 nanoparticles in the immortalized keratinocyte cell line HaCaT. The authors were able to utilize TEM imaging also to monitor the presence of ROS (namely H_2O_2) inside the cell by probing them with Ce^{3+} which forms thorn-like sediments of $Ce(OH)_2OOH$ or $Ce(OH)_3OOH$. For this purpose, $CeCl_3$ was added to the cell after exposure and was incubated for 5 min at room temperature. The formed sediments are well detectable in TEM imaging (**Figure 6**).

These images clearly show that the TiO_2 nanoparticles are surrounded by the thorn-like sediments prior to getting close to the cell membrane (Figure 6A). Hence, anatase TiO_2 nanoparticles are likely to spontaneously produce ROS. Moreover, it was observed that many thorn-like products absorbed at the cell membrane (Figure 6B) indicating that the interaction between TiO_2 nanoparticles and the cell membrane additionally created ROS, which can lead to cell membrane damage. The authors concluded from their studies that TiO_2 induced ROS generation could lead to cellular toxicity if the level of ROS production overwhelms the antioxidant defense.

2.6. Protein Corona

Special considerations apply for the investigation of nanoparticle systems administered in serum containing media. In this case, the constituents of the cell culture media can directly interact with the nanoparticles.[21,82] Frequently, these interactions affect the particles' integrity and particle aggregation as a result of charge shielding by the high salt concentrations of the media is observed. Additionally, cell culture media contain a considerable amount of serum proteins. These may adsorb onto the particles' surface and foster the formation of a protein corona. The protein corona formation entails several implications on the biological activity of the nanoparticle systems. For example, the cytotoxicity or immunotoxic effects[83] are reported as well as a strong influence of the particle uptake mechanism and on the colloidal stability have been observed. The impact of the protein corona in particle stabilization remains controversially discussed and sometimes contradictory results are found in the literature.

As an example, citrate-stabilized AuNPs have been reported to be colloidally stabilized in the presence of proteins,[84] but at the same time, AuNPs were reported to undergo aggregation in protein-containing cultivation medium.[85–87] Protein adsorption has been prominently reported for AuNPs.[88] In many cases, the incubation of citrate-stabilized AuNPs, e.g., with fetal bovine serum (FBS) containing medium, results in the increase of particle size as well as in the occurrence of some particle aggregates, which can be proven by different physicochemical methods.[85–87]

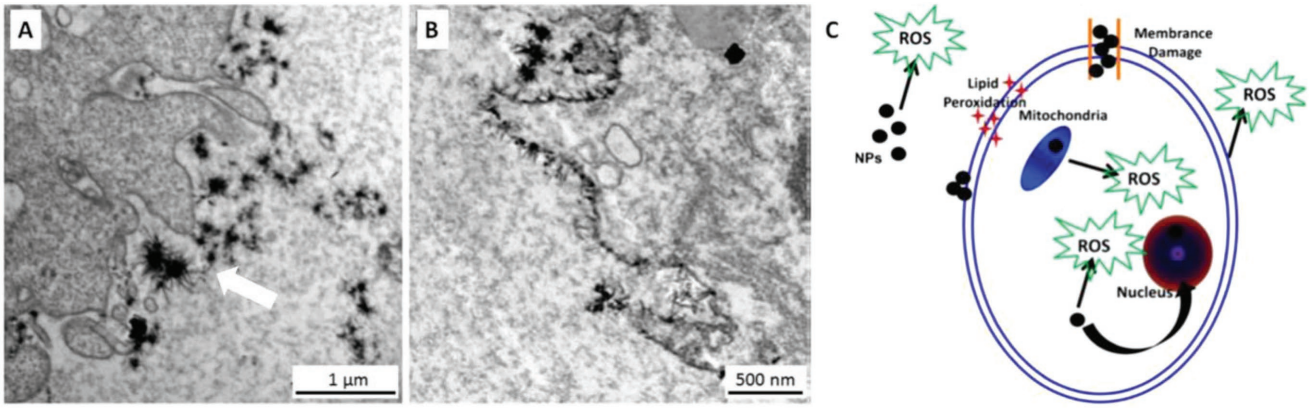

Figure 6. A,B) Visualization of sites of H_2O_2 production by Ce-sediments in HaCaT cells after exposure to TiO_2 nanoparticles. C) Model developed by analysis of the obtained data. Reproduced with permission.[10] Copyright 2011, Springer.

TEM imaging of cells exposed to AuNPs in a serum-containing medium reveals the occurrence of large particle aggregates outside or inside the cell. Taken up into the cell, the AuNPs appear as aggregated structure within vesicular structures.[28,85,87] It is unsurprising that the presence of a protein corona has a strong impact on the mechanism of uptake as well, so that, e.g., caveolae-mediated,[28] clathrin-mediated,[85] or macropinocytic uptake[28] of AuNPs in serum-containing medium could be observed, which points toward the stimulation of active uptake mechanisms. Other studies with SiO_2 NPs revealed that the serum concentration as well as the serum protein itself has considerable effects.[89] These selected literature examples already demonstrate the uncertainties of the role of serum proteins on cellular uptake mechanisms.[25] This can be rationalized by the fact that particle aggregation is not only a result of serum exposure; it rather represents a complex interplay between serum protein as well as protein concentration, salt, and pH value, as well as the nanomaterial itself. As a consequence, the nanoparticle–cell interaction studies should be preceded by a thorough analysis of the behavior of the particle sample with the individual cultivation medium components. This also means that the particle stability in medium is not necessarily predictable. A DLS in addition to supplementary TEM investigations of the nanoparticle systems provide in these studies valuable information that can help to elucidate the appearance of the nanoparticles in respective cell culture media. Due to the complexity of the effect of the protein corona formation a far more detailed discussion about this topic is available in the literature[25] while the present discussion highlights only a few illustrative examples.

For TiO_2 NPs, it has been reported that serum proteins promoted the particle stability.[90,91] A study could confirm that TiO_2 NPs with different morphologies, i.e., anatase and rutile, reacted similarly on serum exposure regarding their impact on the function of enterocytes; however, there was a slight difference in the composition of the respective protein corona.[91]

The formation of a protein corona at the nanoparticle surface is often undesired, since it occurs in an uncontrolled and nonreproducible fashion, which is unfavorable for the nanoparticles' pharmaceutical application. Yu et al. targeted this problem by utilizing albumin-coated iron oxide nanoparticles and their citrate coated analogues.[92] In this study, citrate coated IONPs were incubated with bovine serum albumin (BSA) at high pH values to achieve a controlled coating of the IONPs' surface. The BSA coated particles and the citrate-coated ones were incubated with the adherent cell line MDA-MB231 and the suspension cell line HL60. For both cell lines, it was observed that BSA modified particles internalized in lower amounts compared to the citrate coated ones, which indicates that protein adsorbance decreased the unspecific uptake. It was moreover found, that adherent cell lines internalized iron oxide particles in a threefold higher amount than suspension cells. Representative TEM images revealed a fierce interaction of citrate-stabilized IONPs with the membrane of MDA cells, whereas BSA-coated IONPs approached the cellular membrane in a reduced particle number.

The influence of additives in the cultivation medium was investigated by Siddhanta et al.[93] The authors conducted a study using silver nanoprobes in human prostate cancer cells (PC-3).[93] The cancer cells were exposed to particles with a size of 30–50 nm in a trehalose and a nontrehalose containing environment. Trehalose was used since it constitutes a nonreducing disaccharide capable of inhibiting cell surface receptor denaturation that can prevent membranolysis. This would result in cell apoptosis triggered by the membrane–particle interaction. TEM investigations revealed that AgNPs incubated along with trehalose were localized as particle clusters within intracellular vesicles subsequent to uptake, thus, suggesting an endocytic uptake mechanism. By contrast, in the absence of trehalose during the incubation process most of the particles were found within the cytosol which the authors attributed to a diffusive uptake pathway. Additional surface enhanced Raman spectroscopy (SERS) investigations could reveal characteristic bands corresponding to the α-helical conformation of the polypeptide backbone, which was observed in trehalose-treated cells, while this band was indistinct in the absence of trehalose. This was considered as a clear indication for the disruption of protein structures. The authors concluded that NP uptake in the presence of trehalose led to SERS signals corresponding to vesicular structures, whereas the absence of trehalose resulted in the measurement of collective signals emerging from protein denaturation in the plasma membrane and the cytosol, thus, confirming the observations of the TEM investigations.

2.7. Surface Functionalization

One of the attractive advantages emerging from the utilization of inorganic nanoparticles emerges from the possibility to easily modify their surface properties. This can be achieved by coating of the nanoparticles with surfactants or small molecules self-assembled onto the nanoparticle surface. These molecules can render the surface charge, the polarity, or the chemical interactions of the nanoparticles with their environment, or can add also properties which can change depending on external triggers, i.e., the local pH, light induced changes, or the temperature. In this case, the interaction with the environment changes their behavior in solution as well as strongly influences the nanoparticle interaction with cellular membranes or intracellular organelles. The portfolio of possible surface functionalization schemes is vast[94] (**Figure 7**) and includes next to small molecules also larger molecular species, i.e., polymers or molecules which can tailor the physicochemical properties of the nanoparticles or add stealth properties to the nanoparticle system. Polyethylene glycol polymers are an example for such coatings, which prevent the immune-response of the cellular systems and can help to prolong circulation cycles of the nanoparticles. Owing to the polymer decoration, protein adherence is prevented,[95] which often also impedes particle aggregation. There are a few examples in literature, in which TEM images revealed that PEGylated particles are less aggregated, even within the intracellular vesicles, whereas non-PEGylated nanoparticles form aggregates in the intracellular matrix.[50,96,97]

Additionally, molecular functionalization of the nanoparticle surface can be used, e.g., to direct the interaction of the nanoparticles with the cellular system. As such, e.g., antibodies can address specific receptors of cell walls or proteins can directly stimulate cellular responses.

The immobilization of small molecules for direct surface functionalization or as linkers to attach other molecules

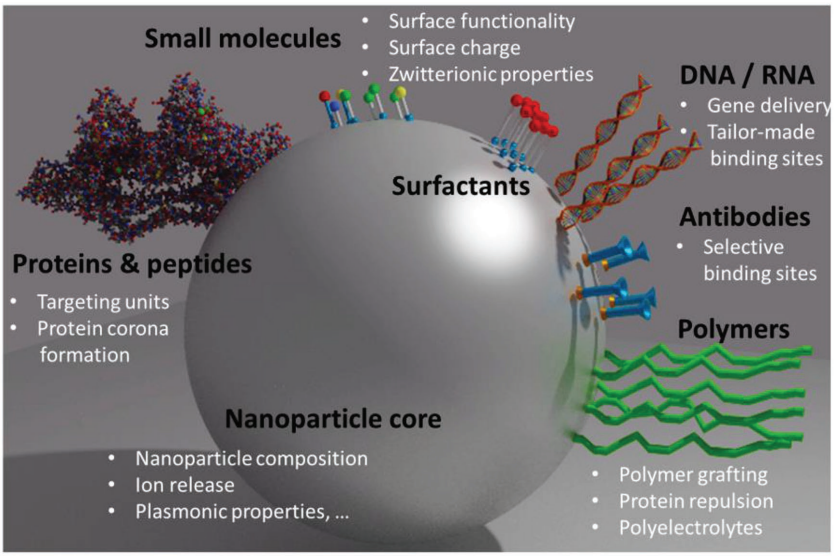

Figure 7. Overview of different possibilities to functionalize the surface of inorganic nanoparticles.

are particularly assessable for gold nanoparticles, which are susceptible for modification with thiolated molecules.[98] This chemical modification works reliably and dense layers of molecular species can be grafted onto the surface of the nanoparticle. For silica nanoparticles, appropriate functionalization strategies include the utilization of silane molecules which attach to the nanoparticle surface.[99,100] Moreover, specific IONP surface modifications result in an increase of the colloidal stability, in particular, under in vivo conditions.[101] Surface modification is achieved by ionic coordination, hydrophobic interactions, or by covalent attachment of molecules using functional alkoxysilanes.[100] A critical point in this functionalization process is the grafting density of the molecules, which is difficult to access but might have significant influence on the nanoparticle cell interactions. In particular, large functional units, i.e., proteins, only feature a limited number of functional units which might impair their efficiency significantly.[94] However, in most studies, this effect is not taken into consideration, which might contribute to a poor comparability of reported results. In general, covalent immobilization strategies are favored compared to processes involving pure electrostatic interactions or physisorption processes as the stability of the functional surface is much higher compared to particle systems modified utilizing physisorption concepts. Electron microscopists have taken advantage of this surface functionalization of colloids for many years by using AuNP–antibody conjugates, which facilitates to combine immunohistochemical methods with the high-resolution capability of TEM. This method, which is referred to as immunogold-labeling, has been applied successfully and enables labeling subcellular constituents in TEM micrographs.[102]

In the aforementioned studies reviewed in Section 2.6, the formation of a protein layer at the particle surfaces as a result of serum–protein interaction was described, and the consequences with respect to uptake and intracellular fate were discussed. Here particle–protein interactions represent uncontrollable processes, however, it is also possible to attach peptides, proteins, or targeting units on purpose to particle surfaces. Representative examples for direct surface functionalization are summarized in the following sections.

2.7.1. Peptides and Proteins

Some detailed TEM studies illustrate the elucidation of protein–membrane interactions. As such, Nativo et al. studied the impact of cell-penetrating peptides (CPPs) on HeLa epithelial cells, using AuNPs (≈16 nm) as nanoprobes.[50] Crossing cellular membranes in a nondestructive fashion represents a major challenge in the development of novel vectors for gene or drug delivery, and CPPs have been explored as functional molecules to efficiently address this issue.[103] In their study, the authors functionalized AuNPs with PEG chains to reduce undesired interaction with serum proteins and prepared as well PEGylated particles further functionalized with a small amount of CPPs.[50] TEM investigations of the PEGylated AuNPs revealed their vesicular distribution and showed that the particles did not undergo any aggregation, as suspected for PEG coated structures (see also Section 2.7.5). An attachment of a small amount of CPPs on PEGylated AuNPs led to an efficient uptake of these particles. CPP modified particles could be found inside the cytosol but not within vesicle structures. In a different study focusing on the role of CPPs, the impact of the protein $S4_{13}$-PV on HeLa endothelial cells was investigated.[104] In order to follow the protein's fate within the cells, the protein was labeled with nanogold (gold clusters with a size ≈1.4 nm). In contrast to the aforementioned study, in which particles approached the cells individually (as a result of PEGylation), it was observed that $S4_{13}$-PV formed uniformly sized assemblies with sizes of 80–100 nm at the cellular membrane. This finding was attributed to the interaction of $S4_{13}$-PV with glycosaminoglycans, which represent membrane constituents, and a cellular membrane response promoting the uptake of these large assemblies was triggered. The assemblies were found initially to be localized within vesicle structures, in which they remained associated with the vesicular membrane. Subsequently, this attachment resulted in a destabilization of the vesicle membrane, which results in the escape of the peptides into the cytosol. By means of TEM investigations, uptake as well as intracellular fate and the disruption of vesicular membranes could be visualized. In another study focusing on CPP–membrane interactions, the translocation of CADY, a secondary amphiphilic peptide with CPP properties which binds to siRNA, was investigated by TEM using nanogold as electron dense label.[105] The authors of this study found a clustered assembly of the CPPs that formed at the cellular membranes. Additionally, an uptake of the NPs could be observed. In contrast to the aforementioned study,[104] peptides were

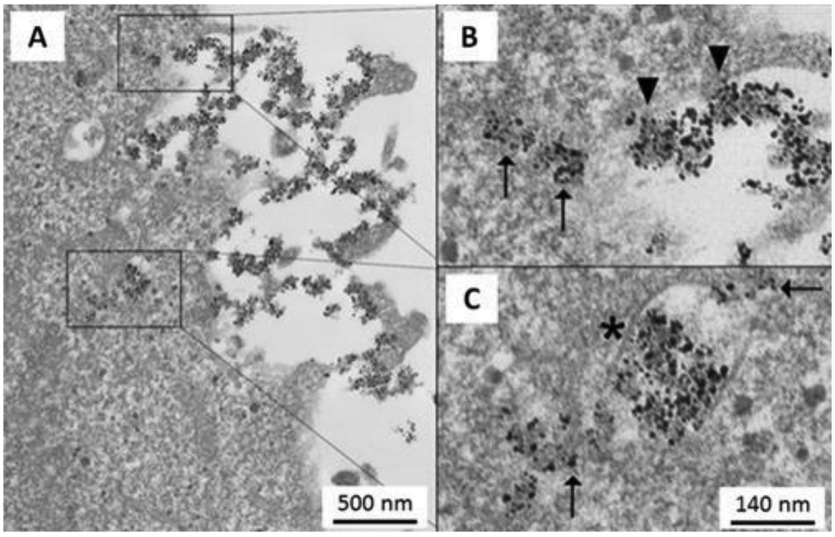

Figure 8. A) Interaction of CADY gold-labeled siRNA nanoparticle complexes with HeLa cells. B) Magnified zoom of the cell membrane area indicating that the complexes associate with the plasma membrane (arrow heads). C) After translocation the nanoparticles localize intracellularly into endosomal vesicles (as marked by the asterix) or are found freely in the cytosol (marked by the arrows). Adapted with permission.[105] Copyright 2011, Public Library of Science.

found directly within the cytosol and could not be found in vesicles.[105] The authors attributed this finding to the direct interaction between CADY and phospholipids of the cellular membrane (**Figure 8**).

Veiseh et al. could observe an increased uptake of iron oxide nanoparticles modified with the functional biomolecule chlorotoxin (CTX) into C6 rat glial tumor cells.[106] CTX represents a small peptide that interacts with the membrane-bound matrix metalloproteinase 2 (MMP-2), an enzyme that is upregulated in gliomal cancer cells. TEM investigations within this study do not only support a substantially increased uptake of CTX-modified particles (**Figure 9**D,E) but can additionally confirm a receptor-mediated uptake mechanism for CTX-modified IONPs by means of membrane investigations as well. In comparison, also the uptake of pristine CTX was studied. TEM images revealed the formation of small endosomes in cells which have only been treated with CTX, whereas larger endosomes occurred in case of cells that were exposed to CTX-modified particles. The authors attributed these findings to the interaction of multiple CTX-molecules at the surface of the individual particle with multiple MMP-2 receptors at the cellular membrane and an internalization of larger lipid membrane fragments. In this work, TEM imaging facilitates a clear elucidation of the hypothesized uptake mechanism (Figure 9A–C).

The surface modification of particles can only be efficient if the functional molecules attached to the particles are oriented in an optimized direction to optimize binding to the receptors. Galbiati et al. critically mentioned this issue and prepared IONPs (≈7 nm) conjugated to the short peptide U11 in such a way that the peptide was bound to the particle surface with a well-defined orientation. This was achieved by a sophisticated surface manipulation strategy involving the enzyme cutinase (CUT), which possesses a high affinity to U11. The particle conjugates were taken up efficiently into MDA-MB-468 breast cancer cells. TEM investigations revealed that particles adhered to the cells' membranes forming invaginations typical for a clathrin-mediated uptake. In addition, small vesicles near the cellular membrane supported their conclusion on a clathrin-mediated uptake. Thus, TEM could reveal the uptake mechanism as hypothesized due the surface properties of the particles.

Proteins can furthermore facilitate the targeted interaction of the nanoparticles with cells, e.g., to improve nucleus penetrability. Targeted nucleus penetrability can be achieved by the utilization of receptor molecules, e.g., the shuttling protein nucleolin. Dam et al. investigated nanostars (diameters ≈25 nm) surface-modified with nucleolin and exposed the particles to human cells.[107] As a first result, the nanostars were freely distributed inside the cytosol, where they can reach the perinuclear region as indicated by TEM micrographs. Furthermore, the stars could be observed at the cell nucleus. There, the particles adhered at the nuclear membrane and caused membrane responses. In this context, membrane invaginations were found, and an uptake in a sense of an active mechanism was hypothesized. Furthermore, the authors observed that these invaginations were observed for cancer cells, but were not that pronounced for noncancerous cells.

The wealth of particle–cell interactions which can be promoted by the utilization of proteins and receptors can be seen as a very valuable tool to study a large variety of different systems. The quality of the surface functionalization, its stability, and the influence on the nanoparticle systems, however, always have to be taken into consideration and a careful characterization of the nanoparticle probes is required.

2.7.2. Antibodies and Receptors

Antibodies facilitate a direct interaction with receptors being present on the cell surface. They have recently been used to target cancer cells in a selective fashion and constitute, thus, a promising tool for cancer therapy.[108] In a study by Baiu et al., starch-modified IONPs were conjugated to the monoclonal antibody hu14.18K332A, which binds efficiently to neuroblastoma cells.[109] TEM images revealed an efficient membrane binding after 1 h of incubation time prior to the uptake in in vitro studies. Furthermore, the particles demonstrated a high-tumor specificity which could be confirmed by magnetic resonance imaging (MRI) measurements in an in vivo mouse model.

As an additional example, the fate of hollow Au nanospheres in B16/F10 melanoma cells was investigated by Lu et al.[96] Within the study, the authors modified the nanospheres (diameter ≈40 nm) with PEG to prevent protein adsorption and additionally functionalized them with the targeting ligand for the

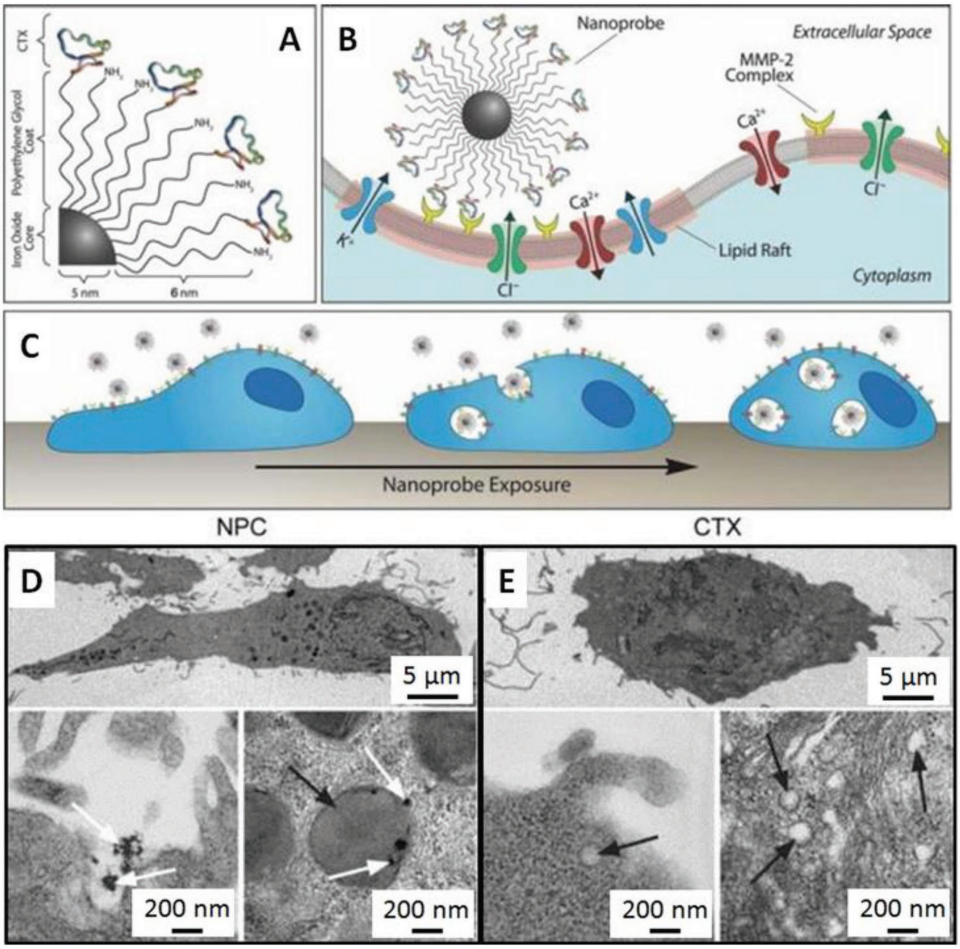

Figure 9. A) CTX-functionalized IONPs were used to study the uptake in glioma cells. B) The uptake is facilitated by nanoparticle binding to lipid rafts containing MMP-2 and selective ion channels. Uptake facilitates the internalization of the nanoparticles and changes the cell morphology. C) Nanoparticle uptake was investigated by TEM and compared to cells treated with an equivalent amount of CTX. D) The white arrows indicate the nanoparticles and E) analysis of the cell membrane (bottom row) showed their internalization into large endosomes (black arrow). Endosomes of nanoparticle treated cells featured a 5–10 times larger size, indicating an increased lipid raft internalization. Adapted with permission.[106] Copyright 2009, Wiley.

melanocortin type-1 receptor, which is expressed by this cancer cell line. The investigators established a tumor model consisting of a multilayer of cells. It was the scope of the experiment to understand the extravascular transport of particles within solid tumors. TEM investigations revealed a receptor-mediated uptake in case of receptor agonist-modified particles, i.e., a protein that activates the ligand–receptor interaction. Subsequently to the cellular uptake, endocytic vesicles were found to transport the cargo toward the cytoplasmic membrane before exocytosis follows. The cargo can undergo additional endocytosis processes into other cells in a subsequent process. The authors suggested a transcytotic pathway for the intratumoral transport.

TEM provides in this respect a smart toolbox, which allows, e.g., by utilization of immune-gold-labeling strategies, to identify also the position of the respective binding sites on the cellular systems itself and to determine potential binding sites even prior to the nanoparticle uptake studies. These additional information could constitute important information on receptor or binding site densities and might provide a more comprehensive understanding of particle uptake.

2.7.3. Drug Molecules

In a similar fashion also drugs can be directly bound to the surface of nanoparticle systems. This allows for a nanoparticle mediated uptake and might facilitate a targeted delivery to specific cell organelles, where the drug can be released. This might occur due to degradation processes or by associated changes of essential parameters in the organelle itself, i.e., the local pH value. Alternatively, external stimuli, i.e., light can be used to release the drug.

Cheng et al.[110] utilized mesoporous silica nanoparticles (NPs) (≈80 nm) functionalized covalently with palladium–porphyrin in order to establish a drug delivery agent which can be used for photodynamic therapy. For this purpose, the efficiency of these particles in a murine model of breast cancer cells was tested. The particles were administered intratumorally into mice and the tumors were harvested after 0, 1, and 6 h subsequently to the treatment. Directly after injection, the particles were found mainly in the periphery of the cells and were not yet taken up. Already after 1 h, a larger number of endocytosed

particles were found, which was even more pronounced after 6 h. The authors emphasized that a covalent attachment of the photosensitizer to the particles prevents the possibility of self-aggregation and self-quenching in the hydrophilic environment.

The release of the drug molecules is difficult to verify by means of TEM investigations, and frequently can only be revealed by the observation of changes in the cellular or organelle morphology.[47,111,112] This was utilized, e.g., in a study focusing on the impact of small particles (≈3 nm) onto B16 melanoma cells.[47] In this study, AuNPs were modified with the cytostatic compound doxorubicin. Combining doxorubicin with ultrasmall AuNPs was shown to enhance their uptake into melanoma cells more efficiently than both components would do individually.[113] TEM investigations confirmed that the AuNPs labeled with doxorubicin entered the cells after 1 h of incubation.[47] AuNPs were found freely inside the nucleus after 6 h and organelle destruction was induced owing to the apoptotic potential emerging from the composites. Evidence for advanced apoptosis was provided by the fact that mitochondria appeared swollen and nuclei were shrunken.

Alternatively, sensitive Raman or fluorescence imaging studies can complement the drug release studies. Ock et al. studied the drug release on the basis of AuNPs (diameters ≈20 nm).[111] Different purine or pyrimidine anticancer drugs were bound onto the AuNP surface and the systems were exposed to HeLa cells. A release of the drugs was achieved by glutathione induction. This reaction could be monitored by means of Raman spectroscopy inside the cell body. Supplementary TEM investigations allowed to gain insights into the aggregation state of the particles within the cell.

Next to the internalization of drug molecules, also the theranostic potential of AuNPs can be utilized. Tam et al.[114] synthesized radiolabeled hollow gold spheres (diameter ≈42 nm) modified with PEG and doxorubicin and applied them to hepatic cancer in New Zealand white rabbits. Within this study, nanoembolization was conducted, a method that is used in cancer therapy to clog blood vessels that supply the tumor. The authors' results indicated that particles were indeed found within blood vessels of tumorous liver tissue, but were not taken up into tumor cells even after 18 h of nanoembolization. The authors attributed this to a retarded endocytic uptake. Subsequent laser-induced thermal therapy led to deformation of the particle shape in the interstitial areas, which might be indicative for efficient drug release. Conversely, the implementation of irreversible electroporation subsequently to embolization led to an uptake of the hollow spheres; however, no change of the particle shape was observed. These findings were complemented by positron emission tomography (PET) and computed tomography (CT) measurements.

2.7.4. DNA, RNA, and siRNA

As a particular application of drug delivery, the transfer of nucleic acids into cells and the cell nucleus constitutes a promising approach in the treatment of inherited disorders, autoimmune diseases and cancer. This approach is referred to as gene therapy and can be realized either by viral gene vectors,[115] stem cell-based approaches,[116] or by means of synthetic, nonviral gene transfer agents.[117] In this context, particularly surface-modified IONPs-based and AuNPs-based systems have been investigated. As an example, Gilleron et al.[118] studied AuNPs modified with small interfering RNA (siRNA), which were exposed to HeLa cells and mice. In the animal studies, particles were observed in the liver, in which they preferably accumulated inside Kupffer cells as well as inside hepatocytes. These cell types could be identified due to their characteristic shapes. Concerning HeLa cell studies, the particles were found inside vesicular structures, but they were also found as free particles inside the cytosol. A statistical analysis of numerous images of HeLa cells facilitated a sustained assessment of the lysosomal escape efficiency: ≈1–2% of the particles were found within the cytosol. Based on these data, a possible transfection mechanism could be concluded. The authors suggest that siRNA itself detaches from the particle surface and leaks out of the lysosomes, perhaps via channels, rather than the particle–siRNA conjugates are released from the lysosomes. The authors explained this hypothesis by the fact that an efficient gene transfection effect was observed; however, no evidence for lysosomal "bursting" could be found during the TEM image analysis, as well as there was only a limited number of particles freely localized in the cells.

2.7.5. Polymers

Polymers represent a very powerful material to establish and promote the internalization of nanoparticles into cells. While all-polymeric nanoparticles have been recently reviewed in detail,[12] here the functionalization of inorganic nanoparticles surface functionalized with polymers is summarized.

This includes functionalization schemes utilizing synthetic but also biopolymers which can be actively used to promote drug or DNA binding and to facilitate the uptake of the nanoparticles or to improve the nanoparticle properties in the cellular environment by introducing, e.g., stealth properties or by preventing the formation of a protein corona. Additionally, further properties, i.e., the surface charge, etc., can be rendered by the utilization of a polymer shell around the inorganic particles. As such, the interaction between poly-L-lysine modified particles and human mesenchymal stem cells was studied, e.g., by Chang et al.[119] In this study, an endocytic pathway was determined due to the formation of membrane protrusions, which interact with particles. Further studies confirmed an efficient uptake of IONPs modified with cationic polymers into transplantable cells compared to the unfunctionalized IONPs used as control.

Schwarz et al. focused on differently polymer functionalized IONPs and studied their interaction with antigen presenting dendritic cells (DCs).[120] In this study, IONPs (≈5–10 nm) were modified using a layer-by-layer approach in order to cover the surface of IONPs with different polymers. The authors could demonstrate that, in particular, poly(diallyldimethylammonium chloride) and oleate stabilized particles were taken up efficiently by the DC cells and provided high intracellular packaging densities (**Figure 10**). The authors found moreover that the subcellular particle density rather than the particle concentration in DCs correlates with the intracellular packaging densities which were determined by TEM images.

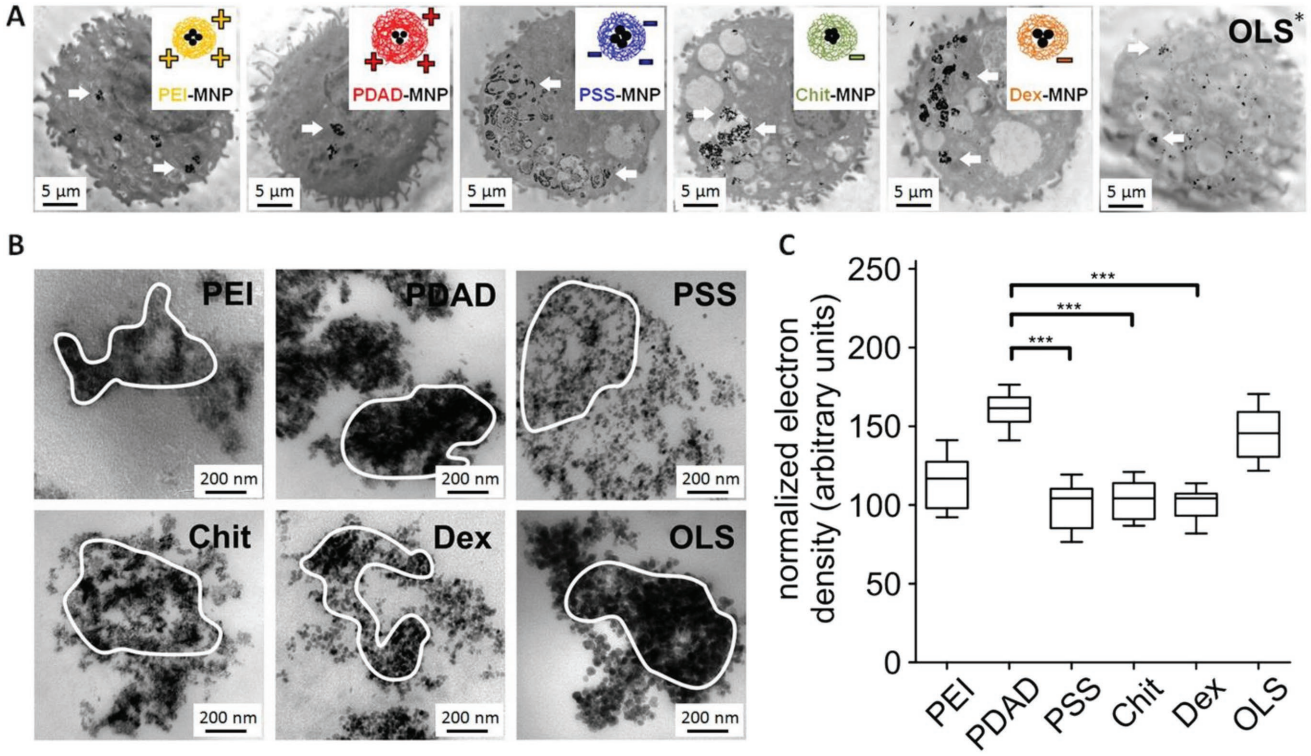

Figure 10. A) TEM micrographs depicting the uptake of IONPs by dendritic cells after 24 h (insets: layer-by-layer functionalization of magnetic nanoparticles by different polyelectrolytes featuring different surface charges). Oleate functionalized magnetic nanoparticles (*) serve as a control. B) Endosomal compartments containing functionalized magnetic nanoparticles. C) Quantitative analysis of the provided electron density of clustered nanoparticles in endosomal compartments. Data are represented as box-and-whiskers plots (middle line: mean; top box 75th quartile; bottom 25th quartile; whiskers represent the lowest and highest values; ***$P < 0.001$). Adapted with permission.[120] Copyright 2010, Elsevier.

Poly(ethylene imine) (PEI) represents a polycationic polymer that can efficiently bind DNA or RNA. Thus, it is frequently utilized as a functional polymer for delivery systems by the formation of polyplexes[121] or by a direct functionalization of the nanoparticles with PEI. An early approach was realized by Thomas et al.[48] The authors attached branched PEI to AuNPs.[122] Since the gold cores were small in size (2–4 nm),[48] they were found within the nucleus in COS-7 monkey kidney cells already after 1 h incubation time. In order to achieve an appropriate polymer attachment on the gold surface 4,4′-dithiodibutyric acid was used, which efficiently binds to the PEI's amine functionalities. In another study, gold particles containing iron oxide nanoparticulate cores were coated with PEI to target BH21 cells.[52] The gold modification of the surface was shown to increase the transfection efficiency. Despite their rather large size (core sizes ≈30–50 nm), the particles were found within the cellular nucleus (**Figure 11**). The authors attributed this observation to the strong interaction between the strongly positively charged particles with the negatively charged nuclear membrane. TEM images provided evidence for a fierce infolding of the nuclear membrane at the aggregated particles, suggesting that this leads to a liberalization of the nuclear membrane from laminas, which represent barriers of the nuclear membrane, and nucleus internalization is facilitated (Figure 11A).

PEG represents another important polymer, which is frequently utilized to introduce a stealth mechanism to nanoparticles. Additionally, PEG can efficiently suppress the formation of a protein corona in cell culture media (see Section 2.6).

In addition to synthetic polymers also biopolymers, i.e., gelatin, can be used to functionalize nanoparticle systems. The development of a gelatin-coated AuNP based system for the delivery of the anticancer agent doxorubicin was reported by Suarasan et al.[112] In this work, gelatin modified AuNPs (gold cores ≈18 nm) were prepared, which were loaded with doxorubicin in a noncovalent fashion. These particles represent a light and pH-responsive drug release system. According to TEM images, the authors concluded that a pinocytic uptake of the particles into the cells takes place. After 48 h, TEM images indicated lysosomal fusion processes. Complementary fluorescence microscopy images revealed an efficient release of the particles.

2.8. Charge

It is generally acknowledged that the surface charge plays an important role in the uptake and internalization of nanoparticles into the cell. This can be rationalized by the fact that the charge can promote or suppress the firm interaction of the nanoparticles with membrane structures.

De Cuyper and co-workers investigated the interaction of differently charged nanoparticles with HepG2 cells.[123] In this study, cationic, anionic, and lactose-bearing metalloliposomes were examined. Even though cationic structures are known to

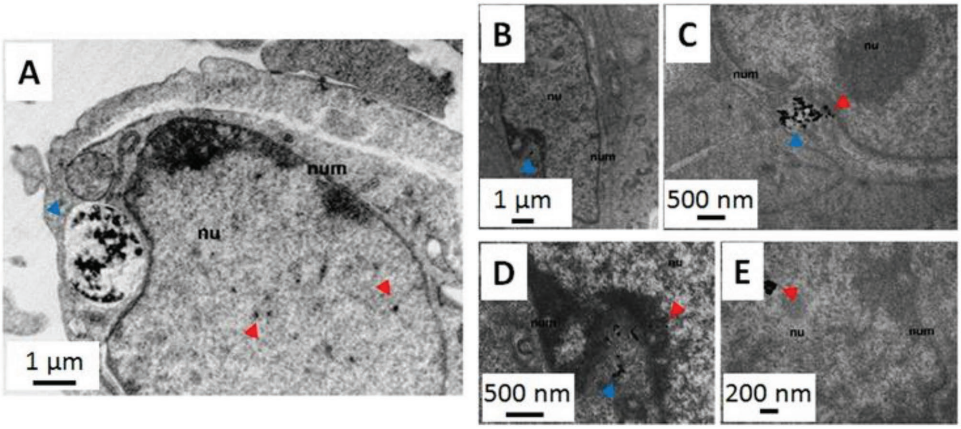

Figure 11. Investigation of the cellular uptake of PEI/DNA complexes in BHK21 cells. A) Gold-coated magnetic and B–E) bare magnetite PEI/DNA nanoparticles. The blue arrow heads point toward association with nuclear membranes. The red arrow heads indicate nanoparticles taken up into the nucleus. Adapted with permission.[52] Copyright 2011, Elsevier.

increase uptake efficiencies, TEM images revealed only little uptake for cationic liposomes; however, a fierce impact onto the membranes of the cells was observed. Anionic liposomes did not show such a severe influence on the membrane structure but their uptake was also not sufficient. Lactose-functionalized liposomes, by contrast, showed a high uptake and internalization of clustered particles within the cells. This study evidences that the surface charge of nanoparticles is an important factor for their internalization but cannot be utilized as a single parameter and has to be discussed in the context of associated effects, i.e., the potential of forming a protein corona or the tendency to form larger aggregates in cell media. Charge screening might occur which directly influences the effective surface charges. Surprisingly few studies address this issue in a systematic fashion taking into account also the various other properties that influence the uptake. Kralj et al.[124] conducted systematic studies on IONPs with a diameter of ≈14 nm and varied the surface charge of these particles. TEM investigations indicated a binding of cationic particles to the membranes of MCF10A neo T and PC-3 cells and observed a highly efficient uptake into the cells. On the other hand, anionic particles were not observed to bind to the outer membrane, which resulted in a significantly lower uptake of the nanoparticles into the cells. The authors attributed their findings to the fact that not only the direct interaction of the nanoparticles with the cells has to be considered as an uptake-governing parameter but also further interactions of the nano-objects with, e.g., biomolecules present in the biological environment, have to be taken into account. A detailed investigation on the influence of the particles' surface charge in relation to serum interactions was reported by Nowak et al.[125] The authors studied the uptake of carboxy-modified and amino-modified silica nanoparticles with a diameter of 23 nm in comparison to similar, nonfunctionalized nanoparticles into A549 human lung epithelial cells. In serum-free media, different uptake rates were observed (COOH > NH_2 > bare). However, this effect only persisted in serum-free media and the difference in the uptake efficiency was not observable anymore when experiments were carried out under serum containing conditions. In addition to the uptake efficiency, the authors could also reveal differences in the nanoparticles' internal localization. Amino-functionalized particles were found within the cytosol as well as in the nucleus, whereas the other particles were internalized into vesicular structures, potentially taken up by macropinocytic uptake pathways as concluded from the electron microsocpy (EM) studies as well as by complementary inhibition studies. Liu et al.[126] identified gold nanoparticles possessing a mixed surface charge, i.e., particles functionalized with cationic and anionic moieties at the same time, as systems, which show an even higher protein-repellent character. The authors studied the uptake of these zwitterionic particles and observed differences in the addressability of immune cells. Particles were intravenously administered to laboratory mice and different organs of the mice were examined one month after injection. TEM images were utilized to determine different cells types in the tissue by their characteristic cell morphologies,[126,127] and it was found that only immunocells, i.e., Kupffer cells in the liver or macrophages in spleen tissue, were addressed by the nanoparticles.[126] These results were compared to PEGylated particles, which additionally showed an increased tendency to aggregate in higher amounts than their zwitterionic counterparts.

2.9. Cell Type

Cell studies are frequently associated to the response of specific cell lines and results are not transferable to other cell types.

Reasons for different uptake behavior are based on the availability of receptors, which might be overexpressed into different cells of receptor cells. These can promote e.g. enhanced receptor-mediated uptake. Also structural peculiarities of specific surface features of different cell types have to be taken into account. Janer et al. investigated the uptake of TiO_2 nanoparticles in carcinomic human alveolar basal epithelial cells (A549) as well as in Caco-2 cells.[128] An efficient particle uptake was observed for the A549 cells, whereas the uptake of the nanoparticles into Caco-2 cells remained low. These findings were attributed to the fact that Caco-2 cells feature microvilli on their

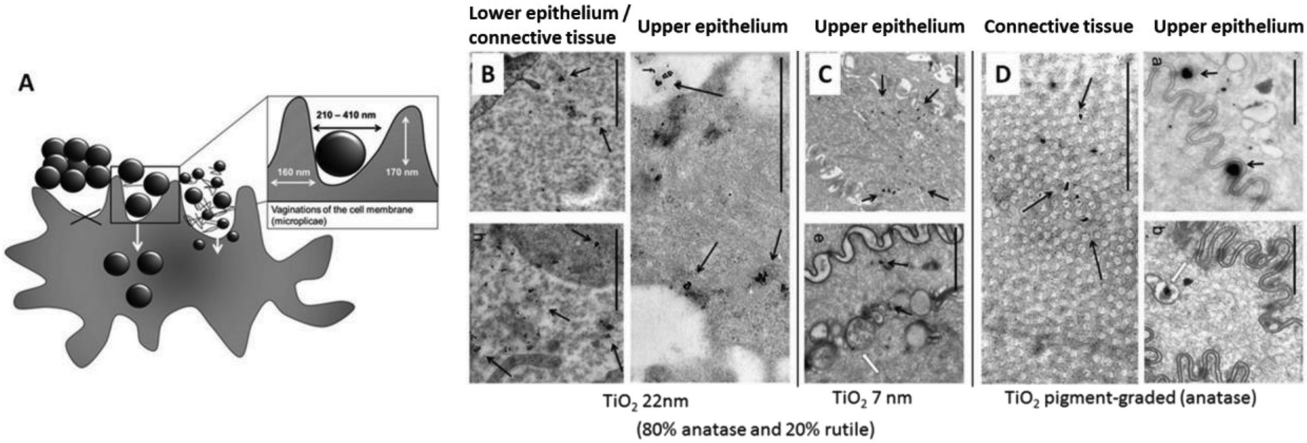

Figure 12. A) Schematic representation of the cross-section buccal mucosa, which features size-dependent uptake of nanoparticles in the oral cavity due to different interaction efficiencies of the particles with the cell membrane and microplicae. B) 22 nm particles were found in the upper and lower epithelium. C) 7 nm particles reached only the upper epithelium, whereas pigment graded TiO_2 nanoparticles D) could be observed in the buccal superficial epithelium, the basal lamina, and in the connective tissue. Scale bars: 1 µm. Adapted with permission.[131] Copyright 2015, Taylor & Francis.

apical side, while the cellular membrane of the A549 cells is rather smooth. Larger aggregates (>1 µm) are more likely to be internalized through a smooth surface rather than through the rough structure of the microvilli.

Also cancer cells can be specifically addressed by suitable targeting strategies. For example, by attachment of molecules onto the nanoparticle surface that address particular receptors which are overexpressed in cancer cells.[129]

As an example showing how surface-modified nanoparticles feature different uptake behaviors into different cell lines, Zhou et al.[130] used Au nanorods surface-modified with different specific ligands, namely, phosphoryl choline (PC), PEG, folic acid (FA), and galactose (Gal). For their experiments, the authors used rhinal epithelial cell lines, CNE-1 cells, L02 cells, H9 cells, 8226 cells, as well as HepG2 cells. ICP-MS data revealed an efficient uptake of PC-modified particles into CNE-1, HepG2, and 8226 cells, whereas Gal-modified rods were efficiently internalization particularly into HepG2. FA-modified rods were taken up by CNE-1 cells most efficiently. PEGylated rods revealed an improved uptake into CNE-1, epithelia, HepG2, and L02 cells; however, their uptake efficiency is not as pronounced as in the case of PC-modified, FA-modified, and Gal-modified rods.

In this context, the interplay of various cells with different functions plays a particular role in the framework of tissues. Teubl et al. investigated the spatiotemporal aspects of three different TiO_2 nanoparticle systems interacting with oral tissue.[131] Their intracellular localization in human epithelial cells was studied and potential toxic effects were evaluated. TiO_2 nanoparticles were observed to assemble into large aggregates in the cell cultivation medium. Thereby, aggregate fractions with different sizes were formed. 10 to 50% of the particle aggregates remained in the nanoscale range and were observed to rapidly interact with the mucus layer and to infect the epithelium. Characteristic differences in their penetration depth were observed to depend on their particle characteristics. TEM investigations revealed that pigment-grade anatase TiO_2 and 22 nm particles consisting of 80% anatase as well as of 20% rutile were found in the upper and lower parts of the buccal mucosa, whereas small anatase nanoparticles with a diameter of 7 nm could only enter the upper parts. Strikingly, also large aggregates of the pigment grade particles were only present in the upper epithelium, while in deeper parts (i.e., the basal lamina and connective tissue) only aggregates in the size range of 100 nm were found. Closer inspection of the particles revealed that the pigment-grade particles were closely aligned to cell membranes or in electron-dense, single-membrane compartments, and were additionally found in collagen fibrils of the connective tissue. Very small anatase nanoparticles were located in the cytosol and partially also in vesicles, whereas the medium size 80:20 anatase/rutile nanoparticles aggregated into cluster-like assemblies in punctuated structures of the cytoplasm. The authors explained their findings by the anatomical/biophysical structure of the buccal/sublingual cells. Their cell membranes exhibit invaginations or ridge-like folds (microplicae) to increase the adsorbance (**Figure 12**). Furrows located in between these microplicae typically feature a size of 200–400 nm. In case that particles or particle aggregates feature comparable sizes of these furrows, preferential settling of the particles is triggered with a tight contact between the nanoparticles and the membrane, which, as a consequence, facilitates their uptake. By contrast, smaller particles exhibit stronger interparticle electrostatic repulsion compared to larger particles and, thus, the particle–cell membrane contact is reduced, resulting in a decreased uptake. The fact that the smallest anatase particles remained in the upper part of the buccal epithelium was explained by the predominate nature of the primary particles, even in their aggregated form. This example nicely shows how cellular morphology determines the uptake of different particle types, despite of the fact that different other parameters also play an essential role in cellular uptake (namely, the aggregate size, the crystalline form, and the bioactivity of TiO_2). In the framework of tissue, several cell types coexist, and each cell type possesses a different affinity toward the particle characteristics.

3. Conclusions

It has to be concluded here that the influence of the parameters which govern and determine the uptake of inorganic nanoparticles into mammalian cells remains a topic of research of significant importance. Due to the large number of parameters that potentially can influence the uptake and metabolism of the nanoparticles, a general overview of the individual parameters is not yet developed and the literature remains partially diverse in terms of the importance of the individual parameters. There is general consensus that each parameter cannot be considered as isolated feature but a careful evaluation of different influences and the peculiar interplay of different factors has to be taken into account. This requires the utilization of well-designed and well-controlled probe nanoparticles, which can separate the different influences and allow controlling the complex interaction with the cell as well as with the biological environment. In this context, a large portfolio of different characterization techniques is at hand which are only briefly mentioned in several examples highlighted in this review. However, we regard TEM investigations as a very valuable tool, which will certainly gain even more importance in future studies, as it allows a direct visualization of internalization processes and thus, allows to obtain a deeper understanding of the processes on the scale of individual nanoparticles. With new developments in the field of TEM, the spectrum of questions regarding how nanoparticles are taken up to cells will prospectively gain increased significance and can help to obtain a better understanding of these processes on the scale of only a few nanometers. To date TEM is the investigation tool of choice if questions on the level of individual nanoparticles are in focus, since its resolution capability is even not matched by newly developed super-resolution fluorescence microscopes. However, the value of these new techniques cannot be underestimated for other aspects of nanoparticle uptake studies, i.e., the possibility to perform live-cell imaging, etc., but the development of routine techniques is still an ongoing process.

In this respect, TEM is a very valuable tool to address the issues of particle internalization and fate in cells, which can benefit from existing and continuously improving sample preparation protocols.

Considering the wealth of possible effects involved in the uptake process of nanoparticles into mammalian cells, it can be concluded that the utilization of inorganic nanoparticles for particle uptake studies is an attractive possibility to utilize their inherent biochemical properties in conjunction with their electron-dense appearance in TEM investigations to further reveal peculiarities and regulating experimental parameters in the complex interplay of cellular function, their interaction with the surrounding media, and metabolism of particles.

Acknowledgements

The authors acknowledge the funding as a part of the Sonderforschunsgbereich "Polytarget" (SFB 1278), project C04, funded by the Deutsche Forschungsgemeinschaft (DFG).

Conflict of Interest

The authors declare no conflict of interest.

Keywords

cellular uptake, nanoparticles, transmission electron microscopy, ultrastructural details

Received: December 18, 2017
Revised: April 9, 2018
Published online:

[1] a) E. Boisselier, D. Astruc, *Chem. Soc. Rev.* **2009**, *38*, 1759; b) T. Curry, R. Kopelman, M. Shilo, R. Popovtzer, *Contrast Media Mol. Imaging* **2014**, *9*, 53; c) X.-H. Peng, X. Qian, H. Mao, A. Y. Wang, Z. Chen, S. Nie, D. M. Shin, *Int. J. Nanomed.* **2008**, *3*, 311; d) A. Z. Wilczewska, K. Niemirowicz, K. H. Markiewicz, H. Car, *Pharmacol. Rep.* **2012**, *64*, 1020; e) F. Peng, Y. Su, Y. Zhong, C. Fan, S.-T. Lee, Y. He, *Acc. Chem. Res.* **2014**, *47*, 612; f) W. Park, K. Na, *Wiley Interdiscip. Rev.: Nanomed. Nanobiotechnol.* **2015**, *7*, 494; g) O.-J. Isaac, C. Joan, G.-F. Lorena, A. M. Zoe, C. Eudald, F. P. Victor, *Curr. Drug Metab.* **2013**, *14*, 518.
[2] D. J. Brayden, S.-A. Cryan, K. A. Dawson, P. J. O'Brien, J. C. Simpson, *Drug Discovery Today* **2015**, *20*, 942.
[3] D. Dutta, J. G. Donaldson, *Cell. Logist.* **2012**, *2*, 203.
[4] a) P. Khanna, C. Ong, B. Bay, G. Baeg, *Nanomaterials* **2015**, *5*, 1163; b) Y. Cao, J. Long, L. Liu, T. He, L. Jiang, C. Zhao, Z. Li, *Life Sci.* **2017**, *186*, 33; c) H. Lujan, C. M. Sayes, *Toxicol. Res.* **2017**, *6*, 580.
[5] R. Tantra, A. Knight, *Nanotoxicology* **2011**, *5*, 381.
[6] P.-C. Lin, S. Lin, P. C. Wang, R. Sridhar, *Biotechnol. Adv.* **2014**, *32*, 711.
[7] J. J. Bozzola, L. D. Russell, *Electron Microscopy: Principles and Techniques for Biologists*, Jones & Bartlett Publishers, Sudbury, Massachusetts, **1999**.
[8] P. V. AshaRani, G. Low Kah Mun, M. P. Hande, S. Valiyaveettil, *ACS Nano* **2009**, *3*, 279.
[9] E. I. Ryabchikova, N. A. Mazurkova, N. V. Shikina, Z. R. Ismagilov, *J. Med. Chem. Biol. Radiol. Def.* **2010**, *8*, pp. 1–18.
[10] J. Chan, T. Ying, Y. F. Guang, L. X. Lin, T. Kai, Z. Y. Fang, Y. X. Ting, L. F. Xing, Y. Y. Ji, *Biol. Trace Elem. Res.* **2011**, *144*, 183.
[11] C. Danciu, A. Falamas, C. Dehelean, C. Soica, H. Radeke, L. Barbu-Tudoran, F. Bojin, S. C. Pînzaru, M. F. Munteanu, *Cancer Cell Int.* **2013**, *13*, 1.
[12] M. Reifarth, S. Hoeppener, U. S. Schubert, *Adv. Mater.* **2018**, *30*, 1703704.
[13] C. Rosman, S. Pierrat, A. Henkel, M. Tarantola, D. Schneider, E. Sunnick, A. Janshoff, C. Sönnichsen, *Small* **2012**, *8*, 3683.
[14] a) A. Elsaesser, C. A. Barnes, G. McKerr, A. Salvati, I. Lynch, K. A. Dawson, C. V. Howard, *Nanomedicine* **2011**, *6*, 1189; b) B. Rothen-Rutishauser, D. A. Kuhn, Z. Ali, M. Gasser, F. Amin, W. J. Parak, D. Vanhecke, A. Fink, P. Gehr, C. Brandenberger, *Nanomedicine* **2013**, *9*, 607.
[15] S. Behzadi, V. Serpooshan, W. Tao, M. A. Hamaly, M. Y. Alkawareek, E. C. Dreaden, D. Brown, A. M. Alkilany, O. C. Farokhzad, M. Mahmoudi, *Chem. Soc. Rev.* **2017**, *46*, 4218.
[16] C. Kinnear, T. L. Moore, L. Rodriguez-Lorenzo, B. Rothen-Rutishauser, A. Petri-Fink, *Chem. Rev.* **2017**, *117*, 11476.
[17] S. Salatin, S. Maleki Dizaj, A. Yari Khosroushahi, *Cell Biol. Int.* **2015**, *39*, 881.
[18] L. Shang, K. Nienhaus, G. U. Nienhaus, *J. Nanobiotechnol.* **2014**, *12*, 5.
[19] A. Albanese, W. C. W. Chan, *ACS Nano* **2011**, *5*, 5478.
[20] E. Fröhlich, *Int. J. Nanomed.* **2012**, *7*, 5577.
[21] D. Docter, D. Westmeier, M. Markiewicz, S. Stolte, S. K. Knauer, R. H. Stauber, *Chem. Soc. Rev.* **2015**, *44*, 6094.
[22] M. A. Maurer-Jones, Y.-S. Lin, C. L. Haynes, *ACS Nano* **2010**, *4*, 3363.

[23] C. Gitrowski, A. R. Al-Jubory, R. D. Handy, *Toxicol. Lett.* **2014**, *226*, 264.
[24] I. Gosens, J. A. Post, L. J. J. de la Fonteyne, E. H. J. M. Jansen, J. W. Geus, F. R. Cassee, W. H. de Jong, *Part. Fibre Toxicol.* **2010**, *7*, 1.
[25] T. L. Moore, L. Rodriguez-Lorenzo, V. Hirsch, S. Balog, D. Urban, C. Jud, B. Rothen-Rutishauser, M. Lattuada, A. Petri-Fink, *Chem. Soc. Rev.* **2015**, *44*, 6287.
[26] a) T.-G. Iversen, T. Skotland, K. Sandvig, *Nano Today* **2011**, *6*, 176; b) T. Kirchhausen, *Annu. Rev. Biochem.* **2000**, *69*, 699.
[27] a) B. Yameen, W. I. Choi, C. Vilos, A. Swami, J. Shi, O. C. Farokhzad, *J. Controlled Release* **2014**, *190*, 485; b) R. G. Parton, K. Simons, *Nat. Rev. Mol. Cell Biol.* **2007**, *8*, 185; c) K. Sandvig, M. L. Torgersen, H. A. Raa, B. van Deurs, *Histochem. Cell Biol.* **2008**, *129*, 267.
[28] M. P. D. Dobay, A. P. Alberola, E. R. Mendoza, J. O. Rädler, *J. Nanopart. Res.* **2012**, *14*, 1.
[29] M. Calero, M. Chiappi, A. Lazaro-Carrillo, M. J. Rodríguez, F. J. Chichón, K. Crosbie-Staunton, A. Prina-Mello, Y. Volkov, A. Villanueva, J. L. Carrascosa, *J. Nanobiotechnol.* **2015**, *13*, 16.
[30] R. Gromnicova, M. Kaya, I. A. Romero, P. Williams, S. Satchell, B. Sharrack, D. Male, *PLoS One* **2016**, *11*, e0161610.
[31] K. Shapero, F. Fenaroli, I. Lynch, D. C. Cottell, A. Salvati, K. A. Dawson, *Mol. Biosyst.* **2011**, *7*, 371.
[32] K. O. Yu, C. M. Grabinski, A. M. Schrand, R. C. Murdock, W. Wang, B. Gu, J. J. Schlager, S. M. Hussain, *J. Nanopart. Res.* **2009**, *11*, 15.
[33] J. J. Corbalan, C. Medina, A. Jacoby, T. Malinski, M. W. Radomski, *Int. J. Nanomed.* **2011**, *6*, 2821.
[34] K. S. Butler, D. J. Peeler, B. J. Casey, B. J. Dair, R. K. Elespuru, *Mutagenesis* **2015**, *30*, 577.
[35] a) B. D. Chithrani, J. Stewart, C. Allen, D. A. Jaffray, *Nanomedicine* **2009**, *5*, 118; b) C. O. Pritz, M. Bitsche, W. Salvenmoser, J. Dudás, A. Schrott-Fischer, R. Glueckert, *Nanomedicine* **2012**, *8*, 239.
[36] I. George, G. Naudin, S. Boland, S. Mornet, V. Contremoulins, K. Beugnon, L. Martinon, O. Lambert, A. Baeza-Squiban, *Nanoscale* **2015**, *7*, 4529.
[37] J. F. Hillyer, R. M. Albrecht, *J. Pharm. Sci.* **2001**, *90*, 1927.
[38] A. Tarantini, R. Lanceleur, A. Mourot, M. T. Lavault, G. Casterou, G. Jarry, K. Hogeveen, V. Fessard, *Toxicol. In Vitro* **2015**, *29*, 398.
[39] Q. Mu, N. S. Hondow, Ł. Krzemiński, A. P. Brown, L. J. Jeuken, M. N. Routledge, *Part. Fibre Toxicol.* **2012**, *9*, 1.
[40] T. Mustafa, F. Watanabe, W. Monroe, M. Mahmood, Y. Xu, L. Saeed, A. Karmakar, D. Casciano, S. Ali, A. S. Biris, *J. Nanomed. Nanotechnol.* **2011**, *2*, 1000118.
[41] U. Taylor, S. Klein, S. Petersen, W. Kues, S. Barcikowski, D. Rath, *Cytometry, Part A* **2010**, *77A*, 439.
[42] a) M. A. Sobhan, V. K. A. Sreenivasan, M. J. Withford, E. M. Goldys, *Colloids Surf., B* **2012**, *92*, 190; b) X. Cai, H.-H. Chen, C.-L. Wang, S.-T. Chen, S.-F. Lai, C.-C. Chien, Y.-Y. Chen, I. M. Kempson, Y. Hwu, C. S. Yang, G. Margaritondo, *Anal. Bioanal. Chem.* **2011**, *401*, 809.
[43] S. N. Tammam, H. M. E. Azzazy, A. Lamprecht, *J. Controlled Release* **2016**, *229*, 140.
[44] M. Belting, S. Sandgren, A. Wittrup, *Adv. Drug Delivery Rev.* **2005**, *57*, 505.
[45] D. P. Devos, R. Gräf, M. C. Field, *Curr. Opin. Cell Biol.* **2014**, *28*, 8.
[46] J. A. Coulter, S. Jain, K. T. Butterworth, L. E. Taggart, G. R. Dickson, S. J. McMahon, W. B. Hyland, M. F. Muir, C. Trainor, A. R. Hounsell, *Int. J. Nanomedicine* **2012**, *7*, 2673.
[47] X. Zhang, S. Shastry, S. E. Bradforth, J. L. Nadeau, *Nanoscale* **2015**, *7*, 240.
[48] M. Thomas, A. M. Klibanov, *Proc. Natl. Acad. Sci. USA* **2003**, *100*, 9138.
[49] A. K. Varkouhi, M. Scholte, G. Storm, H. J. Haisma, *J. Controlled Release* **2011**, *151*, 220.
[50] P. Nativo, I. A. Prior, M. Brust, *ACS Nano* **2008**, *2*, 1639.
[51] a) B. K. Gaiser, S. Hirn, A. Kermanizadeh, N. Kanase, K. Fytianos, A. Wenk, N. Haberl, A. Brunelli, W. G. Kreyling, V. Stone, *Toxicol. Sci.* **2013**, *131*, 537; b) M. Hashimoto, S. Imazato, *Dent. Mater.* **2015**, *31*, 556; c) J. H. Seog, B. Kong, D. Kim, L. M. Graham, J. S. Choi, S. B. Lee, *J. Nanopart. Res.* **2015**, *17*, 6.
[52] M. Arsianti, M. Lim, S. N. Lou, I. Y. Goon, C. P. Marquis, R. Amal, *J. Colloid Interface Sci.* **2011**, *354*, 536.
[53] a) M. Abdel-Wahhab, K. Abdel-Wahhab, F. Mannaa, N. Hassan, R. Safar, R. Diab, B. Foliguet, L. Ferrari, B. Rihn, *Materials* **2014**, *7*, 1555; b) M. Reifarth, D. Pretzel, S. Schubert, C. Weber, R. Heintzmann, S. Hoeppener, U. S. Schubert, *Chem. Commun.* **2016**, *52*, 4361.
[54] L. H. Allen, E. Matijević, *J. Colloid Interface Sci.* **1969**, *31*, 287.
[55] E. Carenza, V. Barceló, A. Morancho, J. Montaner, A. Rosell, A. Roig, *Acta Biomater.* **2014**, *10*, 3775.
[56] J. Reguera, J. Langer, D. Jimenez de Aberasturi, L. M. Liz-Marzan, *Chem. Soc. Rev.* **2017**, *46*, 3866.
[57] W.-S. Kuo, C.-N. Chang, Y.-T. Chang, M.-H. Yang, Y.-H. Chien, S.-J. Chen, C.-S. Yeh, *Angew. Chem., Int. Ed.* **2010**, *122*, 2771.
[58] a) J. Overgaard, *Cancer* **1977**, *39*, 2637; b) P. Wust, B. Hildebrandt, G. Sreenivasa, B. Rau, J. Gellermann, H. Riess, R. Felix, P. M. Schlag, *Lancet Oncol.* **2002**, *3*, 487; c) B. Hildebrandt, P. Wust, O. Ahlers, A. Dieing, G. Sreenivasa, T. Kerner, R. Felix, H. Riess, *Crit. Rev. Oncol. Hematol.* **2002**, *43*, 33.
[59] a) P. Cherukuri, E. S. Glazer, S. A. Curley, *Adv. Drug Delivery Rev.* **2010**, *62*, 339; b) C. B. Collins, R. S. McCoy, B. J. Ackerson, G. J. Collins, C. J. Ackerson, *Nanoscale* **2014**, *6*, 8459.
[60] W. Zhang, Y. Ji, X. Wu, H. Xu, *ACS Appl. Mater. Interfaces* **2013**, *5*, 9856.
[61] Z. Sun, M. Worden, Y. Wroczynskyj, P. K. Manna, J. A. Thliveris, J. van Lierop, T. Hegmann, D. W. Miller, *J. Mater. Chem. B* **2016**, *4*, 5913.
[62] J. Yue, T. J. Feliciano, W. Li, A. Lee, T. W. Odom, *Bioconjugate Chem.* **2017**, *28*, 1791.
[63] a) C. M. Sayes, R. Wahi, P. A. Kurian, Y. Liu, J. L. West, K. D. Ausman, D. B. Warheit, V. L. Colvin, *Toxicol. Sci.* **2006**, *92*, 174; b) J. Petković, B. Žegura, M. Stevanović, N. Drnovšek, D. Uskoković, S. Novak, M. Filipič, *Nanotoxicology* **2011**, *5*, 341.
[64] P. O. Andersson, C. Lejon, B. Ekstrand-Hammarström, C. Akfur, L. Ahlinder, A. Bucht, L. Österlund, *Small* **2011**, *7*, 514.
[65] a) S. A. Thakur, R. Hamilton Jr., T. Pikkarainen, A. Holian, *Toxicol. Sci.* **2009**, *107*, 238; b) H. Zhou, A. Imrich, L. Kobzik, *Part. Fibre Toxicol.* **2008**, *5*, 7.
[66] A. R. Mishra, J. Zheng, X. Tang, P. L. Goering, *Toxicol. Sci.* **2016**, *150*, 473.
[67] a) P. Cronholm, H. L. Karlsson, J. Hedberg, T. A. Lowe, L. Winnberg, K. Elihn, I. O. Wallinder, L. Möller, *Small* **2013**, *9*, 970; b) A. R. Gliga, S. Skoglund, I. Odnevall Wallinder, B. Fadeel, H. L. Karlsson, *Part. Fibre Toxicol.* **2014**, *11*, 11.
[68] E.-J. Park, J. Yi, Y. Kim, K. Choi, K. Park, *Toxicol. In Vitro* **2010**, *24*, 872.
[69] Q. L. Feng, J. Wu, G. Q. Chen, F. Z. Cui, T. N. Kim, J. O. Kim, *J. Biomed. Mater. Res.* **2000**, *52*, 662.
[70] a) R. de Lima, A. B. Seabra, N. Durán, *J. Appl. Toxicol.* **2012**, *32*, 867; b) T. Zhang, L. Wang, Q. Chen, C. Chen, *Yonsei Med. J.* **2014**, *55*, 283; c) L. L. Maurer, J. N. Meyer, *Environ. Sci.: Nano* **2016**, *3*, 311.
[71] X. Jiang, R. Foldbjerg, T. Miclaus, L. Wang, R. Singh, Y. Hayashi, D. Sutherland, C. Chen, H. Autrup, C. Beer, *Toxicol. Lett.* **2013**, *222*, 55.
[72] S. Ahlberg, M. C. Meinke, L. WErner, M. Epple, J. Diendorf, U. Blume-Peytavi, J. Lademann, A. Voght, F. Rancan, *Eur. J. Pharm. Biopharm.* **2014**, *88*, 651.
[73] R. Jin, B. Lin, D. Li, H. Ai, *Curr. Opin. Pharmacol.* **2014**, *18*, 18.
[74] Y. Kohgo, K. Ikuta, T. Ohtake, Y. Torimoto, J. Kato, *Int. J. Hematol.* **2008**, *88*, 7.
[75] J. D. Lopez-Castro, A. V. Maraloiu, J. J. Delgado, J. J. Calvino, M. G. Blanchin, N. Galvez, J. M. Dominguez-Vera, *Nanoscale* **2011**, *3*, 4597.

[76] J. Kolosnjaj-Tabi, Y. Javed, L. Lartigue, J. Volatron, D. Elgrabli, I. Marangon, G. Pugliese, B. Caron, A. Figuerola, N. Luciani, T. Pellegrino, D. Alloyeau, F. Gazeau, *ACS Nano* **2015**, *9*, 7925.
[77] M. Schieber, N. S. Chandel, *Curr. Biol.* **2014**, *24*, R453.
[78] S. Sharifi, S. Behzadi, S. Laurent, M. Laird Forrest, P. Stroeve, M. Mahmoudi, *Chem. Soc. Rev.* **2012**, *41*, 2323.
[79] G. Oberdörster, E. Oberdörster, J. Oberdörster, *Environ. Health Perspect.* **2005**, *113*, 823.
[80] S. Orrenius, *Drug Metab. Rev.* **2007**, *39*, 443.
[81] M. Dusinska, J. Tulinska, N. El Yamani, M. Kuricova, A. Liskova, E. Rollerova, E. Rundén-Pran, B. Smolkova, *Food Chem. Toxicol.* **2017**, *109*, 797.
[82] V. H. Nguyen, B.-J. Lee, *Int. J. Nanomed.* **2017**, *12*, 3137.
[83] C. Corbo, R. Molinaro, A. Parodi, N. E. Toledano Furman, F. Salvatore, E. Tasciotti, *Nanomedicine* **2016**, *11*, 81.
[84] D. Mahl, C. Greulich, W. Meyer-Zaika, M. Koller, M. Epple, *J. Mater. Chem.* **2010**, *20*, 6176.
[85] J. Park, J.-H. Park, K.-S. Ock, E.-O. Ganbold, N. W. Song, K. Cho, S. Y. Lee, S.-W. Joo, *J. Colloid Interface Sci.* **2011**, *363*, 105.
[86] A. K. Murthy, R. J. Stover, W. G. Hardin, R. Schramm, G. D. Nie, S. Gourisankar, T. M. Truskett, K. V. Sokolov, K. P. Johnston, *J. Am. Chem. Soc.* **2013**, *135*, 7799.
[87] C. T. Ng, F. M. A. Tang, J. J. e. Li, C. Ong, L. L. Y. Yung, B. H. Bay, *Anat. Rec.* **2015**, *298*, 418.
[88] J. Liu, Q. Peng, *Acta Biomater.* **2017**, *55*, 13.
[89] E. Izak-Nau, M. Voetz, S. Eiden, A. Duschl, V. F. Puntes, *Part. Fibre Toxicol.* **2013**, *10*, 56.
[90] a) R. Tedja, M. Lim, R. Amal, C. Marquis, *ACS Nano* **2012**, *6*, 4083; b) C. L. Browning, T. The, M. D. Mason, J. P. Wise, J. Environ. *Anal. Toxicol.* **2014**, *4*, 239; c) J. Soto-Alvaredo, E. Blanco, J. Bettmer, D. Hevia, R. M. Sainz, C. Lopez Chaves, C. Sanchez, J. Llopis, A. Sanz-Medel, M. Montes-Bayon, *Metallomics* **2014**, *6*, 1702.
[91] M. Dorier, E. Brun, G. Veronesi, F. Barreau, K. Pernet-Gallay, C. Desvergne, T. Rabilloud, C. Carapito, N. Herlin-Boime, M. Carriere, *Nanoscale* **2015**, *7*, 7352.
[92] S.-M. Yu, L. Gonzalez-Moragas, M. Milla, A. Kolovou, R. Santarella-Mellwig, Y. Schwab, A. Laromaine, A. Roig, *Acta Biomater.* **2016**, *43*, 348.
[93] S. Siddhanta, C. Zheng, C. Narayana, I. Barman, *Chem. Sci.* **2016**, *7*, 3730.
[94] R. A. Sperling, W. J. Parak, *Philos. Trans. R. Soc., A* **2010**, *368*, 1333.
[95] K. Knop, R. Hoogenboom, D. Fischer, U. S. Schubert, *Angew. Chem., Int. Ed.* **2010**, *49*, 6288.
[96] W. Lu, C. Xiong, R. Zhang, L. Shi, M. Huang, G. Zhang, S. Song, Q. Huang, G.-Y. Liu, C. Li, *J. Controlled Release* **2012**, *161*, 959.
[97] G. K. Hinkley, P. Carpinone, J. W. Munson, K. W. Powers, S. M. Roberts, *Part. Fibre Toxicol.* **2015**, *12*, 1.
[98] G. Feng, S. Kun, Z. X. James, Y. Cunzhong, Y. Shi, Y. Qifeng, C. Jie, K. Beihua, *Nanotechnology* **2011**, *22*, 285101.
[99] I. A. Rahman, V. Padavettan, *J. Nanomaterials* **2012**, *2012*, 8.
[100] W. Wu, Q. He, C. Jiang, *Nanoscale Res. Lett.* **2008**, *3*, 397.
[101] M. Muthiah, I.-K. Park, C.-S. Cho, *Biotechnol. Adv.* **2013**, *31*, 1224.
[102] a) M. Amiry-Moghaddam, O. P. Ottersen, *Nat. Neurosci.* **2013**, *16*, 798; b) J. Roth, *Histochem. Cell Biol.* **1996**, *106*, 1.
[103] C. Bechara, S. Sagan, *FEBS Lett.* **2013**, *587*, 1693.
[104] K. Padari, K. Koppel, A. Lorents, M. Hällbrink, M. Mano, M. C. Pedroso de Lima, M. Pooga, *Bioconjugate Chem.* **2010**, *21*, 774.
[105] A. Rydström, S. Deshayes, K. Konate, L. Crombez, K. Padari, H. Boukhaddaoui, G. Aldrian, M. Pooga, G. Divita, *PLoS One* **2011**, *6*, e25924.
[106] O. Veiseh, J. W. Gunn, F. M. Kievit, C. Sun, C. Fang, J. S. H. Lee, M. Zhang, *Small* **2009**, *5*, 256.
[107] D. H. M. Dam, J. H. Lee, P. N. Sisco, D. T. Co, M. Zhang, M. R. Wasielewski, T. W. Odom, *ACS Nano* **2012**, *6*, 3318.
[108] A. M. Scott, J. D. Wolchok, L. J. Old, *Nat. Rev. Cancer* **2012**, *12*, 278.
[109] D. C. Baiu, N. S. Artz, M. R. McElreath, B. D. Menapace, D. Hernando, S. B. Reeder, C. Grüttner, M. Otto, *Nanomedicine* **2015**, *10*, 2973.
[110] S.-H. Cheng, C.-H. Chu, N.-T. Chen, J. S. Souris, C.-T. Chen, L.-W. Lo, *Int. J. Photoenergy* **2014**, *2014*, 11.
[111] K.-S. Ock, E. O. Ganbold, J. Park, K. Cho, S.-W. Joo, S. Y. Lee, *Analyst* **2012**, *137*, 2852.
[112] S. Suarasan, M. Focsan, M. Potara, O. Soritau, A. Florea, D. Maniu, S. Astilean, *ACS Appl. Mater. Interfaces* **2016**, *8*, 22900.
[113] X. Zhang, H. Chibli, R. Mielke, J. Nadeau, *Bioconjugate Chem.* **2011**, *22*, 235.
[114] A. L. Tam, M. P. Melancon, M. Abdelsalam, T. A. Figueira, K. Dixon, A. McWatters, M. Zhou, Q. Huang, O. Mawlawi, K. Dunner, C. Li, S. Gupta, *J. Biomed. Nanotechnol.* **2016**, *12*, 296.
[115] R. Waehler, S. J. Russell, D. T. Curiel, *Nat. Rev. Genet.* **2007**, *8*, 573.
[116] L. Naldini, *Nature* **2015**, *526*, 351.
[117] A. C. Rinkenauer, S. Schubert, A. Traeger, U. S. Schubert, *J. Mater. Chem. B* **2015**, *3*, 7477.
[118] J. Gilleron, W. Querbes, A. Zeigerer, A. Borodovsky, G. Marsico, U. Schubert, K. Manygoats, S. Seifert, C. Andree, M. Stoter, H. Epstein-Barash, L. Zhang, V. Koteliansky, K. Fitzgerald, E. Fava, M. Bickle, Y. Kalaidzidis, A. Akinc, M. Maier, M. Zerial, *Nat. Biotechnol.* **2013**, *31*, 638.
[119] Y.-K. Chang, Y.-P. Liu, J. H. Ho, S.-C. Hsu, O. K. Lee, *J. Orthop. Res.* **2012**, *30*, 1499.
[120] S. Schwarz, J. E. Wong, J. Bornemann, M. Hodenius, U. Himmelreich, W. Richtering, M. Hoehn, M. Zenke, T. Hieronymus, *Nanomedicine* **2012**, *8*, 682.
[121] I. Brezaniova, V. Kral, Z. Černochová, M. Hrubý, presented at 2nd Int. Conf. Infectious Diseases and Nanomedicine, Kathmandu, Nepal, December **2015**.
[122] a) W. T. Godbey, K. K. Wu, A. G. Mikos, *J. Controlled Release* **1999**, *60*, 149; b) P. Midoux, C. Pichon, J.-J. Yaouanc, P.-A. Jaffrès, *Br. J. Pharmacol.* **2009**, *157*, 166.
[123] S. J. H. Soenen, A. R. Brisson, E. Jonckheere, N. Nuytten, S. Tan, U. Himmelreich, M. De Cuyper, *Biomaterials* **2011**, *32*, 1748.
[124] S. Kralj, M. Rojnik, R. Romih, M. Jagodič, J. Kos, D. Makovec, *J. Nanopart. Res.* **2012**, *14*, 1151.
[125] J. S. Nowak, D. Mehn, P. Nativo, C. P. García, S. Gioria, I. Ojea-Jiménez, D. Gilliland, F. Rossi, *Toxicol. Lett.* **2014**, *224*, 84.
[126] X. Liu, H. Li, Y. Chen, Q. Jin, K. Ren, J. Ji, *Adv. Healthcare Mater.* **2014**, *3*, 1439.
[127] N. K. Iversen, S. Frische, K. Thomsen, C. Laustsen, M. Pedersen, P. B. L. Hansen, P. Bie, J. Fresnais, J.-F. Berret, E. Baatrup, T. Wang, *Toxicol. Appl. Pharmacol.* **2013**, *266*, 276.
[128] G. Janer, E. Mas del Molino, E. Fernández-Rosas, A. Fernández, S. Vázquez-Campos, *Toxicol. Lett.* **2014**, *228*, 103.
[129] S. Elliott, A. Sinclair, H. Collins, L. Rice, W. Jelkmann, *Ann. Hematol.* **2014**, *93*, 181.
[130] W. Zhou, X. Liu, J. Ji, *J. Nanopart. Res.* **2012**, *14*, 1.
[131] B. J. Teubl, G. Leitinger, M. Schneider, C.-M. Lehr, E. Fröhlich, A. Zimmer, E. Roblegg, *Nanotoxicology* **2015**, *9*, 253.

Publication P3

"Electron density of polymeric nanoparticles determined by image processing of transmission electron micrographs: Insights into heavy metal staining processes"

M. Reifarth, W. Mueller, B. Shkodra-Pula, H. Goerls, U.S. Schubert, R. Heintzmann, S. Hoeppener

submitted to *Part. Part. Syst. Charact.*

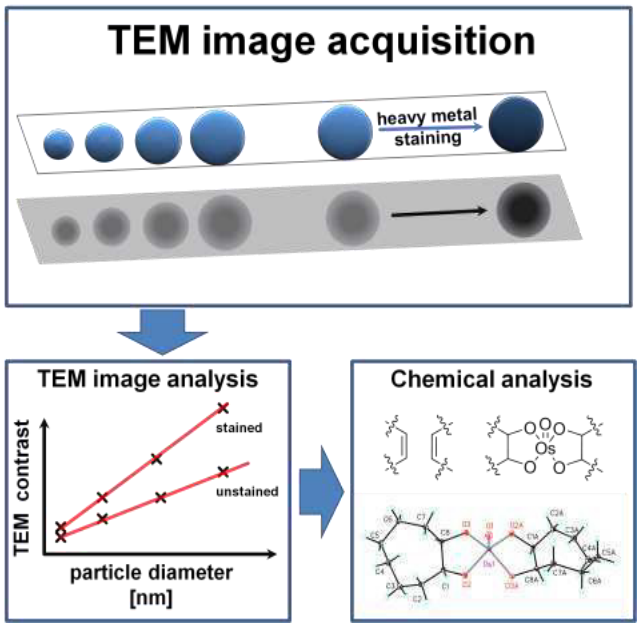

Von: em.particle-journal.0.5cf275.cc37df72@editorialmanager.com <em.particle-journal.0.5cf275.cc37df72@editorialmanager.com> im Auftrag von Particle Journal <em@editorialmanager.com>
Gesendet: Mittwoch, 1. August 2018 18:31
An: Stephanie Höppener
Betreff: Submission Confirmation for Electron density of polymeric nanoparticles determined by image processing of transmission electron micrographs: Insights into heavy metal staining processes (ppsc.201800324)

Dear Mrs. Höppener,

Your submission entitled "Electron density of polymeric nanoparticles determined by image processing of transmission electron micrographs: Insights into heavy metal staining processes" has been received by journal Particle & Particle Systems Characterization. The manuscript number for your submission is ppsc.201800324.

To view your submission, please login to https://particle-journal.editorialmanager.com/ by entering your username (SHoeppener) and password and selecting the "Author Login" option.

This message has been sent to all named co-authors listed in the submission process to serve as notification of submission.

Thank you for submitting your work to the journal.

Kind regards,

Editorial Office
Particle & Particle Systems Characterization
Email:particle@wiley.com
Tel: +49(0)6201-606-432/235

http://www.particle-journal.com/

*****

WILEY-VCH

DOI: 10.1002/((please add manuscript number))

Article type: Communication

Electron density of polymeric nanoparticles determined by image processing of transmission electron micrographs: Insights into heavy metal staining processes

Martin Reifarth, Walter Müller, Blerina Shkodra-Pula, Helmar Görls, Ulrich S. Schubert, Rainer Heintzmann, and Stephanie Hoeppener**

Dipl.-Chem. M. Reifarth, MSc. B. Shkodra-Pula, Prof. U. S. Schubert, Dr. S. Hoeppener

Laboratory of Organic and Macromolecular Chemistry, Friedrich Schiller University Jena, Humboldtstr. 10, 07743 Jena, Germany
and
Jena Center for Soft Matter, Friedrich Schiller University Jena, Philosophenweg 7, 07743 Jena, Germany
E-mail: s.hoeppener@uni-jena.de

Dr. W. Müller, Prof. Dr. R. Heintzmann
Institute of Physical Chemistry, Friedrich Schiller University Jena, Helmholtzweg 4, 07743 Jena, Germany
and
Leibniz Institute of Photonic Technology, Albert-Einstein-Straße 9, 07745 Jena, Germany
and
Jena Center for Soft Matter, Friedrich Schiller University Jena, Philosophenweg 7, 07743 Jena, Germany

E-mail: rainer.heintzmann@uni-jena.de
and
Abbe Center for Photonics
Albert-Einstein-Straße 6, 07745 Jena, Germany

Dr. H. Görls
Institute for Inorganic and Analytical Chemistry, Friedrich Schiller University,
Humboldtstrasse 8, 07743 Jena, Germany

Keywords: electron contrast, polymeric nanoparticles, transmission electron microscopy, heavy metal staining, osmium tetroxide

Introduction

The increasing interest to utilize polymer nanoparticles as efficient delivery and targeting vehicles in biomedical applications or as additives to obtain composites with improved mechanical performances, has fueled continuous interest in studying their distribution in various engineered materials as well as in analyzing their specific mode-of-action. The versatility of polymer synthesis strategies provides access to a virtually unlimited portfolio of different nanoparticles with tailor-made properties, including, e.g., controlled material degradability,[1] stimuli-sensitivity,[2] or thermo-responsiveness.[3] These possibilities to tailor the nanoparticles` properties can be regarded as a major motivation to introduce polymer nanoparticles in a plethora of different lines of research and industrial applications, ranging from materials applications to biomedicine and others.

In the field of materials science, polymeric nanoparticles represent important additives to improve the properties of materials or to introduce novel functions into the system.[4] For instance, polymer particles with suitable properties are utilized as fillers in ductile polymer bulk samples to significantly improve the mechanical properties of the resulting polymeric materials.[5] As a further example, the incorporation of nanoscale capsules into polymer coatings represents a prominent approach in the fabrication of self-healing materials. Here a chemically active compound is released from the capsules in the instance of mechanical damage of the material and initiates an self-healing process of the polymer matrix.[6] In these contexts, the local distribution of the particles, their incorporation and interaction with the matrix materials, their size and shape, their aggregation behavior as well as their ability to incorporate into networks represent questions of tremendous importance, which have to be

considered, if a comprehensive assessment of the nanoparticles' influence on the material properties is addressed.[7] Regarding biomedical applications, polymeric nanomaterials are employed as efficient vehicles for the delivery of pharmaceutically active compounds into cells and tissue with the aim to achieve a controlled release of their cargo.[1, 8] These nanoparticle carriers can be widely adjusted in terms of their surface properties, and the utilization of different polymers or copolymer architectures provides a powerful means to tailor their uptake and localization within cellular systems.[9] Also in this case, a precise investigation of the intercellular distribution, their aggregation state in cellular compartments, as well as their interaction with extracellular membranes and internal cellular compartments is of significant importance and can provide highly valuable information on the intracellular mode-of-action of these particles.[10] In this context, microscopy techniques provide high resolution images and detailed information on the localization and distribution of the nanoparticles and can visualize their interaction with other materials. Thus, electron microscopy techniques are frequently employed to address the question of how nanoparticles are distributed within or interact with a matrix material.[10-11] Transmission electron microscopy (TEM) represents in this respect a powerful technique, since it can provide information on the morphological details of the incorporation of nanoparticles in different materials with a high resolution.[12] One of the major challenges when aiming on localizing polymer nanoparticles in an organic matrix, may it be a polymer bulk material or the intercellular compartments of a cell or the cytosol,[10] is the poor contrast, which is generated by the polymers in TEM imaging. This is based on the fact that polymer nanoparticles almost exclusively consist of the same elements, which are also found in common polymer matrices or even in a cellular system. This situation is different compared to, *e.g.* metal or metal oxide nanoparticles, which consist of atoms with a high atomic number Z. They scatter the electron beam more efficiently, and, as a consequence, an enhanced image contrast is generated by this

class of materials.[12] Researchers employing TEM in cell biology have addressed this issue by selectively introducing heavy elements to lipid membranes, phosphate bearing nucleic acids, and proteins by utilizing staining reagents, *i.e.* osmium tetroxide (OsO_4), uranyl acetate ($UO_2(OOCCH_3)_2$) or lead citrate ($Pb_3(C_6H_5O_7)_2$) – to name only the most common heavy metal compounds employed as electron dense stains.[13] Additionally, immunogold staining approaches utilize small gold nanoparticles functionalized with specific antibodies to localize even individual proteins in cellular compartments, *e.g.* membranes, the nucleus, *etc.*,[14] whereby the easily identifiable gold labels are utilized as colloidal markers to tag, *e.g.*, the location of proteins. These staining protocols have developed over the years and a lot of empirical work has been devoted to optimize the staining protocols. As a result, even though representing a standard method since the 1960s,[13] this approach is today still employed with only minor changes of the protocols.

These staining protocols can be used to efficiently emphasize the morphologies of polymeric nanoparticles within an organic matrix. In this context, heavy metal species accumulate, *e.g.* inside the nanoparticles in a selective manner. In sight of the aforementioned examples, which illustrate the necessity to examine the interplay of polymeric nanomaterials with soft matter, it becomes obvious that there is a demand to understand a relationship between (i) the chemical nature of a polymeric nanoparticle and its TEM image contrast more in detail, and, (ii) in a next step, to estimate, to what extent common heavy metal staining agents are capable of enhancing their image contrast.

To this aim, we introduce a method to analyze different polymers regarding their inherent capability to scatter electrons as well as to study their response to common staining agents. For this reason, an automated image processing algorithm is developed, which analyses the contrast generated in TEM imaging. Subsequently, selected polymeric systems are investigated and exposed to common reactive heavy metal species, and the staining capability

of the agent towards the polymeric structure is evaluated. With this respect, selected results were investigated in more detail. As a point which deserves to be mentioned is the tremendous contrast enhancement of polymers containing isolated double bonds upon staining with OsO_4, which motivated us to examine the chemistry of the underlying process in more detail. OsO_4 staining in this case does not only introduce an electron contrast but it also has a considerable fixation potential and is, therefore, utilized as a common step of improving the structural integrity and density of the materials.[15] In order to investigate in particular the fixation ability of OsO_4 for the staining of double bond containing nanoparticles, we developed a model system, which mimics the staining of a small organic compound in a nanoparticle-like environment and investigated the occurring staining process by means of electron spray ionization time-of-flight (high resolution) mass spectrometry (ESI-ToF-HRMS/ ESI-ToF-MS) and crystal structure analysis.

We finally show the potential of the suggested image processing-based approach to obtain a deeper insight into the TEM image contrast formation of soft matter in their nanoparticle formulation. This approach facilitates a rapid estimation of the staining potential of common heavy metal agents towards the respective polymer class. Nevertheless, we also want to point out that a mere assessment of the contrast enhancement by means of our approach does not necessarily allow for gathering the entirety staining process. As illustrated by the example of OsO_4 fixation of double-bond containing polymers, a more complete comprehension can be obtained by further experiments providing an insight into underlying chemical processes.

Polymer nanoparticle preparation

For the investigation of the staining and electron contrast properties of polymer nanoparticles, in a first instance, different particle systems consisting of relevant homopolymers were

analyzed to investigate the inherent electron attenuation potential[†] of these technologically important homopolymers (**Figure 1**, **P1**-**P3**). Poly(lactic-*co*-glycolic acid) (PLGA, **P1**) was chosen as a representative for a pharmaceutically utilized material, which shows good biocompatibility and is frequently employed for drug administration purposes due to its biodegradability.[16] Furthermore, ester-based poly(methylmethacrylate) (PMMA, **P2**, copolymerized with a small amount of methacrylic acid) and the phenyl group containing poly(styrene) (PS, **P3**) were investigated due to their frequent application in the formation of composite materials[17] or as materials for the formation of carrier particles which can be utilized, *e.g.* in immunoassays.[18]

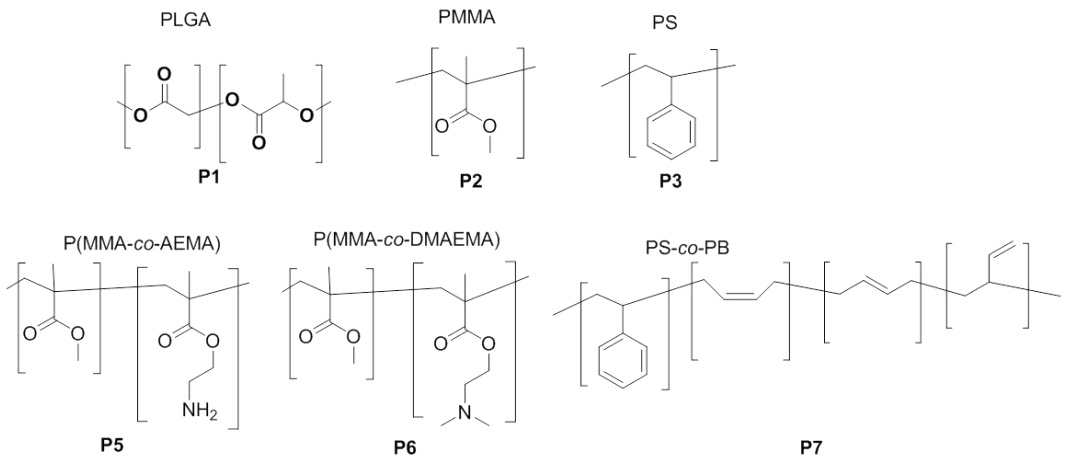

Figure 1: Schematic representation of the chemical structure of the utilized polymers for formulating nanoparticle systems. Top row: Representatives for homopolymers (**P1**–**P3**). Bottom row: Copolymer materials (**P4**–**P6**) used for the formation of nanoparticles. Nanoparticle systems are denoted in the following as **NPx**. Px representing the polymer of which the particles were formulated.

These polymers can be formulated into nanoparticle systems by utilizing nanoprecipitation (NPr), nanoemulsion (NE) and emulsion (EP) polymerization techniques. The formed

[†] In the following text, the decrease of beam intensity due to the interaction of electrons with the nanoparticles will be referred to as electron attenuation. Unlike the attenuation of, *e.g.* visible light as a result its interaction with matter, the attenuation of the electron beam intensity is not attributable to (molecular) absorption of an electron in a quantum-mechanical sense. The loss of beam intensity, in this case, is attributed to the deflexion of electrons from their incident beam direction due to interaction with the nanomaterial. The deflected electrons are blocked by the detection aperture, whereupon they do not reach the detector.

nanoparticle systems were characterized regarding their physico-chemical properties which are summarized in Table 1.

Table 1: Physico-chemical properties of different homo- and copolymer nanoparticle formulations. NE: Nanoemulsion polymerization; NPr: Nano precipitation; EP: Emulsion polymerization. *Determined by Dynamic Light Scattering (DLS).

NP sample	Polymer	Preparation method	Size [nm] Polydispersity (PDI)*	Zeta potential [mV]
NP1	PLGA	NP	199 .138)	–29 ± 1
NP2	PMMA	NPr	107 (0.110)	–46 ± 1
NP3	PS	EP	115 (0.105)	33 ± 1
NP4	P(MMA-*co*-AEMA)	NPr	130 (0.14)	61 ± 1
NP5	P(MMA-*co*-DMAEMA)	NPr	124 (0.06)	33 ± 1
NP6	PS-*co*-PB	NE	214 (0.118)	–5 ± 0.1

In order to define a measure for the electron density of the nanoparticles, all particle systems were prepared on a carbon coated TEM grid by conventional blotting and drying of the remaining solution on the grid. This process might lead to drying artifacts and one could have considered performing measurements by cryo-TEM in vitrified ice samples. However, in this approach of the thickness of the resulting ice layer is hard to control, which would result in problems during the automated analysis of the particles' contrast. Moreover, the position of the nanoparticles within the film along the z-axis is not controllable. As a consequence, the preparation of the polymer nanoparticles by a simple blotting procedure was favored. For the image acquisition, major parameters of the electron beam were kept constant. The beam intensity (approx. 6.000 counts at open carbon support position at a magnification of 19.000 × and a completely spread beam), the spot size (1), the detection aperture (40 µm), and most importantly the defocus (–2.5 µm) from eucentric height were adjusted carefully to the above listed parameters for each image. Thereby, it has to be mentioned that the use of the aperture as well as the defocus of the electron beam were applied to improve the visibility of the polymer nanoparticles (at perfect conditions the nanoparticles are barely – in the optimal case not at all – visible).

The contrast of individual particles is extracted from the so acquired TEM images (**Figure 2**A) using a self-written evaluation algorithm based on the image processing library DIPimage for MATLAB.[19] The theoretical rationales of this algorithm are based on the fact that for amorphous or polycrystalline material, the decrease of the electron beam intensity follows an exponential decay for ultrathin specimens, which has been reported to be used, *e.g.* for the determination of a sample thickness of ideal films.[12, 20] A more detailed derivation of the algorithm and the underlying theoretical considerations are summarized in the Supplementary Information and illustrated by **Figure S1** and **Figure S2**. An exemplary image subjected to image processing is shown in **Figure 2**A. Therefore, in brief, all images are initially normalized by a local background estimate. Particle recognition is implemented by thresholding and supported by a watershed algorithm separating particles in very close proximity. In order to exclude matches with irregular or distorted geometries (*e.g.* inseparable clusters), a routine based on the determination of the Ferret aspect ratio was applied. As a result, only suitable nanoparticles for automated image analysis were reproducibly selected (Figure 2B).

Next, the particle area or rather the diameter d were determined by pixel counting. A measure for the particle volume was determined by a sum, according to Lambert-Beer's law, of logarithmized intensities $I_n(x',y')$ (background normalized pixel values) covering the particle area. Assuming spherical nanoparticles a comparison of both results leads to the electron attenuation coefficient α, describing the electron scattering capability of the polymer:

$$\sqrt[3]{\frac{6}{\pi}\sum_{x',y'}^{\text{area}} \ln I_n(x',y') \cdot p} = \sqrt[3]{\alpha} \cdot \mathrm{d},$$

where p is the area of one pixel. We determine the electron attenuation coefficient α by plotting the cubic root of the sum of the logarithmic intensities (eq. lhs) over particle diameter d (eq. rhs) (Figure 2C). To determine α, we plotted the particle diameter *versus* the

cubic root of the sum of the logarithmic intensities, resulting in a linear fit (Figure 2C). The accuracy of the linear fit improves with a moderate polydispersity of the nanoparticles.

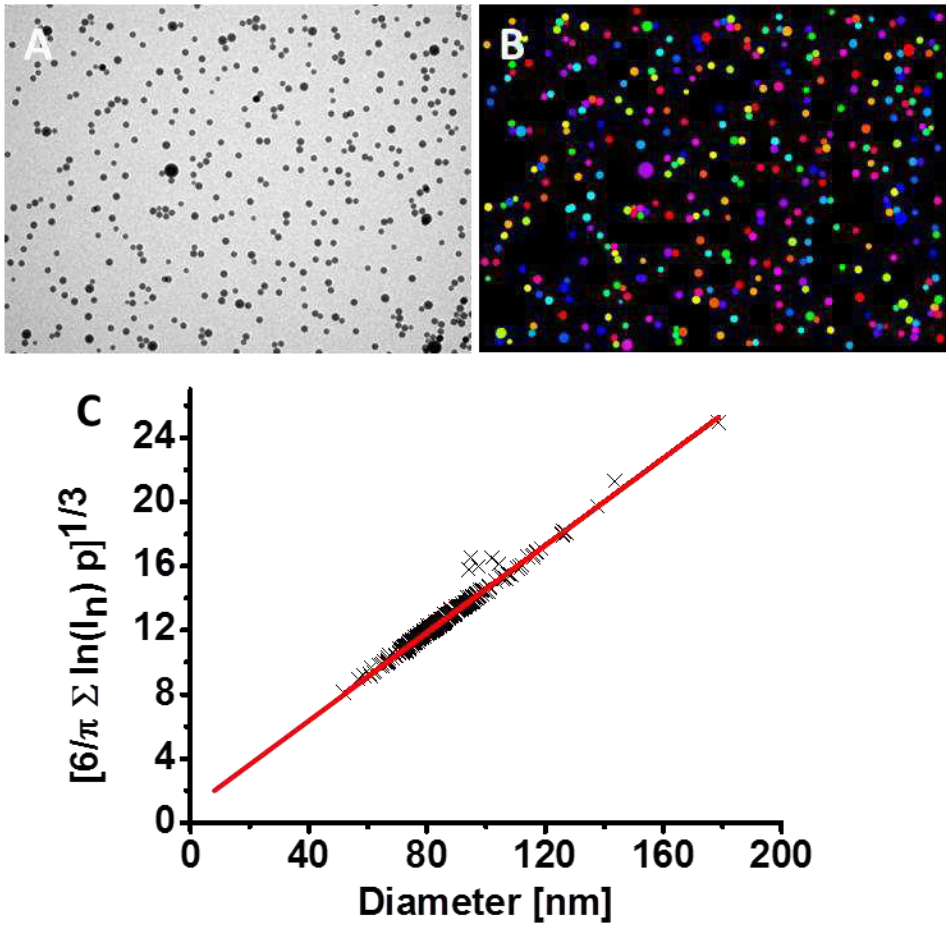

Figure 2: Automatic analysis of the particle contrast and determination of the electron attenuation coefficient α of the slope of the resulting analysis plots. A) Shows a raw image of particle sample. B) Colored spots depict the signals taken into consideration for further data elaboration. C) The electron attenuation, as a measure for the particle contrast, is determined according to Eq. 1. The slope of the linear fit represents the extinction related constant $\alpha^{1/3}$.

High α values correspond to a high electron opaqueness. This directly correlates with the inherent capability of the nanoparticles to attenuate the electrons. In case of stained samples, the electron attenuation coefficient α is a measure for the capability of the polymer nanoparticle to accumulate heavy metals inside the particle material and denotes, as a consequence, the staining efficiency.

Images of all polymer systems were analyzed by this method and the attenuation coefficients α were determined for bare polymer nanoparticles as well as for stained particle systems

(**Table 2**). To this aim, particles were incubated for 24 h with the respective staining solutions. OsO_4 was buffered in PBS (1% OsO_4 in PBS), uranyl acetate was applied as a 1% solution in de-ionized water and lead citrate staining solution was prepared according to the Reynold's procedure.[21] Special care has to be taken that the electron beam does not introduce severe degradation and alterations of the particle contrast. This was carefully checked and image acquisition was performed in the most sensitive manner (*e.g.* minimization of the sample exposure prior to image acquisition under the condition of identical imaging parameters). From each particle sample, a set of multiple images was acquired. At least five images of each sample were taken into consideration for image analysis. The analysis algorithm was applied to each image individually and the slope value α were determined. From all determined constants α an average as well as a standard deviation was calculated and weighted according to the number of particles that were analyzed in each image. Image analysis required the consideration of several parameters which had to be adjusted manually after critical evaluation of the raw images. The respective parameters are listed in **Table S1**.

Based on this procedure the electron attenuation of homopolymer nanoparticles was determined. The respective values are listed in **Table 2** and are compared in **Figure 3**.

Table 2: Electron attenuation coefficients α extracted by image processing.

NP sample	Non-stained NPs α [μm^{-1}]	OsO_4 staining α [μm^{-1}]	Uranyl acetate α [μm^{-1}]	Reynold's Pb α [μm^{-1}]	Europium staining α [μm^{-1}]
PLGA, **P1**	1.13 ± 0.33	1.33 ± 0.21	1.35 ± 0.10	n.d.*	2.19 ± 0.57
PMMA, **P2**	1.64 ± 0.31	1.49 ± 0.3	1.71 ± 0.27	1.61 ± 0.25	n.d.
PS, **P3**	2.14 ± 0.05	2.24 ± 0.17	2.04 ± 0.13	2.04 ± 0.24	n.d.

*Reynold's lead citrate solution possesses a pH value of 12.0. Under these conditions, the PLGA particles were not stable.

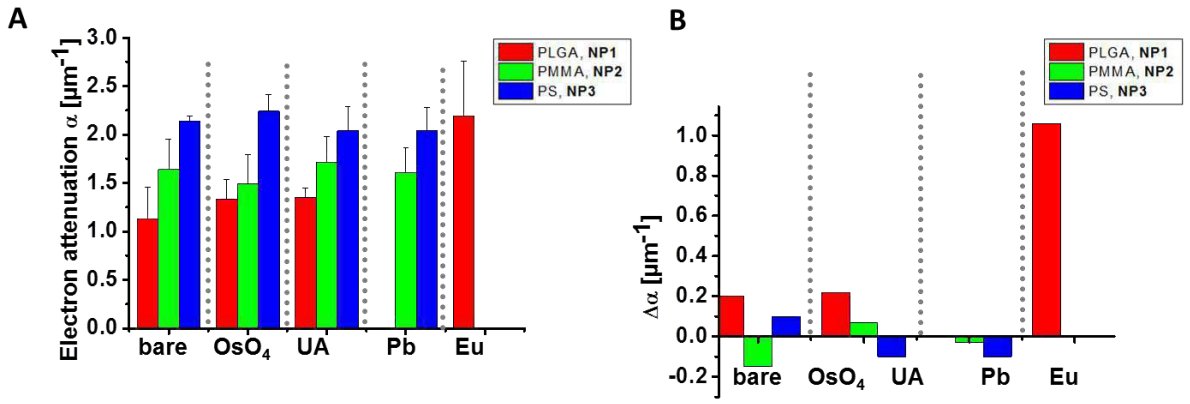

Figure 3: Analysis of the electron attenuation coefficient α of different homopolymer nanoparticles. A) Determined α values obtained after the respective sample treatment (bare particles, and particles after OsO_4 staining, U and Pb staining). B) Electron attenuation differences between untreated and heavy-metal stained particles to highlight changes in the electron attenuation coefficient introduced by the staining process.

The evaluation of the processed images of the untreated PLGA, PMMA and PS homopolymer nanoparticles demonstrates already significant differences in electron attenuation values α, which indicate that the electron attenuation is highest for PS followed by PMMA and PLGA nanoparticles, even though the statistical deviations are rather large. Here it can be seen that the electron attenuation coefficient is a sensitive measure that might be also influenced by other parameters, *e.g.* by the particles' mass density.

Staining with the conventional heavy metal stains did not result in a significant increase of the electron attenuation in this set of homopolymer nanoparticles. This is rationalized by a lack of functional groups capable of interacting actively with the staining agents, which is in agreement with literature reports.[22] Therefore, the validity of the image analysis algorithm was tested by exposure of the polyester structure of **NP1** with europium triflate, which is sensitive towards the PLGA nanoparticles. This treatment resulted in a significant increase of the electron attenuation and an efficient staining of the polymer nanoparticle by a factor of two was observed. Unfortunately, no values could be extracted for **NP1** treated with lead citrate. This is attributed to the fact that Reynold's lead citrate staining requires high pH

values (typically pH = 12), which results in hydrolytic cleavage of ester bonds. These ester bonds constitute the polymer backbone.

In order to demonstrate a further contrast enhancement, other polymers, such as poly[*N*-(2-aminoethyl) methacrylamide] (PAEMA), poly(2-dimethylamino-ethylmethacrylate) (PDMAEMA) or polybutadiene (PB) would represent more promising candidates. These polymers are potentially affine to staining agents due to an enhanced affinity of amino functionalities or carbon-carbon double bonds present in the polymer structure, respectively, resulting in a considerable increase of the contrast. However, these polymers do not form water-stable colloids. A possibility to circumvent this problem is to copolymerize them with PMMA or PS. These respective copolymers (**P4** to **P6)** were formulated into nanoparticles (**NP4** to **NP6**) and their physico-chemical properties were determined by DLS and Zeta-potential measurements as summarized in Table 1. The electron attenuation coefficients for the respective copolymer nanoparticles are listed in Table 3 and are compared in **Figure 4**.

Table 3: Electron attenuation values of copolymer nanoparticles **NP4** to **NP6**.

NP sample	Non-stained NPs α [μm^{-1}]	OsO_4 staining α [μm^{-1}]	Uranyl acetate α [μm^{-1}]	Reynold's Pb α [μm^{-1}]
P(MMA-*co*-AEMA), **P4**	1.71 $\pm$ 0.13	*	2.71 $\pm$ 0.4	1.43 $\pm$ 0.64
P(MMA-*co*-DMAEMA), **P5**	1.23 $\pm$ 0.06	2.41 $\pm$ 0.47	2.64 $\pm$ 0.16	1.45 $\pm$ 0.47
PS-*co*-PB, **P6**	0.26 $\pm$ 0.03	4.73 $\pm$ 0.74	0.29 $\pm$ 0.05	0.29 $\pm$ 0.05

*The electron attenuation characteristics of **P4** treated with OsO_4 could not be determined, since the staining process destabilized the particle stability as indicated by TEM imaging.

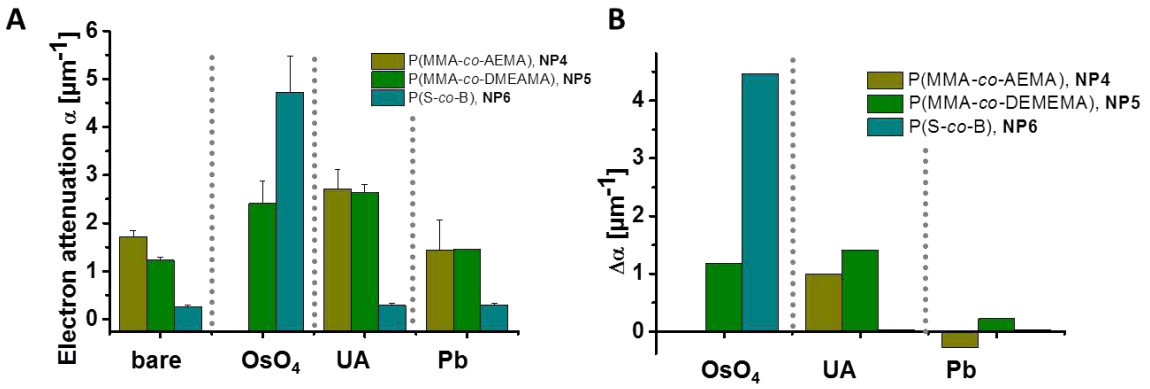

Figure 4: Electron attenuation characteristics of the nanoparticles consisting of copolymers. A) Attenuation coefficients found for the blank and stained nanoparticles after the respective treatment. B) Differences in the electron attenuation coefficient rationalized by plotting the increase of the contrast in relation to the bare polymer.

From the previous investigations of the homopolymer nanoparticles it becomes clear that neither PS nor PMMA can be actively stained with the applied protocol. Observed differences in the electron attenuation are, therefore, ascribed to a staining of the PAEMA, PDMAEMA and the PB only. It is clearly observed (Table 3, Figure 4) that P(MMA-*co*-AEMA) (**NP4**) shows a good stainability towards uranyl acetate, which results in an approximately 1.6-fold enhancement of the attenuation coefficient (whereby it has to be kept in mind that the amino content in the polymer is only 20 mol.-% compared to the methacrylate content, and particle staining is only attributed to the amino functionalities in the polymer). From **NP4** no results could be obtained from image analysis of OsO_4-stained particle samples, since no stable particles were found in TEM micrographs after OsO_4 treatment. We attribute this behavior to a severe oxidative degradation of the primary amino functionality-containing polymer, which causes adverse effects on the particle integrity.

On the contrary, P(MMA-*co*-DMAEMA) (**NP5**) significantly responds to OsO_4 staining, as seen by an approximately two-fold increase of α. Furthermore, this polymer showed an increase of the electron attenuation by a factor of approx. 2 after the treatment with uranyl acetate. Staining with lead citrate resulted in only low staining levels for all copolymer nanoparticles.

The obtained results indicate further, that the imaging contrast not only depends on the electron attenuation introduced by the elemental composition of the nanoparticles. This is reflected in the low attenuation coefficients obtained for the PS-*co*-PB sample system. Even though PS in its homopolymer form (**NP3**) showed an attenuation coefficient of $\alpha = 2.14 \pm 0.05\ \mu m^{-1}$ the copolymer formulation with PB (**NP6**) resulted only in an attenuation coefficient of $\alpha = 0.26 \pm 0.03\ \mu m^{-1}$. Staining with OsO_4 resulted, however, in this case in an 18-fold increase in the observed electron attenuation coefficient α. Exposure of the sample with uranyl acetate and lead citrate, on the contrary, did not result in particle staining, which is reflected in very similar attenuation values of these samples compared to the untreated particle sample. In general it is assumed that the reactive compound consisting of osmium in the highest known oxidation state +8 accumulates into the polymer structure by oxidation of chemical functionalities. OsO_4 is, in this respect, employed not only to introduce an enhanced electron density into the polymer sample due to the heavy metal incorporation into the nanoparticle structure, but it can also contribute to an improved fixation of the samples' fine structure owing to its potential to cross-link certain chemical functionalities. This results in a significant hardening of polymers,[23] similarly as observed in the fixation of biological samples.[13] This aspect is of particular interest since we concluded that the density of the polymer nanoparticles plays an important role when accessing the electron attenuation.

In order to evaluate this effect in more detail and to reveal the interaction mechanism OsO_4 with C=C double bonds, this effect was investigated by utilizing a model system mimicking the stainability of double bond containing polymer nanoparticles.

Insights into OsO_4 staining and fixation mechanisms by mass spectrometry and X-ray crystallography

This model system mimics the strong staining ability observed for nanoparticles containing PB in the previous study. A suitable small molecule providing isolated double bonds is (*Z*)-cyclooctene.[‡] (*Z*)-cyclooctene can be easily formulated into nanoparticle systems by utilizing a hydrophobic solvent as matrix material. As a suitable hydrophobic solvent, which triggers the formation of a stable emulsion of the (*Z*)-cyclooctene under the terms of the experiments, xylene (mixed isomers) was used. Xylene is a chemically inert solvent with a sufficiently high boiling point that provides appropriate stability against evaporation. Moreover, xylene exhibits phenyl moieties, which means that the model compound (*Z*)-cyclooctene is exposed to a similar chemical environment as found in the nanoparticle system **NP6** that contains styrene as a co-monomer unit in the polymer. The model nanoparticle solutions are formulated following the procedure outlined in **Figure 5**.

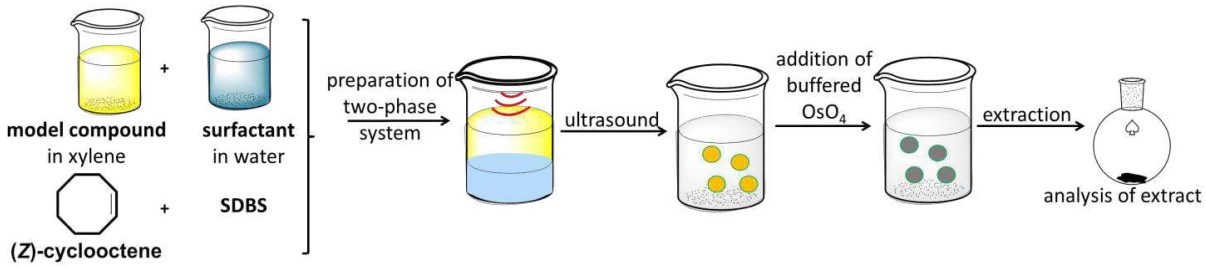

Figure 5: The model compound (*Z*)-cyclooctene was dissolved in xylene to form stable nano-emulsions stabilized by SDBS as surfactant upon ultrasonication. The nano-emulsions were exposed to buffered OsO_4 solution and, consequently, the reaction products were extracted and the resulting black oil was subjected to further analysis.

The nanoemulsions were prepared by dissolving the model compound in xylene and the solution was overlaid with an aqueous solution of the surface-active compound sodium

[‡] In general, polybutadiene as a homopolymer represents a polymer consisting of 1,4- and 1,2-linked monomer (1,3-butadiene) units. Consequently, in the resulting polymer chain, (*Z*)- and (*E*)-substituted (as a result of 1,4-linkage of butadiene units) as well as terminal C=C double bonds (as a result of 1,2-linkage of butadiene units) are present. A proton nuclear magnetic resonance spectrum (Figure S3) suggests, that these three substitution types of olefins are also found in the polymer **P6**.
Hence, we selected (*Z*)-cyclooctene as a model system, not only owing to its presence in **P6**, but also due to the fact that (*Z*)-olefines represent building blocks of, *e.g.* biological membranes.

dodecylbenzenesulfonate (SDBS), whereby ultrasonication of the mixture provided the stable nanoemulsions. The formed droplets can be subjected to OsO_4 staining by applying a 1% staining solution. After a reaction period of 1h, the emulsion was dialyzed thoroughly to remove the residual unreacted osmium tetroxide. Afterwards, the reaction mixture was extracted with toluene and the extract was evaporated to dryness. The matrix can be subsequently easily removed, which allowed for the analysis of the compound **Com-1** by ESI-ToF-MS and crystal structure analysis.

The ESI-ToF-MS spectrum of the OsO_4 treated (*Z*)-cyclooctene is depicted in **Figure 6**.

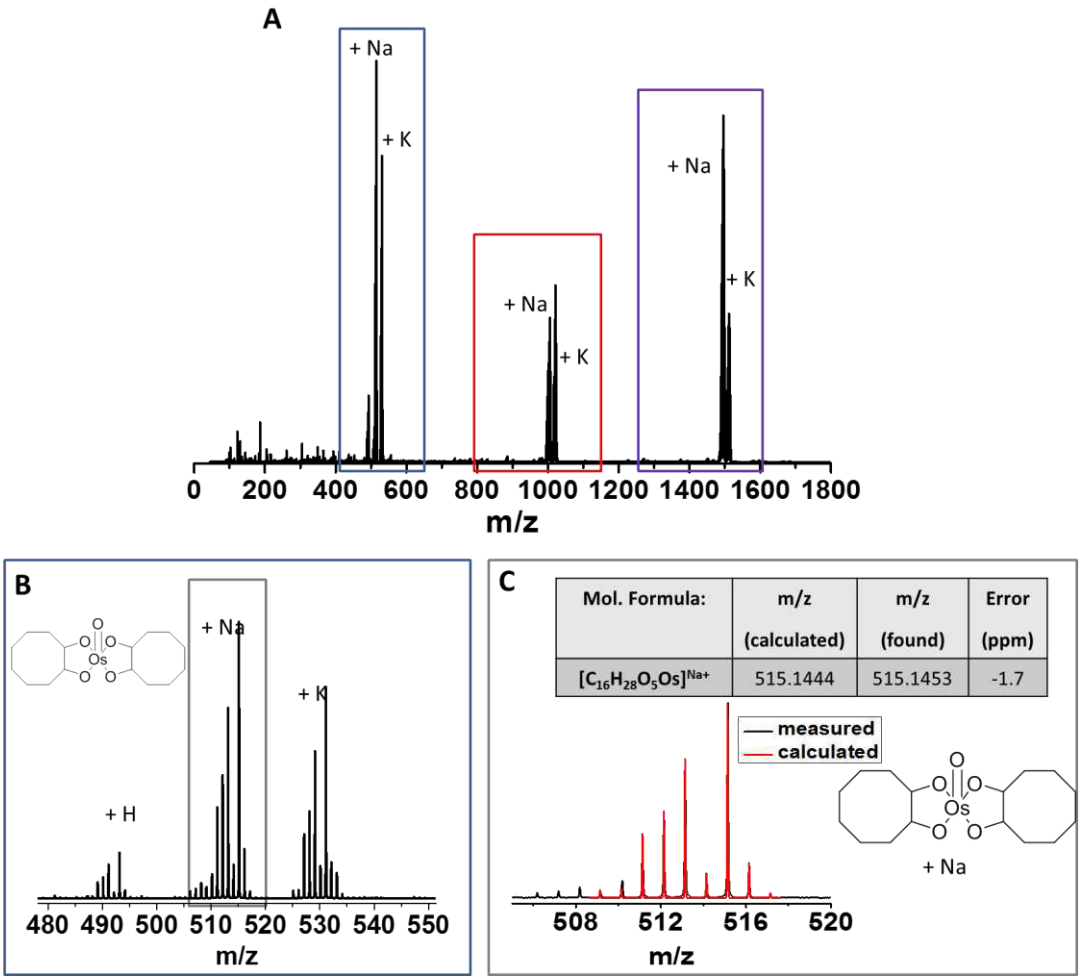

Figure 6: A: ESI-MS of the compound **Com-1** as a result of the treatment of (*Z*)-cyclooctene with OsO_4. Three signal distributions are found as indicated in the blue, red and violet box. The signals found in the blue box are depicted in more detail in (B). Thereby, the occurrence of the signals can be explained by adducts of H^+, Na^+ and K^+ of the species as suggested in the structure as shown in the inset. The isotopic pattern of the measured sample (black box) and the calculated spectrum are in good agreement. Furthermore, high-resolution MS (HRMS) hints towards the suggested structure. The set of signals in the red and violet box are explained more in detail in the SI (**Figure S6**).

The spectrum reveals three main signal distributions as indicated in the blue, red, and violet box (Figure 6A). The first signal distribution (Figure 6B) can be attributed to a chemical structure of **Com-1** with the sum formula $C_{16}H_{28}O_5Os$, which is explained by the formation of a coordinative Os^{VI} compound, whereby the central atom is coordinated by two diolic species in the sense of a cyclic osmium acid ester (structure see the inset in Figure 6B). The spectrum in this m/z-region reveals three peak distributions (Figure 6B), whereby the most intensive abundancy in each set of signals can be ascribed to the adduct of the suggested structure of **Com-1** associated to H^+, Na^+ and K^+,[§] respectively. The signal, as emphasized in the black box in Fig. 6B, is assumed to represent the sodium adduct of the proposed structure. This assumption becomes more evident on the basis of Figure 6C, which reveals that (i) the measured signal distribution is in accordance with the calculated isotopic pattern for the sodium adduct of the suggested structure as well as (ii) the high-resolution mass spectrometry (HRMS) result perfectly agrees with the calculated value (Figure 6C). Furthermore, tandem-ESI-ToF-MS utilizing m/z = 515.15 as parent ion showed no further fragmentation of this signal, which indicates the formation of a stable compound, rather than an adduct that was formed (**Figure S4**).

The set of signals labeled in the red box (Figure 6A) can be explained by the occurrence of dimers **Com-1**, which form adducts with Na^+ and K^+. The signal at m/z = 1005.30 as parental ion was subjected to further MS/MS measurements. The resulting mass spectrum revealed the occurrence of the monomer unit in form of H^+, Na^+ and K^+ adducts (**Figure S5**) as well, which underlines the assumption that this signal basically represents a dimer of species. Likewise, the set of signals labeled in the violet box (Figure 6A) suggests the presence of

[§] Sodium and potassium ions are present ubiquitously in the solvents used for electron-spray ionization MS and form, hence, adducts with the examined species in ESI-ToF-MS.

trimers; MS/MS measurements revealed the formation of dimers and monomers of this species upon further ionization (**Figure S6**).

An additional evidence for the formation of these compounds was found by crystal structure analysis. The obtained crystal structure of the Os^{VI} complex (**Figure 7**) revealed the formation of the Os^{VI} complex with the structure as suggested, which crystallizes in a C2/c space group. This analysis, along with the results from (tandem-)ESI-ToF-MS, provided a reliable proof that osmium coordinates two (*Z*)-olefines in such a way that it cross-links both moieties. It is likely that a similar complex is also formed during the OsO_4 fixation process of within the polymer nanoparticles. Here the cross-linking ability is not limited to an isolated C-C double bond, but a much higher possibility of cross-linking between the polymer chains has to be assumed, which ultimately improves the stability of the formed nanoparticles and results in their hardening.

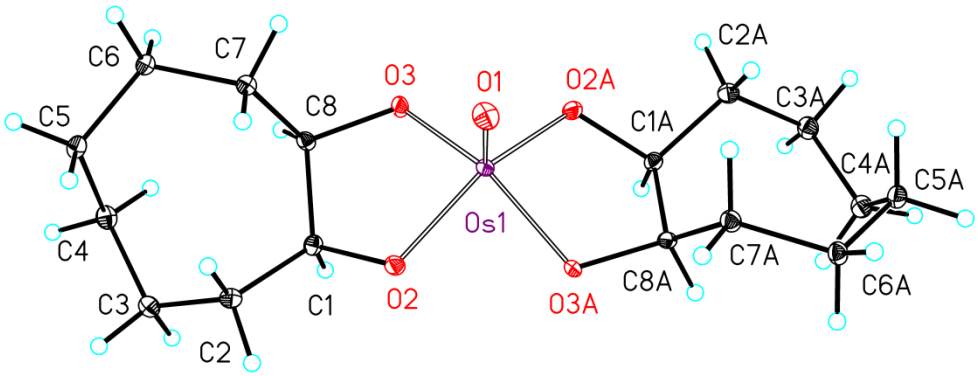

Figure 7: Molecular structure and atom labeling scheme of Bis(cycloocytl-1,2-dioxy)(oxo)osmium (**Com-1**). The ellipsoids represent a probability of 30%. Symmetry-related atoms (-x+1,y,-z+3/2) are marked with the letter "A". Selected bond lengths (Å): Os(1)-O(1) 1.682(3), Os(1)-O(2) 1.895(2), Os(1)-O(3) 1.901(3), O(2)-C(1) 1.461(4), O(3)-C(8) 1.461(4), C(1)-C(8) 1.530(4); angles (deg.): O(1)-Os(1)-O(2) 110.70(7), O(2)-Os(1)-O(3) 82.33(10), O(2)-Os(1)-O(2A) 138.59 (14), C(1)-O(2)-Os(1) 117.56(19), O(2)-C(1)-C(8) 118.4(3).

Conclusion

We developed a robust routine to determine the electron attenuation coefficient α of nanoparticle systems by automated processing of TEM images. The electron attenuation coefficient as a measure for the scattering ability represents a tool to judge the ability of polymers to interact with various staining agents. This tool enables in subsequent studies to also include other aspects and parameters, which can influence the electron scattering abilities of different polymers. In this study, the crucial role of the stabilization and mass density of nanoparticles which was explicitly highlighted for OsO_4 staining, even though detailed studies on this aspect have not been conducted in the framework of this paper. As such, further investigations regarding this particular issue should be conducted by complementary investigations, which relate the density of nanoparticles with the observed contrast.

Further investigations can rely on the introduced image-based analysis routine, which will be further refined in the course of these investigations. In particular the introduction of the particle density might contribute to a better understanding of the obtained electron attenuation factors and will certainly provide a deeper insight into the complex issue of how electron contrast is generated in nanoparticle systems. A fundamental understanding of these processes will inevitably increase the applicability of TEM investigations in this field of research.

Experimental Section

Instrumentation:

Dynamic light scattering (DLS) measurements were conducted using a Zetasizer Nano ZS (Malvern Instruments, Herrenberg, Germany). Therefore, multiple measurements were recorded at 25 °C (wavelength of 633 nm) and the counts were detected under an angle of 173°. Assuming a spherical shape of the particles, the width of the distribution as the polydispersity index of the particles (PDI) was obtained by the cumulants method. In order to determine the zeta potential by electrophoretic light scattering, the Zetasizer Nano ZS (Malvern Instruments, Herrenberg, Germany) using laser Doppler velocimetry was applied. For this purpose, 10 runs were carried out using the slow-field and fast-field reversal mode at 150 V at 25 °C.

Transmission electron microscopy was carried out using a Technai G^2 20 system (FEI), with an acceleration voltage of 200 kV. Imaging conditions were standardized for the acquisition of the images for comparison of the TEM image contrast. Further details are listed in the main text.

ESI-ToF-MS measurements were conducted using a micrOTOF (Bruker Daltonics GmbH) mass spectrometer equipped with an automatic syringe pump for sample injection (KD Scientific) in the positive ion mode. In order to generate ions, the standard electrospray ion (ESI) source was used, employing mixtures of dichloromethane and acetonitrile as solvent. An internal calibration standard (Tunemix solution), which was supplied from Agilent, was used for calibration of the instrument to the m/z range of 50 to 3,000.

Nanoparticle preparation:

The nanoparticles were prepared *via* nanoprecipitation, nanoemulsion or emulsion polymerization route.

NP1

Poly($_{D,L}$-lactide-*co*-glycolide, Resomer® RG502 H, 50:50, 7 to 17 kDa, acid terminated), polyvinyl alcohol (Mowiol® 8-88, partially hydrolysed) and dimethyl sulfoxide were purchased from Sigma-Aldrich.

The nanoparticles were prepared by the nanoprecipitation method. PLGA polymer (40 mg) was dissolved in DMSO (2 mL). Using a syringe pump, the organic solution was injected in 20 mL aqueous PVA solution (0.03 %) at a flow rate of 49 mL h^{-1} under continuous stirring at 800 rpm. To remove the DMSO and excess surfactant, the nanoparticle suspensions were placed in dialysis bags of 50,000 MWCO and dialyzed against water for six days, replacing the dialysate with fresh water every day. Nanoprecipitation and dialysis were performed at room temperature and water used in all processes is milliQ grade. After purification nanoparticles were lyophilized and stored in a refrigerator at 4 °C.

NP2

Polymethylmethacrylate (20 mg, copolymerized with a small amount of 10 mol.-% acrylic acid) was dissolved in 2 mL acetone. To a 50 mL Falcon tube equipped with a magnetic stirrbar, 20 mL water was added. Under vigorous stirring (750 rpm, gas bubbles were removed), the polymer solution was dropped carefully to the water. Therefore, a syringe pump was used and a flow of 49 mL h^{-1} was adjusted. Eventually, the solvent was allowed to evaporate from the suspension overnight.

NP3

Commercially available polystyrene beads were used. Therefore, latex beads, amine-modified polystyrene, fluorescent orange, nominal diameter 0.1 µm in aqueous suspension were purchased from Sigma Aldrich.

NP4 and NP5

The synthesis and characterization of the polymer samples **P4** and **P5** have been described elsewhere.[24] The characterization data of the polymers used in this study are listed below. For experimental details of the respective data see Ref. [24]

P4

SEC (eluent: $CHCl_3$, PMMA calibration, RI detection): M_n = 4,500 g mol^{-1}. Đ = 1.19. DP (determined by ^{1}H-NMR spectroscopy): MMA – 30. AEMA·HCl – 8.2.

P5

SEC (eluent: $CHCl_3$, PMMA calibration, RI detection): M_n = 7,600 g mol^{-1}. Đ = 1.17. DP (determined by ^{1}H-NMR spectroscopy): MMA – 40. DMAEMA – 10.

The nanoparticle samples **NP4** and **NP5** were prepared *via* a nanoprecipitation route. Therefore, the respective polymer samples were dissolved in acetone with a concentration of 10 mg mL^{-1} and added to water as previously described.[24]

NP6

Poly(styrene-*co*-butadiene) was purchased from Sigma Aldrich. Nominal amount of styrene as stated by the manufacturer: 45 wt.-%. Particles were prepared using a single-emulsion method. For this purpose, the polymer was dissolved in dichloromethane to yield a solution with a concentration of 2.5 mg mL^{-1}. 4 mL of an aqueous solution of poly(vinyl alcohol) (Mowiol 4-88, Sigma Aldrich) was added to 2 mL of the polymer solution. The two-phase

system was exposed to ultrasound using a sonicator tip until the system was visibly emulsified. During ultrasonication, the emulsion was cooled to 0 °C. The emulsion was poured on 10 mL deionized water and stirred overnight to allow the solvent to evaporate. The particle suspension was used for subsequent experiments without any further purification. The particle suspension was stored in a refrigerator at 4 °C.

Image acquisition

For image acquisition, nanoparticle samples were blotted onto a carbon support copper grid (400 mesh, Quantifoil, Jena), whereby the particles adhered on the grid surface. In case of staining experiments, the particle samples were incubated with the respective staining solution for 24 h (surfactants were not removed from the particle suspension prior to incubation) and the particles were placed on the grid surface by blotting the solution onto the copper grid. Subsequently, residual heavy metal stains were removed by washing the grid surface three times with deionized water utilizing a drop-to-drop method.

For OsO_4 staining, 100 µL phosphate buffered saline (PBS) and 100 µL OsO_4 solution (2 wt.-% in deionized water) were added to 200 µL of the respective particle suspension.

For uranyl acetate staining, 200 µL uranyl acetate solution (2 wt.-% in deionized water) we added to 200 µL of the respective particle suspension.

Reynold's lead citrate solution was prepared starting from freshly boiled deionized water. 400 mg $Pb(NO_3)_2$ and 528 mg trisodium citrate-dihydrate was suspended in approx. 9 mL water. To this solution, 2.4 mL 1 N NaOH was added, so that the insoluble compounds dissolved completely. The pH value of the resulting solution was adjusted to pH = 12.0 ± 0.1 with NaOH solution. Subsequently, the solution was filled to 15 mL and stored in the refrigerator at 4 °C. For particle staining 50 µL of the particle suspension was added to 150 µL lead citrate solution.

All images were acquired using the transmission electron microscope in transmission mode. In order to warrant comparable experimental conditions, particle samples were imaged using equal magnification values (19,000 ×), equal underfoci of $-2.5\,\mu m$ as well as the same contrast aperture for all measurements. Furthermore, the beam was adjusted in such a way that the background intensities for all measurements exhibited similar grey values (approx. 6,000 Cts., spot size 1). Particle samples were imaged using the camera CCD/TV camera WA-MegaView utilizing the same Bias/Gain correction.

Image processing

Images subjected to image processing were used as TIFF images (16 Bit color depth). Image processing routines were programmed using MATLAB R2014a with the toolbox DIPimage version 2.8.1. Due to a low particle contrast of particle sample **NP6**, an initial rolling ball algorithm was performed for background normalization using ImageJ prior to employing the algorithm in DIPimage. For further details see main text.

Mass spectrometry investigations

The nano-emulsion to study the reactivity of the model compound with OsO_4 was prepared starting from xylene (mixture of isomers). Therefore, (*Z*)-cyclooctene (20 mg) was dissolved in 1 mL xylene. 1 mL of an aqueous solution of sodium dodecyl benzenesulfonate (SDBS, 3 mg mL^{-1}) was added to the xylene phase. The two-phase system was cooled to 0 °C and subjected to ultrasonication using a sonicator tip until the system was visibly emulsified. Afterwards, the stable emulsion was transferred into a dialysis tubing (Roth ZelluTrans, cut-off 3,500 Da, regenerated cellulose) and dialysed for one day to remove an excess of surfactant. Next, the stable emulsion was transferred into a falcon tube and to this amount of

emulsion, the same volume of OsO_4 solution (2% in PBS) was added, so that the final OsO_4 concentration in the reaction mixture was 1%. The reaction mixture was kept for 1 h, whereby a color change from colorless to grey could be observed. Thereafter, the emulsion was dialysed another four days to remove unreacted OsO_4 (ZellutransRoth, regenerated cellulose, cut-off 3.5 kDa). After complete dialysis, the reaction mixture was subjected to extraction with toluene, whereby a small amount of $BaCl_2$ was added to the aqueous phase. The toluene phase was dried over Na_2SO_4 and evaporated to dryness to give a black solid. This black solid was, subsequently, investigated by ESI-ToF-MS.

In order to obtain a crystal of the osmium complex, the black solid was dissolved in a small amount dichloromethane and stored in a glass vial equipped with a teflon cover. In order to ensure slow evaporation of the solvent, the cap was perforated with a thin needle. After complete evaporation of the solvent, a pale-grey crystalline substance could be collected.

Crystal Structure Determination

The intensity data were collected on a Nonius KappaCCD diffractometer, using graphite-monochromated Mo-K_α radiation. Data were corrected for Lorentz and polarization effects; absorption was taken into account on a semi-empirical basis using multiple-scans.[25]

The structure was solved by direct methods (SHELXS)[26] and refined by full-matrix least squares techniques against Fo^2 (SHELXL-97).[26, 27] All hydrogen atoms were included at calculated positions with fixed thermal parameters. All non-hydrogen atoms were refined anisotropically.[28] XP (SIEMENS Analytical X-ray Instruments, Inc.) was used for structure representations.

Crystal Data for **Com-1**: $C_{16}H_{28}O_5Os$, Mr = 490.58 $gmol^{-1}$, pale_grey prism, size 0.112 × 0.062 × 0.024 mm^3, monoclinic, space group C 2/c, a = 24.6179(8), b = 5.3887(2), c = 12.6194(4) Å, β = 100.358(2)°, V = 1646.79(10) $Å^3$, T= -140 °C, Z = 4, $\rho_{calcd.}$ = 1.979 gcm^{-3}, μ (Mo-K_α) =

77.64 cm^{-1}, multi-scan, transmin: 0.5241, transmax: 0.7456, F(000) = 960, 8923 reflections in h(-28/31), k(-6/6), l(-16/16), measured in the range $3.28° \leq \Theta \leq 27.45°$, completeness Θ_{max} = 99.7 %, 1866 independent reflections, R_{int} = 0.0495, 1834 reflections with $F_o > 4\sigma(F_o)$, 101 parameters, 0 restraints, $R1_{obs}$ = 0.0210, wR^2_{obs} = 0.0456, $R1_{all}$ = 0.0216, wR^2_{all} = 0.0459, GOOF = 1.064, largest difference peak and hole: 0.958 / -1.007 e $Å^{-3}$.

References

[1] A. Kumari, S. K. Yadav, S. C. Yadav, *Colloids Surf. B Biointerfaces* **2010**, 75, 1.

[2] a) S. Ganta, H. Devalapally, A. Shahiwala, M. Amiji, *J. Controlled Release* **2008**, 126, 187; b) J. Zhuang, M. R. Gordon, J. Ventura, L. Li, S. Thayumanavan, *Chem. Soc. Rev.* **2013**, 42, 7421; c) F. Wendler, K. R. A. Schneider, B. Dietzek, F. H. Schacher, *Poly. Chem.* **2017**, 8, 2959; d) T. Yildirim, I. Yildirim, R. Yanez-Macias, S. Stumpf, C. Fritzsche, S. Hoeppener, C. Guerrero-Sanchez, S. Schubert, U. S. Schubert, *Polym. Chem.* **2017**, 8, 1328.

[3] a) C. Weber, R. Hoogenboom, U. S. Schubert, *Prog. Polym. Sci.* **2012**, 37, 686; b) Y.-J. Kim, Y. T. Matsunaga, *J. Mater. Chem. B* **2017**, 5, 4307.

[4] a) V. K. Thakur, M. R. Kessler, *Polymer* **2015**, 69, 369; b) M. S. Selim, M. A. Shenashen, S. A. El-Safty, S. A. Higazy, M. M. Selim, H. Isago, A. Elmarakbi, *Prog. Mater. Sci.* **2017**, 87, 1.

[5] a) B. Sandmann, B. Happ, I. Perevyazko, T. Rudolph, F. H. Schacher, S. Hoeppener, U. Mansfeld, M. D. Hager, U. K. Fischer, P. Burtscher, N. Moszner, U. S. Schubert, *Polym. Chem.* **2015**, 6, 5273; b) L. Bécu, H. Sautereau, A. Maazouz, J. F. Gérard, M. Pabon, C. Pichot, *Polymer. Adv. Tech.* **1995**, 6, 316.

[6] a) B. J. Blaiszik, S. L. B. Kramer, S. C. Olugebefola, J. S. Moore, N. R. Sottos, S. R. White, *Annu. Rev. Mater. Res.* **2010**, 40, 179; b) M. Samadzadeh, S. H. Boura, M. Peikari, S. M. Kasiriha, A. Ashrafi, *Prog. Org. Coat.* **2010**, 68, 159.

[7] a) D. R. Paul, L. M. Robeson, *Polymer* **2008**, 49, 3187; b) T. H. Hsieh, A. J. Kinloch, K. Masania, J. Sohn Lee, A. C. Taylor, S. Sprenger, *J. Mater. Sci.* **2010**, 45, 1193.

[8] a) J. Nicolas, S. Mura, D. Brambilla, N. Mackiewicz, P. Couvreur, *Chem. Soc. Rev.* **2013**, 42, 1147; b) J. V. Natarajan, C. Nugraha, X. W. Ng, S. Venkatraman, *J. Controlled Release* **2014**, 193, 122; c) K. Cho, X. Wang, S. Nie, Z. Chen, D. M. Shin, *Clin. Cancer Res.* **2008**, 14, 1310; d) F. Masood, *Mater. Sci. Eng. C.* **2016**, 60, 569.

[9] J. Zhao, M. H. Stenzel, *Polym. Chem.* **2018**, 9, 259.

[10] M. Reifarth, S. Hoeppener, U. S. Schubert, *Adv. Mater.* **2018**, 30, 1703704.

[11] a) R. Tantra, A. Knight, *Nanotoxicology* **2011**, 5, 381; b) Y. Zhang, R.-j. Liang, J.-j. Xu, L.-f. Shen, J.-q. Gao, X.-p. Wang, N.-n. Wang, D. Shou, Y. Hu, *Int. J. Nanomedicine* **2017**, 12, 1201; c) C. Leopold, T. Augustin, T. Schwebler, J. Lehmann, W. V. Liebig, B. Fiedler, *J. Colloid Interface Sci.* **2017**, 506, 620; d) L. Du, H. Z. Xu, T. Li, Y. Zhang, F. Y. Zou, *RSC Adv.* **2017**, 7, 31310.

[12] L. Reimer, *Transmission electron microscopy: Physics of image formation and microanalysis*, Springer, **2013**.

[13] J. J. Bozzola, L. D. Russell, *Electron microscopy: Principles and techniques for biologists*, Jones & Bartlett Learning, **1999**.

[14] a) M. Amiry-Moghaddam, O. P. Ottersen, *Nat. Neurosci.* **2013**, 16, 798; b) J. Roth, *Histochem. Cell Biol.* **1996**, 106, 1.

[15] D. Belazi, S. Solé-Domènech, B. Johansson, M. Schalling, P. Sjövall, *Histochem. Cell Biol.* **2009**, 132, 105.

[16] H. K. Makadia, S. J. Siegel, *Polymers* **2011**, 3, 1377.

[17] a) M. Kaseem, K. Hamad, Y. G. Ko, *Eur. Polym. J.* **2016**, 79, 36; b) A. Afzal, A. Kausar, M. Siddiq, *Polym. Plast. Technol. Eng.* **2016**, 55, 1988; c) N. Roy, R. Sengupta, A. K. Bhowmick, *Prog. Polym. Sci.* **2012**, 37, 781.

[18] a) Y. Murakami, T. Endo, S. Yamamura, N. Nagatani, Y. Takamura, E. Tamiya, *Anal. Biochem.* **2004**, 334, 111; b) R. Gorkin, J. Park, J. Siegrist, M. Amasia, B. S. Lee, J.-M.

Park, J. Kim, H. Kim, M. Madou, Y.-K. Cho, *Lab Chip* **2010**, 10, 1758.
[19] a) *http://www.diplib.org/dipimage, last accessed July 8th, 2018*; b) *http://www.diplib.org/diplib, last accessed July 8th 2018.*
[20] a) R. E. Burge, N. R. Silvester, *J. Biophys. Biochem. Cytol.* **1960**, 8, 1; b) F. Wang, H.-B. Zhang, M. Cao, R. Nishi, A. Takaoka, *Micron* **2010**, 41, 769; c) I. Pozsgai, *Ultramicroscopy* **1997**, 68, 69.
[21] E. S. Reynolds, *J. Cell Biol.* **1963**, 17, 208.
[22] G. H. Michler, *Electron microscopy of polymers*, Springer Heidelberg **2008**.
[23] L. Sawyer, D. Grubb, G. F. Meyers, *Polymer microscopy*, Springer Science & Business Media, **2008**.
[24] T. Yildirim, A. C. Rinkenauer, C. Weber, A. Traeger, S. Schubert, U. S. Schubert, *J. Polym. Sci., Part A: Polym. Chem.* **2015**, 53, 2711.
[25] a) COLLECT, Data Collection Software; Nonius B.V., Netherlands, **1998**; b) Z. Otwinowski & W. Minor, "Processing of X-Ray Diffraction Data Collected in Oscillation Mode", in Methods in Enzymology, Vol. 276, Macromolecular Crystallography, Part A, edited by C.W. Carter & R.M. Sweet, pp. 307-326, Academic Press, San Diego, USA, **1997;** c) SADABS 2016/2: Krause, L., Herbst-Irmer, R., Sheldrick G.M. & Stalke D., *J. Appl. Cryst.* **2015**, *48*, 3.
[26] Sheldrick, G. M. *Acta Cryst.* **2008**, *A64*, 112.
[27] Sheldrick, G. M. *Acta Cryst.* **2015**, *C71*, 3.

Supporting Information

Supporting Information is available from the Wiley Online Library or from the author. Crystallographic data deposited at the Cambridge Crystallographic Data Centre under CCDC-1854637 for **Com-1** contain the supplementary crystallographic data excluding structure factors; this data can be obtained free of charge via www.ccdc.cam.ac.uk/conts/retrieving.html (or from the Cambridge Crystallographic Data Centre, 12, Union Road, Cambridge CB2 1EZ, UK; fax: (+44) 1223-336-033; or deposit@ccdc.cam.ac.uk).

Acknowledgements

This project is part of the DFG Collaborative Research Center 1278 (PolyTarget). Experiments have been conducted in the sub-project C04. Cryo-TEM facilities were funded by the Deutsche Forschungsgesellschaft (DFG) and the European Fond for Regional Development (EFRE). We thank Sabine Armoneit for the preparation of the PMMA particles. Furthermore, we thank Dr. Turgay Yildirim for the preparation of P(MMA-*co*-AEMA) and P(MMA-*co*-DMAEMA).

Received: ((will be filled in by the editorial staff))
Revised: ((will be filled in by the editorial staff))
Published online: ((will be filled in by the editorial staff))

The table of contents entry

Polymer nanoparticles can be visualized by transmission electron microscopy even though their contrast is in most cases only low. We introduce an automated image analysis algorithm which can provide information on the inherent electron attenuation of different polymer nanoparticles before and after staining and present a model system mimicking the staining and fixation of double bond containing polymers in a nanoparticle formulation.

Nanoparticle contrast

M. Reifarth, W. Müller, B. Shkodra-Pula, H. Görls, U. S. Schubert, R. Heintzmann,* S. Hoeppener*

Electron density of polymeric nanoparticles determined by image processing of transmission electron micrographs: Insights into heavy metal staining processes

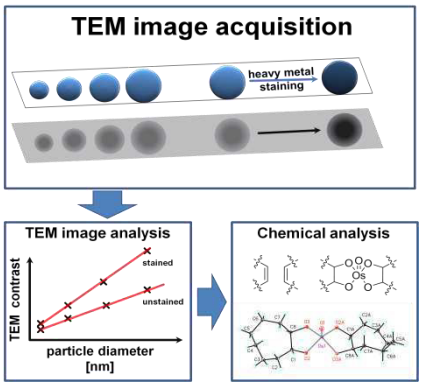

Supporting Information

Electron density of polymeric nanoparticles determined by image processing of transmission electron micrographs: Insights into heavy metal staining processes

Martin Reifarth, Walter Müller, Blerina Shkodra-Pula, Helmar Görls, Ulrich S. Schubert, Rainer Heintzmann, and Stephanie Hoeppener**

Theoretical considerations for the development of the image analysis algorithm

TEM imaging of nanoparticles provides a high resolution view on the particles` features. If a sufficient number of particles is imaged, computational processing routines facilitate the classification of nanoscale objects regarding their size or shape properties with statistical significance. For this purpose, a set pixel intensity is used as a threshold to classify signals emerging from the object and to differentiate them from the background signal. The resulting binary image is subjected to further analyses to obtain a statistical evaluation of size and/or shape of the features.

In transmission electron microscopy, a parallel electron beam propagates through the investigated object. Propagating electrons are scattered due to their interaction with atoms present in the material, where they get deviated and, thus, reach the detection aperture instead of the detector that is located in the beam path of the electron microscope. As a consequence, strongly scattering objects are represented with low intensity values in the TEM image, while the maximum intensity values indicate the background owing to unimpeded propagation of the electrons through the sample. The electron beam is projected only from one direction onto the sample, which is significantly larger than the electron avelength, causing the acquired image to be a 2D projection of the nanomaterial as indicated by the scheme in **Figure S1**. The following assumptions are only valid for particles with isotropic electron scattering properties,

such as polymeric systems, since crystalline materials are known to show anisotropic behavior in TEM. The projection of three-dimensional nanoobjects relates, thus, the object thickness. In case of a well-known geometry, a detailed examination of the pixel intensity profile along the lateral dimensions of the object in the EM image can result in a deeper comprehension of the attenuation characteristics of the electron beam propagating through the nanomaterial.

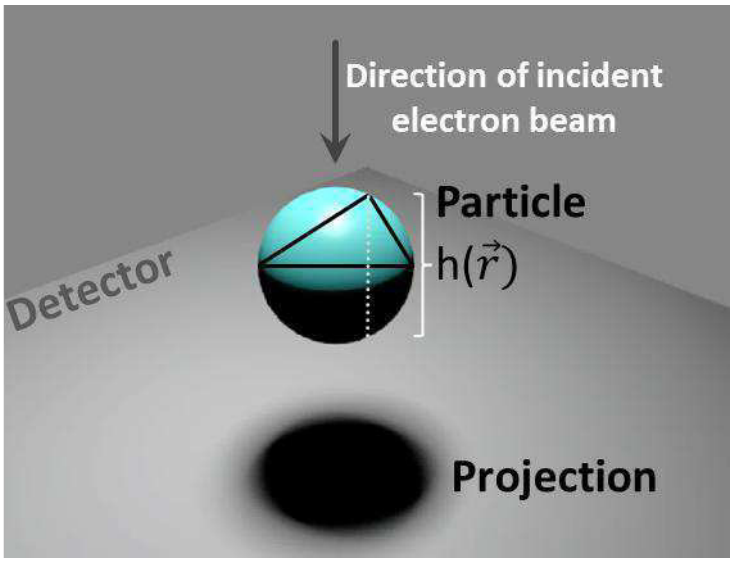

Figure S1: Schematic representation of a spherical nanoparticle imaged by transmission electron microscopy. The image of the particle constitutes its projection on the detector. The white dashed line represents the height $\boldsymbol{h(\vec{r})}$, *i.e.* the transmission path of the incident electron beam through the particle thickness in dependence of the spatial vector $\boldsymbol{\vec{r}}$.

Considering the polymeric particles as an ideal sphere, the height h of the particle, *i.e.* the propagation length of the electron beam through the spherical colloid in dependence of the image coordinates $\vec{r}$, can be described according to equation (1),

$$(1)\ h(\vec{r}) = \begin{cases} 2\sqrt{R^2 - (\vec{r} - \overrightarrow{r_C})^2}, & R^2 - (\vec{r} - \overrightarrow{r_C})^2 \geq 0 \\ 0, & else \end{cases}.$$

where $\overrightarrow{r_C}$ represents the coordinates of the center of the particle with the particle radius R. The decrease of the electron beam intensity has been reported to follow an exponential decay,

which can be employed for instance to determine a sample thickness of ideal films.[1] Equation 2 describes the intensity distribution I as a function of $\vec{r}$ with the background signal intensity I_0 assuming exponential attenuation. Hence, the attenuation profile is dependent on the material-specific attenuation coefficient α and may be considered as a Lambert-Beer-like relation.

$$(2)\ I(\vec{r}) = \begin{cases} I_0 e^{-2\alpha\sqrt{R^2-(\vec{r}-\overrightarrow{r_C})^2}}, R^2-(\vec{r}-\overrightarrow{r_C})^2 \geq 0 \\ I_0, else \end{cases}.$$

In order to support these assumptions, we imaged spherical polystyrene beads with an approximate size of 110 nm by TEM. **Figure S2A** depicts a low-magnification linear raw-image of a number of beads. We selected a representative particle as indicated in the red box and in Figure S2B and in Figure S2C, the intensity values of the particle are plotted in dependence of the pixel positions. It should be noted that the raw data shown here represents the linear detector signal that has not been subjected to contrast enhancement routines. For comparison, the theoretical intensity profile which is expectable according to equation (2) is depicted in Figure S2E (Figure S2D shows the simulated image of an ideally spherically shaped particle). Figure S2F, moreover, displays a cross-section through the intensity plot of the calculated intensity profile (as indicated by red solid line) along with the extracted data of the particle (dotted data). It has to be mentioned that a local background I_0 was calculated which was applied to normalize the pixel intensity of the measured image prior to data extraction.

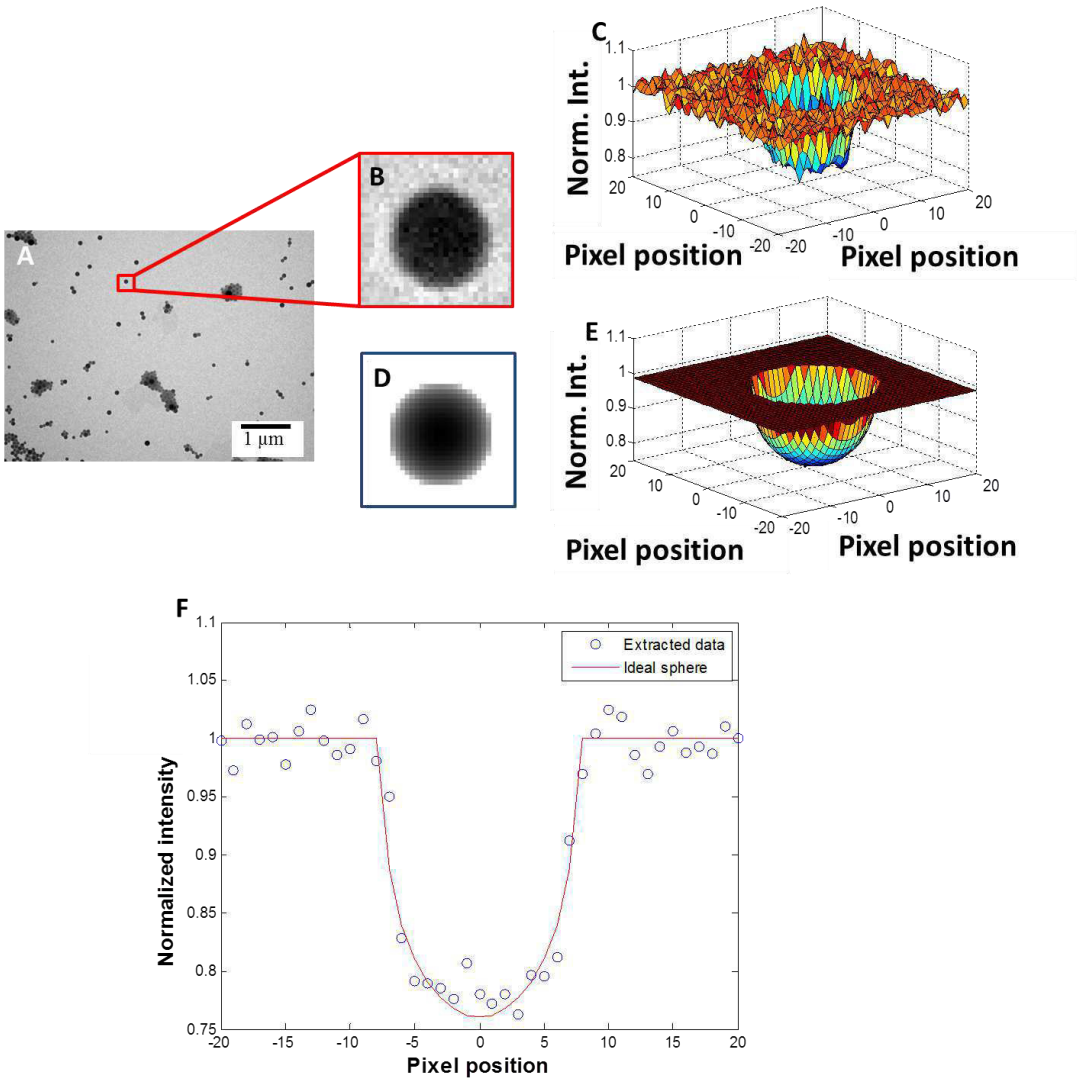

Figure S1: Proving the applicability of Lamber Beers law to the applied contrast method. A) Low-magnification of a raw-image of polystyrene beads. B) Magnification of A). C) Plot of normalized intensity values. D) Simulated image of a particle with ideally spherical shape according to equation (2). E) Plot of predicted normalized intensity values of an ideally spherical particle. F) Intensity profile of the particle (extracted data in blue) compared to intensity profile of an ideal sphere (red solid line).

The developed image analysis algorithm aims to determine the attenuation characteristics of a number of particles imaged simultaneously. Thereby, the attenuation factor α could directly

be deduced from the intensity plot according to equation (2) which would need to be carried out for a certain number of particles individually. However, the analysis of each bead intensity profile individually as shown in Figure S2F and the intricacy to fit the function according to equation (2) *via* the unknown particle parameters α and R would (also with respect to the unknown bead positions) constitute a demanding task particularly with respect to the fact that automated image analysis might in this case be error-prone. In order to overcome this issue, an alternative route was followed to extract the data from TEM images. We made use of the fact that the logarithmic pixel intensity value should be proportional to height of the material at the respective position of the pixel (equation 3, 4).

(3) $\frac{I(\vec{r})}{I_0(\vec{r})} = e^{-\alpha \cdot h(\vec{r})}$,

(4) $\ln I_C(\vec{r}) = \alpha \cdot h(\vec{r})$, Introducing the normalized intensity value $I_c(\vec{r}) = \frac{I_0(\vec{r})}{I(\vec{r})}$.

In order to be robust against intensity noise, we decided not to read out only the maximum intensity value which corresponds to the maximum height of the particle (particle diameter in axial dimension), but to consider all intensity values of the threshold particles. Their summation along both image coordinates x', y' results in a value proportional to the particle volume (equation 5).

(5) $V = \sum_{x',y'} h(\vec{r}) \cdot p = \frac{1}{\alpha} \cdot \sum_{x',y'} \ln I_c(x', y') \cdot p$,

x', y' represent the image coordinates along the particle dimensions and p the pixel area [μm^2].

Knowledge of the particle volume facilitates the determination of the particle diameter d in axial dimension. The particle diameter is, furthermore, accessible by the area of the projected particle in the image. Comparison of the particle diameter deduced from intensity measurements and from the particle area facilitates the determination of the material-specific attenuation coefficient α for each individual particle. To increase the statistical validity of this

value, we investigated a large number of particles. Therefore, we took advantage of the fact that the particles possess a certain size distribution. Data extraction from the raw image facilitated a plot of the diameter determined by the particle area *vs.* the cubic route of the sum of logarithmized intensites (indicating the particle diameter in axial direction). The obtained graphs describe a linear relationship according to equation 6 whose slope characterizes the attenuation.

$$(6)\ d = \sqrt[3]{\frac{6V}{\pi}} = \sqrt[3]{\frac{1}{\alpha}} \cdot \sqrt[3]{\frac{6}{\pi}\sum_{x',y'}^{\text{area}} \ln I_n(x',y') \cdot p}$$

Equation (6) can be expressed in such a way that a linear function follows from the expression of the l.h.s. *vs.* the particle diameter d.

$$(7)\ \sqrt[3]{\frac{6}{\pi}\sum_{x',y'}^{\text{area}} \ln I_n(x',y') \cdot p} = \sqrt[3]{\alpha} \cdot \mathrm{d}$$

From this, the attenuation coefficient α [μm^{-1}] can be determined.

Implementation of the algorithm

In order to achieve a profound data elaboration based on the mathematical relations according to eq. (1) – (7), we developed an evaluation algorithm based on the image processing toolbox DIP*image* for MATLAB.

Initially, the image is normalized by a locally estimated background. This is achieved in two image processing steps. In a first step the image is globally normalized by dividing it by the maximum value of its Gauss filtered version. As a result, the background intensities fluctuate around the value one. In a second step, the normalization is improved by a local background estimate. A thresholding is defined to roughly differentiate between particle signal and image background (typically 91% of brightness). This first background mask is then slightly enlarged. A Gaussian filtering of the scalar normalized image leads, along with an inpainting

of the mask covered parts, to a reasonable estimation of a non-flat background. A further thresholding (typically 95% of brightness) of the locally background corrected image provides a precise second mask which facilitates the discrimination between the background and the particles with the highest precision.

Particle recognition, labeling and geometrical characterization represent central tasks in this algorithm. The recognition is achieved by local maxima determination in the Gaussian-filtered background-corrected image (based on the second mask) which results in appropriate estimations of the particle center positions. A watershed algorithm, seeded by the estimated center positions, facilitates the determination of particle boundaries in case of overlapping particle signals. On the basis of the result achieved by the watershed algorithm and the second mask, most particles are well selected and automatically labeled. In order to exclude geometries which imply shapes other than spherical particles, a routine based on the determination of the Ferret aspect ratio is applied. Consequently to all aforementioned steps, the particle area as well as the sum of intensities is determined for further elaboration according to equation (7).

Table S1: The image processing algorithm requires the pre-selection of some parameters, which are required to be input prior to analysis. These are:

noiseLPrad – parameter to reduce noise in frequency space as initial image processing step

minestmrad – minimal diameter of objects (in pixels) to be considered as particles

maxestmrad – maximal diameter

radBgAre – measure for largest coherent background area

fglimit – threshold used for first analysis to distinguish between particle signal and background area

fglimit2 – threshold used for subsequent analysis

maxEllipt – maximum ellipticity (based on the determination of Feret‘s diameters) of particles considered for analysis

number of images – number of analysed images

number of particles – number of analysed particles

These parameters were selected manually by preliminary inspection of the images.

All images have been processed individually and average values of all determined α weighted by the number of analyzed particles were calculated.

Sample	treatment	noiseLPrad	minestmrad	maxestmrad	radBgAre	fglimit	fglimit2	maxEllipt	number of images	number of particles
NP1	blank Os U Pb	3	10	80	80	0.91	0.96	1.1	132 320 237 ---	5 7 5 ---
NP2	blank Os U Pb	3	4	30	30	0.93	0.96	1.1	147 221 351 510	7 8 6 10
NP3	blank Os U Pb	3	4	30	30	0.93	0.96	1.1	3288 388 4614 612	8 10 8 10
NP4*	blank Os U Pb	8	20	80	40	0.91	0.96	1.1	166 115 133 117	16 13 15 14
NP5	blank Os U Pb	3	4	30	30	0.93	0.96	1.1	271 --- 636 73	6 --- 8 6
NP6	blank Os U Pb	3	4	30	30	0.93	0.96	1.1	626 82 275 57	6 5 7 7
NP7	blank** Os U** Pb**	4 3 4 4	8 4 8 8	30 30 30 30	30 30 30 30	0.96 0.93 0.97 0.97	0.96 0.96 0.97 0.97	1.1 1.1 1.1 1.1	55 231 126 59	8 14 13 8

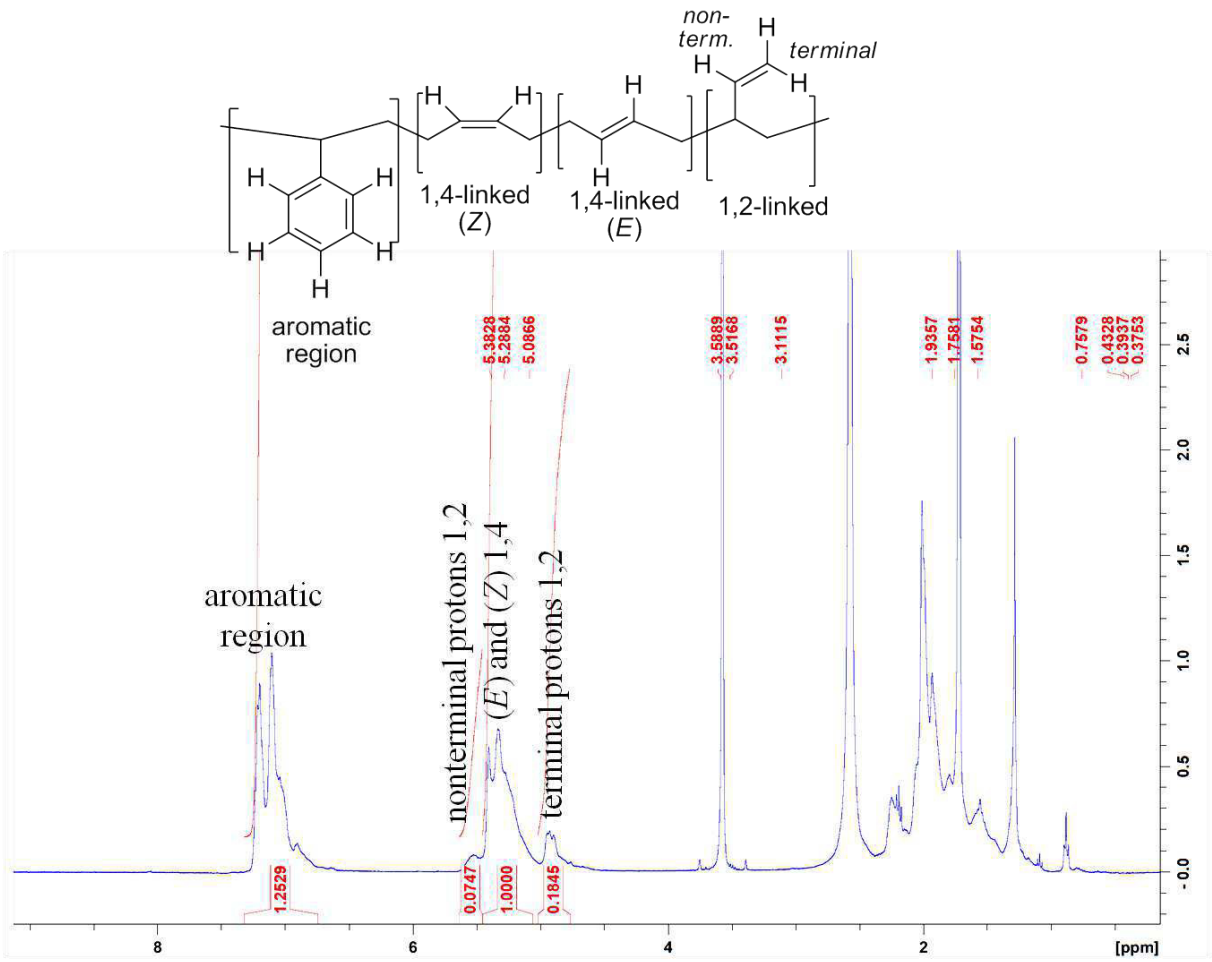

Figure S 2: ^{1}H-NMR spectrum of polymer **P6** (300 MHz, THF-d6). The proton NMR spectrum of the polymer suggests the presence of (*E*) and (*Z*) as well as terminal olefins within the structure of the polymer.

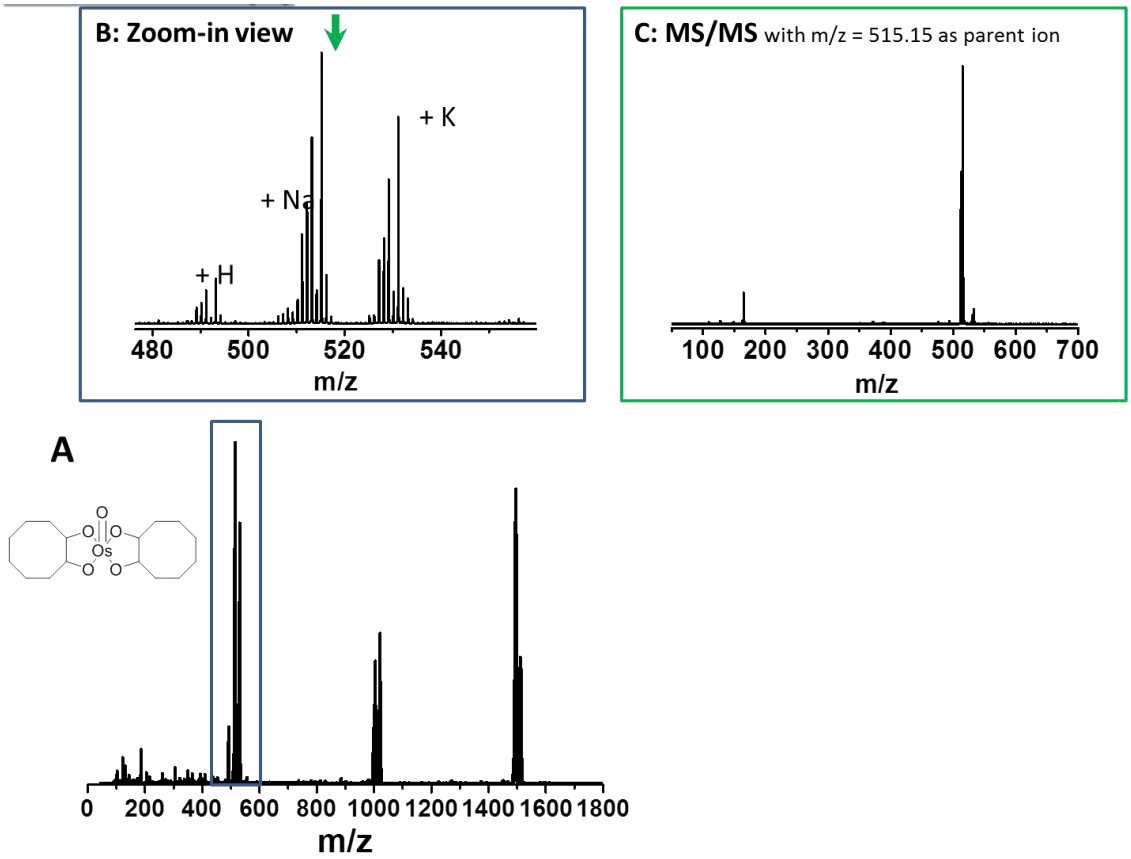

Figure S 3: A) ESI-ToF-MS of (*Z*)-cyclooctene exposed to OsO_4 staining medium. B) Zoom-in view into A. C) MS/MS experiment with m/z = 515.15 as parent ion as indicated with the green arrow in B).

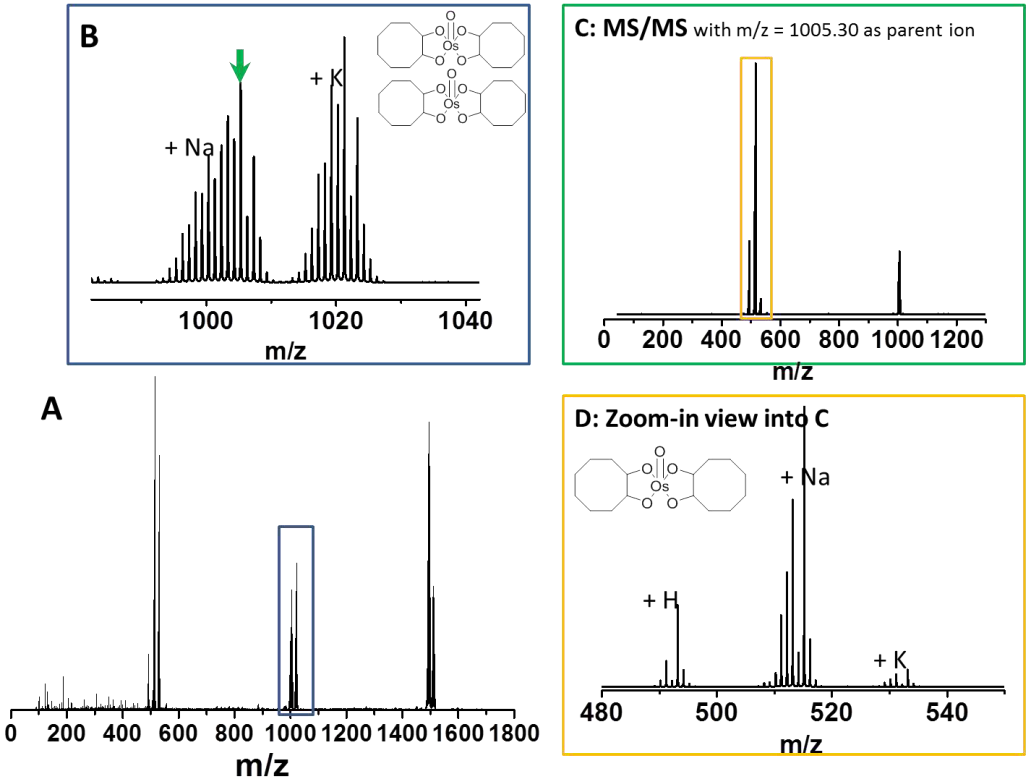

Figure S 4: A) ESI-ToF-MS of (*Z*)-cyclooctene exposed to OsO_4 staining medium. B) Zoom-in view into A. C) MS/MS experiment with m/z = 1005.30 as parent ion as indicated with the green arrow in B. D) Zoom-in view into C).

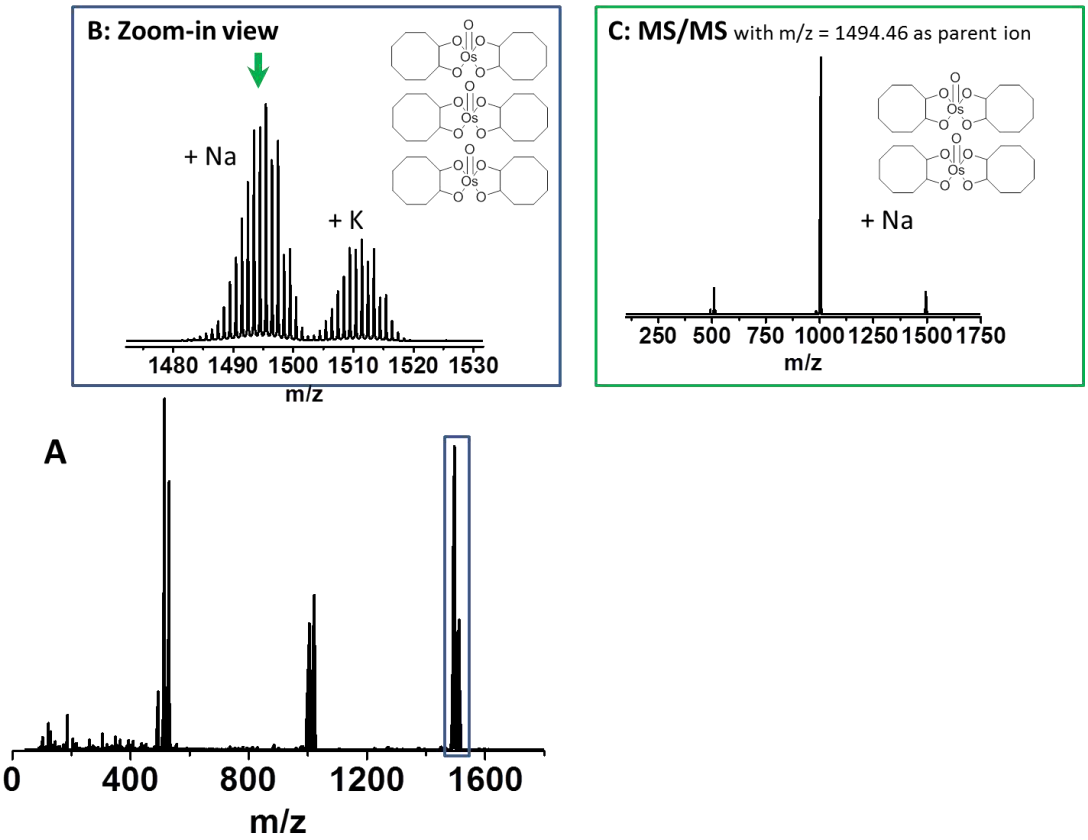

Figure S 5: A) ESI-ToF-MS of (*Z*)-cyclooctene exposed to OsO_4 staining medium. B) Zoom-in view into A). C) MS/MS experiment with m/z = 1494.46 as parent ion as indicated with the green arrow in B).

[1] a) R. E. Burge, N. R. Silvester, *J. Biophys. Biochem. Cytol.* **1960**, 8, 1; b) F. Wang, H.-B. Zhang, M. Cao, R. Nishi, A. Takaoka, *Micron* **2010**, 41, 769; c) I. Pozsgai, *Ultramicroscopy* **1997**, 68, 69; d) L. Reimer, *Transmission electron microscopy: physics of image formation and microanalysis*, Springer, **2013**.

Publication P3

"Electron density of polymeric nanoparticles determined by image processing of transmission electron micrographs: Insights into heavy metal staining processes"

M. Reifarth, W. Mueller, B. Shkodra-Pula, H. Goerls, U.S. Schubert, R. Heintzmann, S. Hoeppener

Published as: *Part. Part. Syst. Charact.* **2019**, *36*, 1800324.

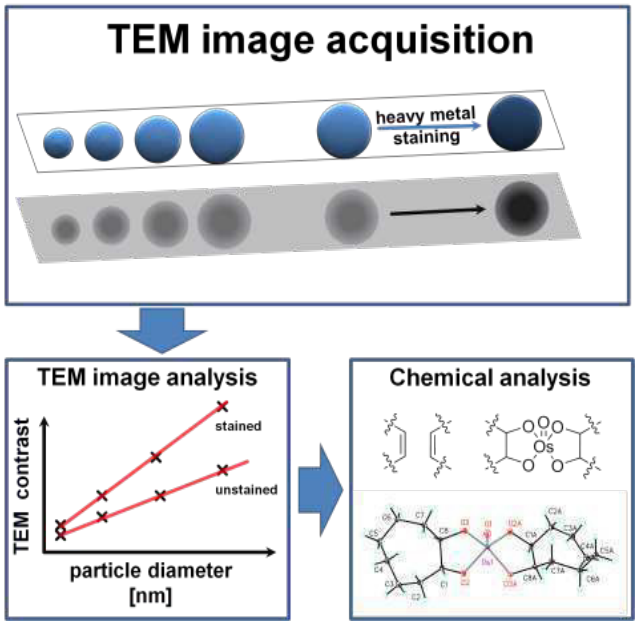

Particle & Particle Systems Characterization

www.particle-journal.com

Electron Density of Polymeric Nanoparticles Determined by Image Processing of Transmission Electron Micrographs: Insights into Heavy Metal Staining Processes

Martin Reifarth, Walter Müller, Blerina Shkodra-Pula, Helmar Görls, Ulrich S. Schubert, Rainer Heintzmann, and Stephanie Hoeppener**

A crucial parameter for the investigation of in particular low electron scattering materials by transmission electron microscopy is their ability to attenuate the electron beam and by this to generate appropriate contrast. Surprisingly little attempts have been devoted to at least qualitatively judge on this property of materials. Here an automated imaging analysis algorithm is introduced for the determination of a characteristic electron attenuation factor for homo- and (co)polymer nanoparticles which provides a means to access a measure for the contrast in a systematic study of the inherent contrast as well as of the contrast of the nanoparticles after staining procedures. The determination is based on similar imaging conditions for different nanoparticle systems, which enables a comparative approach. Additionally, based on the importance and versatility of osmium tetroxide staining, experiments are conducted elucidating the staining process of model nanoparticle systems bearing olefinic groups. The binding of osmium tetroxide in the environment of the nanoparticle is investigated by means of high-resolution electrospray mass spectrometry.

Dr. M. Reifarth, B. Shkodra-Pula, Prof. U. S. Schubert, Dr. S. Hoeppener
Laboratory of Organic and Macromolecular Chemistry (IOMC)
Friedrich Schiller University Jena
Humboldtstr. 10, 07743 Jena, Germany
E-mail: s.hoeppener@uni-jena.de

Dr. M. Reifarth, B. Shkodra-Pula, Prof. U. S. Schubert,
Prof. R. Heintzmann, Dr. S. Hoeppener
Jena Center for Soft Matter (JCSM)
Friedrich Schiller University Jena
Philosophenweg 7, 07743 Jena, Germany
E-mail: rainer.heintzmann@uni-jena.de

Dr. W. Müller, Prof. R. Heintzmann
Institute of Physical Chemistry
Friedrich Schiller University Jena
Helmholtzweg 4, 07743 Jena, Germany

Dr. W. Müller, Prof. R. Heintzmann
Leibniz Institute of Photonic Technology
Albert-Einstein-Straße 9, 07745 Jena, Germany

Dr. W. Müller, Prof. R. Heintzmann
Abbe Center for Photonics
Albert-Einstein-Straße 6, 07745 Jena, Germany

Dr. H. Görls
Institute for Inorganic and Analytical Chemistry
Friedrich Schiller University
Humboldtstrasse 8, 07743 Jena, Germany

The ORCID identification number(s) for the author(s) of this article can be found under https://doi.org/10.1002/ppsc.201800324.

DOI: 10.1002/ppsc.201800324

The increasing interest to utilize polymer nanoparticles as efficient delivery and targeting vehicles in biomedical applications or as additives to obtain composites with improved mechanical performances, has fueled continuous interest in studying their distribution in various engineered materials as well as in analyzing their specific mode of action. The versatility of polymer synthesis strategies provides access to a virtually unlimited portfolio of different nanoparticles with tailor-made properties, including, e.g., controlled material degradability,[1] stimuli sensitivity,[2] or thermo responsiveness.[3] These possibilities to tailor the nanoparticles' properties can be regarded as a major motivation to introduce polymer nanoparticles in a plethora of different lines of research and industrial applications, ranging from materials applications to biomedicine and others.

In the field of materials science as well as in biomedicine, it often represents a central scientific task to determine the localization of nanoscale particles in a functional material.[1,4,5] In these contexts, microscopy techniques provide high-resolution images and detailed information on the localization and distribution of the nanoparticles and can visualize their interaction with other materials.[6] In particular transmission electron microscopy (TEM) represents in this respect a powerful technique, since it can provide information on the morphological details of the incorporation of nanoparticles in different materials with a high resolution.[7] One of the major challenges when aiming on localizing polymer nanoparticles in an organic matrix, may it be a polymer bulk material or the compartments of a biological system,[6b] is the poor contrast, which is generated by the polymers in TEM imaging. Researchers employing TEM have addressed this issue by replacing polymer nanoparticles by metal nanoparticles[7] or by selectively introducing heavy elements, i.e., osmium tetroxide (OsO_4), uranyl acetate ($UO_2(OOCCH_3)_2$), or lead citrate ($Pb_3(C_6H_5O_7)_2$)-to name only the most common heavy metal compounds employed as electron dense stains used in cell biology studies.[8]

Here we introduce a method to comparatively analyze different polymers regarding their inherent capability to scatter electrons as well as to study their response to common staining

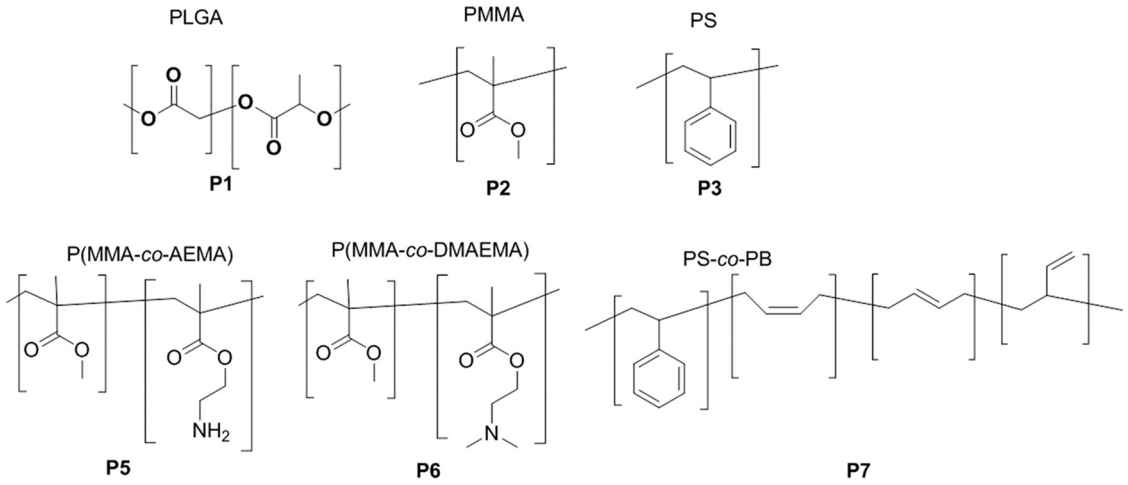

Figure 1. Schematic representation of the chemical structure of the utilized polymers for formulating nanoparticle systems. Top row: representatives for homopolymers (**P1**–**P3**). Bottom row: copolymer materials (**P4**–**P6**) used for the formation of nanoparticles. Nanoparticle systems are denoted in the following as **NPx**. Px representing the polymer of which the particles were formulated.

agents. For this purpose, an automated image processing algorithm was developed, which can analyze the contrast generated in TEM imaging. This approach facilitates a rapid estimation of the staining potential of common heavy metal agents toward the respective polymer class.

Special attention deserves the excellent staining ability of polymers containing double bonds toward OsO_4, which additionally stabilizes the polymeric structures.[9] In this context we studied a model system, which mimics the staining of a small organic compound in a nanoparticle-like environment and investigated the occurring staining process by means of electrospray ionization time-of-flight mass spectrometry (ESI-ToF-MS) and crystal structure analysis.

For the investigation of the staining and electron contrast properties of polymer nanoparticles different technologically important homopolymer particle systems were studied to compare their inherent electron attenuation potential (**Figure 1**, **P1**–**P3**). Poly(lactic-*co*-glycolic acid) (PLGA, **P1**) was chosen as a representative for a pharmaceutically utilized material, which shows good biocompatibility and is frequently employed for drug administration purposes due to its biodegradability.[10] Furthermore, ester-based poly(methylmethacrylate) (PMMA, **P2**, copolymerized with a small amount of methacrylic acid) and the phenyl group containing poly(styrene) (PS, **P3**) were investigated due to their frequent application in the formation of composite materials[11] or as materials for the formation of carrier particles which can be utilized, e.g., in immunoassays.[12]

These polymers can be formulated into nanoparticle systems by utilizing nanoprecipitation (NPr), nanoemulsion (NE), and emulsion (EP) polymerization techniques. The formed nanoparticle systems were characterized regarding their physico-chemical properties which are summarized in **Table 1**.

TEM imaging was performed with identical beam settings for this set of polymers (pixel size (3.94 nm), beam intensity (electron density ≈ 0.28 electrons per $Å^2$ s), objective aperture (40 µm), and defocus (–2.5 µm from eucentric focus)) in order to ensure comparability of the results.

In order to extract an electron attenuation value from the TEM images, a condition in which scattering absorption contrast dominates the image contrast has to be applied. Ideally a combination of zero defocus and small objective aperture is a useful image condition. However, in order to ease automatic particle detection for our algorithms we performed measurements with an additional phase contrast, aiding the edge detection. Phase contrast produced by slight defocus can, in contrast to an image post processing step, enhance the sharpness of particle edges without enhancing shot noise. In order to still be able to apply Lambert–Beer's law the effect of defocus has to be neglectable for determining the electron attenuation coefficient. To ensure this we choose a defocus of –2.5 µm where in our case the diameter of the blur circle (2.3 nm) and the feature size which is maximum pronounced by phase contrast (3.5 nm) is below the nominal pixel size (3.94 nm) (see the Supporting Information).

In particular the defocus and the size of the objective aperture are critical parameters which directly influence the contrast generated in TEM brightfield images. While the choice of the

Table 1. Physico-chemical properties of different homo- and copolymer nanoparticle formulations. NE: nanoemulsion polymerization; NPr: nanoprecipitation; EP: emulsion polymerization. *Determined by DLS.

NP sample	Polymer	Preparation method	Size [nm] Polydispersity (PDI)*	Zeta potential [mV]
NP1	PLGA	NP	199 (0.138)	–29 ± 1
NP2	PMMA	NPr	107 (0.110)	–46 ± 1
NP3	PS	EP	115 (0.105)	33 ± 1
NP4	P(MMA-*co*-AEMA)	NPr	130 (0.14)	61 ± 1
NP5	P(MMA-*co*-DMAEMA)	NPr	124 (0.06)	33 ± 1
NP6	PS-*co*-PB	NE	214 (0.118)	–5 ± 0.1

aperture is straightforward a careful tuning of the defocus level has to be conducted. By measuring at underfocus conditions, the image contrast is enhanced as a result of phase contrast. Since this additional phase contrast is not directly linked to the mass contrast, a series of experiments was conducted to relate the influence of the defocus level to the observed changes in the obtained electron attenuation values. The determination of the electron attenuation values of polystyrene beads **NP3** revealed that the method suggested in our contribution is robust against measuring in defocus, since approximately the same electron attenuation values could be extracted from a set of images measured under different defocus conditions (Figure S1, Supporting Information). This moderate defocus greatly improves the reliability of the image analysis routine.

In this context it has to be mentioned that the electron attenuation, unlike the attenuation of, e.g., visible light, which is a result of the interaction of the photons with matter (like absorption of the photons), refers to the deflection of electrons from their incident beam. The scattered electrons are partially blocked by the objective aperture and enhance the contrast.

By choosing standardized imaging conditions, the influence of instrumental factors (i.e., camera sensitivity) can be excluded. As a consequence, the obtained values for the electron attenuation are not absolute values but can be used to obtain a classification within a set of polymer nanoparticle samples for qualitative comparison. Figure S2 in the Supporting Information displays TEM micrographs of **NP1-3** for illustration.

The contrast of individual particles is extracted from the acquired TEM images (**Figure 2**A) using an automated imaging analysis algorithm based on the image processing

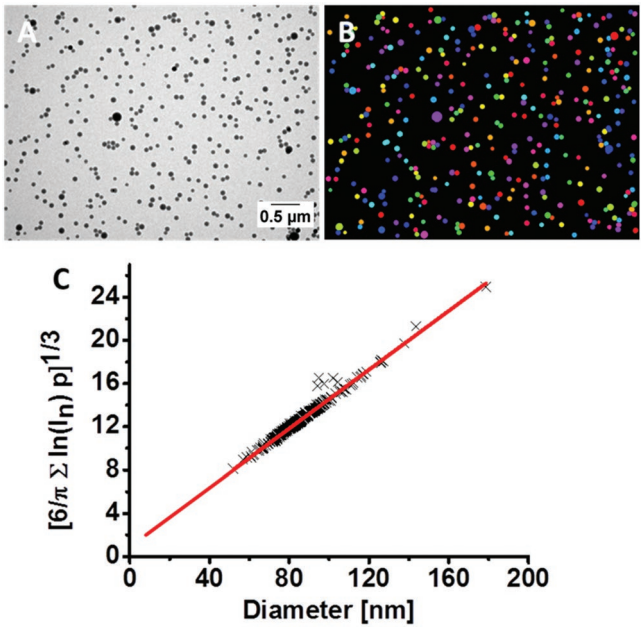

Figure 2. Automatic analysis of PS nanoparticle contrast and determination of the electron attenuation coefficient α, which is the slope of the linear fit of the analysis plots. A) Shows a raw image of particle sample. B) Colored spots depict the signals taken into consideration for further data elaboration. C) The electron attenuation, as a measure for the particle contrast, is determined according to Equation (1). The slope of the linear fit represents the extinction related constant $\alpha^{1/3}$.

library DIPimage for MATLAB.[13] The theoretical rationales of this algorithm are based on the fact that for amorphous or polycrystalline material the decrease of the electron beam intensity follows an exponential decay for ultrathin specimens, which has been reported to be used, e.g. for the determination of a sample thickness of ideal films.[7,14] A more detailed derivation of the algorithm and the underlying theoretical considerations are summarized in the Supporting Information and are illustrated in Figures S3 and S4 in the Supporting Information. An exemplary image subjected to image processing is shown in Figure 2. In brief, all images are initially normalized by a local background estimate. This background correction compensates, e.g., inaccuracies in the thickness of the carbon support film across the image. Furthermore, in this step of the algorithm the full image intensity I is defined. Particle recognition is implemented by thresholding and supported by a watershed algorithm separating particles in very close proximity. In order to exclude matches with irregular or distorted geometries (e.g., inseparable clusters), a routine based on the determination of the Ferret aspect ratio was applied. As a result, only suitable nanoparticles are reproducibly selected for automated image analysis (Figure 2B).

Next, the particle area or rather the diameters d were determined by pixel counting. A measure for the particle volume was determined by a sum, according to Lambert–Beer's law, of logarithmized intensities $I_n(x',y')$ (background normalized pixel values) covering the particle area. Assuming spherical nanoparticles a comparison of both results leads to the electron attenuation coefficient α, describing the electron scattering capability of the polymer:

$$\sqrt[3]{\frac{6}{\pi}\sum_{x',y'}^{\text{area}} \ln I_n\left(x',y'\right)\cdot p} = \sqrt[3]{\alpha}\cdot d \tag{1}$$

where p is the area of one pixel. We determine the electron attenuation coefficient α by plotting the cubic root of the sum of the logarithmic intensities (equation left-hand side) over particle diameter d (equation right-hand side) (Figure 2C) which results in a linear fit (Figure 2C). The accuracy of the linear fit improves with increasing polydispersity of the nanoparticles.

High α values correspond to a relatively higher electron opaqueness. This directly correlates with the inherent capability of the nanoparticles to attenuate the electrons. In case of stained samples, the electron attenuation coefficient α is a measure for the capability of the polymer nanoparticle to accumulate heavy metals inside the particle material and denotes, as a consequence, the staining efficiency.

Images of all polymer systems were analyzed by this method and the attenuation coefficients α were determined for bare polymer nanoparticles as well as for stained particle systems (**Table 2**). Particles were incubated for 24 h with the respective staining solutions. OsO_4 was buffered in PBS (1% OsO_4 in PBS), uranyl acetate was applied as a 1% solution in de-ionized water and lead citrate staining solution was prepared according to the Reynold's procedure.[15] From each particle sample, a set of multiple images was acquired. At least five images of each sample were taken into consideration for image analysis. The

Table 2. Electron attenuation coefficients α extracted by image processing.

NP sample	Nonstained NPs α [μm^{-1}]	OsO_4 staining α [μm^{-1}]	Uranyl acetate α [μm^{-1}]	Reynold's Pb α [μm^{-1}]	Europium staining α [μm^{-1}]
PLGA, **P1**	1.13 ± 0.33	1.33 ± 0.21	1.35 ± 0.10	n.d.[a)]	2.19 ± 0.57
PMMA, **P2**	1.64 ± 0.31	1.49 ± 0.3	1.71 ± 0.27	1.61 ± 0.25	n.d.
PS, **P3**	2.14 ± 0.05	2.24 ± 0.17	2.04 ± 0.13	2.04 ± 0.24	n.d.

[a)]Reynold's lead citrate solution possesses a pH value of 12.0. Under these conditions, the PLGA particles were not stable.

analysis algorithm was applied to each image individually and the slope values α were determined. From all determined constants α an average as well as a standard deviation was calculated and weighted according to the number of particles that were analyzed in each image. Image analysis required the consideration of several parameters which had to be adjusted manually after critical evaluation of the raw images. The respective parameters are listed in Table S1 in the Supporting Information.

Based on this procedure the electron attenuation of the homopolymer nanoparticles was determined. The respective values are listed in Table 2 and are compared in **Figure 3**.

The evaluation of the processed images of the untreated PLGA, PMMA, and PS homopolymer nanoparticles demonstrates already significant differences in electron attenuation values α, which indicate that the electron attenuation is highest for PS followed by PMMA and PLGA nanoparticles. It can be seen that the electron attenuation coefficient is a sensitive measure that might also be influenced by other material's properties. This can be concluded in view of the fact that PLGA possesses a higher mass density than polystyrene in bulk. As a consequence, one would expect a different trend of the obtained attenuation values. However, the mass density of polymeric nanoparticles does not necessarily correspond to the polymer's density in bulk. For this purpose additional parameters should be taken into consideration. These are not taken into account in the actual algorithms as the respective parameters are not straightforward to be implemented. For example, a reliable experimental method has to be developed which determines the mass density of particles, which could be determined, e.g., by analytical ultracentrifugation.[16]

Staining with the conventional heavy metal stains did not result in a significant increase of the electron attenuation in this set of homopolymer nanoparticles. This is rationalized by a lack of functional groups capable of interacting actively with the staining agents, which is in agreement with literature reports.[17] Therefore, the validity of the image analysis algorithm was tested by exposure of functions **NP1** to europium triflate, which is sensitive toward the polyester structures of the PLGA nanoparticles. This treatment resulted in a significant increase of the electron attenuation and an efficient staining of the polymer nanoparticle by a factor of two was observed.

In order to investigate the contrast enhancement by staining other polymers, such as poly[*N*-(2-aminoethyl) methacrylamide] (PAEMA), poly(2-dimethylamino-ethylmethacrylate) (PDMAEMA), or polybutadiene (PB), would represent more promising case studies. These polymers are potentially affine to staining agents due to an enhanced affinity of amino functionalities or carbon–carbon double bonds present in the polymer structure, resulting in a considerable increase of the contrast. However, these polymers do not form water-stable colloids. A possibility to circumvent this problem is to copolymerize them with PMMA or PS. These respective copolymers (**P4–P6**) were formulated into nanoparticles (**NP4–NP6**) and their physico-chemical properties were determined by dynamic light scattering (DLS) and Zeta-potential measurements as summarized in Table 1. The electron attenuation coefficients for the respective copolymer nanoparticles are listed in **Table 3** and are compared in **Figure 4**.

From the previous investigations of the homopolymer nanoparticles it becomes evident that neither PS nor PMMA can be actively stained with the applied protocols. Observed differences in the electron attenuation are, as a consequence, ascribed to a staining of the PAEMA, PDMAEMA, and the PB only. It is clearly observed (Table 3, Figure 4) that P(MMA-*co*-AEMA) (**NP4**) shows a good staining ability toward uranyl acetate, which results in an approximately 1.6-fold enhancement

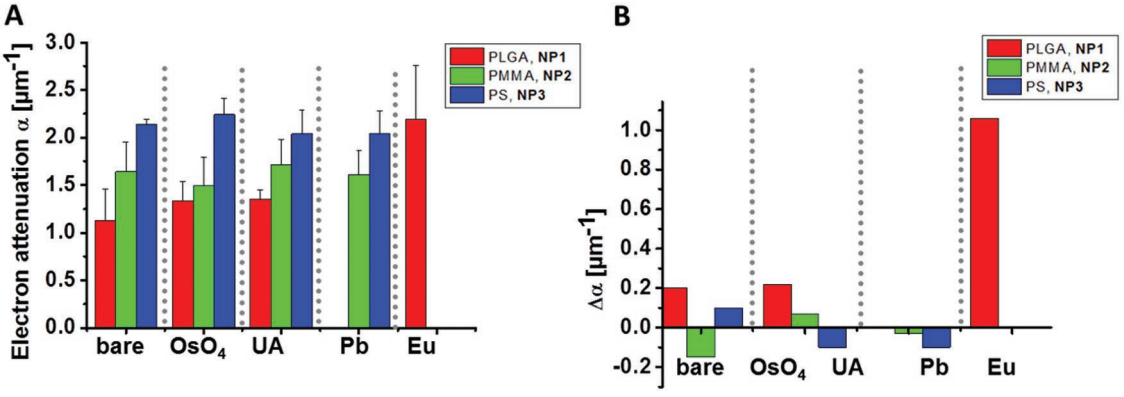

Figure 3. Analysis of the electron attenuation coefficient α of different homopolymer nanoparticles. A) Determined α values obtained after the respective sample treatment (bare particles, and particles after OsO_4 staining, U and Pb staining). B) Electron attenuation differences between untreated and heavy-metal stained particles to highlight changes in the electron attenuation coefficient introduced by the staining process.

Table 3. Electron attenuation values of copolymer nanoparticles **NP4** to **NP6**.

NP sample	Nonstained NPs α [μm^{-1}]	OsO_4 staining α [μm^{-1}]	Uranyl acetate α [μm^{-1}]	Reynold's Pb α [μm^{-1}]
P(MMA-*co*-AEMA), **P4**	1.71 ± 0.13	[a)]	2.71 ± 0.4	1.43 ± 0.64
P(MMA-*co*-DMAEMA), **P5**	1.23 ± 0.06	2.41 ± 0.47	2.64 ± 0.16	1.45 ± 0.47
PS-*co*-PB, **P6**	0.26 ± 0.03	4.73 ± 0.74	0.29 ± 0.05	0.29 ± 0.05

[a)]The electron attenuation characteristics of **P4** treated with OsO_4 could not be determined, since the staining process destabilized the particle stability as indicated by TEM imaging.

of the attenuation factor, even though the amino content in the polymer is only 20 mol.% compared to the methacrylate content, and particle staining is only attributed to the amino functionalities in the polymer. From **NP4** no results could be obtained from image analysis of OsO_4-stained particle samples, since no stable particles were found in TEM micrographs after OsO_4 treatment. We attribute this behavior to a severe oxidative degradation of the primary amino functionality of the polymer, which causes adverse effects on the particle integrity.

In contrast, P(MMA-*co*-DMAEMA) (**NP5**) significantly responds to OsO_4 staining, as seen by an approximately twofold increase of α. Furthermore, this polymer showed an increase of the electron attenuation by a factor of approx. 2 after the treatment with uranyl acetate. Staining with lead citrate resulted in only low staining levels for all copolymer nanoparticles.

The obtained results confirm furthermore, that the imaging contrast not only depends on the electron attenuation introduced by the elemental composition of the nanoparticles. This is reflected in the low attenuation coefficients obtained for the PS-*co*-PB sample system. Even though PS in its homopolymer form (**NP3**) showed an attenuation coefficient of $\alpha = 2.14 \pm 0.05\ \mu m^{-1}$ the copolymer formulation with PB (**NP6**) resulted only in an attenuation coefficient of $\alpha = 0.26 \pm 0.03\ \mu m^{-1}$. Staining with OsO_4 resulted, however, in this case in an 18-fold increase in the observed electron attenuation coefficient α. Exposure of the sample to uranyl acetate and lead citrate did not result in particle staining, which is reflected by the very similar attenuation values of these samples compared to the untreated particle sample. In general it is assumed that osmium in the highest known oxidation state +8 accumulates into the polymer structure by oxidation of chemical functionalities. OsO_4 is, in this respect, employed not only to introduce an enhanced electron density into the polymer sample due to the heavy metal incorporation into the nanoparticle structure, but it can also contribute to an improved fixation of the samples' fine structure owing to its potential to crosslink certain chemical functionalities. This results in a significant hardening of polymers,[18] similarly as observed in the fixation of biological samples.[8] This aspect is of particular interest since we concluded that the density of the polymer nanoparticles plays an important role when accessing the electron attenuation.

In order to evaluate this effect in more detail and to reveal the interaction mechanism of OsO_4 with C=C double bonds, a model system mimicking the staining ability of double bond containing polymer nanoparticles was investigated by ESI-ToF MS and X-ray crystallography.

This model system mimics e.g. the strong staining ability observed for nanoparticles containing PB which was reflected by the extraordinary high electron attenutation factors for the nanoparticle system **NP6**. A suitable small molecule providing isolated double bonds is (*Z*)-cyclooctene. H-NMR (Figure S5, Supporting Information) suggests the presence of three substituted types of olefins in the polymer **P6**. PB as a homopolymer represents a polymer consisting of 1,4- and 1,2-linked monomer (1,3-butadiene) units. As a consequence, in the polymer chain (Z)- and (E)-substituted (as a result of 1,4-linkage of butadiene units) as well as terminal C=C double bonds (as a result of 1,2-linkage of butadiene units) are present. (*Z*)-cyclooctene can be easily formulated into nanoparticle systems by utilizing a hydrophobic solvent as matrix material. As a suitable hydrophobic solvent, which triggers the formation of a stable emulsion of the (*Z*)-cyclooctene under the terms of the experiments, xylene (mixed isomers) was used. Xylene is a chemically inert solvent with a sufficiently high boiling point which provides appropriate stability against evaporation. Moreover, xylene exhibits phenyl moieties, which means that the model compound (*Z*)-cyclooctene is exposed to a similar

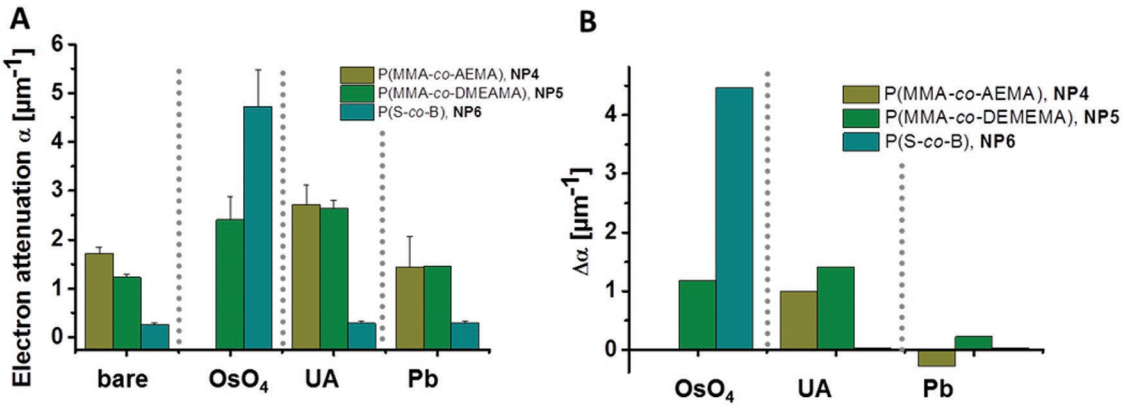

Figure 4. Electron attenuation characteristics of the nanoparticles consisting of copolymers. A) Attenuation coefficients found for the blank and stained nanoparticles after the respective treatment. B) Differences in the electron attenuation coefficient rationalized by plotting the increase of the contrast in relation to the bare polymer.

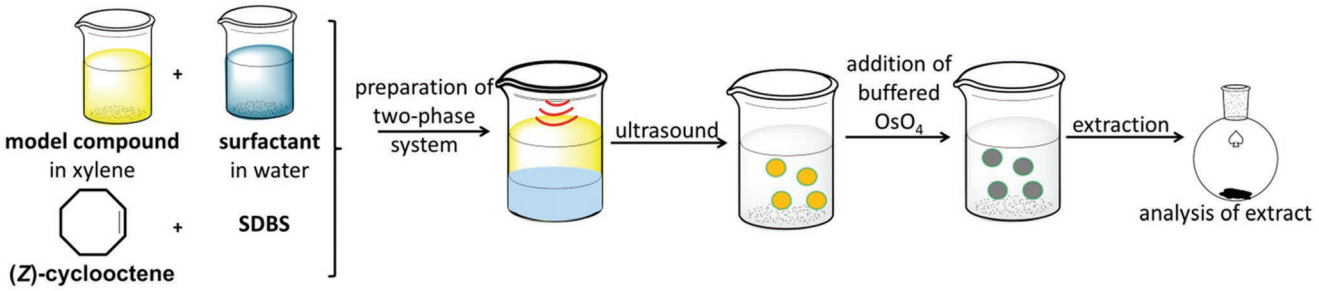

Figure 5. The model compound (*Z*)-cyclooctene was dissolved in xylenes to form stable nanoemulsions stabilized by SDBS as surfactant upon ultrasonication. The nanoemulsions were exposed to buffered OsO_4 solution, the reaction products were extracted and the resulting black oil was subjected to further analysis.

chemical environment as found in the nanoparticle system **NP6** that contains styrene as a co-monomer unit in the polymer. The model nanoparticle solutions are formulated following the procedure outlined in **Figure 5**.

The nanoemulsions (NEs) were prepared by dissolving the model compound in xylene and the solution was overlaid with an aqueous solution of the surface-active compound sodium dodecylbenzenesulfonate (SDBS), whereby ultrasonication of the mixture provided stable NEs. The formed droplets can be subjected to OsO_4 staining by applying a 1% staining solution. After a reaction period of 1 h, the emulsion was dialyzed to remove the residual unreacted osmium tetroxide. Afterward, the reaction mixture was extracted with toluene and the extract was evaporated to dryness. The matrix can be subsequently easily removed, which allowed for the analysis of the compound **Com-1** by ESI-ToF-MS and crystal structure analysis.

The ESI-ToF-MS spectrum of the OsO_4 treated (*Z*)-cyclooctene is depicted in **Figure 6**.

The spectrum reveals three main signal distributions as indicated in the blue, red, and violet box (Figure 6A). The first signal distribution (Figure 6B) can be attributed to a chemical structure of **Com-1** with the sum formula $C_{16}H_{28}O_5Os$, which is explained by the formation of a coordinative Os^{VI} compound, whereby the central atom is coordinated by two diolic species in the sense of a cyclic osmium acid ester (structure see the inset in Figure 6B). The spectrum in this m/z region reveals three peak distributions (Figure 6B), whereby the most intensive abundancy in each set of signals can be ascribed to the adduct of the suggested structure of **Com-1** associated to H^+, Na^+, and K^+, respectively. Sodium and potassium ions are present ubiquitously in the solvents used for electrospray ionization MS and form, hence, adducts with the examined species in ESI-ToF-MS. The signal, as emphasized in the black box in Figure 6B, is assumed to represent the sodium adduct of the proposed structure. This assumption becomes more evident on the basis of Figure 6C, which reveals that i) the measured signal distribution is in accordance with the calculated isotopic pattern for the sodium adduct of the suggested structure as well as ii) the high-resolution HRMS result perfectly agrees with the calculated spectrum (Figure 6C). Furthermore, tandem-ESI-ToF-MS utilizing m/z = 515.15 as parent ion showed no further fragmentation of this signal, which indicates the formation of a stable compound (Figure S6, Supporting Information).

The set of signals labeled in the red box (Figure 6A) can be explained by the occurrence of dimers of **Com-1**, which form adducts with Na^+ and K^+. The signal at m/z = 1005.30 as parental ion was subjected to further MS/MS measurements. The resulting mass spectrum revealed the occurrence of the monomer unit in form of H^+, Na^+, and K^+ adducts (Figure S7, Supporting Information) as well, which underlines the assumption that this signal basically represents a dimer species. Likewise, the set of signals labeled in the violet box (Figure 6A) suggests the presence of trimers; MS/MS measurements revealed the formation of dimers and monomers of this species upon further ionization (Figure S8, Supporting Information).

An additional evidence for the formation of these compounds was found by crystal structure analysis. The obtained crystal structure of the Os^{VI} complex (**Figure 7**) revealed the formation of the complex with the structure as suggested, which crystallizes in a C2/c space group. This analysis, along with the results from (tandem-)ESI-ToF-MS, provided a reliable proof that osmium coordinates two (*Z*)-olefines in such a way that it cross-links both moieties. It is likely that a similar complex is also formed during the OsO_4 fixation process within the polymer nanoparticles. Here the cross-linking ability is not limited to an isolated C=C double bond, but a much higher possibility of crosslinking between the polymer chains has to be assumed, which ultimately improves the stability of the formed nanoparticles and results in their hardening.

In conclusion, we developed a robust routine to determine the electron attenuation coefficient α of nanoparticle systems by automated processing of TEM images of a comparative series of different nanoparticles systems. The electron attenuation coefficient as a measure for the scattering ability represents a tool to judge the ability of polymers to interact with various staining agents. At the present stage this routine can be used as a fast screening tool to judge on the electron attenuation. Important parameters which influence the electron attenuation (i.e., the mass density of the polymer nanoparticles) will be gradually included into the analysis routine to derive a more quantitative tool. This relies on sophisticated methods to determine the density of the nanoparticles, which could be performed e.g. by analytical ultracentrifugation or related methods.

A refined algorithm can in this respect provide a deeper insight into the complex issue of how electron contrast is generated in nanoparticle systems. A fundamental understanding of these processes will certainly support the applicability of TEM investigations in this field of research. The importance

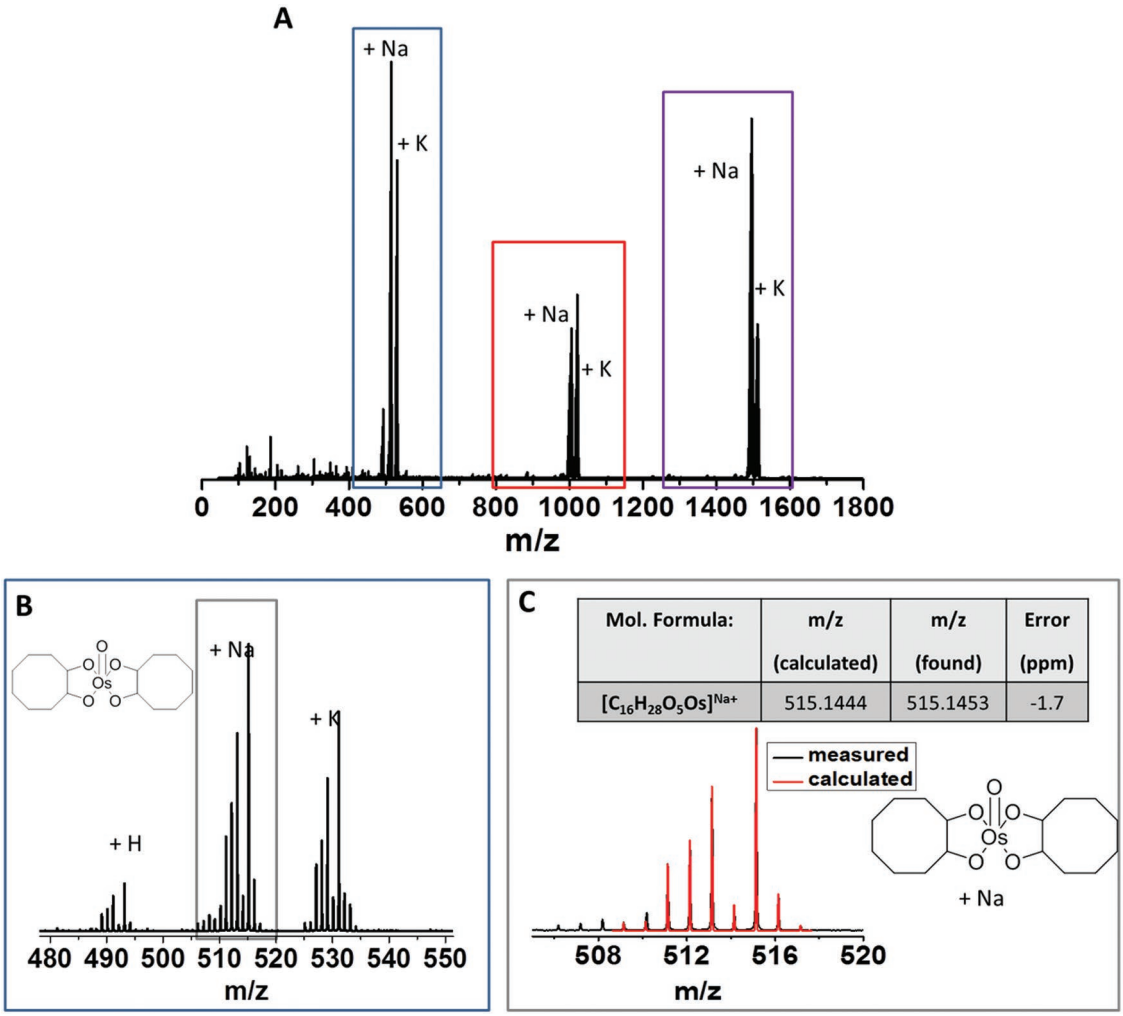

Figure 6. A) ESI-MS of the compound Com-1 as a result of the treatment of (*Z*)-cyclooctene with OsO_4. Three signal distributions are found as indicated in the blue, red and violet box. The signals found in the blue box are depicted in more detail in B). The occurrence of the signals can be explained by adducts of H^+, Na^+, and K^+ of the species as suggested in the structure as shown in the inset. The isotopic pattern of the measured sample (black box) and the calculated spectrum are in good agreement. Furthermore, high-resolution MS (HRMS) hints toward the suggested structure. The set of signals in the red and violet box are explained more in detail in the Supporting Information (Figure S6, Supporting Information). C) The isotopic pattern of the measured sample (black box) and the calculated spectra are in good agreement.

of the molecular structure and the interaction of the staining agents with functional units within the nanoparticle structure was demonstrated by a careful investigation of the staining process of a C=C double bond containing model system.

Experimental Section

Instrumentation: DLS measurements were conducted using a Zetasizer Nano ZS (Malvern Instruments, Herrenberg, Germany). Multiple measurements were recorded at 25 °C (wavelength of 633 nm) and the counts were detected under an angle of 173°. Assuming a spherical shape of the particles, the width of the distribution as the polydispersity index (PDI) of the particles was obtained by the cumulants method. In order to determine the Zeta potential by electrophoretic light scattering, the Zetasizer Nano ZS (Malvern Instruments, Herrenberg, Germany) using laser Doppler velocimetry was applied. For this purpose, 10 runs were carried out using the slow-field and fast-field reversal mode at 150 V at 25 °C.

TEM was carried out using a Technai G^2 20 system (FEI), with an acceleration voltage of 200 kV. Imaging conditions were standardized for the acquisition of the images for comparison of the TEM image contrast. Further details are listed in the main text.

ESI-ToF-MS measurements were conducted using a micrOTOF (Bruker Daltonics GmbH) mass spectrometer equipped with an automatic syringe pump for sample injection (KD Scientific) in the positive ion mode. In order to generate ions, the standard electrospray ion (ESI) source was used, employing mixtures of dichloromethane and acetonitrile as solvent. An internal calibration standard (Tunemix solution), which was supplied from Agilent, was used for calibration of the instrument to the *m/z* range of 50–3000.

Nanoparticle preparation: The nanoparticles were prepared via NPr, NE or emulsion polymerization route.

NP1: Poly($_{D,L}$-lactide-*co*-glycolide, Resomer RG502 H, 50:50, 7 to 17 kDa, acid terminated), polyvinyl alcohol (Mowiol8-88, partially hydrolysed) and dimethyl sulfoxide were purchased from Sigma-Aldrich.

The nanoparticles were prepared by the NPr method. PLGA polymer (40 mg) was dissolved in DMSO (2 mL). Using a syringe pump, the organic solution was injected in 20 mL aqueous PVA solution (0.03 %) at

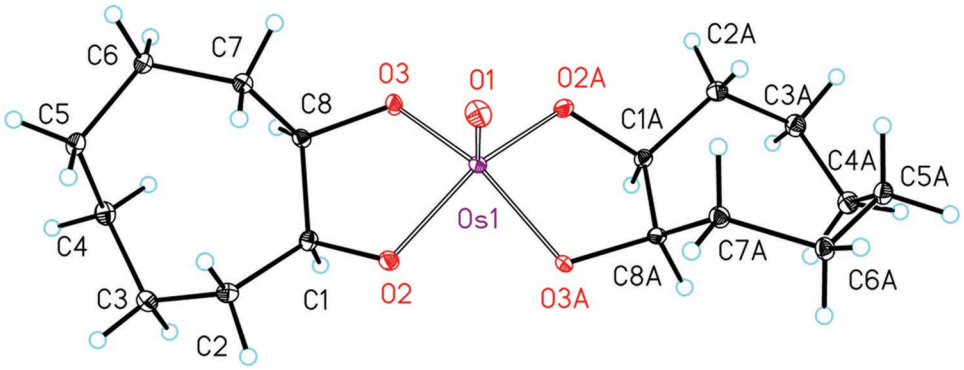

Figure 7. Molecular structure and atom labeling scheme of Bis(cyclooctyl-1,2-dioxy)(oxo)osmium(VI) (**Com-1**). The ellipsoids represent a probability of 30%. Symmetry-related atoms ($-x+1, y, -z+3/2$) are marked with the letter "A." Selected bond lengths (Å): Os(1)–O(1) 1.682(3), Os(1)–O(2) 1.895(2), Os(1)–O(3) 1.901(3), O(2)–C(1) 1.461(4), O(3)–C(8) 1.461(4), C(1)–C(8) 1.530(4); angles (deg): O(1)–Os(1)–O(2) 110.70(7), O(2)–Os(1)–O(3) 82.33(10), O(2)–Os(1)–O(2A) 138.59 (14), C(1)–O(2)–Os(1) 117.56(19), O(2)–C(1)–C(8) 118.4(3).

a flow rate of 49 mL h^{-1} under continuous stirring at 800 rpm. To remove the DMSO and excess surfactant, the nanoparticle suspensions were placed in dialysis bags of 50 000 MWCO and dialyzed against water for 6 d, replacing the dialysate with fresh water every day. NPr and dialysis was performed at room temperature and water used in all processes is milliQ grade. After purification nanoparticles were lyophilized and stored at 4 °C.

NP2: PMMA (20 mg, copolymerized with a small amount of 10 mol% acrylic acid) was dissolved in 2 mL acetone. To a 50 mL Falcon tube equipped with a magnetic stirrbar, 20 mL water was added. Under vigorous stirring (750 rpm, gas bubbles were removed), the polymer solution was dropped carefully to the water. Therefore, a syringe pump was used and a flow of 49 mL h^{-1} was adjusted. Eventually, the solvent was allowed to evaporate from the suspension overnight.

NP3: Commercially available polystyrene beads were used. Therefore, latex beads, amine-modified polystyrene, fluorescent orange, nominal diameter 0.1 µm in aqueous suspension were purchased from Sigma-Aldrich.

NP4 and NP5: The synthesis and characterization of the polymer samples **P4** and **P5** have been described elsewhere.[19] The characterization data of the polymers used in this study are listed below. For experimental details of the respective data see ref. [19].

P4: SEC (eluent: $CHCl_3$, PMMA calibration, RI detection): M_n = 4500 g mol^{-1}. $Đ$ = 1.19. DP (determined by ^{1}H-NMR spectroscopy): MMA—30. AEMA·HCl—8.2.

P5: SEC (eluent: $CHCl_3$, PMMA calibration, RI detection): M_n = 7600 g mol^{-1}. $Đ$ = 1.17. DP (determined by ^{1}H-NMR spectroscopy): MMA—40. DMAEMA—10.

The nanoparticle samples **NP4** and **NP5** were prepared via an NPr route. Therefore, the respective polymer samples were dissolved in acetone with a concentration of 10 mg mL^{-1} and added to water as previously described.[19]

NP6: Poly(styrene-*co*-butadiene) was purchased from Sigma-Aldrich. The nominal amount of styrene as stated by the manufacturer is: 45 wt%. Particles were prepared using a single-emulsion method. For this purpose, the polymer was dissolved in dichloromethane to yield a solution with a concentration of 2.5 mg mL^{-1}. 4 mL of an aqueous solution of poly(vinyl alcohol) (Mowiol 4-88, Sigma-Aldrich) was added to 2 mL of the polymer solution. The two-phase system was exposed to ultrasound using a sonicator tip until the system was visibly emulsified. During ultrasonication, the emulsion was cooled to 0 °C. The emulsion was poured in 10 mL deionized water and stirred overnight to allow the solvent to evaporate. The particle suspension was used for subsequent experiments without any further purification. The particle suspension was stored at 4 °C.

Image Acquisition: For image acquisition, nanoparticle samples were blotted onto a carbon support copper grid (400 mesh, Quantifoil, Jena), whereby the particles adhered on the grid surface. In case of staining experiments, the particle samples were incubated with the respective staining solution for 24 h (surfactants were not removed from the particle suspension prior to incubation) and the particles were placed on the grid surface by blotting the solution onto the copper grid. Subsequently, residual heavy metal stains were removed by washing the grid surface three times with deionized water utilizing a drop-to-drop method.

For OsO_4 staining, 100 µL phosphate buffered saline (PBS) and 100 µL OsO_4 solution (2 wt% in deionized water) were added to 200 µL of the respective particle suspension. Prior to staining with uranyl acetate and lead citrate the respective staining solutions were thoroughly centrifuged to remove precipitates.

For uranyl acetate staining, 200 µL uranyl acetate solution (2 wt% in deionized water) we added to 200 µL of the respective particle suspension.

Reynold's lead citrate solution was prepared starting from freshly boiled deionized water. 400 mg $Pb(NO_3)_2$ and 528 mg trisodium citrate-dihydrate was suspended in approx. 9 mL water. To this solution, 2.4 mL 1 M NaOH was added, so that the insoluble compounds dissolved completely. The pH value of the resulting solution was adjusted to pH = 12.0 ± 0.1 with NaOH solution. Subsequently, the solution was filled to 15 mL and stored at 4 °C. For particle staining 50 µL of the particle suspension was added to 150 µL lead citrate solution.

All images were acquired using the transmission electron microscope in transmission mode. In order to ensure comparable experimental conditions, particle samples were imaged using equal pixel sizes of 3.94 nm, equal underfoci of −2.5 µm as well as the same objective aperture (40 µm) for all measurements. Furthermore, the beam was adjusted in such a way that the background intensities for all measurements exhibited similar grey values (approx. 6000 Cts., spot size 1, for 1 s exposure time). Particle samples were imaged using a WA-MegaView CCD camera utilizing the same Bias/Gain correction.

Image Processing: Images subjected to image processing were used as TIFF images (16 Bit color depth). Image processing routines were programmed using MATLAB R2014a with the toolbox DIPimage version 2.8.1. Due to a low particle contrast of particle sample **NP6**, an initial rolling ball algorithm was performed for background normalization using ImageJ prior to employing the algorithm in DIPimage. For further details see the main text.

Mass Spectrometry Investigations: The nanoemulsion to study the reactivity of the model compound with OsO_4 was prepared starting from xylene (mixture of isomers). Therefore, (*Z*)-cyclooctene (20 mg) was dissolved in 1 mL xylene. 1 mL of an aqueous solution of sodium dodecyl benzenesulfonate (SDBS, 3 mg mL^{-1}) was added to the xylene phase. The two-phase system was cooled to 0 °C and subjected to ultrasonication using a sonicator tip until the system was visibly emulsified. Afterward, the stable emulsion was transferred into a dialysis tubing (Roth ZelluTrans, cut-off 3500 Da, regenerated cellulose) and dialysed for 1 d to remove the excess of surfactant. Next, the stable emulsion was transferred into a falcon tube and to this amount of

emulsion the same volume of OsO_4 solution (2% in PBS) was added, so that the final OsO_4 concentration in the reaction mixture was 1%. The reaction mixture was kept for 1 h, whereby a color change from colorless to grey could be observed. Afterward the emulsion was dialysed another 4 d to remove unreacted OsO_4 (ZellutransRoth, regenerated cellulose, cut-off 3.5 kDa). After complete dialysis, the reaction mixture was subjected to extraction with toluene, whereby a small amount of $BaCl_2$ was added to the aqueous phase. The toluene phase was dried over Na_2SO_4 and evaporated to dryness to obtain a black solid. This black solid was, subsequently, investigated by ESI-ToF-MS.

In order to obtain a crystal of the osmium complex, the black solid was dissolved in a small amount dichloromethane and stored in a glass vial equipped with a teflon cover. In order to ensure slow evaporation of the solvent, the cap was perforated with a thin needle. After complete evaporation of the solvent, a pale-grey crystalline substance could be collected.

Crystal Structure Determination: The intensity data were collected on a Nonius KappaCCD diffractometer, using graphite-monochromated Mo-K_α radiation. Data were corrected for Lorentz and polarization effects; absorption was taken into account on a semi-empirical basis using multiple scans.[20]

The structure was solved by direct methods [21] and refined by full-matrix least squares techniques against Fo^2 (SHELXL-97).[21,22] All hydrogen atoms were included at calculated positions with fixed thermal parameters. All nonhydrogen atoms were refined anisotropically. XP (SIEMENS Analytical X-ray Instruments, Inc.) was used for structure representations.

Crystal Data for **Com-1**: $C_{16}H_{28}O_5Os$, Mr = 490.58 gmol^{-1}, pale_grey prism, size 0.112 × 0.062 × 0.024 mm^3, monoclinic, space group C 2/c, a = 24.6179(8), b = 5.3887(2), c = 12.6194(4) Å, β = 100.358(2)°, V = 1646.79(10) Å^3 , T = –140 °C, Z = 4, $\rho_{calcd.}$ = 1.979 gcm^{-3}, μ (Mo-K_α) = 77.64 cm^{-1}, multiscan, transmin: 0.5241, transmax: 0.7456, F(000) = 960, 8923 reflections in h(–28/31), k(–6/6), l(–16/16), measured in the range 3.28° ≤ Θ ≤ 27.45°, completeness Θ_{max} = 99.7%, 1866 independent reflections, R_{int} = 0.0495, 1834 reflections with $F_o > 4\sigma(F_o)$, 101 parameters, 0 restraints, $R1_{obs}$ = 0.0210, wR^2_{obs} = 0.0456, $R1_{all}$ = 0.0216, wR^2_{all} = 0.0459, GOOF = 1.064, largest difference peak and hole: 0.958/–1.007 e Å^{-3}.

Supporting Information

Supporting Information is available from the Wiley Online Library or from the author. Crystallographic data deposited at the Cambridge Crystallographic Data Centre under CCDC-1854637 for **Com-1** contain the supplementary crystallographic data excluding structure factors; this data can be obtained free of charge via www.ccdc.cam.ac.uk/conts/retrieving.html (or from the Cambridge Crystallographic Data Centre, 12, Union Road, Cambridge CB2 1EZ, UK; fax: (+44) 1223-336-033; or deposit@ccdc.cam.ac.uk.

Acknowledgements

This project is part of the DFG Collaborative Research Center 1278 (SFB PolyTarget). Experiments have been conducted in the subproject C04. Cryo-TEM facilities were funded by the Deutsche Forschungsgesellschaft (DFG) and the European Fond for Regional Development (EFRE). The authors thank Sabine Armoneit for the preparation of the PMMA particles. Furthermore, the authors thank Dr. Turgay Yildirim for the preparation of P(MMA-*co*-AEMA) and P(MMA-*co*-DMAEMA).

Conflict of Interest

The authors declare no conflict of interest.

Keywords

electron contrast, heavy metal staining, osmium tetroxide, polymeric nanoparticles, transmission electron microscopy

Received: August 1, 2018
Revised: January 8, 2019
Published online: February 15, 2019

[1] A. Kumari, S. K. Yadav, S. C. Yadav, *Colloids Surf., B* **2010**, *75*, 1.
[2] a) S. Ganta, H. Devalapally, A. Shahiwala, M. Amiji, *J. Controlled Release* **2008**, *126*, 187; b) J. Zhuang, M. R. Gordon, J. Ventura, L. Li, S. Thayumanavan, *Chem. Soc. Rev.* **2013**, *42*, 7421; c) F. Wendler, K. R. A. Schneider, B. Dietzek, F. H. Schacher, *Polym. Chem.* **2017**, *8*, 2959; d) T. Yildirim, I. Yildirim, R. Yanez-Macias, S. Stumpf, C. Fritzsche, S. Hoeppener, C. Guerrero-Sanchez, S. Schubert, U. S. Schubert, *Polym. Chem.* **2017**, *8*, 1328.
[3] a) C. Weber, R. Hoogenboom, U. S. Schubert, *Prog. Polym. Sci.* **2012**, *37*, 686; b) Y.-J. Kim, Y. T. Matsunaga, *J. Mater. Chem. B* **2017**, *5*, 4307.
[4] a) V. K. Thakur, M. R. Kessler, *Polymer* **2015**, *69*, 369; b) M. S. Selim, M. A. Shenashen, S. A. El-Safty, S. A. Higazy, M. M. Selim, H. Isago, A. Elmarakbi, *Prog. Mater. Sci.* **2017**, *87*, 1; c) B. Sandmann, B. Happ, I. Perevyazko, T. Rudolph, F. H. Schacher, S. Hoeppener, U. Mansfeld, M. D. Hager, U. K. Fischer, P. Burtscher, N. Moszner, U. S. Schubert, *Polym. Chem.* **2015**, *6*, 5273; d) L. Bécu, H. Sautereau, A. Maazouz, J. F. Gérard, M. Pabon, C. Pichot, *Polym. Adv. Technol.* **1995**, *6*, 316; e) B. J. Blaiszik, S. L. B. Kramer, S. C. Olugebefola, J. S. Moore, N. R. Sottos, S. R. White, *Annu. Rev. Mater. Res.* **2010**, *40*, 179; f) M. Samadzadeh, S. H. Boura, M. Peikari, S. M. Kasiriha, A. Ashrafi, *Prog. Org. Coat.* **2010**, *68*, 159; g) D. R. Paul, L. M. Robeson, *Polymer* **2008**, *49*, 3187; h) T. H. Hsieh, A. J. Kinloch, K. Masania, J. Sohn Lee, A. C. Taylor, S. Sprenger, *J. Mater. Sci.* **2010**, *45*, 1193.
[5] a) J. Nicolas, S. Mura, D. Brambilla, N. Mackiewicz, P. Couvreur, *Chem. Soc. Rev.* **2013**, *42*, 1147; b) J. V. Natarajan, C. Nugraha, X. W. Ng, S. Venkatraman, *J. Controlled Release* **2014**, *193*, 122; c) K. Cho, X. Wang, S. Nie, Z. Chen, D. M. Shin, *Clin. Cancer Res.* **2008**, *14*, 1310; d) F. Masood, *Mater. Sci. Eng., C* **2016**, *60*, 569; e) J. Zhao, M. H. Stenzel, *Polym. Chem.* **2018**, *9*, 259.
[6] a) R. Tantra, A. Knight, *Nanotoxicology* **2011**, *5*, 381; b) M. Reifarth, S. Hoeppener, U. S. Schubert, *Adv. Mater.* **2018**, *30*, 1703704; c) Y. Zhang, R. J. Liang, J. J. Xu, L. F. Shen, J. Q. Gao, X. P. Wang, N. N. Wang, D. Shou, Y. Hu, *Int. J. Nanomed.* **2017**, *12*, 1201; d) C. Leopold, T. Augustin, T. Schwebler, J. Lehmann, W. V. Liebig, B. Fiedler, *J. Colloid Interface Sci.* **2017**, *506*, 620; e) L. Du, H. Z. Xu, T. Li, Y. Zhang, F. Y. Zou, *RSC Adv.* **2017**, *7*, 31310.
[7] L. Reimer, *Transmission Electron Microscopy: Physics of Image Formation and Microanalysis*, Springer, Berlin **2008**.
[8] J. J. Bozzola, L. D. Russell, *Electron Microscopy: Principles and Techniques for Biologists*, Jones & Bartlett Learning, Boston **1999**.
[9] D. Belazi, S. Solé-Domènech, B. Johansson, M. Schalling, P. Sjövall, *Histochem. Cell Biol.* **2009**, *132*, 105.
[10] H. K. Makadia, S. J. Siegel, *Polymers* **2011**, *3*, 1377.
[11] a) M. Kaseem, K. Hamad, Y. G. Ko, *Eur. Polym. J.* **2016**, *79*, 36; b) A. Afzal, A. Kausar, M. Siddiq, *Polym.-Plast. Technol. Eng.* **2016**, *55*, 1988; c) N. Roy, R. Sengupta, A. K. Bhowmick, *Prog. Polym. Sci.* **2012**, *37*, 781.
[12] a) Y. Murakami, T. Endo, S. Yamamura, N. Nagatani, Y. Takamura, E. Tamiya, *Anal. Biochem.* **2004**, *334*, 111; b) R. Gorkin, J. Park, J. Siegrist, M. Amasia, B. S. Lee, J.-M. Park, J. Kim, H. Kim, M. Madou, Y.-K. Cho, *Lab Chip* **2010**, *10*, 1758.
[13] a) http://www.diplib.org/dipimage (accessed: July 2018); b) http://www.diplib.org/diplib (accessed: July 2018).

[14] a) R. E. Burge, N. R. Silvester, *J. Cell Biol.* **1960**, *8*, 1; b) F. Wang, H.-B. Zhang, M. Cao, R. Nishi, A. Takaoka, *Micron* **2010**, *41*, 769; c) I. Pozsgai, *Ultramicroscopy* **1997**, *68*, 69.
[15] E. S. Reynolds, *J. Cell Biol.* **1963**, *17*, 208.
[16] a) K. L. Planken, H. Cölfen, *Nanoscale* **2010**, *2*, 1849; b) C. Minelli, A. Sikora, R. Garcia-Diez, K. Sparnacci, C. Gollwitzer, M. Krumrey, A. G. Shard, *Anal. Methods* **2018**, *10*, 1725.
[17] G. H. Michler, *Electron Microscopy of Polymers*, Springer, Heidelberg **2008**.
[18] L. Sawyer, D. Grubb, G. F. Meyers, *Polymer Microscopy*, Springer Science & Business Media, New York **2008**.
[19] T. Yildirim, A. C. Rinkenauer, C. Weber, A. Traeger, S. Schubert, U. S. Schubert, *J. Polym. Sci., Part A: Polym. Chem.* **2015**, *53*, 2711.
[20] a) COLLECT, Data Collection Software; Nonius B.V., Netherlands **1998**; b) Z. Otwinowski, W. Minor, Processing of X-Ray Diffraction Data Collected in Oscillation Mode, in Methods in Enzymology, Vol. *276*, Macromolecular Crystallography, Part A (Eds: C. W. Carter, R. M. Sweet), pp. 307–326; c) L. Krause, R. Herbst-Irmer, G. M. Sheldrick, D. Stalke, *J. Appl. Cryst.* **2015**, *48*, 3.
[21] G. M. Sheldrick, *Acta Cryst.* **2008**, *A64*, 112.
[22] G. M. Sheldrick, *Acta Cryst.* **2015**, *C71*, 3.

Particle
& Particle Systems Characterization

Supporting Information

for *Part. Part. Syst. Charact.,* DOI: 10.1002/ppsc.201800324

Electron Density of Polymeric Nanoparticles Determined by Image Processing of Transmission Electron Micrographs: Insights into Heavy Metal Staining Processes

Martin Reifarth, Walter Müller, Blerina Shkodra-Pula, Helmar Görls, Ulrich S. Schubert, Rainer Heintzmann, and Stephanie Hoeppener**

Supporting Information

Electron density of polymeric nanoparticles determined by image processing of transmission electron micrographs: Insights into heavy metal staining processes

Martin Reifarth,[1,2] Walter Müller,[3,4,5] Blerina Shkodra-Pula,[1,2] Helmar Görls,[6] Ulrich S. Schubert,[1,2] Rainer Heintzmann,[2,3,4,5] and Stephanie Hoeppener[1,2]**

1 Laboratory for Organic and Macromolecular Chemistry (IOMC)
Friedrich Schiller University Jena
Humboldtstr. 10
07743 Jena, Germany
e-mail: s.hoeppener@uni-jena.de

2 Jena Center for Soft Matter (JCSM)
Friedrich Schiller University Jena
Philosophenweg 7
07743 Jena, Germany

3 Institute of Physical Chemistry
Friedrich Schiller University Jena
Helmholtzweg 4
07743 Jena, Germany
e-mail: rainer.heintzmann@uni-jena.de

4 Leibniz Institute of Photonic Technology
Albert-Einstein-Straße 9
07745 Jena, Germany

5 Abbe Center for Photonics
Albert-Einstein-Straße 6
07745 Jena, Germany

6 Institute for Inorganic and Analytical Chemistry
Friedrich Schiller University
Humboldtstr. 8
07743 Jena, Germany

Determination of the influence of the defocus on the imaging contrast

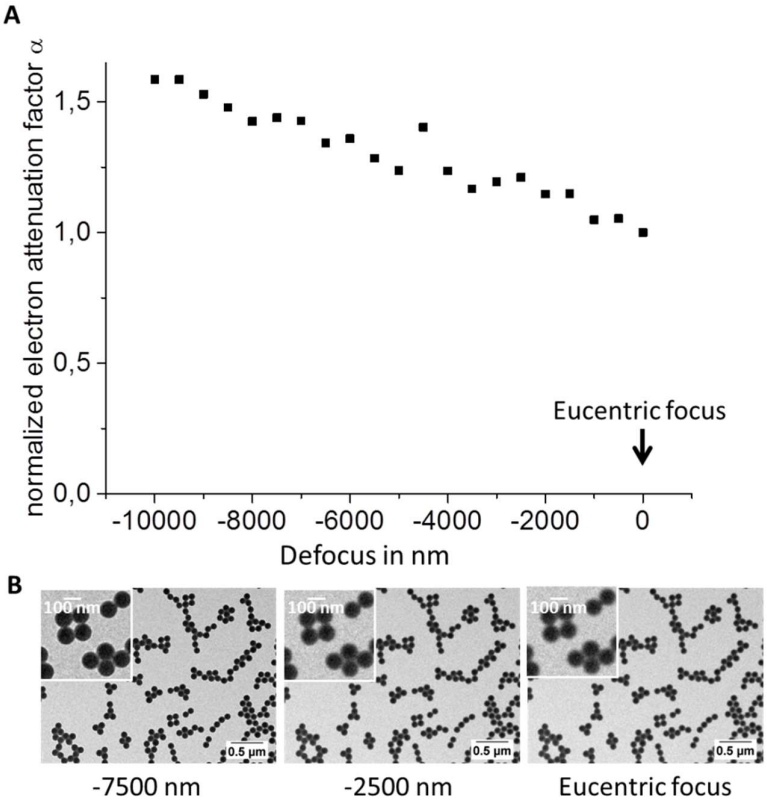

Figure S1: A: Dependence of the electron attenuation factor on the defocus level. Details on the determination of the electron attenuation factor α are discussed in the following section. B: Comparison of the obtained images at different defocus levels. At eucentric focus the outline of the nanoparticles appears to be fuzzy. Reliable automatic image analysis greatly benefits from a certain defocus.

Theoretical estimations

1) Estimation of the depth-of-field and blur circle:

1.1) Illumination numerical aperture

For all images we used a C2 illumination aperture of 100 µm diameter. With this we estimate the half opening angle of the illumination aperture to be 0.45 mrad. Considering -2.5 µm

defocus, this leads to a blur circle with 2.3 nm in diameter, being less than one pixel (nominal pixel size 3.94 nm).

1.2) Detection numerical aperture

For detection we used a SuperTWIN lens with f = 1.7 mm focal length in combination with an objective aperture of 2·r = 40 µm diameter to get the scattering absorption contrast. The half opening angle theta can be estimated to be:

$$\theta = \frac{r}{f} = \frac{20\ \mu m}{1.7\ mm} = 11.8\ mrad$$

This leads to the conclusion that the illumination aperture is in terms of scattering absorption contrast the limiting one to define the depth of field and the defocus blur circle.

2) Estimation of maximum pronounced feature by phase contrast:

As we did argue already in the paper, phase contrast produced by slight defocus can, in contrast to software image sharpening, enhance the sharpness of particle edges without enhancing shot noise. The choice of defocus $l = -2.5\ \mu m$ was made such that spatial features Λ slightly below nominal pixel size of 3.94 nm are maximum enhanced. With a relativistic electron wavelength of $\lambda = 2.50 \cdot 10^{-12}$ m (200 kV acceleration) diffraction theory gives the estimation:

$$\Lambda = \sqrt{2 \cdot l \cdot \lambda} = 3.5\ nm$$

In principle phase contrast is violating Lambert-Beer's, but the violation does mainly occur below pixel sized objects not at our particle size which is more than 25 times above pixel size. Figure S1 is supporting this statement.

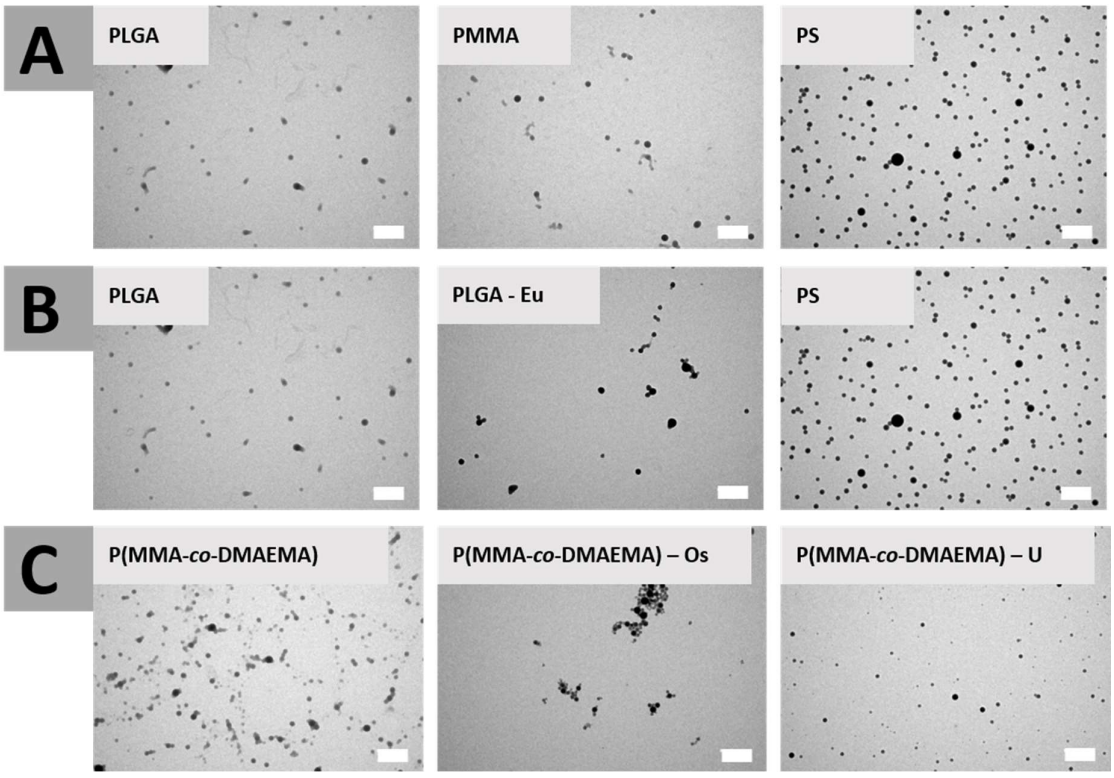

Figure S2: Represented images of investigated nanoparticle samples. All samples were recorded under the same beam conditions. The images of the particles are displayed under the same histogram settings, *i.e.* the same range of grey values (4,000 to 6,200 cts.). This representation enables a rough estimation of the particle image contrast on the basis of a visual observation. Scale bar: 0.5 μm.

Theoretical considerations for the development of the image analysis algorithm

TEM imaging of nanoparticles provides a high resolution view on the particles` features. If a sufficient number of particles is imaged, computational processing routines facilitate the classification of nanoscale objects regarding their size or shape properties with statistical significance. For this purpose, a fixed pixel intensity is used as a threshold to classify signals emerging from the object and to differentiate them from the background signal. The resulting

binary image is subjected to further analyses to obtain a statistical evaluation of size and/or shape of the features.

In transmission electron microscopy, a parallel electron beam propagates through the investigated object. Propagating electrons are scattered due to their interaction with atoms present in the material, where they get deviated and, thus, reach the detection aperture instead of the detector that is located in the beam path of the electron microscope. As a consequence, strongly scattering objects are represented with low intensity values in the TEM image, while the maximum intensity values indicate the background owing to unimpeded propagation of the electrons through the sample. The electron beam is projected only from one direction onto the sample, which is significantly larger than the electron wavelength, causing the acquired image to be a 2D projection of the nanomaterial as indicated by the scheme in **Figure S3**. The following assumptions are only valid for particles with isotropic electron scattering properties, such as polymeric systems, since crystalline materials are known to show anisotropic behavior in TEM. The projection of three-dimensional nanoobjects relates as a consequence to the object thickness. In case of a well-known geometry, a detailed examination of the pixel intensity profile across the lateral dimensions of the object in the EM image can result in a deeper comprehension of the attenuation characteristics of the electron beam propagating through the nanomaterial.

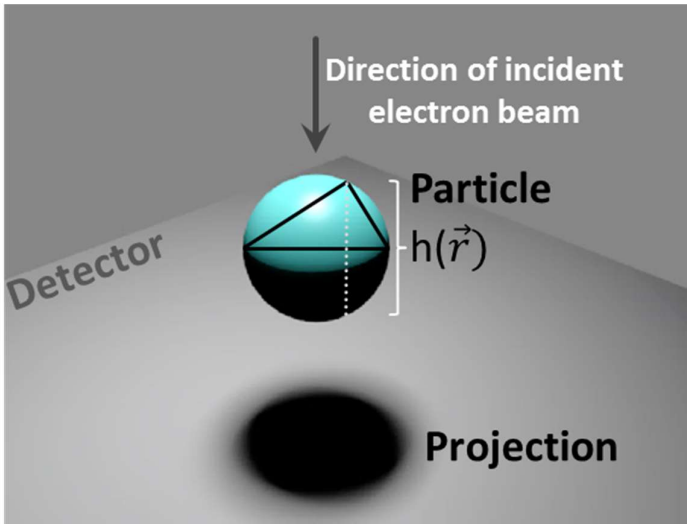

Figure S3: Schematic representation of a spherical nanoparticle imaged by transmission electron microscopy. The image of the particle constitutes its projection on the detector. The white dashed line represents the height $\boldsymbol{h(\vec{r})}$, *i.e.* the transmission path of the incident electron beam through the particle thickness in dependence of the spatial vector $\boldsymbol{\vec{r}}$.

Considering the polymeric particles as an ideal sphere, the height h of the particle, *i.e.* the propagation length of the electron beam through the spherical colloid in dependence of the image coordinates $\vec{r}$, can be described according to equation (1),

$$(1)\ h(\vec{r}) = \begin{cases} 2\sqrt{R^2 - (\vec{r} - \overrightarrow{r_C})^2},\ R^2 - (\vec{r} - \overrightarrow{r_C})^2 \geq 0 \\ 0,\ else \end{cases}.$$

where $\overrightarrow{r_C}$ represents the coordinates of the center of the particle with the particle radius R. The decrease of the electron beam intensity has been reported to follow an exponential decay, which can be employed for instance to determine a sample thickness of ideal films.[1] Equation 2 describes the intensity distribution I as a function of $\vec{r}$ with the background signal intensity I_0 assuming exponential attenuation. Hence, the attenuation profile depends on the material-specific attenuation coefficient α and may be considered as a Lambert-Beer-like relation.

$$(2)\ I(\vec{r}) = \begin{cases} I_0 e^{-2\alpha\sqrt{R^2-(\vec{r}-\overrightarrow{r_C})^2}}, R^2-(\vec{r}-\overrightarrow{r_C})^2 \geq 0 \\ I_0, else \end{cases}.$$

In order to support these assumptions, we imaged spherical polystyrene beads with an approximate size of 110 nm by TEM. **Figure S4A** depicts a low-magnification linear raw-image of a number of beads. We selected a representative particle as indicated in the red box and in Figure S4B and in Figure S4C, the intensity values of the particle are plotted in dependence of the pixel positions. It should be noted that the raw data shown here represents the linear detector signal that has not been subjected to contrast enhancement routines. For comparison, the theoretical intensity profile which is expectable according to equation (2) is depicted in Figure S4E (Figure S4D shows the simulated image of an ideally spherically shaped particle). Figure S4F, moreover, displays a cross-section through the intensity plot of the calculated intensity profile (as indicated by the red solid line) along with the extracted data of the particle (dotted data). It has to be mentioned that a local background I_0 was calculated which was applied to normalize the pixel intensity of the measured image prior to data extraction.

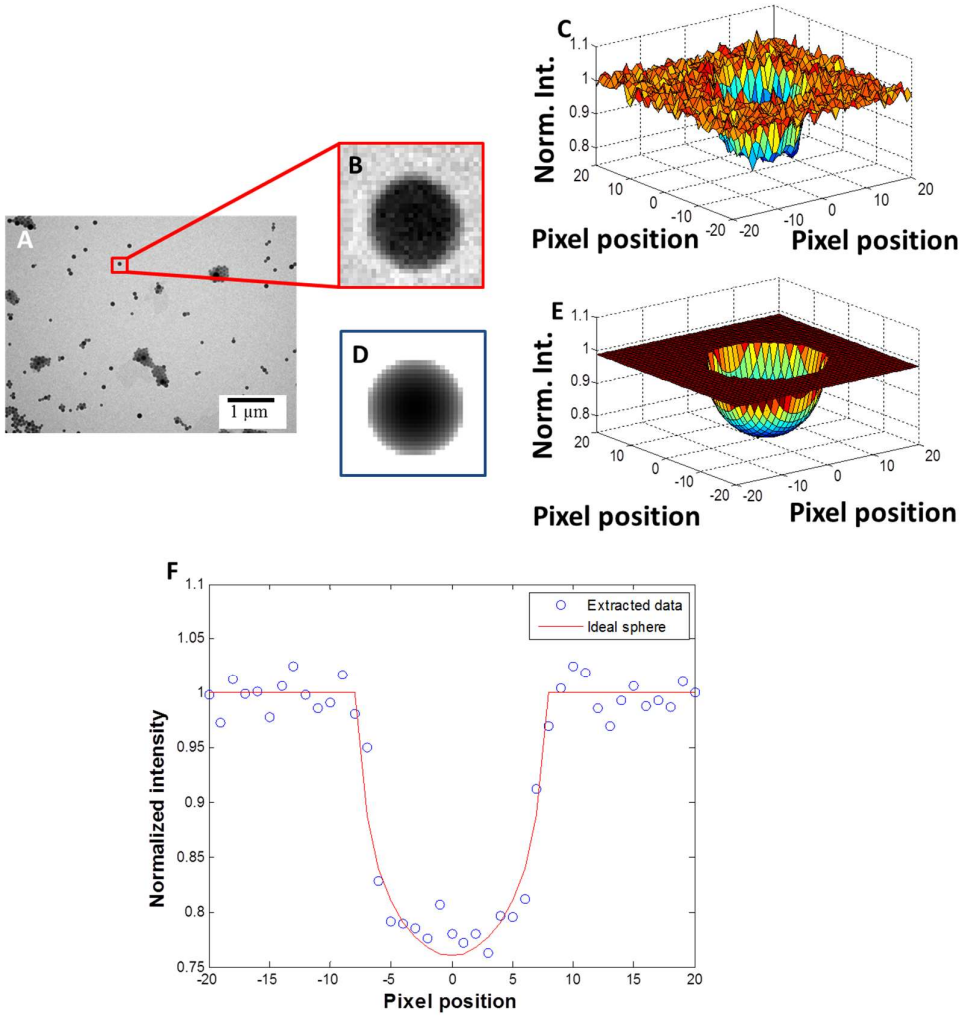

Figure S4: Applicability of Lambert Beer's law to the applied contrast method. A) Low-magnification of a raw-image of polystyrene beads. B) Magnification of A). C) Plot of normalized intensity values. D) Simulated image of a particle with ideally spherical shape according to equation (2). E) Plot of predicted normalized intensity values of an ideally spherical particle. F) Intensity profile of the particle (extracted data in blue) compared to intensity profile of an ideal sphere (red solid line).

The developed image analysis algorithm aims to determine the attenuation characteristics of a number of particles imaged simultaneously. As a consequence, the attenuation factor α can

directly be deduced from the intensity plot according to equation (2) which would need to be carried out for a certain number of particles individually. However, the analysis of each bead intensity profile individually as shown in Figure S4F and the intricacy to fit the function according to equation (2) *via* the unknown particle parameters α and R would (also with respect to the unknown bead positions) constitute a demanding task particularly with respect to the fact that automated image analysis might in this case be error-prone. In order to overcome this issue, an alternative route was followed to extract the data from TEM images. We made use of the fact that the logarithmic pixel intensity value should be proportional to height of the material at the respective position of the pixel (equation 3, 4).

(3) $\frac{I(\vec{r})}{I_0(\vec{r})} = e^{-\alpha \cdot h(\vec{r})}$,

(4) $\ln I_C(\vec{r}) = \alpha \cdot h(\vec{r})$, Introducing the normalized intensity value $I_c(\vec{r}) = \frac{I_0(\vec{r})}{I(\vec{r})}$.

In order to be robust against intensity noise, we decided not to read out only the maximum intensity value which corresponds to the maximum height of the particle (particle diameter in axial dimension), but to consider all intensity values of the thresholded particles. Their summation along both image coordinates x', y' results in a value proportional to the particle volume (equation 5).

(5) $V = \sum_{x',y'} h(\vec{r}) \cdot p = \frac{1}{\alpha} \cdot \sum_{x',y'} \ln I_c(x', y') \cdot p$,

x', y' represent the image coordinates along the particle dimensions and p the pixel area [μm^2].

Knowledge of the particle volume facilitates the determination of the particle diameter d in axial dimension. The particle diameter is, furthermore, accessible by the area of the projected particle in the image. Comparison of the particle diameter deduced from intensity measurements and from the particle area facilitates the determination of the material-specific attenuation coefficient α for each individual particle. To increase the statistical validity of this

value, we investigated a large number of particles. Therefore, we took advantage of the fact that the particles possess a certain size distribution. Data extraction from the raw image facilitated a plot of the diameter determined by the particle area *vs.* the cubic route of the sum of logarithmized intensities (indicating the particle diameter in axial direction). The obtained graphs describe a linear relationship according to equation (6) whose slope characterizes the attenuation.

$$(6)\ d = \sqrt[3]{\frac{6V}{\pi}} = \sqrt[3]{\frac{1}{\alpha}} \cdot \sqrt[3]{\frac{6}{\pi}\sum_{x',y'}^{\text{area}} \ln I_n(x',y') \cdot p}$$

Equation (6) can be expressed in such a way that a linear function follows from the expression of the l.h.s. *vs.* the particle diameter d.

$$(7)\ \sqrt[3]{\frac{6}{\pi}\sum_{x',y'}^{\text{area}} \ln I_n(x',y') \cdot p} = \sqrt[3]{\alpha} \cdot \mathrm{d}$$

From this, the attenuation coefficient α [μm^{-1}] can be determined.

Implementation of the algorithm

In order to achieve a profound data elaboration based on the mathematical relations according to eqs. (1) – (7), we developed an evaluation algorithm based on the image processing toolbox DIP*image* for MATLAB.

Initially, the image is normalized by a locally estimated background. This is achieved in two image processing steps. In a first step the image is globally normalized by dividing it by the maximum value of its Gauss filtered version. As a result, the background intensities fluctuate around the value one. In a second step, the normalization is improved by a local background estimate. A thresholding is defined to roughly differentiate between particle signal and image background (typically 91% of brightness). This first background mask is then slightly enlarged. A Gaussian filtering of the scalar normalized image leads, along with an inpainting

of the mask covered parts, to a reasonable estimation of a non-flat background. A further thresholding (typically 95% of brightness) of the locally background corrected image provides a precise second mask which facilitates the discrimination between the background and the particles with the highest precision.

Particle recognition, labeling and geometrical characterization represent central tasks in this algorithm. The recognition is achieved by local maxima determination in the Gaussian-filtered background-corrected image (based on the second mask) which results in appropriate estimations of the particle center positions. A watershed algorithm, seeded by the estimated center positions, facilitates the determination of particle boundaries in case of overlapping particle signals. On the basis of the result achieved by the watershed algorithm and the second mask, most particles are well selected and automatically labeled. In order to exclude geometries which imply shapes other than spherical particles, a routine based on the determination of the Ferret aspect ratio is applied. Consequently to all aforementioned steps, the particle area as well as the sum of intensities is determined for further elaboration according to equation (7).

Table S1: The image processing algorithm requires the pre-selection of some parameters, which are required to be input prior to analysis. These are:

noiseLPrad – parameter to reduce noise in frequency space as initial image processing step

minestmrad – minimal diameter of objects (in pixels) to be considered as particles

maxestmrad – maximal diameter

radBgAre – measure for largest coherent background area

fglimit – threshold used for first analysis to distinguish between particle signal and background area

fglimit2 – threshold used for subsequent analysis

maxEllipt – maximum ellipticity (based on the determination of Feret‘s diameters) of particles considered for analysis

number of images – number of analysed images

number of particles – number of analysed particles

These parameters were selected manually by preliminary inspection of the images.

All images have been processed individually and average values of all determined α weighted by the number of analyzed particles were calculated.

Sample	treatment	noiseLPrad	minestmrad	maxestmrad	radBgAre	fglimit	fglimit2	maxEllipt	number of images	number of particles
NP1	blank Os U Pb	3	10	80	80	0.91	0.96	1.1	132 320 237 ---	5 7 5 ---
NP2	blank Os U Pb	3	4	30	30	0.93	0.96	1.1	147 221 351 510	7 8 6 10
NP3	blank Os U Pb	3	4	30	30	0.93	0.96	1.1	3288 388 4614 612	8 10 8 10
NP4*	blank Os U Pb	8	20	80	40	0.91	0.96	1.1	166 115 133 117	16 13 15 14
NP5	blank Os U Pb	3	4	30	30	0.93	0.96	1.1	271 --- 636 73	6 --- 8 6
NP6	blank Os U Pb	3	4	30	30	0.93	0.96	1.1	626 82 275 57	6 5 7 7
NP7	blank** Os U** Pb**	4 3 4 4	8 4 8 8	30 30 30 30	30 30 30 30	0.96 0.93 0.97 0.97	0.96 0.96 0.97 0.97	1.1 1.1 1.1 1.1	55 231 126 59	8 14 13 8

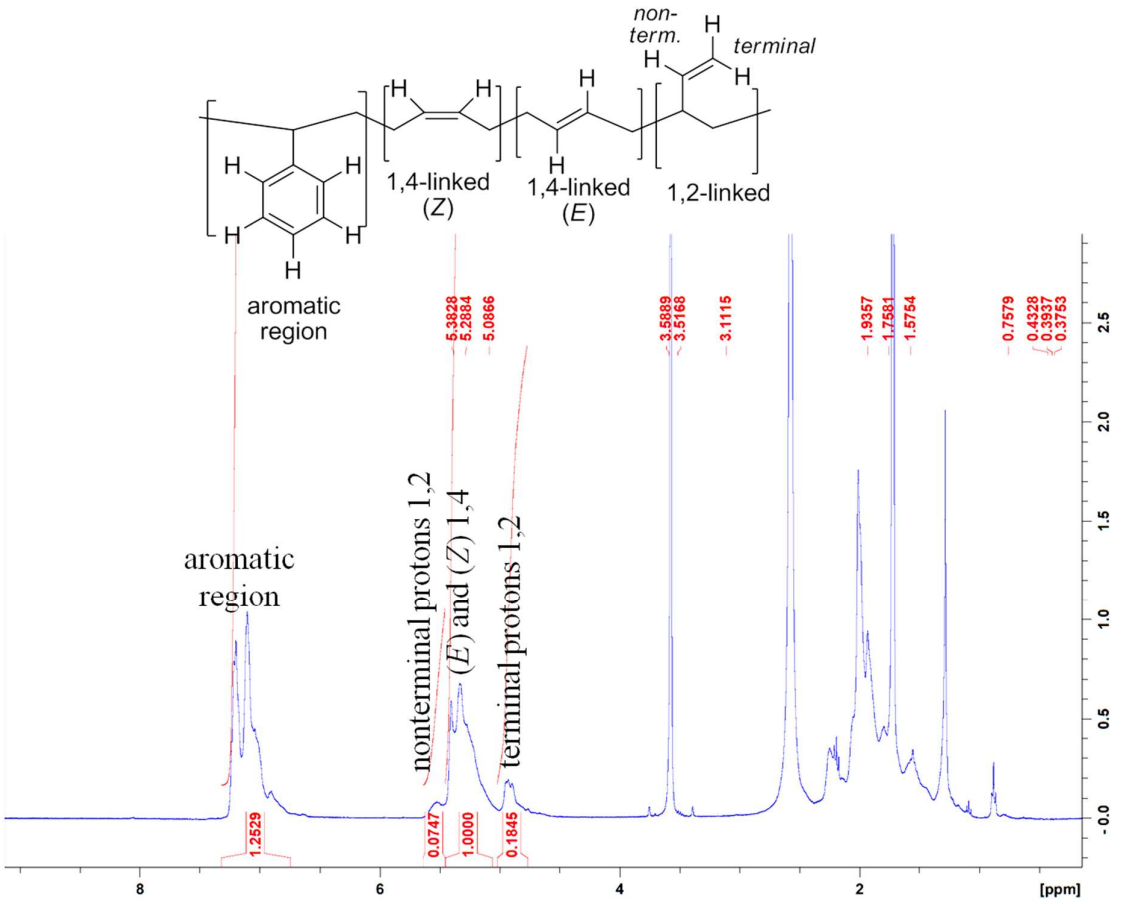

Figure S5: ^{1}H-NMR spectrum of polymer **P6** (300 MHz, THF-d6). The proton NMR spectrum of the polymer suggests the presence of (*E*) and (*Z*) as well as terminal olefins within the structure of the polymer.

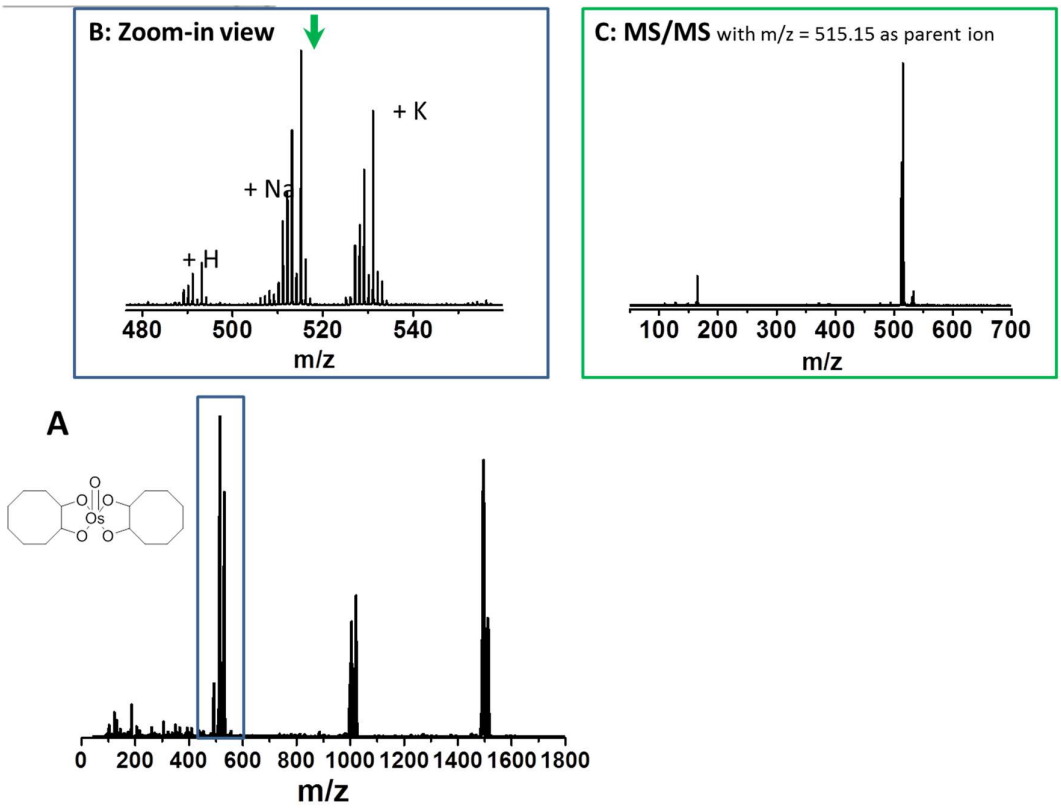

Figure S6: A) ESI-ToF-MS of (*Z*)-cyclooctene exposed to OsO_4 staining medium. B) Zoom-in view into A. C) MS/MS experiment with m/z = 515.15 as parent ion as indicated with the green arrow in B).

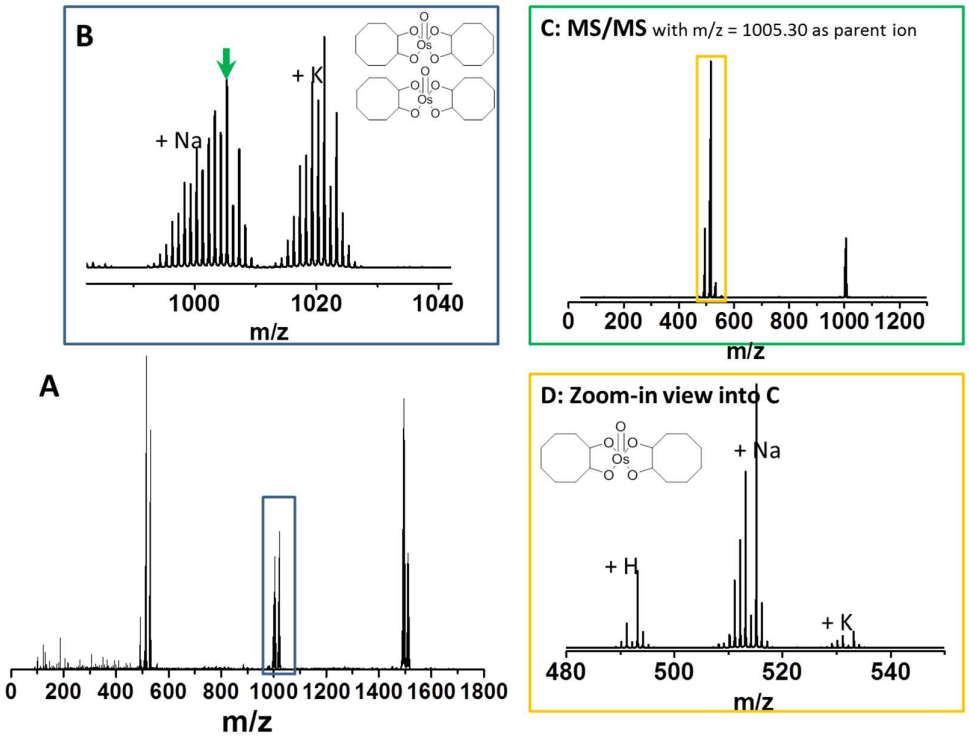

Figure S7: A) ESI-ToF-MS of (*Z*)-cyclooctene exposed to OsO_4 staining medium. B) Zoom-in view into A. C) MS/MS experiment with m/z = 1005.30 as parent ion as indicated with the green arrow in B. D) Zoom-in view into C).

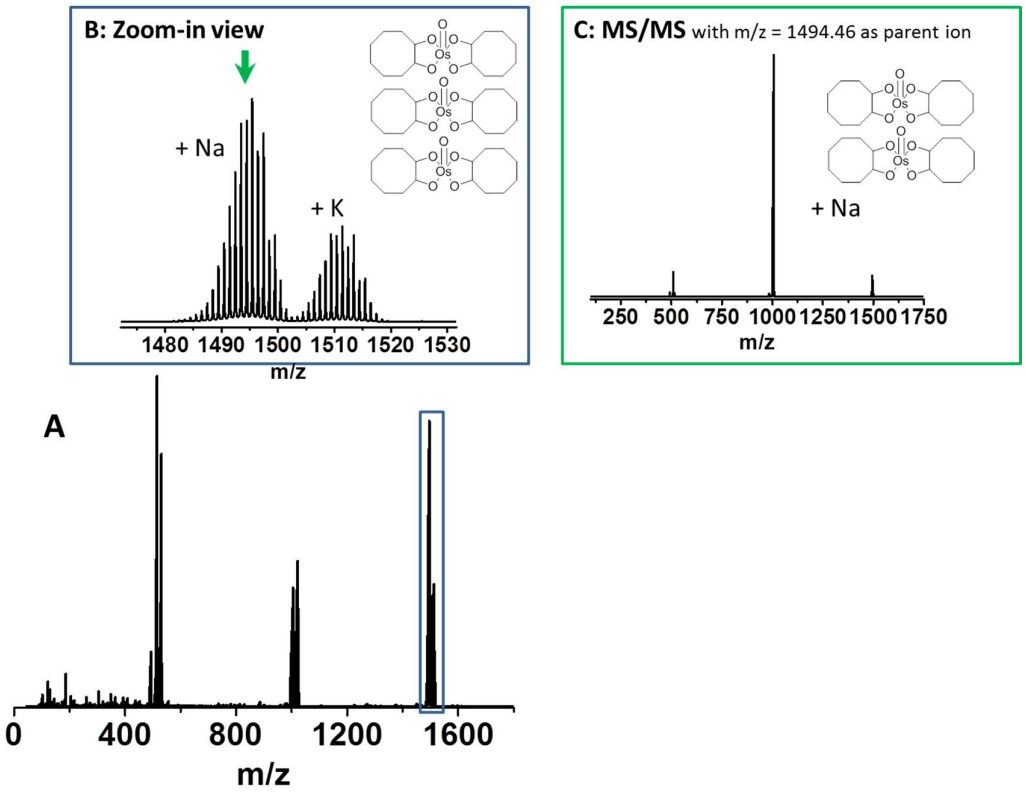

Figure S 8: A) ESI-ToF-MS of (*Z*)-cyclooctene exposed to OsO_4 staining medium. B) Zoom-in view into A). C) MS/MS experiment with m/z = 1494.46 as parent ion as indicated with the green arrow in B).

[1] a) R. E. Burge, N. R. Silvester, *J. Biophys. Biochem. Cytol.* **1960**, 8, 1; b) F. Wang, H.-B. Zhang, M. Cao, R. Nishi, A. Takaoka, *Micron* **2010**, 41, 769; c) I. Pozsgai, *Ultramicroscopy* **1997**, 68, 69; d) L. Reimer, *Transmission electron microscopy: physics of image formation and microanalysis*, Springer, **2013**.

Publication P4

"Cellular uptake of PLA nanoparticles studied by light and electron microscopy: synthesis, characterization and biocompatibility studies using an iridium(III) complex as correlative label"

M. Reifarth, D. Pretzel, S. Schubert, C. Weber, R. Heintzmann, S. Hoeppener, U. S. Schubert:

Chem. Commun. **2016**, *52*, 4361-4364

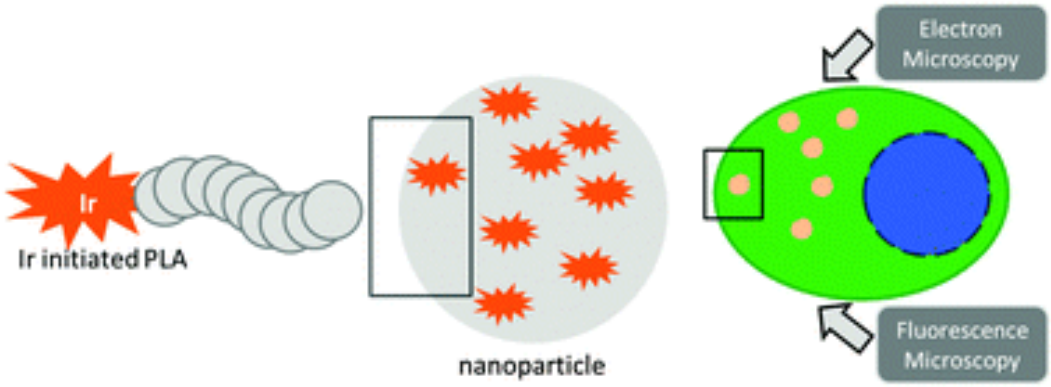

ChemComm

COMMUNICATION

View Article Online
View Journal | View Issue

Cite this: *Chem. Commun.*, 2016, 52, 4361

Received 30th November 2015,
Accepted 22nd February 2016

DOI: 10.1039/c5cc09884j

www.rsc.org/chemcomm

Cellular uptake of PLA nanoparticles studied by light and electron microscopy: synthesis, characterization and biocompatibility studies using an iridium(III) complex as correlative label†

Martin Reifarth,[abcd] David Pretzel,[ab] Stephanie Schubert,[be] Christine Weber,[ab] Rainer Heintzmann,*[cd] Stephanie Hoeppener*[ab] and Ulrich S. Schubert*[ab]

We present the synthesis of polylactide by ring-opening polymerization using a luminescent iridium(III) complex acting as initiator. The polymer was formulated into nanoparticles, which were taken up by HEK-293 cells. We could show that the particles provided an appropriate contrast in both superresolution fluorescence and electron microscopy, and, moreover, are non-toxic, in contrast to the free iridium complex.

The biodegradable polyester polylactide (PLA)[1,2] has found a wide range of applications in medicine and technology, since it is both nontoxic and biorenewable.[3–7] Therefore, it has become a standard material for application in many drug carrier systems.[8–11] In order to gain deeper insight into the particles' mode of action, it is necessary to track them within cells and tissue. While fluorescence labeling of nanoparticles represents a standard method to understand the fate of particles in single cells[10,12] or entire organisms,[13,14] transmission electron microscopy (TEM) is less of a standard. Since TEM images provide knowledge about the cellular ultrastructural details with a resolution far better than the particle size, electron microscopy should yet be considered as a useful tool. Due to the intrinsic low contrast provided by biological specimens, it has to be enhanced by treating the sample with heavy metal salts. PLA particles, uptaken by cells, do not provide a reliable contrast either and can thus only be identified as they are slightly less electron dense compared to their surrounding biological environment.[15,16] Alternatively, their electron density can be enhanced *via* incorporation of nanocrystals[17] or heavy metal complexes.[18,19] Cyclometalated iridium(III) complexes seem ideal for this purpose, since they exhibit large extinction coefficients, good luminescent quantum yields as well as large Stokes shifts,[20] which is desirable in fluorescence imaging.‡ Additionally, iridium as a heavy element provides a suitable TEM contrast. Although the utilization of cyclometallated iridium complexes in cell imaging *in vivo* was reported,[21–23] leakage of a dye from the particles can result in severe toxic effects.[24] This can be prevented by the covalent attachment of the label to the polymer used for the particle formation (Fig. 1). In this article, we describe the synthesis and characterization of PLA nanoparticles covalently labeled with a luminescent iridium–coumarin coordination compound to provide appropriate contrast in fluorescence as well as in TEM imaging. This method is not limited to the end group functionalization of polylactide only, but it can also be applied in the synthesis of other polyesters such as poly(ε-caprolactone).[25] Also functionalization of polymers, such as poly(acrylic acid) derivatives, is feasible, which could potentially be applied to emphasize a selected block within complex polymeric architectures or to target specific cell types.

We synthesized a 2,2′-bipyridine analogous ligand **1** with a hydroxyl functionality *via* a copper-mediated azide alkyne click reaction (Scheme 1, NMR spectra of all compounds Fig. S1–S5 and S7, ESI†).[26,27] The final cationic luminescent complex was obtained from an iridium precursor complex[28] **2** and ligand **1**. Subsequent to an ion exchange, the organo-soluble iridium(III) complex with PF_6^- as counter ion **3** was obtained with high purity. Due to its absorption

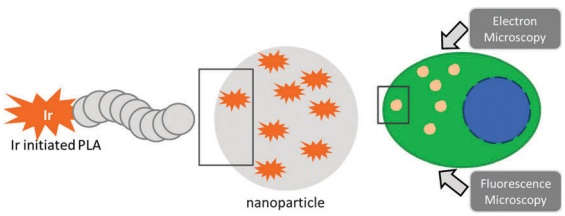

Fig. 1 Sketch of experiments. Iridium(III) complex initiated PLA was used to form nanoparticles. Cellular uptake was studied by electron and fluorescence microscopy.

[a] *Laboratory of Organic and Macromolecular Chemistry (IOMC), Friedrich Schiller University Jena, Humboldtstr. 10, D-07743 Jena, Germany. E-mail: s.hoeppener@uni-jena.de, ulrich.schubert@uni-jena.de*
[b] *Jena Center for Soft Matter (JCSM), Friedrich Schiller University Jena, Philosophenweg 7, D-07743 Jena, Germany*
[c] *Institute of Physical Chemistry and Abbe Center of Photonics, Friedrich-Schiller-University Jena, Helmholtzweg 4, D-07743 Jena, Germany. E-mail: rainer.heintzmann@uni-jena.de*
[d] *Leibniz Institute of Photonic Technology, Albert-Einstein-Straße 9, D-07745 Jena, Germany*
[e] *Institute of Pharmacy, Department of Pharmaceutical Technology, Friedrich Schiller University Jena, Otto-Schott-Str. 41, D-07745 Jena, Germany*

† Electronic supplementary information (ESI) available: Experimental part, NMR spectra, kinetic plots, polymer and particle characterization. See DOI: 10.1039/c5cc09884j

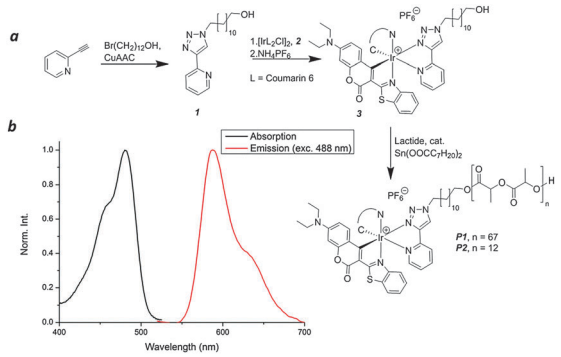

Scheme 1 (a) Reaction scheme. (b) Absorption and emission spectrum of compound **P1**.

maximum at 483 nm, caused by ligand-based electronic transitions,[26] and a high extinction coefficient, it can ideally be illuminated by the 488 nm transition of an Ar^+ ion laser or appropriate solid-state substitutes, which are widely applied in high resolution fluorescence microscopy. In many applications described in literature, 2-phenylpyridine and derivatives, respectively, are utilized as cyclometallating ligands, absorbing in the UV and near VIS range which results in cell damage and scattering loss of the high energetic radiation.[29–32] In addition, the emission of the air-stable complex is independent of the pH value of the surrounding medium (Fig. S10, ESI†), facilitating stable and quantifiable emission microscopy of acidic as well as basic regions in cells and tissue.[33]

To covalently attach the dye molecule to PLA, **3** was applied as initiator for the ring opening polymerization (ROP) of L-lactide[34,35] using the well-established catalyst tin(II)2-ethylhexanoate (characterization data of the polymers are summarized in Table 1). Despite the amine and lactone structures present in the coumarin ligands that could potentially interfere with the ROP mechanism, kinetic studies revealed a linear increase of the polymer molar mass with monomer conversion as well as a linear pseudo-first-order kinetic plot as monitored by size-exclusion chromatography (SEC, $[M]_0/[I]_0$ = 90, k_P = 0.15 L mol^{-1} s^{-1}). Together with the fact that monomodal and narrow molar mass distributions ($Đ$ < 1.2) were observed, this shows that the ROP could be efficiently controlled in terms of molar mass (kinetic plots Fig. S9, ESI†). The signals derived from the initiator could be well assigned in the ^{1}H NMR spectrum of the purified PLA **P1**. The fact that the molar mass determined from the NMR spectrum $M_{n,NMR}$ corresponds to the expected molar mass $M_{n,theo}$ hints towards a high end-group fidelity. In addition, the covalent attachment of the iridium complex was confirmed by SEC using diode array detection (DAD, Fig. 2), revealing a DAD signal at the absorption maximum of the complex (λ = 485 nm) that overlaps with the corresponding refractive index signal (Fig. S6, ESI†). Moreover, the luminescence spectra recorded from the polymer and the free complex are in good agreement (Fig. S8, ESI†). To further prove the covalent attachment of the iridium complex at the α-chain end of the PLA, a second polymer **P2** with a lower degree of polymerization (DP) was prepared. Since both polymers carry a positive charge (due to the complex attached), the singly charged chains could be well ionized by matrix-assisted laser desorption/ionization time of flight mass spectrometry (MALDI-ToF-MS, Fig. 2). Two major distributions with a *m/z* difference corresponding to the mass of one lactide monomer ($\Delta m/z$ = 144) were observed. As shown by the overlay of the measured and the calculated isotopic patterns, the *m/z* distribution E (as marked in Fig. 2) can be assigned to PLA chains with the positively charged complex as end group. The less abundant species O correspond to PLA chains with the same end group but with an odd number of lactic acid repeating units, which result from intermolecular trans-esterification reactions occurring

Table 1 Selected characterization data of the synthesized polymers[f]

	[M]:[I]:[C]	Conv.[a] [%]	$M_{n,theo}$[b] [g mol^{-1}]	$M_{n,NMR}$[c] [g mol^{-1}]	$M_{n,SEC}$[d] [g mol^{-1}]	$Đ_{SEC}$[d]	$M_{n,MALDI}$[e] [g mol^{-1}]	$Đ_{MALDI}$[e]
P1	90:1:1	80	11 400	11 700	6800	1.17	5000	1.04
P2	15:1:1	82	2900	3000	2180	1.21	2460	1.06

[a] Conversion determined from the ^{1}H-NMR spectra of the polymerization mixtures. [b] M_{theo} = $[M]_0:[I]_0$ conv. 144 g mol^{-1} + 1366 g mol^{-1}. [c] Referred to ^{1}H-NMR peak at δ = 8.52 ppm (m, 1H). [d] Eluent: DMAc-LiCl, PMMA calibration, RI detection. [e] DCTB, NaCl. [f] Polymerization conditions: $[M]_0$ = 0.5 M, toluene, reflux.

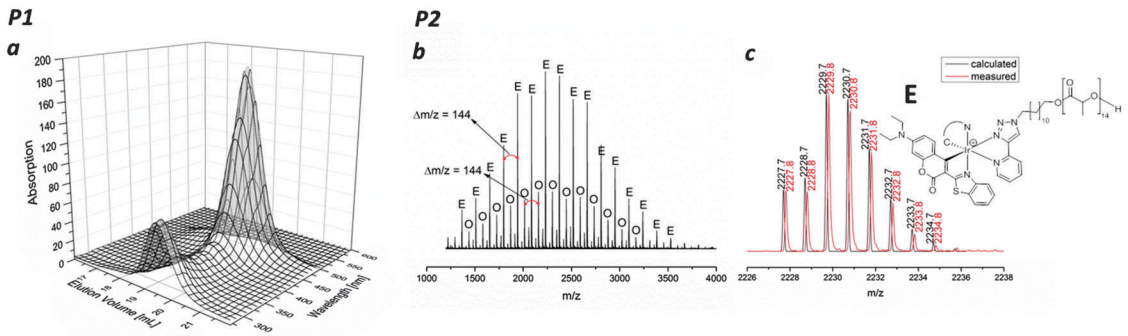

Fig. 2 (a) 3D plot of the SEC trace of **P1** (eluent: DMAc-LiCl, PMMA calibration, DAD detection). (b) MALDI-ToF mass spectrum of **P2** (DCTB, NaCl). An *m/z* difference of 144 can be observed. High abundance intensities can be assigned to the positively charged complex attached to an even number of lactic acid repeating units (c) overlay of measured and calculated isotopic pattern of the most abundant peak.

Table 2 Characterization of the nanoparticle samples.[a] Particle size did not change after lyophilization

	After preparation		After lyophilization		Zeta potential [mV]
	d [nm]	PDI	*d* [nm]	PDI	
NP1[b]	323	0.201	301	0.213	0.2
NP2[c]	307	0.151	293	0.206	7.8

[a] Diameters and PDI determined by DLS measurements. [b] Prepared from 100 wt.-% **P1**. [c] Prepared from 50 wt% **P1** and 50 wt% unlabeled polymer.

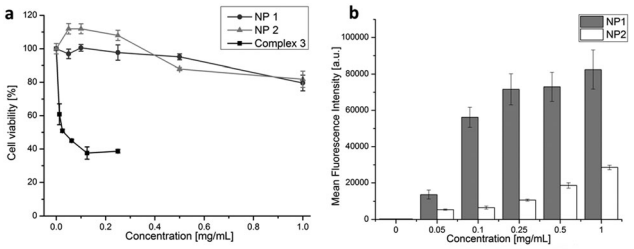

Fig. 3 (a) Viability of HEK cells after 24 hours incubation with the complex **3** resp. **NP1**, **NP2**. (b) Flow cytometry investigation of concentration dependent uptake of **NP1** and **NP2** following 24 h incubation are displayed as mean fluorescence intensities of the analyzed cell populations. Cells cultivated with culture medium served as control. All data are expressed as mean ± SD of triplicates.

during the tin(II) 2-ethylhexanoate catalyzed ROP.[36,37] Hence, ROP using **3** as initiator represents an efficient method to incorporate a defined amount of metal into a well-defined PLA.

Polymer **P1** was formulated into nanoparticles using the single emulsion technique (Table 2). Assuming one complex per polymer chain, two nanoparticle formulations were prepared resulting in particles with an estimated metal content of 2% (**NP1**) and 1% (**NP2**, Table 2), respectively. DLS measurements show unimodal size distributions of both nanoparticle suspensions with particle sizes of approximately 300 nm. Though having a low positive zeta potential, which we attribute to the attachment of the positively charged complex, the particles remained stable in suspension and did not tend to aggregate (TEM images Fig. S11, ESI†).

The toxicity of the nanoparticles **NP1**, **NP2** and compound **3** was determined using the human embryonic kidney cell line HEK-293. The *in-vitro* cytotoxicity experiments were performed *via* a XTT assay. After 24 h of incubation with different concentrations of complex **3**, the whole applied concentration range led to a significant reduction of cell viability pointing out a clear cytotoxic potential of the free complex. In case of **NP1** and **NP2**, the metabolic activity of the treated cells was found to be at the level of the untreated control within the duration of the experiment (Fig. 3). A possible explanation for this observation could be related to the shielding of the majority of the toxic complex within the structure of the formulated NP, hence, reducing the accessibility of the harmful complex, particularly, since complex leakage is prevented due to its covalent attachment to the polymer chains. The concentration-dependent uptake of the complex containing **NP1** and **NP2** was quantified by flow cytometry (FC) measurements after particle incubation with different concentrations. The measured mean fluorescence intensities display a parameter for the relative amount of labeled NPs associated with the cells (internalized or attached to the outer cell membrane). A clear concentration-dependent increase in fluorescence intensity was observed for both **NP1** and **NP2**. Due to the reduced complex content a lower signal level was expected and observed for **NP1** – still, the level of decrease was more pronounced than the actual metal content and fluorescence measurement of the pure particles would suggest (Fig. S12, ESI†). Hence a weaker uptake efficiency caused by an interaction of **NP2** with serum proteins present in the cell culture media is most likely the reason for that observation.[38] It is known that positively charged particles like **NP2** show an increased interaction with proteins as compared to particles with a neutral surface charge like **NP1** – resulting in the formation of a protein corona on the particle surface.[39] The protein-decoration of **NP2** could result in a

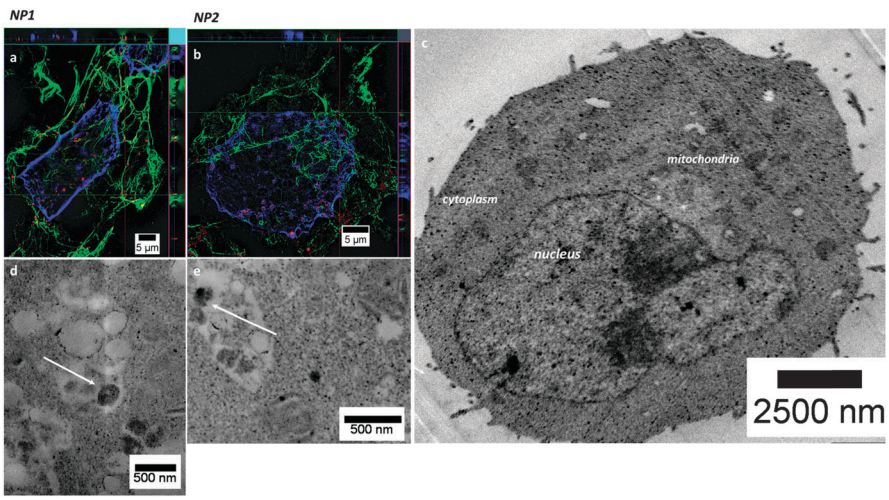

Fig. 4 HEK cells incubated with **NP1** (a and d) und **NP2** (b and e) 24 h, 250 µg mL^{-1}. (a and b): HR SIM. 63 × 1.4 NA oil obj. Blue: nucleus. Green: cytoskeleton. Red: NP. The 3D ortho plot displays the distribution of NPs throughout the cell body. (c–e): HAADF-STEM images. (c) Low magnification image of a HEK-293 cell. Nucleus, cytoplasm and NPs mitochondria are observable. Zoomed-in views of a cell incubated with **NP1** (d) and **NP2** (e). White arrows highlight the uptaken nanoparticles that are localized in cellular endosomes. See also Fig. S13 (ESI†).

reduced cellular uptake due to an altered cell-membrane interaction and recognition of the particles.[40] Whereas FC methods provide statistical information about the cellular uptake efficiency, high resolution imaging techniques facilitate the visualization of internalized particles and, thus, enable an understanding of the fate of the particles in a single cell. Structured illumination microscopy, as a superresolution microscopy technique, was chosen, since it allows image acquisition with a large variety of dyes. The HEK-293 cells, adherently grown on coverslips, were stained by applying standard nucleus and cytoskeleton specific dyes. Alexa488-phalloidin, staining the actin-cytoskeleton, as well as the internalized nanoparticles were excited with the 488 nm laser line simultaneously. Due to the large Stokes shift of complex **3**, the resulting emission could easily be separated from the Alexa488 dye fluorescence by appropriate choice of emission filters. In order to gain information about the particle distribution in axial direction inside the cell, for SIM image acquisition, optical z-sectioning through the cell body was carried out. It could be shown that the fluorescent NPs show intracellular, cytoplasmic localization (Fig. 4). In addition, TEM images were acquired. For this purpose, cells were fixed with glutaraldehyde and osmium tetroxide prior to embedding. Since further contrast-enhancing methods were omitted, the sections were imaged in high-angle annular darkfield scanning transmission electron microscopy (HAADF-STEM) mode. For STEM imaging, ultrathin sections of 80 nm were cut using an ultra-microtome. By imaging ultrathin slices with TEM, the internationalization of the nanoparticles could also be confirmed (Fig. 4). Uptaken particles were found in endosomes. Both nanoparticle probes provide a contrast that is sufficient to point them out within the cellular context.

In conclusion, we synthesized a luminescent cyclo-metallated iridium(III) complex for the utilization as a label in fluorescence microscopy. The complex was used as an initiator for the ROP of lactide to form well-defined polylactides with various chain lengths. The polymers were formulated into nontoxic nanoparticles.

Cellular uptake was proven by FC, SIM and TEM. We could demonstrate that the nanoparticle probes provide both appropriate contrasts for TEM imaging in cellular context as well as a good fluorescence signal in SIM. In further studies, this system will be used as a label for correlative light and electron microscopy.

We thank E. Preußger for cell cultivation experiments, I. Yildirim for providing the unlabeled PLA and Dr. A. Winter for valuable discussions. S. Crotty and N. Fritz are acknowledged for their support with MALDI- and ESI-ToF-MS as well as N. Blaubach for ICP-OES measurements. M. R. is grateful for the financial support in the frameworks of "Carl-Zeiss-Strukturmaßnahme" and ProExzellenzinitiative "NanoPolar" of the state of Thuringia. The TEM was obtained with a grant from the European Funds for Regional Developments (EFRE) and the DFG.

Notes and references

‡ Although the luminescence of the described complex is attributed to phosphorescence, the applied microscopy technique is referred to as fluorescence microscopy.

1 K. E. Uhrich, S. M. Cannizzaro, R. S. Langer and K. M. Shakesheff, *Chem. Rev.*, 1999, **99**, 3181–3198.
2 A.-C. Albertsson and I. K. Varma, *Biomacromolecules*, 2003, **4**, 1466–1486.
3 C. M. Thomas and J.-F. Lutz, *Angew. Chem., Int. Ed.*, 2011, **50**, 9244–9246.
4 N. Hernandez, R. C. Williams and E. W. Cochran, *Org. Biomol. Chem.*, 2014, **12**, 2834–2849.
5 R. Auras, B. Harte and S. Selke, *Macromol. Biosci.*, 2004, **4**, 835–864.
6 R. E. Drumright, P. R. Gruber and D. E. Henton, *Adv. Mater.*, 2000, **12**, 1841–1846.
7 J. M. Anderson and M. S. Shive, *Adv. Drug Delivery Rev.*, 1997, **28**, 5–24.
8 N. Yang, Y. Jiang, H. Zhang, B. Sun, C. Hou, J. Zheng, Y. Liu and P. Zuo, *Mol. Pharmaceutics*, 2015, **12**, 232–239.
9 S. K. Pandey, D. K. Patel, R. Thakur, D. P. Mishra, P. Maiti and C. Haldar, *Int. J. Biol. Macromol.*, 2015, **75**, 521–529.
10 E. Jabbari, X. Yang, S. Moeinzadeh and X. He, *Eur. J. Pharm. Sci.*, 2013, **84**, 49–62.
11 O. O. Maksimenko, L. V. Vanchugova, E. V. Shipulo, G. A. Shandryuk, G. N. Bondarenko, S. É. Gel'perina and V. I. Shvets, *Pharm. Chem. J.*, 2010, **44**, 151–156.
12 A. Reisch, P. Didier, L. Richert, S. Oncul, Y. Arntz, Y. Mély and A. S. Klymchenko, *Nat. Commun.*, 2014, **5**, 4089.
13 A. Vollrath, S. Schubert and U. S. Schubert, *J. Mater. Chem. B*, 2013, **1**, 1994–2007.
14 X. Wu, X. Sun, Z. Guo, J. Tang, Y. Shen, T. D. James, H. Tian and W. Zhu, *J. Am. Chem. Soc.*, 2014, **136**, 3579–3588.
15 A. Höcherl, M. Dass, K. Landfester, V. Mailänder and A. Musyanovych, *Macromol. Biosci.*, 2012, **12**, 454–464.
16 A. Musyanovych, J. Dausend, M. Dass, P. Walther, V. Mailänder and K. Landfester, *Acta Biomater.*, 2011, **7**, 4160–4168.
17 A.-K. Barthel, M. Dass, M. Dröge, J.-M. Cramer, D. Baumann, M. Urban, K. Landfester, V. Mailänder and I. Lieberwirth, *Beilstein J. Nanotechnol.*, 2014, **5**, 1905–1917.
18 J. Panyam, S. K. Sahoo, S. Prabha, T. Bargar and V. Labhasetwar, *Int. J. Pharm.*, 2003, **262**, 1–11.
19 W. Sun, H. Wang, C. Xie, Y. Hu, X. Yang and H. Xu, *J. Controlled Release*, 2006, **115**, 259–265.
20 S.-Y. Takizawa, C. Pérez-Bolívar, P. Anzenbacher and S. Murata, *Eur. J. Inorg. Chem.*, 2012, 3975–3979.
21 K. K.-W. Lo and K. K.-S. Tso, *Inorg. Chem. Front.*, 2015, **2**, 510–524.
22 Y. Hisamatsu, A. Shibuya, N. Suzuki, T. Suzuki, R. Abe and S. Aoki, *Bioconjugate Chem.*, 2015, **26**, 857–879.
23 Q. Zhang, R. Cao, H. Fei and M. Zhou, *Dalton Trans.*, 2014, **43**, 16872–16879.
24 H. Sun, A. M. Scharff-Poulsen, H. Gu and K. Almdal, *Chem. Mater.*, 2006, **18**, 3381–3384.
25 M. Schulze, M. Jäger and U. S. Schubert, *Macromol. Rapid Commun.*, 2012, **33**, 579–584.
26 B. Happ, J. Kübel, M. G. Pfeffer, A. Winter, M. D. Hager, B. Dietzek, S. Rau and U. S. Schubert, *Macromol. Rapid Commun.*, 2015, **36**, 671–677.
27 B. Happ, C. Friebe, A. Winter, M. D. Hager, R. Hoogenboom and U. S. Schubert, *Chem. – Asian J.*, 2009, **4**, 154–163.
28 C. Haensch, M. Chiper, C. Ulbricht, A. Winter, S. Hoeppener and U. S. Schubert, *Langmuir*, 2008, **24**, 12981–12985.
29 Q. Zhao, M. Yu, L. Shi, S. Liu, C. Li, M. Shi, Z. Zhou, C. Huang and F. Li, *Organometallics*, 2010, **29**, 1085–1091.
30 K. Y. Zhang and K. K.-W. Lo, *Inorg. Chem.*, 2009, **48**, 6011–6025.
31 W. Jiang, Y. Gao, Y. Sun, F. Ding, Y. Xu, Z. Bian, F. Li, J. Bian and C. Huang, *Inorg. Chem.*, 2010, **49**, 3252–3260.
32 M. Yu, Q. Zhao, L. Shi, F. Li, Z. Zhou, H. Yang, T. Yi and C. Huang, *Chem. Commun.*, 2008, 2115–2117.
33 Y. Hama, Y. Urano, Y. Koyama, M. Bernardo, P. L. Choyke and H. Kobayashi, *Bioconjugate Chem.*, 2006, **17**, 1426–1431.
34 E. J. Chaney, L. Tang, R. Tong, J. Cheng and S. A. Boppart, *Mol. Imaging*, 2010, **9**, 153–162.
35 I. Yildirim, S. Crotty, C. H. Loh, G. Festag, C. Weber, P.-F. Caponi, M. Gottschaldt, M. Westerhausen and U. S. Schubert, *J. Polym. Sci., Part A: Polym. Chem.*, 2016, **54**, 437–448.
36 M. Jalabert, C. Fraschini and R. E. Prud'homme, *J. Polym. Sci., Part A: Polym. Chem.*, 2007, **45**, 1944–1955.
37 S. Sosnowski and P. Lewinski, *Polym. Chem.*, 2015, **6**, 6292–6296.
38 J. Li, N. Wu, J. Wu, Y. Wan and C. Liu, *J. Appl. Polym. Sci.*, 2016, **133**, DOI: 10.1002/app.42884.
39 G. J. Pillai, M. M. Greeshma and D. Menon, *Colloids Surf., B*, 2015, **136**, 1058–1066.
40 F. Catalano, L. Accomasso, G. Alberto, C. Gallina, S. Raimondo, S. Geuna, C. Giachino and G. Martra, *Small*, 2015, **11**, 2919–2928.

Supplementary information

Cellular uptake of PLA nanoparticles studied by light and electron microscopy: Synthesis, characterization and biocompatibility studies using an iridium(III) complex as correlative label

Martin Reifarth,[a-d] David Pretzel,[a,b] Stephanie Schubert,[a,b,e] Christine Weber,[a,b] Rainer Heintzmann,[c,d]* Stephanie Hoeppener[a,b]* and Ulrich S. Schubert[a,b]*

[a]Laboratory of Organic and Macromolecular Chemistry (IOMC), Friedrich Schiller University Jena, Humboldtstr. 10, 07743 Jena,
[b]Jena Center for Soft Matter (JCSM), Friedrich Schiller University Jena, Philosophenweg 7, 07743 Jena, Germany
[c]Institute of Physical Chemistry and Abbe Center of Photonics, Friedrich-Schiller-University Jena, Helmholtzweg 4, Jena D-07743, Germany
[d]Leibniz Institute of Photonic Technology, Albert-Einstein-Strasse 9, Jena D-07745, Germany
[e]Institute of Pharmacy, Department of Pharmaceutical Technology, Friedrich Schiller University Jena, Otto-Schott-Str. 41, 07745 Jena, Germany

Experimental section

The solvents dichloromethane, methanol and toluene were dried with a PureSolv-EN™ Solvent Purification System (Innovative Technology). Unless otherwise noted, the starting materials were purchased from commercial sources and used as obtained. Reaction progress was monitored by thin layer chromatography on 0.2 mm Merck silica gel plates (60 F254). Column chromatographic purifications were performed on silica gel 60 (Merck).

^{1}H and ^{13}C NMR spectra were recorded on a Bruker AC 250 MHz respectively AC 300 MHz spectrometer at room temperature. Chemical shifts are reported in parts per million (ppm, δ scale) relative to the residual proton signal of the deuterated solvent. Elemental analyses were carried out on a Vario ELIII–Elementar Euro and an EA–HekaTech. Size-exclusion chromatography was performed on an Agilent 1200 series system, equipped with a G1362A refractive index detector, and both a PSS Gram30 and a PSS Gram1000 column in series, applying *N,N'*-dimethylacetamide (DMAc) + 0.21% LiCl as eluent, flow rate 1 mL/min, temperature: 40 °C. MALDI-ToF MS spectra were measured on an Ultraflex III TOF/TOF (Bruker Daltonics GmbH) that was equipped with a Nd:YAG laser and a collision cell. The spectra were recorded in the positive reflector or linear mode using DCTB (*trans*-2-[3-(4-tert.-butylphenyl)-2-methyl-2-propenylidene]malononitrile) as matrix. ESI-Q-ToF MS measurements were executed on a micrOTOF (Bruker Daltonics GmbH) mass spectrometer, which was equipped with an automatic syringe pump for sample injection. The pump was supplied from KD Scientific. It was operated in the positive ion mode. The standard electrospray ion (ESI) source was used to generate ions. Mixtures of dichloromethane and acetonitrile were utilized as solvent. The ESI-Q-TOF-MS instrument was calibrated in the m/z range of 50 to 3,000 using an internal calibration standard (Tunemix solution) which was supplied from Agilent. UV/vis absorption spectra were measured on a Perkin-Elmer Lambda 750 UV/vis spectrophotometer. Emission spectra were recorded with a Perkin-Elmer LS 50 spectrometer and corrected according to the spectral sensitivity function of the detector.

Spectroscopic measurements were carried out in a 1 cm quartz cuvette using spectroscopy grade solvents.

Dynamic light scattering (DLS) experiments were carried out using a Zetasizer Nano ZS (Malvern Instruments, Herrenberg, Germany). For this purpose, 3×30 runs were recorded at 25 °C (wavelength of 633 nm). The counts were detected under an angle of 173°. Each measurement was performed three times. The mean particle size was approximated as the effective diameter (z-average diameter). The width of the distribution as the polydispersity index of the particles (PDI) was obtained by the cumulants method assuming a spherical shape of the particles. The zeta potential was determined by electrophoretic light scattering. The measurements were carried out on a Zetasizer Nano ZS (Malvern Instruments, Herrenberg, Germany) by applying laser Doppler velocimetry. Therefore, 10 runs were carried out using the slow-field and fast-field reversal mode at 150 V (three times at 25 °C).

12-[4-(Pyridin-2-yl)-1*H*-1,2,3-triazol-1-yl]dodecanol (*1*)

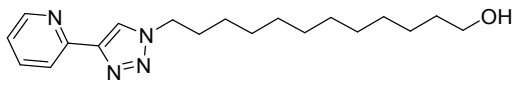

12-[4-(Pyridin-2-yl)-1*H*-1,2,3-triazol-1-yl]dodecanol was synthesized according to a procedure described in literature.[1] Sodium azide (195 mg, 3.0 mmol), 2-ethinylpyridine (290 mg, 2.8 mmol), 12-bromododecanol (740 mg, 2.8 mmol), copper(II) sulfate pentahydrate (23 mg, approx. 5 mol-%) and sodium ascorbate (90 mg, approx. 25 mol-%) were suspended in 8 mL ethanol/water (7:3 v/v) in a microwave vial which was subsequently sealed. The suspension was heated to 125 °C under microwave irradiation for 20 min. After cooling to room temperature, the vial was opened and another portion of copper(II) sulfate pentahydrate (23 mg, approx. 5 mol-%) was added to the mixture. The mixture was then heated to 125 °C by microwave irradiation for further 25 min. The brown suspension was poured on 100 mL distilled water and the resulting brown precipitate was separated and then dried *in-vacuo*. The crude material was suspended in ethyl acetate and copper was removed by a short silica column (ethyl acetate as eluent). The resulting yellowish solid was dissolved in a small amount of dichloromethane and dropped to *n*-pentane, by what **1** precipitated as an off-white solid (678 mg, 2.1 mmol, 73 %). ^{1}H-NMR (CD_2Cl_2, 250 MHz): δ 8.57 (s, 1H), 8.19 (s, 2H), 7.81 (s, 1H), 7.25 (s, 1H) 4.43 (t, J = 7.2 Hz, 2H), 3.61 (t, J = 6.6 Hz, 2H), 1.97 (s, 1H), 1.84 (s, 1H), 1.55 (m, 2H), 1.33 (m, 16H) ppm. ^{13}C-NMR (CD_2Cl_2, 63 MHz): δ 150.5, 149.4, 148.1, 136.8, 122.7, 121.9, 119.8, 62.6, 50.4, 32.9, 30.6, 30.2, 29.5, 29.4, 29.4, 29.3, 28.9, 26.4, 25.7 ppm. ESI-MS: 331.0 (100) $[M+H]^+$, 353.3 (20) $[M+Na]^+$. Elemental Analysis: C: 69.05%, H: 9.15%, N: 16.95% (Calc.), C: 68.80%, H: 9.17%, N: 16.72% (Found).

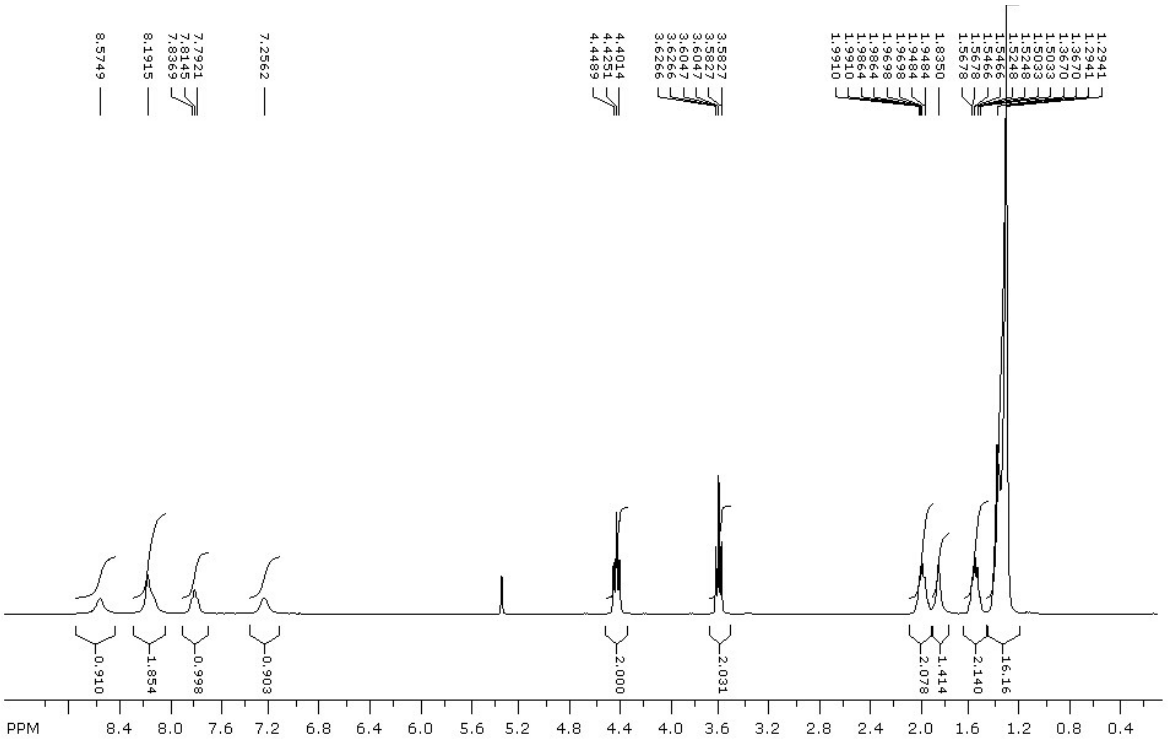

Figure S1: ^{1}H-NMR spectrum of compound ***1*** (CD_2Cl_2, 250 MHz).

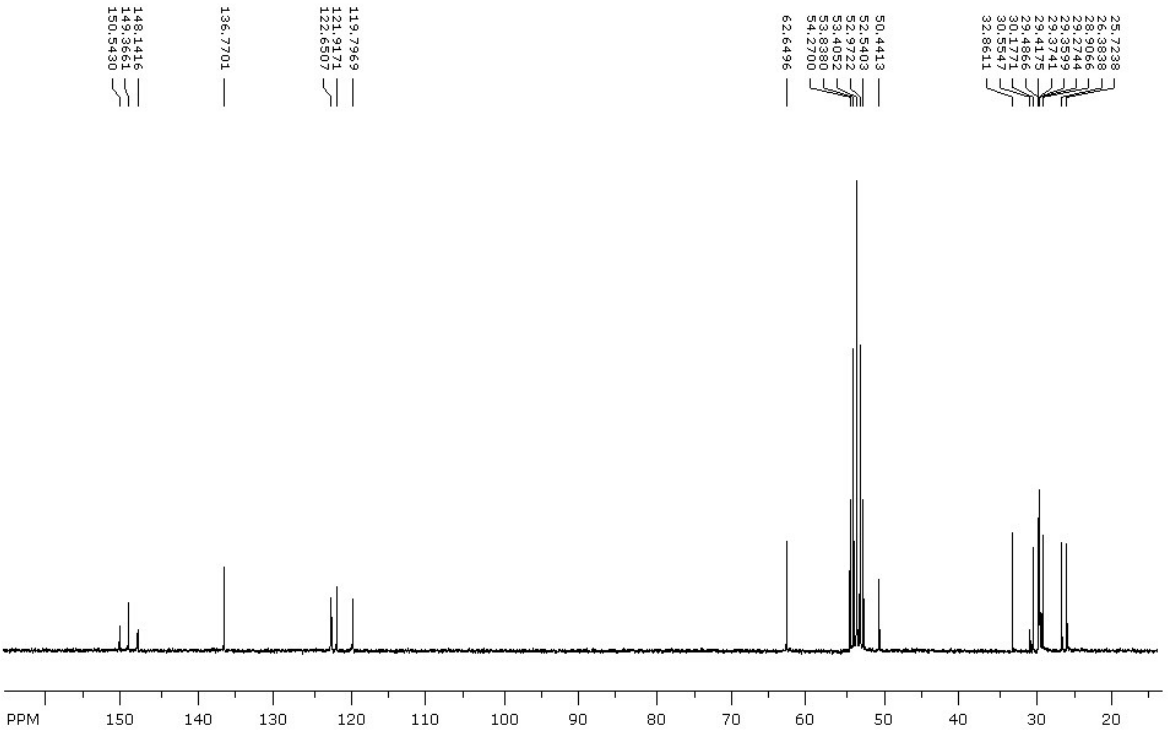

Figure S2: ^{13}C-NMR spectrum of compound ***1*** (CD_2Cl_2, 63 MHz).

Tetrakis[3-(2-benzothiazolyl)-7-(diethylamino)-2H-1-benzopyran-2-onato-N',C^{4}]-di-μ-chlorodi-iridium(III) (*2*)

The precursor complex was synthesized according to a standard method described in literature.[2]

Iridium(III) bis[3-(2-benzothiazolyl)-7-(diethylamino)-2H-1-benzopyran-2-onato-N',C^4]- 12-[4-(pyridin-2-yl)-1*H*-1,2,3-triazol-1-yl]dodecanol hexafluorophosphate (*3*)

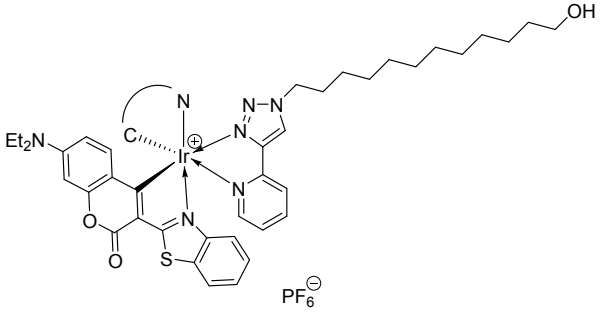

Tetrakis[3-(2-benzothiazolyl)-7-(diethylamino)-2H-1-benzopyran-2-onato-N',C^4]-di-μ-chlorodi-iridium(III) (50 mg, 0.027 mmol) and 12-[4-(pyridin-2-yl)-1*H*-1,2,3-triazol-1-yl]dodecanol (18 mg, 0.054 mmol) were suspended in 15 mL of a degassed mixture of dichloromethane/methanol (5:4 v/v) and heated under reflux for 24 h, whereupon all insoluble compounds dissolved. The solution was then cooled to room temperature and stirred for three hours in the presence of NH_4PF_6 (58 mg, 0.355 mmol, 6.5 eq). The reaction mixture was evaporated to dryness. The residue was resuspended in 100 mL dichloromethane and the organic phase was washed with water, dried over anhydrous Na_2SO_4 and evaporated to dryness. The crude product was purified by silica gel chromatography with dichloromethane/methanol 15:1 (v/v) as eluent to give **3** (65 mg, 88%) as an orange powder. ^{1}H-NMR (CD_2Cl_2, 250 MHz): δ 8.61 (m, 2H), 8.01 (m, 2H), 7.83 (dd, J = 7.8, 2.5 Hz, 2H), 7.55 (t, J = 6.4 Hz, 1H), 7.24 (q, J = 7.0 Hz, 2H), 7.03 (t, J = 7.8 Hz, 1H), 6.90 (t, J = 7.8 Hz, 1H), 6.38 (dd, J = 9.1, 2.5 Hz, 2H), 6.27 (d, J = 8.2 Hz, 2H), 6.19 (d, J = 9.5 Hz, 1H), 5.59 (m, 3H), 4.49 (t, J = 6.6 Hz, 2H), 3.59 (t, J = 6.4 Hz, 2H), 3.27 (m, 8H), 2.55 (s, 1H), 1.90 (m, 2H), 1.52 (m, 2H), 1.92 (m, 16 H), 1.06 (t, J = 7.5 Hz, 12H) ppm. ^{13}C-NMR (CD_2Cl_2, 63 MHz): δ 181.3, 178.0, 177.1, 176.5, 157.7, 157.4, 155.2, 154.8, 152.7, 152.4, 149.6, 149.5, 148.3, 148.1, 147.7, 141.3, 132.5, 131.9, 131.3, 131.2, 127.6, 127.3, 127.2, 126.1, 124.7, 124.5, 123.3, 123.2, 123.0, 121.9, 118.9, 118.8, 116.2, 115.6, 109.8, 109.5, 96.5, 96.4, 62.7, 44.8, 44.7, 41.0, 32.9, 30.9, 30.1, 29.52, 29.45, 29.4, 29.3, 28.8, 26.0, 25.7, 12.2 ppm. HRMS (ESI, m/z): 1221.4066 (calc. for $C_{59}H_{64}IrN_8O_5S_2$ [M-PF_6]$^+$), 1221.4033 (found).

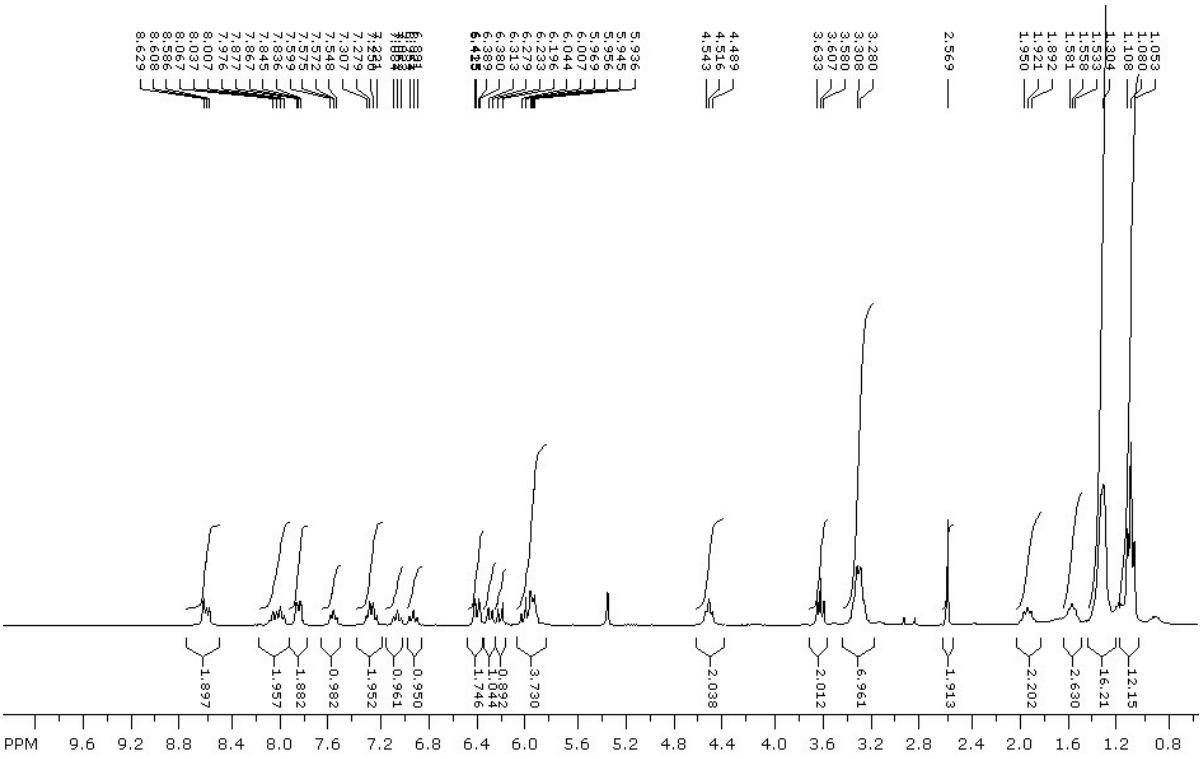

Figure S3: ^{1}H-NMR spectrum of compound ***3*** (CD_2Cl_2, 250 MHz).

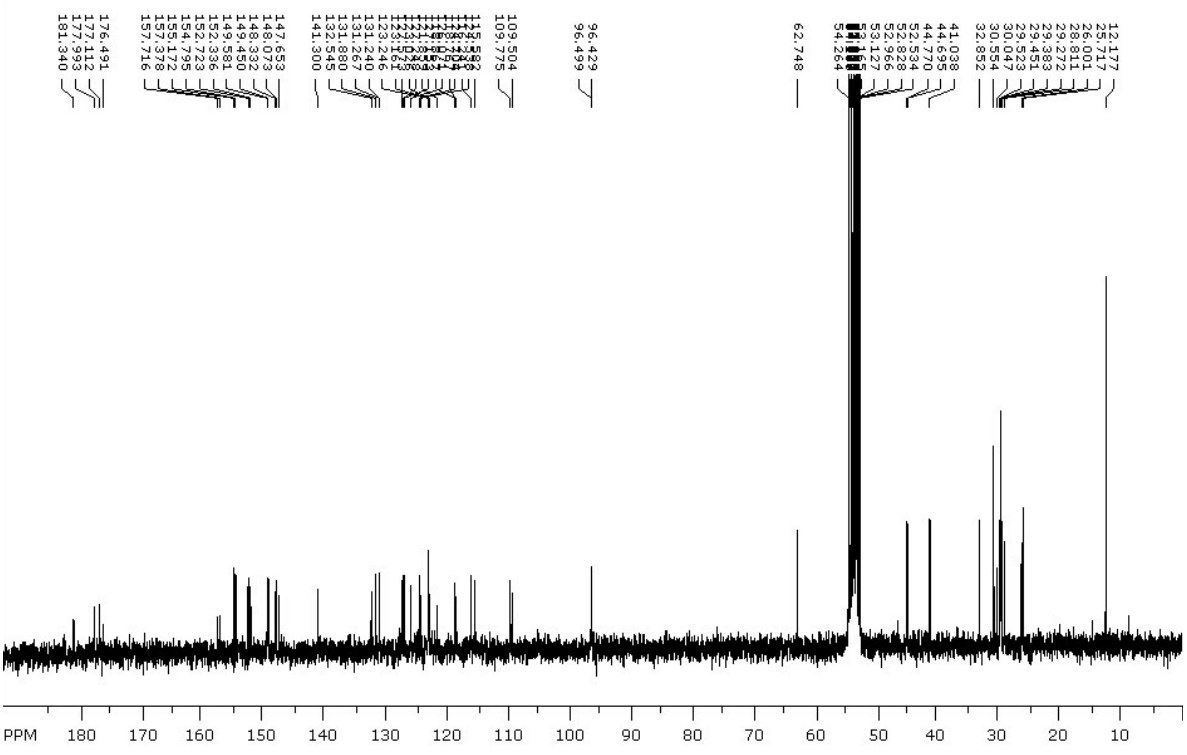

Figure S4: ^{13}C-NMR spectrum of compound ***3*** (CD_2Cl_2, 63 MHz).

End-functionalized polylactide (P1, P2)

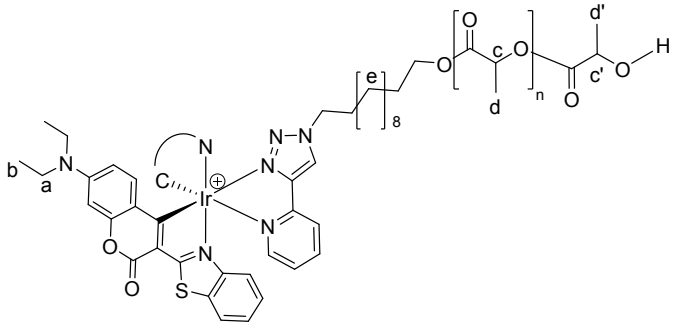

General procedure

All polymerization reactions were carried out in oven-dried glassware under an argon atmosphere using standard Schlenk technique. All solvents were dried using standard techniques and stored over molecular sieves. (3*S*)-*cis*-3,6-Dimethyl-1,4-dioxane-2,5-dione was recrystallized from dried toluene and tin(II) 2-ethylhexanoate was distilled *in-vacuo* prior to usage and stored under an argon atmosphere.

(3*S*)-*cis*-3,6-Dimethyl-1,4-dioxane-2,5-dione, tin(II) 2-ethylhexanoate (catalyst C) and complex **3** (initiator I, molar conc. ratio [I]:[C] = 1:1) were dissolved in degassed toluene and heated to reflux for 21 min. The orange solution was cooled to room temperature and exposed to air moisture for further 20 min. The reaction solution was precipitated in ice-cold *n*-pentane, redissolved in dichloromethane and precipitated two more times in *n*-pentane. The polymers were obtained as orange amorphous substances.

P1

(3*S*)-*cis*-3,6-Dimethyl-1,4-dioxane-2,5-dione (212 mg, 1.47 mmol, 0.5 mmol·mL^{-1}), complex **3** (20 mg, 0.016 mmol), tin(II) 2-ethylhexanoate (6 mg, 0.016 mmol). Conversion: 80% (according to ^{1}H-NMR). ^{1}H-NMR ($CDCl_3$, 300 MHz): 8.52, 8.12, 8.07, 7.71, 7.17, 6.31, 6.14, 5.91, 5.81 (complex aromatic region), 5.00-5.21 (c), 4.43-4.32 (c'), 4.05 (a), 3.20, 1.86, 1.34-1.64 (d, d') 1.33-1.12 (e), 1.11-0.92 (b) ppm. SEC (eluent: DMAc-LiCl, PMMA calibration, RI detection): M_n = 6,800 g mol^{-1}, M_W = 7,800 g mol^{-1}, Đ = 1.18. MALDI-ToF (DCTB, NaCl): M_n = 5,000 g mol^{-1}, M_W = 5,400 g mol^{-1}, Đ = 1.04.

P2

(3*S*)-*cis*-3,6-Dimethyl-1,4-dioxane-2,5-dione (21 mg, 0.15 mmol, 0.3 mmol·mL^{-1}), complex **3** (12 mg, 0.01 mmol), tin(II) 2-ethylhexanoate (4 mg, 0.01 mmol). Conversion: 82% (according to ^{1}H-NMR). ^{1}H-NMR: 8.52, 8.41, 8.12, 7.94, 8.07, 7.42, 7.71, 7.17, 6.94, 6.80, 6.31, 6.14, 5.91, 5.81 (complex aromatic region), 5.00-5.21 (c), 4.43-4.32 (c'), 4.05 (a), 3.20, 1.86, 1.34-1.64 (d, d') 1.33-1.12 (e), 1.11-0.92 (b). SEC (eluent: DMAc-LiCl, PMMA-standard, RI detection): M_n = 2,200 g mol^{-1}, M_W = 2,700 g mol^{-1}, Đ = 1.22. MALDI-ToF (DCTB, NaCl): M_n = 2,460 g mol^{-1}, M_W = 2,600 g mol^{-1}, Đ = 1.06.

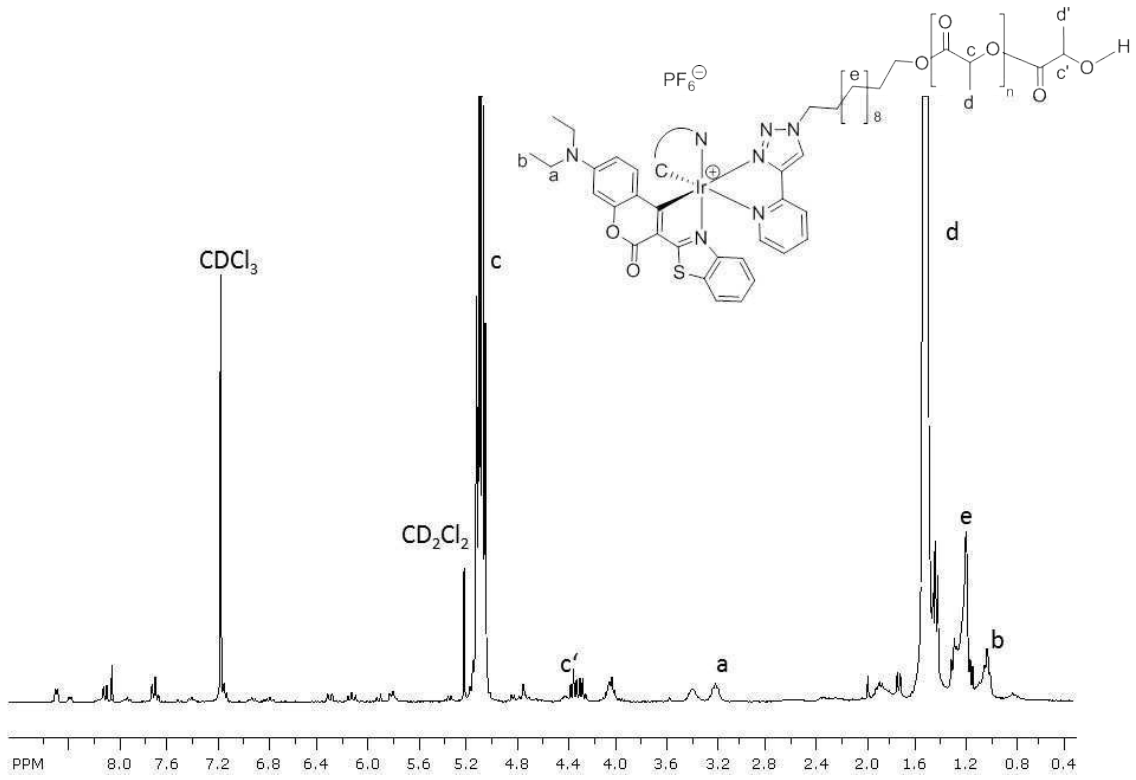

Figure S5: ^{1}H-NMR spectrum of compound ***P1*** ($CDCl_3$, 300 MHz).

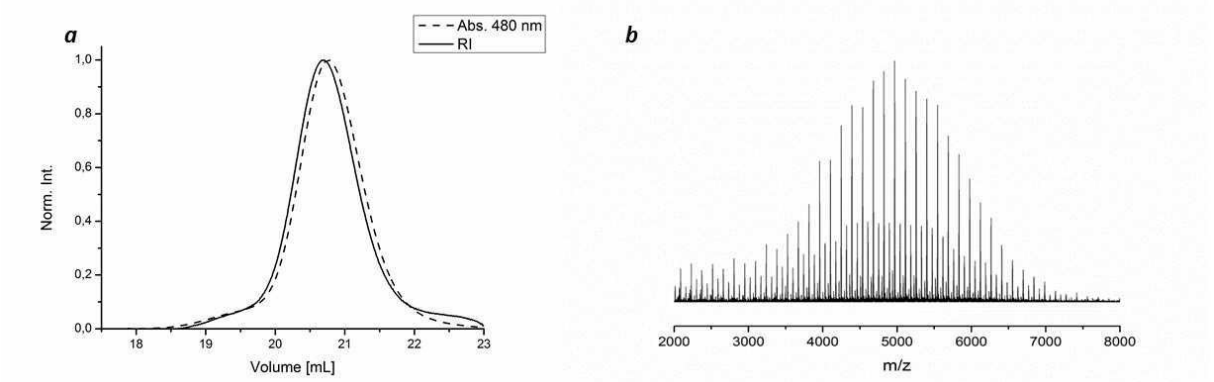

Figure S6: (a) SEC traces of polymer ***P1*** (DMAc-LiCl). Overlay of the RI signal and abs. UV/vis signal at 480 nm. (b) MALDI-ToF MS spectrum (DCTB, NaCl).

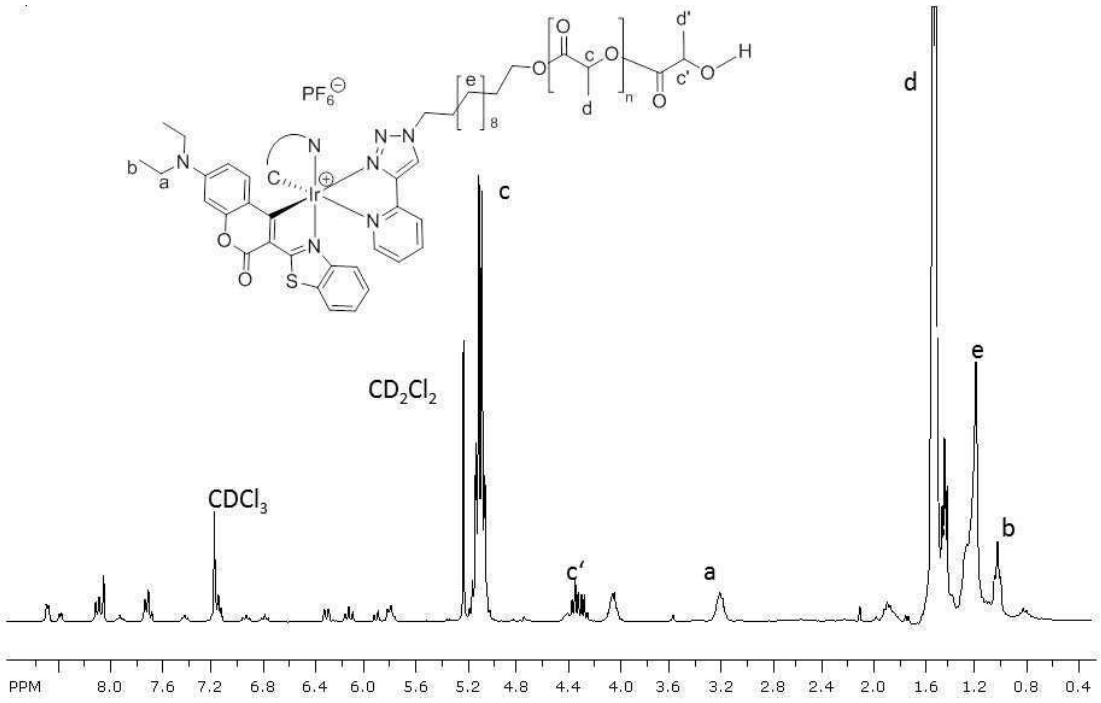

Figure S7: ^{1}H-NMR spectrum of compound ***P1*** ($CDCl_3$, 300 MHz).

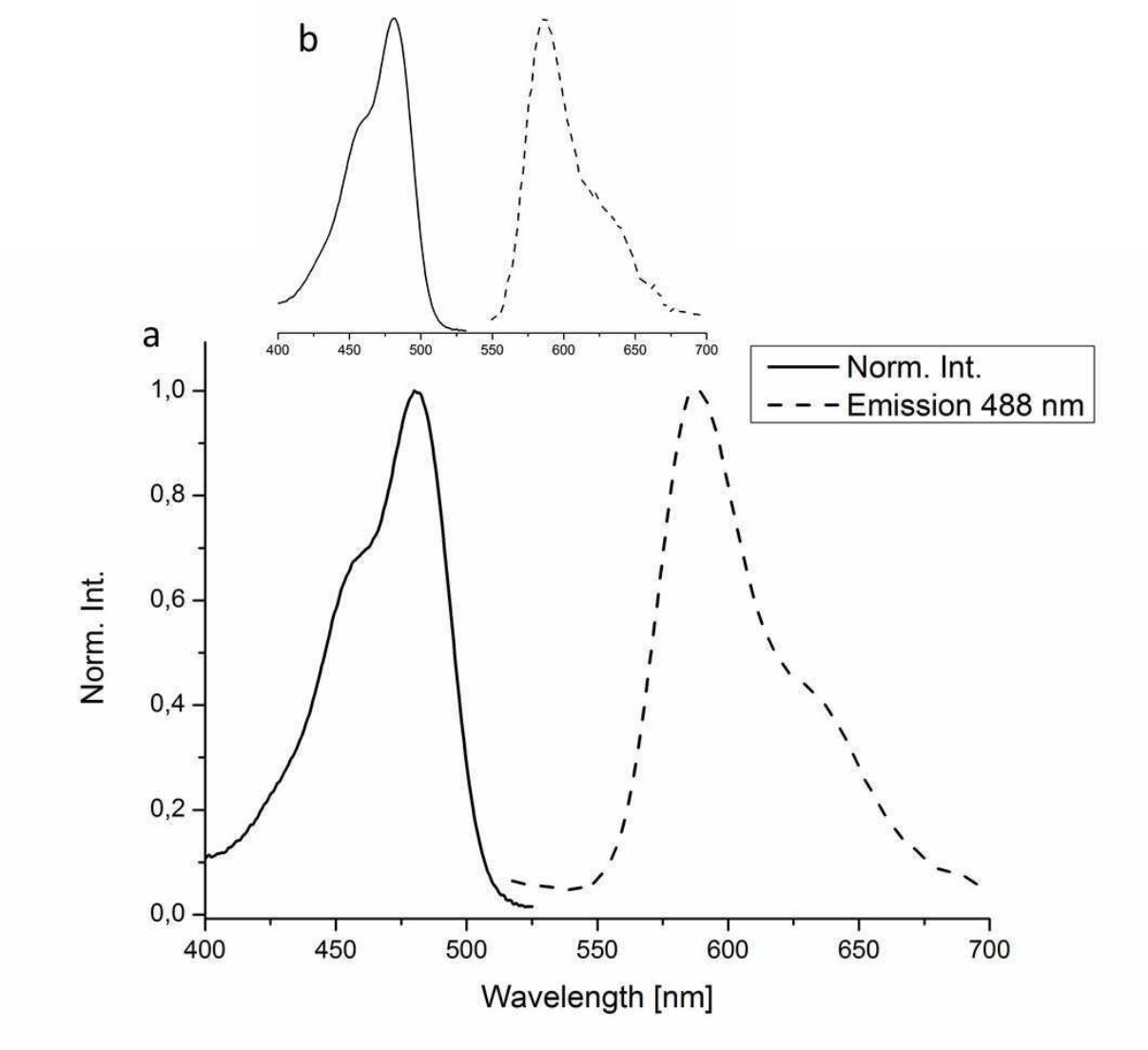

Figure S8: Absorption and emission spectrum of (a) polymer ***P2*** and (b) complex ***3*** (10^{-6} mol·L^{-1}). Absorption and emission spectra of both compounds are in good accordance (excitation slit width 5 nm, emission slit width 10 nm).

Kinetic measurements

For kinetic measurements, (3*S*)-*cis*-3,6-dimethyl-1,4-dioxane-2,5-dione (212 mg, 1.47 mmol, 0.5 mmol·mL^{-1}), complex ***3*** (20 mg, 0.016 mmol) and tin(II) 2-ethylhexanoate (6 mg, 0.016 mmol, [M]:[I] = 90:1) were dissolved in 3 mL toluene. From the reaction mixture, aliquots of 200 µL were taken with a syringe purged with argon. The aliquots were analyzed by ^{1}H-NMR spectroscopy to estimate the conversion. Therefore, the ratio of the integrals of the signals at 5.04 ppm (methine proton of monomer) and 5.13–5.25 ppm (methine proton of polymer)[3] were calculated. SEC measurements were carried out using DMAc-LiCl in order to estimate the molar masses using a PMMA calibration.

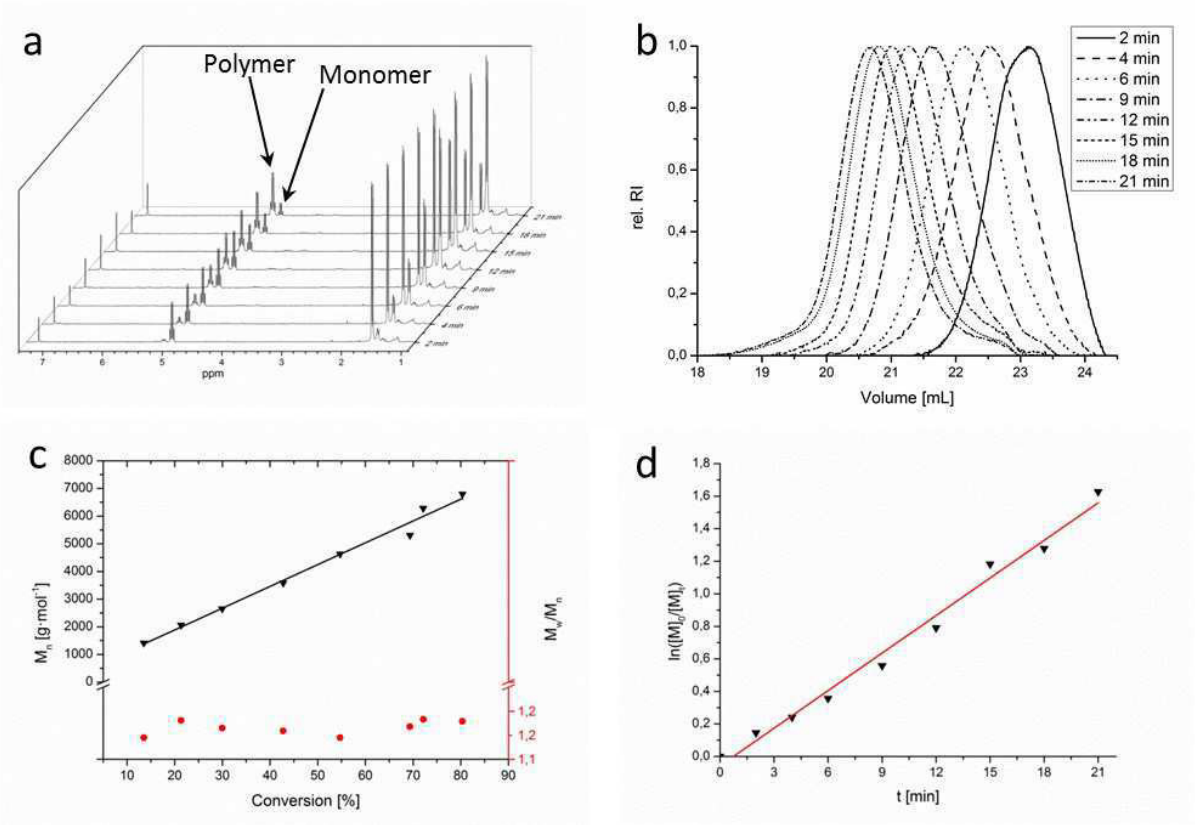

Figure S9: (a) ^{1}H-NMR spectra and (b) SEC traces of the samples taken during kinetic measurements (DMAc-LiCl, PMMA calibration and RI detection). (c) Molar mass versus conversion. Conversions were determined by ^{1}H-NMR measurements of the polymerization mixtures and molar masses as well as polydispersity indices by SEC measurements (DMAc-LiCl, PMMA calibration and RI detection). (d) Semilogarithmic plot. k_P = 0.15 L·mol^{-1}·s^{-1}.

pH-dependence

For the determination of the pH-dependence of the complex, a suspension of 10 µg·mL^{-1} complex in buffer solution was prepared. Therefore, ***2*** was predissolved in acetonitrile (1 mg·mL^{-1}) and 10 µL stock solution was given to 1 mL buffer solution (pH 4-6: acetate buffer, 0.1 mol·L^{-1}, pH 7-9: phosphate buffer, 0.1 mol·L^{-1}).

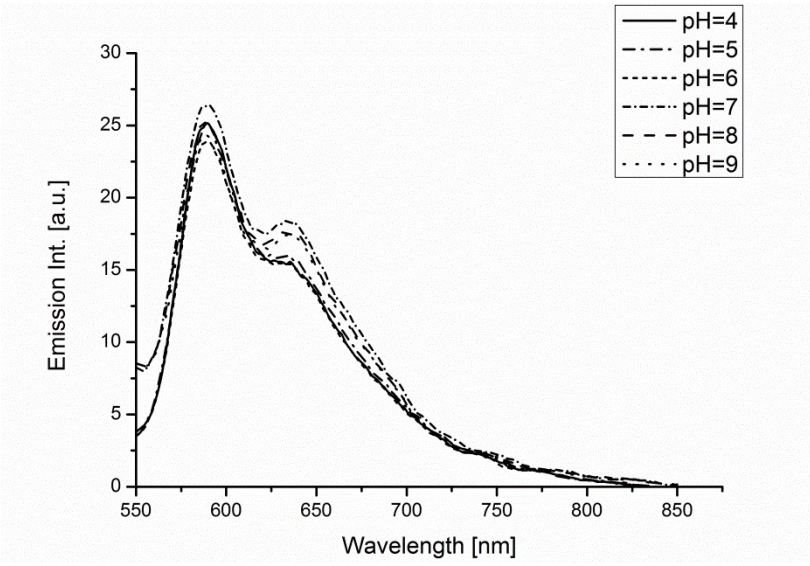

Figure S10: Emission from complex suspended in aqueous buffers. The emission intensity is barely dependent of the pH value of the surrounding medium.

Nanoparticle preparation

The nanoparticle suspensions were prepared using a single emulsion technique. Therefore, 25 mg of ***P1*** for ***NP1*** (1:1 mixture of ***P1*** and PLA, isopropanol initiated, M_n = 5,800 g mol^{-1}, $Đ$ = 1.18 acc. to SEC measurements, THF eluation and PLA calibration for ***NP2***) were dissolved in 0.5 mL dichloromethane and added to 1 mL poly(vinyl alcohol) (PVA) solution (3 wt%). The two-phase system was emulsified with a sonicator tip (10 s, 50 W), poured into 10 mL of 0.3 wt% PVA solution and stirred overnight at room temperature. The particles were washed twice by centrifugation and resuspension. A solution of Hepes buffered glucose (0.5 mL) was added as cryoprotectant to stabilize the particles during lyophilization. DLS measurements before and after lyophilization prove that the particles can be easily resuspended resulting in same particle size distributions.

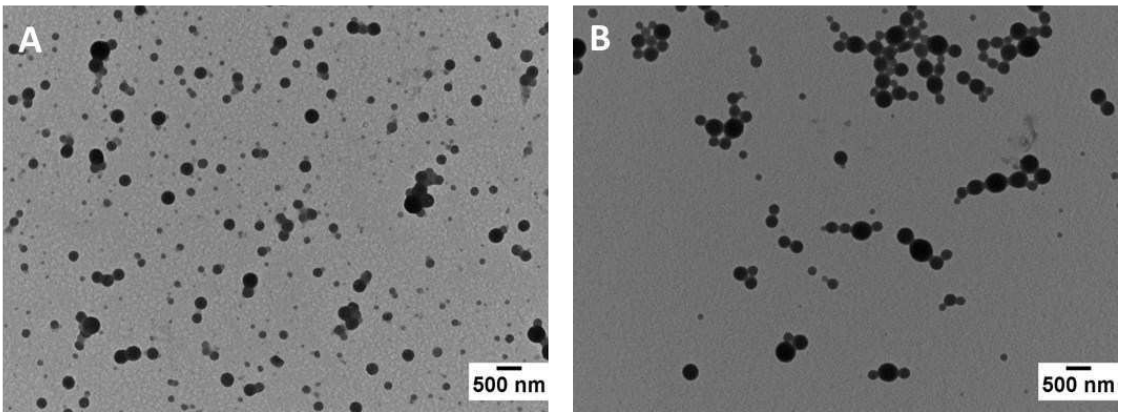

Figure S11: TEM images of (a) NP1 and (b) NP2.

The iridium content of the particles was determined *via* ICP-OES. For this purpose, the lyophilized particle samples were weighted out into a beaker and heated to reflux in suprapure nitric acid (approx. 35%, diluted with miliQ water) for 20 minutes and diluted with miliQ water prior to the measurement. The measurements were carried out using a Varian 725-ES spectrometer (ICP-725).

NP1: 0.262% Ir (w/w, referred mass of the lyophilized particles including stabilizers and buffer) and ***NP2:*** 0.182% Ir (w/w).

The luminescence behavior of the particles at different concentrations (miliQ water) was determined using a Tecan M200 Pro fluorescence microplate reader (Crailsheim, Germany), excitation wavelength 488 nm (exc. bandwith 9 nm), emission wavelength 580 nm (em. bandwith 20 nm).

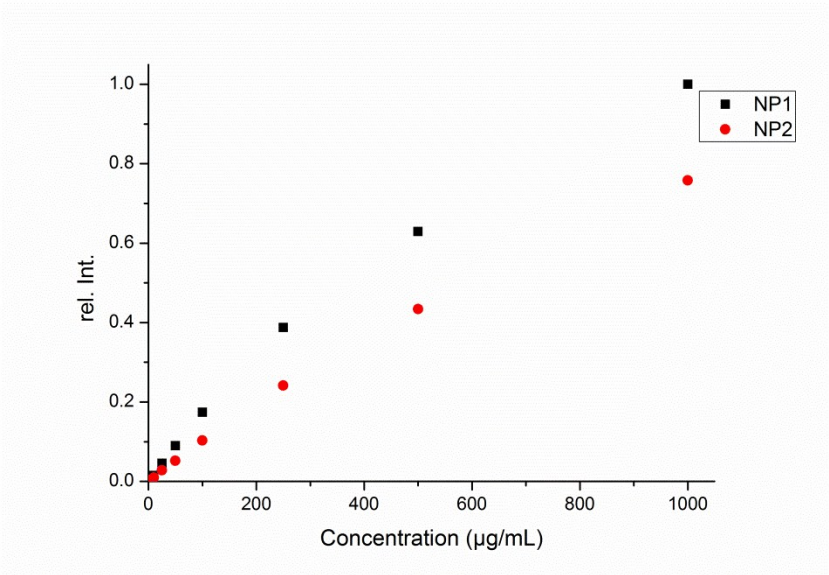

Figure S12: Luminescence intensities in dependence of the particle concentration. At concentrations up to 250 µg·mL^{-1}, a linear dependence was observed. For higher concentration, a saturation behavior was observed.

Cell Cultivation, Toxicity and Flow Cytometry Tests

Cell cultivation

The human embryonic kidney cell line HEK-293 used in the biological experiments was purchased from the German Collection of Microorganisms and Cell Cultures (DSMZ, Braunschweig, Germany). Cells were cultured in Eagle's Minimum Essential Medium (EMEM) supplemented with 2 mmol L^{-1} L-glutamine, 1% non-essential amino acids, 1.0 mmol sodium pyruvate, 10% fetal bovine, 100 U mL^{-1} penicillin and 100 µg mL^{-1} streptomycin (all components from Biochrom, Berlin, Germany) at 37 °C in a humidified atmosphere with 5% (v/v) CO_2.

Toxicity tests

The *in-vitro* cytotoxicity experiments were performed via an XTT assay according to the German standard institution guideline DIN ISO 10993-5 as a reference for biomaterial testing. HEK-293 cells were seeded in 96-well plates at a density of $1 \cdot 10^4$ cells/well and were grown as monolayer cultures for 24 h. The cells were then incubated separately with different concentrations of the NP (1.0, 0.5, 0.25, 0.1, 0.05 mg·mL^{-1}) and the complex ***3*** (0.25, 0.125, 0.0625, 0.025 and 0.0125 mg·mL^{-1}) for 24 h. Control cells were incubated with fresh culture medium. After incubation, cells were washed once and 150 µL of medium containing 50 µL XTT solution prepared according to the manufacturer's instructions were added to each well. After 4 h at 37 °C 100 µL of each solution was transferred to a new microtiter plate and the optical density (OD) at 450 nm was measured photometrically. The negative control was standardized as 0% of metabolism inhibition and referred as 100% viability.

Cellular uptake studied by flow cytometry

The concentration dependent uptake of the complex containing NP1 and NP2 was quantified by flow cytometry measurements. For this purpose, HEK cells were incubated with different concentrations (1, 0.5, 0.25, 0.1 and 0.05 mg·mL^{-1}) of the NP for 24 h at 37 °C. Following the incubation, the excess of NP was removed by washing with PBS. Subsequently, the adherent cells were detached by trypsin treatment, the cell suspension was washed twice with PBS supplemented with 10% fetal calf serum. For the identification of dead cells, a propidium iodide (PI) staining was performed for 15 minutes at room temperature using 100 µg PI/mL PBS. A total of $2 \cdot 10^4$ cells were resuspended and directly subjected to flow cytometry on a FACS Canto II (BD, Heidelberg, Germany) using gates of forward and side scatters to exclude debris and cell aggregates.

Microscopy

Structured illumination microscopy

HEK-293 cells were grown on coverslips (Zeiss, thickness no 1 ½, high-performance 18 mm × 18 mm, thickness 170±5 µm) and incubated for 24 h with the respective nanoparticle samples (250 µg·mL^{-1}). After rinsing with PBS to remove the excess of NP, the cells were stained for fluorescence microscopy according to manufactures instructions. The Hoechst dye was applied to viable cells at a concentration of 1 µg·mL^{-1}. Cells were then fixed for 10 minutes at room temperature using 4% paraformaldehyde dissolved in PBS, permeabilized with 0.1% TritonX100 solution and subsequently stained with AlexaFluor488 Phalloidin (Thermo Fisher Scientific, Schwerte, Germany) at a concentration of 165 nmol·mL^{-1} for 20 min. After rinsing with PBS, the coverslips were mounted on glass slides using 25 µL Mowiol 4-88 solution containing 625 µg 1,4-diazabicyclo-(2,2,2)octane (Sigma-Aldrich, Buchs, Switzerland). Imaging was performed on an Elyra S1 system (Zeiss, Oberkochen, Germany, excitation wavelengths of 405 nm, 488 nm, 561 nm and 642 nm) applying an 63× 1.4 NA plan apochromat oil objective. For structured illumination, excitation gratings with 23

resp. 28 µm were applied. Three channels were acquired: blue displaying nucleus (Hoechst 33342 staining, excitation wavelength 405 nm, BP 420-480 + LP 750), green displaying cytoskeleton (Alexa Fluor 488™ Phalloidin staining, excitation wavelength 488 nm, BP 495-550 + LP 750), red displaying nanoparticles (complex ***3***, excitation wavelength 488 nm, BP 570-620 + LP 750). The grating position and axial position of the sample table were controlled by piezo controllers (Physik Instrumente, Germany). An axial stack of images was acquired (Δz = 120 nm). Images were recorded with a CCD camera (Andor, USA), cooled to −63 °C. Reconstructions were performed with the commercial ZEN software installed on the system.

Electron microscopy

For electron microscopy, HEK-293 cells were grown in a 6-well plate and incubated for 24 h with the respective nanoparticle samples (250 µg·mL^{-1}). Subsequent to incubation, cells were suspended by treatment with trypsin. The cell suspension was fixed for 2 h with glutaraldehyde (2% in PBS 1x, prepared from 8% EM grade stock solution) on ice and subsequently fixed with osmium tetroxide (1% in PBS, prepared from 4% EM grade stock solution, both purchased from EMS, Hatfield). After washing with pure water, the samples were dehydrated by an ethanol/water series (50%, 70%, 90%, 2 × 100% dry EtOH, purified with a Solvent Purification System, stored over molecular sieves). The dehydrated samples, which were transferred into BEEM capsules (Plano, Wetzlar), were immersed in mixtures of Embed 812 (EMS, Hatfield) and ethanol (Embed/EtOH = 1:1 *v/v* for 1 hour, 2:1 *v/v* for 12 h) and subsequently in pure Embed 812 for 4 h. After a further change of the embedding medium, the samples were stored in a drying oven at 70 °C for 24 h, until the resin hardened. Ultrathin sections of 80 nm were cut with an ultramicrotome (PT-XL PowerTome, RMC, Tucson) using a diamond knife (RMC, Tucson). The sections were put on a carbon supported copper grid (400 mesh, Quantifoil, Jena) imaged with a Technai G^2 system (FEI), with 200 kV acceleration voltage in STEM mode (HAADF detection).

Comparison of contrast generated by gold nanoparticles and polymer nanoparticles

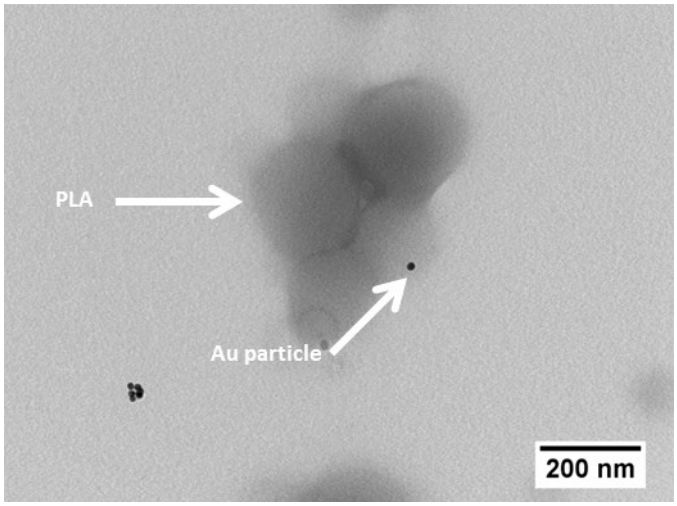

Fig. S13: Comparison of the contrast generated by gold nanoparticles and polymer nanoparticles PLA particles. PLA provides poor contrast in comparison to the gold particles. The Au particles were prepared according to a standard procedure[4] (diameter 23.9 nm, PDI 0.204 according to DLS).

References

1. B. Happ, C. Friebe, A. Winter, M. D. Hager, R. Hoogenboom and U. S. Schubert, *Chem. Asian J.*, 2009, **4**, 154-163.
2. C. Haensch, M. Chiper, C. Ulbricht, A. Winter, S. Hoeppener and U. S. Schubert, *Langmuir*, 2008, **24**, 12981-12985.
3. J. L. Robert and K. B. Aubrecht, *J. Chem. Educ.*, 2008, **85**, 258.
4. F. Kretschmer, U. Mansfeld, S. Hoeppener, M. D. Hager and U. S. Schubert, *Chem. Commun.*, 2014, **50**, 88-90.

Publication P5

"3rd generation poly(ethylene imine)s for gene delivery"

T. Bus, C. Englert, M. Reifarth, P. Borchers, M. Hartlieb, A. Vollrath, S. Hoeppener, A. Traeger, U. S. Schubert

J. Mater. Chem. B **2017**, *5*, 1258-1274

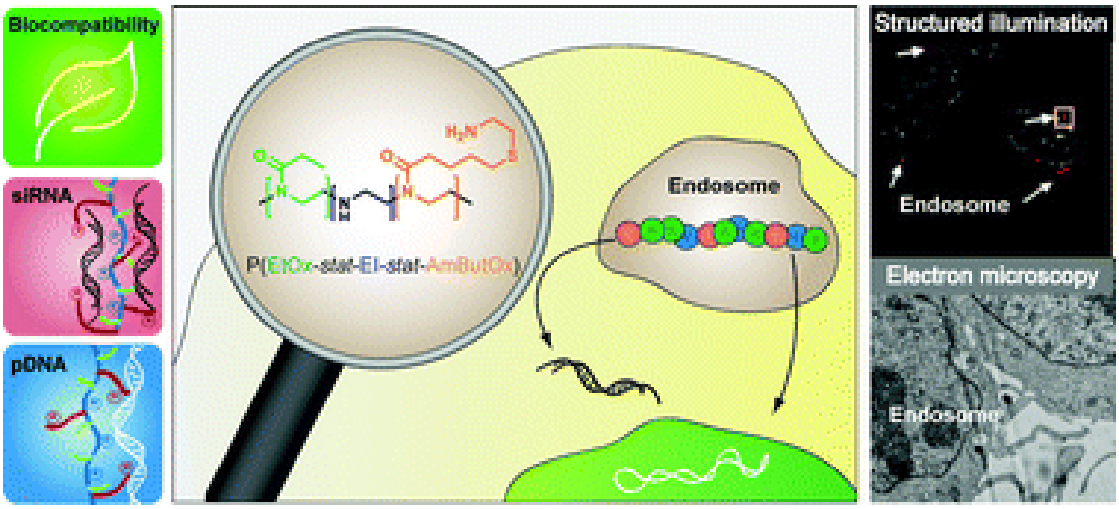

Journal of Materials Chemistry B

PAPER

View Article Online
View Journal | View Issue

Cite this: J. Mater. Chem. B, 2017, 5, 1258

3rd generation poly(ethylene imine)s for gene delivery†

Tanja Bus,‡[ab] Christoph Englert,‡[ab] Martin Reifarth,[abcd] Philipp Borchers,[ab] Matthias Hartlieb,§[ab] Antje Vollrath,[ab] Stephanie Hoeppener,[ab] Anja Traeger*[ab] and Ulrich S. Schubert*[ab]

Received 4th October 2016,
Accepted 20th December 2016

DOI: 10.1039/c6tb02592g

www.rsc.org/MaterialsB

Cationic polymers play a crucial role within the field of gene delivery offering the possibility to circumvent (biological) barriers in an elegant way. However, polymers are accompanied either by a high cytotoxicity or low efficiency. In this study, a series of high molar mass poly(2-oxazoline)-based copolymers was synthesized introducing 2-ethyl-2-oxazoline, ethylene imine, and primary amine bearing monomer units representing a new generation of poly(ethylene imine) (PEI). The potential of these modified PEIs as non-viral gene delivery agents was assessed and compared to linear PEI by studying the cytotoxicity, the polyplex characteristics, the transfection efficiency, and the cellular uptake using plasmid DNA (pDNA) as well as small interfering RNA (siRNA). High transfection efficiencies, even in serum containing media, were achieved using pDNA without revealing any cytotoxic effects on the cell viability at concentrations up to 1 mg mL^{-1}. The delivery potential for siRNA was further investigated showing the importance of polymer composition for different genetic materials. To elucidate the origins for this superior performance, super-resolution and electron microscopy of transfected cells were used, identifying the endosomal release of the polymers as well as a reduced protein interaction as the main difference to PEI-based transfection processes. In this respect, the investigated copolymers represent remarkable alternatives as non-viral gene delivery agents.

Introduction

Within the last decades synthetic polymers emerged as versatile tools in the field of gene delivery.[1] They represent promising alternatives to viral vectors or lipid-based, non-viral transfection agents, since they combine the advantages of large scale production, simple storage conditions, and the availability of a variety of architectures with tailored properties, *e.g.* defined molar masses, end groups, and functionalities.[2] The most prominent representative of synthetic, cationic polymers utilized for nucleic acid delivery is the gold standard poly(ethylene imine) (PEI).[3,4] Subdivided into a linear (lPEI) and a branched (bPEI) topology, it reveals one of the highest cationic-charge-densities of all organic macromolecules.[5] Under physiological conditions, every sixth nitrogen (N) is protonated[6] and able to interact with the phosphate groups (P) of deoxyribonucleic acid (DNA) as well as ribonucleic acid (RNA) to form nanoscale interelectrolyte complexes, so-called polyplexes.[7–9]

lPEI offers the benefit to be synthesized by hydrolysis of poly(2-alkyl-2-oxazoline)s (POx) using a living polymerization process resulting in well-defined structures.[10] However, these advantages are accompanied by a severe cytotoxicity and undesired non-specific interactions with cellular and non-cellular components, both *in vitro* and *in vivo*.[11–13] Various attempts have been made to optimize PEI by focusing on the design of biodegradable[14–16] and biocompatible[17,18] derivatives, which represent the 2nd generation of PEI-based polymers. Carbohydrates, *e.g.* dextran[19] or hydroxyethyl starch (HES),[20] as well as stealth polymers like poly(ethylene glycol) (PEG)[21,22] are extensively studied.[23] Approaches as the introduction of biodegradable linkers, such as disulfide bonds,[24–26] the combination with liposomes[27,28] or the utilization of micelles or nanoparticles in combination with PEI[29,30] are further concepts partially fulfilling the complex requirements. Besides the post-modification of the PEI backbone, the partial hydrolysis of POx, resulting in P(Ox-*stat*-EI) copolymers, represents a

[a] Laboratory of Organic and Macromolecular Chemistry (IOMC), Friedrich Schiller University Jena, Humboldtstrasse 10, 07743 Jena, Germany. E-mail: ulrich.schubert@uni-jena.de, anja.traeger@uni-jena.de
[b] Jena Center for Soft Matter (JCSM), Friedrich Schiller University Jena, Philosophenweg 7, 07743 Jena, Germany
[c] Institute of Physical Chemistry and Abbe Center of Photonics, Friedrich Schiller University Jena, Helmholtzweg 4, 07743 Jena, Germany
[d] Leibniz Institute of Photonic Technology, Albert-Einstein-Strasse 9, 07745 Jena, Germany

† Electronic supplementary information (ESI) available: Fig. S1–S21. See DOI: 10.1039/c6tb02592g

‡ The authors contributed equally to this work.

§ Current address: Department of Chemistry, University of Warwick, Gibbet Hill Road, Coventry, CV4 7AL, UK.

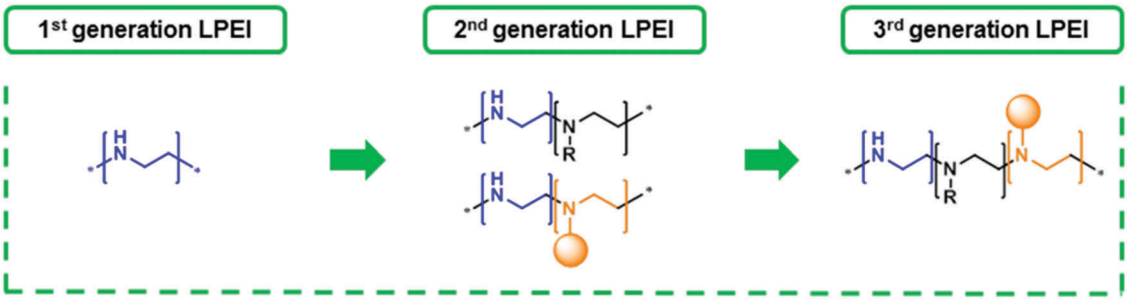

Fig. 1 Overview of different generations of linear poly(ethylene imine) (lPEI). Compared to the original lPEI (1st generation), which has been established over the last decades, the 2nd generation lPEI contains functional monomer units (black or orange) besides the present ethylene imine units (blue). The 3rd generation lPEI describes the presence of multiple functional units comprising cationic functionalities (blue), functional groups to increase cell viability (black) as well as a third group of functionalities (orange, *e.g.* primary amine functionalities or targeting molecules).

promising approach.[31,32] The "stealth behavior" of POx, comparable to PEG, facilitates a reduction of cytotoxicity.[32,33] Although the cytotoxicity problem might be solved, the modifications often result in inefficient gene delivery presumably due to weak DNA complexation and decreased cell interaction.[34] Hence, the design criteria for a perfect polymeric vector are still unknown and other polymer characteristics, *i.e.* the degree of hydrophobicity or synergistic effects of different polycationic species within one polymeric vector, have to be considered.[17,35]

The present contribution focusses on the synthesis of high molar mass copolymers of lPEI and POx. A combination of primary and secondary amines as well as non-charged 2-ethyl-2-oxazoline (EtOx) units was aspired. While different amine species were used to support the polyplex formation, biocompatibility is achieved *via* the integration of EtOx. To realize the synthesis of the targeted polymer structure, a post-polymerization functionalization of partially hydrolyzed high molar mass poly(2-ethyl-2-oxazoline) (PEtOx) was used. The insertion of alkenes is followed by the functionalization *via* thiol–ene click chemistry. This extraordinary combination of modification techniques offers a new platform of copolymers which marks the beginning of a new generation – the 3rd generation of PEI (see Fig. 1).

The designed copolymers were investigated concerning their *in vitro* transfection potential including polyplex characterization, competitor/serum interaction and the cellular uptake mechanism using plasmid DNA as well as siRNA. For a detailed understanding of the mechanism during the gene delivery process super-resolution fluorescence as well as electron microscopy were utilized.

Materials and methods

Materials

2-Ethyl-2-oxazoline (EtOx) and methyl tosylate were obtained from Acros Organics, distilled to dryness (over barium oxide in the case of EtOx), and stored under argon atmosphere. Pyridine, methanol, dichloromethane, 4-*N*,*N*-dimethylaminopyridine (DMAP), 2-(boc-amino)ethanethiol, 2,2-dimethoxy-2-phenylacetophenone (DMPA), trifluoroacetic acid and Amberlyst® A21 (free base) were obtained from Sigma Aldrich (Steinhausen, Germany) and are of analytical grade and were used without further purification. Acetonitrile was purified on a MBraun solvent purification system (MB SPS-800). The dye Cy5 was purchased from Lumiprobe GmbH (Hannover, Germany). *N*-Succinimidyl-4-pentenate was prepared according to literature procedures.[36] The commercially available poly(ethylene imine)s, both the branched (bPEI) as well as the linear (lPEI) type, were purchased from Polysciences (USA). Poly(methacrylic acid) (PMAA, DP = 200) was synthesized according to literature procedures.[37] The transfection reagent jetPRIME, used as positive control for siRNA delivery, was obtained from Polyplus (Polyplus transfection SA, USA). 5-(*N*-Ethyl-*N*-isopropyl)amiloride (EIPA) was purchased from Sigma-Aldrich (Merck, Darmstadt). Ethidium bromide solution (1%, 10 mg mL^{-1}) was purchased from Carl Roth (Karlsruhe, Germany). AlamarBlue, YOYO-1 iodide, Hoechst 33342 trihydrochloride as well as all other indicated CLSM dyes were obtained from Life Technologies (Thermo Fisher Scientific, Germany). If not stated otherwise, cell culture media and solutions (L-glutamine, antibiotics) were obtained from Biochrom (Berlin, Germany). Plasmid pEGFP-N1 (4.7 kb, Clontech, USA) encoding green fluorescent protein (EGFP) was isolated with the Giga Plasmid Kit provided by Qiagen (Hilden, Germany). The siRNA negative controls (scrambled siRNA, 21 nucleotides, double-stranded) and the siRNA against *egfp* (sense 5′-GCAAGCTGACCCTGAAGTTCAT-3′, antisense 5′-ATGAACTTCAGGGTCAGCTTGC-3′) were purchased from Eurogentech (Seraing, Belgium).

General methods and instrumentation

An Initiator Sixty single-mode microwave synthesizer from Biotage, equipped with a noninvasive IR sensor (accuracy: 2%), was used for polymerizations and hydrolyses under microwave irradiation.

Proton (^{1}H) nuclear magnetic resonance (NMR) spectra were acquired in deuterated methanol, at room temperature using a Bruker AC 300 MHz spectrometer; chemical shifts (δ) are expressed in parts per million relative to TMS.

Size exclusion chromatography (SEC) was performed using an Agilent Technologies 1200 Series gel permeation chromatography system equipped with a G1329A auto sampler, a G131A isocratic pump, a G1362A refractive index detector, and both a PSS Gram 30 and a PSS Gram 1000 column placed in series. As eluent a 0.21% LiCl solution in *N*,*N*-dimethylacetamide (DMAc) was used at 1 mL min^{-1} flow rate and a column oven temperature of 40 °C. Molar masses were calculated using a poly(styrene) calibration.

Asymmetric flow field-flow fractionation (AF4) was performed on an AF2000 MT System (Postnova Analytics, Landsberg, Germany) coupled to an UV (PN3211, 260 nm (Postnova)), RI (PN3150), multi-angle light scattering (MALLS, PN3070, 633 nm (Postnova)) and DLS (ZetaSizer Nano ZS; Malvern) detector. The eluent was delivered by three different pumps (tip, focus, cross-flow) and the sample was injected by an autosampler (PN5300) into the channel. The channel has a trapezoidal geometry and an overall area of 31.6 cm^2. The nominal height of the spacer was 500 μm. A regenerated cellulose membrane with a molar mass cut-off of 10 kDa served as accumulation wall. All experiments were carried out at 25 °C with pure water as eluent. A sample of 10 μL (1 mg mL^{-1}) was injected with an injection flow rate of 0.2 mL min^{-1} and a cross-flow rate of 1.2 mL min^{-1} for 7 min (detector flow rate 0.5 ml min^{-1}, focus flow rate 1.5 mL min^{-1}). After the focusing step, the cross-flow rate was reduced under an exponential gradient (0.4) within 10 min to 0 mL min^{-1}. The cross-flow was kept constant at 0 mL min^{-1} for 40 min to ensure complete elution. All measurements were in triplicate.

For the acid/base titration the copolymers **P1** to **P3** ($m \sim 20$ mg) were dissolved in 4 mL deionized water, and 20 μL conc. hydrochloric acid were added (0.06 M). The titration was performed against 0.1 M aqueous sodium hydroxide solution using a 765 Dosimat from Metrohm, a digital pH/mV-thermometer GMH 3530 from Greisinger electronic, and the EBS9 M Recorder software.

Synthesis of poly(2-ethyl-2-oxazoline) (PEtOx)

The monomer 2-ethyl-2-oxazoline (3.965 g) and the initiator methyl tosylate (12.42 mg, 0.067 mmol) were dissolved in dry acetonitrile (6.0 mL) in a microwave vial within a glovebox under nitrogen atmosphere. After stirring for 2 minutes the vessel was transferred to a microwave synthesizer and heated for 128 min at 140 °C. After cooling to room temperature, a sample was taken to determine the chain length by ^{1}H NMR. The polymerization mixture was diluted with 5 mL of dichloromethane, followed by precipitation in 250 mL ice-cold diethyl ether. The precipitate was filtered off, dissolved in deionized water and lyophilized (yield: 3.720 g, 94%).

PEtOx. DP = 575. ^{1}H NMR (300 MHz, D_2O): δ 3.70–3.20 (–NR–CH_2–CH_2), 2.41–2.08 (CH_2–CH$_3$), 1.09–0.79 (CH$_2$–CH_3) ppm. SEC (DMAc, LiCl): M_n = 69 000 g mol^{-1}, $Đ$ = 1.3. AF4: M_n = 57 000 g mol^{-1}, $Đ$ = 1.23.

Synthesis of poly(2-ethyl-2-oxazoline-*stat*-ethylene imine) (P(EtOx-*stat*-EI))

To obtain a specific degree of hydrolysis of **P(EtOx-*stat*-EI)**, kinetic studies were performed previously according to literature procedures.[38] The results were used to synthesize PEtOx with defined degree of hydrolysis in larger scale. Accordingly, **PEtOx** (3.510 g, 0.062 mmol) was dissolved in 6 M hydrochloric acid (36 mL). The reaction mixture was heated in a microwave synthesizer at 100 °C for 100 min. Subsequently, the excess of HCl and the resulting propionic acid were distilled off and the residue was dissolved in 15 mL water. The obtained solution was neutralized with 3 M aqueous NaOH to a pH value >8, and the remaining solvent was removed under reduced pressure. The residue was dissolved in DMF and the filtered polymer solution was precipitated two times in 500 mL cold diethyl ether. The obtained product was dried at 85 °C under reduced pressure. ^{1}H NMR spectroscopy was used to determine the conversion of the PEtOx to lPEI. Therefore, the signals from the released lPEI backbone and the signals from the remaining CH_3 group in the side chain of PEtOx were used (yield: 2.350 g, 91%).

P(EtOx-*stat*-EI). EtOx : EI [%] = 54 : 46. ^{1}H NMR (300 MHz, MeOD): δ 3.69–3.41 (NR–CH_2–CH_2), 2.93–2.63 (NH–CH_2–CH_2), 2.55–2.31 (CH_2–CH$_3$), 1.19–1.03 (CH$_2$–CH_3) ppm. SEC (DMAc, LiCl): M_n = 48 000 g mol^{-1}, $Đ$ = 1.28. AF4: M_n = 31 300 g mol^{-1}, $Đ$ = 1.03.

Synthesis of P(EtOx-*stat*-EI-*stat*-ButEnOx) (preP1 to preP3)

The partially hydrolyzed PEtOx, **P(EtOx-*stat*-EI)** (**1**: 659 mg, **2**: 654 mg, **3**: 647 mg), and the catalyst 4-*N*,*N*-dimethylaminopyridine (DMAP, 100 mg, 0.82 mmol) were dissolved in a microwave vial in pyridine (V = 8 mL) at 80 °C. In a second vial, a defined quantity of *N*-succinimidyl-4-pentenate (645 mg, 483 mg, 318 mg) was dissolved in the same solvent (4 mL) and heated up to 80 °C. The two solutions were combined and solvent was added (3 mL) to yield a 4 wt% mixture of **P(EtOx-*stat*-EI)**. The reaction mixture was stirred for 20 h at 80 °C. After cooling to room temperature the sample was filtered and precipitated into 400 mL ice-cold diethyl ether. The copolymer was filtered off and washed with 40 mL of diethyl ether. Due to the negligible effect of the side product *N*-hydroxysuccinimide on subsequent reaction steps, no further purification steps were required. The residue was dried under reduced pressure to constant weight (yield: **1**: 619 mg, 68%, **2**: 650 mg, 75%, **3**: 625 mg, 77%).

preP1. EtOx : EI : ButEnOx = 54 : 12 : 34%. ^{1}H NMR (300 MHz, MeOD): δ 6.00–5.77 (*H*C═CH$_2$), 5.18–4.95 (HC═C*H*$_2$), 3.81–3.40 (NR–CH_2–CH_2), 3.00–2.74 (NH–CH_2–CH_2), 2.67 (NHS), 2.60–2.20 (CH_2–CH$_3$, CH_2–CH_2–C$_2$H$_3$), 1.20–0.97 (CH$_2$–CH_3) ppm. SEC (DMAc, LiCl): M_n = 36 000 g mol^{-1}, $Đ$ = 2.12. AF4: M_n = 25 500 g mol^{-1}, $Đ$ = 1.41.

preP2. EtOx : EI : ButEnOx = 54 : 17 : 29%. ^{1}H NMR (300 MHz, MeOD): δ 6.00–5.78 (*H*C═CH$_2$), 5.17–4.95 (HC═C*H*$_2$), 3.81–3.40 (NR–CH_2–CH_2), 2.95–2.68 (NH–CH_2–CH_2), 2.59 (NHS), 2.57–2.21 (CH_2–CH$_3$, CH_2–CH_2–C$_2$H$_3$), 1.21–1.00 (CH$_2$–CH_3) ppm. SEC (DMAc, LiCl): M_n = 34 500 g mol^{-1}, $Đ$ = 1.63. AF4: M_n = 30 900 g mol^{-1}, $Đ$ = 1.33.

preP3. EtOx : EI : ButEnOx = 54 : 23 : 23%. ^{1}H NMR (300 MHz, MeOD): δ 5.99–5.76 (*H*C═CH$_2$), 5.19–4.96 (HC═C*H*$_2$), 3.81–3.40 (NR–CH_2–CH_2), 2.94–2.66 (NH–CH_2–CH_2), 2.57 (NHS), 2.55–2.25 (CH_2–CH$_3$, CH_2–CH_2–C$_2$H$_3$), 1.22–0.99 (CH$_2$–CH_3) ppm. SEC (DMAc, LiCl): M_n = 36 000 g mol^{-1}, $Đ$ = 1.55. AF4: M_n = 30 400 g mol^{-1}, $Đ$ = 1.33.

Synthesis of P(EtOx-*stat*-EI-*stat*-bocAmButOx) *via* thiol–ene functionalization (*boc*P1 to *boc*P3)

In a microwave vial, **P(EtOx-*stat*-EI-*stat*-ButEnOx)** (**preP1**: 253 mg, **preP2**: 351 mg, **preP3**: 360 mg) was dissolved in methanol (2 mL). In a second vial, the photoinitiator 2,2-dimethoxy-2-phenylacetophenone (DMPA, 49 ± 0.5 mg, 0.19 mmol) and a 1.3-fold excess per double bond of 2-(boc-amino)ethanethiol (193 μL, 239 μL, 205 μL)

were dissolved in methanol (2 mL), likewise. The combined solutions (10 wt%) were degassed with nitrogen for 20 min and the clear solution was stirred in a UV chamber (λ = 365 nm) overnight. Subsequently, the copolymer was precipitated in 200 mL ice-cold diethyl ether. After filtration, the copolymer was dried under reduced pressure for two days (yield: ***boc*P1**: 361 mg, 89%, ***boc*P2**: 493 mg, 92%, ***boc*P3**: 476 mg, 92%).

***boc*P1.** EtOx : EI : bocAmButOx = 54 : 12 : 34%. ^{1}H NMR (300 MHz, MeOD): δ 3.81–3.40 (NR–CH_2–CH_2), 3.27–3.16 (S–CH_2–CH_2), 3.00–2.74 (NH–CH_2–CH_2), 2.64 (NHS), 2.63–2.55 (S–CH_2–CH_2), 2.54–2.27 (CH_2–CH$_3$, CH_2–C$_2$H$_4$–CH_2), 1.82–1.57 (CH$_2$–C$_2$H$_4$–CH$_2$), 1.55–1.39 (C(CH_3)$_3$), 1.21–1.00 (CH$_2$–CH_3) ppm.

***boc*P2.** EtOx : EI : bocAmButOx = 54 : 17 : 29%. ^{1}H NMR (300 MHz, MeOD): δ 3.81–3.41 (NR–CH_2–CH_2), 3.28–3.16 (S–CH_2–CH_2), 2.92–2.72 (NH–CH_2–CH_2), 2.69–2.59 (S–CH_2–CH$_2$), 2.58 (NHS), 2.54–2.29 (CH_2–CH$_3$, CH_2–C$_2$H$_4$–CH_2), 1.82–1.56 (CH$_2$–C$_2$H$_4$–CH$_2$), 1.55–1.39 (C(CH_3)$_3$), 1.21–1.03 (CH$_2$–CH_3) ppm.

***boc*P3.** EtOx : EI : bocAmButOx = 54 : 23 : 23%. ^{1}H NMR (300 MHz, MeOD): δ 3.79–3.41 (NR–CH_2–CH_2), 3.27–3.17 (S–CH_2–CH_2), 2.91–2.71 (NH–CH_2–CH_2), 2.67–2.59 (S–CH_2–CH$_2$), 2.58 (NHS), 2.54–2.29 (CH_2–CH$_3$, CH_2–C$_2$H$_4$–CH_2), 1.80–1.56 (CH$_2$–C$_2$H$_4$–CH$_2$), 1.55–1.39 (C(CH_3)$_3$), 1.20–1.02 (CH$_2$–CH_3) ppm.

Synthesis of P(EtOx-*stat*-EI-*stat*-AmButOx) *via* deprotection (P1 to P3)

The copolymer **P(EtOx-*stat*-EI-*stat*-bocAmButOx)** (***boc*P1**: 321 mg, ***boc*P2**: 402 mg, ***boc*P3**: 420 mg) was dissolved in dichloromethane (3 mL). Trifluoroacetic acid was added (5 mL) and the reaction mixture was stirred overnight at room temperature. The copolymer was precipitated in 400 mL ice-cold diethyl ether. The precipitate was filtered, washed with 40 mL diethyl ether, dissolved in methanol and shaken overnight with Amberlyst A21 (free base) ($\sim$0.5 g). The solvent was removed and the copolymer lyophilized (yield: **P1**: 240 mg, 95%, **P2**: 293 mg, 91%, **P3**: 330 mg, 95%).

P1. EtOx : EI : bocAmButOx = 54 : 12 : 34%. ^{1}H NMR (300 MHz, MeOD): δ 3.76–3.29 (NR–CH_2–CH_2), 3.11–2.98 (S–CH_2–CH_2), 2.84–2.65 (NH–CH_2–CH_2), 2.58 (NHS), 2.57–2.46 (S–CH_2–CH$_2$), 2.45–2.16 (CH_2–CH$_3$, CH_2–C$_2$H$_4$–CH_2), 1.83–1.44 (CH$_2$–C$_2$H$_4$–CH$_2$), 1.10–0.89 (CH$_2$–CH_3) ppm. SEC (DMAc, LiCl): M_n = 30 500 g mol^{-1}, $Đ$ = 1.60. AF4: M_n = 35 300 g mol^{-1}, $Đ$ = 1.74.

P2. EtOx : EI : bocAmButOx = 54 : 17 : 29%. ^{1}H NMR (300 MHz, MeOD): δ 3.68–3.21 (NR–CH_2–CH_2), 3.01–2.87 (S–CH_2–CH_2), 2.72–2.56 (NH–CH_2–CH_2), 2.50 (NHS), 2.48–2.37 (S–CH_2–CH$_2$), 2.37–2.08 (CH_2–CH$_3$, CH_2–C$_2$H$_4$–CH_2), 1.70–1.36 (CH$_2$–C$_2$H$_4$–CH$_2$), 1.03–0.82 (CH$_2$–CH_3) ppm. SEC (DMAc, LiCl): M_n = 39 000 g mol^{-1}, $Đ$ = 1.58. AF4: M_n = 43 700 g mol^{-1}, $Đ$ = 1.72.

P3. EtOx : EI : bocAmButOx = 54 : 23 : 23%. ^{1}H NMR (300 MHz, MeOD): δ 3.87–3.40 (NR–CH_2–CH_2), 3.23–3.03 (S–CH_2–CH_2), 2.97–2.75 (NH–CH_2–CH_2), 2.74–2.57 (S–CH_2–CH$_2$), 2.56–2.28 (CH_2–CH$_3$, CH_2–C$_2$H$_4$–CH_2), 1.88–1.56 (CH$_2$–C$_2$H$_4$–CH$_2$), 1.22–0.98 (CH$_2$–CH_3) ppm. SEC (DMAc, LiCl): M_n = 31 500 g mol^{-1}, $Đ$ = 1.45. AF4: M_n = 30 500 g mol^{-1}, $Đ$ = 1.62.

Copolymer labeling with Cy5

Copolymer **P3** (40 mg) and triethylamine (150 μL) were dissolved in DMF (10 mL). After addition of the cyanine-5-NHS-ester (0.4 mg) the reaction was stirred at room temperature overnight. The labeled copolymer was precipitated in 500 mL ice-cold diethyl ether, filtered and re-dissolved in H_2O (15 mL). Further purification was performed by dialysis against water using a Spectra/Por 3 dialysis membrane (3500 g mol^{-1} cut-off). Finally, the product was lyophilized and obtained as a blue powder. The calculated labeling efficiency (*via* UV-Vis) for conjugation was 65% for **P3–Cy5** (yield: 27 mg, 67%). **lPEI** was treated likewise but dialyzed against a water/methanol mixture and dried under reduced pressure, subsequently (yield: 2.6 mg, 26%; labeling efficiency: 2%).

Synthesis of linear poly(ethylene imine) (lPEI)

The synthesized copolymer **P(EtOx-*stat*-EI)** (DP = 575, 100 mg) was treated with an excess of 6 M aqueous hydrochloric acid (1.5 mL) for 2 hours at 100 °C in a microwave synthesizer to yield a hydrolyzed linear poly(ethylene imine) (DP = 575). Neutralization and purification *via* precipitation were performed analogous to the described synthesis of **P(EtOx-*stat*-EI)** (see above). The product **lPEI** was dried at 85 °C under high vacuum for 2 days and the degree of hydrolysis was determined by ^{1}H NMR by correlating the integrals of the PEI backbone and the remaining methyl group of the PEtOx side chain (yield: 51 mg, 87%).

lPEI. EtOx : EI [%] = 5 : 95. ^{1}H NMR (300 MHz, MeOD): δ 3.58–3.41 (NR–CH_2–CH_2), 2.91–2.61 (NH–CH_2–CH_2), 2.56–2.36 (CH_2–CH$_3$), 1.18–1.06 (CH$_2$–CH_3) ppm.

Polyplex preparation

Polyplexes of pDNA and polymers were prepared by mixing stock solutions of 15 μg mL^{-1} pDNA and different amounts of polymers (1 mg mL^{-1}) to obtain various N/P ratios (nitrogen of polymer to phosphate of pDNA) in HBG buffer (20 mM 4-(2-hydroxyethyl)piperazine-1-ethanesulfonic acid (HEPES) and 5% (w/v) glucose, pH 7.2). The solutions were vortexed for 10 s at maximal speed and incubated at room temperature for 20 min to ensure complex formation. For the preparation of polyplexes with siRNA, 1 μM siRNA (final concentration) was used as described above.

Ethidium bromide quenching assay

The formation of polyplexes with pDNA as well as siRNA was examined by quenching of the ethidium bromide fluorescence. Briefly, pDNA (15 μg mL^{-1}) or siRNA (1 μM) in a total volume of 100 μL HBG buffer were incubated with ethidium bromide (0.4 μg mL^{-1}) for 10 min at room temperature. Subsequently, polyplexes with different amounts of polymer (various N/P ratios) were prepared in black 96-well plates (Nunc Thermo Fisher). The samples were incubated at room temperature for 15 min. The fluorescence of the samples was measured at an excitation wavelength of 525 nm and an emission wavelength of 605 nm using a microplate reader (TECAN Infinite M200 Pro, Crailsheim, Germany). A sample containing only pDNA and ethidium bromide was used to calibrate the device to 100% fluorescence against a background of 0.4 μg mL^{-1} of ethidium bromide in

HBG solution. The percentage of dye displaced upon polyplex formation was calculated using eqn (1):

$$\mathrm{RFU}[\%] = \frac{F_{\mathrm{sample}} - F_0}{F_{\mathrm{pDNA}} - F_0} \times 100 \quad (1)$$

Here, RFU is the relative fluorescence and F_{sample}, F_0, and F_{pDNA} are the fluorescence intensities of a given sample, the ethidium bromide in HBG alone, and the ethidium bromide intercalated into pDNA alone.

Heparin dissociation assay

To investigate the release of pDNA from polyplexes, the heparin dissociation assay was performed. Polyplexes with an N/P ratio of 30 were prepared as described above in a total volume of 100 μL HBG buffer containing ethidium bromide (0.4 μg mL^{-1}). After incubation in the dark at room temperature for 15 min, the polyplexes were transferred into a black 96-well plate, and heparin of indicated concentrations was added. The solution was mixed and incubated for further 30 min at 37 °C in the dark. The fluorescence of ethidium bromide was measured at Ex 525 nm/Em 605 nm with a Tecan microplate reader. The percentage of intercalated ethidium bromide was calculated as described before.

Dynamic and electrophoretic light scattering

Dynamic light scattering (DLS) was performed on a Zetasizer Nano ZS (Malvern Instruments, Herrenberg) with a He–Ne laser operating at a wavelength of λ = 633 nm. All measurements (30 runs, triplicate) were carried out at 25 °C after an equilibration time of 120 s. The counts were detected at an angle of 173°. The mean particle size was approximated as the effective (*z*-average) diameter and the width of the distribution as the polydispersity index of the particles (PDI) obtained by the cumulants method assuming a spherical shape. Electrophoretic light scattering (ELS) was used to measure the zeta potential (ζ). The measurement was performed on a Zetasizer Nano ZS (Malvern Instruments, Herrenberg, Germany) by applying laser Doppler velocimetry. For each measurement, 20 runs were carried out using the slow-field reversal and the fast-field reversal mode at 150 V. Each experiment was performed in triplicate a 25 °C. The zeta potential was calculated from the electrophoretic mobility (μ) according to the Henry equation. Henry coefficient f(ka) was calculated according to Oshima.

Determination of the cytotoxicity

Cytotoxicity studies were performed with the mouse fibroblast cell line L929 (CCL-1, ATCC), as recommended by ISO10993-5. The cells were routinely cultured in Dulbecco's modified eagle's medium (DMEM, Lonza, Basel) supplemented with 10% fetal calf serum (FCS), 100 U mL^{-1} penicillin and 100 μg mL^{-1} streptomycin at 37 °C in a humidified 5% (v/v) CO_2 atmosphere.

In detail, cells were seeded at 10^4 cells per well in a 96-well plate and incubated for 24 h, whereas no cells were seeded in the outer wells. Subsequently, the testing substances (polymers) at indicated concentrations (from 0.25 μg mL^{-1} to 1 mg mL^{-1}) were added to the cells and the plates were incubated for further 24 h. Control cells were incubated with fresh culture medium. Subsequently, the medium was replaced by a mixture of fresh culture medium and Alamar-Blue solution (Life technologies, Darmstadt, Germany), prepared according to the manufacturer's instructions. After a further incubation of 4 h at 37 °C, the fluorescence was measured at Ex 570/Em 610 nm, with untreated cells on the same well plate serving as negative controls. The negative control was standardized as 0% of metabolism inhibition and referred as 100% viability. Cell viability below 70% was considered indicative of cytotoxicity. Data are expressed as mean ± SD of three determinations.

Hemolysis assay

The interaction of polymers with cellular membranes was investigated by analyzing the release of hemoglobin from erythrocytes. Blood from sheep, collected in heparinized tubes, was provided by the Institute of Laboratory Animal Science and Animal Welfare, Friedrich-Schiller University Jena. The blood was centrifuged at 4500 × *g* for 5 min, and the pellet was washed three times with cold 1.5 mM phosphate buffered saline (PBS, pH 7.4). After dilution with PBS in a ratio of 1 : 7, aliquots of erythrocyte suspension were mixed 1 : 1 with the polymer solution and incubated in a water bath at 37 °C for 60 min. After centrifugation at 2400 × *g* for 5 min, the hemoglobin release into the supernatant was determined spectrophotometrically using a microplate reader (TECAN Infinite M200 Pro, Crailsheim, Germany) at a wavelength of 544 nm. Complete hemolysis (100%) was achieved using 1% Triton X-100 serving as positive control. Pure PBS was used as negative control (0% hemolysis). The haemolytic activity of the polycations was calculated as follow (2):

$$\%\ \mathrm{Hemolysis} = 100 \times \frac{\left(A_{\mathrm{Sample}} - A_{\mathrm{Negative\ control}}\right)}{A_{\mathrm{Positive\ control}}} \quad (2)$$

A value less than 2% hemolysis rate were classified as non-hemolytic, 2 to 5% as slightly haemolytic and values >5% as hemolytic. Experiments were run in triplicates and were performed with three different batches of donor blood.

Erythrocyte aggregation

Erythrocytes were isolated as described above. The erythrocyte suspension were mixed 1 : 1 with the polymer solutions (100 μL total volume) in a clear flat bottomed 96-well plate. The cells were incubated at 37 °C for 2 h, and the absorbance was measured at 645 nm in a microplate reader. Cells, which were treated with PBS served as negative control and 25 kDa bPEI (50 μg mL^{-1}, Polysciences) was used as positive control. Absorbance values of the test solutions lower than the negative control were regarded as aggregation. Experiments were run in triplicates and were performed with three different batches of donor blood.

Polyplex uptake

HEK-293 cells (CRL-1573, ATCC) were cultured in RPMI 1640 medium (Lonza, Basel) supplemented with 10% FCS, 100 μg mL^{-1} streptomycin, 100 U mL^{-1} penicillin and 2 mM L-glutamine at 37 °C in a humidified 5% CO_2 (v/v) atmosphere.

For uptake studies, cells were seeded at a density of 10^5 cells per mL in 24-well plates and cultured for 24 h. One hour prior to the addition of the polyplexes, the medium was changed to OptiMEM (Life Technologies, Darmstadt, Germany). The polyplexes were prepared as described above and at least 50 μL polyplexes in solution were added to the cells. The plates were incubated for 4 h at 37 °C, 5% CO_2.

For kinetic studies of the polyplex uptake within 4 h, pDNA was labeled with YOYO-1 iodide prior to the polyplex preparation. For labeling of 1 μg pDNA, 0.026 μL of 1 M YOYO-1 solution was mixed with pDNA and incubated for 20 min at 4 °C protected from light. Afterwards, HBG buffer and polymers were added at the indicated N/P ratio and the polyplexes were formed as described previously. The cells were harvested 0.5, 1, 2 and 4 h after polyplex addition and 10% trypan blue was added to quench the outer fluorescence of the cells. For energy-dependent uptake studies, cells were equilibrated in OptiMEM at 4 °C 1 h prior polyplex addition. The plates were incubated at 4 °C for 4 h. To determine the relative uptake of the polyplexes, 10^4 cells were measured by flow cytometry using a Cytomics FC 500 (Beckman Coulter) and the amount of viable cells showing YOYO-1 signal were gated. Dead cells were identified *via* counterstaining with propidium iodide (PI). The experiments were performed at least three times independently.

For inhibition experiments, cells were treated with 100 μM 5-(*N*-ethyl-*N*-isopropyl)amiloride (EIPA) in standard culture media 30 min prior to polyplex addition. Subsequently, **P3** and **lPEI** polyplexes were added to the cells and incubated for further 4 h. Afterwards, the cells were harvested and analyzed as described above *via* flow cytometry or were further prepared for STEM imaging.

Transfection of adherent cells

For transfection of adherent HEK-293 cells, the cells were seeded at a density of 10^5 cells per mL in 24-well plates and incubated for 24 h at 37 °C, 5% CO_2. One hour prior to transfection, the cells were washed with PBS and supplemented with 0.5 mL OptiMEM or fresh serum containing growth medium (RPMI 1640). The polyplexes were prepared as described above, and were added to the cells (50 μL per well). After an incubation time of 4 h at 37 °C, the supernatant was replaced by fresh growth medium and the cells were incubated for further 20 h. For analysis *via* flow cytometry (Cytomics FC 500, Beckman Coulter), cells were harvested by trypsinization. For determination of the viability during flow cytometry, dead cells were identified *via* counterstaining with propidium iodide. For determination of the transfection efficiency, 10^4 viable cells expressing EGFP were gated. The experiments were performed three times independently. Regarding the Bafilomycin experiments, 175 nM Bafilomycin was added to the cells in OptiMEM and incubated for 20 min, prior to the polyplex addition. The knockdown studies were performed with stable EGFP expressing CHO cells (CCL-61, ATCC, stable transfected with pEGFP-N1) and the corresponding siRNA (against *egfp*, riboxx, Germany). The polyplexes were incubated in OptiMEM for 6 h and measured after 72 h *via* flow cytometry.

Electron microscopy

Scanning transmission electron microscopy with high-angle annular dark-field detection (STEM-HAADF) was carried out using a Technai G^2 system (FEI), with 120 kV or 200 kV acceleration voltage on ultrathin slices of resin-embedded cell samples.

For cell preparation, HEK-293 cells (10^5 cells mL^{-1}) were seeded on 6-well plates and incubated for 4 h at 37 °C with the respective polyplex samples (N/P 30). The cells were harvested, washed with PBS and fixed for 2 h with glutaraldehyde (2% in PBS, prepared from 8% EM grade stock solution) on ice. Subsequent to aldehyde fixation, the cells were washed with PBS prior to the fixation with OsO_4 for 1 h (1% in PBS, prepared from 4% EM grade stock solution, both purchased from EMS, Hatfield). After this, the cells were washed with MilliQ water and staining with uranyl acetate solution was carried out for 1 h and protected from light (1% in solution in MilliQ water prepared from depleted uranyl acetate dihydrate purchased from EMS, Hatfield). Subsequently, the sample was washed with pure water prior to dehydration by an ethanol/water series (50%, 70%, 90%, 2 × 100% dry EtOH, purified with a Solvent Purification System and stored over molecular sieves). Thereafter, the cells were transferred into BEEM capsules (Plano, Wetzlar), in which the cell suspension was immersed in mixtures of Embed 812 (EMS, Hatfield) and ethanol (Embed/EtOH = 1 : 1 v/v for 1 hour, 2 : 1 v/v for 12 h, pure Embed 812 for 4 h). Subsequent to a further exchange of the embedding medium, the resin was allowed to harden at 70 °C for 24 h. From the resin block, ultrathin sections with a thickness of 80 nm were cut with an ultramicrotome (PT-XL PowerTome, RMC, Tucson) using a diamond knife (RMC, Tucson). The ultrathin resin sections were applied on a carbon supported copper grid (400 mesh, Quantifoil, Jena).

Confocal microscopy and structured illumination microscopy

Live cell imaging was performed for uptake studies. In detail, HEK cells (10^5 cells mL^{-1}) were seeded on glass-bottomed dishes (ibidi, Germany, thickness 170 ± 5 μm for high-resolution fluorescence microscopy) and cultivated for 24 h in a humidified atmosphere. One hour prior to the polymer addition, the cells were rinsed with phosphate buffered saline (PBS) and the medium was changed to OptiMEM. The polyplexes were formed with Cy5-labeled **P3** and YOYO-labeled pDNA or Cy3-labeled siRNA, added to the cells and incubated for further 4 h. Subsequently, medium was replaced by fresh culture medium or PBS supplemented with Hoechst 33342 for nucleus staining, LysoTracker Red DND-99 or LysoTracker Green DND-26 (all from Thermo Fisher Scientific) for lysosome staining.

Imaging was performed with LSM880, Elyra PS.1 system (Zeiss, Oberkochen, Germany) applying a 63× 1.4 NA plan apochromat oil objective. For SIM imaging, cells were grown on high precision cover glasses (Marienfeld-Superior, 18 × 18 mm, 170 ± 5 μm certified thickness) at a density of 5×10^4 cells mL^{-1}, fixed with paraformaldehyde (2% in PBS) and embedded in prolong gold antifading reagent (Thermo Fisher Scientific). Regarding the SIM performance, excitation wavelengths of 405 nm

(exc. grating 28.0 μm), 488 nm (exc. grating 34.0 μm), 561 nm (exc. grating 42.0 μm) and 642 nm (exc. grating 42.0 μm resp. 51.0 μm) were used. The following four color channels were used for both microscopy techniques: Nucleus (Hoechst 33342 staining, excitation wavelength 405 nm, BP 420–480 + LP 750, grey), pDNA (YOYO-1 Iodide, excitation wavelength 488 nm, BP 495–550 + LP 750, green), polymer **P3** (Cy-5 labeling, excitation wavelength 642 nm, LP 655, blue) and lysosome (CellLight Lysosomes-RFP BacMam 2.0, excitation wavelength 561 nm, BP 570–620 + LP 750, red). The grating position and axial position of the sample table were controlled by piezo controllers. Images were recorded with a sCMOS camera (pco.edge, Kehlheim, German), cooled to 5 °C. Reconstructions and deconvolution were performed with the commercial ZEN2 software installed on the system (Zeiss, Oberkochen, Germany).

Statistical analysis

The values represent the mean ± SD. For the calculation of the standard derivation of two or more different groups, the two sample *t*-test (student's *t*-test) or the ANOVA was used. Statistical significance was defined as * for *p*-values of <0.05 and # for *p*-values <0.005.

Results and discussion

Polymer synthesis

As chain transfer reactions are more likely to occur during polymerization of 2-methyl-2-oxazoline,[39] 2-ethyl-2-oxazoline was used as monomer for the polymerization of the precursor homopolymer, being able to decrease cytotoxicity of aspired copolymers.[40]

PEtOx was synthesized according to a literature procedure by microwave supported cationic ring-opening polymerization (CROP).[41] The degree of polymerization of 575 was calculated from the tosylate ^{1}H NMR signals of MeOTos before purification. In order to ensure the absence of water, the polymerization solutions were prepared in a glove box under nitrogen atmosphere yielding **PEtOx** with a dispersity *Đ* of 1.3 (SEC: DMAc, 0.21% LiCl, standard: PS, Table 1). This homopolymer served as precursor for the subsequent copolymer synthesis.

PEtOx was hydrolyzed in a microwave synthesizer (Scheme 1a) to yield the copolymer poly(2-ethyl-2-oxazoline-*stat*-ethylene imine) (**P(EtOx-*stat*-EI)**) with an EtOx content of 54% (calc. from ^{1}H NMR).[38]

To introduce primary amines to the polymers, a fraction of the ethyleneimine units was functionalized with *N*-succinimidyl-4-pentenate to introduce alkene functionalities (Scheme 1b).[42] While the synthesis of poly(2-butenyl-2-oxazoline) is possible *via* the polymerization of the respective monomers,[36] these units do not withstand the conditions of the acidic hydrolysis of PEtOx. Three different copolymers of P(EtOx-*stat*-EI-*stat*-ButEnOx) (**preP1** to **preP3**) with varying ratios of secondary amines and 2-(3-butenyl-2-oxazoline)s (1 : 3, 1 : 2, 1 : 1) were synthesized while maintaining a constant EtOx content of 54% (Table 1). The introduction of primary amines was performed by thiol–ene photoaddition. Hence, the copolymers P(EtOx-*stat*-EI-*stat*-AmButOx) (**P1** to **P3**) were synthesized by reaction of the corresponding precursor copolymers (**preP1** to **preP3**) with a protected aminothiol under UV irradiation and subsequent deprotection to yield the primary amine group (Scheme 1c and d).

Characterization by ^{1}H NMR spectroscopy confirms the presence of 2-ethyl-2-oxazoline (EtOx) as well as ethylene imine (EI) units (Fig. 2, **PEtOx** and **P(EtOx-*stat*-EI)**). The integrals of the signals of the EtOx side chain (A, B) as well as the signals of the backbone (C) remain constant during further reactions and are, therefore, used as reference.

The successful functionalization with the activated acid *N*-succinimidyl-4-pentenate is exemplified by the proton signals of the double bond (ButEnOx) that appear at 5.9 ppm (–*H*C═CH_2, H) and 5.1 ppm (–HC═CH_2, I) for the copolymer **preP3**. The first signal is used to calculate the composition of the formed copolymer by comparing the signals of the ethylene imine backbone (between 3.00 to 2.66, NH–CH_2–CH_2, D) and the methyl protons of the EtOx side chain (between 1.22 to 0.97, CH_2–CH_3, A). The successful functionalization of **preP1** to **preP3** with the thiol is shown by the disappearance of the double bond signals after the photoaddition (***boc*P3**). The signals of the newly formed CH_2 groups appear at 2.40 (I′) and 1.70 ppm (H′), respectively. Furthermore, a singlet of the *tert*-butyloxycarbonyl (boc) protecting group is obtained at 1.50 ppm (L). After treatment with

Table 1 Composition and molar masses for **PEtOx**, **P(EtOx-*stat*-EI)**, **preP1** to **preP3** and **P1** to **P3**

		Composition[a]		Amine ratio	NMR[b]	AF4		SEC	
Abbr.	Name	*X* [%]	*Y* [%]	$sec_X : prim_Y$	M_n [g mol^{-1}]	M_n [g mol^{-1}]	*Đ*	M_n [g mol^{-1}]	*Đ*
PEtOx	$PEtOx_{575}$	—	—	—	57 000	57 000	1.2	69 000	1.3
P(EtOx-*stat*-EI)	$P(EtOx_{54\%}$-*stat*-$EI_X)$	46	—	—	42 100	31 300	1.3	48 000	1.3
preP1	$P(EtOx_{54\%}$-*stat*-EI_X-$ButEnOx_Y)$	12	34	—	58 100	25 500	1.4	36 000	2.1
preP2	$P(EtOx_{54\%}$-*stat*-EI_X-$ButEnOx_Y)$	17	29	—	55 800	30 900	1.3	34 500	1.6
preP3	$P(EtOx_{54\%}$-*stat*-EI_X-$ButEnOx_Y)$	23	23	—	53 000	30 400	1.3	36 000	1.6
P1	$P(EtOx_{54\%}$-*stat*-EI_X-$AmButOx_Y)$	12	34	1 : 2.8	73 200	35 300	1.7	30 500	1.6
P2	$P(EtOx_{54\%}$-*stat*-EI_X-$AmButOx_Y)$	17	29	1 : 1.7	68 600	43 700	1.7	39 000	1.6
P3	$P(EtOx_{54\%}$-*stat*-EI_X-$AmButOx_Y)$	23	23	1 : 1	63 100	30 500	1.6	31 500	1.5

[a] Determined by ^{1}H NMR (calculated from the ratio of EtOx, ButEnOx signals and EI backbone). [b] Determined by ^{1}H NMR (calculated from tosylate signals of MeOTos before purification).

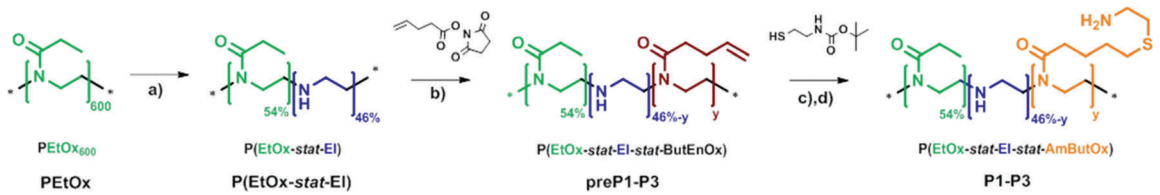

Scheme 1 Schematic representation of the synthesis of cationic copolymers. (a) Partial hydrolysis of poly(2-ethyl-2-oxazoline) in a microwave synthesizer, (b) post-polymerization functionalization with *N*-succinimidyl-4-pentenate, (c) thiol–ene photo-addition of 2-(boc-amino)ethanethiol at 365 nm and (d) deprotection using trifluoroacetic acid.

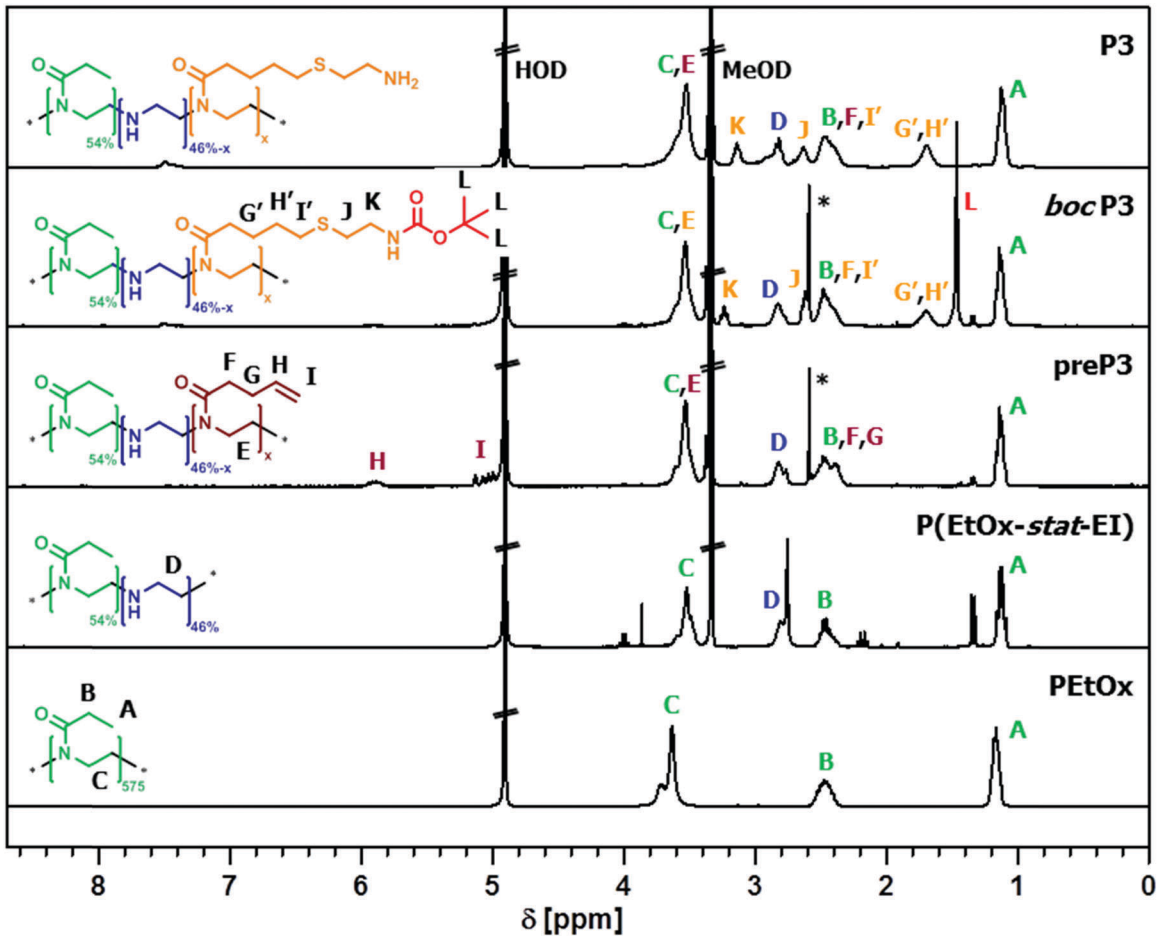

Fig. 2 Comparison of ^{1}H NMR spectra of **PEtOx**, **P(EtOx-*stat*-EI)**, **preP3**, ***boc*P3** and the final product **P3** (* side product *N*-hydroxysuccinimide) (300 MHz, MeOD).

trifluoroacetic acid (TFA) and precipitation into diethyl ether, the signal of the protecting group disappears, indicating the successful deprotection of ***boc*P1** to **bocP3** and, consequently, the synthesis of P(EtOx-*stat*-EI-*stat*-AmButOx) (**P1** to **P3**).

A comparison of the composition and molar masses of the prepared copolymers obtained by asymmetric flow field-flow fractionation (AF4) and size exclusion chromatography (SEC) is shown in Table 1. Although a trend is clearly visible, the obtained values should be handled with care due to the fact that the introduction of double bond containing ButEnOx units as well as the cationic amine units (primary and secondary) could lead to undesired column and membrane interactions and, hence, to a change in the elution behavior. SEC traces, exemplified for the synthesis of **P2**, are depicted in the ESI† (Fig. S1).

To enable *in vitro* imaging, copolymer **P3** was labeled using one equivalent of Cy5–NHS per polymer chain. Successful dye functionalization and purification *via* dialysis (3500 g mol^{-1} cut-off) was verified by size exclusion chromatography (SEC), revealing no trace of unbound dye (ESI,† Fig. S2).

Bio- and hemocompatibility

Biocompatibility represents a critical parameter for PEI based polymers. One option to reduce the known cytotoxicity of PEI[12,13,43]

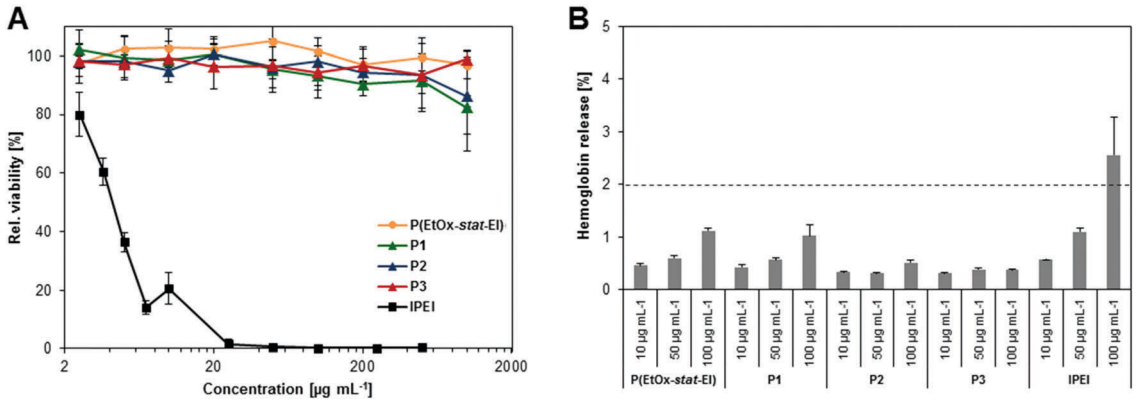

Fig. 3 Determination of bio- and hemocompatibility. (A) Relative viability of L929 cells after 24 h incubation with the polymers at different concentrations according to ISO10993-5. (B) Hemolysis assay of erythrocytes after incubation with polymers at the indicated concentrations. Triton X-100 served as positive control (98.8% hemolysis) and PBS as negative control (0.2%). A value less than 2% hemolysis rate was classified as non-hemolytic, 2 to 5% as slightly hemolytic and values >5% as hemolytic. Values represent the mean ± S.D. (n = 3).

is the introduction of EtOx units.[31] The copolymers introduced here (**P1** to **P3**) possess an oxazoline content of 54%, expected to decrease severe cytotoxic effects. The cytotoxicity of **P1** to **P3** was investigated in comparison to **lPEI** (Fig. 3A), obtained by full hydrolysis of **P(EtOx-*stat*-EI)**. Besides **lPEI**, commercial available linear poly(ethylene imine) (**comlPEI**, 25 kDa, Polyscience) was used as internal control. The results of the following *in vitro* experiments performed with **comlPEI** are summarized in the ESI† (Fig. S18–S20).

As assumed, **lPEI** leads to a significant reduction of cell viability at low concentrations (IC_{50} of 3.6 µg mL^{-1}), which is in accordance to literature data.[3] Despite a high molar mass (>25 kDa), **P(EtOx-*stat*-EI)** as well as **P1** to **P3** showed no cytotoxicity after 24 h using polymer concentrations up to 1 mg mL^{-1} (IC_{50} > 1 mg mL^{-1}, Fig. 3A). This improvement on cell viability is attributed to the introduced EtOx content of 54% within the copolymers and is consistent with literature reports on partially hydrolyzed POx.[32]

The blood compatibility of the copolymers was further investigated by assessment of the hemolytic activity (Fig. 3B) as well as the aggregation of erythrocytes. The treatment of **P(EtOx-*stat*-EI)** and **P1** to **P3** did not show any hemolytic activity in a concentration range from 10 to 50 µg mL^{-1}. A slight hemolysis (~1% hemoglobin release) could be revealed at higher concentrations of **P(EtOx-*stat*-EI)** and **P1** (100 µg mL^{-1}). In contrast, **lPEI** revealed an increased interaction with the cellular membranes of the blood cells resulting in hemoglobin releases above 2% (100 µg mL^{-1}) and, moreover, in a strong agglomeration of erythrocytes (see ESI,† Fig. S3 and S4). The later was not observed with EtOx containing copolymers (**P(EtOx-*stat*-EI)**, **P1** to **P3**) indicating a good hemo- and biocompatibility.

Characterization of the polyplexes

Despite the beneficial impact of EtOx on the biocompatibility of the polymers, their impact on the polyplex formation was investigated. For this purpose, the ethidium bromide quenching assay (EBA) was used to investigate the condensation of plasmid DNA (pDNA) by **P1** to **P3** as well as **P(EtOx-*stat*-EI)**, at different nitrogen (polymer) to phosphate (DNA) ratios (N/P). Ethidium bromide is excluded from its binding sites within the oligonucleotides because of the electrostatic and hydrophobic interactions between polymer and the nucleic acid, leading to a reduction in fluorescence that can be correlated to the affinity of the complexation.[44,45] All copolymers (**P1** to **P3**) revealed decreasing fluorescence intensities below 40% relative fluorescence units (RFU, Fig. 4A). Stable polyplexes indicated by a plateau were reached at higher N/P ratios 5 to 40, whereby no significant differences between **P1**, **P2**, **P3** and **lPEI** were observed. In contrast, the precursors **PEtOx** (data not shown) and **P(EtOx-*stat*-EI)** did not form appropriate polyplexes. It can be assumed that the EtOx units prevent a strong binding of the DNA to the secondary amines of the PEI backbone. This reduced complexation affinity is compensated by the introduction of the more flexible side chains consisting of AmButOx (primary amines) within **P1** to **P3**, which apparently are essential for the polyplex formation. Interestingly, the combination of EI and AmButOx seems to be beneficial, since a comparable copolymer **P(MeOx-*stat*-AmButOx)** without ethylene imine units revealed reduced pDNA complexation around 60% RFU in a previous study.[17] A synergistic effect between both, primary amines in the side chain and secondary amines in the backbone, leads to an improved binding of DNA despite an EtOx content of 54%. The following studies of **P1** to **P3** were performed with polyplexes formed at N/P 30 as this guarantees stable polyplex formation.

To analyze the stability and the dissociation properties of the formed polyplexes, the heparin dissociation assay was performed.[46–48] Heparin, a sulfated glycosaminoglycan, has an anionic character and competes with the nucleic acid of the polyplex. With increasing amount of heparin, the pDNA dissociates from the polymer and the polyplex dissolves. As indicated in Fig. 4B, polyplexes formed with partially hydrolyzed PEtOx (**P(EtOx-*stat*-EI)**) as well as **P2** and **P3** polymers revealed a reversible binding, achieving 80% dissociation at 5 U mL^{-1} heparin. A higher heparin concentration (20 U mL^{-1}) was required for **P1** reaching 80% dissociation. One reason for

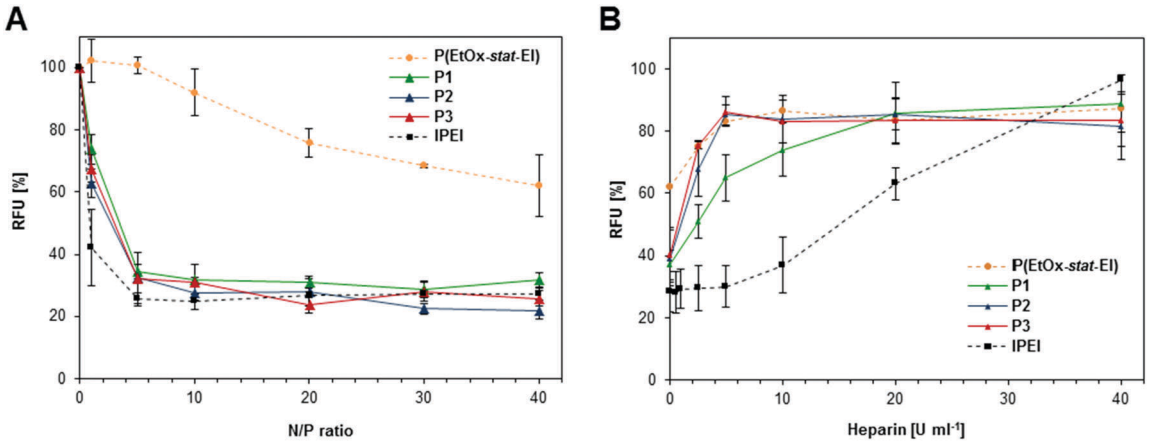

Fig. 4 Polyplex formation and stability with pDNA using the polymers **P(EtOx-*stat*-EI)**, **P1**, **P2**, **P3** as well as **lPEI**, which was used as positive control. (A) Complexation affinity (ethidium bromide quenching assay) of all polymers at the indicated N/P ratios. (B) Dissociation assay of polyplexes formed at N/P 30 using heparin. Values represent the mean ± S.D. (n = 3).

this might be the higher amount of AmButOx, responsible for an enhanced binding to the genetic material. However, a full release from the copolymers **P1** to **P3** could not be achieved using heparin. Therefore, another polyanion, namely poly(methacrylic acid) (PMAA, DP = 200), was successfully used as competitor (Fig. S5, ESI†). **lPEI** required an increased amount of heparin (40 U mL^{-1}) as compared to the copolymers. These results confirm the weakening of the electrostatic interactions caused by the presence of EtOx units, which are beneficial for a fast release of the genetic material.

As polyplexes are usually internalized into cells *via* endocytic pathways, the size as well as the charge of the complexes is of crucial importance. For efficient delivery, critical sizes of polymeric nanocarriers up to 200 nm are recommended.[33,49] As depicted in Table 2, the polyplexes formed with **P1** to **P3** at N/P 30 exhibit a favorable size of approximately 150 nm with a positive net charge, as determined by dynamic and electrophoretic light scattering. **P(EtOx-*stat*-EI)** formed complexes with a z-average of 242 ± 73.4 nm and high polydispersity (0.46) supporting the inefficient polyplex formation as observed by EBA.[50] Polyplexes formed with **lPEI** revealed a smaller complex size of 80 nm with a positive net charge comparable to previous studies.[46] These results support our assumption that the EtOx units impede the compact packaging of the genetic material into small polyplexes. This can be compensated by the presence of AmButOx units resulting in polyplex sizes between **lPEI** and loosely bound **P(EtOx-*stat*-EI)** polyplexes. Therefore, the tailored combination of EtOx and AmButOx units within the copolymer structure can be used to design polyplexes with required properties.

Table 2 Size and surface charge (zeta potential) of pDNA complexes at N/P 30 measured *via* dynamic light as well as electrophoretic light scattering

Polymeric system	z-Average [d, nm]	PDI	Zeta potential [mV]
P(EtOx-*stat*-PEI)	242 ± 73.4	0.46	20 ± 0.44
P1	158 ± 1.0	0.23	27 ± 0.25
P2	143 ± 1.4	0.21	23 ± 0.11
P3	154 ± 1.4	0.23	23 ± 0.12
lPEI	80 ± 2.3	0.17	33 ± 4.23

Transfection efficiency

Based on the previous results, the polymers **P1** to **P3** appear to be promising candidates as non-viral gene delivery agents and were, therefore, analyzed regarding their transfection efficiency (TE) using human embryonic kidney (HEK) cells and pDNA containing a enhanced green fluorescence protein reporter gene (*egfp*). The TE was determined by flow cytometry analyzing all viable cells (PI staining) which successfully express EGFP (see ESI,† Fig. S6 and S7). To investigate the interaction with serum proteins, a side effect of cationic polymers, the cells were transfected in serum reduced media (OptiMEM) and in serum containing media (RPMI1640 supplemented with 10% FCS) (Fig. 5). The use of serum offers test conditions more comparable to an *in vivo* situation and represents a known challenge for the performance of the polymers due to the inhibitory effect of serum proteins on the cellular uptake process.[51,52]

It should be noted that higher N/P ratios were required for the copolymers as all nitrogen atoms were taken into account for the N/P calculations. This includes also the amide functionalities of EtOx and AmButOx although they are not capable to interact with the pDNA. **P1**-based polyplexes were less efficient as indicated by a TE below 50%. High TEs over 60% were achieved in serum reduced conditions for **P2** and **P3** polyplexes at N/P 30 to 50. Comparable TEs were obtained for **lPEI** at N/P20. Compared to the transfection in OptiMEM, the EGFP transfection level of **P1** to **P3** at N/P 50 in serum containing media did not change considerably. Due to the cytotoxic effect of **lPEI** and the influence of serum proteins the cell viability as well as the TE decreased rapidly with increasing N/P ratios.

The combination of high cell viability (no cyto-/hemotoxicity) and formidable transfection performance even in the presence of proteins underlines the potential of **P2** and, in particular, **P3** as preferable gene delivery vectors. Moreover, **P3** also withstands

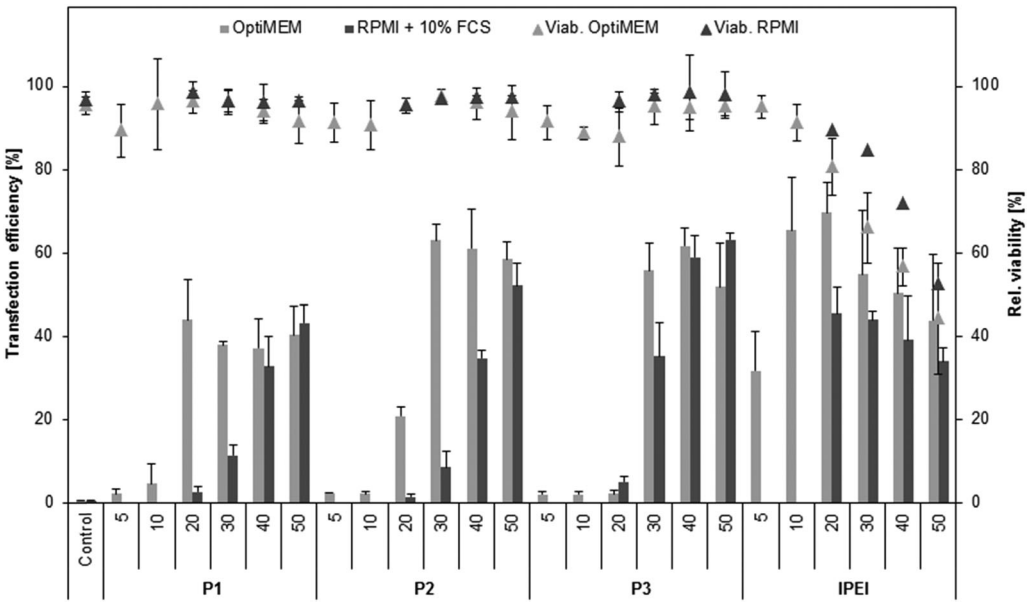

Fig. 5 Transfection efficiency of copolymers **P1** to **P3** and **lPEI** for adherent HEK cells in serum reduced (OptiMEM, light grey) and serum containing media (RPMI + 10% FCS, dark grey) at different N/P ratios after 24 h. Values represent the mean ± S.D. (n = 3).

a comparison to **lPEI** and the literature known 'gold standard for transfection', **comlPEI** (see ESI,† Fig. S18).

Uptake mechanism

For cationic polyplexes, the internalization into cells by endocytosis followed by the endosomal release of the pDNA into the cytosol and the subsequent transport into the nucleus is reported.[53,54] To clarify this process and to understand the excellent transfection performance of the copolymers, the uptake mechanism was investigated. An uptake kinetic using polyplexes formed with YOYO-1 labeled pDNA was performed to detect the internalization within cells by flow cytometry (Fig. 6). All tested polymers exhibited a fast and time-dependent cellular uptake. In detail, almost 90% of measured cells internalized polyplexes after 4 h when medium is changed

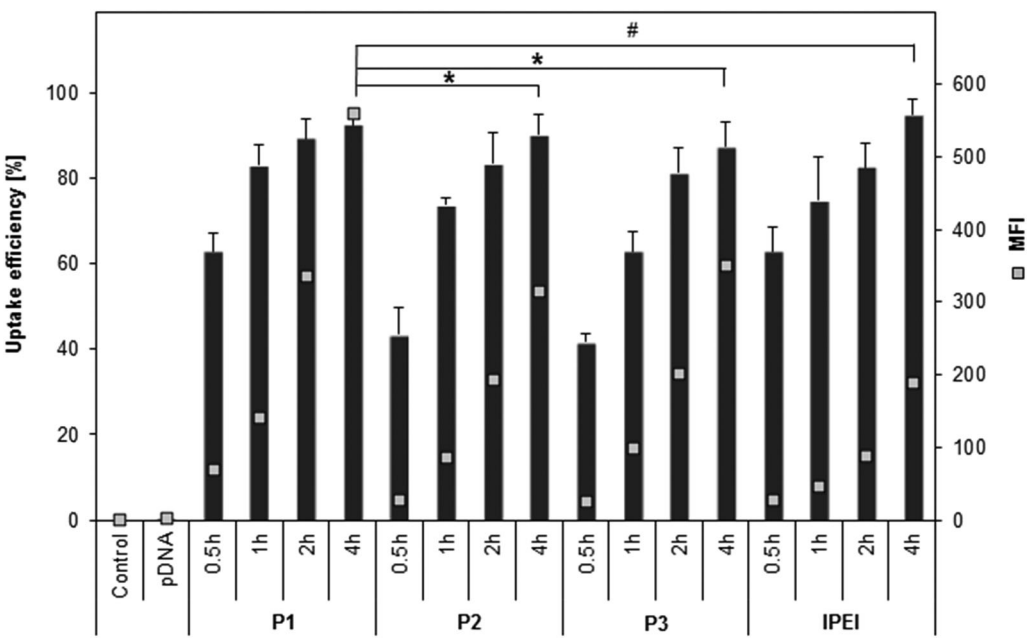

Fig. 6 Uptake study. Polyplexes formed with YOYO-1 labeled pDNA were incubated with HEK cells in OptiMEM for indicated time points using the copolymers **P1** to **P3** and **lPEI** (N/P ratio 30) as control. Statistical analysis (t-test) was used to compare the MFI after 4 h of **P1** with **P3** and **lPEI**, * represents $p < 0.05$ and # $p < 0.005$ of MFI values using student's t-test. Values represent the mean ± S.D. (n = 3).

according to standard transfection protocol. In particular, **P1** as well as **lPEI** showed an enhanced uptake efficiency after 30 min (~60%) compared to **P2** and **P3** (40%). Although most of the cells internalized polyplexes, the quantities (mean fluorescence intensities, MFI) differ significantly after 4 h (Fig. 6). Higher internalized polyplex concentrations were detected in cells using **P2**, **P3** (twofold) and **P1** (threefold) compared to **lPEI**. An explanation might be the introduction of AmButOx to the copolymers for enhanced complexation with the genetic material and cellular uptake, while the EtOx content possessing reduced membrane disruption.

To preclude an uptake by passive membrane diffusion, the uptake of YOYO-1 stained polyplexes was performed at 4 °C and 37 °C, respectively (Fig. S8B, ESI†). Polyplexes of all tested polymers were internalized into cells at 37 °C with approximately 90% efficiency. In contrast, the uptake efficiency was significantly decreased to approximately 10% at 4 °C for all samples. This indicates an energy-dependent uptake (endocytotic process). Furthermore, bafilomycin, a proton pump (H^+-ATPase) inhibitor, was used to prevent endosomal release caused by acidification (Fig. S8A, ESI†). The inhibition of an endosomal escape prevents the release of pDNA into the cytoplasm, the transfer into the nucleus and the EGFP expression. As expected, the TE significantly decreased after treatment with bafilomycin for all tested polymers to <5%. This indicates the involvement of the endosomal uptake and release as critical steps during the transfection mechanism, as it is reported for PEI.[43,55]

High resolution microscopy of polyplex–cell interactions

Deeper insights into the uptake mechanism and the fate of polyplexes within the cells were obtained with microscopic studies including confocal microscopy, structured illumination microscopy (SIM) and high-angular annular dark-field scanning transmission electron microscopy (HAADF-STEM).

Confocal microscopy as well as SIM studies were performed with HEK cells and polyplexes based on YOYO-1 labeled pDNA and Cy5-labeled **P3** representing the polymer with the overall highest transfection efficiency compared to **lPEI**. Fluorescence imaging of cells, in particular SIM images, revealed a co-localization of pDNA-bound **P3** polyplexes (blue) within the lysosomes/late endosomes (red, RFP labeling, Fig. 7 and Fig. S9 and S10, ESI†). The detection of the YOYO-signal within the cytoplasm that was not co-localized with lysosomal structures reveals that pDNA is released from the polyplex itself. Considering the low concentration of heparin required to destabilize the polyplex, an efficient release of pDNA into the cytoplasm can be assumed. As SIM provides a resolution of approx. 100 nm, a more detailed insight into the polyplex behavior within the lysosomes/late endosomes was obtained compared to conventional confocal imaging. A non-centrically localization of **P3** polyplexes

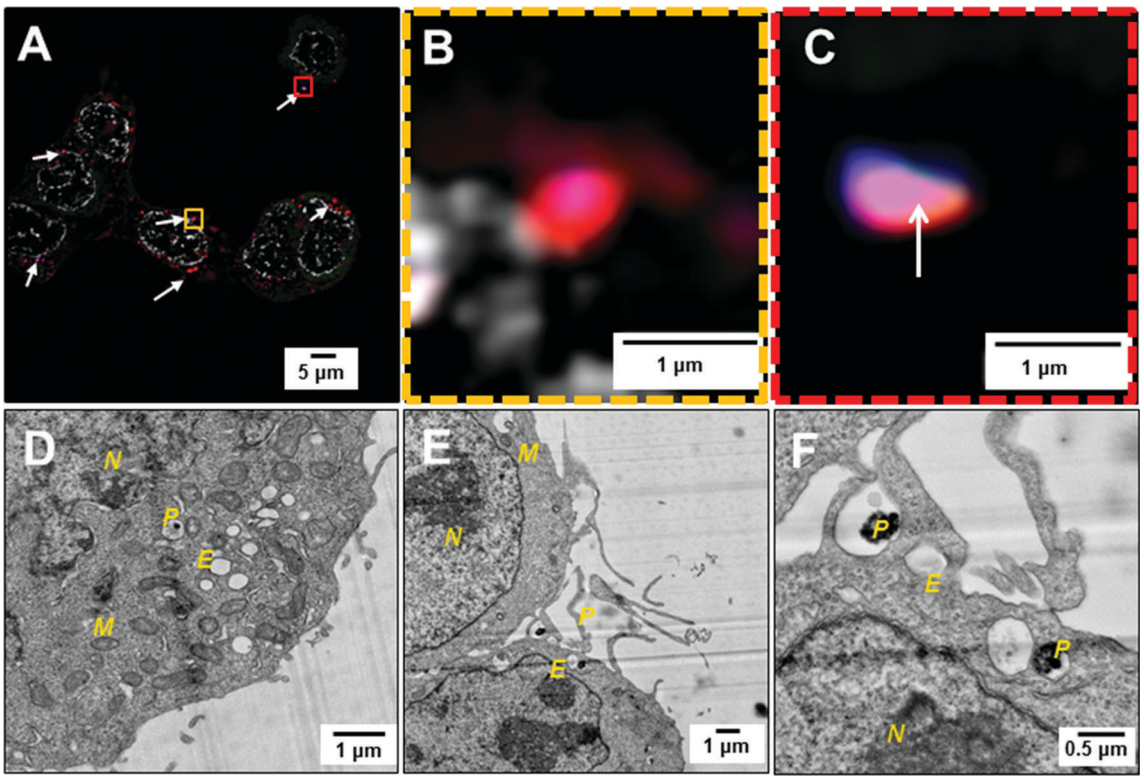

Fig. 7 High resolution imaging. (A) Structured illumination image of **P3**-based polyplexes within cells (deconvolved data). White arrows indicate co-localization of **P3**-pDNA polyplexes within lysosomes. (B and C) Magnified view of the yellow and red, dash-lined frame in (A): **P3**-Cy5 polyplex within the endosome. 63× Oil Obj. 1.4 NA. Grey: Hoechst 33342. Red: lysosomal membrane (RFP). Green: plasmid DNA labeling (YOYO-1). Blue: polymer labeling (Cy-5). (D–F) HAADF-STEM images of **P3**-based polyplexes taken up by HEK cells. The following letters correspond to cell organelles: N = cell nucleus, M = mitochondria, E = endosomal compartment, P = polyplex.

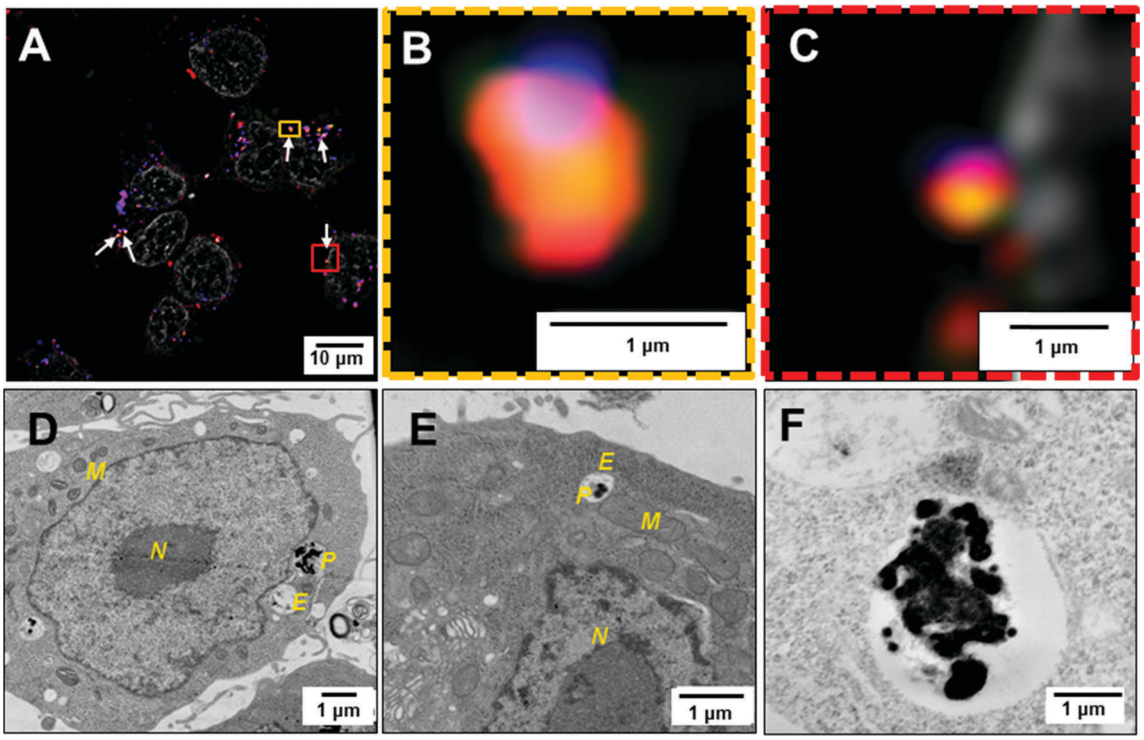

Fig. 8 High resolution imaging. (A) Structured illumination image of **lPEI**-based polyplexes within HEK cell, white arrows indicates full co-localization (deconvolved data). (B and C) Magnified zoom of yellow and red, dash-lined frame in (A): **lPEI-Cy5** polyplex within the endosome. 63× oil obj. 1.4 NA. Grey: Hoechst 33342. Red: lysosomal membrane (RFP). Green: plasmid DNA labeling (YOYO-1). Blue: polymer labeling (Cy-5). (D–F) HAADF-STEM images of **lPEI**-based polyplex taken up by HEK-293 cell. The following letters correspond to cellular structures: N = cell nucleus, M = mitochondria, E = endosomal compartment, P = polyplex.

(Cy5 and YOYO-1 signal) within the endosome (red) was observed, being in close vicinity to the endosomal membrane (Fig. 7A and zoom-in Fig. 7B and C, single channel splitting: Fig. S11, ESI†). This could be attributed to a strong interaction between the polyplex and the cytoplasmic membrane at the time of the cellular uptake or a strong interaction of the polyplex with the endosomal membrane caused by acidification. However, also **lPEI** polyplexes (Cy5 and YOYO-1 signal) were localized in close vicinity to the endosomal membrane (Fig. 8A and zoom-in Fig. 8B and C, single channel splitting: Fig. S12, ESI†). Interestingly, a higher number of larger endosomes bearing polyplex signals with an apparent larger spatial dimension was found for **lPEI** in contrast to **P3**. To study the interaction of both polymers with the endosomal membrane in more detail, STEM on embedded sections was carried out to confirm this assumption. STEM provides a resolution in the low nanometer range, elucidating the subcellular ultrastructural context, and particularly, highlighting membrane structures. EM images revealed an uptake of single **P3** polyplexes into vesicles with sizes of 200 to 500 nm ($n > 10$ vesicles of different sections were analyzed, Fig. S13, ESI†). Although, the polyplexes themselves provide only poor electron contrast, their structures were highlighted efficiently within the cellular environment (Fig. 7D–F) in the sample by sample staining. This can be explained by the strong affinity of the amines of the polymer and phosphates of the DNA to the heavy metal stains (OsO_4 and uranylacetate, respectively). The close vicinity between **P3** polyplex and the endosomal membrane was confirmed. We attribute this observation to a preceding active cell membrane-driven uptake event, initiated by strong interaction of a single polyplex with the membrane. We observed an uptake event involved by membrane ruffles and lamellipodia-like structures (Fig. 7E and F), supporting our previous findings concerning an energy-dependent uptake, such as by macropinocytosis. We therefore investigated cells after incubation with **P3** polyplexes in the presence of the inhibitor, 5-(*N*-ethyl-*N*-isopropyl)amiloride (EIPA, 100 μM). Our experiments support the assumption, since only 25% of the cells internalized **P3** polyplexes after 4 h (see ESI,† Fig. S14). Performing STEM imaging, we observed no **P3** polyplexes within the cytoplasm (see ESI,† Fig. S15A and B). This underlines an uptake mechanism *via* macropinocytosis.

STEM images of **lPEI** polyplexes revealed larger endosomes with sizes of 500 to 1500 nm ($n > 10$ vesicles of different sections were analyzed, Fig. S16, ESI†) bearing more than a single polyplex as well as increased cellular membrane rupture (Fig. 8D–F). The presence of multiple polyplexes within large endosomes explains the large spatial dimension of the polyplex signals as being found in SIM images (Fig. 8F). STEM images of cells, which were incubated with **lPEI** polyplexes in the presence of a macropinocytosis inhibitor (EIPA), revealed indeed a cellular internalization (see ESI,† Fig. S15C and D). However, the uptake efficiency was apparently lower compared to the

standard uptake protocol (~65% YOYO-positive cells after 4 h) and hints towards alternative uptake mechanisms in addition to macropinocytosis. It was already demonstrated that **lPEI** possesses a high membrane activity (see erythrocyte aggregation, Fig. S3 and S4, ESI†), which is in association with polymer aggregation in serum containing media[5] and could lead to enhanced uptake of multiple polyplexes within single endosomes. Aggregated polyplexes could be also responsible for a reduced uptake because of a size-limited uptake mechanism, *e.g.* endocytosis. The presence of EtOx subunits within **P3** shields the formed polyplexes from aggregation caused by protein interaction prior to uptake. This might be a reason for a more efficient cellular uptake and the high transfection efficiency of the respective copolymer. Based on this data, the efficient endosomal release of single **P3** polyplexes is impressive compared to agglomerated **lPEI** polyplexes. Due to the high buffer capacity of **lPEI**, an enhanced protonation of amines followed by the swelling of the endosomes might occur, as it is hypothesized for the "proton sponge" effect.[6,51,53,54,56] In case of **P3**, the full protonation of the primary/secondary amines could lead to a destabilization of the membrane indicating a membrane rupture and the subsequent release of the cargo into the cytosol. A previous study of Zuhorn and co-workers describes a similar process for PEI polyplexes supporting these findings.[52] Additionally, the authors showed that the release did not come along with a complete rupture of the endosome. As the polymers **P1** to **P3** possess a content of 12 to 23% secondary amines and a content of primary amines of 34 to 23%, they do not show such a severe swelling of endosomal compartments like **lPEI** polyplexes. Nevertheless, it can be assumed that a protonation of the primary amines in the side chain within the endosomal compartments forces the interaction of the polymers with the endosomal membrane leading to an efficient endosomal release. These results indicate that not only the buffer capacity and the swelling of endosomal compartments but also the interaction of the polymer with the endosomal membrane facilitate the escape from the endosome, which is in accordance to literature data and visualized in detail.[51,52]

siRNA delivery

To further investigate the potential of the modified PEI copolymers, the delivery efficiency for siRNA was determined. Although DNA and siDNA represent genetic material they differ in certain characteristics. Most importantly, siRNA is smaller (<30 base pairs (bp) compared to 4700 bp pDNA) and more rigid. From a biological point of view, pDNA has to be transferred across the nuclear barrier to the cell nuclei, whereas siRNA has to be released from the polyplex in the cytoplasm to form the RNA-induced silencing complex (RISC).[57]

The copolymers **P1** to **P3** were further investigated regarding the influence of primary and secondary amines for siRNA delivery. High binding affinity to siRNA (<40%) of all tested polymers was observed by EBA (Fig. 9A). Positively charged polyplexes with a size of <200 nm were formed, whereas **lPEI** polyplexes exhibited a compact size of around 83 nm (Table 3). This trend was also observed for the pDNA based polyplexes (see Table 2).

A GFP-expressing CHO cell line was used to estimate the knockdown efficiency (Fig. 9B). Interestingly, **P1** showed superior knockdown efficiency for siRNA (244 ± 50.3 MFI), compared to **P3** (317 ± 19.3 MFI), which was identified as best performer for pDNA transfection. Both, **P1** and **P2**, led to a significant reduction of around 40% of the fluorescence intensity of EGFP-expressing cells. In contrast, **P3** showed only 10 to 20% reduction of MFI. Interestingly, **lPEI** as well as branched PEI

Table 3 Size and surface charge (zeta potential) of the siRNA complexes at N/P 30 measured *via* dynamic light as well as electrophoretic light scattering in water-based HBG buffer

Polymeric system	*z*-Average [d, nm]	PDI	Zeta potential [mV]
P1	102 ± 1.2	0.15	21 ± 1.2
P2	124 ± 1.5	0.13	25 ± 1.0
P3[a]	149 ± 12.6	0.49	22 ± 0.1
lPEI	83 ± 2.3	0.23	33 ± 1.6

[a] Intensity weighted size distribution revealed a mean peak of 257 nm (68%).

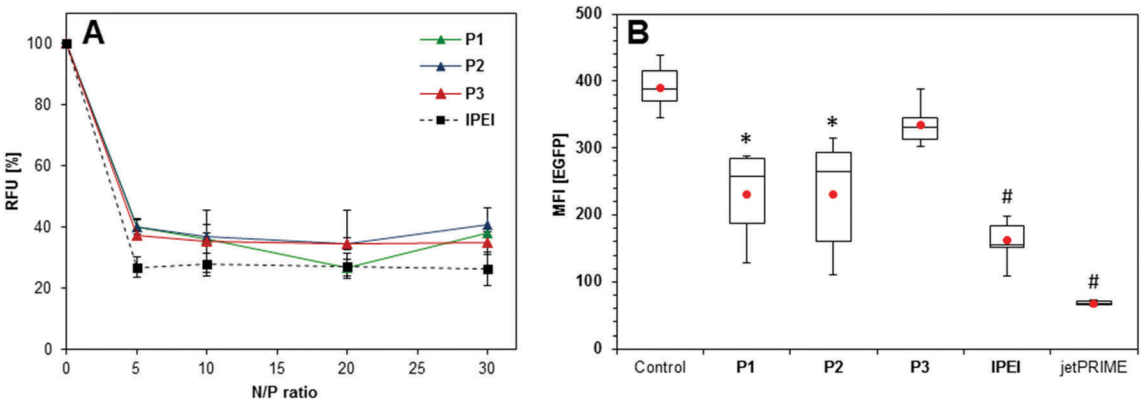

Fig. 9 Investigations of the siRNA delivery. (A) Binding affinity of siRNA to **P1** to **P3** and **lPEI** at different N/P ratios measured by the fluorescence quenching of ethidium bromide. The fluorescence of pure siRNA represents 100% RFU. (B) siRNA knockdown mediated by **P1** to **P3**, **lPEI** and jetPRIME polyplexes at N/P 30 after 72 h. Stable EGFP-expressing CHO cells were transfected with polyplexes formed using siRNA able to knock down *egfp*. Statistical analysis (*t*-test) was used to compare the mean fluorescence intensity (MFI) of the control with **P1** to **P3** and **lPEI**, * represents $p < 0.05$ and # $p < 0.005$. The values represent the mean ± S.D. ($n \geq 3$).

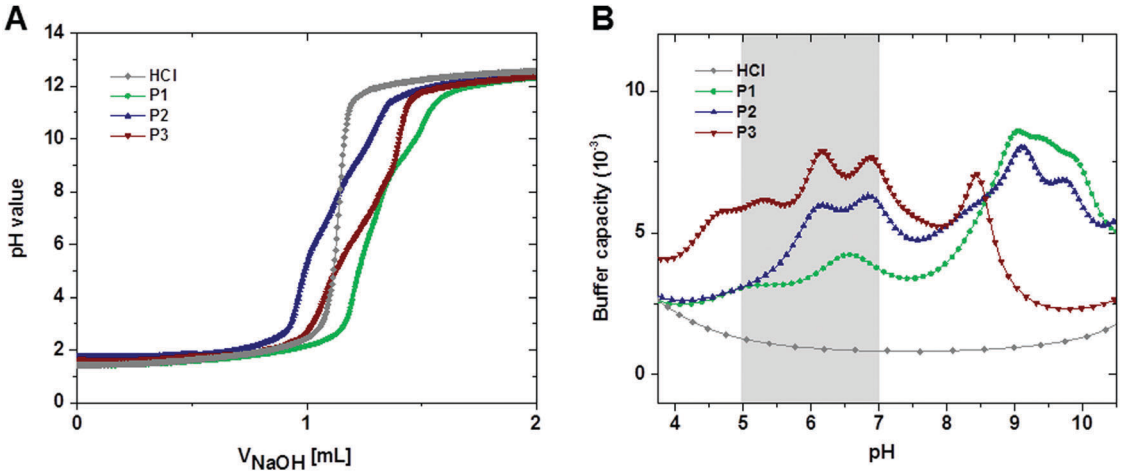

Fig. 10 (A) Acid–base titration curves of an acidified solution of the cationic copolymers **P1** to **P3** (~5 mg mL^{-1}) dissolved in 4 mL hydrogen chloride (HCl, 0.06 M) and neutralized with sodium hydroxide (0.1 M). For comparison, 0.06 M HCl was titrated accordingly. Precipitation of **lPEI** at pH 7 prevents the interpretation of the respective titration curve. (B) The buffer capacities of the cationic copolymers **P1** to **P3** were calculated from A utilizing the relation $\beta = dn(OH^-)/dpH$ and presented as a function of the pH value. For comparison, the buffer capacity of HCl is included.

(**bPEI**) revealed high knockdown potentials of around 60% (Fig. 9B). **ComlPEI** was less efficient and exhibited comparable efficiencies to the copolymers **P1** and **P2** (Fig. S20, ESI†). However, the highest knockdown (>80%, ~68 ± 3.9 MFI) was achieved with the positive control jetPRIME (cationic, polymeric transfection reagent, Polyplus). The fluorescence intensities were not reduced when using scrambled siRNA (negative control, see ESI,† Fig. S17). The polymers **P1** and **P2** revealed adequate knockdown levels, but are not as effective as commercially available siRNA transfection agents. Nevertheless, the promising performance and high biocompatibility of these 3rd generation PEIs could be developed in future studies by optimizing the polymeric design and composition as a higher AmOx content shows improved performance.

To understand the different performances of the copolymers depending on the genetic material, the endosomal release has to be considered. For successful delivery of siRNA a fast and efficient release from the endosome into the cytosol is beneficial, whereas the transfection efficiency of pDNA is increased, when it is transported to the perinuclear region inside endosomal compartments.[58]

From the titration of the polymers **P1** to **P3** (Fig. 10A) the buffer capacities of the respective copolymers were calculated ($\beta = dn(OH^-)/dpH$) and expressed as a function of the pH value (Fig. 10B). The copolymers show considerable higher buffer capacities with increasing EI content for pH values between 5 and 7 (endosomal release environment). As **P3** revealed the

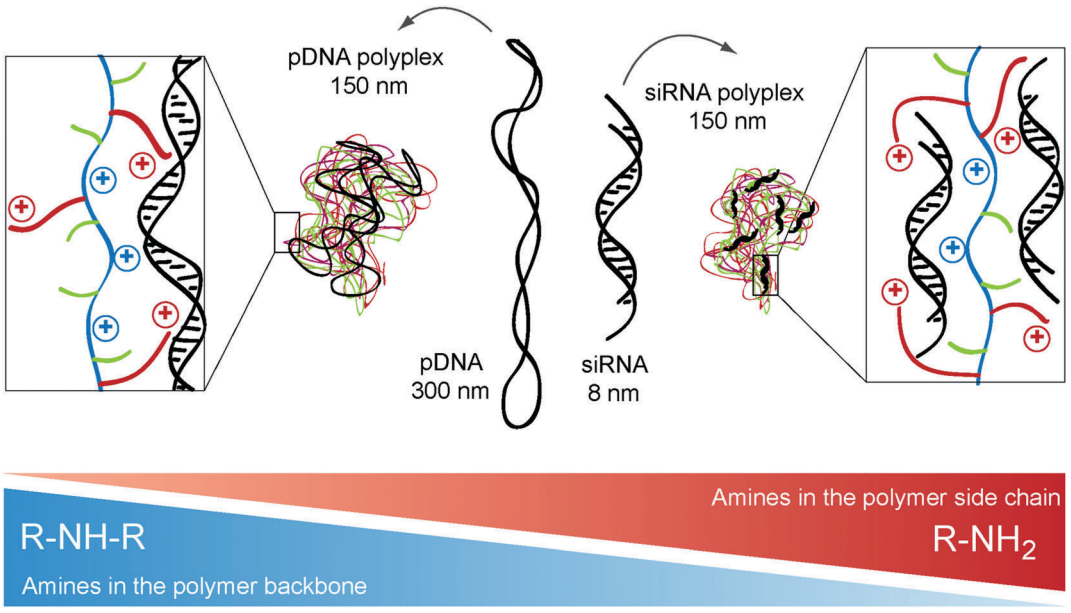

Fig. 11 Schematic representation of the polyplex formation illustrating the interaction of 3rd generation poly(ethylene imine) with pDNA or siRNA.

highest buffer capacity at acidic conditions, this could be an explanation for the diminished performance for siRNA delivery due to a delayed endosomal escape. In contrast, **P1** showed the highest degree of protonation at endosomal pH values facilitating a faster endosomal release into the cytosol by interaction of the charged amines with the endosomal membrane. It should be kept in mind, that **P1** and **P2** revealed also a high buffer capacity at a pH value around 9, in contrast to **P3**, which could be a hint for different performances.

Moreover, it could be assumed that the different physicochemical parameters of the genetic material (size, topology) play a crucial role for the interaction with the 3rd generation PEIs (Fig. 11). siRNA is small and stiff preferentially interacting with the primary amines in the polymer side chain. In contrast to that, the large pDNA requires the interaction with the primary amines (flexible side chains) as well as the secondary amines (backbone). This enabled an tremendous enhancement of pDNA delivery compared to literature reported polymer systems, *e.g.* P(EtOx-*stat*-MeOx).[17]

Conclusion

The introduced 3rd generation PEI copolymers has shown to present several advantages in contrast to 1st (PEI) and 2nd (single PEI modifications) generation approaches in terms of efficient polymeric gene delivery. Starting from high molar mass PEtOx, partially hydrolyzed **P(EtOx-*stat*-EI)** copolymers were synthesized. Subsequently, different amounts of the ethylene imine subunits were functionalized, introducing alkene groups which, in turn, could be used to attach primary amine groups in the side chains using thiol–ene chemistry. While the EtOx content of these polymers remained constant, the ratio between primary and secondary amine groups was varied to obtain a series of copolymers. It should be highlighted that no adverse effects on the cell viability was observed for polymer concentrations up to 1 mg mL^{-1} in contrast to **lPEI** (IC_{50} = 3.6 μg mL^{-1}). Remarkably, these 3rd generation PEIs were, in contrast to the 2nd generation **P(EtOx-*stat*-EI)**, able to form well-defined complexes with various genetic materials, in detail pDNA and siRNA. Besides a fast uptake, the delivery of pDNA revealed comparable transfection efficiencies to **lPEI**. In serum containing media, the performance of copolymer-based polyplexes could even exceed the efficiency of **lPEI**. Furthermore, the copolymers (in particular **P1** and **P2**) revealed siRNA delivery capability as well. Nevertheless, an optimization of this approach should be further pursued in future studies. Noteworthy, a different ratio of primary to secondary amines is required to form appropriate polyplexes with siRNA emphasizing the multivalence and potential of the presented polymeric system.

Using live cell confocal microscopy, super-resolution microscopy as well as transmission electron microscopy of ultrathin sections of embedded cell samples, the transfection mechanism was elucidated in more detail. In contrast to **lPEI**, where endosomes contained multiple polyplexes in swollen endosomes, copolymer based polyplexes present themselves individually within the endosomal compartments. This was attributed to a lower protein interaction of **PEtOx** containing vectors, preventing agglomeration in serum containing media prior to uptake as well as to a diminished membrane interaction. This feature also leads to a release process based on membrane interactions of the described polyplexes in contrast to the ''proton sponge'' effect hypothesized for PEI. The 3rd generation PEI outperforms PEI of former generations (1st and 2nd) concerning an overall concept in terms of toxicity as well as transfection efficiency for a wide range of genetic materials. Thus, it represents a promising alternative for more complex transfection approaches including hard-to-transfect cells or *in vivo* studies.

Acknowledgements

The authors would like to thank Dr. Michael Wagner for AF4 measurements and Carolin Fritzsche for support of the cyto- and hemocompatibility assays. This project was funded by the German Federal Ministry of Education & Research (BMBF, #031A518B Vectura, #13N13416 smart-dye-livery), the Thüringer Ministerium für Wirtschaft, Wissenschaft, und Digitale Gesellschaft (TMWWDG, ProExzellenzI, NanoConSens; ProExzellenzII, NanoPolar). The funding of the collaborative research center ChemBioSys (SFB 1127) by the Deutsche Forschungsgemeinschaft (DFG) is highly acknowledged. MR and AT are grateful for the financial support in the frameworks of ''Carl-Zeiss-Strukturmaßnahme'' and the Carl-Zeiss Stiftung. MH gratefully acknowledges the DFG (GZ: HA 7725/1-1) for funding. The LSM880 ELYRA PS.1 was further funded with a grant from the DFG. The transmission electron microscope was obtained with a grant from the European Funds for Regional Developments (EFRE) and the DFG.

References

1 U. Laechelt and E. Wagner, *Chem. Rev.*, 2015, **115**, 11043–11078.
2 A. C. Rinkenauer, S. Schubert, A. Traeger and U. S. Schubert, *J. Mater. Chem. B*, 2015, **3**, 7477–7493.
3 U. Lungwitz, M. Breunig, T. Blunk and A. Göpferich, *Eur. J. Pharm. Biopharm.*, 2005, **60**, 247–266.
4 M. A. Mintzer and E. E. Simanek, *Chem. Rev.*, 2009, **109**, 259–302.
5 M. Neu, D. Fischer and T. Kissel, *J. Gene Med.*, 2005, **7**, 992–1009.
6 O. Boussif, F. Lezoualc'h, M. A. Zanta, M. D. Mergny, D. Scherman, B. Demeneix and J. P. Behr, *Proc. Natl. Acad. Sci. U. S. A.*, 1995, **92**, 7297–7301.
7 W. T. Godbey, M. A. Barry, P. Saggau, K. K. Wu and A. G. Mikos, *J. Biomed. Mater. Res.*, 2000, **51**, 321–328.
8 S. De Smedt, J. Demeester and W. Hennink, *Pharm. Res.*, 2000, **17**, 113–126.
9 I. Y. Perevyazko, M. Bauer, G. M. Pavlov, S. Hoeppener, S. Schubert, D. Fischer and U. S. Schubert, *Langmuir*, 2012, **28**, 16167–16176.
10 M. Jager, S. Schubert, S. Ochrimenko, D. Fischer and U. S. Schubert, *Chem. Soc. Rev.*, 2012, **41**, 4755–4767.

11 P. Chollet, M. C. Favrot, A. Hurbin and J.-L. Coll, *J. Gene Med.*, 2002, **4**, 84–91.
12 J. H. Jeong, S. H. Song, D. W. Lim, H. Lee and T. G. Park, *J. Controlled Release*, 2001, **73**, 391–399.
13 Y. Yue, F. Jin, R. Deng, J. Cai, Z. Dai, M. C. M. Lin, H.-F. Kung, M. A. Mattebjerg, T. L. Andresen and C. Wu, *J. Controlled Release*, 2011, **152**, 143–151.
14 M. Thomas, Q. Ge, J. J. Lu, J. Chen and A. Klibanov, *Pharm. Res.*, 2005, **22**, 373–380.
15 W. Y. Seow, K. Liang, M. Kurisawa and C. A. E. Hauser, *Biomacromolecules*, 2013, **14**, 2340–2346.
16 C. Englert, M. Hartlieb, P. Bellstedt, K. Kempe, C. Yang, S. K. Chu, X. Ke, J. M. García, R. J. Ono, M. Fevre, R. J. Wojtecki, U. S. Schubert, Y. Y. Yang and J. L. Hedrick, *Macromolecules*, 2015, **48**, 7420–7427.
17 A. C. Rinkenauer, L. Tauhardt, F. Wendler, K. Kempe, M. Gottschaldt, A. Traeger and U. S. Schubert, *Macromol. Biosci.*, 2015, **15**, 414–425.
18 S. Taranejoo, J. Liu, P. Verma and K. Hourigan, *J. Appl. Polym. Sci.*, 2015, 132.
19 S. Ochrimenko, A. Vollrath, L. Tauhardt, K. Kempe, S. Schubert, U. S. Schubert and D. Fischer, *Carbohydr. Polym.*, 2014, **113**, 597–606.
20 M. Noga, D. Edinger, E. Wagner, G. Winter and A. Besheer, *J. Biomater. Sci., Polym. Ed.*, 2014, **25**, 855–871.
21 M. Ogris, S. Brunner, S. Schuller, R. Kircheis and E. Wagner, *Gene Ther.*, 1999, **6**, 595–605.
22 H. Petersen, P. M. Fechner, D. Fischer and T. Kissel, *Macromolecules*, 2002, **35**, 6867–6874.
23 K. Knop, R. Hoogenboom, D. Fischer and U. S. Schubert, *Angew. Chem., Int. Ed.*, 2010, **49**, 6288–6308.
24 J. Liu, X. Jiang, L. Xu, X. Wang, W. E. Hennink and R. Zhuo, *Bioconjugate Chem.*, 2010, **21**, 1827–1835.
25 N. Zhao, S. Roesler and T. Kissel, *Int. J. Pharm.*, 2011, **411**, 197–205.
26 G. Zhang, J. Liu, Q. Yang, R. Zhuo and X. Jiang, *Bioconjugate Chem.*, 2012, **23**, 1290–1299.
27 Y. Yamazaki, M. Nango, M. Matsuura, Y. Hasegawa, M. Hasegawa and N. Oku, *Gene Ther.*, 2000, **7**, 1148–1155.
28 A. Sato, S. Kawakami, M. Yamada, F. Yamashita and M. Hashida, *J. Drug Targeting*, 2001, **9**, 201–207.
29 X. Wang, D. Niu, C. Hu and P. Li, *Curr. Pharm. Des.*, 2015, **21**, 6140–6156.
30 A. T. Press, A. Traeger, C. Pietsch, A. Mosig, M. Wagner, M. G. Clemens, N. Jbeily, N. Koch, M. Gottschaldt, N. Bézière, V. Ermolayev, V. Ntziachristos, J. Popp, M. M. Kessels, B. Qualmann, U. S. Schubert and M. Bauer, *Nat. Commun.*, 2014, **5**, 5565–5577.
31 H. P. C. Van Kuringen, J. Lenoir, E. Adriaens, J. Bender, B. G. De Geest and R. Hoogenboom, *Macromol. Biosci.*, 2012, **12**, 1114–1123.
32 R. Shah, Z. Kronekova, A. Zahoranová, L. Roller, N. Saha, P. Saha and J. Kronek, *J. Mater. Sci.: Mater. Med.*, 2015, **26**, 1–12.
33 R. Luxenhofer, G. Sahay, A. Schulz, D. Alakhova, T. K. Bronich, R. Jordan and A. V. Kabanov, *J. Controlled Release*, 2011, **153**, 73–82.
34 S.-D. Li and L. Huang, *J. Controlled Release*, 2010, **145**, 178–181.
35 A. C. Rinkenauer, A. Schallon, U. Günther, M. Wagner, E. Betthausen, U. S. Schubert and F. H. Schacher, *ACS Nano*, 2013, **7**, 9621–9631.
36 A. Gress, A. Völkel and H. Schlaad, *Macromolecules*, 2007, **40**, 7928–7933.
37 A. Krieg, C. Pietsch, A. Baumgaertel, M. D. Hager, C. R. Becer and U. S. Schubert, *Polym. Chem.*, 2010, **1**, 1669–1676.
38 H. M. L. Lambermont-Thijs, F. S. van der Woerdt, A. Baumgaertel, L. Bonami, F. E. Du Prez, U. S. Schubert and R. Hoogenboom, *Macromolecules*, 2010, **43**, 927–933.
39 M. Litt, A. Levy and J. Herz, *J. Macromol. Sci., Chem. A*, 1975, **9**, 703–727.
40 M. Bauer, S. Schroeder, L. Tauhardt, K. Kempe, U. S. Schubert and D. Fischer, *J. Polym. Sci., Part A: Polym. Chem.*, 2013, **51**, 1816–1821.
41 M. Bauer, C. Lautenschlaeger, K. Kempe, L. Tauhardt, U. S. Schubert and D. Fischer, *Macromol. Biosci.*, 2012, **12**, 986–998.
42 C. Englert, L. Tauhardt, M. Hartlieb, K. Kempe, M. Gottschaldt and U. S. Schubert, *Biomacromolecules*, 2014, **15**, 1124–1131.
43 T. Bieber, W. Meissner, S. Kostin, A. Niemann and H. P. Elsasser, *J. Controlled Release*, 2002, **82**, 441–454.
44 J. B. Lepecq and C. Paoletti, *J. Mol. Biol.*, 1967, **27**, 87–106.
45 A. J. Geall and I. S. Blagbrough, *J. Pharm. Biomed. Anal.*, 2000, **22**, 849–859.
46 A. Kwok and S. L. Hart, *Nanomedicine*, 2011, **7**, 210–219.
47 M. Ruponen, S. Ylä-Herttuala and A. Urtti, *Biochim. Biophys. Acta*, 1999, **1415**, 331–341.
48 S. Sundaram, S. Viriyayuthakorn and C. M. Roth, *Biomacromolecules*, 2005, **6**, 2961–2968.
49 J. Rejman, V. Oberle, I. S. Zuhorn and D. Hoekstra, *Biochem. J.*, 2004, **377**, 159–169.
50 R. V. Benjaminsen, M. A. Mattebjerg, J. R. Henriksen, S. M. Moghimi and T. L. Andresen, *Mol. Ther.*, 2013, **21**, 149–157.
51 M. Wagner, A. C. Rinkenauer, A. Schallon and U. S. Schubert, *RSC Adv.*, 2013, **3**, 12774–12785.
52 Z. U. Rehman, D. Hoekstra and I. S. Zuhorn, *ACS Nano*, 2013, **7**, 3767–3777.
53 A. M. Funhoff, C. F. van Nostrum, G. A. Koning, N. M. E. Schuurmans-Nieuwenbroek, D. J. A. Crommelin and W. E. Hennink, *Biomacromolecules*, 2004, **5**, 32–39.
54 A. Akinc, M. Thomas, A. M. Klibanov and R. Langer, *J. Gene Med.*, 2005, **7**, 657–663.
55 J. Rejman, A. Bragonzi and M. Conese, *Mol. Ther.*, 2005, **12**, 468–474.
56 J. P. Behr, *Acc. Chem. Res.*, 2012, **45**, 980–984.
57 A. T. Da Poian, F. A. Carneiro and F. Stauffer, *Braz. J. Med. Biol. Res.*, 2005, **38**, 813–823.
58 C. Scholz and E. Wagner, *J. Controlled Release*, 2012, **161**, 554–565.

Electronic Supplementary Material (ESI) for Journal of Materials Chemistry B.

SUPPORTING INFORMATION:

3rd Generation Poly(ethylene imine)s for Gene Delivery

Tanja Bus,[a,b,†] Christoph Englert,[a,b,†] Martin Reifarth,[a,b,c,d] Philipp Borchers,[a,b]
Matthias Hartlieb,[a,b,#] Antje Vollrath,[a,b] Stephanie Hoeppener,[a,b]
Anja Traeger,[a,b,] Ulrich S. Schubert[a,b,]**

[a] *Laboratory of Organic and Macromolecular Chemistry (IOMC), Friedrich Schiller University Jena, Humboldtstrasse 10, 07743 Jena, Germany*

[b] *Jena Center for Soft Matter (JCSM), Friedrich Schiller University Jena, Philosophenweg 7, 07743 Jena, Germany*

[c] *Institute of Physical Chemistry and Abbe Center of Photonics, Friedrich Schiller University Jena, Helmholtzweg 4, 07743 Jena, Germany*

[d] *Leibniz Institute of Photonic Technology, Albert-Einstein-Strasse 9, 07745 Jena, Germany*

[†] *The authors contributed equally to this work*

[#] *Current address: Department of Chemistry, University of Warwick, Gibbet Hill Road, Coventry, CV4 7AL, UK.*

Email: ulrich.schubert@uni-jena.de, anja.traeger@uni-jena.de

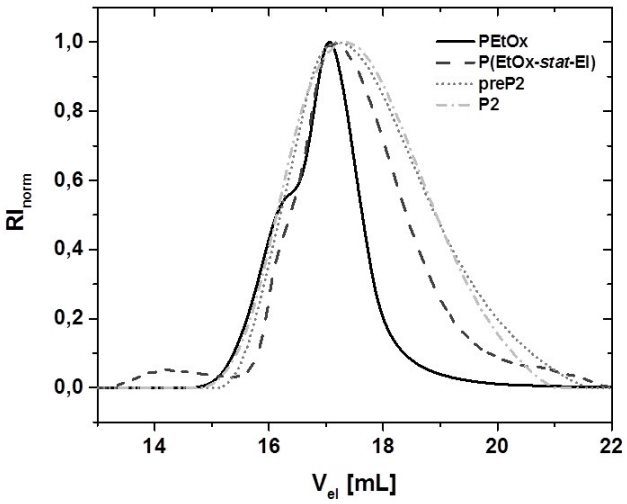

Figure S1. Size exclusion chromatography traces of the starting homopolymer **PEtOx** and the copolymers **P(EtOx-*stat*-EI)**, **preP2** and **P2** (*N*,*N*-dimethylacetamide, 0.21% LiCl, calibration: polystyrene).

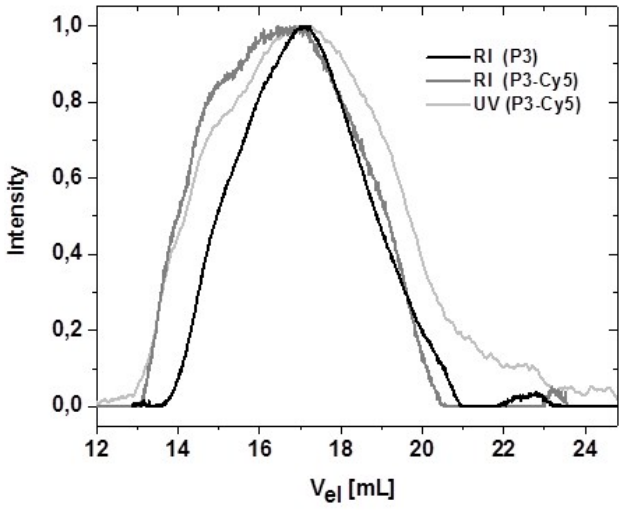

Figure S2. Size exclusion chromatography elugrams of the labeled copolymer **P3** (**P3-Cy5**) in comparison to the unlabeled starting material (**P3**) (*N*,*N*-dimethylacetamide, 0.21% LiCl, calibration: polystyrene).

Hemocompatibility of PEI-based polyplexes

The erythrocyte aggregation of the PEI copolymers was performed in parallel with high molar mass lPEI polymers as positive controls. **lPEI** show membrane-perturbing activity at high concentrations (100 µg mL^{-1}) leading to the aggregation of erythrocytes as indicated in the photospectrometrically measurement and by light microscopy. This effect was not seen with the copolymers **P1** to **P3**.

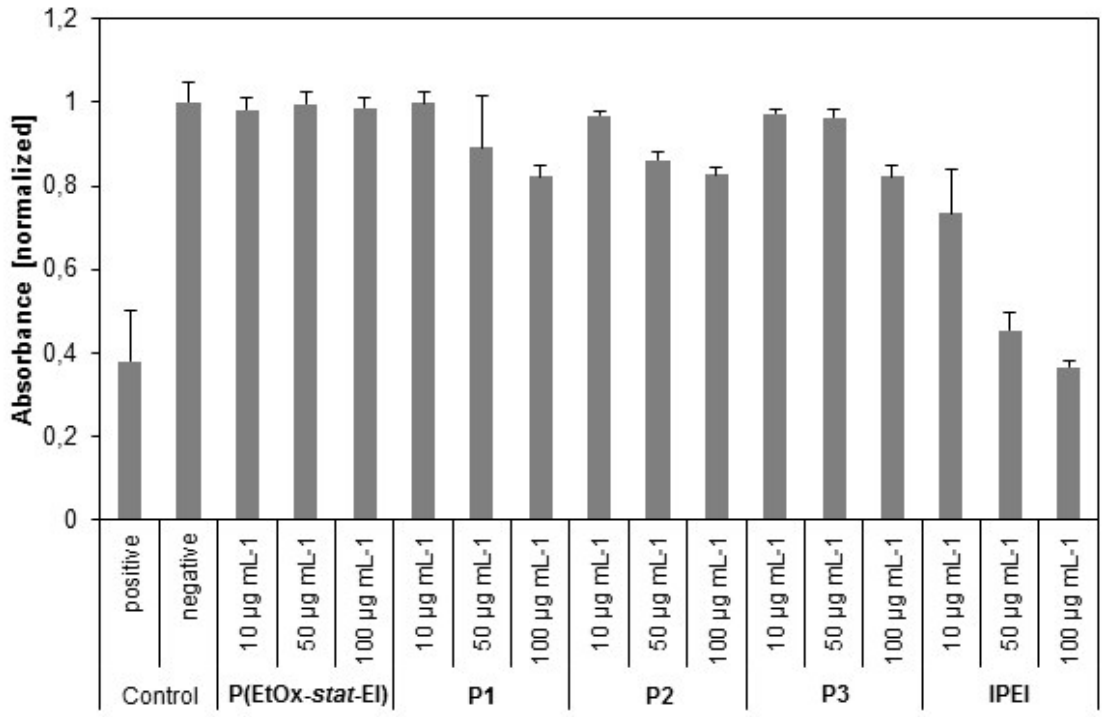

Figure S3. Erythrocyte aggregation of the tested polymers at indicated concentrations. bPEI (25 kDa) served as positive control resulting in high aggregation formation and PBS as negative control. Values represent the mean ± S.D. (n=3).

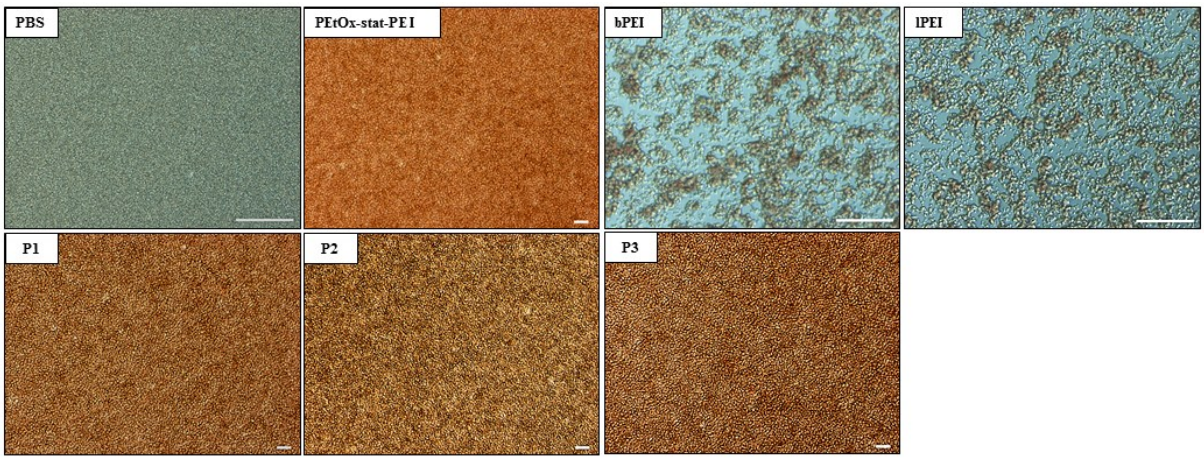

Figure S4. Light microscopy of erythrocyte aggregation of the polymers **P1** to **P3**, **PEtOx** and both **lPEI** polymers. PBS served as negative control, while bPEI (25kDa) was served as positive control. Scale bar = 50 µm.

Interaction of polymers with genetic material

The polyplex dissociation assay was performed aside from heparin with poly(methacrylic acid) (PMAA) (DP = 200) as competing factor. To keep equal conditions, same PMAA concentrations as for heparin were used during the measurement.

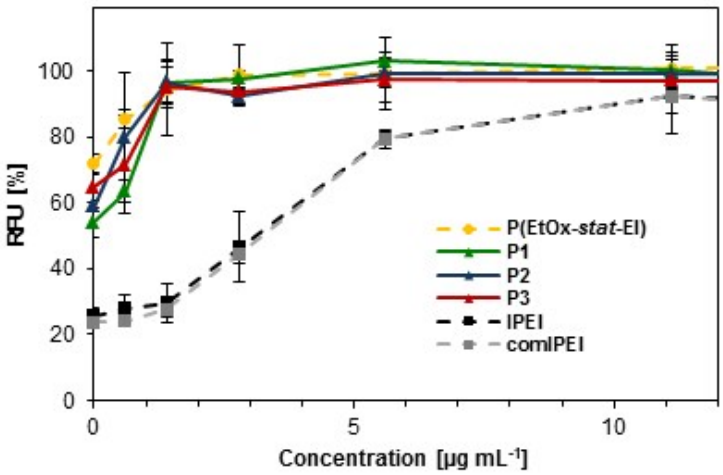

Figure S5. Dissociation assay of polyplexes formed with pDNA at N/P 30 and with increasing PMAA concentrations, which correlates to heparin concentrations.

Analysis of polyplex uptake and transfection of cells

The uptake and transfection studies were performed with HEK cells and pDNA encoding the EGFP (enhanced green fluorescence protein) or with YOYO-labeled pDNA. Transfection efficiency was determined by measuring the amount of viable cells (PI stained) expressing EGFP after 24 h *via* flow cytometry, whereas non-transfected cells served as negative control. To determine the amount of EGFP expressing cells, the histogramm of control cells was used and the percentage of cells within the gated area was defined as transfection efficiency in percentage.

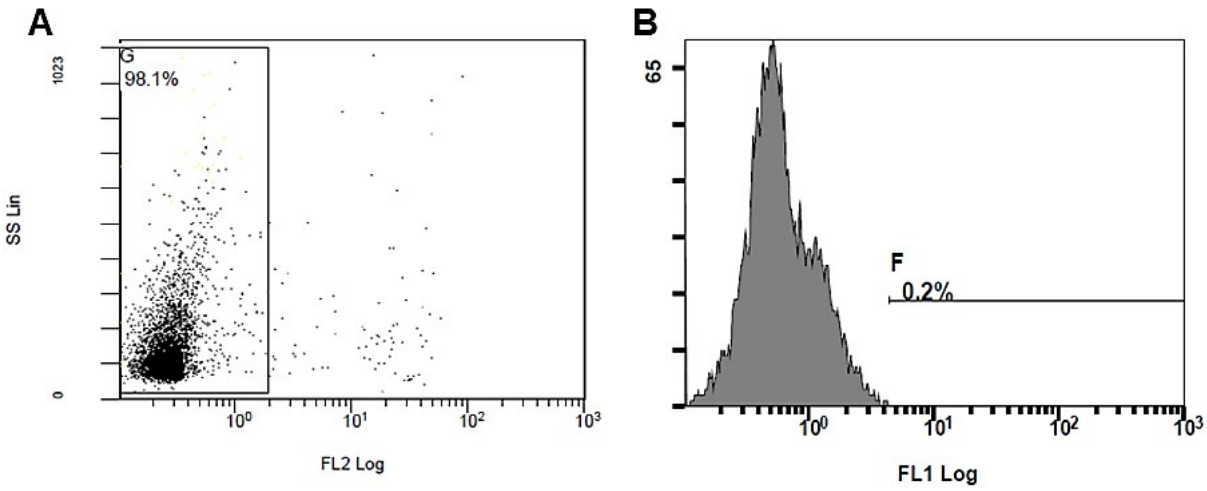

Figure S6. Flow cytometry measurements. A) Dot-plot of PI stained HEK cells for determining cell viability. FL2 Log represents red fluorescence of PI stained cells. All cells within the specified area G represent all measured viable cells. B) Histogramm of non-transfected cells served as control. FL1 Log represents green fluorescence by EGFP expression.

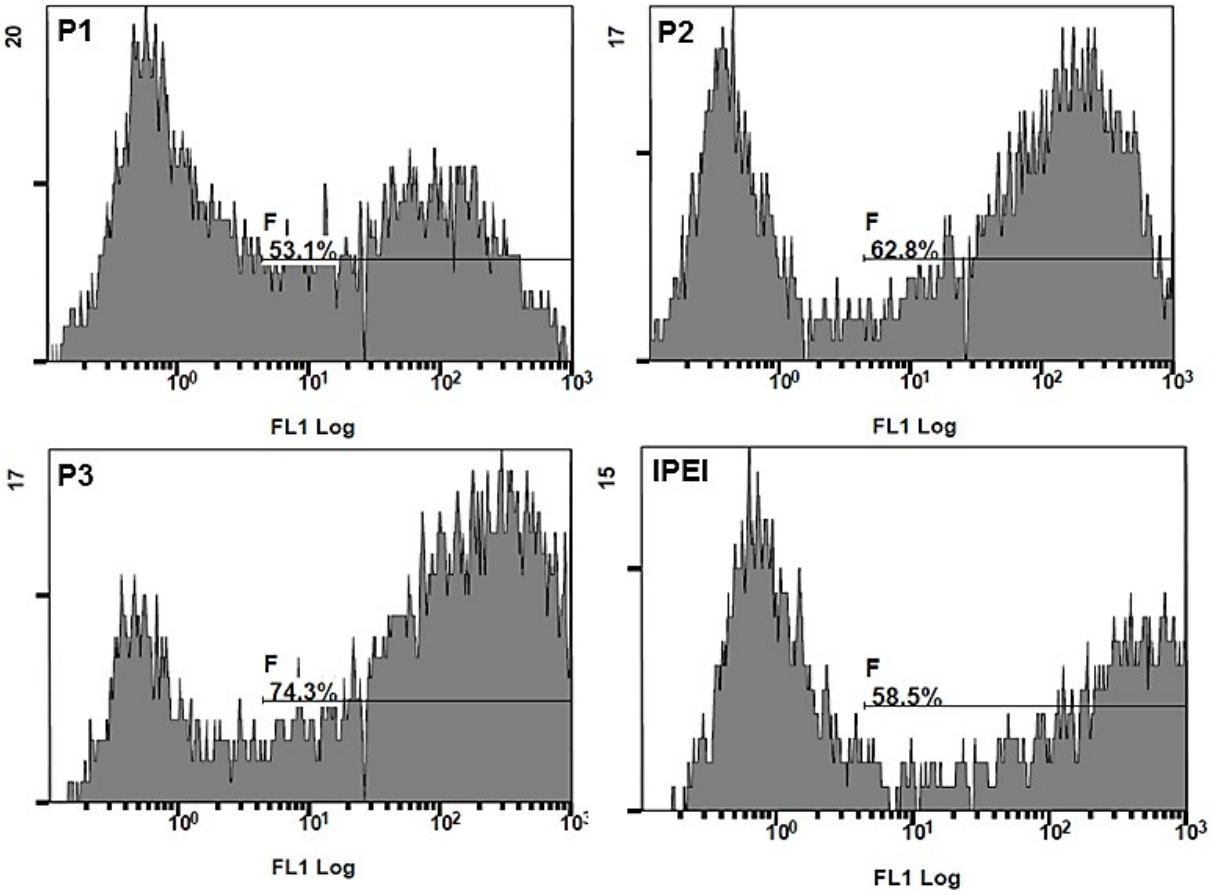

Figure S7. Histograms of flow cytometry measurements determining positive EGFP-expressing HEK cells after 24 h post-transfection with **P1** to **P3** and lPEI (N/P 30). Only viable HEK cells (PI staining) were gated. FL1 Log represents green fluorescence by EGFP expression.

To investigate the uptake mechanism in detail, cells were treated at different conditions with bafilomycin (proton pump inhibitor) or at 4 °C and 37 °C.

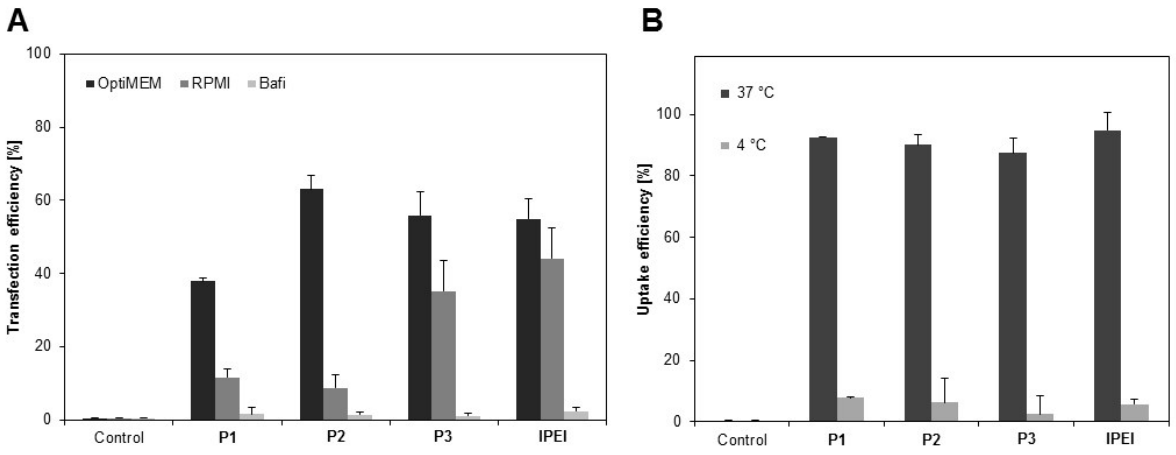

Figure S8. A) Uptake study: amount of cells taken up YOYO-1 labeled pDNA after 4 h at different temperatures (4 °C and 37 °C) using the copolymers **P1** to **P3** and **lPEI** (N/P ratio 30) as controls. Values represent the mean (n = 3). B) Comparison of the transfection efficiency of **P1** to **P3** and **lPEI** for adherent HEK cells in serum reduced (OptiMEM) and serum containing media (RPMI + 10% FCS) as well as after bafilomycin treatment at N/P 30. Values represent the mean (n = 3).

Live cell imaging

Confocal as well as structured illumination microscopy were used to investigate the uptake process of polyplexes in more detail and for visualization purposes. Therefore, non-treated control HEK cells as well as **P3** polyplexes added to HEK cells in serum reduced media were analyzed.

Control: pDNA transfection

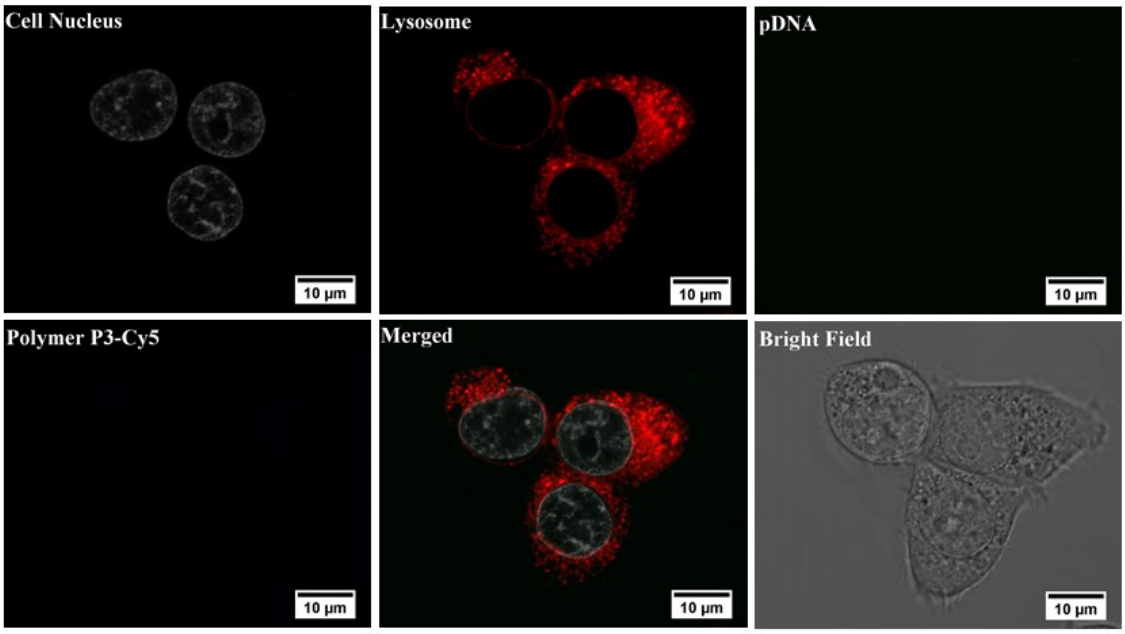

Figure S9. Uptake studies: HEK cells in serum reduced media without polyplexes served as negative controls. The cells were analyzed after 4 h *via* confocal laser scanning microscopy. The cell nucleus was stained with Hoechst 33342, the lysosomes with LysoTracker Red.

P3-Cy5: pDNA transfection

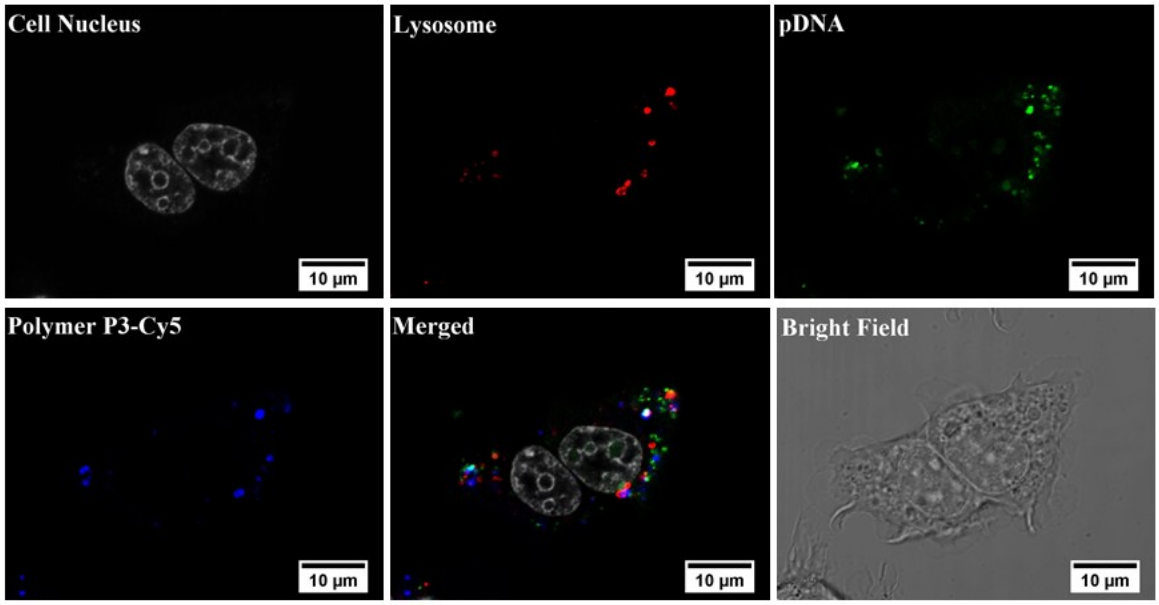

Figure S10. Uptake studies: Pure YOYO-labeled pDNA was added to HEK cells in serum reduced media. The cells were analyzed after 4 h *via* confocal laser scanning microscopy. The cell nucleus was stained with Hoechst 33342, the lysosomes with LysoTracker Red.

Structured illumination microscopy (SIM)

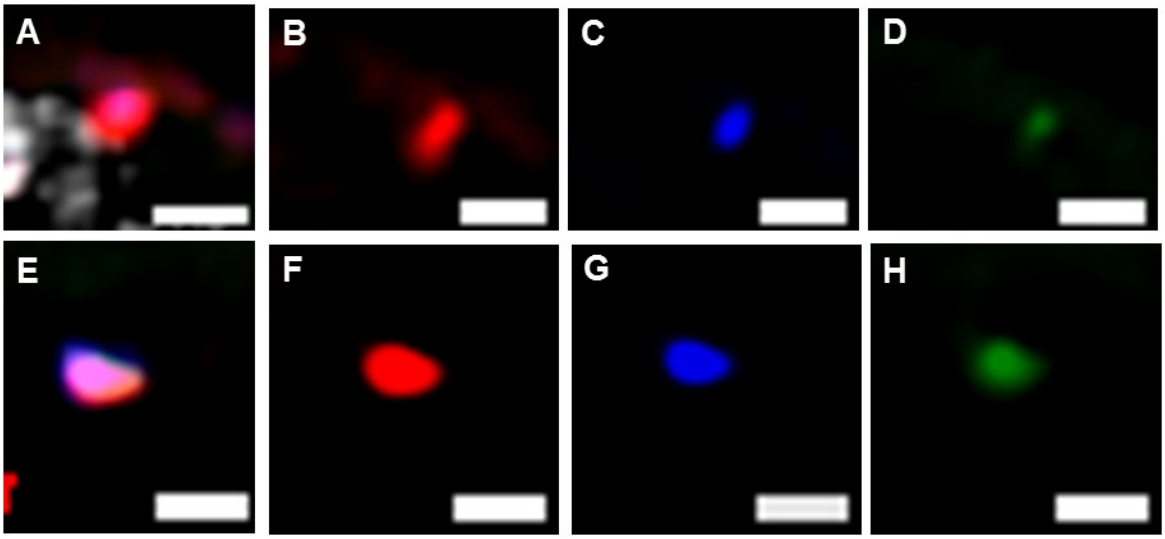

Figure S11. Magnified SIM images of endosome bearing polyplexes formed with **P3** in the presence of DNA (SIM data, deconvolved, acquired with 63x Oil Obj. 1.4 NA). Red; Lysosomal membrane (RFP). Green: pDNA labeling (YOYO-1). Blue: Polymer labeling (Cy5). A and E: Merged channels. B-D, F-H: split channels. Scale bars = 1 µm,

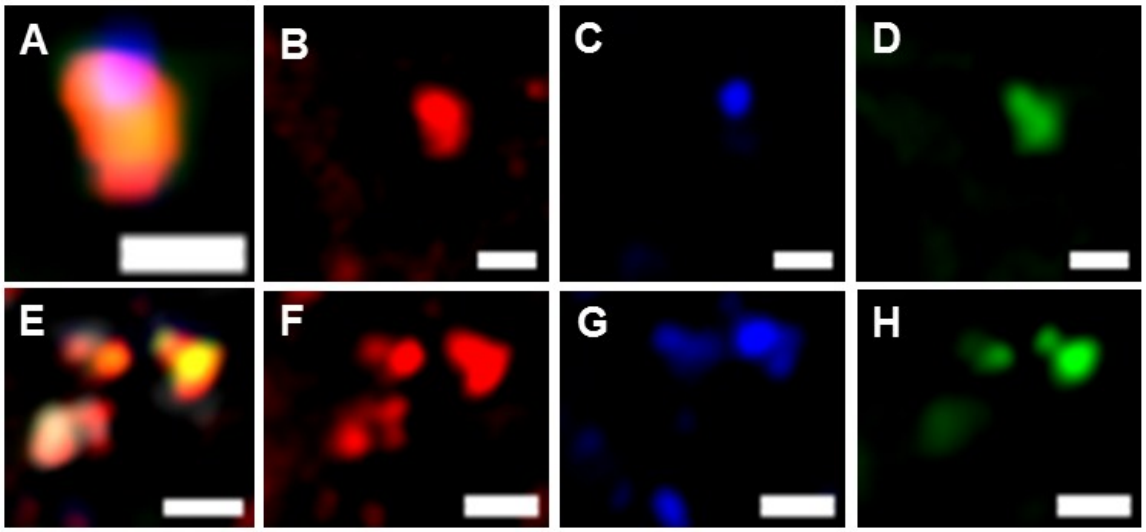

Figure S12. Magnified SIM images of endosome bearing polyplexes formed with **lPEI** in the presence of DNA (SIM data, deconvolved, acquired with 63x Oil Obj. 1.4 NA). Red; Lysosomal membrane (RFP). Green: pDNA labeling (YOYO-1). Blue: Polymer labeling (Cy5). A and E: Merged channels. B-D, F-H: split channels. Scale bars = 1 µm,

Scanning transmission electron microscopy (STEM)

To obtain deeper insights into the uptake mechanism and the fate of polyplexes inside the cell as well as the endosomal environment, scanning transmission electron microscopy (STEM) were performed. The images display a section (thickness of the resin slice: 80 nm) through the cell and sizes are determined by a two-dimensional section through the cell. This can only conditionally make a statement of the actual size of the three-dimensional vesicle. More than 5 sections (and ~ 10 vesicles) of different cells were analyzed to evaluate our findings.

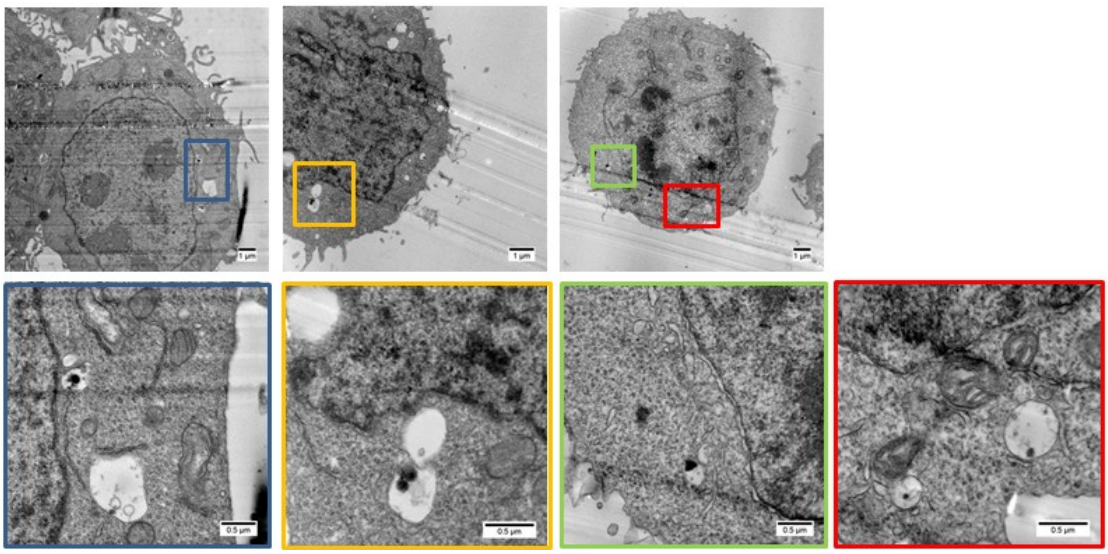

Figure S13. STEM images of polyplex uptake in HEK cells at standard conditions. Polyplexes were formed with **P3** and pDNA. Cells were harvested after 4 h.

Macropinocytosis inhibitor

For inhibition experiments, cells were treated with 100 µM 5-(*N*-ethyl-*N*-isopropyl)amiloride (EIPA) in standard culture media 30 min prior to polyplex addition. Subsequently, **P3** and lPEI polyplexes were added to the cells and incubated for further 4 h. Afterwards, the cells were harvested and analyzed as described above *via* flow cytometry or were further prepared for STEM imaging.

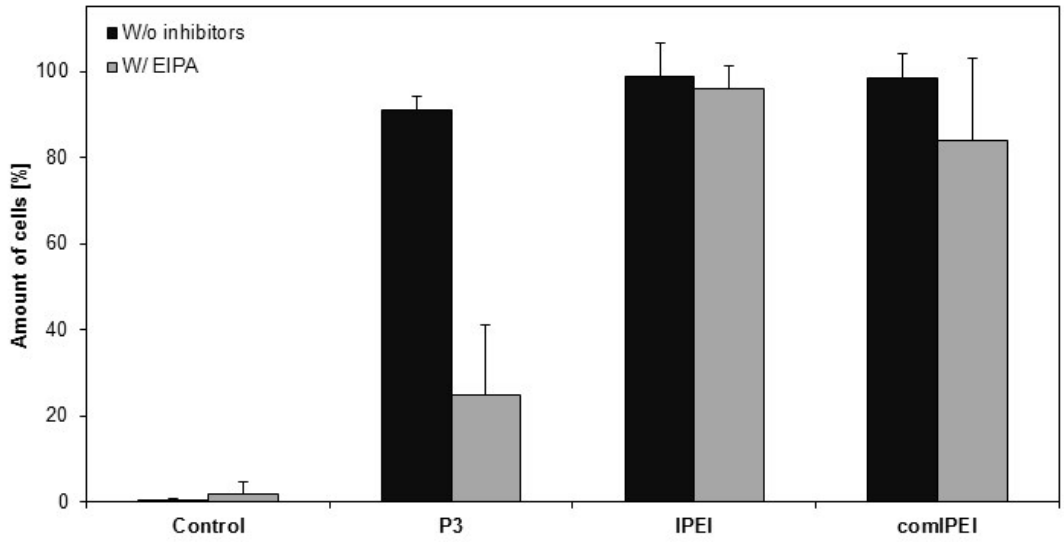

Figure S14. Polyplex uptake (YOYO-labeled pDNA) in HEK cells after treatment with EIPA (macropinocytosis inhibitor).

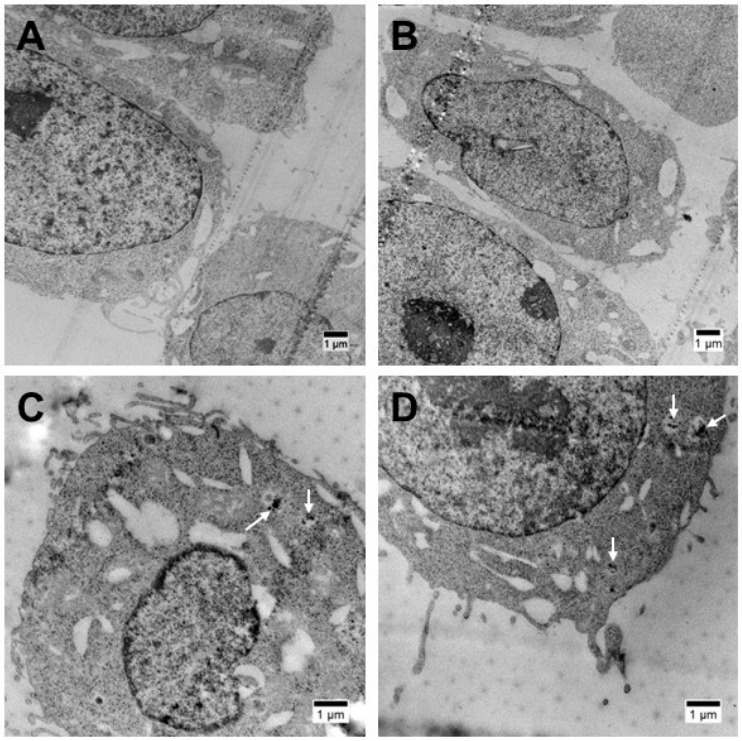

Figure S15. STEM images of polyplex uptake in HEK cells after treatment with EIPA (macropinocytosis inhibitor). A-B) Uptake of **P3** polyplexes. C-D) Uptake of **lPEI** polyplexes. White arrows indicate vesicles with polyplexes.

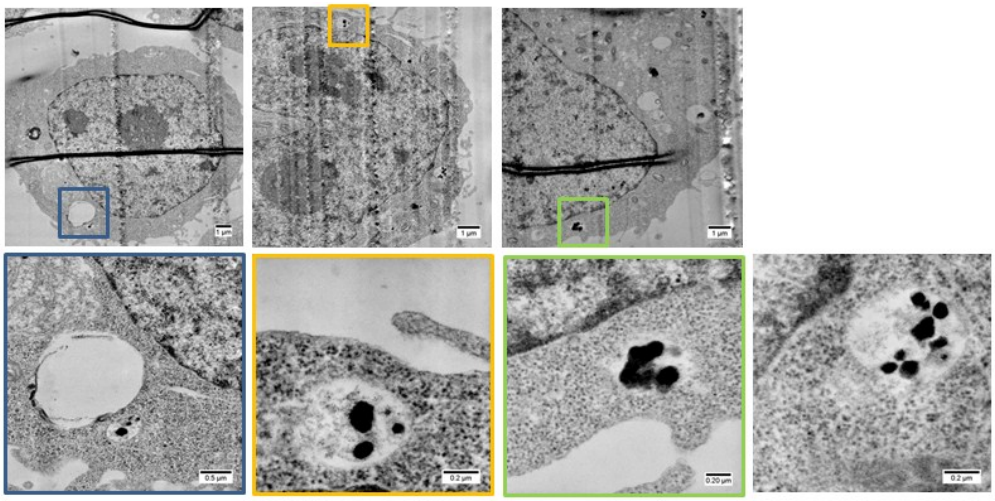

Figure S16. STEM images polyplex uptake in HEK cells at standard conditions. Polyplexes were formed with **lPEI** and pDNA. Cells were harvested after 4 h.

siRNA delivery

A stable GFP-expressing CHO cell line was transfected with the polymers **P1** to **P3** as well as PEI using scrambled siRNA as negative control. The knockdown of EGFP was analyzed *via* flow cytometry by measuring the MFI of all viable cells (PI staining).

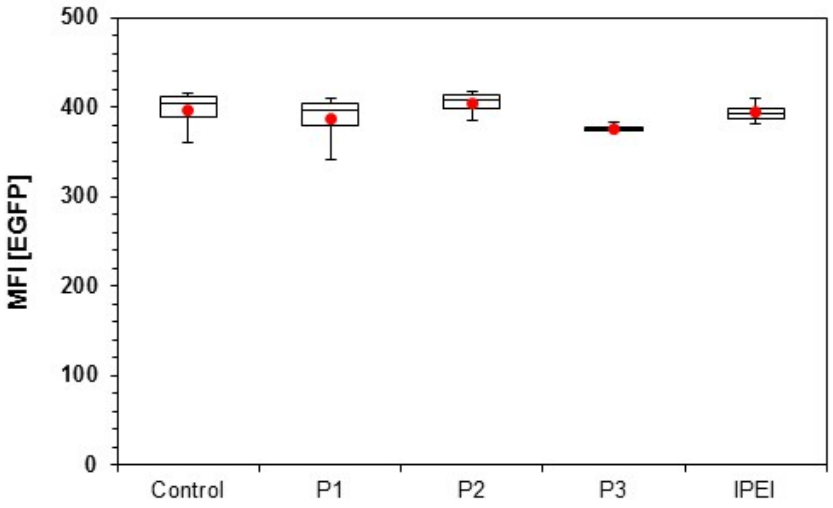

Figure S17. siRNA transfection efficiency mediated by **P1** to **P3** as well as PEI polyplexes at N/P 30 after 72 h. Stable EGFP-expressing CHO cells were transfected with scrambled siRNA served as negative control. The values represent the mean ± S.D., $n \geq 3$.

Comparison of lPEI and commercial lPEI25k (comlPEI, Sigma Aldrich)

The cytotoxicity tests of the PEI copolymers were performed in parallel with high molar mass lPEI polymers as positive controls. Fully hydrolyzed PEtOx, thus lPEI as well as the commercially available lPEI (25 kDa, **comlPEI**) obtained from Polysciences were used. The synthesized lPEI shows a higher cytotoxicity (IC_{50} at ~ 4 µg mL^{-1}), whereas the commercial PEI reaches 50% cell viability at 25 µg mL^{-1}. The reduced cytotoxicity could be attributed to residual, N-acyl groups from polymerization, which is also stated by the supplier.[39] Furthermore, the hemolysis and the erythrocyte aggregation assay were performed with both PEIs. Both polymers show membrane-perturbing activity at high concentrations (100 µg mL^{-1}) leading to hemoglobin release and the aggregation of erythrocytes. This effect was not seen with the copolymers **P1** to **P3**.

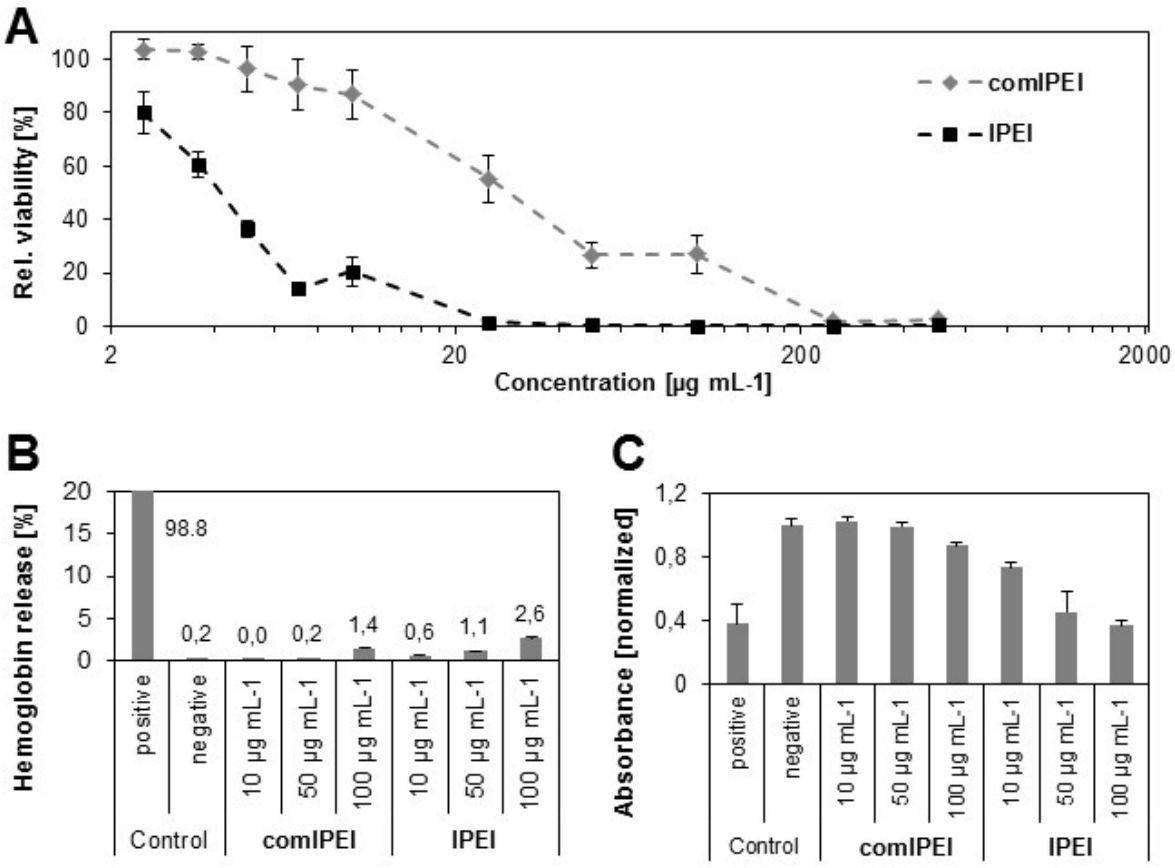

Figure S18. Comparison of **lPEI** and commercially available PEI (**comlPEI**, Polysciences). A) Cytotoxicity assay treating L929 cells with the synthesized **lPEI** as well as **comlPEI** at indicated concentrations. B) Hemolysis assay of erythrocytes after incubation with polymers at indicated concentrations. Triton X-100 served as positive control (100% hemolysis) and PBS as negative control. C) Erythrocyte aggregation of the tested polymers at indicated concentrations. bPEI (25 kDa) served as negative control resulting in high aggregation formation and PBS as negative control. Values represent the mean ± S.D. (n=3).

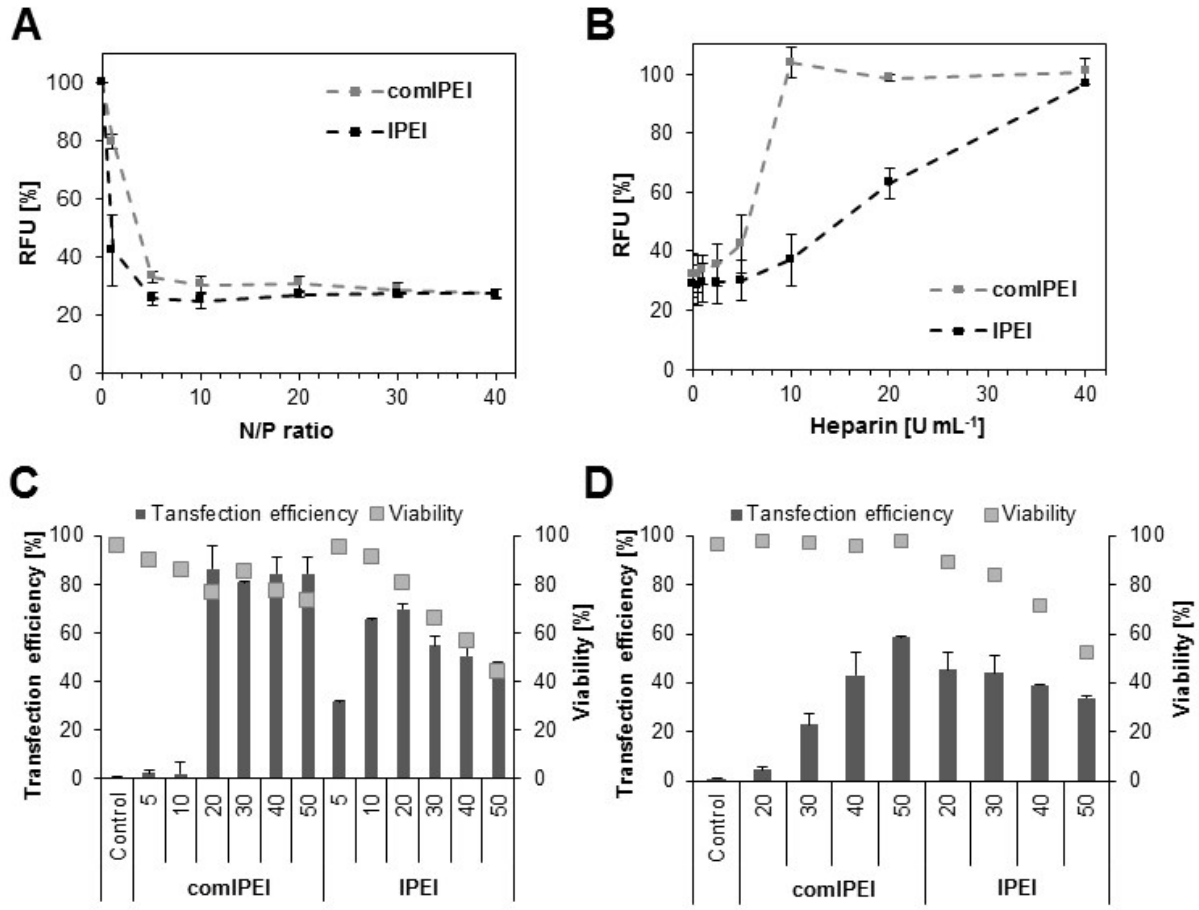

Figure S19. Comparison of **lPEI** and commercially available PEI (**comlPEI**, Polysciences). A) Complexation affinity (EBA) of mentioned polymers using pDNA at the indicated N/P ratios. B) Dissociation assay with heparin of polyplexes formed with pDNA at N/P 30. C-D) Transfection efficiency of both PEI polymers for adherent HEK cells in serum reduced (C) as well as serum containing (D) media at different N/P ratios after 24 h. Values represent the mean ± S.D. (n=3).

Besides the synthesized lPEI, comlPEI was used as control for the ethidium bromide quenching assay (Figure S18A). Both polymers show a high complexation affinity with pDNA, while a faster polyplex formation of lPEI could be detected at N/P 5. Regarding the heparin dissociation assay, comlPEI achieved a full decomplexation of genetic material at a heparin concentration of 10 U mL^{-1} (Figure S19B). For the complete release of pDNA (100% RFU) from lPEI polyplexes, 40 U mL^{-1} heparin was required. The uptake and transfection studies were

performed with HEK cells and pDNA encoding the EGFP (enhanced green fluorescence protein). Transfection efficiency was determined by measuring the amount of cells expressing EGFP after 24 h *via* flow cytometry. ComlPEI shows high TE > 80% at N/P ratios of 20 to 50 in serum reduced media, which is comparable to other studies. It has to be mentioned that with increasing N/P ratio, i.e. the polyplex concentration, the cell viability is reduced. This effect could be prevented using serum containing media for transfection, whereas a significant reduction of up to 70% (at N/P 20) of TE is occured.

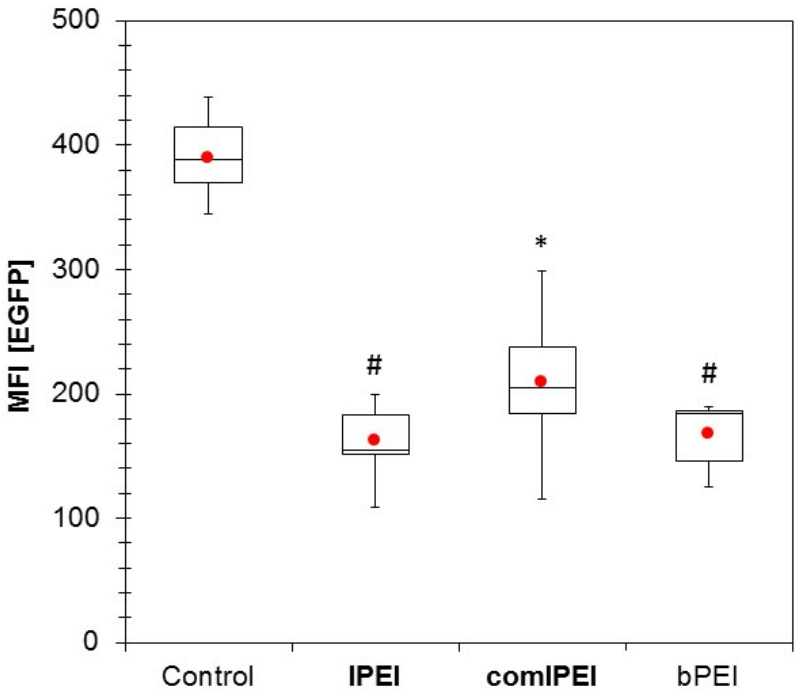

Figure S20. siRNA transfection efficiency mediated by PEI polyplexes at N/P 30 after 72 h. Stable EGFP-expressing CHO cells were transfected with polyplexes formed using siRNA able to knock down *egfp*. Statistical analysis (t-test) was used to compare the MFI of the control with PEI, * represents $p < 0.05$ and # $p < 0.005$. The values represent the mean ± S.D., n ≥

Publication P6

"Metal–Polymer Hybrid Nanoparticles for Correlative High-Resolution Light and Electron Microscopy"

M. Reifarth, E. Preußger, R. Heintzmann, U. S. Schubert, S. Hoeppener

Part. Part. Syst. Charact. **2017**, *34*, 1700180

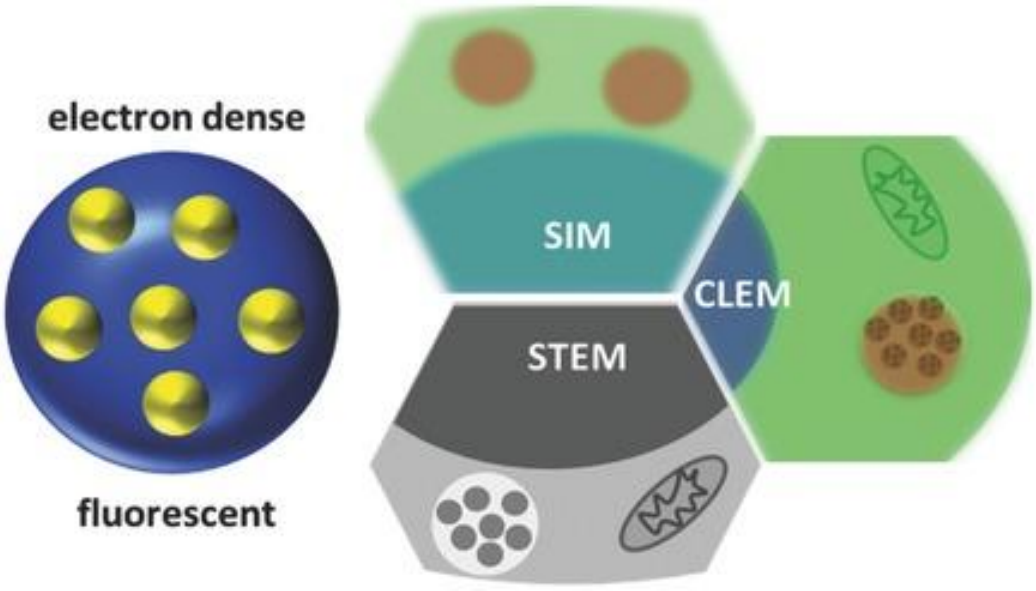

Particle & Particle Systems Characterization

www.particle-journal.com

Metal–Polymer Hybrid Nanoparticles for Correlative High-Resolution Light and Electron Microscopy

Martin Reifarth, Elisabeth Preußger, Ulrich S. Schubert, Rainer Heintzmann,* and Stephanie Hoeppener**

The combination of fluorescence microscopy and electron microscopy promises a deeper insight into the ultrastructural features of cell organelles, e.g., after drug administration. Both methods complement each other and provide, as a correlative approach, a keen insight into the fate of nanoparticles within the cell. Moreover, it represents a promising tool to determine alterations of the cellular environment as a response to particle uptake. However, the availability of suitable correlative markers is mandatory for such correlative approaches. In this contribution, the utilization of poly(ethylene imine) based metal–polymer hybrid particles labeled with small gold nanoparticles and Rhodamine B facilitating the observation of the particles by means of fluorescence as well as by transmission electron microscopy is suggested. Correlative light and electron microscopy is used to study uptake and intracellular fusion processes of endosomal/lysosomal structures.

Polymeric nanoparticles have gained increasing attention in biomedicine as efficient drug and gene delivery agents.[1] The large variety of properties covered by different polymeric systems promises a tailored approach to the targeted delivery of drugs into cells as well as an improved biocompatibility.[2] In order to achieve a keen understanding of the mode-of-action of polymer-based nanoparticles in vitro, the utilization of high-resolution imaging techniques is indispensable. These insights are important in order to improve the particles' performance by reducing cytotoxic effects, understand their fate within the cell and enhancing the controllability of the cargo release etc. Whereas fluorescence techniques are widely used for the investigation of uptake and internalization in the cellular or tissue context[3] and facilitate to image particles in the intact biological sample without confusing them with the cellular matrix, their resolution is still limited. Novel super-resolution fluorescence microscopy methods,[4] such as structured illumination microscopy (SIM), can improve the resolution capabilities; however, the level of individual particles is still difficult to reach. This level of information requires the utilization of electron microscopy in particular transmission electron microscopy (TEM), which provides a resolution down to the nanometer level, facilitating the visualization of individual particles and their localization in a cellular environment. Moreover, TEM allows a deeper insight into the ultrastructural cellular features down to the membrane level; however, these advantages are at the expense of tedious preparation routines, a limited field of view and the impediment to acquire dynamic information on the uptake process.[5] Additionally, in the context of the investigation of polymer nanoparticles, frequently only poor material contrast is achieved compared to the interior of the cellular structures since polymeric particles possess an intrinsic low electron density, which complicates their identification within the cellular context.[5b–d] For this purpose, a combination of fluorescence and electron microscopy (EM) represents a promising approach to obtain a more complete set of information on a cellular system and its response to the exposure of drug delivery and nanoparticle systems than each of the applied methods can provide alone. Fluorescence and electron microscopy pose special requirements on the nanoparticles under investigation as well as on the sample condition and the preparation methods. Fluorescence microscopy depends on the introduction of suitable fluorescence dyes into the cell. The samples require optimized fluorescence labeling as well as fixation protocols preventing autofluorescence, dye quenching, or a destruction of the dyes' properties while maintaining the cellular microstructure of the cell. Whereas fluorescence imaging can be carried out on the intact biological sample and even live cell imaging is possible, electron microscopy requires optimized staining steps for visualization of membranes and organelles being present in the cell structure as well as sectioning of the cells into thin slices.

M. Reifarth, E. Preußger, Prof. U. S. Schubert, Dr. S. Hoeppener
Laboratory of Organic and Macromolecular Chemistry (IOMC)
Friedrich Schiller University Jena
Humboldtstr. 10, 07743 Jena, Germany
E-mail: ulrich.schubert@uni-jena.de; s.hoeppener@uni-jena.de

M. Reifarth, E. Preußger, Prof. U. S. Schubert, Dr. S. Hoeppener
Jena Center of Soft Matter (JCSM)
Friedrich Schiller University Jena
Philosophenweg 7, 07743 Jena, Germany

Prof. U. S. Schubert, Prof. R. Heintzmann
Abbe Center of Photonics
Albert-Einstein-Str. 6, 07745 Jena, Germany
E-mail: rainer.heintzmann@uni-jena.de

Prof. R. Heintzmann
Institute of Physical Chemistry
Friedrich Schiller University Jena
Helmholtzweg 4, 07743 Jena, Germany

Prof. R. Heintzmann
Leibniz Institute of Photonic Technology
Albert-Einstein-Str. 9, 07745 Jena, Germany

DOI: 10.1002/ppsc.201700180

Despite the diverse preparation requirements, both methods can complement each other in a synergistic fashion. Whereas the nanoparticle cargo can be observed by means of fluorescence microscopy, the ultrastructural cellular context can be elucidated most efficiently by electron microscopy. Thus, a combination of both techniques can provide a deeper insight into cellular processes at a level of information that is unmatched by each technique on its own or by other techniques. The combination of both methods and a correlation of the obtained data are excellently suited to investigate cellular and nanoparticle uptake processes and might be very valuable to understand the mode-of-action of tailored nanoparticle systems in the cellular context. Therefore, suitable nanoparticles with correlative labels are required.

For drug delivery applications, amino functionalized polymers have gained significant interest in the field of delivery of nucleic acids. In particular, poly(ethylene imine) (PEI) has become the gold standard in gene transfection via nonviral gene delivery.[6] Due to its high amino content PEI can interact electrostatically with phosphate bearing nucleic acids to form polyplexes which can be used to transfer, e.g., DNA or RNA into cells.[6,7] However, poly(ethylene imine)s are limited in their medical use since they are known to be cytotoxic,[8] possess a low blood compatibility,[9] and are nonbiodegradable.[10] To overcome these drawbacks, PEIs have been modified regarding their chemical structure to form less toxic polyplexes[11] or to build more complex polymeric architectures.[12]

So far, strategies to enhance the contrast of the polymer nanoparticles employ the enhancement of the electron contrast by incorporation of smaller, dense nanoparticles[5a] or heavy metal complexes.[13] In particular, studies of poly(ethylene imine) uptake supported by the incorporation of electron dense labels have been reported.[14]

Uptake studies as well as the elucidation of the intracellular fate using correlative light and electron microscopy (CLEM) as an investigation tool have mainly been focusing on the interaction of bacteria[15] or viruses[16] with cells. Nanoparticle uptake studied by CLEM[17] has, so far, only sparsely been reported and the availability of suitable correlative dyes has been identified as a critical issue. In this contribution, we introduce a CLEM approach to study the uptake and intracellular fate of a selected polymeric nanoparticle system based on poly(ethylene imine), which can serve, first, as a suitable correlative label for both electron and fluorescence microscopy and, second, act as a model system to mimic drug delivery of PEI-based systems. In this context we will also discuss technological challenges as well as the synergistic character of fluorescence and electron microscopy techniques and will highlight the benefit that is gained by combining both methods.

Here, we introduce a metal–polymer hybrid nanoparticle system, recently developed in our group as a nanoparticle system for plasmonic applications, consisting of a PEI polymer nanosphere which incorporates smaller gold nanoparticles.[18] In the present study, the plasmonic properties of the nanoparticles do not play a predominant role; however, we realized that the particle system is additionally well suited for biological uptake studies. This is motivated by the exceptional role of the utilized PEI as a gene transfection agent as well as a sufficient biocompatibility of the system. Furthermore, the fact that the particles incorporate small gold nanoparticles, which are perfectly suitable as easily identifiable markers for TEM, along with the free amino functionalities present in the PEI that enable a facile covalent attachment of a reactive fluorescent dye pose excellent properties for their utilization as object of study in CLEM.

To obtain a metal–polymer hybrid nanoparticle system that can be utilized as a correlative dye for CLEM, nanoparticles have been prepared following the synthesis introduced by Kretschmer et al.[18] In this approach, gold nanoparticles are formed within nanoparticles consisting of branched PEI by the reaction of branched PEI with $HAuCl_4$ (**Figure 1**A) in *N,N′*-dimethylfomamide (DMF). This approach allowed the synthesis of different metal–polymer hybrid systems (Figure 1B) in which the size of the PEI polymer nanoparticles as well as the fill factor with gold nanoparticles of the resulting particles can be controlled. The particles used in our study possess an average diameter of 32 ± 7 nm and carry gold particles with a mean diameter of 10 ± 4 nm according to TEM image analysis (Figure 1C). The primary amino functionalities being present in the PEI polymer can additionally act as efficient anchor groups for fluorescence labels. Fluorescence labeling was introduced by the covalent attachment of Rhodamine B isothiocyante or Fluoresceine isothiocyanate, respectively. In contrast to Rhodamine B, Fluoresceine labeled particles showed a limited long-term stability and aggregation occurred after few days (absorption and emission spectra of Fluorescein-labeled gold-PEI particles in *N,N′*-dimethylformamide are depicted in Figure S1 in the Supporting Information). The nonlabeled gold-PEI particles exhibit a strong positive zeta potential of 44.0 ± 0.1 mV. Whereas Rhodamine B functionalized nanoparticles keep their positive charge (41.5 ± 2.3 mV), the dye labeling with the uncharged Fluorescein significantly decreases the surface potential of the nanoparticles to 24.4 ± 0.5 mV which results in severe particle aggregation after short time. The strongly positive zeta potential of the Rhodamine B-labeled particles moreover is beneficial for their cellular uptake.[19]

Cellular uptake studies on Rhodamine B-labeled nanoparticles were conducted on the human cell line HEK-293. Cell Proliferation Kit II assays (XTT, (2,3-bis(2-methoxy-4-nitro-5-sulfophenyl)-2H-tetrazolium-5-carboxanilide)) were performed to verify the nontoxic nature of Rhodamine-functionalized and nonfunctionalized nanoparticles at appropriate working concentrations.

The particle concentration (in μg branched PEI per mL) of the stock solution was estimated assuming a complete conversion of the reacted polymer. A severe toxic effect could not be observed up to a concentration of 30 μg mL^{-1} (**Figure 2**A) for the Rhodamine B-labeled as well as for the nonlabeled particle systems. At higher concentrations, the cell viability decreased significantly. At concentrations >50 μg mL^{-1} Rhodamine B-functionalized particles exhibited a significantly higher toxicity compared to the nonfunctionalized nanoparticles. Based on these toxicity studies all cell uptake experiments were performed at moderate particle concentrations of 25 μg mL^{-1}. Flow cytometry investigations revealed the uptake efficiency of the nanoparticles for up to 24 h. Already after 4 h an uptake of >60% of the nanoparticles was determined and an uptake efficiency of almost 90% was reached after 8 h (Figure 2B).

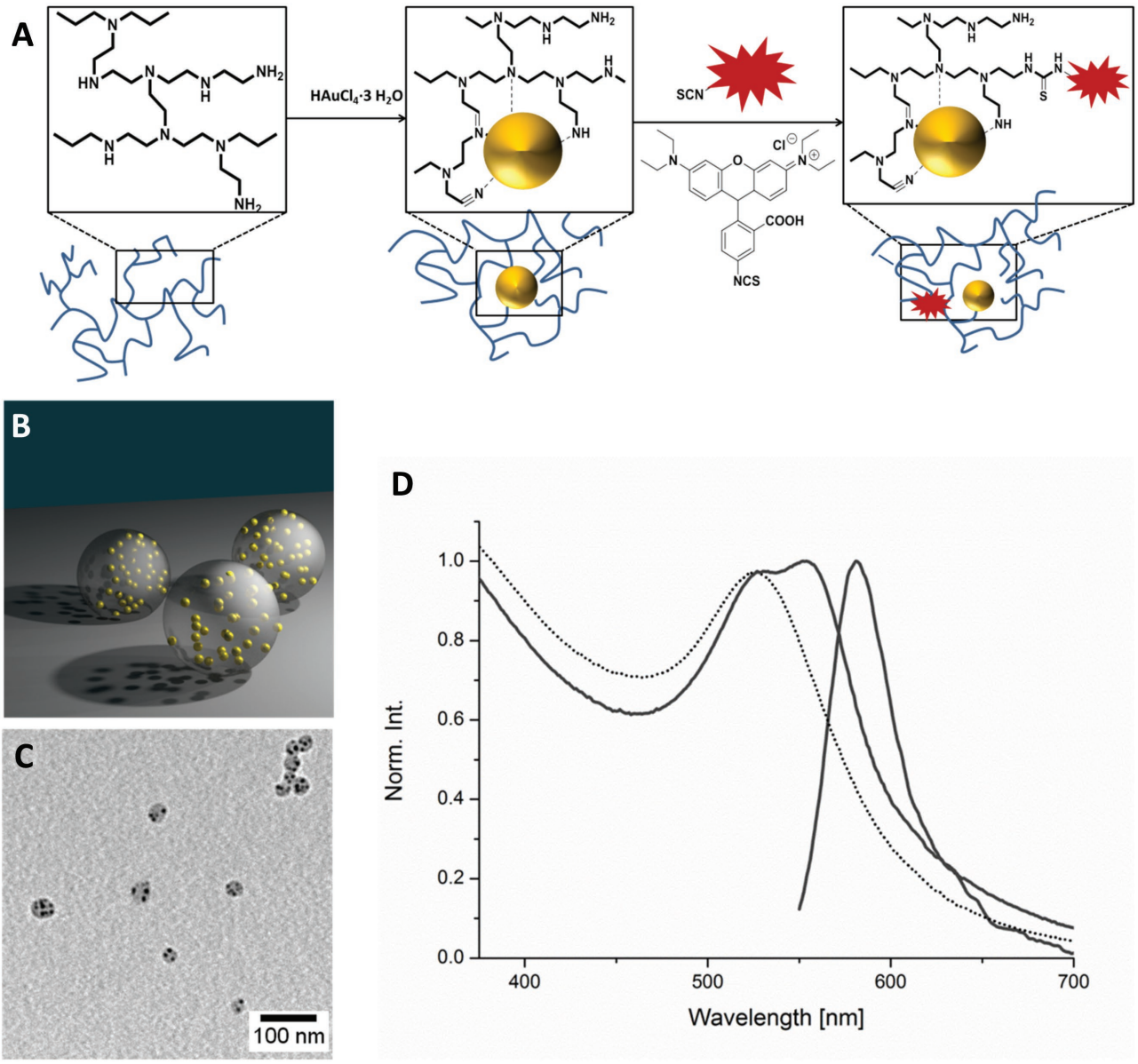

Figure 1. A) Schematic representation of the synthesis of gold-PEI hybrid metal–polymer nanoparticles. B) Schematic representation of the nanoparticles and C) TEM images of the the gold-PEI Rhodamine B-labeled nanoparticles. D) Absorption spectrum of nonfunctionalized (dotted line) and absorption and emission sprectra of Rhodamine B-labeled (solid line) gold-PEI nanoparticles measured in DMF.

Since flow cytometry cannot prove the internalization but also indicates an association of the nanoparticles to the extracellular membrane, additional SIM imaging was performed.

Figure 3A,B depicts representative cells after a particle incubation time of 24 h. The nucleus of the cells is stained in blue (Hoechst 33342), the cytoskeleton in green (Alexa Fluor 488 phalloidin), and the gold-PEI nanoparticles appear red (Rhodamine B isothiocyanate). The gold-PEI nanoparticles can be clearly located within the cell, thus, confirming their cellular uptake. Furthermore, bright fluorescence spots with a spatial dimension of ≈1–2 µm were identified, indicating that the nanoparticles were internalized into cellular compartments. A closer inspection of the intracellular nanoparticle locations revealed areas of fairly high particle incorporation. They appear to consist of compartments which are in close proximity of each other. This close proximity might be indicative for subsequent lysosomal fusion processes. Figure 3B provides a magnified view of an area which partially indicates an elongated appearance of the compartment, which is regarded as a further indication for fusion processes. However, the lateral resolution of wide-field fluorescence microscopy is not sufficient to provide an additional proof for this assumption. Moreover, from these images it is not clear if individual or rather the uptake of a large number of gold-PEI nanoparticles generates the fluorescence contrast within the cellular compartments and how the particles are arranged within the cell. In addition to the intracellular distribution of fluorescence signals, nanoparticles were also found at the extracellular membrane of the cells (these findings are

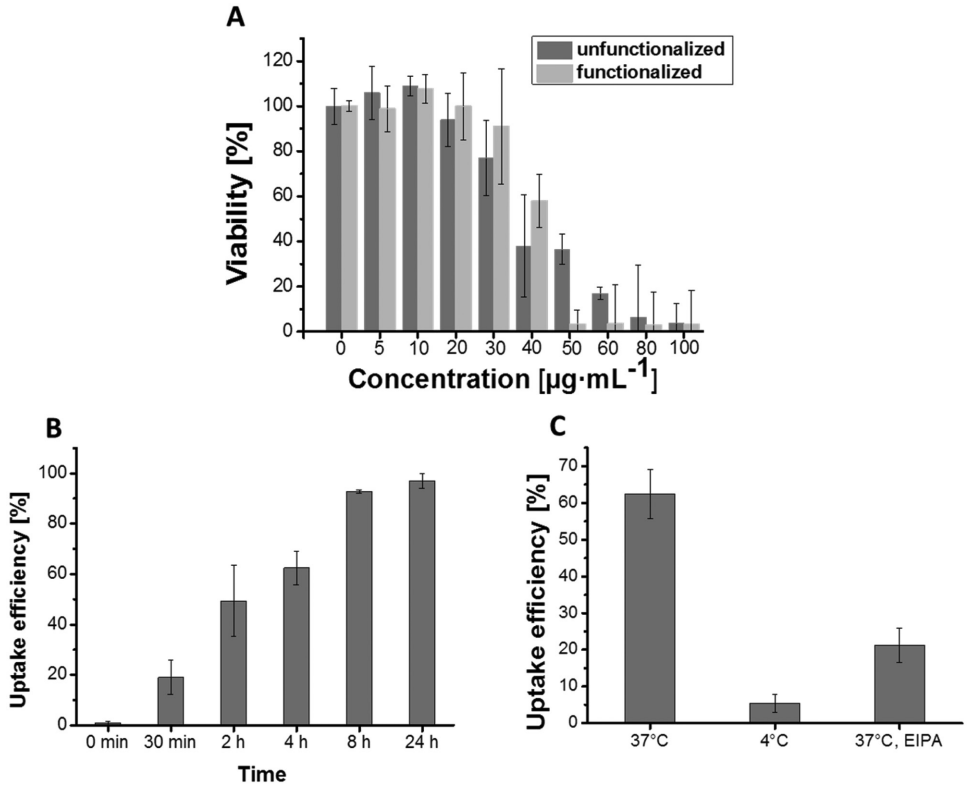

Figure 2. A) XTT cytotoxicity test with Rhodamine B-labeled nanoparticle samples and the unlabeled particle sample at different nanoparticle concentrations (0–100 µg mL^{-1}). In the course of these experiments incubation times of 24 h were chosen to enable uptake of the metal–polymer hybrid nanoparticles into HEK-293 cells. All data are expressed as mean and SD ($n \geq 3$). B) Time-dependent uptake efficiency determined by flow cytometry (labeled particles with a conc. of 25 µg mL^{-1}). All data are expressed as mean and SD ($n \geq 4$). C) Uptake efficiency after exposure to labeled particles (conc. 25 µg mL^{-1}) examined after 4 h of incubation at 37 and 4 °C, and subsequent to exposure to 30 µg mL^{-1} EIPA, a macropinocytosis inhibitor, respectively. All data are expressed as mean and SD ($n \geq 4$).

based on confocal laser scanning microscopy (CLSM) images, see Figure S2 in the Supporting Information). They indicate an interaction of the gold-PEI nanoparticles with the membrane and could originate either from particle uptake, release processes, or from attached particles which interact with the membrane. Again, limitations in the resolution capabilities of fluorescence imaging do not allow obtaining detailed information on these interaction processes. The resolution of wide-field microscopy can significantly be enhanced if structured illumination is used. SIM potentially provides an enhanced resolution down to 100 nm to access more detailed information on the distribution of the fluorescent particles within the cellular framework. Figure 3C,D demonstrates the improved resolution capabilities of this method on the same cellular structure as previously investigated by laser wide-field imaging. In contrast to the wide-field images (Figure 3A,B), a more detailed insight

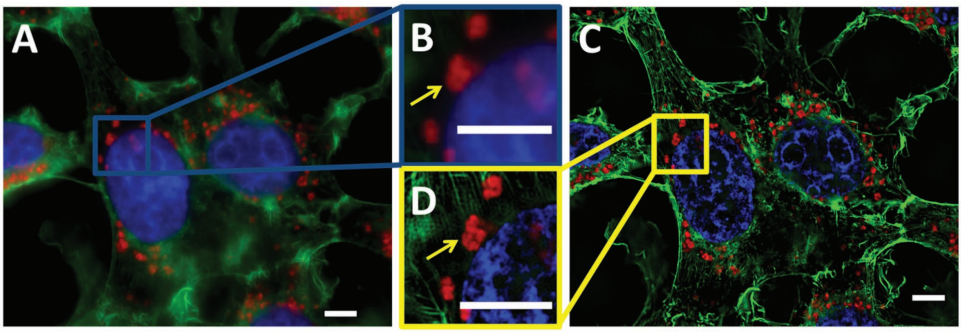

Figure 3. Fluorescence images of HEK-293 cells incubated with functionalized nanoparticles (25 µg mL^{-1}, 24 h). 63× oil objective 1.4 NA. Blue: Nucleus (Hoechst 33342). Green: Cytoskeleton (Alexa-green phalloidin). Red: Functionalized nanoparticle. A) Laser wide-field image. B) Magnification of the highlighted area in panel (A). C) Structured illumination microscopy (SIM) image. D) Magnification of the highlighted area in panel (C). D) SIM is capable of resolving the particle arrangement inside lysosomes far better than conventional wide-field microscopy (C). Scale bars: 5 µm.

into the ultrastructural arrangement of nanoparticles internalized into the cells is facilitated by SIM (Figure 3C,D) due to the enhanced lateral resolution provided by this method. The shape of the particle-containing compartments can be clearly discriminated and the evidence for the previously observed fusion processes is more pronounced compared to the wide-field imaging.

However, still the resolution is not high enough to provide a clear impression of the internalization on the single particle level as well as on the endosomal/lysosomal fusion processes itself. The resolution of SIM is, in this context, sufficient to select cells of interest and to provide information on areas of particular interest that show internalization of nanoparticles as well as to clearly identify the elongated structures. The lack of fine-structural resolution capabilities of conventional and super-resolution fluorescence methods, i.e., CLSM, laser wide-field, and SIM can be compensated by performing additional TEM as a method that provides a resolution sufficiently high enough to resolve single particles and to visualize details of the ultrastructural context. This information is very valuable to complement the observations of the fluorescence microscopy studies.

In a first study, cells were trypsinated and embedded into Epon-resin with the aim to obtain a general insight of uptake processes involved in the internalization of the nanoparticles. For this purpose, their interaction with the extracellular membrane as well as their association to intracellular compartments was investigated in a screening approach. Slices with a thickness of 80 nm were prepared and investigated by scanning transmission electron microscopy (STEM). This method was chosen owing to the good material contrast provided by this measurement mode. **Figure 4** depicts STEM images of the ultrastructural features of the cell, in particular, focusing on the localization of the nanoparticles within the cytoplasm and at the extracellular membrane. It is clearly observable that the gold-PEI nanoparticles tend to aggregate at the extracellular membrane and are engulfed by protrusions (Figure 4A,B) facilitating their internalization into membrane-surrounded endosomal or lysosomal compartments (Figure 4C,D).

The observed morphologies of the extracellular membrane are characteristic for macropinocytosis mediated uptake processes. Furthermore, the localization of the nanoparticles inside the cytoplasm within membrane-surrounded endosomal/lysosomal structures are indicative for the active uptake of larger nanoparticles or even nanoparticle aggregates and further supports the involvement of macropinocytosis in the uptake mechanism. Additional temperature-dependent uptake investigations provided further evidence for this assumption. HEK293 cells incubated at 4 °C showed a significantly reduced uptake of the gold-PEI nanoparticles (flow cytometry data, see Figure 2C). This observation was furthermore confirmed by flow cytometry analysis and TEM imaging of cell samples that were exposed to the macropinocytosis inhibitor 5-(*N*-ethyl-*N*-isopropyl)amiloride (EIPA) prior to nanoparticle incubation (Figure 2C; Figure S3, Supporting Information). The results showed a significantly reduced uptake in the presence of EIPA which indicates that macropinocytosis represents the predominant uptake process; however, the remaining, small uptake efficiency of <10% suggests that also alternative uptake pathways might be involved in the internalization of nanoparticles. Since the incubation temperature of 4 °C is not optimal for HEK-293 cells as cells

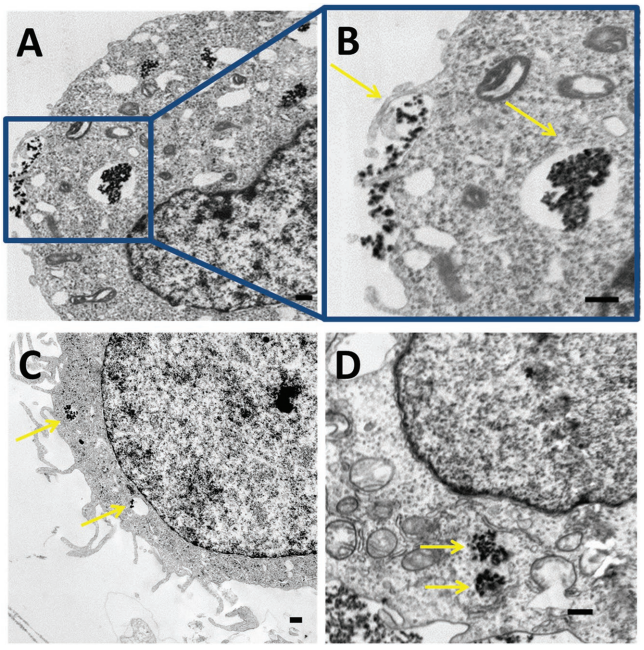

Figure 4. STEM images of HEK-293 cells after gold-PEI nanoparticle uptake after 24 h of particle incubation (conc. 25 µg mL^{-1}). Particles inside the cellular body are highlighted by yellow arrows. A) Macropinocytosis triggered uptake of nanoparticles and nanoparticle aggregates at the extracellular membrane. B) Magnification thereof. C,D) Internalized particles. Intracellular localization of nanoparticle aggregates within membrane surrounded endosomal/lysosomal compartments. Scale bars: 0.5 µm.

of human origin and EIPA as macropinocytosis inhibitor is, moreover, known to inhibit Na^+/H^+ exchangers (and, thus, to influence the cellular live processes),[20] we chose short incubation periods of only 4 h for the control tests to ensure appropriate cell viability at the timescale of the experiment.

For further investigation of the suspected fusion processes of cellular compartments, a correlative approach was chosen in order to elucidate details of these processes. Regions of interest were initially identified by CLSM and later subjected to electron microscopy investigations. Hereby, advantage was taken on the fact that the gold-PEI nanoparticles can serve as easily traceable objects for both techniques. For this purpose, it is possible to define cells which show evidence for the anticipated fusion processes, to identify interesting time points and to perform a prescreening by taking advantage of the strengths of fluorescence microscopy.

In the present case, a cell showing a large number of elongated intracellular compartments was chosen. Subsequently, a detailed investigation on the ultrastructural details of the same cells was carried out by electron microscopy to investigate peculiarities of the membrane structures and the association state of the internalized particles.

For correlating light and electron microscopy it is essential that the preparation protocols are carefully adjusted and optimized for both techniques. A respective scheme of the entire procedure is outlined in the workflow summarized in Figure S4 (Supporting Information).[21] This includes first the optimization of the preparation conditions for CLSM under consideration

of factors that might impair the later preparation steps. For example, glutaraldehyde fixation represents a standard method for electron microscopy, however, it is not compatible with fluorescence microscopy since the autofluorescence of the samples is unacceptably strong.[22] Autofluorescence does not occur on formaldehyde fixed samples; nevertheless, its fixation efficiency is not sufficient for EM sample processing. A mixture of 2% formaldehyde and 0.5% glutaraldehyde did not interfere with the fluorescence microscopy performance and was, thus, applied in the correlation protocol. Subsequently, CLSM imaging was carried out through the entire body of the adherent cells in phosphate buffer saline (PBS) as immersion medium (the CLSM image of the slice of interest is displayed in **Figure 5**A; for a 3D representation of the entire cell see CLSM stack representation displayed in Figure 5B).

Subsequently to fluorescence imaging, the aqueous medium was removed and standard TEM sample preparation was performed, including glutaraldehyde fixation as well as OsO_4 post-fixation, uranyl acetate staining, dehydration, and embedding in Epon resin. The Epon resin was removed from the glass bottom dish by plunging the sample into liquid nitrogen. After that, sectioning with an ultramicrotome and subsequent in-block staining with lead citrate was performed. Generally, in this approach the relocation of cells subjected to the preceding fluorescence imaging inside the resin block constitutes a challenge. For relocation, cells were initially seeded on a gridded glass-bottom dish with a mesh size of 500 µm. In order to simplify the relocation, the area previously imaged by fluorescence microscopy was pretrimmed to an ≈500 × 500 µm^2 cutting window prior to sectioning using a razorblade. Due to the relatively small size of the pretrimmed cutting window, reidentification of the cells in the resin slice was possible by means of cell shape and the organization of the cells in the sample.

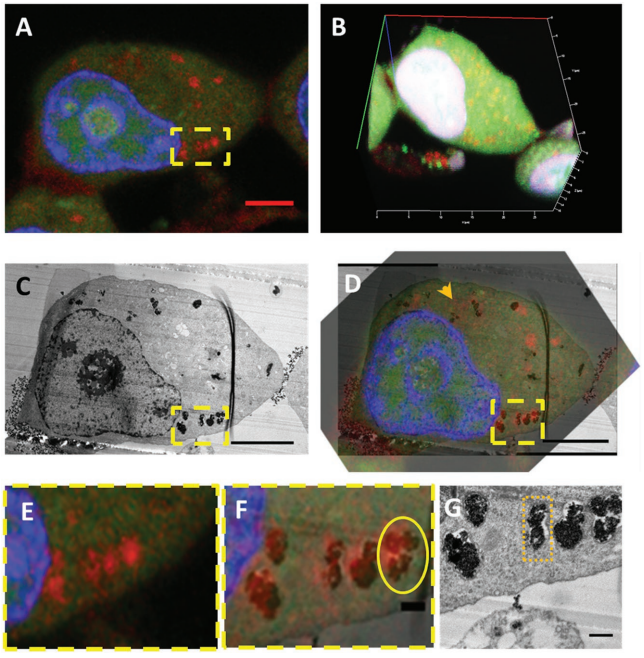

Figure 5. Correlative light and electron microscopy of a HEK-293 cell 24 h incubated with functionalized gold-PEI nanoparticles (25 µg mL^{-1}). A) Cell imaged by CLSM. 63× oil objective 1.4 NA. Blue: Nucleus (Hoechst 33342). Green: Cytoplasm (Hoechst 33342). Red: Functionalized nanoparticles (Rhodamine B). B) 3D representation of the entire cell imaged by CLSM. C) STEM image of the same cell. D) Overlay. Orange arrow: Fluorescence signal which cannot be assigned to nanoparticles in the EM image. E) Magnified image of (A) (as indicated by yellow box). F) Magnified image of (D) (as indicated by yellow box). G) High-magnification STEM image of selected area. Scale bars: A,C,D) 5 µm. D) Scale bar extracted from STEM image. F,G) 0.5 µm. All STEM images are displayed with equalized histogram.

Figure 5 displays the results of a correlated data set obtained by CLSM and STEM. Figure 5A depicts the fluorescence image of a HEK-293 cell exposed to nanoparticles after an incubation period of 24 h. Red fluorescence highlights the Rhodamine B-functionalized gold-PEI particles, blue represents the fluorescence emerging from the nucleus (Hoechst 33342 staining) and the cytoplasm is depicted in green (Hoechst 33342 staining). This particular cell was selected, since the CLSM image indicated endosomal/lysosomal fusion processes. Subsequently to the fluorescence data acquisition, STEM imaging was carried out. The same cell as previously imaged by CLSM could be reidentified according to the characteristic cellular shape (Figure 5C). An overlay of CLSM and STEM images further validates the reidentification. The correct registration of the green (cytoplasm) and blue channel (nucleus) in the fluorescence image with the corresponding signals in STEM reveals a clear correlation between the red fluorescence spots and the presence of nanoparticles in the STEM images (Figure 5D).

The fluorescence images clearly indicate red, fluorescent compartments. These spots feature the previously observed elongated structure of the particles which are suspected to indicate the endosomal/lysomal fusion processes, in particular, in the area which is highlighted by the yellow dashed-lined box in Figure 5A. Images acquired at higher magnification allow revealing the ultrastructural features in this area of interest, thus, enabling the elucidation of the particle arrangement inside the vesicular structures. Special focus is placed on the appearance of the compartments' membrane features. Whereas conventional, noncorrelated STEM investigations frequently reveal a spherical structure of the endosomal features (see, e.g., Figure 4D), the correlative data set in the region of the fusion processes mark clear signs for a merging of the individual endosomal/lysosomal structures. As highlighted in Figure 5F (circle) it can be observed that the structure of the resulting endosomes appears segmented and packages of Au-PEI nanoparticle cluster aggregates are located within one structure without being segregated by membranes anymore. The membrane, however, surrounds the entire packages of aggregated Au-PEI nanoparticles. The most evident example demonstrating the fusion of endosmal/lysosomal structures seen in the process is highlighted by the highlighted area in Figure 5G. Here, the original shape of two merging endosomes is still visible with a membrane constriction being observed in the middle of the fusing structures marking the fusion process. Thus, the correlation of fluorescence and electron microscopy images clearly proves the additional information value gained by the combination of both methods and helps to reveal the fusion processes in great detail. However, it has also to be mentioned critically that the correlation of both images is not straightforward. As can be observed in the overlay images, in the present data set fluorescence

spots are visible, which cannot directly be associated to internalize cluster arrangements (Figure 5D, indicated by the orange arrow). Here, the corresponding STEM images do not reveal the presence of nanoparticles although fluorescence signals are identified. This obstacle is a direct result of the different vertical resolution capabilities of both techniques. Whereas the depth of information is limited in case of STEM studies by the thickness of the prepared slices (thus, typically 80 to 120 nm), the focus depth of CLSM is in the range of 500–700 nm[4a] due to light-optical diffraction limitation and, thus, particles might be located in adjacent slices of the STEM sample even though they can still be observed in the fluorescence images.

In this study, we investigated cellular uptake and intracellular fate of polymeric nanoparticles by means of light and electron microscopy. For this purpose a metal–polymer hybrid particle system was utilized on the basis of branched PEI bearing small gold particles. Due to the incorporation of these electron-dense Au particles, these metal–polymer composites are suitable as markers for electron microscopy investigations. The particles could also be labeled efficiently with Rhodamine B which enabled their utilization for fluorescence imaging. Flow cytometry investigations revealed an efficient uptake of the particles into HEK-293 cells after an incubation time of 24 h. In combination with fluorescence and STEM investigations, a mainly active uptake mechanisms of the gold-PEI nanoparticles by macropinocytosis could be determined.

A correlative investigation of intracellular compartments provided detailed insight into the fate of particles within the cells and intracellular endosomal/lysosomal fusion processes could be revealed. In this context, CLSM investigations provided in a prescreening process evidence for these processes which were investigated subsequently by electron microscopy, which could demonstrate details of this process by providing information on the ultrastructural level.

Experimental Section

N,N′-Dimethylformamide was dried with a PureSolv-EN Solvent Purification System (Innovative Technology). Branched poly(ethylene imine) (bPEI, 25 kDa) was received from Sigma-Aldrich. Hydrogen tetrachloroaurate(III) trihydrate ($HAuCl_4 \cdot 3H_2O$, 99.99%) was purchased from Alfa Aesar. Rhodamine B isothiocyanate (mixed isomers) and Fluorescein isothiocyanate (mixed isomers) were purchased from Sigma-Aldrich. Triethylamine (puriss. p.a.) was purchased from Sigma-Aldrich and stored over Argon.

UV–vis absorption spectra were measured on a Varian Cary 5000 UV–vis–NIR double beam spectrophotometer (Agilent) with a spectral resolution of 1 nm. Emission spectra were recorded using a Perkin-Elmer LS 50 spectrometer and corrected according to the spectral sensitivity function of the detector. Spectroscopic measurements were carried out using a 1 cm quartz cuvette using spectroscopy grade solvents. Centrifugation was performed with a Heraeus Biofuge Primo with a fixed angle rotor in 1.5 mL Eppendorf tubes.

Zeta potential measurements were carried out using electrophoretic light scattering. The zeta potentials were determined using a Zetasizer Nano ZS (Malvern Instruments, Herrenberg, Germany) by applying laser Doppler velocimetry. Therefore, 10 runs were carried out using the slow-field and fast-field reversal mode at 150 V. The measurement results are expressed as mean and SD of triplicates. For zeta potential determinations, the sample was suspended in milliQ water and measured at 25 °C.

Transmission electron microscopy was carried out using a Technai G^2 20 system (FEI), with 120 or 200 kV acceleration voltage.

Particle sizes were determined on the basis of TEM images using ImageJ. For this purpose, particle areas were measured and diameter equivalents were calculated assuming a spherical shape. For size determination, at least 300 particles were analyzed.

Nanoparticle Synthesis: To 1 mL of DMF, 40 µL of a solution of bPEI in DMF (10 mg mL^{-1}) as well as 40 µL of a solution of $HAuCl_4 \cdot 3H_2O$ (10 mg mL^{-1}) was added under thorough stirring. The solution, which turned orange immediately after addition, was heated in an oil bath and the temperature was set to 150 °C. The solution was stirred for 20 min. After 2 min, the solution turned red. Subsequently, the particle suspension was allowed to cool to room temperature. The particles were centrifuged (1 h, 15 000 rpm) and washed twice with fresh DMF.

For further biological tests, the particles were centrifuged and washed three times with milliQ water. The suspension was filled up to 1 mL yielding a stock solution of 400 µg mL^{-1} PEI decorated with Au particles (assuming a full conversion of PEI during the synthesis).

Particle size: 32 ± 7 nm.

Zeta potential: 41.5 ± 2.3 mV.

Particle Labeling: For particle labeling, the particles synthesized as described above were washed with DMF, centrifuged (1 h, 15 000 rpm), and resuspended in a few drops of DMF. To this suspension, 2 µL trimethylamine and the respective reactive dye was added (2.5 mg Rhodamine B isothiocyanate resp. 1.9 mg Fluorescein isothiocyanate). The reaction mixture was filled up to 1 mL DMF and stirred for four days in the dark. Subsequently, the reaction mixture was centrifuged (1 h, 15 000 rpm) and washed until no residual dye was observable (2 to 3 times). The particles were stored in DMF. For cell experiments, the particles were finally washed at least two times with milliQ water.

Zeta potential (Fluorescein labeled): 24.4 ± 0.5 mV

Zeta potential (Rhodamine labeled): 41.5 ± 2.3 mV.

Cell Experiments: HEK-293 cell line (CRL-1573, ATCC) was maintained in DMEM culture medium (Biochrom) supplemented with 10% fetal calf serum (Capricorn), 100 IU mL^{-1} penicillin, 100 µg mL^{-1} streptomycin, and 20 mM L-glutamine (Merck Millipore). The cells were cultured in a humidified 5% CO_2 atmosphere at 37 °C.

Toxicity Tests: For cytotoxicity studies of the particles, the XTT assay (Proliferation Kit II, Roche) was performed. In detail, 10^4 HEK-293 cells per well were grown in a 96-well microplate for 24 h. The outer wells were left blank. Afterward, nanoparticles were added at the indicated concentrations and the cells were incubated for further 24 h at 37 °C. Subsequently, the medium was replaced by fresh medium containing XTT labeling mixture as recommended by the supplier. After an incubation period of 4 h, the absorbance was measured with a Tecan M200 Pro fluorescence microplate reader (Crailsheim, Germany) at 450 nm with 630 nm as reference wavelength. Untreated cells on the same well plate served as controls. The experiment was repeated three times independently.

Flow Cytometry: The time-dependent uptake efficiency of Rhodamine labeled gold-PEI nanoparticles was determined by flow cytometry. In detail, HEK 293 cells were grown in a 12-well plate at a density of 2×10^5 cells mL^{-1} for 24 h. Afterward, particles were added at a concentration of 25 µg mL^{-1} and incubated at 37 °C. Cells were then harvested 30 min, 2, 4, 8, and 24 h after nanoparticle addition. All data shown are expressed as mean ± SD of triplicates.

Otherwise, cells were incubated at 4 °C for 4 h or cells were incubated at 37 °C for 4 h in the presence of the macropinocytosis inhibitor EIPA (Sigma, concentration of 30 µg mL^{-1}) which was added immediately

before nanoparticle incubation, respectively. For determination of relative uptake, 10 000 viable cells per sample were measured by flow cytometry using a Cytomics FC 500 (Beckman Coulter). The results represent $n = 4$ experiments independently.

Fluorescence Microscopy: For structured illumination microscopy, HEK-293 cells were seeded on high precision cover glasses (Marienfeld-Superior, 18 × 18 mm, 170 ± 5 µm certified thickness) at a density of 5×10^4 cells mL^{-1} for 24 h at 37 °C. Cell culture medium was renewed and particles were applied to the cells at a concentration of 25 µg mL^{-1}. After 24 h, cells were washed with 1× PBS (Merck Millipore). Hoechst 33342 (Life Technologies) was applied 1:1000 in cell culture medium and incubated for 45 min at 37 °C. For cell fixation, the medium was replaced by 2% paraformaldehyde (BDH Prolabo). After 20 min of incubation, cells were permeabilized with 0.1% Triton X-100 (Carl Roth) in PBS for 10 min at room temperature. Cells were washed again with PBS and stained with Alexa Fluor 488 Phalloidin (Thermo Fisher) 1:40 in PBS for 20 min at room temperature. Subsequently, the cells were embedded in Prolong Gold antifade reagent (Thermo Fisher). Imaging was performed on an Elyra S1 system (Zeiss, Oberkochen, Germany, excitation wavelengths of 405, 488, 561, and 642 nm, respectively) applying an 63× 1.4 NA plan apochromat oil objective. For structured illumination, three channels were acquired: Blue (nucleus, Hoechst 33342 staining, excitation wavelength 405 nm, excitation grating with 23 µm, BP 420–480 + LP 750), green (cytoskeleton, Alexa Fluor 488 Phalloidin staining, excitation wavelength 488 nm, excitation grating with 28 µm, BP 495–550 + LP 750), and red (Rhodamine B, excitation wavelength 561 nm, excitation grating with 34 µm, BP 570–620 + LP 750). The grating position and axial position of the sample table were controlled by piezo controllers (Physik Instrumente, Germany). Images were recorded with a CCD camera (iXon 885 from Andor, UK), cooled to −63 °C. Reconstructions were performed with the commercial ZEN software installed on the system. The laser wide-field image was reconstructed from SIM raw data.

For confocal laser scanning microscopy, cells were seeded and incubated with the nanoparticle samples as described above. Subsequently, Hoechst 33342 (10 µg, Life Technologies) as well as CellTracker Green CMFDA dye (10 µM, Thermo Fisher) was applied to cell culture medium and incubated for 45 min at 37 °C. After this, cells were fixed and embedded as aforementioned. Three color channels have been acquired: Blue (405 nm excitation wavelength, Hoechst 33342 nucleus staining), green (488 nm excitation wavelength, CellTracker Green CMFDA dye), and red (561 nm excitation wavelength, Rhodamine labeled particles). The images were processed using the commercial ZEN 2.0 software installed on the system. In order to achieve an improved separation of the color channels, linear unmixing was carried out on the basis of emission spectra (Hoechst, Fluorescein, Rhodamine B) implemented in the system.

Scanning Transmission Electron Microscopy: HEK-293 cells were seeded on 6-well plates with a cell density of 10^5 cells mL^{-1} and incubated for 24 h at 37 °C with the nanoparticles samples (unfunctionalized particles, 25 µg mL^{-1}). The cells were detached using trypsin 1× trypsin-EDTA solution (Sigma-Aldrich). The cell suspension was washed (PBS 1×) and fixed for 1 h with glutaraldehyde (2% in PBS 1×, prepared from 8% EM grade stock solution) at 0 °C. After the aldehyde fixation, the cells were washed with PBS and postfixed with OsO_4 for 1 h (1% in PBS, prepared from 4% EM grade stock solution, both purchased from EMS, Hatfield) in the dark. Afterward, the cells were stained with uranyl acetate solution for 1 h and protected from light (1% in solution in milliQ water prepared from depleted uranyl acetate dihydrate purchased from EMS, Hatfield). Subsequently, the sample was dehydrated by an ethanol/water series with rising EtOH content (50%, 70%, 90%, 2× 100% dry EtOH, purified with a Solvent Purification System and stored over molecular sieves). Afterward, the cells were transferred into BEEM capsules (Plano, Wetzlar). There, the cell suspension was immersed in mixtures of Embed 812 (EMS, Hatfield) and ethanol (Embed/EtOH = 1:1 v/v for 1 h, 2:1 v/v for 12 h, pure Embed 812 for 4 h). After a further change of the embedding medium, the resin was hardened in an oven at 70 °C for 24 h. Ultrathin sections of 80 nm were cut with an ultramicrotome (PT-XL PowerTome, RMC, Tucson) using a diamond knife (RMC, Tucson) from the resin block. The ultrathin resin sections were put on a carbon supported copper grid (400 mesh, Quantifoil, Jena). Poststaining using lead citrate (according to Reynold's procedure) was carried out. Scanning transmission electron microscopy with high-angle annular dark-field detection was carried out using a Technai G^2 20 system (FEI), with 120 or 200 kV acceleration voltage.

Images were processed using ImageJ software. In order to represent the nanoparticles that possess a high contrast along with the cellular interior that possesses a low contrast at a similar contrast level, histogram equalization was carried out.

Correlative Light and Electron Microscopy: HEK-293 cells were grown on gridded µ-glass bottom dishes (ibidi, Martinsried, 500 µm grid size, 170 ± 5 µm certified thickness) with a cell density of 5×10^4 cells mL^{-1} and incubated for 24 h at 37 °C with the nanoparticles samples (25 µg mL^{-1}). For microscopy, the cells were stained with Hoechst 33342 as well as CellTracker Green CMFDA dye (Thermo Fisher) and fixed (2.0% formaldehyde and 0.5% glutaraldehyde) for 1 h at 0 °C. Confocal laser scanning microscopy was carried out on the sample immersed in PBS using a LSM880, Elyra PS.1 system (Zeiss, Oberkochen, Germany) applying a 63× 1.4 NA plan apochromat oil objective. Three color channels were acquired: Blue (405 nm excitation wavelength, Hoechst 33342 nucleus staining), green (488 nm excitation wavelength, CellTracker Green CMFDA dye), red (561 nm excitation wavelength, Rhodamine labeled particles). A stack of images was acquired with varying focus positions through the entire cell volume ($\Delta z = 0.5$ µm). Linear unmixing was carried out on the basis of emission spectra (Hoechst, Fluorescein, Rhodamine B) implemented in the system.

Subsequently to fluorescence microscopy, PBS was removed and a postfixation was carried out (glutaraldehyde 2% in PBS, OsO_4 1% in PBS), washed with water, followed by contrast enhancement (uranyl acetate 1% in milliQ water), dehydration, and embedding as previously described. Herein, a BEEM capsule filled with the embedding components was placed upside-down onto the afore fluorescently imaged area and hardened in a drying oven overnight at 70 °C.

After hardening, the glass bottom dish was removed manually. Residual glass adhering on the resin surface was burst by plunge-freezing the resin sample (heated up to 100 °C) into liquid nitrogen several times. The region of interest on the resin surface was trimmed with a razorblade to trapezoidal shaped cutting window (base area ≈0.5 × 0.5 mm^2). For ultrathin sectioning, the pretrimmed sample was adjusted in the ultramicrotome such, that the cutting window was oriented parallel to the diamond knife blade in order to yield slices of 80 nm thickness. The slices were placed on a finder grid (200 mesh, copper, Plano, Wetzlar), which were covered with formvar (Plano, Wetzlar) and carbon prior to usage. Prior to STEM imaging, poststaining with lead citrate was carried out.

The acquired images were correlated using ImageJ (bilinear TurboReg routine) and Inkscape.

Supporting Information

Supporting Information is available from the Wiley Online Library or from the author.

Acknowledgements

The authors thank Dr. Florian Kretschmer for competent discussions. Carolin Fritzsche and Dr. David Pretzel are acknowledged for performing cell toxicity tests. M.R. is grateful for the financial support within the frameworks of "Carl-Zeiss-Strukturmaßnahme" as well as the Proexzellenzinitiative "Nanopolar" of the state of Thuringia. The transmission electron microscope was obtained with a fund from the European Funds for Regional Developments (EFRE) and the Deutsche

Forschungsgemeinschaft (DFG). The confocal microscope LSM880 ELYRA PS.1 was funded with a grant from the German Research Council (DFG).

Conflict of Interest

The authors declare no conflict of interest.

Keywords

correlative light and electron microscopy, gold nanoparticles, poly(ethylene imine), scanning transmission electron microscopy, structured illumination microscopy, uptake studies

Received: May 24, 2017
Revised: June 20, 2017
Published online: July 26, 2017

[1] a) F. Masood, *Mater. Sci. Eng. C* **2016**, *60*, 569; b) T. Patel, J. Zhou, J. M. Piepmeier, W. M. Saltzman, *Adv. Drug Delivery Rev.* **2012**, *64*, 701; c) M. Elsabahy, K. L. Wooley, *Chem. Soc. Rev.* **2012**, *41*, 2545.

[2] N. Kamaly, B. Yameen, J. Wu, O. C. Farokhzad, *Chem. Rev.* **2016**, *116*, 2602.

[3] A. Vollrath, S. Schubert, U. S. Schubert, *J. Mater. Chem. B* **2013**, *1*, 1994.

[4] a) L. Schermelleh, R. Heintzmann, H. Leonhardt, *J. Cell Biol.* **2010**, *190*, 165; b) B. O. Leung, K. C. Chou, *Appl. Spectrosc.* **2011**, *65*, 967; c) T. Kohl, V. Westphal, S. W. Hell, S. E. Lehnart, *J. Mol. Cell. Cardiol.* **2013**, *58*, 13.

[5] a) A.-K. Barthel, M. Dass, M. Dröge, J.-M. Cramer, D. Baumann, M. Urban, K. Landfester, V. Mailänder, I. Lieberwirth, *Beilstein J. Nanotechnol.* **2014**, *5*, 1905; b) A. Höcherl, M. Dass, K. Landfester, V. Mailänder, A. Musyanovych, *Macromol. Biosci.* **2012**, *12*, 454; c) A. Musyanovych, J. Dausend, M. Dass, P. Walther, V. Mailänder, K. Landfester, *Acta Biomater.* **2011**, *7*, 4160; d) W. Sun, H. Wang, C. Xie, Y. Hu, X. Yang, H. Xu, *J. Controlled Release* **2006**, *115*, 259.

[6] a) M. A. Mintzer, E. E. Simanek, *Chem. Rev.* **2009**, *109*, 259; b) M. Jäger, S. Schubert, S. Ochrimenko, D. Fischer, U. S. Schubert, *Chem. Soc. Rev.* **2012**, *41*, 4755.

[7] W. T. Godbey, K. K. Wu, A. G. Mikos, *J. Controlled Release* **1999**, *60*, 149.

[8] a) S. M. Moghimi, P. Symonds, J. C. Murray, A. C. Hunter, G. Debska, A. Szewczyk, *Mol. Ther.* **2005**, *11*, 990; b) B. I. Florea, C. Meaney, H. E. Junginger, G. Borchard, *AAPS PharmSci* **2002**, *4*, E12; c) A. C. Hunter, *Adv. Drug Delivery Rev.* **2006**, *58*, 1523.

[9] D. Fischer, Y. Li, B. Ahlemeyer, J. Krieglstein, T. Kissel, *Biomaterials* **2003**, *24*, 1121.

[10] Y. Wen, S. Pan, X. Luo, X. Zhang, W. Zhang, M. Feng, *Bioconjugate Chem.* **2009**, *20*, 322.

[11] a) W. Y. Seow, K. Liang, M. Kurisawa, C. A. E. Hauser, *Biomacromolecules* **2013**, *14*, 2340; b) C. Englert, M. Hartlieb, P. Bellstedt, K. Kempe, C. Yang, S. K. Chu, X. Ke, J. M. Garcı a, R. J. Ono, M. Fevre, R. J. Wojtecki, U. S. Schubert, Y. Y. Yang, J. L. Hedrick, *Macromolecules* **2015**, *48*, 7420; c) H. Yamada, B. Loretz, C.-M. Lehr, *Biomacromolecules* **2014**, *15*, 1753.

[12] a) Z. Zhong, J. Feijen, M. C. Lok, W. E. Hennink, L. V. Christensen, J. W. Yockman, Y.-H. Kim, S. W. Kim, *Biomacromolecules* **2005**, *6*, 3440; b) D. G. Abebe, R. Kandil, T. Kraus, M. Elsayed, O. M. Merkel, T. Fujiwara, *Macromol. Biosci.* **2015**, *15*, 698; c) H. Petersen, P. M. Fechner, D. Fischer, T. Kissel, *Macromolecules* **2002**, *35*, 6867.

[13] a) M. Reifarth, D. Pretzel, S. Schubert, C. Weber, R. Heintzmann, S. Hoeppener, U. S. Schubert, *Chem. Commun.* **2016**, *52*, 4361; b) J. Panyam, S. K. Sahoo, S. Prabha, T. Bargar, V. Labhasetwar, *Int. J. Pharm.* **2003**, *262*, 1.

[14] a) S. Huth, J. Lausier, S. W. Gersting, C. Rudolph, C. Plank, U. Welsch, J. Rosenecker, *J. Gene Med.* **2004**, *6*, 923; b) M. Thomas, A. M. Klibanov, *Proc. Natl. Acad. Sci. USA* **2002**, *99*, 14640.

[15] a) V. Krieger, D. Liebl, Y. Zhang, R. Rajashekar, P. Chlanda, K. Giesker, D. Chikkaballi, M. Hensel, *PLoS Pathog.* **2014**, *10*, e1004374; b) L.-A. Ligeon, N. Barois, E. Werkmeister, A. Bongiovanni, F. Lafont, *Methods* **2015**, *75*, 61; c) D. M. van Elsland, E. Bos, W. de Boer, H. S. Overkleeft, A. J. Koster, S. I. van Kasteren, *Chem. Sci.* **2016**, *7*, 752.

[16] Y. S. Bykov, M. Cortese, J. A. G. Briggs, R. Bartenschlager, *FEBS Lett.* **2016**, *590*, 1877.

[17] a) P. de Boer, J. P. Hoogenboom, B. N. G. Giepmans, *Nat. Methods* **2015**, *12*, 503; b) J. T. Ngo, S. R. Adams, T. J. Deerinck, D. Boassa, F. Rodriguez-Rivera, S. F. Palida, C. R. Bertozzi, M. H. Ellisman, R. Y. Tsien, *Nat. Chem. Biol.* **2016**, *12*, 459; c) E. B. Bloss, M. S. Cembrowski, B. Karsh, J. Colonell, R. D. Fetter, N. Spruston, *Neuron* **2016**, *89*, 1016; d) C. L. Moore, D. Cheng, G. J. Shami, C. R. Murphy, *Micron* **2016**, *84*, 61; e) S. Vale-Costa, M. Alenquer, A. L. Sousa, B. Kellen, J. Ramalho, E. M. Tranfield, M. J. Amorim, *J. Cell Sci.* **2016**, *129*, 1697; f) M.-B. Fares, B. Maco, A. Oueslati, E. Rockenstein, N. Ninkina, V. L. Buchman, E. Masliah, H. A. Lashuel, *Proc. Natl. Acad. Sci. USA* **2016**, *113*, E912.

[18] F. Kretschmer, U. Mansfeld, S. Hoeppener, M. D. Hager, U. S. Schubert, *Chem. Commun.* **2014**, *50*, 88.

[19] K. Kettler, K. Veltman, D. van de Meent, A. van Wezel, A. J. Hendriks, *Environ. Toxicol. Chem.* **2014**, *33*, 481.

[20] a) M. Koivusalo, C. Welch, H. Hayashi, C. C. Scott, M. Kim, T. Alexander, N. Touret, K. M. Hahn, S. Grinstein, *J. Cell Biol.* **2010**, *188*, 547; b) M. A. West, M. S. Bretscher, C. Watts, *J. Cell Biol.* **1989**, *109*, 2731.

[21] H. H. Hanson, J. E. Reilly, R. Lee, W. G. Janssen, G. R. Phillips, *Microsc. Microanal.* **2010**, *16*, 747.

[22] K. Lee, S. Choi, C. Yang, H.-C. Wu, J. Yu, *Chem. Commun.* **2013**, *49*, 3028.

Particle
& Particle Systems Characterization

Supporting Information

for *Part. Part. Syst. Charact.,* DOI: 10.1002/ppsc.201700180

Metal–Polymer Hybrid Nanoparticles for Correlative High-Resolution Light and Electron Microscopy

Martin Reifarth, Elisabeth Preußger, Ulrich S. Schubert, Rainer Heintzmann,* and Stephanie Hoeppener**

Supporting Information

Metal-polymer Hybrid Nanoparticles for Correlative High-Resolution Light and Electron Microscopy

Martin Reifarth, Elisabeth Preußger, Ulrich S. Schubert, Rainer Heintzmann*, and Stephanie Hoeppener**

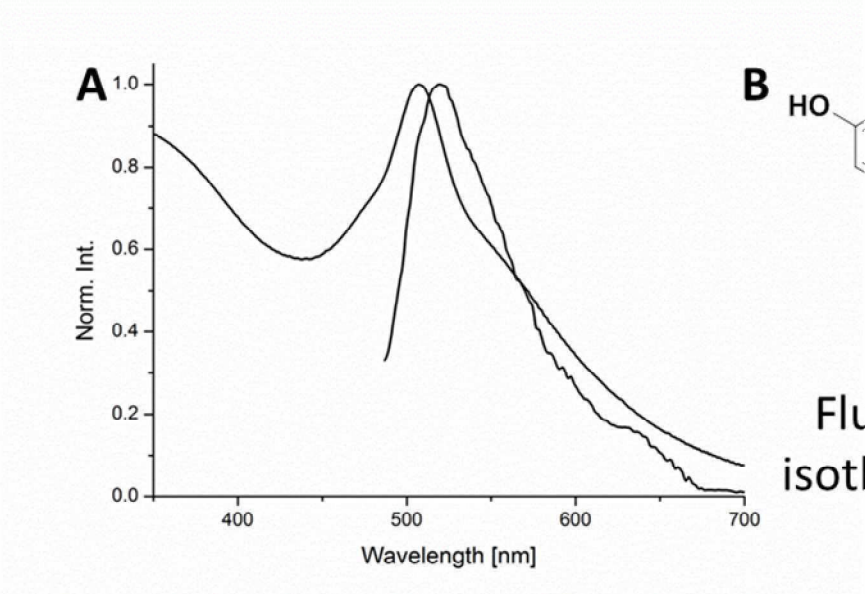

Figure S1: (A) Absorption and fluorescence spectrum of Fluorescein-labeled gold-PEI particles in DMF. (B) Schematic representation of the chemical structure of Fluorescein-isothiocyanate.

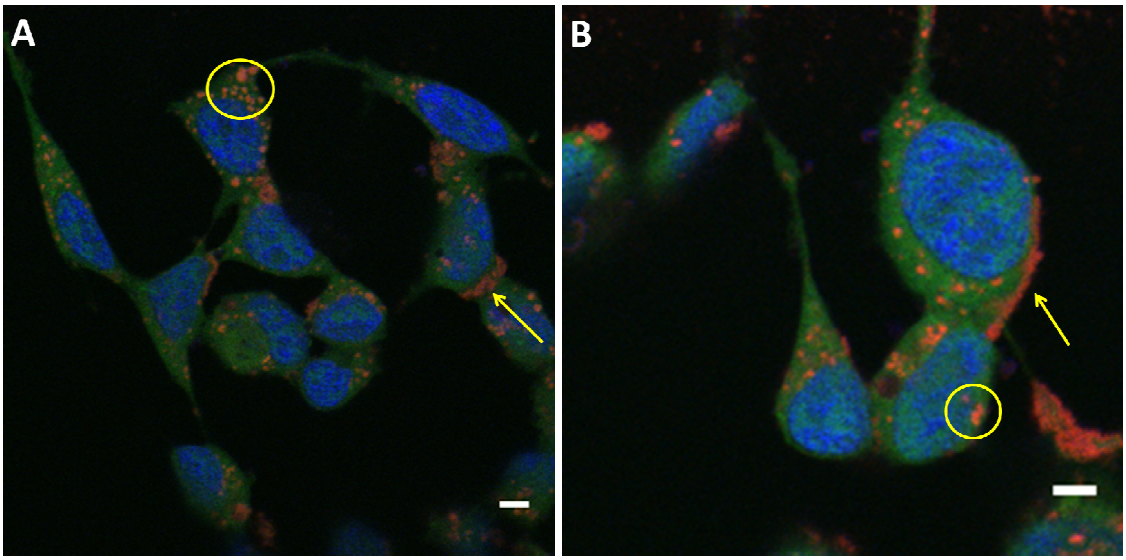

Figure S2: (A),(B): Confocal laser scanning microscopy images of HEK-293 cells incubated for 24 h with Rhodamine B-labeled particle sample (25 µg·mL^{-1}). 63× oil obj. 1.4 NA. Blue: Nucleus (Hoechst 33342). Green: Cytoplasm (CellTracker Green CMFDA). Red: Functionalized nanoparticles. Yellow arrows emphasize particles located at the cellular membrane. Lysosomal arrangements are highlighted by yellow circles. Scale bar: 5 µm.

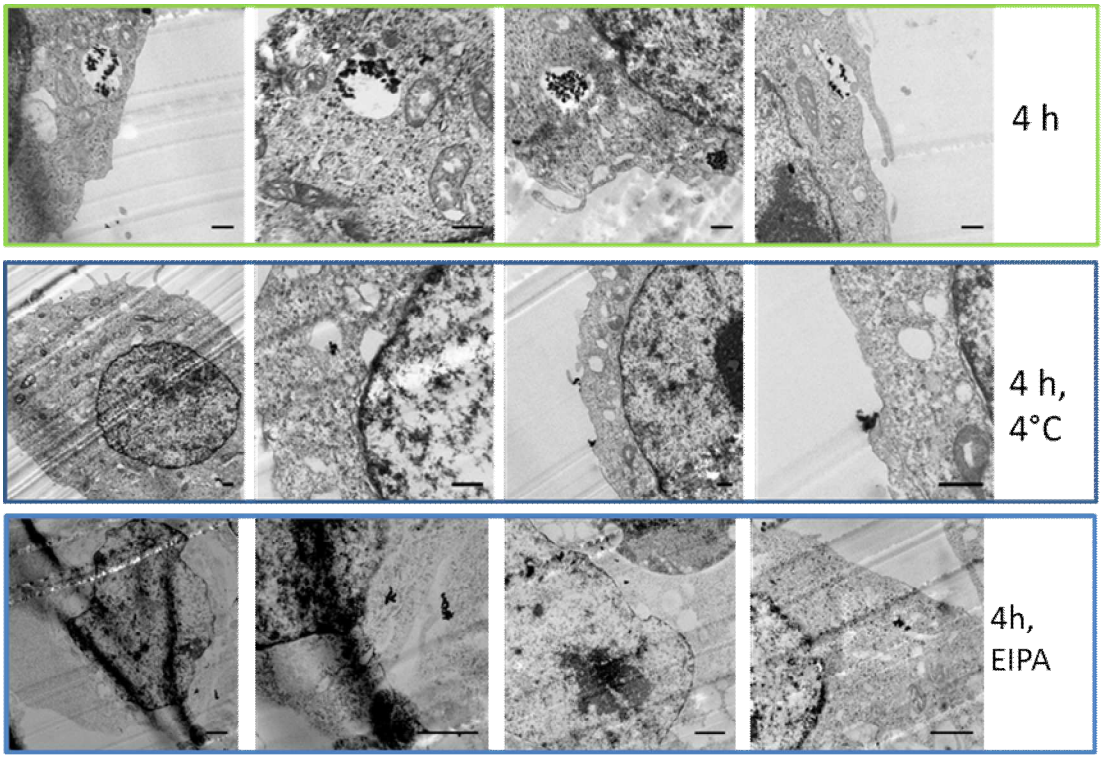

Figure S3: Upper row: STEM images of HEK-293 cells incubated with unlabeled Au-PEI particles for 4 h at 37 °C (25 µg·mL^{-1}). Middle row: HEK-293 cells exposed to particles with the same concentration for 4 h. Incubations were performed at a temperature of 4 °C. A substantially lower uptake can be observed at this temperature, which points towards an active uptake process. Lower row: Incubation in the presence of the macropinocytosis inhibitor 5-(*N*-ethyl-*N*-isopropyl)amiloride (EIPA). Since particles are still internalized into cells, also other active uptake processes may take place. All EM images are displayed with equalized histograms. Scale bars: 0.5 µm.

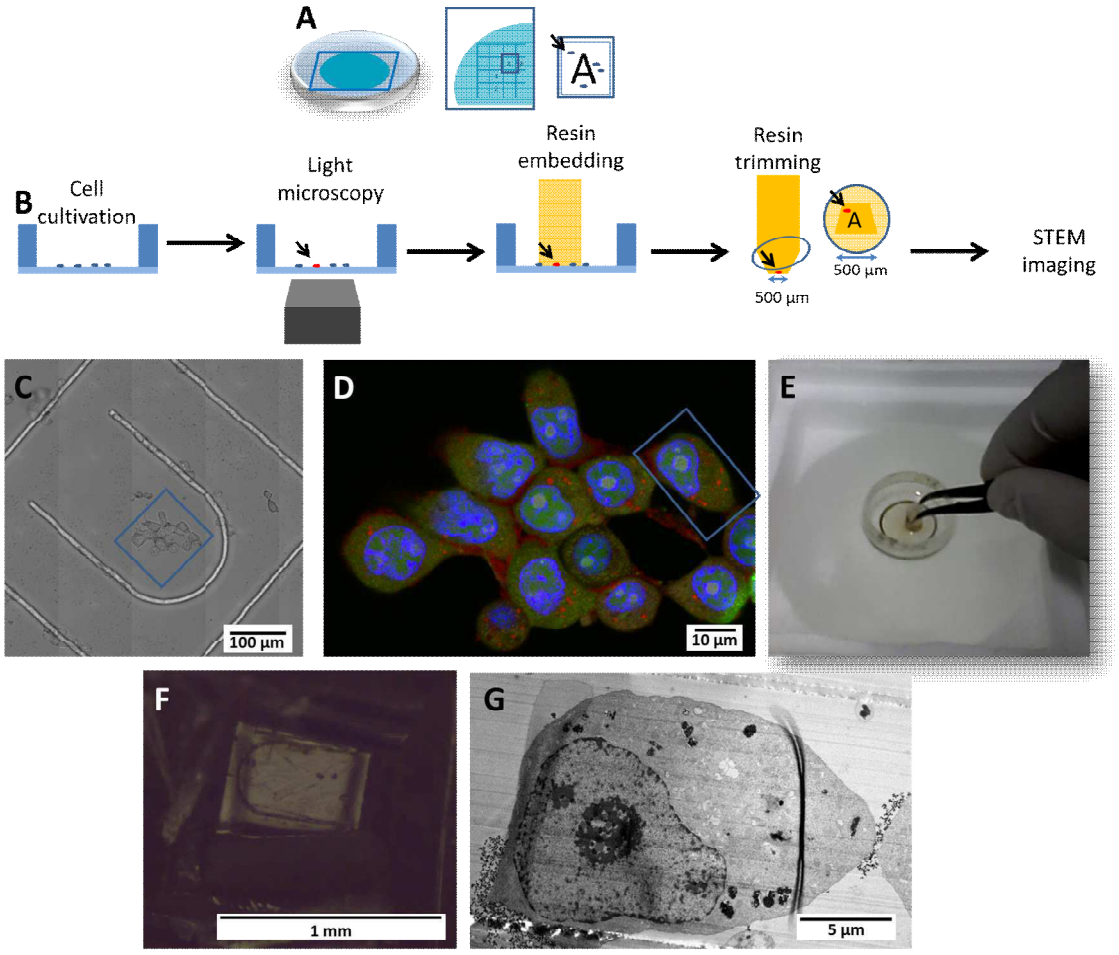

Figure S4 (A): Gridded glass-bottom dish and detailed views on graduated pattern used for correlative light and electron microscopy. (B): Schematic representation of the workflow for correlative microscopy. Cells are initially seeded onto the gridded glass-bottom dish. Subsequently, fluorescence imaging is carried out. A selected area of cells, as highlighted by an arrow, is imaged. Afterwards, TEM sample preparation including fixation, heavy metal staining, resin embedding is carried out. Subsequent to fluorescence imaging, the glass bottom is removed by plunging the sample into liquid nitrogen. Subsequently, resin slicing is carried out. In this connection, the area of interest is trimmed to such a size, that cell identification via electron microscopy can be carried out with a moderate effort. (C): Bright-field light microscopy image of interesting cell assembly. Blue box highlights cell assembly of interest. (D): CLSM image thereof. Cell further imaged by STEM is highlighted (blue box). (E): Glass-bottom dish equipped with resin-filled BEEM capsule plunged into liquid nitrogen in order to remove adherent glass residues. (F): Pre-trimmed cutting window of the sample. (G): STEM image of selected cell.